Peer-Reviewed Abstracts

of the

Tenth Conference on Electromagnetic & Light Scattering

Edited by

Gorden Videen

Army Research Laboratory
Adelphi, USA

Michael Mishchenko

NASA Goddard Institute for Space Studies
New York, USA

M. Pinar Mengüç

University of Kentucky
Lexington, USA

Nadia Zakharova

Sigma Space Partners
New York, USA

OBJECTIVE

The 10th Electromagnetic and Light Scattering Conference is held in Bodrum, a resort town on the Aegean Coast of Turkey. ELS-X is built on the success of previous meetings held in Amsterdam, Helsinki, New York, Vigo, Halifax, Gainesville, Bremen, Salobreña, and St. Petersburg, along with the various Bremen workshops. The main objective is to bring together scientists and engineers researching various aspects of light scattering and to provide a relaxed atmosphere for in-depth discussion of theory, measurements, and applications.

The 10th Electromagnetic and Light Scattering Conference is co-located with the 5th Symposium on Radiative Transfer, which follows meetings held in Kusadasi, in 1995, 1997, in Antalya in 2001, and in Istanbul in 2004.

CONVENERS

Michael Mishchenko, *NASA Goddard Institute for Space Studies, New York, USA*
Gorden Videen, *Army Research Laboratory, Adelphi, MD, USA*
M. Pinar Mengüç, *University of Kentucky, Lexington, KY, USA*

ORGANIZING COMMITEE

Jay Eversole, *Naval Research Laboratory, Washington, DC, USA*
Keith I. Hopcraft, *University of Nottingham, Nottingham, UK*
James Hough, *Astronomy Research Centre, University of Hertfordshire, UK*
Joop Hovenier, *Astronomical Institute "Anton Pannekoek", University of Amsterdam, The Netherlands*
Hal Maring, *NASA HQ, Washington, DC, USA*
Fernando Moreno, *Institute of Astrophysics of Andalucia, Spain*
Karri O. Muinonen, *University of Helsinki, Finland*
Yuri Shkuratov, *Kharkiv University, Kharkiv, Ukraine*
Nikolai Voshchinnikov, *Sobolev Astronomical Institute, St. Petersburg University, Russia*
Thomas Wriedt, *University of Bremen, Germany*

INVITED SPEAKERS

Ferdinando Borghese, *Universita di Messina, Messina, Italy*
Shane R. Cloude, *AEL Consultants, Fife, Scotland, UK*
Oleg Dubovik, *University of Lille, Lille, France*
Michael Kahnert, *Swedish Meteorological and Hydrological Institute, Norrkping, Sweden*
Nikolai Khlebtsov, *Saratov State University, Saratov, Russian Federation*
Daniel W. Mackowski, *Auburn University, Alabama, USA*
Michael Wolff, *Space Science Institute, Milwaukee, Wisconsin, USA*

CONFERENCE LOCALE

The conference will be held at Hapimag Sea Garden Hotel, a resort about 20 km outside Bodrum. Bodrum is a lovely town on the shores of the Aegean Sea. It spreads over the ancient Halicarnassus, where its mausoleum was one of the Seven Wonders of the World. The town and its surroundings are rich with history and natural beauty. The modern Bodrum is a busting town with many cafes, restaurants, bars and beaches. To many it is everything and anything they want it to be: historic, interesting, relaxing, or rich.

An imposing Crusader Castle, built by the knights of Rhodes, overlooks the harbor and the international marina. The nearby peninsula is rich in history and has many hidden beaches and traditional small villages. Bodrum houses the impressive Museum of Underwater Archeology.

ACKNOWLEDGMENTS

We wish to acknowledge Faruk Arinç and the International Centre for Heat and Mass Transfer (ICHMT) for the organizational support. Generous funding was provided by the NASA Radiation Sciences Program managed by Hal Maring and by the Office of Naval Research Global. Any opinions, findings and conclusions or recommendations expressed in this material are those of the authors and do not necessarily reflect the views of the Organizing Committee, ICHMT, NASA, or the Office of Naval Research Global.

NOTES:

Table of Contents

Microstructures located on flat substrates contaminated with small bosses: Backscattering and substrate effects

P. Albella, F. Moreno, J.M. Saiz, F. González

Grupo de Óptica. Departamento de Física Aplicada. Universidad de Cantabria
tel: +34 942201868, fax: +34 942201402, e-mail: albellap@unican.es

Abstract

The influence of the optical properties of the substrate in the backscattering of Micron-sized structures supporting sub-micron defects is analyzed by means of a parameter based on integrated backscattering calculations. This analysis is performed for two different configurations (defect on the microstructure or on the substrate), considering both dielectric and metallic substrates.

1 Introduction

During the last decades, researchers on light scattering by surfaces have focused on the electromagnetic problem of particles on substrates. Their results have generated non-invasive light scattering techniques for particle sizing with applications in different fields. In previous works[1-2], the authors have extensively studied light scattering by particles on substrates from both numerical and experimental points of view.
Among the types of far-field scattering measurements the backscattering detection has proved itself very sensitive to small variations in the geometry and/or optical properties of scattering systems with structures comparable to the incident wavelength[3-4].

In a recent work [1], we described how a small defect located on a micron-sized cylinder on a substrate changes the backscattered intensity. Also, we showed that an integration of the backscattered intensity over either the positive or negative quadrant (corresponding to the defect side or the opposite one, respectively) yields to a parameter, β_{br}, (see ref.[1]) sensitive not only to the existence of the defect but also to its size and location on the microstructure. These results were obtained for a homogeneous system, where substrate, cylinder and defect were supposed perfect conductors. Later on, another work was presented showing results for more realistic systems: dielectric or metallic defect on a metallic cylinder located on a metallic substrate[2] . Also, other geometries, where the small defect was in the substrate nearby the cylinder, were considered. Those works suggests the measurement of s_{br} as an experimental technique for monitoring, sizing and characterization of small defects adhered to microstructures. From a practical point of view, detection and sizing of very small defects on microstructures located over substrates by some reliable and non-invasive method could be useful in quality control technology and in nano-scale monitoring processes. In this context, the objective of this work is to study the sensitivity of this technique to the optical properties of the substrate in two configurations: A) defect on cylinder and B) defect on substrate nearby the cylinder. This abstract is organized as follows: Section 2 is devoted to describe the geometry and the numerical method proposed to solve the problem. Section 3 is devoted to show the main results and their corresponding discussion. Finally Section 4 summarizes the main conclusions of this research.

2 Scattering Geometry and Numerical Method

The scattering geometry is similar to that described in a previous work[1], i.e a cylindrical metallic microstructure of diameter $D=l$ located on a flat conducting substrate, and supporting a much smaller defect. Its shape will be assumed cylindrical with diameter $d=0.1l$. Two situations will be analyzed: Configuration A) The defect is located on the cylinder and its position is given by the angle j, which is considered always in the right side, $j>0$, with no loss of generality. Configuration B) The defect is located on the substrate nearby the cylinder. In principle, we want to show the differences, if any, appearing between these two configurations in order to extract the most important conclusions leading to a possible distinction between them. This could give more insight in the solution of the inverse problem.

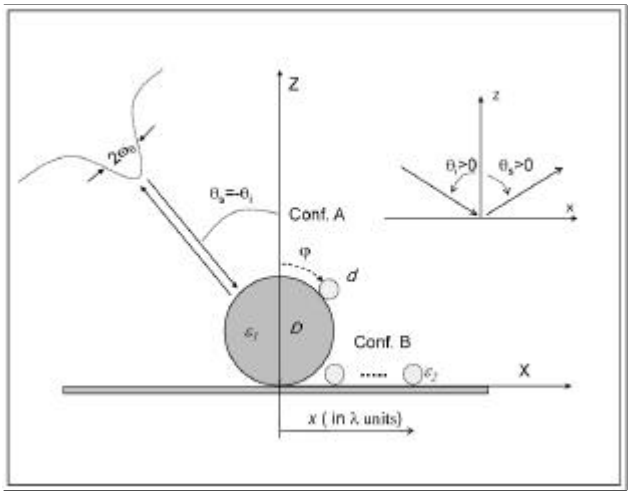

Figure 1: Scattering geometry.

The scattered field in each medium is obtained by numerically solving the Maxwell's integral equations using the Extinction Theorem formulation applied to the 2-D geometry for multiple connected domains[5].

3 Results

3.1 Configuration A

Figure 2 shows a comparison of s_{br} for different dielectric and metallic substrates, as a function of the angular position of the defect on the main cylinder. An interesting result that can be observed in Fig.2 is that $|s_{br}+|$ increases as we increase e, being maximum for the case of metals. An opposite behavior appears for $|s_{br}-|$.

It can also be seen that s_{br} is more sensitive to e , when $e\in[1.2,4]$ and it saturates for big values of e, tending to the metal case. Another difference in $s_{br}+$, is that the maxima and minima shift to the right as we increase e, tending to the metal case for big values of e. The main difference between dielectric and metallic substrate in this configuration is that for the dielectric case, sb- is not close to zero and therefore it is more difficult to predict the side of the cylinder where there is a defect.

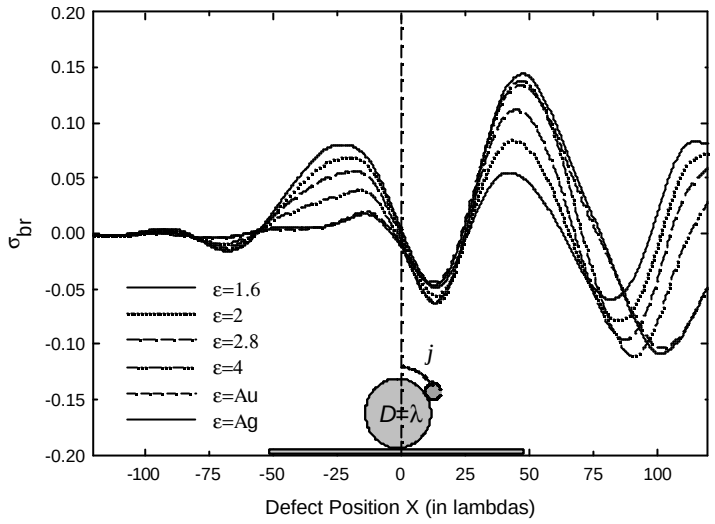

Figure 2: $s_{br}^{\pm}$ as a function of the defect angular position j for a silver cylinder of *D=?* with a silver defect of *d=0.1*λ and located on different types of substrate (*e*).

3.2 Configuration B

Figure 3. shows the evolution of s_{br} for different dielectric and metallic substrates, as a function of the position *x*, of the defect in the substrate. The shadowed area represents defect positions "under" the cylinder, not considered in the calculations. In this configuration, s_{br} is still more sensitive for dielectric substrates than metallic substrates. In fact, silver and gold substrates give almost the same values of s_{br}.

An interesting feature of s_{br} in this configuration is that, s_{br} is always positive for dielectric substrates whereas is always negative for metallic substrates. As it happened in configuration A, s_b- present bigger values for the case of dielectric substrate, but this time this is not critical, as s_b^- is always smaller than s_b^+.

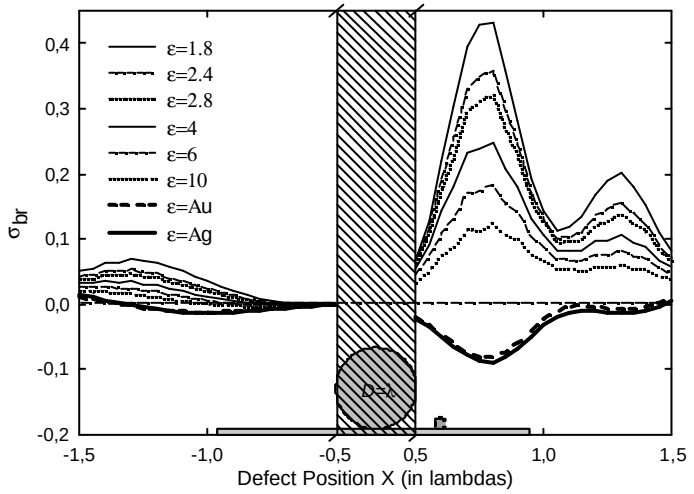

Figure 3: $s_{br}^{\pm}$ for a silver cylinder of *D=?* with a silver defect *d*=0.1λ and located on different types of substrate (*e*). Defect position *x* ranging from 0.5*? to* 1.5*?*

4 Conclusions

In this work, the influence of the optical properties of the substrate in the sensitivity of the parameter s_{br} has been analyzed for two different configurations: A) defect on cylinder and B) defect on substrate nearby the cylinder. In both cases, s_b- present bigger values for the case of dielectric substrate. s_{br} also present an opposite behavior in configurations A and B for different types of substrate. In configuration A, metallic substrates allow an easier detection and characterization of a defect. In configuration B, s_{br} is more sensitive if the substrate is dielectric, giving very high values of s_{br} (up to 0.6) for small values of e.

Finally, if we focus on the inverse problem, information about the optical properties of the substrate could be obtained in both configurations by studying the maximum value of $s_{br.}$

Acknowledgments

This research has been supported by the Ministry of Education of Spain under project #FIS2004-06785. P. Albella wants to express his gratitude to the Ministry of Education for his FPI grant.

References

[1] P.Albella, F.Moreno, J.M.Saiz and F.González, "Monitoring small defect on microstructures through backscattering measurements" Opt. Lett, **31**, 1744 (2006)

[2] P.Albella, F.Moreno, J.M.Saiz and F.González, "Backscattering of metallic microstructures with small defects located on flat substrates (Submitted to Opt. Express, 2007)

[3] J.M.Saiz, P.J.Valle,F.Gonzalez, F.Moreno and D.L.Jordan, "Backscattering from particulate surfaces: experiment and theoretical modeling" Opt.Eng **33(4)**, 1261 (1994)

[4] J.L. de la Peña, J.M. Saiz and F. González, "Profile of a fiber from backscattering measurements" Opt. Lett. **25**, 1699 (2000).

[5] M. Nieto-Vesperinas, Scattering and diffraction in physical optics (John Wiley and Sons,1991)

Effect of hemoglobin localization in erythrocytes on optical absorption by human blood

Vladimir V. Barun and Arkady P. Ivanov

B.I. Stepanov Institute of Physics, National Academy of Sciences of Belarus
68 Nezavisimosti Pr., Minsk 220072, Belarus
Tel: +375(17)284-0796, fax: +375(17)284-0879; e-mail barun@dragon.bas-net.by

Abstract

Hemoglobin localization in erythrocytes is shown to lead to a decrease of their apparent absorption coefficient in the blue spectral range. This effect is quantitatively evaluated by using analytical relations. The replacement of erythrocytes by equivalent spheres is considered to simplify the final calculation formulas. The spheres with the same volume as that of erythrocytes is shown can be used for single red blood cells or for their rouleau with small number of erythrocytes. For rather a long rouleau, the spheres with the same ratio of their volume to surface are applicable. The asymptotic behavior of the absorption decrease and its influence on absorption coefficient of skin dermis are studied.

1 Introduction

There are known and widely used a lot of procedures to study human blood by optical means. Among them are diffuse reflectance and transmittance spectroscopy [1], time- and frequency-domain investigations [1], optical measurements of blood samples in a cell [2], etc. The two first procedures are usually used under multiple light scattering by *in vivo* tissues. The latter one is applicable for both multiple and single scattering conditions. All the above procedures are highly affected by optical blood absorption coefficient that itself is often a subject of the studies to indicate various blood pathologies. The main absorbing components of blood are well known to be hemoglobins in different forms, the major of which are oxy- and deoxyhemoglobins. Their optical absorption is reliably referenced [2 – 4]. How does hemoglobin, which is localized in erythrocytes, affect the optical absorption coefficient of blood? At the first glance, one could average the hemoglobin absorption over a blood unit volume according to its volume fraction $f_{\mathrm{H}}H$ in blood, where f_{H} is the volume fraction of hemoglobin in an erythrocyte and H is the hematocrit (volume fraction of erythrocytes in blood). Let $f_{\mathrm{H}} = 0.25$ and $H = 0.4$ [1] below. However, such an averaging is not correct always. Really, let, for a moment, hemoglobin have infinitely large absorption. Then the averaged absorption coefficient will be infinitely large too. It is clear, however, that some light portion will pass through "holes" that do not contain any absorbing substance. So averaging weight $f_{\mathrm{H}}H$ is not applicable here. What will be the consequences of using another weight for calculating the absorption coefficient of a biological tissue as a whole? The paper will answer these questions.

The effect of light transmission through the above "holes" is sometimes called by the "sieve" effect [5]. We proposed earlier [6] an analytical procedure to treat the localized absorption of light by chaotically or regularly oriented cylindrical capillaries. Hemoglobin absorption was uniformly spread over blood volume there. On the other hand, the "sieve" effect of hemoglobin in erythrocytes was already evaluated [5] by replacing an erythrocyte with a spherical particle. It is shown that the hemoglobin localization leads effectively to some decrease in the volume fraction of the absorbing substance. The effect is physically understood, because internal portions of an erythrocyte, where light comes highly attenuated, participate in the absorption to a less degree that the periphery. The decrease has the clearest manifestation in the blue spectral range or in the Soret band, where blood absorbs light strongly. Meanwhile, an erythrocyte is a disk-shaped particle, not a spherical one as is validly mentioned in [5]. How one can replace an erythrocyte by an equivalent sphere? What will be its radius? How does erythrocyte aggregation in a rouleau affect the absorption? These topics are considered in the paper.

2 Calculation scheme

Let an erythrocyte be a disk with diameter D_e = 8.8 μm and thickness L = 2 μm [1, 7]. Although an erythrocyte is really a concavo-concave disk, we will approximate it by a cylinder with flat bases for the estimations below. Absorption coefficient $\mu_{a,e}$ of erythrocytes occupying volume fraction H is

$$\mu_{a,e} = C_e(\mu_H) H \mu_H = C_e(\mu_H) H f_H [S\mu_{HbO} + (1-S)\mu_{Hb}], \quad (1)$$

where C_e is the correction factor due to the hemoglobin localization; μ_H is the absorption coefficient of hemoglobins uniformly spread over an erythrocyte volume; S is the blood oxygenation degree (fraction of oxyhemoglobin with respect to total hemoglobin); μ_{HbO} and μ_{Hb} are the oxy- and deoxyhemoglobin absorption coefficients, respectively. Our aim is to find the correction factor for chaotically oriented erythrocytes. The following analytical relation [6] will be used for this purpose:

$$C_e(\mu_H) = \frac{0.25\pi L_{ag} + 0.5a_{ef} - \int_0^{\pi/2} \sin\vartheta d\vartheta \int_0^{L_{ag}\sin\vartheta + a_{ef}\cos\vartheta} \tau(x,\vartheta)dx}{0.25\mu_H L_{ag} \pi D_e}, \quad (2)$$

where $L_{ag} = NL$ is the length of an erythrocyte rouleau, N is the number of erythrocytes in the aggregate,

$$a_{ef} = (1/\mu_H)\ln[\int_0^1 \exp(-\mu_H D_e \sqrt{1-x^2})dx], \quad (3)$$

$\tau(x,\vartheta)$ is the transmission coefficient of erythrocytes with their generatrix (of length L_{ag}) set at angle ϑ to light propagation direction. While deriving Eq.(3), an erythrocyte disk or cylinder was replaced by a parallelepiped with the same generatrix L_{ag} and two bases with sides a_{ef} and D_e. Its light transmission is strictly the same as that of the cylinder [6]. The first two terms in the numerator and integration of Eq.(2) correspond to the averaged light transmission over all possible erythrocyte orientations. The integral over x of Eq.(2) can be calculated analytically [6]. We do not give its explicit, but cumbersome form here.

We will also consider the correction factor for equivalent spheres of two kinds. The first one is a sphere with the same volume as an erythrocyte. Its diameter is $D_s = [1.5(D_e)^2 L]^{1/3}$. Another sphere kind has the same ratio of its volume to its surface as that of an erythrocyte. In this case, the sphere diameter is $D_s = 1.5D_e$. The light transmission coefficient and the correction factor for a sphere are, respectively, $T_s(\mu_H) = [1-(1+D_s\mu_H)\exp(-D_s\mu_H)]/[0.5(D_s\mu_H)^2]$ and $C_s(\mu_H) = 1.5[1 - T_s(\mu_H)]/(D_s\mu_H)$.

3 Sample results

Figure 1 shows correction factors C_e (solid lines) or C_s (marks) as a function of optical diameter $\mu_H D_e$ of the erythrocyte base. Points on the abscissa axis indicate wavelengths, where the corresponding values of $\mu_H D_e$ occur. Different curves (1 to 4) give the C_e values for N = 1, 2, 8, and ∞, respectively. One can see that, due to the "sieve" effect, the decrease in the apparent absorption coefficient of erythrocytes can be up to about 3 times within the real range of $\mu_H D_e$ variations. The data of Fig.1 answer the question on possible approximation of erythrocyte aggregates by equivalent spherical particles. When number N of erythrocytes in a rouleau is small (N = 1 ÷ 4), the aggregate can be represented by a sphere with the same volume (■ and ▲). When N > 8 (+), one can use the spheres with the same ratio of their volume to surface for calculating the correction factor. The more erythrocytes are in an aggregate (rouleau), the more pronounced is the "sieve" effect.

As one can see from Fig.1, absorption coefficient $\mu_{a,e}$ depends on how many erythrocytes form an aggregate. This dependence is explicitly shown in Fig.2. The more erythrocytes are in a rouleau, the smaller the correction factor and, hence, the smaller the absorption coefficient. The problem on the influence of erythrocyte aggregation on blood optical characteristics has been studied in [7] too. However, wavelength λ = 632 nm selected for the investigations there shows no "sieve" effect (C_e = 1), as follows from Figs.1 and 2 (see also Fig.4 below). So the dependence of C_e on N was omitted in [7].

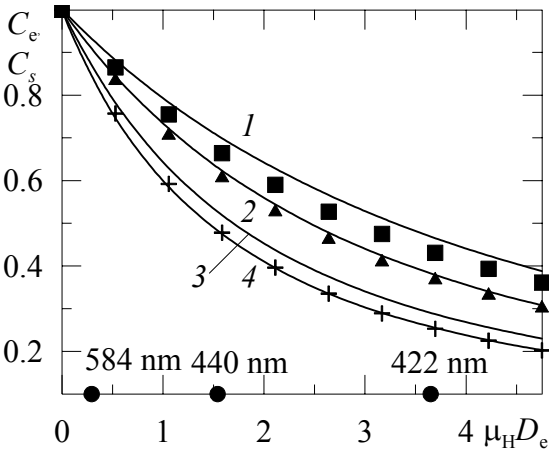

Figure 1: Correction factor as a function of $\mu_H D_e$ for single erythrocyte (curve 1), rouleau of two (2) and eight (3) erythrocytes, and for $L_{ag} = \infty$. Marks ■ ($N = 1$) and ▲ ($N = 2$) correspond to spheres of the same volume, **+'s** correspond to spheres with the same ratio of their volume to surface.

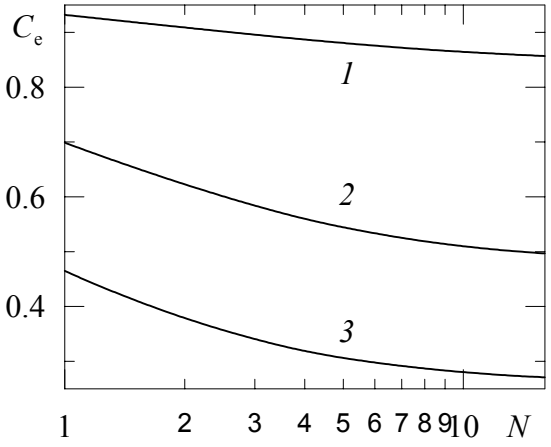

Figure 2: Correction factor as a function of erythrocyte number N in a rouleau for $\mu_H D_e = 0.29$ (curve 1), 1.5 (2), and 3.7 (3).

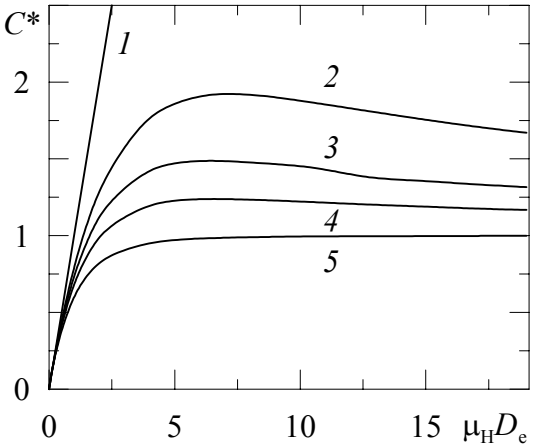

Figure 3: Normalized correction factor C^* as a function of $\mu_H D_e$ for uniform distribution of absorbing substance (curve 1), single erythrocyte (2), aggregates of two (3) and four (4) erythrocytes (4), and for $L_{ag} = \infty$ (5).

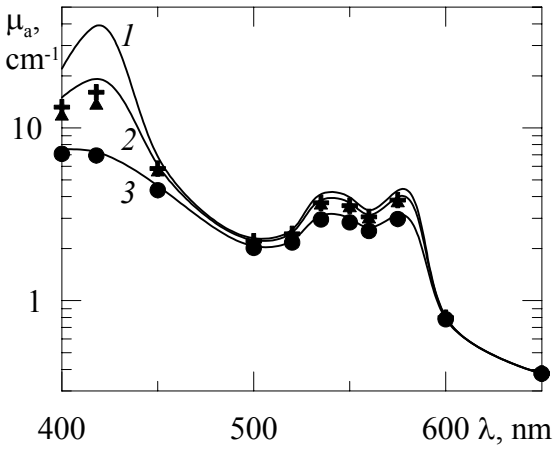

Figure 4: Absorption spectra of dermis without (curve 1) and with "sieve" effect by capillaries only (2 and 3, $D_c = 10$ and 40 μm, respectively). Marks show the effect of erythrocyte aggregates additional to that of capillaries for $N = 1$, $D_c = 10$ μm (+) and for $N = 8$, $D_c = 10$ (▲) and 40 μm (●).

It follows from Eqs.(2) and (3) that product $C_e \mu_H D_e \to 1$ as $\mu_H D_e$ or simply μ_H (D_e is fixed) $\to \infty$. Although the optical diameter of an erythrocyte cannot be infinitely large in the optical wavelength range, it is interesting to study the asymptotic behavior of the correction factor. Fig.3 shows the dependence of normalized correction factor $C^* = C_e \mu_H D_e$ on $\mu_H D_e$ for a single erythrocyte and its aggregation. Note first that for usual uniform distribution of hemoglobins over blood volume one has the linear dependence (curve 1). This corresponds to the weakly absorbing substance for $\lambda > 600$ nm. With increasing optical erythrocyte diameter, one observes deviations from the linearity that leads to the decrease in the blood absorption coefficient as compared to the homogeneous distribution of hemoglobins over blood volume. It is worthwhile to note the non-monotonic behavior (with a maximum) of the curves for single erythrocytes (curve 2) or for rouleaux with small number N (curves 3 and 4). The more number of erythrocytes in a rouleau, the less pronounced is the maximum. It disappears for large enough N (curve 5).

The maximum can be explained by follows. As μ_H increases, a_{ef} and $t(x,J)$ are obviously to decrease. So the competition between these two terms entering Eq.(2) with opposite signs provides the maximum.

How does the hemoglobin localization in erythrocytes affect the optical absorption of biotissue? The absorption spectra of dermis containing blood vessels are illustrated in Fig.4 without and with accounting for the "sieve" effect by both the capillaries and erythrocytes. Eqs.(2) and (3) with $L_{ag} = \infty$ and D_e replaced with vessel diameter D_c were used for the calculations of the correction factor for capillaries. The absorption coefficient of dermis is

$$m_a = C_c(m_{a,e})f_c m_{a,e} + (1 - f_c)m_{a,t}, \quad (4)$$

where $f_c = 0.02$ is the volume fraction of blood vessels in dermis and $\mu_{a,t}$ is the absorption coefficient of bloodless tissue. One can see from Fig.4 that the "sieve" effect of the vessels only gives rise to a considerable decrease in μ_a of the blue spectral range (up to 5 times). As for erythrocytes too, the larger the optical diameter $\mu_{a,e}D_c$ of a vessel, the more pronounced the effect is. Additional accounting for the hemoglobin localization in erythrocytes leads to a further decrease in the absorption coefficient in the blue for small capillary diameter (D_c = 10 μm, + and ▲) and is practically inessential for large vessels (D_c = 40 μm, ●). Such a behavior is physically transparent. Really, the "sieve" effect by erythrocytes decreases absorption coefficient $\mu_{a,e}$ of blood inside a vessel. In its own turn, this makes the "sieve" effect by capillaries less significant. In other words, the two effects somewhat compensate each other for large vessels. The compensation for small capillaries occurs to a less degree.

4 Conclusion

The decrease in absorption coefficient $\mu_{a,e}$ illustrated in Figs.1 and 2 can be observed for a suspension of intact erythrocytes in a cell. This effect opens a new opportunity to essentially detect the erythrocyte aggregation degree in a blood sample by optical means. For example, comparing the transmittance values of the erythrocyte suspension and of the solution with the same quantity of broken erythrocytes at several wavelengths in the blue can directly give the correction factor. The latter is analytically related with the aggregation degree and other unknown parameters of erythrocytes. The solution to a set of equations for used wavelengths can, in principle, simplify the unknown characteristics. As to the determination of erythrocyte parameters *in vivo*, this topic requires additional investigations. In any case, the screening of the "sieve" effect in skin by melanin, which strongly absorbs blue light too, should be taken into consideration. The screening can hide the hemoglobin localization effect.

References

[1] *Handbook of optical biomedical diagnostics*, Ed. V. V. Tuchin (SPIE, USA, 2002).

[2] G. S. Dubova, A. Ya. Khairullina, and S. F. Shumilina, "Determination of hemoglobin absorption spectra by light-scattering methods", J. Appl. Spectroscopy **27**, 871 – 878 (1977).

[3] A. Isimaru, *Waves propagation and scattering in randomly nonisotropic media* (Academic Press, New York, 1978).

[4] S. A. Prahl, http://omlc.ogi.edu/spectra/hemoglobin/index.html.

[5] J. S. Finlay and T. H. Foster, "Effect of pigment packaging on diffuse reflectance spectroscopy of samples containing red blood cells", Opt. Lett. **29**, 965 – 967 (2004).

[6] V. V. Barun and A. P. Ivanov, "Estimate of the contribution of localized blood absorption by blood vessels to the optical properties of biological tissue", Opt. Spectroscopy **96**, 1019 – 1024 (2004).

[7] E. K. Naumenko, "Effect of erythrocyte aggregation on the blood scattering characteristics", J. Appl. Spectroscopy **70**, 375 – 380 (2003).

Extinction and the Electromagnetic Optical Theorem

Matthew J.Berg, Christopher M. Sorensen, and Amit Chakrabarti

Kansas State University, Department of Physics, Manhattan, KS 66502-2601, USA
tel: +1 785-317-3378, e-mail: mberg@phys.ksu.edu

Abstract

The energy flow caused by single particles is examined to form a physically based understanding for extinction and the electromagnetic optical theorem. The behavior of the energy flow is explained in terms of wave interference. The optical theorem is shown to be a relationship based on the relative phase between the wave incident on a particle and the wave scattered by it. The relative phase is determined by the refractive and absorptive properties of the particle and reveals how extinction depends on both scattering and absorption.

1 Introduction

The optical theorem has a long history; its occurrence in electromagnetic theory begins more than one hundred years ago and analogs of the theorem are found in quantum mechanical and acoustical scattering [1]. Over the years, many derivations and implementations of the theorem have been given [2]-[5]. However, we have found no previous work that provides an explicit interpretation of the theorem in a physical (not mathematical) context. This work examines the optical theorem in detail and achieves a physical understanding of its meaning based on simulations of the energy flow caused by specific single particles.

2 The Optical Theorem

Consider a single particle that is illuminated by a plane wave polarized along the x-axis and traveling in the $\hat{\mathbf{n}}^{inc}$ direction, see Fig. (1) and Eq. (2) below. By expanding this wave into counter-propagating spherical waves using Jones' lemma, one can obtain an expression for the extinction cross section C^{ext} of the particle as

$$C^{ext} = \frac{4\pi}{k\mathcal{E}_o^{inc}} \operatorname{Im}\{\hat{\mathbf{x}} \cdot \mathbf{E}_1^{sca}(\hat{\mathbf{n}}^{inc})\} . \tag{1}$$

This is the *electromagnetic optical theorem* [5].

To the unfamiliar investigator, Eq. (1) can appear mysterious. The optical theorem relates C^{ext} to the imaginary part of the scattering amplitude $\mathbf{E}_1^{sca}$ evaluated in only the forward direction $\hat{\mathbf{n}}^{inc}$. However, extinction is due to scattering and absorption [3]. Scattering involves all directions whereas absorption is often independent of direction, so why should the optical theorem depend on only the forward direction, and how is absorption involved?

3 Theoretical Considerations

Suppose that the particle is located at the origin of the Cartesian coordinate system and surrounded by vacuum, see Fig. (1). The particle is described by a complex-valued refractive index m. Let $\mathcal{S}$ and V denote the surface and interior volume of the particle, respectively. The fields of the incident plane wave are

$$\mathbf{E}^{inc}(\mathbf{r}) = \mathcal{E}_o^{inc} \exp(ikr\hat{\mathbf{r}} \cdot \hat{\mathbf{n}}^{inc})\, \hat{\mathbf{x}} , \qquad \mathbf{B}^{inc}(\mathbf{r}) = \frac{k}{\omega} \hat{\mathbf{n}}^{inc} \times \mathbf{E}^{inc}(\mathbf{r}) . \tag{2}$$

The wave number of the incident wave is $k = 2\pi/\lambda$ where λ is the wavelength. A harmonic time dependence given by $\exp(-i\omega t)$, where ω is the angular frequency, is assumed for all field quantities. Surrounding the particle is a spherical surface $\mathcal{S}_l$ of radius R_l that is large enough that points on its surface are in the far-field of the particle. The intersection of $\mathcal{S}_l$ with the y-z plane forms the C_l contour, see Fig. (1). The wave scattered by the particle can be found by solving Maxwell's equations using the volume integral relation [5]. In the far-field of the particle, the scattered wave takes the form of an outward traveling spherical wave with an angular profile given by the scattering amplitude $\mathbf{E}_1^{sca}$.

The Poynting vector $\mathbf{S}$ describes the energy flow in an electromagnetic wave [6]. Because both the incident and scattered waves exist at the observation point $\mathbf{r}$, $\mathbf{S}$ factors into three distinct terms. One of these terms, the cross term $\mathbf{S}^{cross}$, involves the fields of *both* the incident and scattered waves whereas the other terms involve the fields of only *either* the incident or scattered waves. The integral of the flow of the time-averaged cross term $\langle \mathbf{S}^{cross} \rangle_t$ through $\mathcal{S}_l$ gives the extinction cross section C^{ext}, and, it is this integral that forms a starting point for the derivation of the optical theorem, Eq. (1) [5].

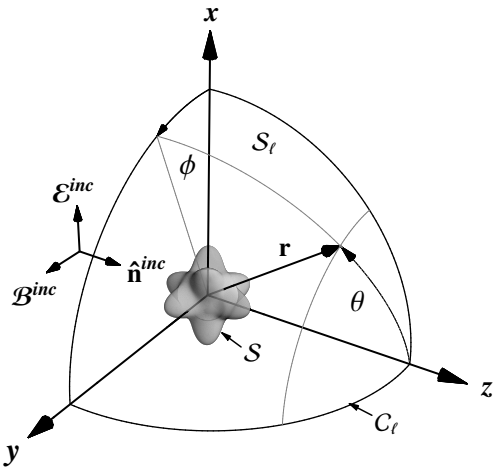

Figure 1: A scattering arrangement with a star-shaped particle at the origin. The incident wave is shown with the direction of its electric $\mathcal{E}^{inc}$ and magnetic $\mathcal{B}^{inc}$ fields pointing along the x and y-axes respectively and its propagation direction along $\hat{\mathbf{n}}^{inc}$. The observation point $\mathbf{r}$ is shown along with the surface $\mathcal{S}_l$ of radius R_l and the intersection of $\mathcal{S}_l$ with the y-z plane that forms the circular contour, C_l.

4 A Physical Picture of the Optical Theorem

Figure (2) reveals a major qualitative aspect of the behavior of the radial component of the $\langle \mathbf{S}^{cross} \rangle_t$ energy flow; the flow alternates from being inward to outward and does so more rapidly with direction as R_l increases. To see how integration of the $\langle \mathbf{S}^{cross} \rangle_t$ energy flow through $\mathcal{S}_l$ yields the extinction cross section, the integral $I^{cross}(\theta_s) = \int_{\partial \mathcal{S}_l} \langle \mathbf{S}^{cross} \rangle_t \cdot \hat{\mathbf{r}} \, da$ is also shown in Fig. (2). This integral is taken over the open surface $\partial \mathcal{S}_l$ which is formed by the part of $\mathcal{S}_l$ extending from $\theta = \pi$ to $\theta = \theta_s$. Because of energy conservation considerations, there is a negative sign in the relation $I^{cross}(\theta_s = 0) = -C^{ext} I^{inc}$, (where I^{inc} is the flux of the incident wave), which is why the curves in Fig. (2) for I^{ext} stop at the negative of $C^{ext} I^{inc}$ when $\theta_s = 0$.

By expressing the scattered wave as a spherical wave with an amplitude and phase shift given by the scattering amplitude $\mathbf{E}_1^{sca}$, we demonstrate that the optical theorem can be understood in a more 'physical' setting than is done in existing literature. The 'physical' understanding relies on the interpretation of extinction as being caused by the interference of the incident wave with the scattered wave. This interference causes the alternating energy flow shown in Fig. (2) and ultimately accounts for the value of C^{ext} via a phase shift relationship between the two waves. This phase depends, in part, on the wave inside of the particle. As the refractive ($\mathrm{Re}\, m$), or the absorptive ($\mathrm{Im}\, m$) properties of the particle vary, the internal wave changes which effects the phase of the scattered wave and hence forms the connection between extinction and the optical properties of the particle. In addition, the energy-flow interpretation of the optical theorem naturally

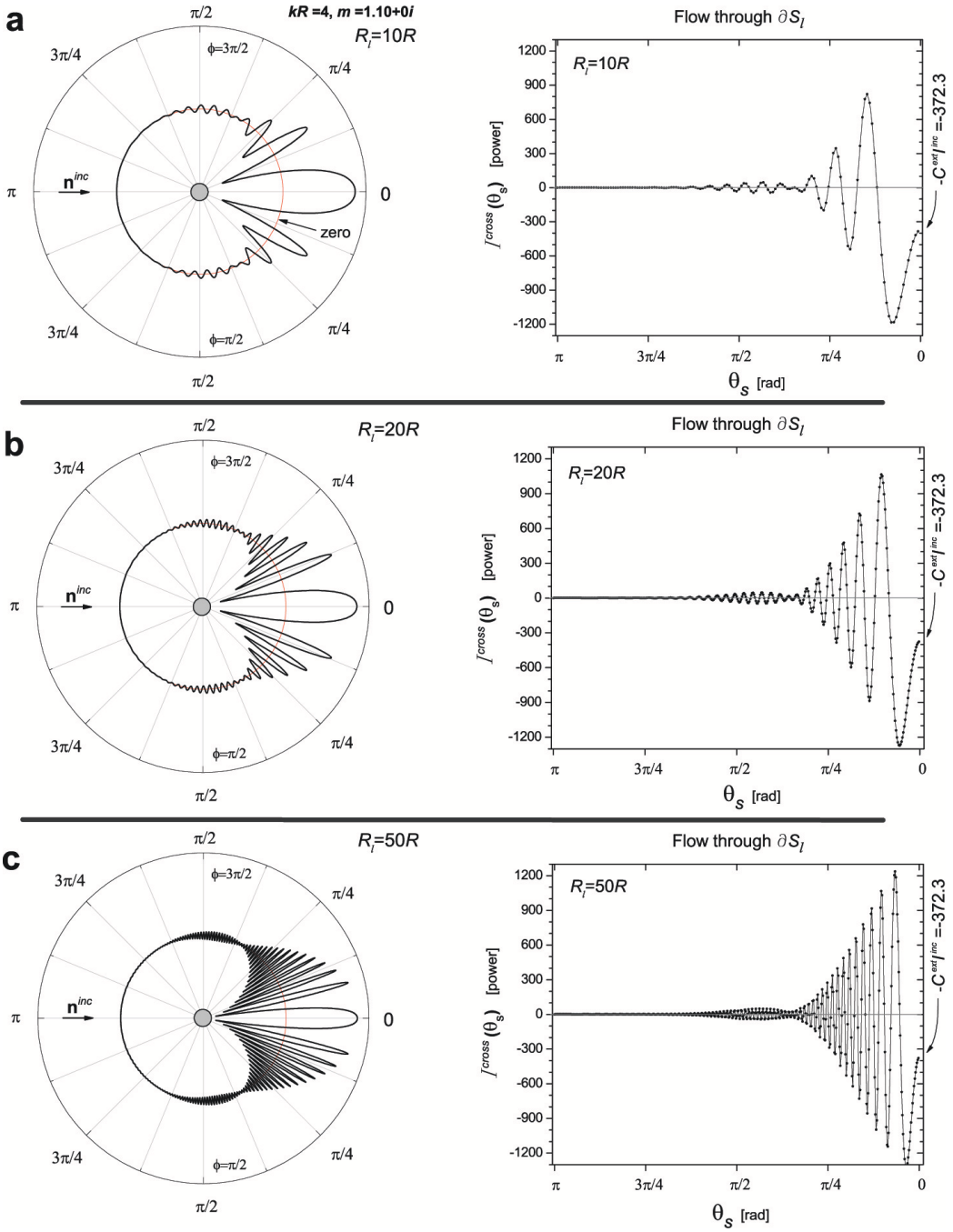

Figure 2: **Left column:** Polar plots of the radial component of the $\langle \mathbf{S}^{cross} \rangle_t$ energy flow through the C_l contour shown in Fig. (1). The particle is a sphere with a size parameter $kR = 4.08$ and refractive index $m = 1.10 + 0i$ and the scattered wave is calculated from Mie theory. The three polar plots labeled **a**, **b** and **c** show the energy flow for increasing contour radii $R_l = 10R$, $R_l = 20R$ and $R_l = 50R$, respectively. **Right column:** Plots of the integral I^{cross} for the contour radii corresponding to the matching polar plots in the left-hand column. The value of C^{ext} as calculated directly from Mie theory is indicated in the plots.

leads one to an understanding of the requirement regarding the size of a detector that is used to measure extinction, as discussed in Ref. [5].

Acknowledgments

This work was supported by the NASA GSRP.

References

[1] Newton, R. G., 'Optical Theorem and Beyond,' Am. J. Phys. **44** (7), 639-642 (1976).

[2] van de Hulst, H. C., *Light Scattering by Small Particles*, (Dover, New York, 1981).

[3] Bohren, C. F., and Huffman, D. R., *Absorption and Scattering of Light by Small Particles* (Wiley, New York, 1983).

[4] Jackson, J. D., *Classical Electrodynamics* (Wiley, New York, 1999).

[5] Mishchenko, M. I., Travis, L. D. and Lacis A. A., *Scattering, Absorption, and Emission of Light by Small Particles* (Cambridge University Press, Cambridge, 2002).

[6] Rothwell, E. J. and Cloud, M. J., *Electromagnetics* (CRC Press, New York, 2001).

Optical trapping of nonspherical particles in the T-matrix formalism

Ferdinando Borghese,[1] Paolo Denti,[1] Rosalba Saija,[1] Maria Antonia Iatì,[1]
Onofrio Maragò[2]

[1] *Università di Messina, Dipartimento di Fisica della Materia e Tecnologie Fisiche Avanzate*
Salita Sperone 31, 98166 Messina, Italy
tel: +39-090-6765396, fax: +39-090-391382, e-mail: borghese@ortica.unime.it
[2] *Istituto per i Processi Chimico-Fisici del CNR, Via La Farina 237, 98122 Messina,Italy*
e-mail: marago@its.me.cnr.it

Abstract

We discuss the optical trapping of nonspherical particles in the transition matrix formalism. We also present some results of the application of the theory to trapping and manipulation of carbon nanotubes.

1 Introduction

The pioneering work of Ashkin et al. [1] has proved the practical feasibility of the trapping of small particles by highly focused laser beams. Actually, the configuration of the field focused by a high numerical aperture lens may be such that the resulting radiation force traps the particles within the focal region. The configuration of the field focused by an aplanatic lens has been described by Richards and Wolf [2] in terms of the rays that actually traverse the exit pupil. Although the Maxwell stress tensor enters the general expression of the radiation force [3], the literature reports several procedures to avoid using it when dealing with the optical trapping [4, 5].

In a recent paper the calculation of the trapping force on dielectric ellipsoids has been formulated in terms of the transition matrix approach [6] on the assumption that the incident field is a gaussian beam.

In this paper we reformulate the theory of optical trapping of nonspherical particles making full use of the Maxwell stress tensor and resorting to the transition matrix approach [7] in such a way that the final formulas are easily applicable to trapping of clusters of spherical scatterers. Actually, the radiation force that the field exerts on a particle is calculated by expanding the field in a series of spherical multipole fields and the field scattered by the particle is calculated through the transition matrix approach, which, in principle, does not require the particle to be spherical or small. Our aim is to apply the theory so formulated to the study of nanowires of silicon and nanotubes of carbon [8, 9] which present unique difficulties of trapping and manipulation.

2 Theory

The coordinate system that we adopt in our calculations is depicted in Fig. 1. The origin coincides with the focus of the lens whose optical axis coincides with the z axis. The particle under study lies at $\mathbf{R}_{O'}$ and the force exerted by the radiation is given by the equation

$$\mathbf{F}_{\mathrm{Rad}} = r'^2 \int_{\Omega'} \hat{\mathbf{r}}' \cdot \langle \mathsf{T}_{\mathrm{M}} \rangle \, \mathrm{d}\Omega' \,, \tag{1}$$

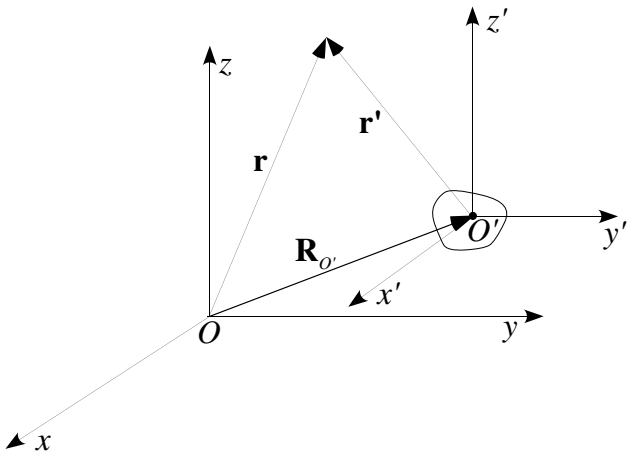

Figure 1: Coordinates

where the integration is over the full solid angle, r' is the radius of a large sphere S' with center O' at $\mathbf{R}_{O'}$ surrounding the particle, and $\langle \mathsf{T}_{\mathrm{M}} \rangle$ is the time averaged Maxwell stress tensor

$$\langle \mathsf{T}_{\mathrm{M}} \rangle = \frac{1}{8\pi} \mathrm{Re}\left[n^2 \mathbf{E}' \otimes \mathbf{E}'^{*} + \mathbf{B}' \otimes \mathbf{B}'^{*} - \frac{1}{2}(n^2 |\mathbf{E}'|^2 + |\mathbf{B}'|^2) \mathsf{I} \right] . \tag{2}$$

In Eq. (2), $\otimes$ denotes dyadic product, the asterisk indicates complex conjugation, the prime indicates that the fields are functions of $\mathbf{r}'$, and I is the unit dyadic. Of course, the fields that enter the definition of $\langle \mathsf{T}_{\mathrm{M}} \rangle$ are the superposition of the incident and of the scattered field. In our calculations we assumed that the incident field is a superposition of plane waves of the kind described by Richards and Wolf [2] and the scattered wave is calculated through the transition matrix of the particle. In this respect we stress that, in the calculation of the radiation force found convenient not to start from the formula obtained by Mishchenko [10] through the use of the optical theorem. We found more convenient to perform the integration in Eq. (1) using the asymptotic expansion of the multipole fields [11] up to terms of order $1/r$. In fact, higher order terms are easily seen to give a vanishing contribution to the radiation force. We cannot report here the mathematical details but a few points deserve a comment.

First we proved rigorously that the dyadic products $n^2 \mathbf{E}' \otimes \mathbf{E}'^{*} + \mathbf{B}' \otimes \mathbf{B}'^{*}$ in Eq. (2) give no contribution to the radiation force not only when the incident field is a plane wave but also when it is the superposition of the plane waves, with different direction of propagation, that traverse the exit pupil of the lens.

Second, we were also able to demonstrate that, for the same superposition of plane waves, no contribution to the radiation force comes from the dot products $\mathbf{E}'_{\mathrm{I}} \cdot \mathbf{E}'^{*}_{\mathrm{I}}$ and $\mathbf{B}'_{\mathrm{I}} \cdot \mathbf{B}'^{*}_{\mathrm{I}}$.

Third, we used the fact that the incident field in the focal region can formally be written as a single plane wave whose amplitudes depend on the position of the particle. This allows us to calculate the scattered field through the usual transition matrix.

At present the work sketched here is still in progress and is carried on in collaboration with the experimental group at the Istituto per i Processi Chimico-Fisici of the CNR in Messina (Italy) and the group A. Ferrari at the University of Cambridge (UK).

References

[1] A. Ashkin, J. M. Dziedzic, J. E. Bjorkholm and S. Chu, " Optics Lett. **11**, 288–290 (1986).

[2] B. Richards and E. Wolf, "Electromagnetic diffraction in optical systems. II. Structure of the image field in an aplanatic system," Proc. Roy. Soc. (London) **253**, 358–379 (1959).

[3] J. D. Jackson, *Classical electrodynamics*, 2nd edition (Wiley, New York, 1975).

[4] A. Rohrbach and E. H. K. Stelzer, "Optical trapping of dielectric particles in arbitrary fields," J. Opt. Soc. Am. A **18**, 839–853 (2001).

[5] A. R. Zakharian, P. Polynkin, M. Mansuripur and J. V. Moloney, "Single-beam trapping of micro-beads in polarized light: Numerical simulations," Optics Express **14**, 3660–3676 (2006).

[6] S. H. Simpson and S. Hanna, "Optical trapping of spheroidal particles in gaussian beams," J. Opt. Soc. Am. A **24**, 430–442 (2007).

[7] P. C. Waterman, "Symmetry, unitarity and geometry in electromagnetic scattering," Phys. Rev. D **4**, 825–839 (1971).

[8] R. Gauthier, M. Ashman and P. Grover, "Experimental confirmation of optical-trapping properties of cylindrical objects," Appl. Opt. **38**, 4861–4869 (1999).

[9] P. J. Pauzauskie, A. Radenovic, E. Trepagnier, H. Schroff, P. Yang, and J. Lipphardt, "Optical trapping and integration of semiconductor nanowires assemblies in water," Nature Materials **5**, 97–101 (2006).

[10] M. I. Mishchenko, "Radiation force caused by scattering, absorption and emission of light by nonspherical particles," J. Quant. Spectros. Radiat. Transfer **70**, 811–816 (2001).

[11] F. Borghese, P. Denti and R. Saija, *Scattering from model nonspherical particles*, 2nd edition (Springer, Berlin, 2007).

Phase matrix for horizontally oriented ice crystals of cirrus clouds

Anatoli Borovoi,[1] Aleksey Burnashov,[1] Ariel Cohen [2]

[1] *Institute of Atmospheric Optics, Rus. Acad. Sci., pr. Akademicheski 1, 634055 Tomsk, Russia*
[2] *Hebrew University of Jerusalem, Safra Campus 1, 91904 Jerusalem, Israel*
tel: +7 (3822)492864, fax: +7 (3822) 492086, e-mail: borovoi@iao.ru

Abstract

The phase matrices for horizontally oriented ice plates of cirrus clouds are calculated within the framework of geometric optics. A method for retrieving aspect ratios of the plates by means of polarization measurements is discussed.

1 Introduction

The problem of light scattering by ice crystals of cirrus clouds is one of the current problems of the atmospheric optics. Optical properties of cirrus clouds are needed for incorporation in numerical models of radiative budget of the Earth and, consequently, in numerical models of weather forecasting and climate change. These optical properties have been calculating for last 20-30 years within the framework of geometric optics where the ice crystals were mainly assumed to be 3D randomly oriented (e.g. [1,2]). However, the ice crystals often reveal the tendency to be horizontally oriented because of aerodynamics laws. In particular, the horizontal orientation is manifested through numerous halo phenomena that are watched and classified for centuries [3]. As for quantitative data on the light scattering by preferably oriented ice crystals, they are rather poor [4-6]. The available data are represented as a number of figures that can be hardly used by other authors for some calculations. Moreover, a set of input parameters in these data is so small that they can be considered as preliminary or illustrative ones.

In this contribution, we focus on both the quantitative data and their physical interpretation. For brevity, this consideration is restricted by the most conventional and simple case of hexagonal ice plates that are horizontally oriented.

2 Reduced phase matrices

The conventional phase matrix $\mathbf{Z}$ (e.g. [7]) transforms the incident Stokes vector $\mathbf{I}_0 = (I_0, Q_0, U_0, V_0)$ into the Stokes vector $\mathbf{I} = (I, Q, U, V)$ of the scattered field

$$\mathbf{I}(\mathbf{n}) = \mathbf{Z}(\mathbf{n}, \mathbf{n}_0)\mathbf{I}_0(\mathbf{n}_0) \tag{1}$$

where $\mathbf{n}_0$ and $\mathbf{n}$ are the incident and scattering directions, respectively. This matrix is convenient for mathematical processing but the physical meaning of its elements is not intuitive. We prefer to use a reduced matrix $\mathbf{R}$ with more simple interpretation of its elements. Namely, let us consider the initial phase matrix $\mathbf{Z}$ as a set of four column vectors $\mathbf{Z} = (\mathbf{Z}_1. \mathbf{Z}_2, \mathbf{Z}_3. \mathbf{Z}_4,)$ where $\mathbf{Z}_1 = (Z_{11}, Z_{21}, Z_{31}, Z_{41},)$ and so on. The reduced matrix $\mathbf{R}$ is determined by the linear transformations of the column vectors as follows

$$\mathbf{R}_1 = \mathbf{Z}_1; \qquad \mathbf{R}_2 = \mathbf{Z}_2 + \mathbf{Z}_1; \qquad \mathbf{R}_3 = \mathbf{Z}_3 + \mathbf{Z}_1; \qquad \mathbf{R}_4 = \mathbf{Z}_4 + \mathbf{Z}_1 \tag{2}$$

Then the column vectors $\mathbf{R}_j$ mean the Stokes vectors of the scattered field for different states of polarization of the incident light. They correspond to nonpolarized ($Q_0 = U_0 = V_0 = 0$), linearly polarized at 0º ($Q_0 = 1$, $U_0 = V_0 = 0$), linearly polarized at 45º ($U_0 = 1$, $Q_0 = V_0 = 0$), and circularly polarized ($V_0 = 1$, $Q_0 = U_0 = 0$) incident light, respectively. Thus, all elements of the matrix $\mathbf{R}$ mean the results of the obvious experimental measurements. Here the first row means the intensities of the scattered light in the proper experiments. We shall normalize the other elements of a column vector to these intensities

resulting in the degree of polarization of the scattered light for every polarization state of the incident light. This normalized matrix **N** with the elements

$$N_{1j} = R_{1j} \ ; \qquad N_{ij} = R_{ij} / R_{1j} \quad \text{for } i = 2, 3, 4 \tag{3}$$

is the goal of our numerical calculations. For the case of horizontally oriented crystals, the conventional spherical coordinate system is assumed where the azimuth angle θ is accounted from the vertical downward direction. The azimuth angle φ is accounted from an arbitrary chosen zero meridian in the direction of the unit vector $\mathbf{e}_\varphi$ that is determined by means of three right-handed basic unit vectors $\mathbf{n} = \mathbf{e}_\theta \times \mathbf{e}_\varphi$.

3. The reduced phase matrix N for horizontally oriented hexagonal ice plates

3.1 Phase functions

In a recent paper [8], we studied the phase functions of the horizontally oriented hexagonal plates in details. As known, the phase functions are concentrated along four horizontal circles. Two of them (the parhelic and subparhelic circles) reveal four sharp angular peaks. They are the forward peak, sundog, parhelion 120º, and peak 150º. As an example, a typical phase function is shown in Fig.1.

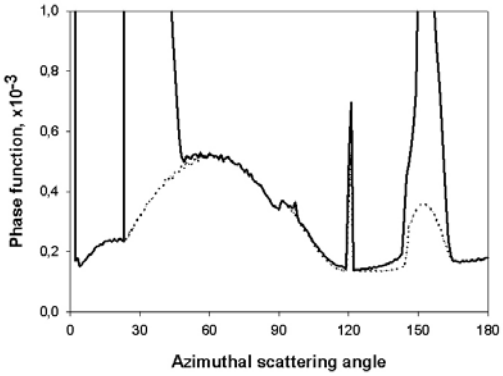

Fig.1. The phase function in the parhelic circle for a horizontally oriented hexagonal ice plate of the aspect ratio 0.2 at the incident angle of 75º. The dotted line corresponds to the residue after a subtraction of the abovementioned four peaks.

3.2 Degrees of polarization

Because of great intensity, these four peaks are easy measured in experiments. Hence, they are the most promising values for the inverse scattering problems, i.e. for retrieving crystal shapes and orientations from optical measurements. Polarization measurements inside these peaks should bring valuable additional information in the inverse problems since the polarization measurements are relational, i.e. they do not need some absolute detector calibration. So, the phase matrix calculated is a promising instrument for the scattering inverse problems.

We note that the parhelic circle is usually watched by an observer on the Earth when the sun radiation propagates through cirrus clouds. In this case, it is natural to assume that the incident light is nonpolarized, i.e. only the first column of the phase matrix is of practical interest. The subparhelic circle,

on the contrary, can be watched from the Earth when a light source is located on the ground. This light source can be either a nonpolarized floodlight beam or a polarized laser beam. In the latter case, all columns of the phase matrix are of practical importance.

Let us consider the brightest peaks, i.e. the forward scattering peaks and sundogs. Table 1 and Fig.2 show the phase matrix **N** of Eq. (3) obtained for certain typical situations

Table 1: The normalized reduced matrix **N** of Eq. (3) in the forward scattering peak for the hexagonal plate of the aspect ratio of 0.1. The 2-4th rows are given in percents.

0.9	0.9	0.9	0.9	0.75	0.79	0.75	0.75	0.45	0.53	0.45	0.45
<1	100	<1	<1	4.59	100	4.59	4.59	16.6	100	16.6	16.6
0	0	>99	0	0	0	99.8	0	0	0	94.7	-10.1
0	0	0	>99	0	0	0	99.8	0	0	10.1	94.7

Parhelic circle, the incident angle are equals 15º, 45º, and 75º, respectively

0.03	0.03	0.03	0.03	0.05	0.02	0.05	0.05	0.21	0.14	0.21	0.21
-10.6	100	-10.6	-10.6	-61.9	100	-61.9	-61.9	-35.9	100	-35.9	-35.9
0	0	-99.4	0	0	0	-56.3	-14.1	0	0	91.2	-3.0
0	0	0	-99.4	0	0	14.1	-56.3	0	0	3.0	91.2

Subparhelic circle, the incident angle are equals 15º, 45º, and 75º, respectively

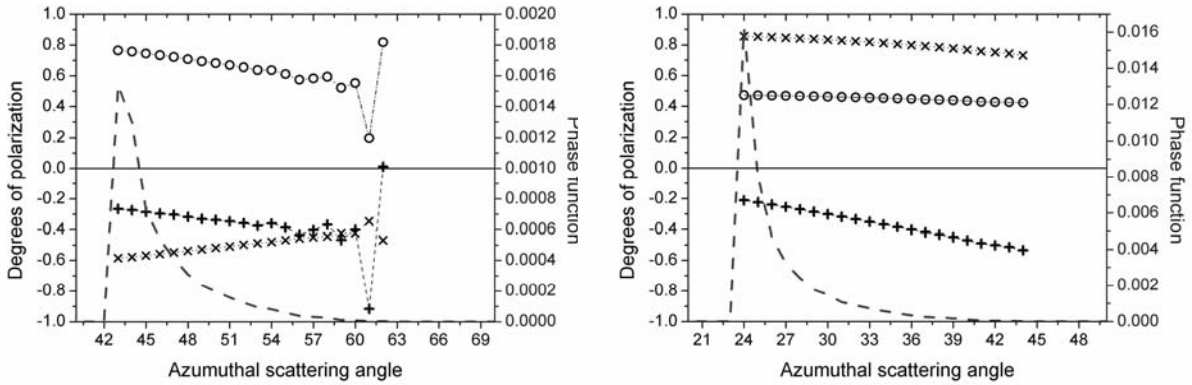

Fig.2. Polarization of sundog in the parhelic circle for the incident polarized light (i.e. the Stokes vector $N_{i3}(\varphi)$). The phase function N_{13} is shown by the dashed curves with the right ordinate axis. The left ordinate presents the other elements: N_{23} (+), N_{33} (×), and N_{43} (o). Aspect ratio is equal to 0.1. The incidence angles are 45 º (left) and 75 º (right)

Considering such kind of numerical data we conclude the following. The case of small incident angle (up to ≈ 30º) is not promising for retrieval of aspect ratios of the plates from the scattered radiation. For the large incident angles (> 30º), these are the elements N_{34} and N_{43} that prove to be sensitive to either the incident angles or the particle's aspect ratios. Moreover, their behaviors are rather regular. There is a simple physical explanation of this fact. Namely, the element N_{34} describes appearance of circular polarization in the case of incidence of linearly polarized light. A transformation of the linearly polarized light into circular polarization can be caused by only total internal reflections. So, the degree of circular polarization is an indicator for the number of the total internal reflections among the photon trajectories giving an essential contribution to the scattered light. The number of total internal reflections for the

typical trajectories reflecting from the horizontal facets is a simple function of either the incident angle or particle's aspect ratio. Such physical regularities are true for other peaks, too, in the case of plates of arbitrary shape but of small aspect ratios. Therefore a method for diagnostics of aspect ratios of the plates by means of polarization measurements appears.

So, this is the bistatic lidar sounding of cirrus clouds that can be promising for diagnostics of horizontally oriented ice plates. In the bistatic lidar sounding scheme, not only the forward scattering peak, but other peaks, for example, sundogs can be used, too. In particular, Fig.2 demonstrates the strong dependence of the element N_{34} on the incidence angle within the sundog. Though our calculations are performed within the framework of geometric optics approach, they can be easy expanded to include diffraction. It is obvious that diffraction will not essentially distort the values describing degree of polarization. Therefore diffraction will not prevent to apply the method proposed for diagnostic of the aspect ratios of ice crystals in practice.

Acknowledgments

This research is supported by the Russian Foundation for Basic Research (grants 06-05-65141 and 05-05-39014) and by the International Association for the Promotion of Cooperation with Scientists through the New Independent States of the Former Soviet Union (INTAS) under the grant 05-1000008-8024.

References

[1] K.N. Liou, Y. Takano, and P. Yang "Light scattering and radiative transfer in ice crystal clouds: Applications to climate research". In: Mishchenko M.I, Hovenier J.W., Travis L.D., editors. *Light scattering by nonspherical particles: Theory, measurements, and applications*, Acad. Press, San Diego, 2000, p. 417-449

[2] K. Muinonen, K. Lumme, J. Peltoniemi, and W.M. Irvine, "Light scattering by randomly oriented crystals", *Appl. Opt*. **28**, 3051-3060 (1989)

[3] W. Tape, *Atmospheric Halos*, (American Geophysical Union, Antarctic Research Series v.64. Washington, 1994)

[4] Y. Takano and K.N. Liou, "Solar radiative transfer in cirrus clouds. Part1: Single scattering and optical properties of hexagonal ice crystals", *J. Atmos. Sci*., **46**, 3-19 (1989)

[5] Y. Takano and K.N. Liou, "Transfer of polarized infrared radiation in optically anisotropic media: application to horizontally oriented ice crystals", *J. Opt. Soc. Am*. **A 10**, 1243-1256 (1993)

[6] V. Noel, G. Ledanois, H. Chepfer and P.H. Flamant, "Computation of a single-scattering matrix for nonspherical particles randomly or horizontally oriented in space", *Appl. Opt.* **40**, 4365-4375 (2001)

[7] M.I. Mishchenko, L.D. Travis, and A.A. Lacis, *Scattering, Absorption, and Emission of Light by Small Particles* (Cambridge University Press, Cambridge, 2002)

[8] A.G. Borovoi, A.V. Burnashov, and A.Y.S. Cheng, "Light scattering by horizontally oriented ice crystal plates", *JQSRT* (2007, *in press*)

The spatial polarization distribution over the dome of the sky for abnormal irradiance of the atmosphere

V.P. Budak, S.V. Korkin

Moscow Power-Engineering Institute (TU), Light Engineering Department
14, Krasnokazarmennaya str., Moscow, 111250, Russia
tel: +7 (495) 362-7067, fax: +7 (495) 362-7594, e-mail: BudakVP@mpei.ru

Abstract

The paper deals with the polarized radiative transfer within a slab irradiated by a collimated infinity-wide beam of arbitrary polarized light. The efficiency of the proposed analytical solution lies in the assumption that the complete vectorial radiative transfer solution is the superposition of the most anisotropic and smooth parts, computed separately. The vectorial small angle modification of the spherical harmonics method is used to evaluate the anisotropic part and the vectorial discrete ordinates method is used to obtain the smooth one. The azimuthal expansion is used in order to describe the light field spatial distribution for the case of abnormal irradiance and to obtain some known neutral points in the sky especially useful for polarized remote sensing of the atmosphere.

1 Introduction

It is well known in optics that polarization state of light described by four-element Stokes vector (SV) contains all the information about an object under consideration available for optical methods of remote sensing (RS). Nevertheless today the amount of scalar (neglecting polarization) studies is much more grater than polarimetric ones. This relates with the comparatively small amount of polarimetric systems all over the world. And this fact in its turn can be explained by two main reasons: design problems in electro-optical polarimetric systems (high accuracy of measurements must be apply to determine the polarization state of light) and mainly by absence of a reliable mathematical model including polarization for interpretation of the experimental results (see SPIE vol. 5888 "Polarization Science and Remote Sensing II", 2005 for example – quite many polarimetric systems and simultaneously only a few theoretical investigations). Following the scalar case the polarized radiative transfer (RT) mathematical model must be of a high efficiency from the result convergence to the exact one point of view. It must allow to compute highly anisotropic scattering of natural formations (clouds, ocean, galaxy dust and others), be valid for arbitrary optical thickness τ and the irradiance angle θ_o of a scattering media (the last one allows to describe known directions of neutral polarization of atmosphere-scattered light – Arago, Babinet and Brewster points). The model must include multiple scattering and if possible it must be expressed in analytical form to make the solution of inverse problems a little simpler. This paper deals with a described model applied to a slab irradiated by infinity wide collimated beam (plain unidirectional (PU) source of radiation with $\hat{\mathbf{l}}_0$ as a direction of the irradiation). The incident light assumed to be both natural and arbitrary polarized.

2 The complete solution of the polarized radiative transfer problem

2.1 The anisotropic part

We will use the following notation: «→» is the 4-elements column vector; «↔» - the 16-elemnts square Mueller matrix, Λ – single scattering albedo; θ and φ – are zenithal and azimuthal angles respectively; $\mu = \cos\theta$, the unit directionality is $\hat{\mathbf{l}}$. The SV and its component we note as $\vec{L}(\tau,\hat{\mathbf{l}}) = [\mathrm{I} \quad \mathrm{Q} \quad \mathrm{U} \quad \mathrm{V}]$. In RT

one of the main problems is to take mathematical specialties of the boundary problem for the vectorial radiative transfer equation (VRTE) into account. For the PU-source such speciality is the unscattered radiation expressed as Dirac δ-singularity. This singularity needs ∞ elements to be represented in a series and hence can not be computered analytically. *Chandrasekhar* separated the light field within the slab into two parts - δ-singularity and scattered light - and computed the diffuse transparent and reflected light field. But for real turbid media the scattered light field still remains a highly anisotropic function which needs lots of terms of the series to be computed. This leads to the ill-conditionality of the evaluations and besides computation time increases.

We follow with an idea that showed good results for scalar case [1] and represent the desired vectorial radiation field as the superposition of the anisotropic part that includes the δ-singularity and smooth non-mall angle part (indexed by «~»). So we write for the desired spatial distribution of SV

$$\vec{\mathrm{L}}(\tau,\hat{\mathbf{l}}) = \vec{\mathrm{L}}_{\mathrm{VMSH}}(\tau,\hat{\mathbf{l}}) + \vec{\mathrm{L}}_{\sim}(\tau,\hat{\mathbf{l}}). \tag{1}$$

We use the definition, the addition theorem and some recurrence formulas from *Gelfand* for generalized spherical functions (GSF) $\vec{\mathrm{P}}^{k}_{m}(\mu)$ which represent the eigen-functions for the scattering operator of the VRTE and write down the standard series to express SV and the scattering matrix as follows

$$\vec{\mathrm{L}}(\tau,\hat{\mathbf{l}}) = \sum_{m=-\infty}^{\infty}\sum_{k=0}^{\infty}\frac{2k+1}{4\pi}\vec{\mathrm{P}}^{k}_{m}(\mu)\vec{\mathbf{f}}^{k}_{m}(\tau)\exp(im\varphi), \quad \vec{x}(\hat{\mathbf{l}}\hat{\mathbf{l}}') = \sum_{k=0}^{\infty}(2k+1)\vec{\mathrm{P}}_{k}(\hat{\mathbf{l}}\hat{\mathbf{l}}')\vec{x}_{k}. \tag{2}$$

The anisotropic part is computed in the vectorial small-angle modification of the spherical harmonics method (VMSH) [2]. The VMSH is built upon the substitution of the discrete spatial spectrum of the SV $\vec{\mathbf{f}}$ in (2) with respect to zenithal index *k* by a smooth *k*-continuous one. Its Taylor expansion with respect to *k* cut to two terms. This gives quite simple differential equation for the VMSH. The solution expresses as matrix exponent. So the VMSH can be evaluated as

$$\vec{\mathrm{L}}_{\mathrm{VMSH}}(\tau,\hat{\mathbf{l}},\hat{\mathbf{l}}_0) = \sum_{m=-2}^{0,2}\sum_{k=0}^{\infty}(2k+1)\vec{\mathrm{P}}^{m}_{k}(\hat{\mathbf{l}}\hat{\mathbf{l}}_0)\exp\left\{-(\vec{\mathrm{I}}-\Lambda\vec{x}_{k})\tau/\mu_0\right\}\vec{\mathbf{f}}^{m}_{k}(0)/4\pi, \tag{3}$$

where all $\vec{\mathbf{f}}(0)$ are known from boundary conditions. The VMSH (3) allows evaluating the light field for some solid angle of the forward hemisphere (co-directionally with the incident radiation). This zone of validity depends greatly upon the slab properties. The more is the anisotropy state of the slab scattering properties the wider is the zone of accurate result. More deeply we discuss (3) and gave some results in our recent work [3]. Here we note only that the main advantage of (3) is its keeping both the anisotropic part of light field and the direct non-scattered singularity. Approximation (3) neglects the back-scattered radiation and so we are going to describe the determination the smooth regular part in the following subsection.

2.2 The smooth part

As we noted above we depart from *Chandrasekhar* and formulate the boundary problem not for the whole diffuse radiation but for the smooth part only as follows

$$\begin{cases} \mu\dfrac{\partial}{\partial\tau}\vec{\mathrm{L}}_{\sim}(\tau,\hat{\mathbf{l}}) + \vec{\mathrm{L}}_{\sim}(\tau,\hat{\mathbf{l}}) = \dfrac{\Lambda}{4\pi}\oint\vec{\mathrm{S}}(\hat{\mathbf{l}}\hat{\mathbf{l}}',\chi',\chi)\vec{\mathrm{L}}_{\sim}(\tau,\hat{\mathbf{l}})d\hat{\mathbf{l}}' + \vec{\Delta}(\tau,\hat{\mathbf{l}})/4\pi, \\ \vec{\mathrm{L}}_{\sim}(0,\hat{\mathbf{l}})\big|_{\mu>0} = \vec{0}; \quad \vec{\mathrm{L}}_{\sim}(\tau_0,\hat{\mathbf{l}})\big|_{\Omega_{\sim}} = -\vec{\mathrm{L}}_{\mathrm{VMSH}}(\tau,\hat{\mathbf{l}})\big|_{\mu<0}, \end{cases} \tag{4}$$

where $\vec{\mathrm{S}}$ contains the scattering matrix and the rotator in order to take the multiple transformations of the reference plane during scattering into account. The VMSH as the source function is described by $\vec{\Delta}$ and can be expressed as follows

$$\vec{\Delta}(\tau,\hat{\mathbf{l}}) = -\mu\frac{\partial}{\partial\tau}\vec{\mathrm{L}}_{\mathrm{VMSH}}(\tau,\hat{\mathbf{l}},\hat{\mathbf{l}}_0) + \vec{\mathrm{L}}_{\mathrm{VMSH}}(\tau,\hat{\mathbf{l}},\hat{\mathbf{l}}_0) + \frac{\Lambda}{4\pi}\oint\vec{\mathrm{S}}(\hat{\mathbf{l}}\hat{\mathbf{l}}',\chi,\chi')\vec{\mathrm{L}}_{\mathrm{VMSH}}(\tau,\hat{\mathbf{l}}',\hat{\mathbf{l}}_0)d\hat{\mathbf{l}}'. \tag{5}$$

Both in scalar and vectorial theory the evaluation of scattering integral of the transport equation is on a par with the δ-singularity subtraction. In vectorial case the complex circular basis (CP - representation) was offered by *Kuščer* and *Ribarič*. The matrix relation between the CP- and Stokes polarization (SP-) representations is well known. The advantage point of CP is in the fact the rotator in this basis becomes a diagonal matrix and the scattering integral can be evaluated (we used this to obtain (3)). But it is impossible to use matrix scaling transformation (*Karp*) for complex numbers in order to prevent ill-conditionality of the system of equations while τ or anisotropy increases. So after evaluating of the scattering integral we transform the obtained system for $\vec{\mathbf{f}}_m^k(\tau)$ (2) from complex CP- back to real energetic SP-basis.

The vectorial discrete ordinates method with Mark's boundary condition is used because of its efficiency [4]. In [5] *Chandrasekhar's* δ-singularity subtraction was used to obtain the diffuse radiation so it's convenient to use some notations from [5] in our method of solution. As we have previously mentioned we use the CP-representation, the GSF addition theorem and back CP→SP transformation to evaluate scattering integrals both in (4) and (5). Besides we note that the frame of reference for (3) differs from that in (4). So we use the linear transformation to reduce (3) and (4) to the same frame of reference. Here we omit intermediate evaluations and give the main results.

For the scattering integral in (4) we have

$$\vec{\mathrm{I}}_{\mathrm{S}} = \frac{\Lambda}{2}\sum_{k=0}^{\infty}(2k+1)\sum_{m=0}^{k}\left[\ddot{\phi}_1(m\varphi)\int_{-1}^{1}\ddot{\mathrm{A}}_k^m(\mu,\mu')\tilde{\mathrm{L}}_1^m(\tau,\mu') + \ddot{\phi}_2(m\varphi)\int_{-1}^{1}\ddot{\mathrm{A}}_k^m(\mu,\mu')\tilde{\mathrm{L}}_2^m(\tau,\mu')d\mu\right], \tag{6}$$

where

$\ddot{\phi}_1(\varphi) = \mathrm{diag}\{\cos\varphi, \cos\varphi, \sin\varphi, \sin\varphi\}$; $\ddot{\phi}_2(\varphi) = \mathrm{diag}\{-\sin\varphi, -\sin\varphi, \cos\varphi, \cos\varphi\}$; $\ddot{\mathrm{A}}_k^m(\mu,\mu') = \ddot{\Pi}_k^m(\mu)\ddot{\chi}_k\ddot{\Pi}_k^m(\mu')$.

$\ddot{\chi}_k$ are the matrix coefficients of scattering matrix (2) in SP-representation, and matrix polynomials are

$$\ddot{\Pi}_k^m(\mu) = \begin{bmatrix} \mathrm{Q}_k^m(\mu) & 0 & 0 & 0 \\ 0 & \mathrm{R}_k^m(\mu) & \mathrm{T}_k^m(\mu) & 0 \\ 0 & \mathrm{T}_k^m(\mu) & \mathrm{R}_k^m(\mu) & 0 \\ 0 & 0 & 0 & \mathrm{Q}_k^m(\mu) \end{bmatrix}; \quad \begin{aligned} \mathrm{R}_k^m(\mu) &= \frac{1}{2}\left(\mathrm{P}_{m,2}^k(\mu) + \mathrm{P}_{m,-2}^k(\mu)\right); \\ \mathrm{T}_k^m(\mu) &= \frac{1}{2}\left(\mathrm{P}_{m,2}^k(\mu) - \mathrm{P}_{m,-2}^k(\mu)\right). \end{aligned}$$

$\mathrm{Q}_k^m(\mu)$ are semi-normalized Schmidt polynomials and $\mathrm{P}_{m,2}^k(\mu)$ are GSF. It can be seen from (6) that it is convenient to present the smooth part as two azimuthally-dependent items

$$\vec{\mathrm{L}}(\tau,\mu,\varphi) = \sum_{m=0}^{\infty}\left[\ddot{\phi}_1(m\varphi)\vec{\mathrm{L}}_1^m(\tau,\mu) + \ddot{\phi}_2(m\varphi)\vec{\mathrm{L}}_2^m(\tau,\mu)\right],$$

each of which can be obtained from the following boundary-condition problem (i = 1 and 2) similar to (4)

$$\begin{cases} \mu\dfrac{\partial}{\partial\tau}\tilde{\mathrm{L}}_i^m(\tau,\mu) + \tilde{\mathrm{L}}_i^m(\tau,\mu) = \dfrac{\Lambda}{2}\displaystyle\sum_{k=0}^{\infty}(2k+1)\int_{-1}^{1}\ddot{\mathrm{A}}_k^m(\mu,\mu')\tilde{\mathrm{L}}_i^m(\tau,\mu')d\mu' + \Delta_i(\tau,\mu) \\ \tilde{\mathrm{L}}_i^m(0,\mu)\big|_{\mu>0} = \vec{0};\ \tilde{\mathrm{L}}_i^m(\tau_0,\mu)\big|_{\mu<0} = -\vec{\mathrm{L}}_{\mathrm{VMSH}}^m(\tau_0,\mu)\big|_{\mu<0}; \end{cases} \tag{7}$$

if the source function $\vec{\Delta}(\tau,\mu)$ is derived.

For the source function after reduction of frames of reference we use the same methods as described above. Namely, we'll use the SP→CP→SP transformation, the addition theorem for the GSF to evaluate the scattering integral in (5) and the recurrence formulas for the GSF to obtain the system of equations for the vectorial coefficients. As a result we have the following for the source function

$$\vec{\Delta}(\tau,\hat{\mathbf{l}},\hat{\mathbf{l}}_0) = \sum_{k=0}^{\infty}\sum_{m=-k}^{k}\frac{2k+1}{4\pi}\ddot{\Pi}_k^m(\mu)\ddot{\Phi}_k(\tau)\ddot{\Pi}_k^m(\mu_0)\vec{\mathrm{L}}_0\exp(im(\varphi-\varphi_0)), \tag{8}$$

where $\vec{\mathrm{L}}_0 = \begin{bmatrix} 1 & p\sin 2\varphi_0 & -p\cos 2\varphi_0 & q \end{bmatrix}$ is the initial Stokes vector with the linear polarization degree p, the ellipticity q and φ_0 – gives the azimuth of the reference plane. Further on

$$\vec{\Phi}_k(\tau)=\left\{\frac{1}{2k+1}\left[\vec{A}_{k+1}(\vec{1}-\Lambda\vec{\chi}_{k+1})\vec{Z}_{k+1}(\tau)\vec{a}_k+4\frac{(2k+1)}{k(k+1)}(\vec{1}-\Lambda\vec{\chi}_k)\vec{Z}_k(\tau)\vec{b}+\vec{A}_k(\vec{1}-\Lambda\vec{\chi}_{k-1})\vec{Z}_{k-1}(\tau)\vec{a}_k\right]-\right.$$
$$\left.-(\vec{1}-\Lambda\vec{\chi}_k)\vec{Z}_k(\tau)\right\},\qquad \vec{Z}_k=\exp\left(-(\vec{1}-\Lambda\vec{\chi}_k)\tau_0/\mu_0\right),$$

and $\vec{a}_k=\mathrm{diag}[k\quad\sqrt{k^2-4}\quad\sqrt{k^2-4}\quad k]$; $\vec{A}_k=\vec{a}_k/k$; $\vec{b}=\mathrm{diag}[0\quad 1\quad 1\quad 0]$. This being substituted in (8) together with (7), the VMSH (3) gives and the assumption (1) the complete solution of the VRTE boundary problem for an arbitrary irradiated slab.

3 Conclusion

In summary we would like to note one thing, we've mentioned above, for the second time: δ-singularity subtraction and the subsequent determination of the scattered radiation seems to be inefficient for the cases of highly anisotropic scattering and the VRTE boundary condition's mathematical specialty presence. One can find such specialties not only for PU-source but for point-sources too. So the only way to build an efficient model for such cases is to consider the anisotropic and the regular part superposition. We particularly note that the efficiency of the proposed method increases together with the degree of scattering anisotropy, the number of stratification layers of a slab (for example, 4 layers to simulate a real atmosphere), for 2D and 3D geometry (point-source is the simple example).

The neutral polarization points following the direction of the slab irradiance have the day and annually variation. So the method described here and considered the azimuthal asymmetry (*m*- or, the same, *Fourier*-expansion) of the SV spatial distribution seems to be an efficient basis for polarized remote sensing that uses both atmosphere neutral points and any SV-component analysis for different media especially for highly anisotropic one.

Acknowledgments

The authors would like to thank the members of "The Light Field in the Turbid Medium" seminar held in the Light Engineering Department in Moscow Power-Engineering Institute (TU).

References

[1] V. P. Budak, A. V. Kozelskii, E. N. Savitskii, "Improvement of the spherical harmonics method convergence at strongly anisotropic scattering," Atm. and Ocean. Opt. **17**, №1, pp 28–33 (2004).

[2] I. E. Astakhov, V. P. Budak, D. V. Lisitsin and V.A. Selivanov, "Solution of the vector radiative transfer equation in the small-angle approximation of the spherical harmonics method", Atm. and Ocean. Opt. **7**, № 6, pp 398 - 402 (1994).

[3] V. P. Budak, S. V. Korkin, "The vectorial radiative transfer equation problem in the small angle modification of the spherical harmonics method with the determination of the solution smooth part", Proc. SPIE, Vol. 6408, pp 1I-1 – 1I-8 (2006).

[4] V. P. Budak, S.V. Korkin, "On the solution of the vectorial radiative transfer equation in arbitrary three-dimensional turbid medium with an anisotropic scattering", Proc. The Fifth Int. Symp. On Radiative transfer, RAD – V – 038 (collocated conference).

[5] C. E. Siewert, "A discrete-ordinates solution for radiative-transfer models that include polarization effects", JQSRT 64, №3, pp 227 – 254 (2000).

Polarization Symmetries in Electromagnetic Scattering

Shane R Cloude,

AEL Consultants,
26 Westfield Avenue, Cupar, Fife, KY15 5AA, Scotland, UK
tel: +44 (1334) 650761, fax: +44 (1334) 650761, e-mail aelc@mac.com

Abstract

In this paper we consider ways in which macroscopic symmetries impact on the structure and information content of scattering matrices in vector electromagnetic theory. We show how these symmetries can lead to a consistent and complete parameterization of depolarization behaviour and examine the potential for using these ideas to extract information about non-spherical and complex particles in random media scattering applications.

1 Introduction

Polarization effects in wave scattering by non-spherical particles forms a topic of great interest in many applications. While several powerful modeling techniques have been developed for predicting the quantitative vector nature of such scattering, there remains a need to augment this with methods for validation and interpretation of the predictions of such models. In addition, advances in measurement techniques have opened the possibility of fully populating scattering matrices from experimental data and this in turn offers the possibility of improved parameter retrieval, such as particle shape and composition, from scattered field measurements of complex random media.

In the absence of suitable canonical wave solutions for many complex geometries of interest, scattering symmetries and physical constraints provide an important means of satisfying such needs. In this paper we look at a new way of integrating these constraints into a self-consistent parameterization of wave depolarization by complex particle clouds. That scattered powers are always non-negative and wave coherences lies between 0 and 1 are simple physical constraints, but ones with a subtle impact in vector scattering theory. For example, we shall show that parameterization of an important class of depolarizers defines a cube in Stokes space [1], but do all points inside the cube satisfy even these two simple physical constraints? We shall show in this paper that they do not and that only a subset of the cube contains valid physical depolarizers. Given this shortcoming, we can then ask if there is not a better way of studying depolarizers with symmetry and physical constraints built into the parameterization from the start. Such a scheme forms the central focus of this paper.

In polarization studies, interest centers on the Mueller matrix [M] that relates incident and scattered Stokes vectors. Importantly, the structure of [M] reflects symmetries in the underlying complex amplitude or [S] matrix. For example, the vector wave reciprocity theorem in backscatter causes a symmetry in [S] which limits the form of the Mueller matrix (for arbitrary random scattering problems) to that shown in equation 1 [2], where we note that there is an important constraint equation on the diagonal elements, leaving [M] with only 9, rather than 16 degrees of freedom. Reciprocity symmetry then limits the types of depolarization we can observe in backscatter.

In general [M] = f([S]) changes the degree of polarization of the wave but has the property that if the incident wave entropy is zero (a purely polarized incident wave) then the scattered wave entropy is also zero. This ‘conservation of zero wave entropy’ is an important idea in polarization theory. Fundamentally, this property has to do with the reversibility of the mapping from [S] to [M] as $[M] = f([S]) \Rightarrow [S] = f^{-1}([M])$?

$$[S]=\begin{bmatrix} a & b \\ -b & d \end{bmatrix} \Rightarrow [M]=\begin{bmatrix} m_{11} & m_{12} & m_{13} & m_{14} \\ m_{12} & m_{22} & m_{23} & m_{24} \\ -m_{13} & -m_{23} & m_{33} & m_{34} \\ m_{14} & m_{24} & -m_{34} & m_{44} \end{bmatrix} \quad \text{Reciprocity} \Rightarrow m_{11}-m_{22}+m_{33}-m_{44}=0 \quad (1)$$

However there exists the possibility of formulating a set of Mueller matrices that do not correspond to a single [S] matrix at all, called depolarizers. The most extreme example of these is the isotropic depolarizer, with a Mueller matrix of the form shown on the left hand side of equation 2 [1]

$$[M]=\begin{bmatrix} 1 & 0 & 0 & 0 \\ 0 & 0 & 0 & 0 \\ 0 & 0 & 0 & 0 \\ 0 & 0 & 0 & 0 \end{bmatrix} \Rightarrow [M]=\begin{bmatrix} 1 & 0 & 0 & 0 \\ 0 & \delta & 0 & 0 \\ 0 & 0 & \delta & 0 \\ 0 & 0 & 0 & \delta \end{bmatrix} \Rightarrow [M_{III}]=\begin{bmatrix} 1 & \underline{0}^T \\ \underline{0} & [O]_3[\Delta][O]_3^T \end{bmatrix} \quad [\Delta]=\begin{bmatrix} \delta_1 & 0 & 0 \\ 0 & \delta_2 & 0 \\ 0 & 0 & \delta_3 \end{bmatrix} \quad (2)$$

This matrix converts all Stokes vector into a randomly polarized wave, but there is no corresponding single [S] matrix. This form leads to a standard generalization of the depolarizer as shown in two stages from left to right in equation 2. The middle is a partial depolarizer while the right hand form generalizes to an anisotropic partial depolarizer with arbitrary direction in Stokes space (the matrix O_3 is a 3 x 3 real rotation matrix of the Poincaré sphere). However, we can ask if all such depolarizers are physically consistent and do these forms exhaust all possibilities? To answer these questions we need to look in more detail at the nature of depolarization. To do this we introduce the scattering coherency matrix.

2. Scattering Coherency Matrix Formulation

The Mueller matrix can be conveniently converted into a 4 x 4 Hermitian coherency matrix [T] which is positive semi-definite and so guarantees that all scattered powers will be non-negative and coherences less than or equal to 1 [3,4]. The mapping from [M] into this 4x4 matrix [T] is shown for reference in equation 3.

$$<[M]>=\begin{bmatrix} m_{11} & m_{12} & m_{13} & m_{14} \\ m_{21} & m_{22} & m_{23} & m_{24} \\ m_{31} & m_{32} & m_{33} & m_{34} \\ m_{41} & m_{42} & m_{43} & m_{44} \end{bmatrix} \Rightarrow <[T]>=$$

$$\frac{1}{2}\begin{bmatrix} m_{11}+m_{22}+m_{33}+m_{44} & m_{12}+m_{21}-i(m_{34}-m_{43}) & m_{13}+m_{31}+i(m_{24}-m_{42}) & m_{14}+m_{41}-i(m_{23}-m_{32}) \\ m_{12}+m_{21}+i(m_{34}-m_{43}) & m_{11}+m_{22}-m_{33}-m_{44} & m_{23}+m_{32}+i(m_{14}-m_{41}) & m_{24}+m_{42}-i(m_{13}-m_{31}) \\ m_{13}+m_{31}-i(m_{24}-m_{42}) & m_{23}+m_{32}-i(m_{14}-m_{41}) & m_{11}-m_{22}+m_{33}-m_{44} & m_{34}+m_{43}+i(m_{12}-m_{21}) \\ m_{14}+m_{41}+i(m_{23}-m_{32}) & m_{24}+m_{42}+i(m_{13}-m_{31}) & m_{34}+m_{43}-i(m_{12}-m_{21}) & m_{11}-m_{22}-m_{33}+m_{44} \end{bmatrix} \quad (3)$$

As [T] is positive semi-definite (PSD) Hermitian it has real non-negative eigenvalues and orthogonal eigenvectors. For example, by mapping the general depolarizer D of equation 2 into [T] we see that the real diagonal elements δ_1, δ_2 and δ_3 are constrained by the four inequalities shown in equation 4. If we consider δ_1, δ_2 and δ_3 as defining a unit cube in Stokes space then equation 4 represents four planes in this

space that further constrain the region of physical depolarizers. By using [T] we can then avoid problems of considering non-physical [M] matrices inside this cube by mistake.

$$\begin{bmatrix} 1 & 1 & 1 & 1 \\ 1 & 1 & -1 & -1 \\ 1 & -1 & 1 & -1 \\ 1 & -1 & -1 & 1 \end{bmatrix} \begin{bmatrix} 1 \\ \delta_1 \\ \delta_2 \\ \delta_3 \end{bmatrix} \geq 0 \tag{4}$$

For the case of a 'general' depolarizer proposed on the far right in equation 2, obtained by a rotation of the Poincaré sphere, the coherency matrix [T] is transformed as shown in equation 5

$$\begin{aligned} &\underline{g}' = \begin{bmatrix} 1 & 0 \\ 0 & [O_3] \end{bmatrix} \underline{g} \xrightarrow{SU(2)-O_3^+} [S]' = [U_2][S][U_2]^{*T} \\ &\Rightarrow <[T]>' = [U_{4B}] <[T]> [U_{4B}]^{*T} \quad [U_{4B}] = [U_2] \otimes [U_2]^* \end{aligned} \tag{5}$$

We shall see that this represents only a subset of possible depolarizers and leads to a more general classification based on 4 x 4 unitary matrix transformations of $[T]' = [U_4][T][U_4]^{*T}$ as follows.

3. General Theory of Depolarization

In this section we formulate a general model of depolarization that scales to arbitrary dimension of the coherency matrix N x N. The basic idea is to identify the 'polarizing' contribution with the dominant eigenvector of the coherency matrix, i.e. the eigenvector corresponding to the largest eigenvalue. The other eigenvectors then contribute to depolarization with a strength given by the remaining minor eigenvalues. By employing multidimensional unitary transformations we will then be able to parameterize all possible types of depolarization. We first start with the general formulation and then specialize it to the three important cases for N = 2,3 and 4. We then consider the effects of scattering symmetries on constraining the degrees of freedom involved in both polarized and depolarized components [4].

The starting point for our analysis is the idea of a unitary reduction operator [U_{-1}], which acts to reduce the dimensionality of an N x N unitary matrix to N-1 x N-1 as shown in equation 6

$$[U_{-1}][U_N] = \begin{bmatrix} 1 & \underline{0}^T \\ \underline{0} & U_{N-1} \end{bmatrix} = \begin{bmatrix} 1 & \underline{0}^T \\ \underline{0} & \exp(iH_{N-1}) \end{bmatrix} \tag{6}$$

$$H_{N-1} = \sum_{k=1}^{M} h_k \Psi_k \quad \Rightarrow \underline{h} = \textit{depolarisation state vector}$$

We then identify the submatrix U_{N-1} with the depolarizing aspects of the scattering process. In this way U_{N-1} involves continuous smooth transformation away from the polarized reference state (the dominant eigenvector). The submatrix U_{N-1} may be further parameterized in terms of an N-1 x N-1 Hermitian matrix, related to the unitary transformation by a matrix exponential and itself conveniently expanded in terms of a set of scalar parameters, being the basis elements of the underlying algebra [5].

This then leads us to propose the following notation to characterize the number of parameters involved in polarizing and depolarizing components of the decomposition of a general N x N coherency matrix T_N

$$T_N = [E + L] + (E + L) \tag{7}$$

where [..] are the depolarizing parameters and (..) the polarizing terms and for each, E are those parameters associated with the eigenvectors and L the eigenvalues. From the general structure of N x N coherency matrices we then have the following constraints:

- [L] + (L) = N
- [E] + (E) = dim(SU(N)) - rank(SU(N))=N(N-1)

Note that the total number of eigenvector parameters = [E] + (E) = dim(SU(N)) – r(SU(N)) where dim()=N^2-1 is the dimension of the group and r = N-1 is the rank of the Cartan sub-algebra or the number of mutually commuting generators [5]. For example for N=1 there are no useful eigenvector parameters, for N=2 we only have two, while for N= 4 (the most general scattering case) we have twelve parameters available. In this case [T]/[M] have up to 16 parameters and SU(4) is the governing unitary group. SU(4) has dimension 16 and rank 4 so [E]+(E) = 16-4 = 12 and [L] + (L)= 4 . By application of the unitary reduction operator, depolarization in general scattering systems is controlled by [L] = 3 eigenvalues and the SU(3) group for eigenvectors. SU(3) has dimension 8 and rank 2 [5] so that we can write the polarizing/depolarizing decomposition in compact form as shown in equation 8

$$T_{bistatic} = [6 + 3] + (6 + 1) \tag{8}$$

which shows that there are now up to 6 eigenvector parameters associated with depolarization. However there are several important symmetries that reduce further the number of parameters. In the paper we shall show that depolarization is limited by the following cascades in the presence of increasing levels of scattering symmetry

$$T_4^{recip} = [2+3]+(4+1) \qquad T_4^{plane} = [2+3]+(2+1)$$

$$T_4^{bi\,sec\,trix} = [2+3]+(4+1) \quad T_4 \xrightarrow{bistatic+symmetry} [0+3]+(3+1) \tag{9}$$

We shall give examples and further discussion of these results in the full paper.

References

[1] S.Y. Lu, R.A. Chipman, 1996, “Interpretation of Mueller matrices based on the Polar decomposition”, JOSA A Vol 13, No 5, May, pp. 1106-1113

[2] J. W.Hovenier, D W Mackowski, “Symmetry Relations for Forward and Backward Scattering by Randomly Oriented Particles”, J. Quant. Spectrosc. Radiat. Transfer Vol 60, pp 483-492,1998

[3] S.R Cloude, “Polarimetry in Wave Scattering Applications”, Chapter 1.6.2 in SCATTERING, Volume 1,Eds R Pike, P Sabatier, Academic Press, 2001, ISBN 0-12-613760-9

[4] S.R. Cloude, “A New Method for Characterising Depolarisation Effects in Radar and Optical Remote Sensing”, Proceedings of IEEE International Geoscience and Remote Sensing Symposium (IGARSS 2001), Sydney, Australia, Vol.2, pp 910-912, July 2001

[5] S.R.Cloude, " Lie Groups in EM Wave Propagation and Scattering", Chapter 2 in Electromagnetic Symmetry, Eds. C Baum, H N Kritikos, Taylor and Francis, Washington, USA, ISBN 1-56032-321-3, pp 91-142, 1995

Spectropolarimetry of planets: what observational data can be essential for correct microphysical retrievals of atmospheric aerosols

Janna M. Dlugach[1] and Michael I. Mishchenko[2]

[1] *Main Astronomical Observatory of the National Academy of Sciences of Ukraine, 27 Zabolotny Str., 03680, Kyiv, Ukraine, e-mail: dl@mao.kiev.ua*
[2] *NASA Goddard Institute for Space Studies, 2880 Broadway, New York, NY 10025, U.S.A., e-mail: mmishchenko@giss.nasa.gov*

Abstract

We present the results of computations of the degree of linear polarization for the center of a planetary disk in the phase angle range $0° < \alpha < 90°$. The computations were performed for various models of the cloud layer of Jupiter derived in [1–3] on the basis of spectropolarimetric observations of Jupiter [4]. For $\alpha \geq 15°$, our results show a noticeable difference in the value of polarization depending on the adopted cloud-particle model. We conclude that the availability of observational data in a wide range of phase angles can provide critical constraints on the particle shape.

1 Introduction

In our previous publications [2, 3], we have used Jupiter as a "testing ground" and have demonstrated that the optical properties of cloud particles (especially the refractive index) cannot be reliably estimated on the basis of measurements performed in a narrow range of phase angles. Using the results of ground–based spectropolarimetric observations of the center of the Jovian disk [4], we found that the assumed shape of atmospheric aerosols is essential in estimating their microphysical properties. Specifically, varying the assumed particle shape resulted in significant changes in the retrieved refractive index, size, and atmospheric structure. In this paper, we analyze how an extension of the phase angle range can help in the determination of the particle shape and, as a consequence, yield more accurate retrievals of the optical properties of cloud particles.

2 Atmosphere models and computational techniques

A detailed analysis of ground-based observation of Jupiter, using the model of a cloud layer composed of spherical cloud particles was performed in [1]. Subsequently, the case of nonspherical particles was considered in [2, 3]. In all three publications, we used spectropolarimetric data for the center of the Jovian disk collected by Morozhenko [4] at wavelengths λ = 0.423, 0.452 0.504, 0.600, and 0.798 μm in the phase angle range $0° < \alpha < 11°$. Two models of the Jovian atmosphere were considered: (A) a homogeneous semi-infinite layer composed of gas and cloud particles; and (B) a two-layered medium with a layer of pure gas of optical thickness τ_0 on top of a semi-infinite homogeneous layer composed of gas and cloud particles. The semi-infinite homogeneous layer was supposed to consist of spheres, randomly oriented oblate or prolate spheroids, or randomly oriented cylinders with varying aspect ratios *E*. Particle polydispersity was characterized by a simple gamma size distribution. As a result, a good agreement between the observational data and the model results was found for the values of the real part of the refractive index m_R, the effective radius r_{eff}, the effective variance v_{eff}, and the model of atmosphere listed in Table 1.

Table 1. Best-fit microphysical parameter values for various particle models, derived in [1–3]

Shape	E	m_R	r_{eff}, μm	v_{eff}	Model
Spheres	1.0	1.386	0.385	0.45	A
Oblate spheroids	1.3	1.45	0.35	0.40	B
Oblate spheroids	1.5	1.52	0.40	0.35	B
Prolate .spheroids	1.3	1.50	0.35	0.30	B
Prolate spheroids	1.5	1.54	0.90	0.30	A
Oblate cylinders	1.3	1.43	0.47	0.40	B
Prolate cylinders	1.3	1.49	0.60	0.40	B

To interpret polarimetric data for the center of a planetary disk, it is necessary to calculate the degree of linear polarization $P = -Q/I$. The first two components, I and Q, of the Stokes vector **I** of the reflected radiation are given by

$$I(-\mu, \varphi) = \mu_0 R_{11}(\mu, \mu_0, \varphi - \varphi_0), \tag{1}$$

$$Q(-\mu, \varphi) = \mu_0 R_{21}(\mu, \mu_0, \varphi - \varphi_0), \tag{2}$$

where (μ_0, φ_0) and $(-\mu, \varphi)$ specify the directions of light incidence and reflection, respectively, and R_{11} and R_{21} are elements of the 4×4 Stokes diffuse reflection matrix **R**. In our computations, we first used the T-matrix approach to determine the elements of the single-scattering matrix **F** [5]. Then the elements R_{11} and R_{21} for model A were computed by means of a numerical solution of the Ambartsumian's nonlinear integral equation [6]. The overlaying gas layer in model B was incorporated by means of a computational algorithm based on the invariant imbedding technique as described in [7].

3 Results of computations and discussion

We performed calculations of the degree of linear polarization for the center of a planetary disk ($\mu_0 = \cos\alpha$, $\mu = 1$) for the range of phase angles $0° \le \alpha \le 90°$, spectral interval of $\lambda = 0.423 \div 0.798$ μm, and the models of cloud particles listed in the Table 1. The results of the computations are shown in Figs. 1 and 2. Figure 1 depicts the calculated phase-angle dependences of the degree of linear polarization for $0º \le \alpha \le 30º$ (left-hand column), $30° \le \alpha \le 60°$ (middle column), and $60° \le \alpha \le 90°$ (right-hand column). For $\alpha > 15°$ and all wavelengths, one can see a significant difference in the behavior of the polarization curves depending on the adopted cloud-particle model. For instance, in the wavelength range $0.423 \div 0.504$ μm in the case of spheres, the negative polarization has a minimum absolute value (compared to the cases of other particle shapes), and the sign of polarization changes twice (at $\alpha \approx 15$–20 and $30°$). For longer wavelengths, the sign of polarization changes once at $\alpha \approx 25°$, and then the magnitude of the positive polarization increases with increasing phase angle. In the case of prolate spheroids with $E = 1.5$, for $\lambda = 0.423 \div 0.504$ μm the behavior of polarization is somewhat similar to that in the case of spheres, but in a longer wavelength range polarization is always negative. For other particle shapes, one can see that the absolute value of the negative polarization first increases with increasing phase angle, reaches its maximum value, and then starts to decrease. At some value of phase angle, the polarization becomes positive and increases with increasing phase angle. However, for different particle shapes we see a noticeable difference in the position of minumum of the negative polarization and the polarization inversion point, as well as in values of polarization. It is possible that such different behavior of polarization at the center of a disk for $\alpha > 15°$ is caused by a specific behavior of the single-scattering matrix element F_{12}. To confirm this supposition, we include Fig. 2 which depicts the calculated dependences of $-F_{12}/F_{11}$ on the scattering angle Θ $(= \pi - \alpha)$ for all cloud-particle models used.

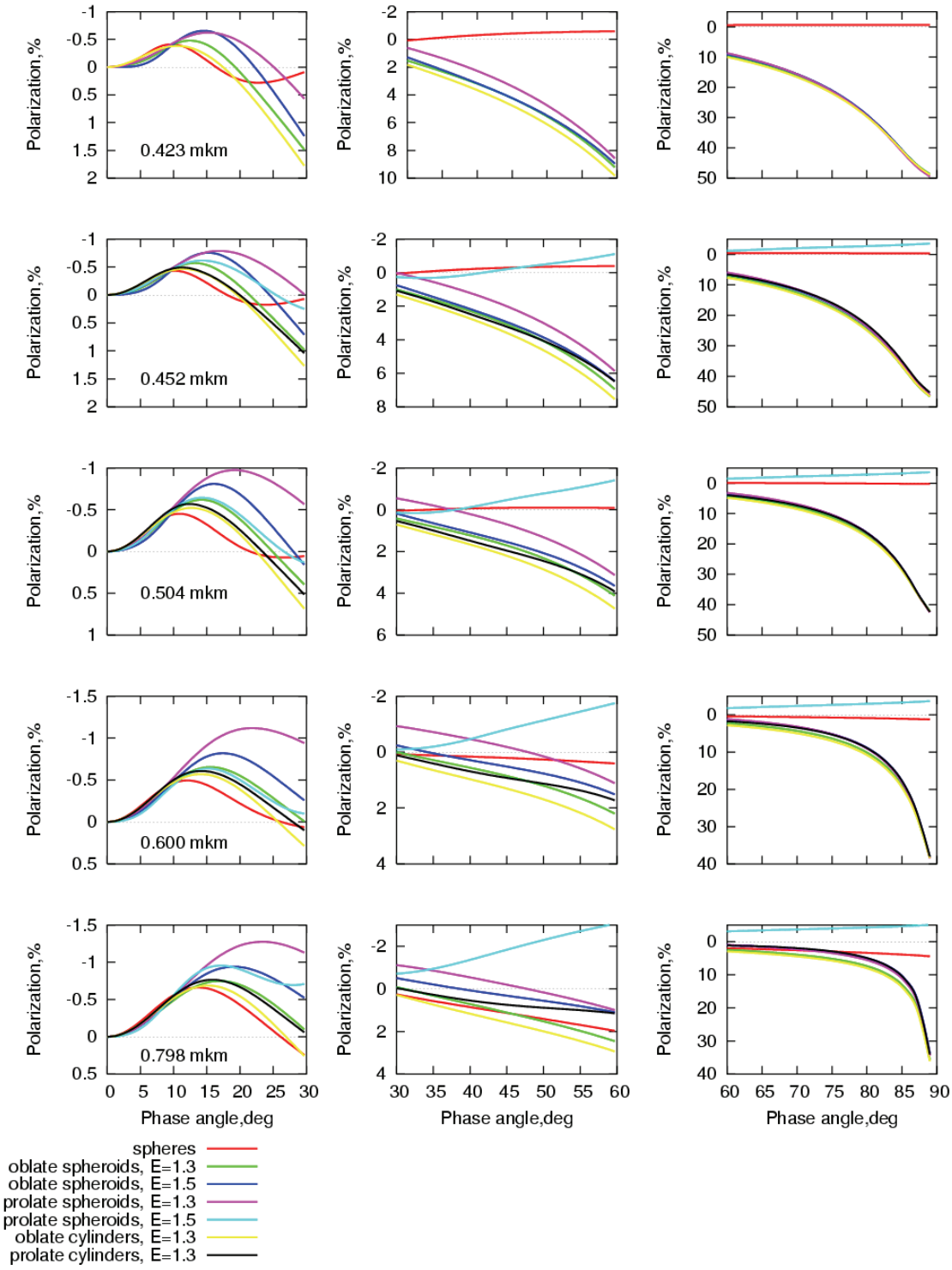

Figure 1. Calculated phase-angle dependence of the polarization at the center of a planetary disk for $0° \leq \alpha \leq 30°$ (left-hand column), $30° \leq \alpha \leq 60°$ (middle column), and $60° \leq \alpha \leq 90°$ (right-hand column).

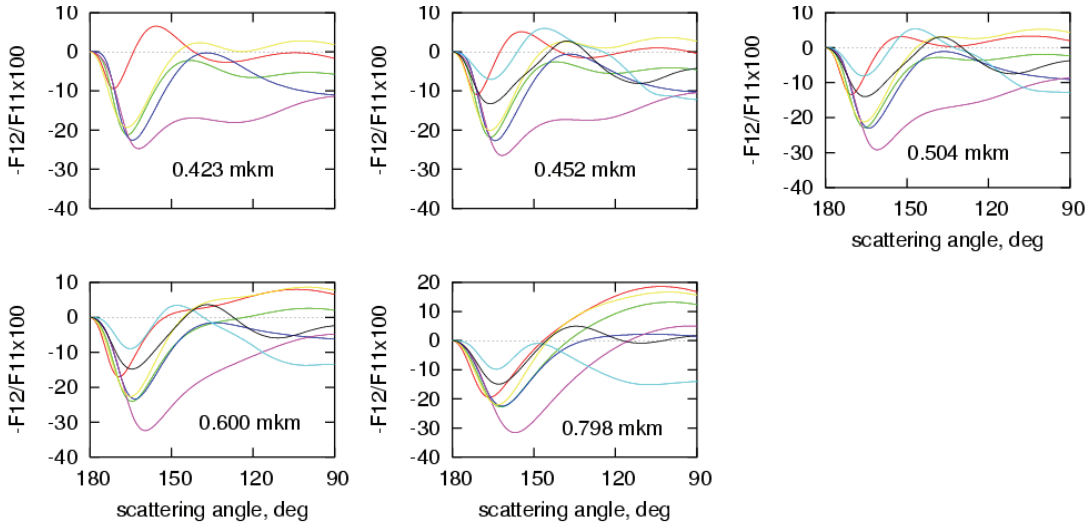

Figure 2. Calculated scattering-angle dependence of the scattering-matrix element ratio $-F_{12} / F_{11}$.

4 Conclusion

Thus, we have demonstrated that phase-angle dependences of the polarization at the center of a planetary disk calculated for various particle cloud models exhibit noticeable differences at larger values of the phase angle. So, we can conclude that the availability of observational data obtained in a wide range of phase angles, e.g., from spacecraft, can provide the necessary constraints on aerosol particle shape and make the problem of the interpretation of polarimetric observations better defined.

Acknowledgments

This research was sponsored by the NASA Radiation Sciences Program managed by Hal Maring.

References

1. M. I. Mishchenko, "Physical properties of the upper tropospheric aerosols in the equatorial region of Jupiter", *Icarus* **84**, 296-304 (1990).
2. J. M. Dlugach and M. I. Mishchenko, "The effect of particle shape on microphysical properties of Jovian aerosols retrieved from ground-based spectropolarimetric observations", *JQSRT* **88**, 37-46 (2004).
3. J. M. Dlugach and M. I. Mishchenko, "The effect of aerosol shape in retrieving optical properties of cloud particles in the planetary atmospheres from the photopolarimetric data. Jupiter", *Solar Syst. Res.* **39**, 102-111 (2005).
4. A. V. Morozhenko,. "Results of polarimetric investigations of Jupiter", *Astrometriya Astrofizika* **30**, 47–54 (1976) (in Russian).
5. M. I. Mishchenko and L. D. Travis, "Capabilities and limitations of a current FORTRAN implementation of the *T*-matrix method for randomly oriented rotationally symmetric scatters", *JQSRT* **60**, 309–324 (1998).
6. W. A. de Rooij, *Reflection and transmission of polarized light by planetary atmospheres*, PhD dissertation (Amsterdam: Vrije Universiteit, 1985).
7. M. I. Mishchenko, "The fast invariant imbedding method for polarized light: computational aspects and numerical results for Rayleigh scattering", *JQSRT* **43**, 163–171 (1990).

Extinction coefficient in absorbing media: a theoretical and numerical study

Stéphane Durant[1], Jean-Jacques Greffet[1], Olivier Calvo-Perez[2] and Nicolas Vukadinovic[2]

[1] *Laboratoire d'Energétique Moléculaire et Macroscopique, Combustion;*
Ecole Centrale Paris, Centre National de la Recherche Scientifique
92295 Châtenay-Malabry Cedex, France
[2] *Direction Général Technique; Dassault Aviation;*
78 Quai Marcel Dassault St Cloud 92214, France

Abstract

We report a theoretical and numerical investigation of the light scattering in an absorbing medium with randomly distributed scatterers. The extinction coefficient is derived from the imaginary part of the effective index derived using a diagrammatic approach. The accuracy of the result is assessed by comparison with a numerical solution of Maxwell's equations that fully accounts for multiple scattering.

1 Introduction

Modelling transport of light in scattering random media when the host medium is absorbing is a fundamental topic of practical importance. In this paper, we focus on the extinction coefficient in absorbing media containing a random distribution of scatterers of arbitrary size. No general satisfying form of the extinction coefficient has been derived yet. Indeed, the presence of the particles modifies the field in the host medium. Hence the absorption in the host medium is also modified by the presence of particles. In other words, particles and host medium cannot be treated as two uncoupled systems. This entails that the scattering and absorption cross-section are not intrinsic characteristics of the particle when the latter is embedded into an absorbing medium. This issue has already been raised by Bohren *et al.*[3] and more recently by Videen *et al.*[2].

The purpose of this paper is to introduce a new model of the extinction coefficient in absorbing media based on the effective medium theory (EMT) arising from the well developed multiple scattering theory[4, 5, 6]. The second section outlines the key ideas of our model. In order to assess the validity of the model, we have implemented a numerical solution of Maxwell equations for a set of 2D particles (cylinders) embedded in an absorbing host medium. We solve the problem for a large number of realizations and perform an ensemble average over typically 500 realizations. Section 3 is devoted to the outline of this procedure. Section 4 shows an example of comparison between numerical simulations and theory.

2 Diagrammatic expansion of the extinction coefficient

The key of our approach is to derive an equation for the mean field in a random medium. This equation has the form of a Helmholtz equation with an effective refractive index. As this effective refractive index is homogeneous, the energy flux due to the mean field coincides with the contribution of the collimated part of the specific intensity. The extinction coefficient K_{ext} is simply related to the imaginary part of the effective wavevector $Im(k_{eff})$:

$$K_{ext} = 2Im(k_{eff}). \tag{1}$$

Within the independent scattering approximation, we show[1] that the effective wave vector is given by:

$$k^2 = k_h^2 + i\frac{f}{v_p}\frac{4\pi S_{k_h}(0)}{k_h}, \tag{2}$$

where $S_{k_h}(0)$ is the scattering matrix as defined by Bohren and Huffman [7] evaluated in the forward direction, v_p is the volume of a particle, f is the filling ratio of particles and the wavevector in the matrix is $k_h = n_h k_0$ where n_h is the host medium refractive index and k_0 is the wavenumber in free space. The effective medium theory can be improved by taking into account the correlation between two particles[6, 1]. It yields the following equation for the effective wavevector:

$$\begin{aligned} k^2 &= k_h^2 + i\frac{f}{v_p}\frac{4\pi S_{k_h}(0)}{k_h} \\ &+ \left(i\frac{f}{v_p}\frac{4\pi S_{k_h}(0)}{k_h}\right)^2 \frac{1}{k}\int_0^\infty e^{ik_h r}\sin(kr)g_2(r)dr, \end{aligned} \tag{3}$$

where $g_2(r)$ is the pair-correlation function[5, 1]. This expression is strictly rigorous only for small particles and assuming a scalar behavior of the corrective terms due to the correlations[1]. We note that this equation can be cast in the form:

$$k^2 = k_0^2 n_{eff}^2(\omega, k), \tag{4}$$

where n_{eff} is an effective index that depends on ω so that the medium is dispersive and on k so that the medium is non-local. In what follows, we will refer to this model as a non-local effective medium. The non-local correction has to be taken into account when correlations cannot be ignored, this is the so-called dependent scattering regime. For the sake of comparison, we report the phenomenological expression introduced by Kuga *et al.*[8] :

$$K_{ext} = 2k_0 Im(n_h)(1-f) + \frac{f}{v_p}C_{ext}, \tag{5}$$

where C_{ext} is the extinction cross section of a scatterer evaluated as if the host medium was not absorbing. This model is based on the simple idea that absorption is a local phenomenon and that the field is essentially uniform. Within this approximation, absorption in the host medium is proportional to the host volume. There are many cases where this approximation is very good. Yet, it is clear that if the particle has a resonance, the field at the boundary is enhanced. In turn, this produces a strong field in the host medium along the boundary. It follows that the presence of the particle may increase the absorption in the host medium. This discussion suggests that it is necessary to account for the exact scattering operator of the particle including the losses of the host medium. In order to compare the 2D numerical simulation with the effective medium theory, we have developped a 2D version of the effective medium theory[1].

3 Derivation of the extinction coefficient from a numerical simulation

We outline in this section the derivation of the extinction coefficient from the exact numerical solution of Maxwell's equation in a slab with a thickness e containing a 2D random distribution of dielectric disks. The host medium is absorbing. We consider a p-polarized incident plane wave. The geometry described in Fig.1 is periodic along the slab with a period L large compared to the wavelength and the particle size in order to avoid edge effects. The periodic system diffracts the incident plane wave into a large number of discrete directions given by the transverse wave number $k_{x,p} = k_{inc,x} + p\frac{2\pi}{L}$, where p is the diffraction order. Disk particles are randomly distributed in the slab with the condition that particles cannot overlap and that each

disk is entirely in the rectangular box. For each realization of a random distribution of particles, the reflected and transmitted field is computed exactly using the method of moment as it was described in ref.[9]. Since the scatterers are randomly located, each realization produces a speckle pattern. When considering the set of solutions corresponding to a set of realizations, it proves useful to split the field as the sum of the statistical average and a fluctuating component:

$$\mathbf{E} =< \mathbf{E} > +\delta\mathbf{E}, \tag{6}$$

where $< \delta\mathbf{E} >= 0$. Between 200 and 1000 realizations were generated to compute the average field. When averaging the intensity, the speckle pattern is smoothed and one finds the scattered intensity pattern. When averaging the field, the speckle structure disappears and the mean field is the response of the average system with the effective index. For a slab, we find two plane waves specularly transmitted or reflected.

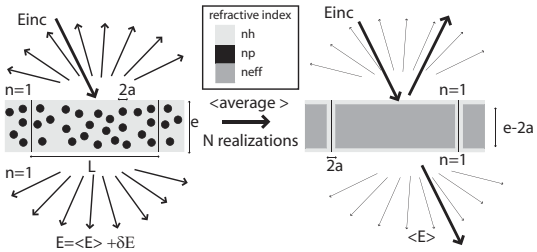

Figure 1: Geometry of the system

4 Comparison between numerical simulations and approximate theories

We have investigated the extinction coefficient in an absorbing medium when the correlation effects are important. Results are displayed in Fig.2 for different cases. We shall discuss the effect of dielectric contrast, losses in the particles and correlation between particles. Our main conclusions can be summarized

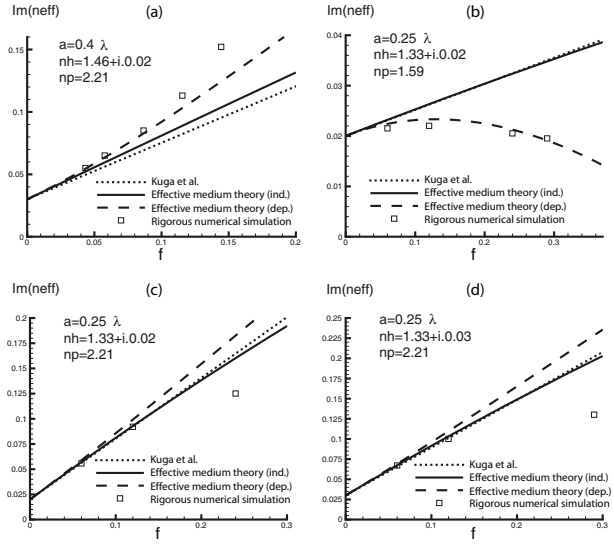

Figure 2: Comparison between theory and numerical simulation

as follows. The comparison shows a very good agreement in the independent scattering regime. When the dielectric contrast between particles and the host medium is small, the EMT model which takes into account the correlation between pair of scatterers is in excellent agreement with the exact result up to 30% as seen in Fig.2. For a filling ratio above 5%, we find that for small particles, the effect of correlations leads to a smaller extinction coefficient than predicted by the independent scattering approximation, while the tendency is reversed for large particles. It is worth noticing that there is a particle size for which the correlation effects are negligible up to 15 $\%$. It is also observed that in general, the absorption of the host medium reduces the effect of the correlations allowing one to use the independent scattering approximation for larger filling ratio. The case of large dielectric contrast, large volume fraction and size parameter on the order of one (the so-called resonance regime) remains an open issue.

5 Conclusion

The evaluation of the extinction coefficient for particles embedded in an absorbing medium is a long standing problem. Using the multiple scattering theory in random media, we have derived the expression of the extinction coefficient from the imaginary part of the effective index for two-dimensional and three-dimensional cases. Taking into account correlation between particles position yields a non-local effective index. In order to assess the accuracy of the model, we have presented in this paper a direct comparison with two-dimensional exact solution of Maxwell's equations in an absorbing slab filled with randomly distributed scatterers.

Bibliography

[1] S. Durant, O. Calvo-Perez, N. Vukadinovic and J.-J. Greffet, "Light scattering in absorbing media: diagrammatic expansion of the extinction coefficient", To be published in J. Opt.Soc.Am.A (2007)

[2] G. Videen, W. Sun, " Yet another look at light scattering from particles in absorbing media", Appl.Opt. **42**, 6724-6727 (2003)

[3] C.F. Bohren and D.P. Gilra, "Extinction by a Spherical Particle in an Absorbing Medium", Journal of Colloid and Interface Science, **72**, 215-221 (1979).

[4] J.B. Keller, *Stochastic equation and wave propagation in random media*, in "Stochastic processes in mathematical physics and engineering", Proc. Symposium Appl. Math., New-York, 145-170 (1964)

[5] U. Frisch, *Wave Propagation in Random Media*, in "Probabilistic Methods in Applied Mathematics", In Bharuch-Reid, editor, Academic Press, **1**, (1968).

[6] S. Durant, "Propagation de la lumière en milieu aléatoire. Rôle de l'absorption, de la diffusion dépendante et du couplage surface-volume", Ph.D thesis, Ecole Centrale Paris, France, (2003).

[7] C.F. Bohren and D.R. Huffman, *Absorption and Scattering of Light by Small Particles*, Wiley-Interscience Publication (1983).

[8] Y. Kuga, F.T. Ulaby, T.F. Haddock and R.D. DeRoo, "Millimeter-wave radar scattering from snow 1. Radiative transfer model", Radio Science, **26**, 329-341 (1991).

[9] L. Roux, P. Mareschal and N. Vukadinovic, J.-B. Thibaud, and J.-J. Greffet, "Scattering by a slab containing randomly located cylinders: comparison between radiative transfer and electromagnetic simulation", J. Opt. Soc. Am. A **18**, 374-384 (2001).

Monte Carlo for Very Thin Layered Media

Reginald Eze[1], Sunil Kumar [1], Nabil Elkouh[2], Paul Sorenson[2], and Roger Hill[2]

[1] Polytechnic University, Department of Mechanical, Aerospace and Manufacturing Engineering,
6 Metro Tech Center, Brooklyn, NY 11201 USA
tel: +1 (718) 260-3270, fax: +1 (718) 260-3532, e-mail:cjkstar@gmail.com
[2] Creare Inc., P.O. Box 71 Hanover, NH 03755 USA
tel: +1 (603) 643-3800, fax: +1 (603) 643-4657

Abstract

Many modern applications of lasers involve modeling of radiation energy transport through very thin layers. The interactions of continuous wave and pulsed lasers with skin in dermatological use related to surgery and cosmetic procedures are examples of such. Highly scattering thin layers in skin are best modeled by Monte Carlo method since their interfaces are not perfectly planar and the thicknesses are non-uniform. Due to scattering, interference and other thin film wave effects are not important. Additionally, the common diffusion approximation utilized extensively in modeling bio-medical laser transport is invalid because of the proximity of interfaces where the diffusion approximation is known to be inaccurate.

Traditional Monte Carlo models may, however, inaccurately capture the effect of thin layers. As an example, the very thin epidermis with its highly absorbing melanin is known to influence the laser penetration significantly. If the Monte Carlo model is implemented without special features then the results of the simulation would show no effect of the outer thin layer since the path length of most photons would be significantly larger than the layer thickness and the resulting predicted photon travel would simply not notice the presence of the layer.

In this paper we present the results of using Monte Carlo to accurately model transport of radiation through very thin layers using both the traditional Monte Carlo and that with the new features incorporated. The results have profound implications in the diagnostic and therapeutic applications of laser in biomedicine and surgery.

1 Introduction

Monte Carlo simulations have become increasingly important in developing new diagnostic and therapeutic applications of laser in biomedicine and surgery. Monte Carlo computational models have been used to chart new direction in the development and advancement of new clinical applications, new clinical procedures, resulting in better clinical outcomes. For instance, Monte Carlo based models are being used to develop and optimize treatment procedures, speed wound healing, minimize pain, reduce subjacent tissue damage or injury and predict the extent of tissue damage resulting from a particular thermal treatment method.

Many clinical conditions rely on the ability to deliver energy to biological tissue in order to modify the properties or health of the tissue. Monte Carlo based laser diagnostics [1] and therapeutics [2] applications have become widely accepted as the benchmark for the management and treatment of many clinical conditions. Modern therapies require accurate deposition of thermal energy into biological tissues and laser based therapies have become widely accepted. Photodynamic therapy, selective photothermolysis, laser surgery, tissue welding and cryosurgery are examples of this laser based modern therapies. These therapeutic procedures require accurate modeling of transient deposition and absorption of energy in the regions of interest in the affected tissue. Most previous studies on numerical models that are used to predict energy distribution in illuminated biological tissue layers during laser therapies and diagnostics have been studied extensively. Parabolic diffusion approximation [3] and Monte Carlo simulation models [4] have been considered by many researchers, but models to predict precisely deposition of energy in very thin tissue layers are yet to be fully developed.

For optically thin tissues like the epidermis and the epithelial layer of the esophagus, numerical models used to predict energy distributions fail partly because of the microscale nature of these layers. Results from traditional Monte Carlo simulations have been shown not to match those obtained from

parabolic diffusion results for tissue samples of thickness less than their mean free path [5]. Experimental investigations of short pulse laser transport through tissue have indicated that although the diffusion approximation seems adequate for very thick tissue samples, it does not match experimental results in other cases [6]. Also when the energy is pulsed, has very short time scale with attendant high heat fluxes, current approaches used in modeling biological thermal phenomena are not proficient at capturing important physical events occurring at or near boundaries or tissue interfaces.

In this paper, laser light scattering for thin layers has been examined for both the traditional Monte Carlo and that with new features added and its effect on the reflection, transmission, and absorption presented.

2 Method

Monte Carlo simulation technique is a common statistical method used to model light propagation in tissue and is based on the concept that photons can be scattered, absorbed or exit the model under investigation Fig. 1 [7].

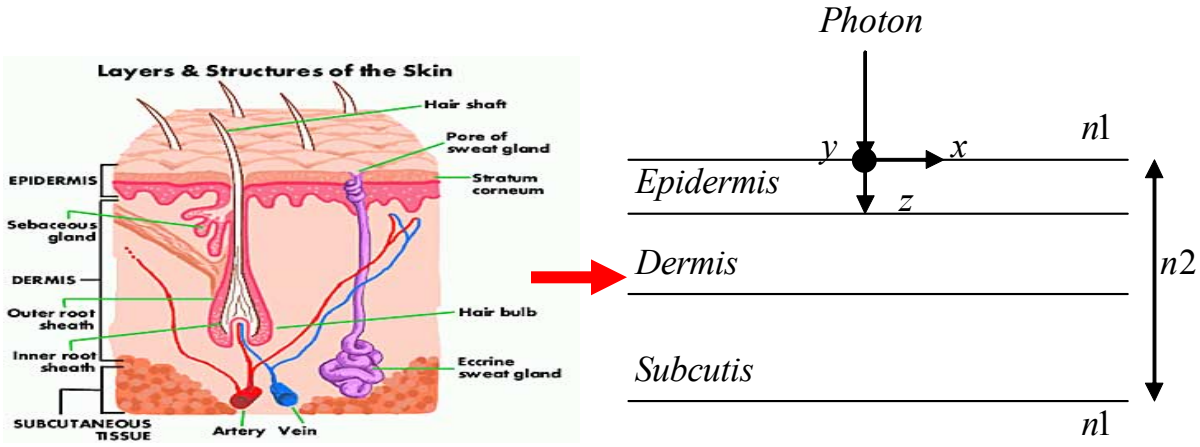

(a) (b)

Figure 1: (a) Typical skin sample [7], (b) Multi layer skin model used in the simulation.

The simulation process is initiated by launching light beam which is considered to be split into many photon packets, each with initial weight, W, into the biological medium in a given direction. After a distance, L, the photon packet is assumed to interact with the medium, and a fraction, ΔW of this packet is deposited at the point of interaction after which a new direction for the photon packet is simulated. A repetition of this process continues until the photon packet is absorbed or exits the medium. Termination roulette is used to avoid simulating small weights. The path length between two successive interactions or scattering event L, the deflection angle after the interaction in the polar and azimuthal directions θ & φ, respectively, and the deposited fraction at j^{th} interaction are determined by the following equations [8]:

$$L = -\frac{\ln(R1)}{\mu_a + \mu_s} \tag{1}$$

$$\theta = f^{-1}(R2) \tag{2}$$

$$\varphi = 2\pi(R3) \tag{3}$$

$$\Delta W(j) = W(j-1)\frac{\mu_a}{\mu_a + \mu_s} \tag{4}$$

$$f(\theta) = \frac{\int_0^{\theta} p(\varphi)\sin(\varphi)d\varphi}{\int_0^{\pi} p(\varphi)\sin(\varphi)d\varphi} \tag{5}$$

For time resolved analysis, the total optical path length of each photon bundle inside the medium is converted to time of flight, *t*, of photon by using the speed of light of the medium c thus:

$$t = \frac{L_{total}}{c} \tag{6}$$

3 Results and Discussion

The distribution of photon energy absorbed in each layer is shown in Fig. 2, while reflection and transmittance from the layered media is shown in Fig. 3. The top surface of the epidermal layer is considered as a black or a reflecting boundary. Black boundary, for the purpose of this work implies that a photon packet once inside the tissue cannot be reflected out to the surrounding media. This is equivalent to insulation boundary condition. For reflecting boundary the photon after multiple scattering and not being absorbed in the tissue escapes from the tissue surface. The traditional Monte Carlo profile has a continuous photon absorption distribution. The exact transition from layer to layer is not dramatic as there is no clear dividing line between layers, despite the large difference in layers absorption contrast.

For the Monte Carlo with special features shown in Fig. 2 as 'New' and 'Traditional', the absorption profile in the layered skin media has a sharp discontinuity at each layer to layer interface. Photon interaction with the turbid skin model is captured explicitly at each level and on each layer, and gives a vivid picture of events occurring during each step of the simulation. In the traditional method, there is no clear delineation of photon absorption between respective layers.

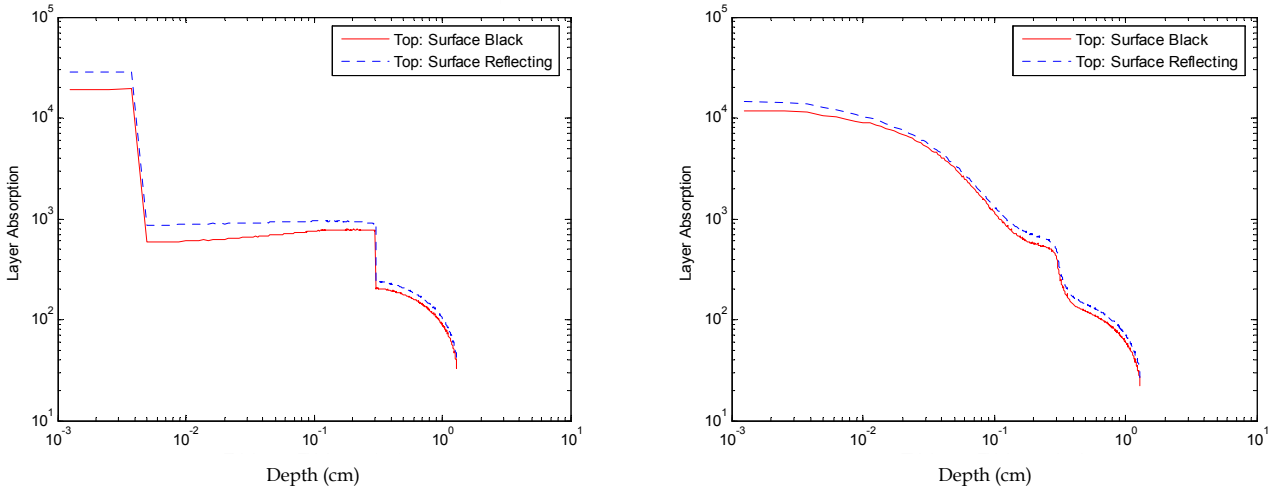

Figure 2: (a) Monte Carlo with new features added (b) Traditional Monte Carlo: Energy deposition in epidermis (L1), dermis (L2) and subcutaneous (L3) layers for both reflecting and non-reflecting epidermal layer with L1 = 0.005 cm, L2 = 0.30 cm, L3 = 0.99 cm, μ_a = 8.8, 0.26 and 0.07 cm^{-1} for epidermis, dermis and subcutis, μ_a = 20 cm^{-1} for all layers, and n1 = 1.0, and n2 = 1.37.

The reflection and transmission intensity for Monte Carlo with new features added and the traditional Monte Carlo for situation where the epidermal layer is black and reflecting is shown in Fig. 3. This enhancement was made possible by using the optical distance of each layer as intermediate start and end boundary condition and hence photon path length traveled after an interaction event is captured in the layered where the event occurred. The result presented above may provide a route to more realistic

determination of energy deposition in very thin layered media, noting however that these results are also dependent upon chosen optical properties, age, race and physiological factors of each individual.

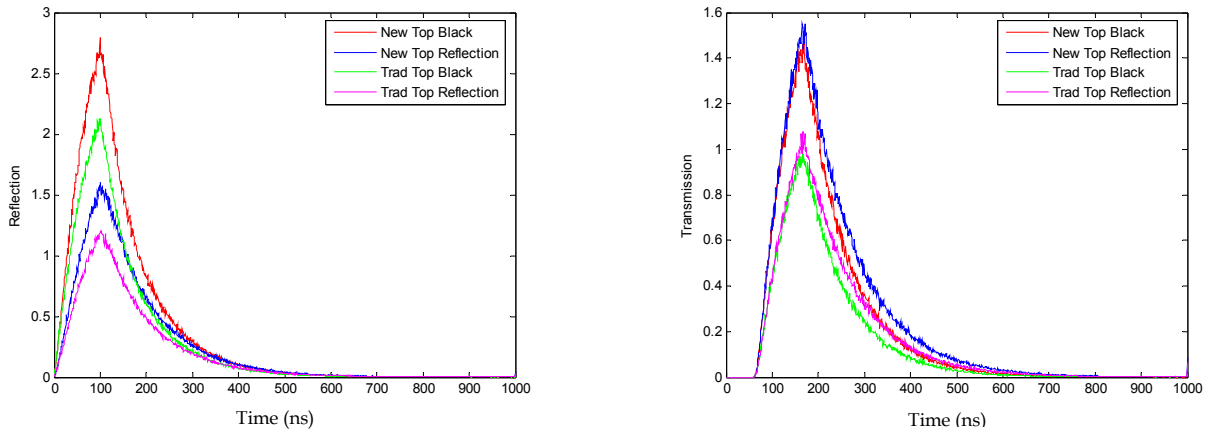

(a) (b)

Figure 3: (a) Reflection intensity and (b) Transmission intensity: For epidermis (L1), dermis (L2) and subcutaneous (L3) layers for both reflecting and non-reflecting epidermal layer with L1 = 0.005 cm, L2 = 0.30 cm, L3 = 0.99 cm, μ_a = 8.8, 0.26 and 0.07 cm^{-1} for epidermis, dermis and subcutis, respectively, μ_a = 20 cm^{-1} for all layers, and n1 = 1.0, and n2 = 1.37.

4 Conclusion

In this paper, we have presented a novel Monte Carlo simulation with features that calculates photon propagation and energy deposition, reflection and transmission in multi layered skin explicitly for each layer. This result will improve our understanding of light tissue interaction and its effect on dermatological applications relating to surgery and skin rejuvenation.

Acknowledgments

The authors would like to acknowledge the support of Thermal Optics Lab., Dept. of Mechanical Eng., Polytechnic University, Brooklyn, NY, USA. Authors also like to acknowledge the support from AGEP.

References

[1] Thueler, P. Charvet, I. Bevilacqua, F. Ghislain, M. Ory, G. Marquet, P., Meda, P. Vermuelen, B. & Depeursinge, C. "In Vivo Endoscopic Tissue Diagnostics Based on Spectroscopic Absorption, Scattering, & Phase Function Properties", J. of Biomedical Opt., **8**, 495-503 (2003).

[2] Anderson R R. and Parish, J. A. "Selective Photothermolysis: Precise Microsurgery by Selective Absorption of Pulsed Radiation", Science, **220**, 524-527 (1983).

[3] Gemert, M. J. C. Jacques, S. L., Sterenborg, H. J. C. M. and Star, W. M. "Skin Optics", IEEE Trans. Biomed. Eng., **36**, 1146-1154 (1989).

[4] Wilson, B C. "A Monte Carlo Model for the Absorption and Flux Distributions of Light in Tissue", Med. Phys., **10,** 824-830 (1983).

[5] Gandbakche, A. H. Nossal, R. and Bonner, R. F. "Scaling Relationships for Theories of Anisotropic Random Walks Applied to Tissue Optics", Applied Optics, **32**, 504-516 (1993).

[6] Yodh, A. and Chance, B. "Spectroscopy and Imaging with Diffusing Light", Physics Today, **48,** 34-40 (1995).

[7] Healthy-Skin-Guide, http://www.healthy-skin-guide.com/skin-diagram.html

[8] Yamada, Y., 1995, "Light-tissue Interaction and Optical Imaging in Biomedicine, Annual Review of Heat Transfer, **6**, 1-59 (1995).

Modeling lunar reflectance spectra

Ye. Grynko,[1] Yu. Shkuratov,[1] and G. Videen[2,3]

[1]*Astronomical Institute of Kharkov V.N. Karazin National University, 35 Sumskaya St., Kharkov, 61022, Ukraine, tel: +38(057)7075063, e-mail: egrinko@hotmail.com*
[2]*Astronomical Institute "Anton Pannekoek", University of Amsterdam, Kruislaan 403, 1098 SJ Amsterdam, The Netherlands*
[3]*Space Science Institute, 4750 Walnut St. Suite 205, Boulder CO 80301, USA*

Abstract

We study the dependence of the reflectance spectra of regolith-like surfaces on the phase angle. A computer model based on the ray optics approximation is used. Our calculations reveal a strong non-monotonous dependence of the spectral slopes on the phase angle. Changing observation geometry also influences the depth of the absorption bands. We also calculate the phase angle distribution of the average path lengths <*L*> that rays pass through in the medium between the points of entrance and emergence.

1 Introduction

Progress in the remote sensing of planets and their satellites requires better understanding of light scattering by their regoliths. In particular, interpretation of the reflectance spectroscopy data can provide information about chemical and mineral properties of planetary surfaces. There are unresolved questions that should be considered to make this interpretation more accurate. For instance, it is important to estimate contributions of single particles and multiple scattering between particles at different phase angles. Important problems include transforming photometric data to the same illumination/observation geometry of illumination and accounting for the polarimetric effect on spectra.

During photometric observations of a planet with a spacecraft, the illumination and observation conditions change. The principal parameter for characterizing the conditions is the phase angle α. The continuum slope and parameters of the absorption bands can be different for the same portion of a planetary surface, if spectra are taken under different conditions. Examples are spectrophotometric measurements of the Moon, asteroids Eros *in situ* [1] and Itokawa [2]. Although laboratory experiments have been coupled with regolith structure models [3,4], measurements of lunar samples [5], and telescopic observations of the Moon [6], the solution of the problem is not complete. The interpretation of existing space mission data as well as planning future projects warrant more detailed analyses of the role of photometric geometry in the formation of the reflectance spectra.

We here use light scattering computer simulations to study the phase angle and polarimetric effects on lunar spectra. To simulate light scattering in particulate media we use a ray tracing model [7, 8].

2 Computer experiment description

A detailed description of the ray-tracing model used in this study can be found in [7,8]. To generate random particles with irregular shape we use an auxiliary 3-D random Gaussian field (RGF) [7]. The model of the particulate medium is characterized with the following parameters: volume fraction of particles ρ (packing density), the complex refractive index of the material ($m = n + ik$), and the average particle size d. In our samples the sizes of particles are almost the same, varying from 25 to 1500 μm. The

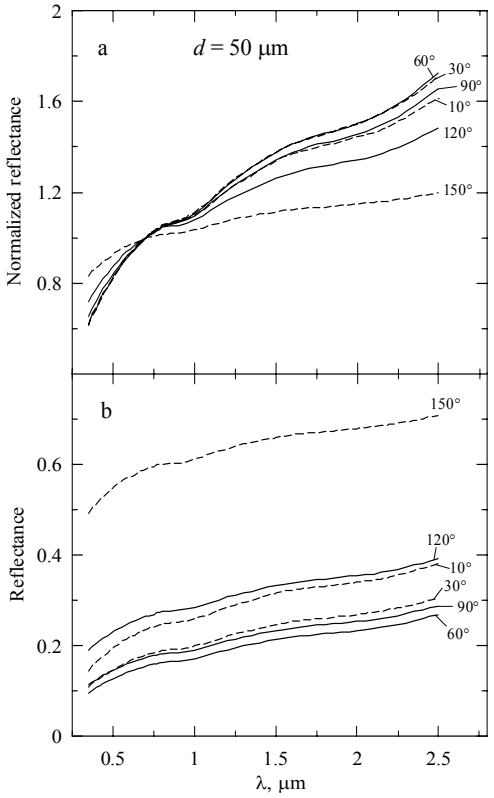

Figure 1: Spectral dependences of reflectance and normalized reflectance at different phase angles for a medium composed of particles d = 50 μm.

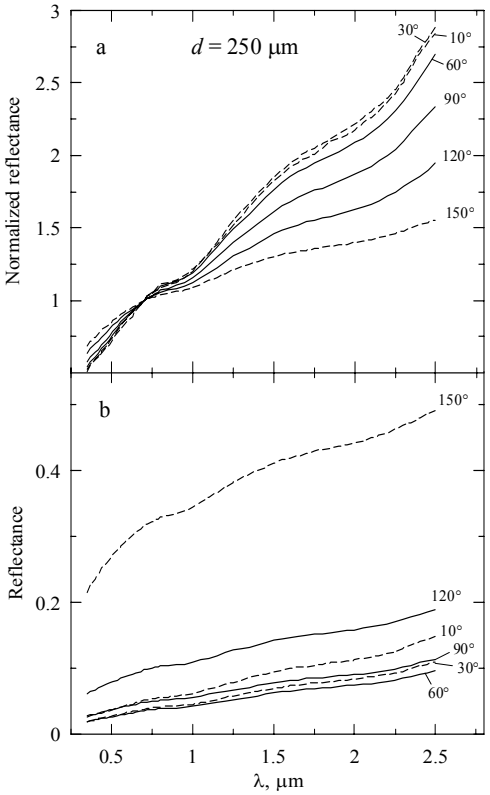

Figure 2: Same as Figure 1 for d = 250 μm.

packing density of particles in all experiments equals to ρ = 0.1. Natural powders usually are denser and our algorithm allows packing up to ρ = 0.4. However, lower density significantly simplifies simulations and, in general, the parameter ρ plays a secondary role in spectral reflectance (e.g., [9]).

In our ray tracing calculations we used 10^6 – 10^7 rays. Each ray is traced from facet to facet until it leaves the particulate surface after a sequence of interactions with the particulate medium. At non-zero absorption each ray propagated inside a particle can be absorbed on the way between two facets with probability exp(-τ), where $\tau = 4\pi k(\lambda) l/\lambda$, l is the path length between facets, and λ is the wavelength. For $k(\lambda)$ we used an average dependence for lunar mare material obtained from spectral observations of the Moon [9]. The real part n of the complex refractive index is considered as a constant, we use n = 1.6.

In order to determine angular scattering characteristics, the phase angle range is divided into a number of angular bins. The number of rays normalized by the solid angle of a given bin is the intensity of scattered light at the bin. The reflectance of a particulate surface at a given phase angle is defined as a ratio of the bin intensities corresponding to arbitrary k and $k = 0$. This simulates comparison with a Lambertian surface. Calculation of reflectance for a set of wavelengths at given photometric geometry provides a spectrum. We made calculations for a fixed incidence angle i = 70° and changing angle of emergence e. Phase angle α varies within 0 – 160°. Scattered intensity is collected in the narrow sector containing a plane perpendicular to the average surface.

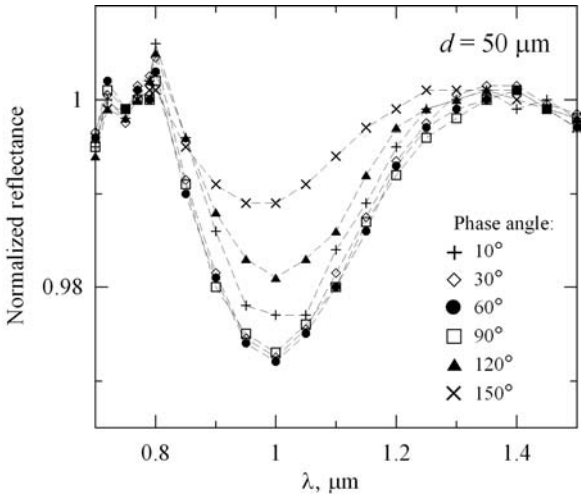

Figure 3: Surface reflectance divided by continuum near the 1 μm absorption feature at different phase angles. The size of constituent particles is d = 50 μm.

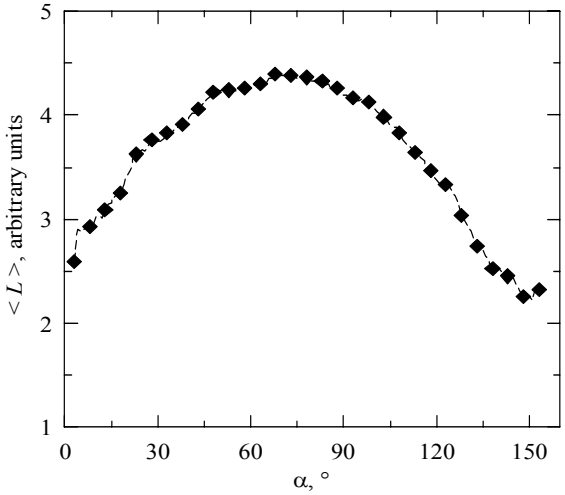

Figure 4: Phase-angle distribution of the average path lengths <L> that rays pass through between the entrance and emergence points of the particulate medium.

3 Results and discussion

Figures 1 and 2 show (a) normalized and (b) absolute reflectance spectra for media consisting of particles with whose average size is 50 and 250 μm measured at λ = 0.7 μm. At first, we note that the surface reflectance becomes lower as particle size increases. This is a widely known effect. The slope of the spectra changes with the phase angle α in all plots. It can be either increasing or decreasing depending on the size of the particles. For a size of 50 μm in the range of phase angles ≈ 0 – 60° the slope increases. This can be attributed to the so called "phase reddening" that is observed for natural surfaces, the albedo of which is higher at larger wavelengths. This was investigated in laboratory experiments (e.g., [3-5, 10]), but has not been adequately studied theoretically before. For particles with sizes larger than ≈ 200 μm the spectral slope decreases monotonously.

The changing illumination/observation geometry also influences the depth of the absorption bands. To illustrate this we plot the spectra divided by the continuum in the wavelength range near the 1 μm absorption feature in Figure 3. We approximated the continuum as a linear function between the band wings. It is seen that beginning from approximately α = 60° the band quickly becomes weaker, and in the range 10° – 120° its depth decreases by a factor of two.

Ray-tracing allows decomposition of the reflected flux into single-particle and multiple-particle scattering components. Our calculations show that for the multiple-scattering component, the spectral slopes are much larger than those for the single-particle-scattering component. The phase dependence of the slopes is monotonous in the case of single-particle scattering and has non-monotonous behavior for the multiple-scattering component.

An explanation can be suggested for the observed behavior of the slope and absorption band. We may consider the total ray path length L in a particulate medium between the points of entrance and emergence from the particulate surface. The intensity of a transmitted ray is proportional to $\exp(-4\pi k(\lambda)L / \lambda)$. The value of L is a function of the phase angle α. These values are different for different orders of scattering. In Figure 4 we show the calculated distribution of $<L(\alpha)>$. As one can see, the average ray path length increases in the range 0 – 80°, which corresponds to the increasing spectral slope, reaches a maximum and then decreases at large α.

3 Conclusions

From the results of our ray-tracing simulations we can conclude the following:

1. The results reveal a strong dependence of the spectral slope on the phase angle. It can be either increasing or decreasing depending on the size of particles. The illumination/observation geometry can also influence the depth of the 1 μm absorption band. In the range 10° – 120° its depth decreases by a factor of two.

2. Single and multiple scattering components both appear to be important and play a significant role in the formation of the reflectance spectra and its behavior with phase-angle change. Multiple light scattering is responsible for the non-monotonous phase dependence of the spectral slope.

Acknowledgments

The authors are grateful to U. Mail who supported this work in its initial stage.

References

[1] Clark, B.E., Helfenstein, P., Bell, J. F., Peterson, C., Veverka, J., Izenberg, N.I., Domingue, D., Wellnitz, D., McFadden, L. "NEAR Infrared Spectrometer Photometry of Asteroid 433 Eros", Icarus, 155. 189–204 (2002).

[2] Abe, M., Takagi, Y., Kitazato, K., Abe, S., Hiroi, T., Vilas, F., Clark, B. E., Abell, P. A., Lederer, S. M., Jarvis, K. S., Nimura, T., Ueda, Y., Fujiwara, A. "Near-Infrared Spectral Results of Asteroid Itokawa from the Hayabusa Spacecraft", Science, 312, 5778, 1334–1338 (2006).

[3] Gradie, J.C., Veverka, J., Buratti, B.J. The effects of scattering geometry on the spectrophotometric properties of powdered material. LPSC, 11, 799–815 (1980).

[4] Pieters, C.M., Pratt, S., Hoffman, H., Helfenstein, P., Mustard, J. "Bidirectional spectroscopy of returned lunar soils: detailed "Ground Truth" for planetary remote sensors", LPSC, 22, 1069 (1991).

[5] Shkuratov, Y. G., Melkumova, L. Y., Opansenko, N. V., Stankevich, D. G. "Phase dependence of the color indices of solid surfaces of celestial bodies", Solar System Res. 30, 71–79 (1996).

[6] Jaumann, R., Grobner, G., Dummel, A., Rebhan, H., Neukum, G. "Dependence of color ratios on the observation geometry", LPSC, 23, 605 (1992).

[7] Grynko, Ye. and Shkuratov, Yu. "Scattering matrix calculated in geometric optics approximation for semi-trasparent particles faceted with various shapes", J. Quant. Spectrosc. Rad. Trans. 78, 319–340 (2003).

[8] Shkuratov, Yu., Grynko, Ye. "Light scattering by media composed of semitransparent particles of different shapes in ray optics approximation: consequences for spectroscopy, photometry, and polarimetry of planetary regoliths", Icarus, 173, 16–28 (2005).

[9] Shkuratov, Yu., L. Starukhina, H. Hoffmann, and G. Arnold, "A model of spectral albedo of particulate surfaces: implication to optical properties of the Moon", Icarus, 137, 235–246(1999).

[10] Akimov, L. A., Antipova-Karataeva, I. I., Shkuratov, Yu.G. "Indicatrix Measurements of Lunar Samples from Landing Sites of Luna 24, Luna 16, and Luna 2", LPSC, 10, 9–11 (1979).

Circular polarization of light scattered by randomly built aggregates

D. Guirado[1,2], F. Moreno[1], and J. W. Hovenier[2]

[1]*Instituto de Astrofísica de Andalucía (CSIC), Cmo. Bajo de Huétor, 50, Granada, 18008, Spain, tel: +34 958 230 615, fax: +34 958 814 530, e-mail: dani@iaa.es*
[2] *Astronomical Institute "Anton Pannekoek", University of Amsterdam, Kruislaan 403, 1098 SJ Amsterdam, The Netherlands*

Abstract

We present calculations of the scattering angle dependence of the degree of circular polarization of light singly scattered at 500 nm by randomly oriented randomly built aggregates of optically inactive homogeneous identical spheres. Using the T-matrix method we analyzed the effect of changing the size of the monomers for two different geometries. The values of the computed degree of circular polarization are comparable to the observed ones for light scattered by dust particles in comets P/Halley, C/1995 O1 (Hale-Bopp) and C/1999 S4 (LINEAR).

1 Introduction

A small but non-zero degree of circular polarization (DCP hereafter) has been persistently observed for light scattered by dust grains in comets. A summary of some of the available observations is presented in Table 1.

The measurements for a given comet are highly variable in time. The time scale of the variations have been reported to be of the order of a few days [1, 2] or as short as a few minutes [3]. The precision of the measurements is, in general, quite low, especially for measurements of comet Halley, where the errors are of the order of the mean values, or even larger.

Some systematic errors might be introduced in the observations of Halley by Metz et al. [3], because they present a strong dependence on the diaphragm aperture: DCP values of -1.0%, 0.2% and -1.3% were obtained for apertures of $10''$, $21''$ and again $10''$, respectively.

In a previous work (Guirado et al. [7]) we presented a systematic study of the DCP of light scattered by model asymmetrical particles. There we used two artificially asymmetrical aggregates of identical spheres (monomers) and calculated the DCP curves, i.e., the DCP as a function of the scattering angle for several sizes, refractive indices and numbers of monomers of the aggregates. We obtained a DCP of up to 2%. From the results of that work we inferred the following: when the substructure (monomer or group of monomers) producing the asymmetry of the aggregate is comparable in size to the wavelength, some principal peaks appear in the DCP curve. These peaks reduce their amplitude when the aggregate becomes larger than the wavelength, but always remain at about the same scattering angles. Also the number of principal peaks keeps constant when varying the size of the aggregate. When the size of the aggregate is increased in such a way that the diameter of each monomer becomes of the order of the wavelength, secondary peaks appear in the DCP curve. The number of these peaks increases while increasing the size of the aggregate, and their positions change. Finally, when making an average of the DCP curve over a size distribution the secondary peaks contribution is cancelled out when these peaks are summed up and only principal peaks remain, because they always contribute in the same sense at the same positions. From these conclusions, we derived that aggregates built in a random way may also produce a significant DCP of scattered light if the substructure producing the asymmetry of the particle is comparable in size to the wavelength of scattered light. The main goal of the present work is to study what is the order of magnitude of the DCP of light

Comet	Author	Wavelength (nm)	Aperture	Phase angle (°)	DCP (%)
Halley	Morozhenko [1]	514	$2.7'' \times 81''$	21.1 - 34.8	(-0.76 ± 0.27) - (0.37 ± 0.20)
Halley	Morozhenko [1]	484	$2.7'' \times 81''$	21.1 - 34.8	(-0.05 ± 0.15) - (0.70 ± 0.28)
Halley	Dollfus [2]	visible*	$2.1''$ to $107''$	40.7 - 22.5	(-0.65 ± 0.39) - (1.18 ± 0.48)
Halley	Metz [3]	560	$10''$, $15''$ and $21''$	66.1	(-2.2 ± 0.1) - (-0.7 ± 0.0)
Hale-Bop	Manset [4]	684	15.5“	40 - 47.4	(-0.24 ± 0.02) - (0.20 ± 0.04)
Hale-Bop	Rosenbush [5]	485	10“	46	(-0.26 ± 0.02) - (-0.06 ± 0.06)
LINEAR	Rosenbush [6]	red**	$15''$	60.9 - 122.1	up to 1%

* Wide band filter centered at 500 nm and covering the whole visible spectrum.
** Wide band R filter.

Table 1: Summary of some observations of circular polarization of light scattered by comets.

scattered by randomly built aggregates. If too small, we could directly rule out real asymmetrical aggregates as producing most of the circular polarization in comets, but if it is of the order of the observations, we should proceed with a systematic study of several geometries, sizes and refractive indices.

A previous approach to this problem was made by Kolokolova et al. [8]. These authors found values of the DCP very close to zero for randomly built aggregates of identical optically inactive homogeneous spheres in random orientation. But only two particular sizes were chosen, and now we know that other sizes could give large values of the DCP so that significant values might remain after size-averaging.

2 Numerical methods

For the generation of the aggregates we implemented a cluster-cluster aggregation (CCA) method in a Fortran code. We chose this mechanism instead of particle-cluster aggregation (PCA) because the former produces aggregates with elongated substructures, which is favourable to the asymmetry of the formed particles. Only if the obtained DCP is comparable to the observations, PCA aggregates should be studied. In order to limit the size of the clusters and the whole aggregates, we fixed a limit to the maximum distance between two monomers of the structure.

For all calculations we used the T-matrix superposition method for aggregates made of spherical monomers. We chose the free available double precision version of the code of Mackowski and Mishchenko [9]. The results depend somewhat on the accuracy parameters of the code, and we needed very accurate results because we expected to obtain small values of the DCP. So, we changed the accuracy parameters until the results became stable. The criterion for stability was the following. We defined the relative error for each element of the scattering matrix as $\frac{F_{ij}(parameters1)-F_{ij}(parameters2)}{F_{ij}(parameters2)}$, where $parameters2$ are ten times smaller than $parameters1$. Then we changed the parameters until the error was smaller than 10^{-9} for all scattering angles and all elements of the scattering matrix.

3 Numerical results

We chose aggregates made of identical homogeneous and optically inactive spheres for this preliminary study. The refractive index was $m = 1.5 + i0.001$. We have calculated the degree of circular polarization, as a function of scattering angle, produced by incident unpolarized light scattered at a wavelength $\lambda = 500$ nm by collections of the above described particles in random orientation.

Two different shapes were used for the aggregates (see Fig. 1). We will denote by x the size parameter of the monomers of the particle, and by X the volume equivalent size parameter of the whole aggregate. All results are plotted as a function of the scattering angle, and the phase angle, which simply is 180° minus the

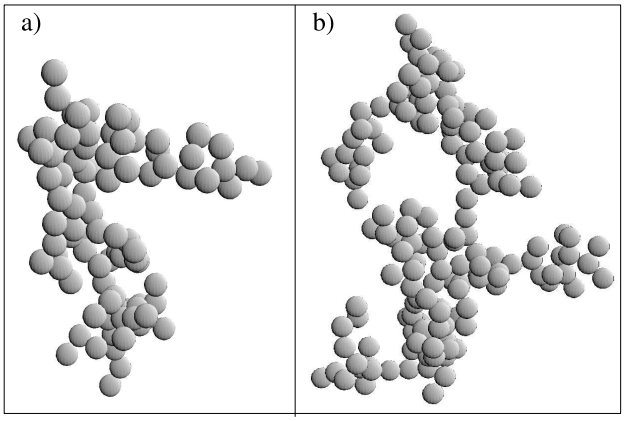

Figure 1: Randomly built asymmetrical aggregates consisting of (a) 93 and (b) 165 identical spherical monomers.

scattering angle.

As seen in Fig. 2 while increasing the size parameter for geometry (a), larger values of the absolute value of the DCP appear, while the substructure producing the asymmetry becomes comparable in size to the wavelength. For geometry (b) even larger values of the absolute value of the DCP are reached.

Secondary peaks are not present in any of the geometries. In our interpretation this is due to the fact that the monomers are much smaller than the wavelength.

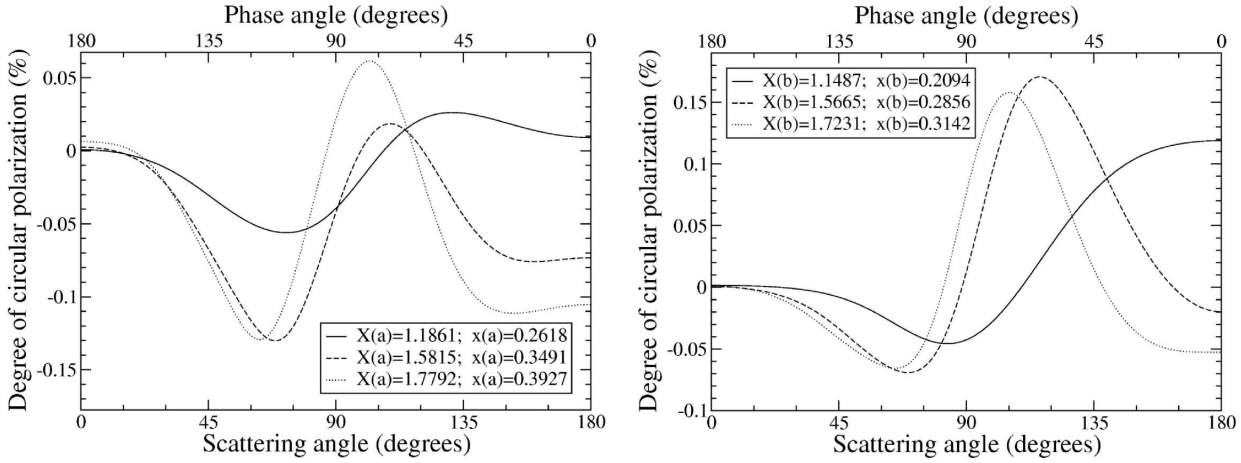

Figure 2: The degree of circular polarization as a function of the scattering angle for three collections of randomly oriented randomly built aggregates differing in volume equivalent size parameter for shape *a* (left) and *b* (right).

4 Conclusions

Single scattering of unpolarized light by randomly built optically inactive particles in random orientation can produce values of the degree of circular polarization comparable to the observed values for light scattered in comets. Further work is in progress.

Acknowledgments

Stimulating discussions with Michiel Min are gratefully acknowledged. The authors thankfully acknowledge the computer resources, technical expertise and assistance provided by the Barcelona Supercomputing Center. This work was partially supported by contract AYA2004-03250.

References

[1] Morozhenko AV, Kiselev NN, Gural'chuk AL. Circular polarization of the light from the head of Halley's comet. Kinematika i Fizika Nebesnykh Tel 1987;2:89-90.

[2] A. Dollfus and J.-L. Suchail, "Polarimetry of grains in the coma of P/Halley," Astron. Astrophys. **187**, 669–688 (1987).

[3] Metz K, Haefner R. Circular polarization near the nucleus of comet P/Halley. Astron Astrophys 1987;187:539-542.

[4] Manset N, Bastien P. Polarimetric observations of comets C/1995 O1 Hale-Bopp and C/1996 B2 Hyakutake. Icarus 2000;145:203-219.

[5] Rosenbush VK, Shakhovskoj NM, Rosenbush AE. Polarimetry of comet Hale-Bopp: linear and circular polarization, stellar occultation. Earth, Moon and Planets 1999;78:381-386.

[6] Rosenbush V, Kolokolova L, Lazarian A, Shakhovskoy N and Kiselev N. Circular polarization in comets: Observations of Comet C/1999 S4 (LINEAR) and tentative interpretation. Icarus 2007;186:317-330.

[7] Guirado D, Hovenier JW and Moreno F. Circular polarization of light scattered by asymmetrical particles. J Quant Spectrosc Radiat Transfer 2007;in press.

[8] L. Kolokolova, H. Kimura, K. Ziegler and I. Mann, "Light-scattering properties of random-oriented aggregates: Do they represent the properties of an ensemble of aggregates?," J. Quant. Spectrosc. Radiat. Transfer **100**, 199–206 (2006).

[9] D. W. Mackowski and M. I. Mishchenko, "Calculation of the T matrix and the scattering matrix for ensembles of spheres," J. Opt. Soc. Am. A **13**, 2226–2278 (1996).

Scattering from a long helix

Ioseph Gurwich,[1] Moshe Kleiman,[2] and Nir Shiloah [2]

[1] ELOP, P.O.Box 1166, Rehovot, 76110, ISRAEL
[2] Israel Institute for Biological Research, P.O.Box 19, Ness-Ziona, 74100, ISRAEL
tel: + 972 8 938-1654, fax: + 972 8 938-1664, e-mail: moshekl@iibr.gov.il

Abstract

We consider here the electromagnetic wave scattering by a long and thin-wire (in comparison to the wavelength) helical particle. In contrast to several previous theoretical works, we adopt here the algorithm developed for scattering by a multi-layered fiber. In the present work a long helical particle is considered as a hollow cylinder with a thin non-homogeneous membrane for which the periodical boundary conditions are imposed.

1 Introduction

A helical particle is an exotic object, and till now it was scarcely considered in literature devoted to light scattering problems.
In rare works concerned with this problem[1, 2], numerical techniques are involved. In contrast to such approach, we develop here a formalism based on representation of a helical particle as thin non-homogeneous membrane and periodical boundary conditions. This allows for using the iterative technique and equations in the form obtained for a coated infinite cylinder[3] on each iteration step.

2 Basic considerations

Consider a helix oriented along *z*-axis (Fig. 1).

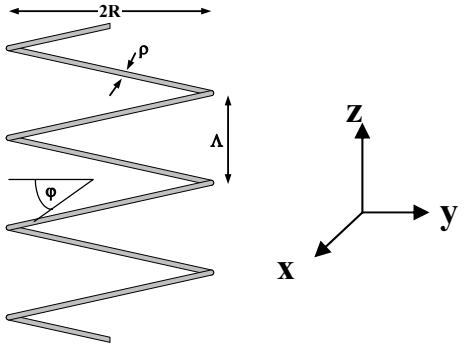

Figure 1: The geometry of helical particle

The equation of its central line is:

$$\begin{aligned} x_C &= R_C \cos\varphi \\ y_C &= R_C \sin\varphi \\ z_C &= R\varphi \end{aligned} \tag{1}$$

with $\varphi \in (-\infty, \infty)$, and the tangent unit vector $\hat{\mathbf{l}}$ is

$$\hat{\mathbf{l}} = \left(\frac{dx_C}{dl}, \frac{dy_C}{dl}, \frac{dz_C}{dl} \right) = \left(\frac{\cos\varphi}{\sqrt{1+h^2}}, -\frac{\sin\varphi}{\sqrt{1+h^2}}, \frac{h}{\sqrt{1+h^2}} \right) \tag{2}$$

where $h = \dfrac{\Lambda}{2\pi R_C}$ and l is the length parameter. Consider the attendant local coordinate (ξ,ψ,ζ),with $\hat{\boldsymbol{\zeta}}$ coinciding with $\hat{\mathbf{l}}$. The outer surface points in these coordinates are $(\xi,\psi,0)$: $\xi^2+\psi^2=\rho^2$. However, for $\rho << \lambda$ (wavelength) we can accept that inside the helix (not in the volume of helix, but in the "wire" itself) the field is homogeneous relative to ξ,ψ coordinates, and thus the boundary conditions can be formulated on the central line: (x_c, y_c, z_c).

The case $R_C \to 0$ corresponds to an infinite thin wire, and the case $\eta = \rho/\Lambda \to \dfrac{1}{2}(0)$ corresponds to a hollow cylinder with a thin homogeneous membrane (absolutely transparent if η=0). In general, the helix can be considered as a hollow cylinder with a thin (non-homogeneous) membrane and periodical boundary condition (the following expression is not accurate, because of the round shape of a wire forming the helix, but for a thin wire we can ignore such an inaccuracy):

$$\varepsilon = \begin{cases} 1, z \in \left[\dfrac{\Lambda}{2\pi}\phi + n\Lambda + \rho, \dfrac{\Lambda}{2\pi}\phi + (n+1)\Lambda - \rho \right) \\ \varepsilon_h, z \in \left[\dfrac{\Lambda}{2\pi}\phi + n\Lambda - \rho, \dfrac{\Lambda}{2\pi}\phi + n\Lambda + \rho \right) \end{cases} \tag{3}$$

with ρ/Λ<<1, and n=…-1,0,1,... The proper Fourier series is

$$\varepsilon(z,\phi) = 1 + 2(\varepsilon_h - 1)\left\{ \eta + \frac{1}{n\pi}\sum_{n=1}^{\infty} \sin(2\pi n\eta)\left[\cos(n\phi)\cos\left(2\pi n\frac{z}{\Lambda}\right) + \sin(n\phi)\sin\left(2\pi n\frac{z}{\Lambda}\right) \right] \right\} \tag{3-1}$$

and the similar series can be written for the refraction index m. Dealing with such a cylinder, we can formulate the periodical boundary conditions for z and τ components of **E** and **H**. Thus we have a hollow cylinder (Fig. 2 shows its cross-section), and three separated regions: 0- the inner medium (air), 1 – the helix, i.e., non-homogeneous membrane (gray area), and 2- the ambient medium (air).

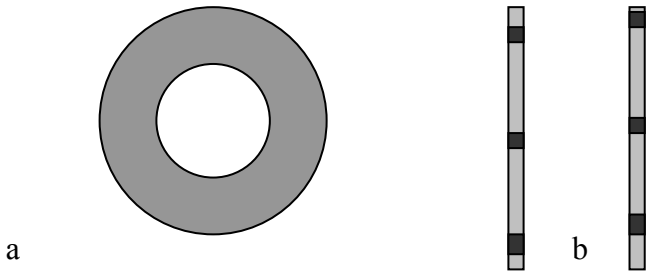

Figure 2: The hollow cylinder cross-section: a) upper view, b) side view

Here the inner radius is $R_1=R_c-\rho$, and the outer radius is $R_2=R_c+\rho$ and $\rho/R_c << 1$ is presumed.

3 Solution for scattered field

Strictly speaking the wave equation does not have a close solution for the present boundary condition. However, this can be shown that in cases where parameter $\eta = \frac{\pi\rho}{4\Lambda}$ is very small or close to 0.5: $\eta << 1$ or $|\eta - 0.5| << 1$, a convenient approximation does exist. In such an approximation one can represent the scattered field by the series of space (angular: θ will be the angle between *z*-axis and the scattering direction) Fourier harmonics.

It seems reasonable to assume that the scattered and inner fields have periodical dependence on the coordinate *z* with the space period Λ. Therefore we suppose the periodical dependence of scattering coefficients on *z*. In the present case the scattering coefficients (except of the incident $a_n^{(in)}$ field) have to be represented as the Fourier series. However, every Fourier term requires its own radial dependence; therefore, we have to write the solution in the form. In a certain approximation the fields in the j^{th} layer (j = 1,2) can be written as :

$$\begin{aligned}
\mathbf{E}_j &= \sum_n \sum_l \left\{ Q_{n,l}^{(1)} \mathbf{N}_{n,j,l}^{(1)} + T_{n,l}^{(j)} \mathbf{M}_{n,j,l}^{(1)} - W_{n,l}^{(j)} \mathbf{N}_{n,j,l}^{(2)} - P_{n,l}^{(j)} \mathbf{M}_{n,j,l}^{(2)} \right\} e^{il\phi} e^{i2\pi lz/\Lambda} \\
\mathbf{H}_j &= -i \frac{km_j'}{\omega} \sum_n \sum_l \left\{ T_{n,l}^{(1)} \mathbf{N}_{n,j,l}^{(1)} + Q_{n,l}^{(j)} \mathbf{M}_{n,j,l}^{(1)} - P_{n,l}^{(j)} \mathbf{N}_{n,j,l}^{(2)} - W_{n,l}^{(j)} \mathbf{M}_{n,j,l}^{(2)} \right\} e^{il\phi} e^{i2\pi lz/\Lambda}
\end{aligned} \tag{4}$$

Where **M** and **N** are cylindrical vector harmonics[4].

By writing *m* as $m(z,\phi) = \overline{m} + \delta m(z,\phi)$, where δm is represented approximately by a Fourier series analogous to (3-1) we write the boundary conditions for the inner and outer boundary in the form similar to that appearing for a case of a layered cylinder[3]. The solving procedure prescribes to use $m(z,\phi) = \overline{m}$ at the first step for getting the zero order space harmonic for the scattered field and the fields in the hollow cylinder layers. The scattering coefficients $\left\{ Q_{n,0}^{(j)}, T_{n,0}^{(j)}, W_{n,0}^{(j)}, P_{n,0}^{(j)} \right\}$ appear as the standard solution[3]. At the following stage one obtains higher order harmonics as perturbations with respect to the small parameter δm. The proper equations take the similar form, where the zero order field solution with the factor δm appears at the place of the incident field. Thus the similar procedure can be used in the iterative manner. This corresponds to the physical interpretation, where the mean-field generates higher order perturbations.

Since the helix is taken as infinitely long, the θ-directions can be found in the same manner as the diffraction angles for the infinitely long gratings. In case of a finite length helix each θ_l is replace by a (narrow) continuous spectral shape. Being interesting in the total energy scattered in a certain θ angular order, one can fulfill integration with respect to θ in the proper interval and then reduce formally the problem to the similar form for the mean value of the scattering coefficients, say $\left\langle Q_{n,l}^{(j)} \right\rangle_{|\theta \in \Delta\theta_l}$ instead of $Q_{n,l}^{(j)}(\theta \in \Delta\theta_l)$. In the case of the infinitely long helix, where a spectral function is reduced to the series of δ-functions we return to the original equations.

4 Extinction and scattering coefficients

Consider the general relations[4]:

$$\begin{aligned}
\mathbf{W}_{sc} &= R \int dz \int d\phi (\mathbf{S}_{sc})_r \\
\mathbf{W}_{ext} &= R \int dz \int d\phi (\mathbf{S}_{ext})_r
\end{aligned} \tag{5}$$

where R is the radius of a cylindrical surface around the helix (integration with respect to *z* can be fulfilled in the interval [0,Λ]) and

$$\mathbf{S}_{sc} = \frac{1}{2}\mathrm{Re}\left\{\mathbf{E}_{sc} \times \mathbf{H}_{sc}^{*}\right\}$$
$$\mathbf{S}_{ext} = \frac{1}{2}\mathrm{Re}\left\{\mathbf{E}_{in} \times \mathbf{H}_{sc}^{*} + \mathbf{E}_{sc} \times \mathbf{H}_{in}^{*}\right\} \tag{6}$$

Since the incident field does not contain terms with factors $e^{ih\Lambda lz}$, coefficients $A_{n,l}^{(sc)}$, $B_{n,l}^{(sc)}$ with $l > 0$ will drop from expression for $\mathbf{W}_{sc}$. Thus in the common relations[4,5] we keep for Q_{ext} :

$$\mathrm{Re}(a_n) = \mathrm{Re}\left\{A_{n,0}^{(sc)}\right\}$$
$$\mathrm{Re}(b_n) = \mathrm{Re}\left\{B_{n,0}^{(sc)}\right\} \tag{7-1}$$

but for Q_{sc} we have to take :

$$|a_n|^2 = \sum_l \left|A_{n,l}^{(sc)}\right|^2$$
$$|b_n|^2 = \sum_l \left|B_{n,l}^{(sc)}\right|^2 \tag{7-2}$$

5. CONCLUSION

In the present work we demonstrated a possibility of treating the problem of light scattering by a helical particle by using a Fourier approach. It is shown, that one can use a calculation procedure developed for a multilayered (hollow) cylinder to find all Fourier (diffraction) order of the scattered field. Thus a calculation technique turns out to be much simpler than it has been suggested before.

6. REFERENCES

1. C. Bustamante, M. F. Maestre, and I. Tinoco, “Circular intensity differential scattering of light by helical structures”, I. Theory*, J. Chem. Phys*, **9**, 4273-4281,1980.
2. A. Cohen, R.D. Haracz and L.D. Cohen, “Scattering from a helix using the exact cylinder theory”, *J. Wave Mater. Interac.*, **3**, pp. 219-225, 1988.
3. I. Gurwich, N. Shiloah and M. Kleiman, “The recursive algorithm for electromagnetic scattering by tilted infinite circular multi-layered cylinder”, *J. Quant. Spectrosc. Radiat.* **63**, 217–229, 1999.
4. C. F. Bohren and D. R. Huffman, *Absorbing and Scattering of Light by Small Particles*, (Wiley, New York, 1983).
5. H. C. Van de Hulst, *Light scattering by Small Particles*, (Dover Publications, Inc,, New York, 1981).

Light scattering simulation by concave, peanut-shaped silver nanoparticles modeled on Cassini-ovals

Jens Hellmers,[1] Norbert Riefler,[1] Thomas Wriedt,[2] Yuri Eremin,[3]

[1] *Universität Bremen, Verfahrenstechnik, Badgasteiner Str. 3, 28359 Bremen, Germany*
[2] *Institut für Werkstofftechnik, Badgasteiner Str. 3, 28359 Bremen, Germany*
[3] *Moscow State University, Fac. of Apl. Math.& Comp. Sc., Lenin's Hills, 119992 Moscow, Russia*
tel: +49 (421) 218-5418, fax: +49 (421) 218-5418, e-mail: hellmers@iwt.uni-bremen.de

Abstract

Light scattering is a useful tool in particle characterization. The simulation of light scattering processes can help to understand scattering characteristics and from this information about particle sizes, materials or shapes can be retrieved. In this paper we demonstrate the application of the Nullfield Method with Discrete Sources for light scattering by concave, peanut-shaped silver nanoparticles. Additionally we use the Discrete Sources Method for result validation. For the shape model a Cassini-oval based model is used, which accords to two sintered silver spheres. This model is compared to a simpler two-sphere approach by calculating the corresponding scattering patterns.

1 Introduction

With the increasing interest in nanotechnology also the interest in light scattering by such nanoparticles increases, as it can help to understand their sometimes complex characteristics and interactions. Often systems or clusters of single nanoparticles are the topics of interest. For metal nanoparticles with their luminous optical properties Gunnarsson et al. [1] point out, that the localized surface plasmon resonance has a key role in nanoparticle optics and that this is connected with the shape of the particles. So suitable particle and cluster models are needed and this includes an adequate description of the connection between two or more single particles. The easiest connection model is made from single spheres touching each other at one point. But this might be a too general approach; the resulting shape of two metallic particles sintered together should be more complex, as e.g. was demonstrated by Shimosaka et al. [2]. Because of this light-scattering studies can lead to wrong interpretations as soon as the intersection of such combined particles has an influence on the scattering pattern. This influence is investigated in this work; it is a preliminary study for better cluster models. We compare light scattering by two identical spheres with optical properties of silver with a more realistically shaped model based on a three-dimensional Cassini-oval. For light-scattering calculations we use an advanced T-matrix approach, the Nullfield Method with Discrete Sources (NFM-DS). Unlike the conventional T-matrix theory the NFM-DS allows to calculate light-scattering by such concave particles. A detailed description of the NFM-DS together with computer codes can be found in the book by Doicu et al. [3]. To make sure that we get reliable results by the NFM-DS we compare the calculated results with those we get from the Discrete Sources Method (DSM). More information about the DSM can be found in the book chapter by Eremin et al. [4]. The approach to check the validity of scattering simulation results by using these two methods worked before when we investigated light scattering by oblate, flat Cassini-oval based particles [5].

2 Particle shape model

We look for a shape model to approximate two similar spheres that are sintered together. For this we use a two-dimensional concave Cassini-oval. The Cassini-oval is defined by

$$\left[(x-a)^2+\left(y/c\right)^2\right]\left[(x+a)^2+\left(y/c\right)^2\right]=\mathrm{b}^4 \quad \Rightarrow \quad y=\pm c\cdot\left(-a^2-x^2\pm\left(4x^2a^2+b^4\right)^{1/2}\right)^{1/2}$$

The shape of a Cassini-oval by definition depends on the two parameters *a* and *b*; by adding a third parameter *c* one can additionally manipulate the overall thickness of the form. Rotating this curve around its main axis delivers a three-dimensional, concave peanut-like shape. Carefully choosing these parameters enables to create a shape model that fits the two initial spheres; additionally we make sure that the volume of the peanut shape is equal to the volume of the two original spheres. Fig. 1 shows an example of such a shape.

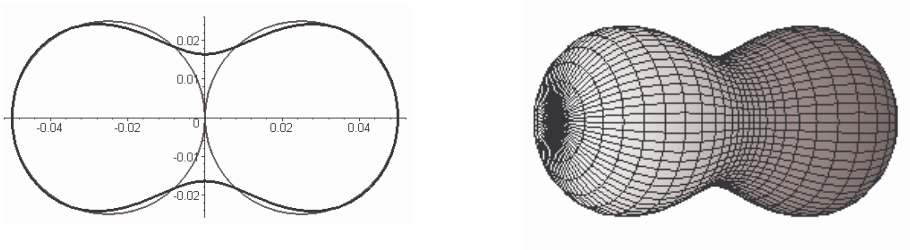

Figure 1: Cassini-oval based shape model; two-dimensional compared to two equi-volumed spheres (left) and the corresponding three-dimensional model (right). a = 0.0340625, b = 0.0365625, c = 1.236; the diameter of the spheres is 50nm. Overall particle size is 100nm.

3 Results

First we compare light scattering results for a peanut-like silver particle calculated by the NFM-DS with those we get from DSM to make sure, that both theories deliver the same scattering patterns. This helps to estimate the quality of the result; in case of accordance it is very likely that the result is correct. Fig. 2 shows the scattering patterns for a silver particle with shape and dimension as shown in Fig. 1.

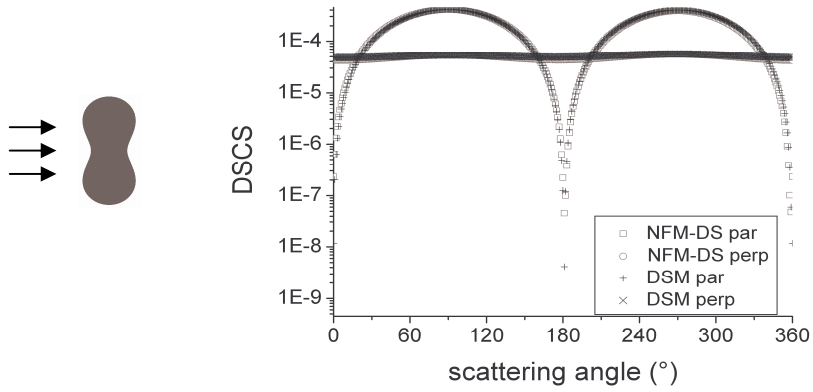

Figure 2: Comparison of light scattering patterns calculated by NFM-DS and DSM. Particle shape is a Cassini-oval based peanut as shown in Fig. 1, particle length is 100nm. Wavelength is 478nm, incident angle is 90° to rotational axis; therefore forward scattering can be observed at 90°. Refractive index is 0.13-2.729i.

As one can see there is a good congruence between both light scattering results.
In the next step we do a spectral analysis of the scattering behavior of the peanut-like silver particle as well as a corresponding two-sphere model as presented in Fig. 1. This spectral analysis will show if the shape model has influence on the scattering patterns and at which wavelengths this influence can be observed best. Fig. 3 shows exemplary scattering diagrams for both parallel and perpendicular polarization for a wavelength range between 250nm and 500nm. The refractive index follows the studies made by Johnson and Christy [5].

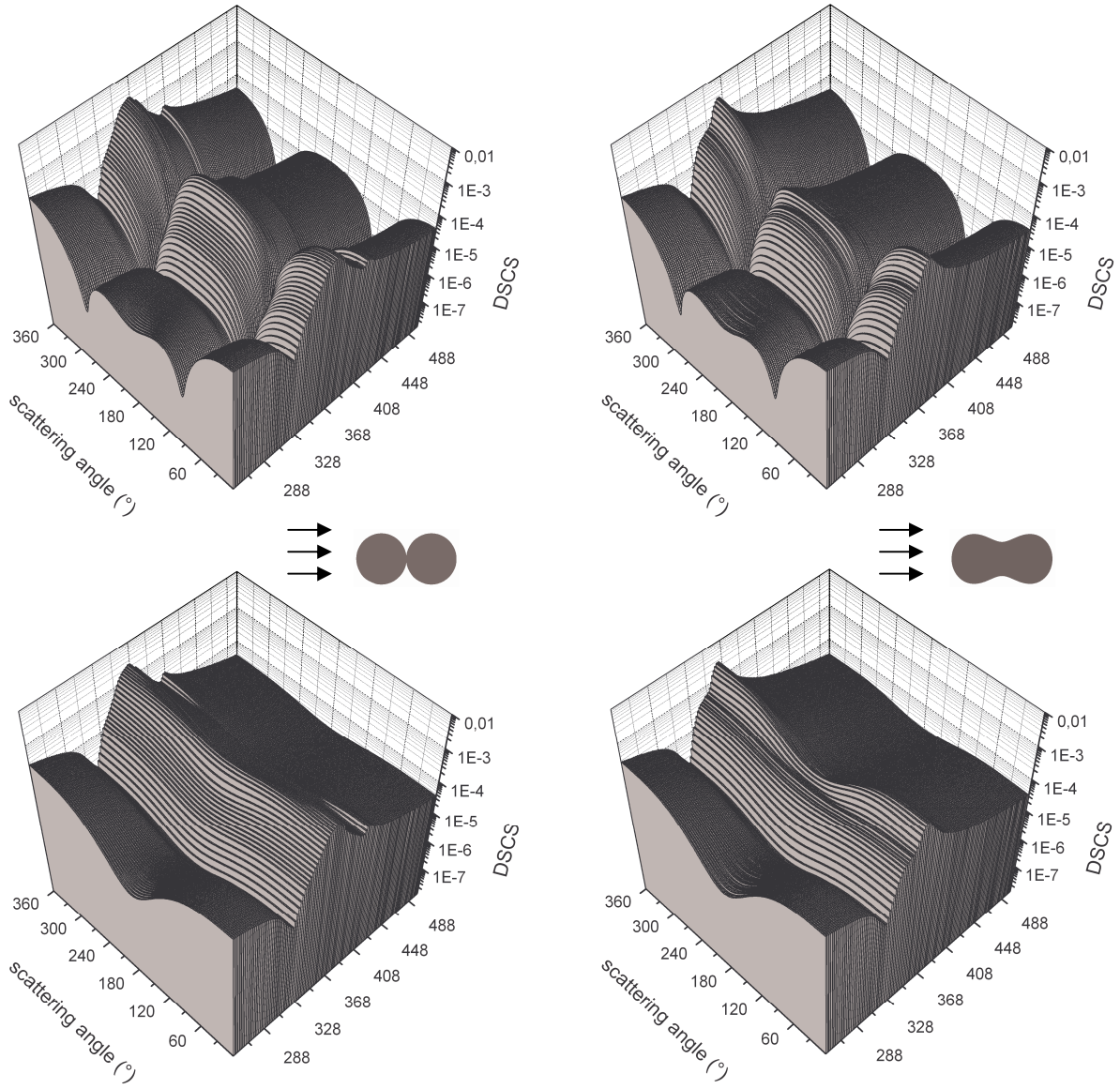

Figure 3: Spectral analysis of two spheres (left) and an equi-volume Cassini-oval based peanut (right) as shown in Fig. 1. Particle length is 100nm. Wavelength-range is from 250nm to 500nm; direction of incident light is along rotational axis. Upper diagrams show parallel, lower diagrams show perpendicular polarization.

Looking at Fig. 3 one can make several observations: comparing the diagrams for parallel polarization one sees, that for both shape models the highest intensity is reached for a wavelength about 366nm (for this particular particle size). But for the two-sphere model there is a small second peak at 404nm while this is not visible for the Cassini-oval model. On the other side this model shows a kind of small plateau before the main peak at 366nm is reached which can not be observed for the two-sphere model. For the perpendicular polarization there are also differences, mostly at the 180° scattering angle for the highest intensity. Here the diagram for the Cassini-oval model shows a significant indentation.

5 Conclusion

Fig. 3 demonstrates that there are different light scattering patterns for the different shape models, two identical spheres touching each other on one side and a single particle with a corresponding volume based on a Cassini-oval on the other side. While this is just one example for a specific particle size, shape and material, it is nevertheless reasonable that similar effects could be observed for other particle sizes as well. Further studies using light scattering simulations now can help to give a better understanding of the characteristics of such particle systems and clusters. One practical application could be to determine from measured scattering characteristics if the observed particles are sintered together or just slightly touch each other. Simulations results could also provide the information, which wavelengths and observation angles are most suitable for observations. Both light scattering theories used for this work are advantageous for this purpose: while the DSM is very fast and reliable, the NFM-DS offers all benefits of the T-matrix approach, for example fast post-processing calculations for incident angles different from the original one or orientation averaging.
To give a better impression on the topic, more detailed results will be presented at the ELS10 conference.

Acknowledgments

We would like to acknowledge support of this work by Deutsche Forschungsgemeinschaft DFG.

References

[1] L. Gunnarsson, T. Rindzevicius, J. Prikulis, B. Kasemo, M. Käll, S. Zou and G. C. Schatz, “Confined Plasmons in Nanofabricated Single Silver Particle Pairs: Experimental Observations of Strong Interparticle Interactions”. J. Phys. Chem. B **109**, 1079-1087 (2005).

[2] A. Shimosaka, Y. Ueda, Y. Shirakawa and J. Hidaka, “Sintering Mechanism of Two Spheres Forming a Homogeneous Solid Solubility Neck”. KONA **21**, 219-233 (2003).

[3] A. Doicu, T. Wriedt and Y. Eremin, *Light Scattering by Systems of Particles* (Springer, 2006).

[4] Y. Eremin, N. Orlov and A. Sveshnikov, *Generalized Multipole Techniques for Electromagnetic and Light Scattering* (ed. T. Wriedt, Elsevier Science, Amsterdam, 1999; 39-80)

[5] J. Hellmers, E. Eremina and T. Wriedt, “Simulation of light scattering by biconcave Cassini ovals using the Nullfield Method with Discrete Sources”. J. Opt. A **8**, 1-9 (2006).

[6] P. B. Johnson and R. W. Christy, “Optical Constants of the Noble Metals”. Phys. Rev. B **6** (12), 4370-4379 (1972).

Temporal scattering of dense scattering media under ultra short laser light illumination: Application for particle sizing.

HESPEL Laurent[1], BARTHELEMY Marie[1], RIVIERE Nicolas[1], DELFOUR André[1], MEES Loic[2] and GREHAN Gerard[2]

[1] *Onera, The French Aerospace Lab, Theoretical and Applied Optics Department*
Light Interaction with Matter, Imaging and Detection Laser Systems Unit
2 avenue Edouard Belin, BP4025, 31055 Toulouse cedex 4, France
tel: +33 562 25 26 69, fax: +33 562 25 25 88, e-mail: laurent.hespel@onera.fr

[2] *CORIA, Université de Rouen, Site Universitaire du Madrillet BP 12*
76801 Saint Etienne du Rouvray, France

Abstract

We intend to demonstrate the contribution of ultra short laser light methods for improving the particle sizing of dense scattering medium like plumes or engine sprays. We especially focus our attention on the time-resolved propagation of ultra short laser pulses in the forward and backward directions considering a Monte-Carlo (MC) scheme. We investigate the influence of the detector-source configurations on the retrieval of spectral backscattering and extinction coefficients derived from the measurements of the spectral transmittance and backscattering power. An efficient method developed to retrieve Particle Size Distribution of aerosols from multi-spectral LIDAR returns is then adapted to the investigated case. This method is finally tested on the numerical spectral backscattering and extinction coefficients derived from MC simulations.

1 Introduction and Context

For aerosols particle sizing, we developed a specific scheme inverting spectral extinction and backscattering coefficients that could be derived from single scattering multispectral LIDAR returns using Klett method [1]. This inverse scheme includes a self-regularization method built from the data uncertainties.

Assuming an homogeneous scattering medium of length L, the extinction $\alpha(\lambda)$ and backscattering $\beta(\lambda)$ spectral coefficients could be retrieved from respectively the measurement of spectral transmittance $T(\lambda) \propto \exp(-\alpha(\lambda) \times L)$ or backscattering power $P(\lambda) \propto \beta(\lambda) \times T^2(\lambda)$.

In LIDAR application, retrieving extinction $\alpha(\lambda)$ and backscattering $\beta(\lambda)$ spectral coefficients is only performed from backscattering power $P(\lambda)$ and consequently, requires to presume a known relation between $\alpha(\lambda)$ and $\beta(\lambda)$. Using simultaneously $P(\lambda)$ and $T(\lambda)$ prevents from this requirement.

Nevertheless, the characterization of the particle size distribution (PSD) in dense scattering media like plumes, engine sprays… using a spectral measurement of the transmission and the backscattering power is a challenge as multiple scattering phenomenon scrambles useful information.

Retrieving the Particle Size Distribution f(R) (PSD) from these spectral data requires:

- a reduction of the contribution of multiple scattering events and consequently of the errors occurring on the derived spectral coefficients. Time-resolved analysis of ultra short laser pulses propagation in the backward and forward directions seems to indicate a temporal separation of ballistic and scattering photons. As a consequence, studying such phenomenon could be used in order to reduce multiple scattering if it is related to appropriate detector configurations (FOV, time gate…).
- an efficient inverse method unaffected by the residual uncertainties. The method developed for LIDAR applications could be adapted for this purpose.

In the first paragraph, we present the Monte-Carlo (MC) scheme developed to simulate ultra short laser pulses propagation in dense scattering media.

2 Monte-Carlo Simulations

The MC scheme developed is based on a temporal photon pursuing method [2] that we have extended to include polarization according to the Stokes formalism. To increase the convergence of the MC results, a pseudo MC approximation is used to evaluate the temporal intensities collected by two small detectors geometries in the forward and backward directions [3].

The statistical scattering properties are derived from the temporal Mueller matrices $P_{ij}(\theta,t)$ or the integrated ones $\overline{P}_{ij}(\theta)=\int_{\Delta t} P_{ij}(\theta,t)dt$. Those matrices are evaluated through a scanning of frequency coupled with a Lorenz-Mie (LM) theory algorithm associated with a FFT transform of the incident pulse and an inverse FFT transform of the scattering matrices [4]. The Figure 1 presents the temporal phase function of a50µm sphere illuminated by a 50fs pulse for different times relative to the transmitted time of flight. We can observe that the angular direction, where occurs the maximum of light scattered, is time dependant.

The Figure 2 compares the integrated linear depolarization ratio to this obtained for the same sphere and a continuous illumination. The pulse integrated ratio smoothes the fluctuations of the "continuous".

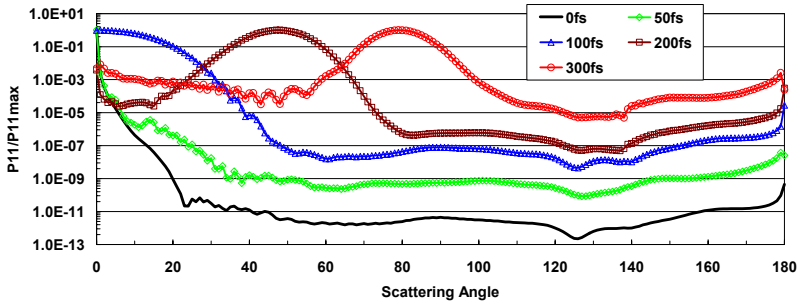

Figure 1: Temporal phase function normalized to maximum $P_{11}(\theta,t)/\max(P_{11}(\theta,t))\ \forall\theta$
(Sphere radius = 50µm and 50fs Pulse)

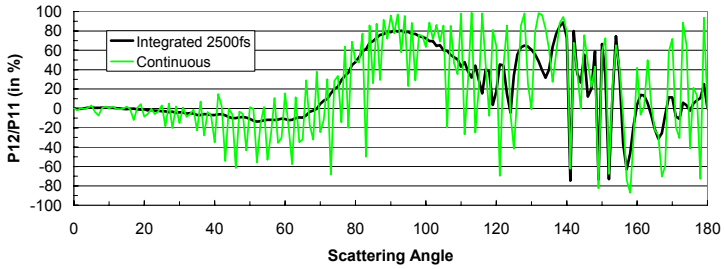

Figure 2: Ratio $\overline{P}_{12}(\theta)/\overline{P}_{11}(\theta)$ for Δt = 2500fs and a 50fs pulse width compared to the same ratio obtained for a continuous wave.

We here specially focused our attention on scattering medium, in which large optical thicknesses (OT), various bimodal Particle Size Distributions (PSD) and concentration gradients could be observed. The spectral transmittances T(λ) or backscattering received powers P(λ) of those media could be then derived considering various detector-source geometries, temporal pulse widths and integration ranges The Figure 3 represents an example of the transmitted temporal intensities considering various collection angles.

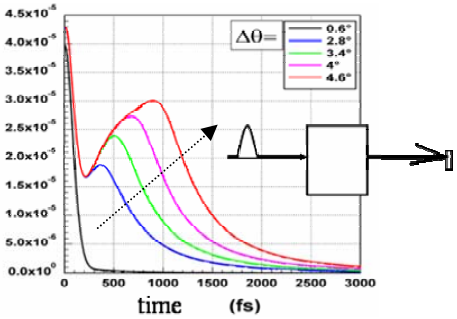

Figure 3: Transmitted temporal intensities considering various collection angles (.the arrow indicates an increase of the collection angle)

2 Inverse scheme

The spectral transmittances $T(\lambda)$ and the backscattering received powers $P(\lambda)$ are affected by multiple scattering, which depends on the optical thickness and the chosen experimental configuration. The first challenge is then to derive an optimal experimental configuration (time gate, spectral range, detector FOV, pulse width…) where the temporal integration of transmitted and backscattered temporal intensities leads to measured intensities that are close to those related respectively to a collimated or a single scattering measurement hypothesis.
Nevertheless, the spectral extinction α(λ) and backscattering β(λ) coefficients derived from the previous relations could be still uncertain. As a consequence, retrieving the Particle Size Distribution f(R) (PSD) from these spectral coefficients requires regularization.

We propose to use an inverse scheme developed for LIDAR applications. It includes a self-regularization method built from the uncertainties $\Delta X(\lambda_i)$ associated to a set of mean data values $X(\lambda_i)$. This method is based on previous works [5] derived for angular scattering data and spectral extinctions [6]. It is adapted to consider simultaneously spectral extinction and backscattering coefficients. This method is actually numerically tested to retrieve the PSD of atmospheric aerosols from extinction α(λ) and backscattering β(λ) spectral coefficients. These coefficients are obtained from Klett inversion [1] of noisy

multispectral LIDAR backscattering signals. The Figure 4 presents the PSD of a maritime bimodal aerosol retrieved from an "8 wavelengths (UV to NIR)" Simulated LIDAR Signals (SLS). A 10% Gaussian noise is added to the theoretical extinction $\alpha(\lambda)$ and backscattering $\beta(\lambda)$ to perform SLS.
The retrieved PSD are derived considering one set of spectral data (extinction or backscattering) or both of them. For this case, we can observe that only considering backscattering data is insufficient and lead to a worth estimation of the PSD.

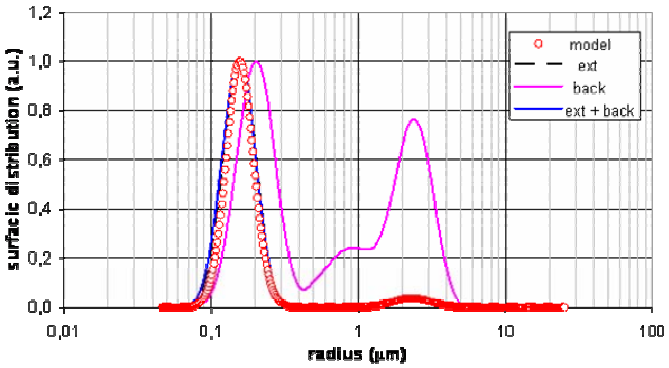

Figure 4: Retrieved PSD compared to theoretical one.

3 Further works

An optimal experimental configuration (time gate, spectral range, detector FOV, pulse width…) reducing multiple scattering contributions for the transmittance $T(\lambda)$ or backscattering received powers $P(\lambda)$ and having a sufficient Signal to Noise Ratio (SNR) is first evaluated. The extinction and backscattering coefficients retrieved from the inversions of the Beer-Lambert law and the single scattering LIDAR return equation are then compared to the theoretical values used for the MC simulations in order to evaluate the residual uncertainties due to multiple scattering.

In parallel and considering various spectral data issued from diverse scattering media, we also try to evaluate the influence of the spectral range and the mesh grid on the PSD recovering method. The influence of the uncertainties level on the inverse scheme efficiency is also estimated and related to the field of application of the proposed method.

Finally, a complete simulation is performed for a specific scattering media and the retrieved PSD are compared to the theoretical ones used in the MC simulation; in order to assess the proposed concept.

These numerical results will be presented in the poster session.

A time gated experimental setup based on a femtosecond laser associated to a Non-colinear Optical Parametric Amplifier (NOPA) is also under development. Preliminary experimental results could be presented if they are available.

References

[1] J.D. Klett, Applied Optics, **20**, No. 2, 211-220 (1981
[2] C. Rozé, T. Girasole, L. Méès, G. Gréhan, L. Hespel and A. Delfour. Opt. Comm., **220** (4-6), 237-245, (2003).
[3] Tinet et al., *J. Opt. Soc. Am. A.*, **14**, No. 9, 1903-1915 (1996)
[4] L. Méès, G. Gouesbet and G. Gréhan. Opt. Comm, **194**, 59-65 (2001)
[5] L. Hespel and A. Delfour, Applied Optics, **39**, Issue 36, 6897-6917, (2000)
[6] S.Gossé, L. Hespel, P. Gossart and A. Delfour, J. Propuls. Power, **22**, Issue 1,127-135 (2006)

The use of derivative spectrum of solution in regularization

Andriy Holdak,[1] Wolodymyr Siwers[2]

[1] *Lviv Polytechnic National University, Department of Informational measuring technics, 28a Bandera str., Lviv, 79013, Ukraine.*
[2]*REMA Research Institute,31 Zavods'ka str., Lviv 79019, Ukraine*
e-mail: fogcake@gmail.com

Abstract

The article is devoted to a new way of choosing the regularization parameters in the Tikhonov method as applied to inverse problems of light scattering. The derivative spectrum of the calculated solution is used as the selection criterion. The suggested method is compared with other well-known techniques such as the L-curve and the Generalized Cross Validation.

1. Introduction

The Fredholm equation of the first kind appears in many applied problems concerned with the determination of geometrical parameters of small particles:

$$\int_c^d K(\theta, a)\cdot \omega(a)\cdot da = I_S(\theta) \tag{1}$$

where $K(\theta,a)$ is the kernel of the integral equation, which characterizes light scattering by one particle with a characteristic dimension of a at an angle θ in the spherical coordinate system; $\omega(a)$ is the probability density function of particles sizes; $I_s(\theta)$ is the intensity of light scattered by the particle ensemble. It should be noted that Eq. (1) convolves the intensity of the light scattered by the particles with their sizes. The case of independent light scattering is considered.

The Tikhonov regularization method is one of the techniques widely used to solve this equation. According to the Tikhonov method, Eq. (1) has the following operator form [1, 2]:

$$\left(\alpha L + A^* A\right)\omega_\alpha = A^* I \tag{2}$$

where A is an operator that corresponds to the integral equation (1), A^* is the complex conjugate counterpart of A; ω_α is the required function corresponding to $\omega(a)$; I denotes $I_s(\theta)$, and the operator L is either the identity matrix or has the following form [1]:

$$L\omega = \omega - \frac{d^2\omega}{da^2} \tag{3}$$

The article deals with the presentation of the operator L in form of Eq. (3).

As the problem (1) is ill-posed, certain additional criteria [1, 2] should be applied in order to get acceptable results. The first derivative spectrum of the calculated $\omega(a)$ is suggested to be used as one of such criteria. It is known [3] that the higher harmonics of the solution of Eq. (1) converge to the exact solution slower than its lower harmonics. One should find the solution the first derivative spectrum of which contains the smallest number of the highesto-order harmonics. In the symbolic form this can be put in the following equation:

$$\min\left(\max\left(F_i\left(\omega_\alpha\right)\Big|_{\alpha_{\min}<\alpha<\alpha_{\max}}\right)\right) \tag{4}$$

where F_i is the magnitude of the i-th harmonic of spectrum F solution's derivative ω_α; $\alpha_{\min}$ and $\alpha_{\max}$ are the boundaries of the range of variation of the parameter α.

In Eq. (4), the regularization parameter α varies within certain boundaries. The boundaries are determined by the application of some additional requirements. The model investigation of the functional given by Eq. (5) below, as described in [4], is used in order to constrain these boundaries:

$$\frac{\|\omega_\alpha - \omega\|_{L_2}}{\|\omega\|_{L_2}} \tag{5}$$

where ω_α is the solution of Eq. (1) corresponding to a certain value of the parameter α; ω is the exact solution of Eq. (1).

In [4] it is shown that the functional (5) has one minimum. Since the mentioned functional is in fact the analog of relative error in the L_2 space, the minimum of the function will be reached when ω_α is the closest to the exact solution in the L_2 space. The optimal regularization parameter value will correspond to that ω_α. One can state that the value of the optimal regularization parameter and the corresponding solution is the best among all possible solutions for a given second term of Eq. (1). The results of a model investigation, shown in the next section, are used to determine the variational boundaries of the parameter α.

2. Simulations

The conventional Mie theory was used in order to compute the kernel of the integral equation (1).

From the physics point of view, there are some requirements to $\omega(a)$: this function should be defined from 0 to ∞ and should have a finite number of extrema; the values of $\omega(a)$ are above zero; it is bounded from above by a given constant C and satisfies the following standardization condition:

$$\int_0^\infty \omega(x)dx = 1 \tag{6}$$

The distributions of Raileigh, χ^2, Nakagami, Gamma etc. satisfy the requirements. In this article the distribution of Raileigh and χ^2 are used as an approximation of the particle size distribution. These approximations are described in [5] and [6].

In order to make the analysis more realistic, families of Raileigh and χ^2 distributions were used instead of one fixed form of the probability density function (PDF). The used PDF families are shown in Fig. 1.

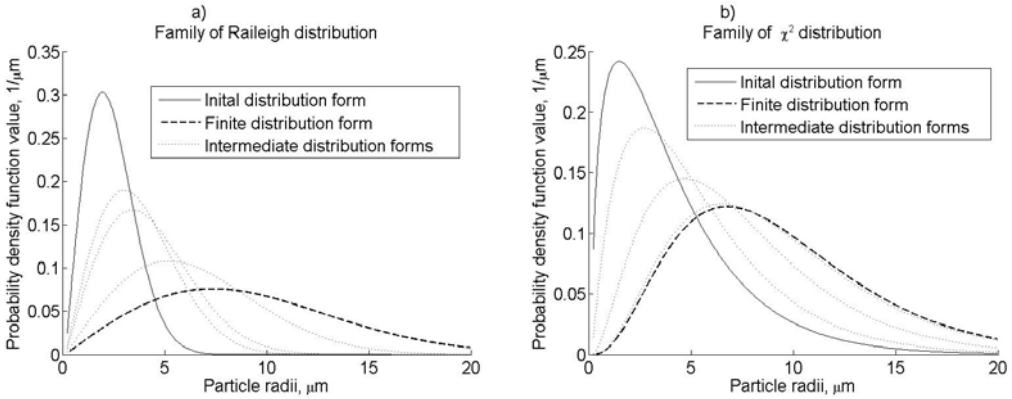

Figure 1: Families of Raileigh and χ^2 distributions

The following simulations were performed to determinate the boundaries of the "best" regularization parameter magnitudes, i.e., the parameter values that in each case, when the equation is solved, correspond to ω_α which is the closest to the exact solution. In the simulations such regularization parameter values, that minimize Eq. (5), were segregated.

The frequency diagrams of the regularization parameter values spread are presented in Fig. 2.

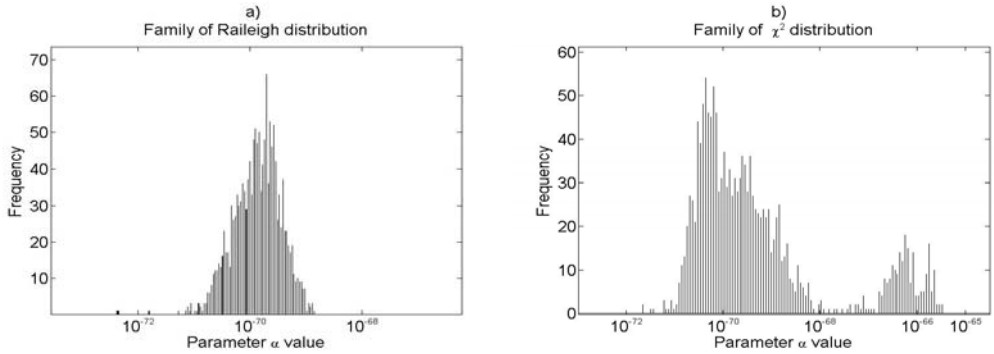

Figure 2: Spread of optimal regularization parameter values.

Figure 2 shows that α values are concentrated in certain limits for both families of distributions. In the case of the Raileigh distribution family the values of α parameter are within 10^{-69} – 10^{-71}, as for the χ^2 distribution family they are within 10^{-65} – 10^{-72}. These regularization parameter limits were used to calculate the solution of the Fredholm equation of the first kind by applying the criterion (4).

It is reasonable to present the solution of Eq. (1) for distribution families in the form of the errors described by Eq. (7):

$$\nu(a_j) = \frac{\bar{\omega}(a_j) - \omega_\alpha(a_j)}{\max\left(\bar{\omega}(a_j)\right)} \cdot 100\%, \tag{7}$$

where $\bar{\omega}(a_j)$ is the exact solution at a_j, $\omega_\alpha(a_j)$ is the calculated solution at a_j.

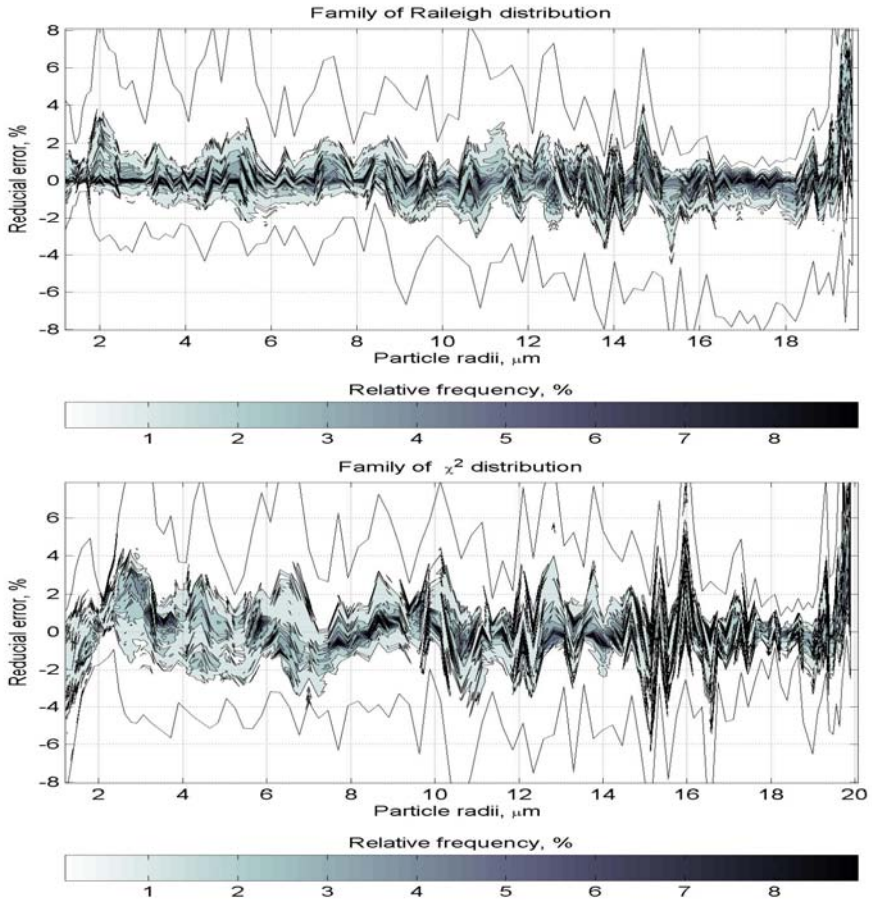

Figure 3: Results of $\omega(a)$ computatation for families of Raileigh and χ^2 distributions.

In Fig. 3 the results of $\omega(a)$ computations for families of Raileigh and χ^2 distributions are shown. By fixing the particle size value *a* one can see the boundary values of $\omega(a_i)$ and relative frequency of calculated $\omega(a_i)$ on the *y* axis. In fact, having the fixed particle radius magnitude we deal with a histogram of the spread of $\omega(a_i)$ determination errors values. Instead of the usual histogram frequency, the relative frequency is used. The same colors correspond to the $\omega(a)$ values that occur with the same relative frequency.

Similar simulations were also performed for other methods of regularization parameter determination such as the *L*-curve [7, 8] and the Generalized Cross Validation [9]. Comparison of the derivative spectrum method with the *L*-curve and Generalized Cross Validation methods proved the advantages of the suggested method.

3. Conclusions

The new way of regularization parameter determination in Tikhonov regularization method is proposed. The advantages of the suggested method over the *L*-curve and Generalized Cross Validation techniques are demonstrated.

References

[1] А. Н. Тихонов, В. Я. Арсенин, *Методы решения некорректных задач* (М., 1979).

[2] А. Б. Бакушинский, А. В. Гончарский *Некорректные задачи. Численные методы и приложения* (М.:Узд-во Моск. ун-та, 1989).

[3] Y. Liu, W. P. Arnott, and J. Hallett, "Particle size distribution retrieval from multispectral optical depth: Influences of particle nonshpericity and refractive index" *J. Geophys. Res*. **104**, 31753 –31762 (1999).

[4] В. С. Сизиков, *Устойчивые методы обработки результатов измерений.* (Специальная литература, СПб, 1999).

[5] S. I. Hwang and S. E. Powers, "Using Particle-Size Distribution Models to Estimate Soil Hydraulic Properties," *J.* Soil Sci. Soc. Amer. **67**, 1103–1112 (2003).

[6] A. Wax, C. Yang, V. Backman, M. Kalashnikov, R. R. Dasari, M. S. Feld, et al., "Determination of particle size by using the angular distribution of backscattered light as measured with low-coherence interferometry", *J. Opt. Soc. Am. A* **19**, 312–337 (2002).

[7] K. Miller, "Least squares methods for ill-posed problems with a prescribed bound," J. Math. Anal. **1**, 52–74 (1970).

[8] C. L. Lawson and R. J. Hanson, *Solving Least Squares Problems* (SIAM, Philadelphia, 1995).

[9] G. Wahba, *Spline Models for Observational Data* (SIAM, Philadelphia, 1990).

Filling a Gap in Multiple Scattering Theory

J. W. Hovenier[1] and D. M. Stam[2]

[1] *Astronomical Institute Anton Pannekoek, University of Amsterdam, Kruislaan 403, 1098 SJ Amsterdam, The Netherlands*
[2] *SRON Netherlands Institute for Space Research, Sorbonnelaan 2, 3584 CA Utrecht, The Netherlands*
tel: +31 (20) 592 5126, fax: +31 (20) 525 7484, e-mail: hovenier@science.uva.nl

Abstract

Horizontal incidence and reflection by a plane-parallel atmosphere is investigated. A peculiar discontinuity of the reflected intensity is discussed. Several interesting properties of the bidirectional reflection function are presented, together with some applications.

1 Introduction

One of the best studied problems in multiple scattering theory is the reflection of radiation by a plane–parallel medium filled with independently scattering particles and illuminated at the top by a parallel beam of radiation, see e.g. [1]-[6]. In most publications the limiting case in which both the direction of incidence and that of reflection become grazing is not treated at all, or only touched upon. To fill this gap in multiple scattering theory we embarked some time ago in an investigation of this intriguing case. This has resulted in two papers, [7] and [8], dealing with the intensity (radiance) and polarization, respectively, of the reflected radiation. Here we focus on properties of the bidirectional reflection function.

2 Theory for horizontal directions

We consider a plane–parallel atmosphere or similar medium filled with randomly oriented particles that scatter radiation independently and without change of wavelength. The medium may be vertically inhomogeneous and semi–infinite or finite with or without a reflecting surface underneath. Suppose a parallel beam of radiation with net flux, πF_0, per unit area normal to itself is incident on every point of the top of the medium. Ignoring polarization we write the (specific) intensity of the reflected radiation emerging at the top of the medium in the form

$$I^{\rm t}(\mu,\mu_0,\phi-\phi_0)=\mu_0 R(\mu,\mu_0,\phi-\phi_0)F_0, \tag{1}$$

with $\arccos\mu$ the angle of the direction of the reflected light with the upward normal, $\arccos\mu_0$ the angle of the direction of the incoming radiation with the downward normal, ϕ and ϕ_0 the corresponding azimuth angles and $R(\mu,\mu_0,\phi-\phi_0)$ the bidirectional reflection function (BRF). It should be noted that $0\leq\mu\leq 1$ and $0\leq\mu_0\leq 1$, where $\mu=0$ means grazing reflection and $\mu_0=0$ grazing incidence.

Before presenting properties of the BRF we summarize some of the main results of [7], in which rigorous proofs are given. For the medium under consideration we have

$$\lim_{\mu_0\to 0} I_n^{\mathrm{t}}(\mu,\mu_0,\phi-\phi_0) = 0 \qquad (\mu\geq 0 \text{ and } n\geq 2), \tag{2}$$

$$\lim_{\mu,\mu_0\to 0} I^{\mathrm{t}}(\mu,\mu_0,\phi-\phi_0) = \lim_{\mu,\mu_0\to 0} I_1^{\mathrm{t}}(\mu,\mu_0,\phi-\phi_0), \tag{3}$$

$$\lim_{\mu,\mu_0\to 0} I^{\mathrm{t}}(\mu,\mu_0,\phi-\phi_0) = \frac{a^{\mathrm{t}}}{4(c+1)} Z^{\mathrm{t}}(\cos(\phi-\phi_0))F_0, \tag{4}$$

where n denotes the order of scattering, a^{t} the albedo of single scattering at the top, $Z^{\mathrm{t}}(\cos\Theta)$ the phase function at the top with Θ the scattering angle, and c a number that depends on how μ and μ_0 approach zero. More precisely, if we approach the origin of a Cartesian co–ordinate system, with μ_0 as the abscissa and μ as the ordinate, along a curve given by the function $\mu = g(\mu_0)$, the slope at the origin of $g(\mu_0)$ is c (see Fig. 1). Thus, for a straight line we have $\mu = c\mu_0$. For all curves we have $0 \leq c \leq \infty$, since μ and μ_0 are nonnegative. Therefore, for grazing incidence and reflection only first order scattering at the top of the medium contributes to the reflected intensity, but it has a peculiar discontinuity. The factor $1/(c+1)$ may take any value in the closed interval $[0,1]$, depending on how μ and μ_0 tend to zero. It is zero if we first let μ_0 tend to zero and then do the same with μ, but it is unity if μ is the first to become zero.

An important consequence of Eq. 4 is that, for a given value of c, the way in which the reflected intensity depends on azimuth in grazing incidence and reflection is proportional to the way in which the phase function at the top depends on the scattering angle. A similar statement was made by Minnaert in 1935 [9], but he did not mention the occurrence of a discontinuity, nor did he provide a rigorous proof.

We can now use the results for the intensity of the reflected light in the case of grazing incidence and reflection to derive properties of the BRF. Combining Eqs. 1 and 4 we find

$$\lim_{\mu,\mu_0\to 0} \mu_0 R(\mu,\mu_0,\phi-\phi_0) = \frac{a^{\mathrm{t}}}{4(c+1)} Z^{\mathrm{t}}(\cos(\phi-\phi_0)). \tag{5}$$

Multiplying both sides of Eq. 1 by μ/μ_0 leads to

$$\lim_{\mu,\mu_0\to 0} \mu R(\mu,\mu_0,\phi-\phi_0) = \frac{a^{\mathrm{t}} c}{4(c+1)} Z^{\mathrm{t}}(\cos(\phi-\phi_0)). \tag{6}$$

Consequently, a peculiar discontinuity occurs, when the BRF is multiplied by μ or μ_0. If $c = 1$ the two limits in Eqs. 5 and 6 are the same. Generally, the one is obtained from the other by replacing c by $1/c$. Since both limits are bounded it is clear that $\mu\mu_0 R(\mu,\mu_0,\phi-\phi_0) = 0$ if $\mu = \mu_0 = 0$.

By adding Eqs. 5 and 6 we obtain the simple relation

$$\lim_{\mu,\mu_0\to 0} (\mu+\mu_0) R(\mu,\mu_0,\phi-\phi_0) = \frac{a^{\mathrm{t}}}{4} Z^{\mathrm{t}}(\cos(\phi-\phi_0)), \tag{7}$$

which is independent of how μ and μ_0 tend to zero. Hence, adding the two peculiar discontinuities results in no discontinuity. We have thus obtained a rigorous proof of Eq. 7 for the general case of an inhomogeneous atmosphere which is semi–infinite or bounded by a reflecting surface. Eq. 7 has been reported without a rigorous proof for a semi–infinite homogeneous atmosphere by e.g. [3].

For natural and realistic model particles the right–hand side of Eq. 7 is always positive. Therefore, we must have

$$\lim_{\mu,\mu_0\to 0} R(\mu,\mu_0,\phi-\phi_0) = \infty, \tag{8}$$

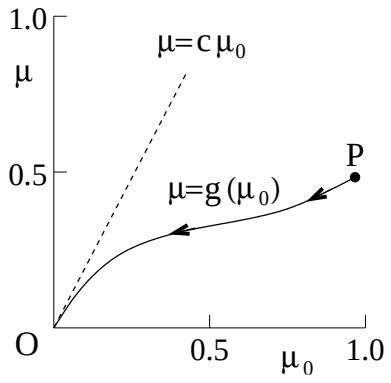

Figure 1: A point, P, approaches the origin, O, along a curve given by $\mu = g(\mu_0)$, which has a slope, c, at O with respect to the positive μ_0-axis. The tangent of the curve at O has also been drawn.

irrespective of the way in which this limit is taken, since any other result would be in conflict with Eq. 7. So the BRF itself has a discontinuity for $\mu = \mu_0$, but not a peculiar one. This is illustrated in Fig. 2 for a homogeneous, non–absorbing, semi–infinite atmosphere with isotropic scattering and $\mu = \mu_0$. As shown by [1] and later by [2] we have in this very simple case

$$R(\mu, \mu, \phi - \phi_0) = \frac{1}{8\mu} H^2(\mu), \tag{9}$$

where $H(\mu)$ is a well–known function that can be calculated by solving an integral equation and increases from 1 for $\mu = 0$ to 2.9 for $\mu = 1$. Figure 2 is based on a table (for $\varphi(\mu) = H(\mu)/2$) given by [10]. Apparently the factor $1/\mu$ is the main cause of the strong increase of the BRF in Fig. 2 as μ tends to zero. For comparison Chandrasekhar's function $S(\mu, \mu_0, \phi - \phi_0)$ [2] for $\mu = \mu_0$ is also shown in Fig. 2, illustrating its simpler behavior for small values of μ as compared to the BRF.

It should not be assumed that the discontinuity of the BRF for $\mu = \mu_0 = 0$ will never cause any problems upon integration. For example, in the case of isotropic scattering in a homogeneous, semi-infinite medium we readily find from the definition of the H-function

$$\int_0^1 R(\mu, \mu_0, \phi - \phi_0) d\mu = \frac{1}{2\mu_0} \left[H(\mu_0) - 1 \right], \tag{10}$$

which tends to infinity if μ_0 tends to zero [4].

3 Applications

The results presented in Sect. 2 can be used for various applications, as shown by the following examples.
1. Checking formulae valid for general μ and μ_0 in multiple scattering theory by letting both tend to zero.
2. Similarly, for numerical results, even for complicated models of atmospheres and oceans.
3. Interpolation of the BRF for small values of μ and μ_0, e.g. by first multiplying the BRF by $(\mu + \mu_0)$.
4. Using Eq. 7, approximate values for the phase function in the upper part of a cloud deck or aerosol layer can be obtained from observations for near grazing incidence and reflection. When this is done for a sufficient number of azimuthal angles integration over these angles yields an approximate value for the albedo of single scattering in the top layers, since the spatial average of the phase function equals unity. The necessary observations can be done, for instance, by a detector at a mountain top or in an airplane.

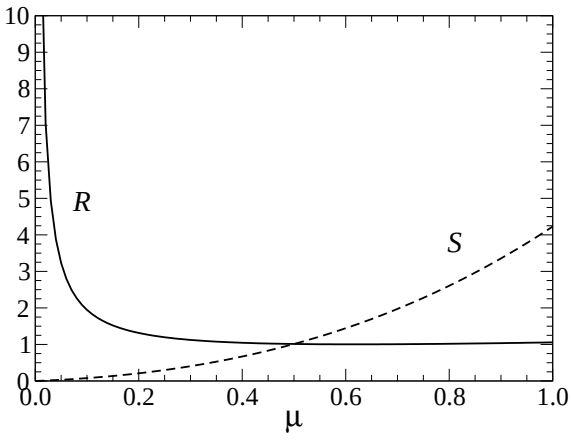

Figure 2: Bidirectional reflection function (R) and Chandrasekhar's function (S) of a non–absorbing, homogeneous, semi–infinite atmosphere with isotropic scattering in case $\mu = \mu_0$. Here, $S = 4\mu^2 R$.

5. Numerous approximation formulae for the BRF of plane-parallel media have been proposed. It is clear now that some of these cannot be accurate for near grazing incidence and reflection. This holds especially for the well-known "Lambert reflection law", which implies that the BRF would remain constant instead of tend to infinity when the directions of incidence and reflection become more and more horizontal.

References

[1] V.A. Ambarzumian, *Nauchni Trudi* (Scientific Works) (V.V. Sobolev, ed., Izd. Akad. Nauk Armyanskoi SSR, Yerevan, 1960).

[2] S. Chandrasekhar, *Radiative Transfer* (Oxford University Press, London, 1950; also Dover, New York, 1960).

[3] V.V. Sobolev, *Light Scattering in Planetary Atmospheres* (Pergamon Press, Oxford, 1975).

[4] H.C. van de Hulst, *Multiple Light Scattering* (Academic Press, San Diego, 1980).

[5] J.W. Hovenier, C. van der Mee, H. Domke, *Transfer of Polarized Light in Planetary Atmospheres. Basic Concepts and Practical Methods* (Kluwer Academic Publishers, Dordrecht, 2004).

[6] M.I. Mishchenko, L.D. Travis, A.A. Lacis, *Multiple Scattering of Light by Particles* (Cambridge University Press, Cambridge, 2006).

[7] J.W. Hovenier and D.M. Stam, "A peculiar discontinuity in the intensity of light reflected by a plane-parallel atmosphere." *JQSRT* **101**, 1–15 (2006).

[8] J.W. Hovenier and D.M. Stam, "Polarized light for horizontal incidence and reflection by plane-parallel atmospheres," *JQSRT* (accepted for publication) (2007).

[9] M. Minnaert, "Die Lichtzerstreuung an Milchglas," *Physica* **2**, 363–379 (1935).

[10] G. Placzek, "The angular distributions of neutrons emerging from a plane surface," *Phys. Rev.* **72**, 556–558 (1947).

A review of point-group symmetries in the T matrix and Green's functions formalisms

Michael Kahnert[1]

[1]*Swedish Meteorological and Hydrological Institute, Folkborgsvägen 1, S-601 76 Norrköping*
tel: +46 11-495 8013, e-mail: michael.kahnert@smhi.se

Abstract

An overview of the exploitation of boundary symmetries in electromagnetic scattering problems is presented. The paper follows the historical development of methodologies, thus starting with method-specific formulations based on boundary-integral equation approaches, followed by more general treatments based on the T matrix formulation, and finally reviewing a unified treatment of symmetries within the self-consistent Green's function formalism.

1 Introduction

Boundary symmetries of particles allow us to simplify the solution to the Helmholtz equation in electromagnetic or acoustic scattering, which results in a reduction of computational costs and and increase in numerical stability. The symmetries can either be inherent in nature, as in the case of spherical raindrops, pristine ice crystals, or cubical dry sodium chloride aerosols, or enter through simplifying assumptions by choosing symmetric model particles. Numerical experiments have demonstrated that the use of symmetries can result in reductions of CPU-time requirements by several orders of magnitude. This has paved the way for applying non-axisymmetric model particles to realistic atmospheric scattering and radiative transfer problems (see e.g. Refs. [1, 2]).

2 Exploitations of symmetries in light scattering problems

The earliest applications of symmetries in electromagnetic scattering theory have focused on specific kinds of symmetries or specific solution methods. In the special case of spherically symmetric particles the scattering problem can be solved analytically [3]. Waterman [4] investigated selected reflection symmetries in his boundary-integral equation (BIE) approach. Mishchenko [5] derived the symmetry properties of the T matrix of axisymmetric particles independent of the method employed for computing the T matrix.

More general treatments of symmetries in electrostatics and in electromagnetic and acoustic scattering theory have been conducted since the 1990's. Symmetries in integral-equation formulations of boundary value problems were studied by Zakharov et al. and applied to problems of electrostatics [6]. Zagorodnov and Tarasov studied symmetry groups in a Green's function approach to boundary value problems [7] and presented applications to integral-equation solutions to the electromagnetic scattering problem [8].

Symmetry properties of the T matrix for arbitrary symmetry groups were studied systematically for reducible [9] and irreducible representations [10]. The main idea is to investigate the transformation properties of the basis functions (usually vector spherical wave functions) under symmetry operations R, and thereby derive matrix representations $\mathbf{R}$ for each symmetry operation R in the vector space on which the T matrix operates. The symmetry properties of the T matrix can then be expressed as commutator relations

$$[\mathbf{T}, \mathbf{R}] = \mathbf{0}, \tag{1}$$

where the commutator is defined as $[\mathbf{T}, \mathbf{R}] = \mathbf{T} \cdot \mathbf{R} - \mathbf{R} \cdot \mathbf{T}$. These commutator relations reduce the number of nonzero, independent T matrix elements that need to be evaluated in numerical applications.

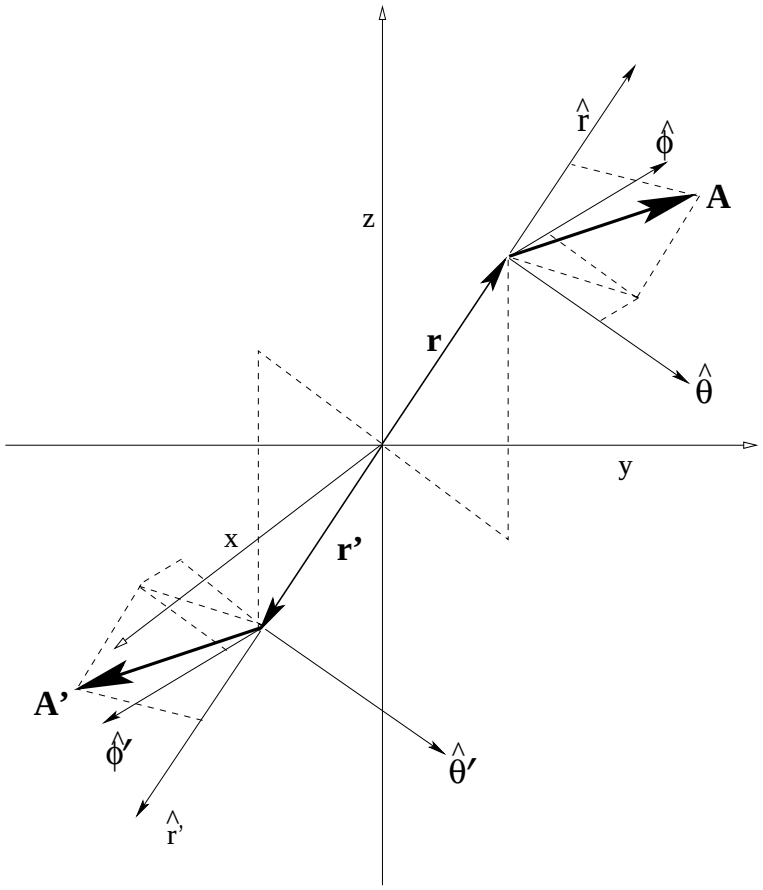

Figure 1: Transformation of a vector function under an inversion of all spatial coordinates.

Consider as an example an inversion I of the spatial coordinates given by $(x, y, z) \longrightarrow (-x, -y, -z)$. As shown in the figure a vector function given in spherical coordinates will transform according to

$$\begin{pmatrix} A_r(r,\theta,\phi) \\ A_\theta(r,\theta,\phi) \\ A_\phi(r,\theta,\phi) \end{pmatrix} \stackrel{I}{\longrightarrow} \begin{pmatrix} A_r(r,\pi-\theta,\pi+\phi) \\ -A_\theta(r,\pi-\theta,\pi+\phi) \\ A_\phi(r,\pi-\theta,\pi+\phi) \end{pmatrix}. \tag{2}$$

By using the properties of the vector spherical wave functions $\mathbf{M}^{(j)}_{n,m,\tau}$ (where $\tau = 1, 2$ and $j = 1, \ldots, 4$) this leads to

$$\mathbf{M}^{(j)}_{n,m,\tau} \stackrel{I}{\longrightarrow} (-1)^{n+\tau} \mathbf{M}^{(j)}_{n,m,\tau}, \quad j = 1, \ldots, 4. \tag{3}$$

Thus a matrix representation of the inversion operation is given in components by

$$I_{n,m,\tau;n',m',\tau'} = \delta_{n,n'}\, \delta_{m,m'}\, \delta_{\tau,\tau'}\, (-1)^{n+\tau}. \tag{4}$$

If the boundary surface is invariant under the inversion operation, then $\mathbf{T} = \mathbf{I} \cdot \mathbf{T} \cdot \mathbf{I}^{-1}$, or, analogous to Eq. (1), $[\mathbf{T}, \mathbf{I}] = \mathbf{0}$. Using Eq. (4), this becomes in explicit form

$$T_{n,m,\tau;n',m',\tau'} = (-1)^{n+\tau+n'+\tau'}\, T_{n,m,\tau;n',m',\tau'}, \tag{5}$$

or equivalently

$$T_{n,m,\tau;n',m',\tau'} = 0, \text{ unless } (n+\tau+n'+\tau') \text{ even.} \tag{6}$$

This method can be used to derive representations and symmetry relations for any symmetry operation encountered in point groups [10].

The representations **R** in the basis of vector spherical wave functions are in general reducible. By means of group theoretical techniques one can construct a similarity transformation to transform the reducible into irreducible representations, thus bringing the matrix representations into block-diagonal form. It can be shown that this transformation also brings the T and Q matrix into irreducible block-diagonal form [10]. The main idea is to construct projection operators

$$\tilde{P}^{(\mu)}_{j,i} = \sum_{g\in\mathcal{G}} \chi^{(\mu)*}(g)\, R_{j,i}(g) \tag{7}$$

that project into the μ-th irreducible invariant subspace. Here $\mathcal{G}$ denotes the symmetry group, $R_{j,i}(g)$ denote the reducible representations of group element g, and $\chi^{(\mu)}(g)$ denote the characters of the irreducible representations, which can be computed by standard group-theoretical techniques [11, 12]without prior knowledge of the irreducible representations. By use of the operators (7) one constructs a similarity transformation into the irreducible basis in which all matrix quantities become block-diagonal.

It was demonstrated by use of irreducible representations in a BIE approach [8] that exploitation of symmetries can reduce CPU-time requirements by a factor of M_0^2, where M_0 represents the order of the symmetry group. Interestingly enough, the same was observed in Ref. [13], in which only reducible representations were exploited. A recent comparison of BIE computations that exploited reducible and irreducible representations, respectively, showed that the latter only saved and additional factor of 3–4 in computation time [10]. However, it was also shown [10] that the block-diagonalisation of the T and Q matrix favourably pre-conditions the Q matrix, thus increasing the numerical stability of the Q matrix inversion problem in T matrix computations.

In a recently published treatment [14] of symmetries (which was focused on the exterior problem) it was shown that one can derive general symmetry relations of the Green's function of an arbitrary linear boundary-value problem. From the general symmetry relations, one obtains for the special case of the Helmholtz equation symmetry relations for the surface Green's function $G_{\partial\Gamma}$ of the form

$$G_{\partial\Gamma}(\mathbf{x},\mathbf{x}_s) = G_{\partial\Gamma}(D_g(\mathbf{x}), D_g(\mathbf{x}_s)) \tag{8}$$

where $\mathbf{x}$ lies in the surrounding medium and $\mathbf{x}_s$ lies on the boundary surface. The D_g denote the representations in three-dimensional space of the symmetry group's elements g. Likewise, one obtains for the volume Green's function G_{Γ_+}

$$G_{\Gamma_+}(\mathbf{x}_0,\mathbf{x}) = G_{\Gamma_+}(D_g(\mathbf{x}_0), D_g(\mathbf{x})), \tag{9}$$

where $\mathbf{x}_0$ and $\mathbf{x}$ lie in the surrounding medium. For the interaction operator $W_{\partial\Gamma}$ one obtains

$$W_{\partial\Gamma}(\mathbf{x}_s,\mathbf{x}'_s) = W_{\partial\Gamma}(D_g(\mathbf{x}_s), D_g(\mathbf{x}'_s)), \tag{10}$$

where $\mathbf{x}_s$ and $\mathbf{x}'_s$ lie on the boundary surface. These three symmetry relations are shown to be equivalent [14]. The volume Green's function is related to volume-integral equation (VIE) methods, the surface Green's function to BIE methods, and the interaction operator to the T-matrix formulation. For instance, from the symmetry relations of the interaction operator, one can derive the commutator relations of the T-matrix. Thus one has a general description of symmetries in acoustic and electromagnetic scattering theory that comprises symmetries in VIE and BIE methods as well as in the T-matrix formalism. This treatment of symmetries is based on the self-consistent Green's function formulation of the electromagnetic and acoustic scattering problem [15, 16].

References

[1] M. Kahnert and A. Kylling. Radiance and flux simulations for mineral dust aerosols: Assessing the error due to using spherical or spheroidal model particles. *J. Geophys. Res.*, 109:D09203, doi:10.1029/2003JD004318, errata: doi:10.1029/2004JD005311, 2004.

[2] T. Nousiainen, M. Kahnert, and B. Veihelmann. Light scattering modeling of small feldspar aerosol particles using polyhedral prisms and spheroids. *J. Quant. Spectrosc. Radiat. Transfer*, 101:471–487, 2006.

[3] G. Mie. Beiträge zur Optik trüber Medien, speziell kolloidaler Metallösungen. *Ann. Phys.*, 25:377–445, 1908.

[4] P. C. Waterman. Matrix formulation of electromagnetic scattering. *Proc. IEEE*, 53:805–812, 1965.

[5] M. I. Mishchenko. Light scattering by randomly oriented axially symmetric particles. *J. Opt. Soc. Am. A.*, 8:871–882, 1991.

[6] E. V. Zakharov, S. I. Safronov, and R. P. Tarasov. Finite-order abelian groups in the numerical analysis of linear boundary-value problems of potential theory. *Comput. Maths. Math. Phys.*, 32:34–50, 1992.

[7] I. A. Zagorodnov and R. P. Tarasov. The problem of scattering from bodies with a noncommutative finite group of symmetries and its numerical solution. *Comput. Maths. Math. Phys.*, 37:1206–1222, 1997.

[8] I. A. Zagorodnov and R. P. Tarasov. Finite groups in numerical solution of electromagnetic scattering problems on non-spherical particles. In *Light Stattering by Nonspherical Particles: Halifax Contributions*, pages 99–102, Adelphi, MD, 2000. Army Research Laboratory.

[9] F. M. Schulz, K. Stamnes, and J. J. Stamnes. Point group symmetries in electromagnetic scattering. *J. Opt. Soc. Am. A*, 16:853–865, 1999.

[10] M. Kahnert. Irreducible representations of finite groups in the T matrix formulation of the electromagnetic scattering problem. *J. Opt. Soc. Am. A*, 22:1187–1199, 2005.

[11] J. D. Dixon. High speed computation of group characters. *Numerische Mathematik*, 10:446–450, 1965.

[12] J. J. Cannon. Computers in group theory: a survey. *Commun. ACM*, 12:3–11, 1969.

[13] F. M. Kahnert, J. J. Stamnes, and K. Stamnes. Application of the extended boundary condition method to homogeneous particles with point group symmetries. *Appl. Opt.*, 40:3110–3123, 2001.

[14] M. Kahnert. Boundary symmetries in linear differential and integral equation problems applied to the self-consistent Green's function formalism of acoustic and electromagnetic scattering. *Opt. Commun.*, 265:383–393, 2006.

[15] T. Rother. Self-consistent Green's function formalism for acoustic and light scattering, Part 1: Scalar notation. *Opt. Commun.*, 251:254–269, 2005.

[16] T. Rother. Self-consistent Green's function formalism for acoustic and light scattering, Part 2: Dyadic notation. *Opt. Commun.*, 251:270–285, 2005.

On the (in)accuracy of the spherical particle approximation in mineral aerosol radiative forcing simulations

Michael Kahner[1], Timo Nousiainen[2], and Petri Räisänen[3]

[1]*Swedish Meteorological and Hydrological Institute, 601 76 Norrköping, Sweden*
[2]*University of Helsinki, Finland*
[3]*Finnish Meteorological Institute, Finland*

Abstract

Errors in mineral aerosol radiative forcing computations due to the spherical particle approximation (SPA) and the uncertainty in refractive index were studied. These two error sources are found to be of comparable magnitude, although strongly dependent on optical depth, surface albedo, and particle size. Thus, the use of the SPA in radiative transfer simulations may be among the major error sources in quantifying the regional climate forcing by mineral aerosols.

1 Introduction

Mineral aerosols are radiatively important owing to their widespread distribution and their relatively high optical depth [1]. Desertification caused by changes in land usage results in rising mineral dust concentrations, which is considered the dominant anthropogenic radiative forcing mechanism in and near arid regions [2]. Quantification of this radiative forcing effect is subject to various error sources, of which the uncertainty in the refractive index m and, to a lesser extent, the uncertainty in the size distribution (SD) have previously been identified as the most important ones [2]. It is common in climate applications to model optical properties of dust aerosols by use of spherical model particles. The validity of the spherical particle approximation (SPA) is rarely questioned in climate research, and it is often taken for granted that the errors caused by the SPA are small compared to those caused by other error sources. In the present study we put this assumption to a test.

2 Optical properties of mineral aerosols

Table 1 shows the aerosol samples employed in the simulations, their effective radii r_{eff}, and the uncertainty ranges of their refractive indices $m = n + i\kappa$. Also shown are the optical depths assumed in the radiative transfer simulations. The optical properties of these nonspherical dust particles are derived from measure-

Sample	r_{eff} (μm)	n	κ	τ
Feldspar	1.0	1.5–1.6	10^{-5}–10^{-3}	0.25
Red Clay	1.5	1.5–1.7	10^{-5}–10^{-3}	0.25
Green Clay	1.55	1.5–1.7	10^{-5}–10^{-3}	0.25
Loess	3.9	1.5–1.7	10^{-5}–10^{-3}	1.10
Sahara	8.2	1.5–1.7	10^{-5}–10^{-3}	1.10

Table 1: Mineral aerosol samples considered in this study.

ments available in the Amsterdam Light Scattering Database [3] (*http* : *//www.astro.uva.nl/scatter*), which

provides particle SDs and phase matrices at wavelengths of 441.6 nm and 632.8 nm for scattering angles of 5°–173°. The full phase function and the asymmetry parameter g are derived by combining the measured phase functions with Mie-computations of the diffraction peak through a variational data analysis method. The details of the procedure and a discussion of analysis errors can be found in Ref. [4].

To obtain corresponding results for spheres, and to estimate the m-uncertainty, we ran Mie simulations based on the measured SDs. The refractive index of each sample has been varied within the uncertainty ranges indicated in Tab. 1. The extreme values of g are obtained for $m_1 = n_{\min} + i\kappa_{\max}$ and $m_2 = n_{\max} + i\kappa_{\min}$. Figure 1 shows a comparison of asymmetry parameters derived from the measurements and the Mie computations. It is evident from the figure that the SPA-errors and m-related errors (estimated for spheres)

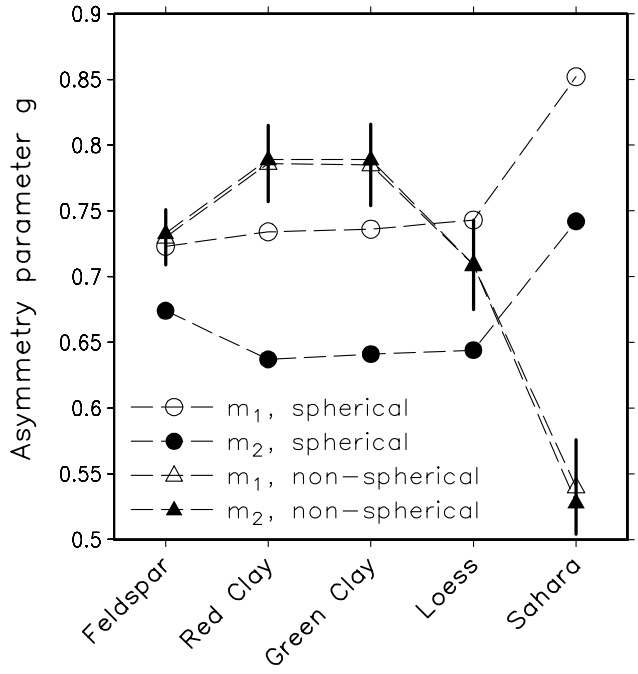

Figure 1: Values of the asymmetry parameter g at λ=441.6 nm for spherical and non-spherical aerosol particles and for refractive indices $m_1 = n_{\min} + i\kappa_{\max}$ and $m_2 = n_{\max} + i\kappa_{\min}$. The vertical bars indicate the uncertainty of g for non-spherical particles, defined as best estimate ± measurement error (one standard deviation). The m-dependence of g for non-spherical particles is artificially small since m affects only the diffraction part of the combined phase function.

in g are of comparable magnitude.

The single-scattering albedo is known to be rather insensitive to particle shape. Hence, values obtained from Mie calculations were used both for spherical and non-spherical particles.

3 Radiative transfer simulations

Radiative transfer simulations were performed for a standard tropical atmosphere. The aerosols are assumed to be spread uniformly between 0 and 5 km. The solar zenith angle is 55° (a yearly daytime-average at an altitude of 20°). Two surface albedos were used: $\alpha_s = 0.1$ (ocean surface) and $\alpha_s = 0.45$ (high-albedo desert). The lower optical depth ($\tau = 0.25$) indicated in Table 1 lies within the range of typical background values near arid regions, whereas the higher value ($\tau = 1.10$) is typical for dust-storm events.

4 Comparison of radiative flux and transmittance errors

We investigate the errors in the net radiative flux at the top of the atmosphere (TOA) (Fig. 2a), the flux absorbed within the atmosphere (Fig. 2b), the downwelling flux at the surface (BOA = bottom of atmosphere) (Fig. 2c), and the net flux at the surface (Fig. 2d). For instance, Fig. 2a shows three normalised net radiative flux errors at the TOA for a wavelength of λ=441.6 nm and for a surface albedo of α_s=0.1:

$$\delta F^{(\mathrm{net})}_{\mathrm{spher}}(m) = 100\% \times \left[F^{(\mathrm{net})}_{\mathrm{spher}}(m_1) - F^{(\mathrm{net})}_{\mathrm{spher}}(m_2)\right] / (2F_{\mathrm{solar}}) \quad (1)$$

$$\delta F^{(\mathrm{net})}_{\mathrm{m_1}}(\mathrm{SPA}) = 100\% \times \left[F^{(\mathrm{net})}_{\mathrm{spher}}(m_1) - F^{(\mathrm{net})}_{\mathrm{nonspher}}(m_1)\right] / F_{\mathrm{solar}} \quad (2)$$

$$\delta F^{(\mathrm{net})}_{\mathrm{m_2}}(\mathrm{SPA}) = 100\% \times \left[F^{(\mathrm{net})}_{\mathrm{spher}}(m_2) - F^{(\mathrm{net})}_{\mathrm{nonspher}}(m_2)\right] / F_{\mathrm{solar}}. \quad (3)$$

Here, $F^{(\mathrm{net})}_{\mathrm{nonspher}}$ and $F^{(\mathrm{net})}_{\mathrm{spher}}$ denote spectral net fluxes computed using optical properties for non-spherical and spherical aerosols, respectively. Hence, $\delta F^{(\mathrm{net})}_{\mathrm{spher}}(m)$ (black bars) is the normalised net flux error related to the uncertainty in m, based on computations for spherical particles. It is defined here by dividing the maximal m-related uncertainty range by a factor of two. Similarly, $\delta F^{(\mathrm{net})}_{\mathrm{m_1}}(\mathrm{SPA})$ (shaded bars) and $\delta F^{(\mathrm{net})}_{\mathrm{m_2}}(\mathrm{SPA})$ (white bars) represent the net radiative flux errors caused by the SPA for refractive indices m_1 and m_2, respectively. The normalised errors in atmospheric absorptance (Fig. 2b), downwelling flux at the surface (Fig. 2c) and net flux at the surface (Fig. 2d) are defined analogously. The main result in Fig. 2a is that the SPA-related errors in the TOA net flux $\delta F^{(\mathrm{net})}_{\mathrm{m_1}}(\mathrm{SPA})$ and $\delta F^{(\mathrm{net})}_{\mathrm{m_2}}(\mathrm{SPA})$ are in most cases comparable to, and sometimes even larger than the error related to the m-uncertainty $\delta F^{(\mathrm{net})}_{\mathrm{spher}}(m)$. Another result is that there are clear differences between $\delta F^{(\mathrm{net})}_{\mathrm{m_1}}(\mathrm{SPA})$ and $\delta F^{(\mathrm{net})}_{\mathrm{m_2}}(\mathrm{SPA})$. Thus the SPA and the uncertainty in the refractive index are strongly correlated error sources in net flux simulations.

Similar observations apply to the BOA transmitted and net fluxes in Figs. 2c and 2d. Thus the SPA- and m-related errors in these radiative quantities are of comparable size. On the other hand, the error in the absorbed flux (Fig. 2b) is entirely dominated by the uncertainty in m.

Computations for a surface albedo of $\alpha_s = 0.45$ indicated that for the TOA net flux, the m-related error is larger and the SPA-error is smaller than for $\alpha_s = 0.10$. The absorbed flux error is, as expected, again dominated by the m-error. At BOA, however, the SPA-error still dominates over the m-error in net-flux and transmitted-flux computations.

Finally, we remark that the flux errors considered here can equivalently be regarded as radiative forcing errors, since radiative forcing is defined as $\Delta F = F_{\text{aerosols included}} - F_{\text{no aerosols}}$, where the aerosol-free case is not impacted by the treatment of aerosol optical properties.

5 Conclusions

The primary conclusion of this study is that the use of spherical model particles (Mie theory) can introduce substantial errors in simulated mineral aerosol radiative forcing at the TOA and at the surface. The errors are comparable to those related to the uncertainty in the refractive index m, which is generally believed to be the largest error source. Due to the widespread use of the SPA in aerosol climate studies, this error source could have far-reaching consequences in assessing the direct climate forcing effect of mineral aerosols.

The SPA errors arise through the misrepresentation of the phase function and the related error in the asymmetry parameter g. Moreover, the radiative flux errors caused by the SPA appear rather unpredictable and defy simplistic corrections, since their magnitude and sign depend on particle size, surface albedo, wavelength, and optical depth, and since they are strongly correlated with the radiative flux errors caused by the m-uncertainty. The SPA-related TOA and surface net-flux errors are more pronounced over the ocean, whereas the significance of the corresponding m-related errors increase over land surfaces. The error in the downwelling flux at the surface is much less sensitive to surface albedo.

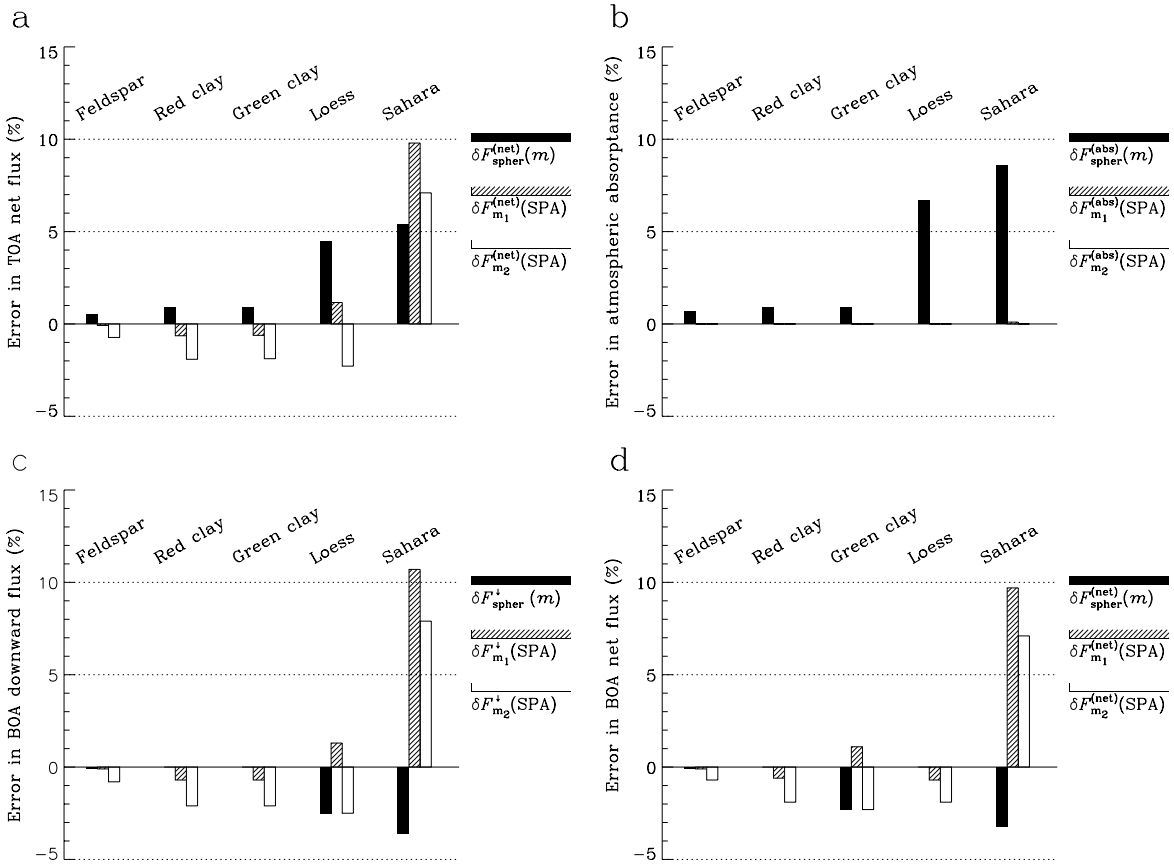

Figure 2: (a) Normalised spectral net flux errors at TOA (as defined by Eqs. (1)–(3)) for the five aerosol samples at a wavelength of 441.6 nm and a surface albedo of 0.1. (b)–(d) Same as (a), but for the errors in atmospheric absorptance, downward flux at the surface (BOA), and net flux at the surface, respectively.

References

[1] I. N. Sokolik, D. M. Winker, G. Bergametti, D. A. Gilette, G. Carmichael, Y. J. Kauman, L. Gomes, L. Schuetz, and J. E. Penner. Outstanding problems in quantifying the radiative impacts of mineral dust. *J. Geophys. Res.*, 106:18015–18027, 2001.

[2] G. Myhre and F. Stordal. Global sensitivity experiments of the radiative forcing due to mineral aerosols. *J. Geophys. Res.*, 106:18193–18204, 2001.

[3] H. Volten, O. Muñoz, E. Rol, J. F. de Haan, W. Vassen, J. W. Hovenier, K. Muinonen, and T. Nousiainen. Scattering matrices of mineral aerosol particles at 441.6 nm and 632.8 nm. *J. Geophys. Res.*, 106:17375–17401, 2001.

[4] M. Kahnert and T. Nousiainen. Variational data analysis method for combining laboratory-measured light scattering phase functions and forward-scattering computations. *J. Quant. Spectrosc. Radiat. Transfer*, 103:27–42, 2007.

Engineering of plasmon-resonant nanostructures for biomedical applications

Boris Khlebtsov,[1] Vitaly Khanadeev,[2]
Vladimir Bogatyrev,[1,2] Lev Dykman,[1] and Nikolai Khlebtsov[1,2]

[1]*Institute of Biochemistry and Physiology of Plants and Microorganisms Russian Academy of Sciences, 13 Pr. Entuziastov, Saratov 410049, Russia*
[2]*Saratov State University, 83 Astrakhanskaya St., Saratov 410026, Russia*

Abstract

Interest in metal nanostructures stems from their unique optical properties related with single-particle or collective plasmons. This report is focused on optical properties of gold nanorods and silica/gold nanoshells, whereas the synthesis protocols and biomedical applications are discussed shortly. Our consideration includes the following topics: (1) depolarized light scattering by gold nanorods; (2) sensitivity of longitudinal dipole plasmon to dielectric environment; (3) scaling properties of nanorod multipole plasmons; (4) engineering of silica/gold nanoshells for tunable optical properties; (5) collective plasmons in self-assembled nanoshell monolayers; (6) applications of plasmon-resonant particles to solid-phase immunoassay, photothermal therapy, and OCT.

1 Introduction

Gold plasmon-resonant nanoparticles have found various applications in nanobiotechnology and biomedicine [1] due to their exceptional biocompatibility. An additional advantage of such nanostructures is related to their spectral tuning of the localized plasmon resonance (LPR) by variation of metal, size, shape, structure and dielectric environment. The last property includes both the local dielectric environment formed by adsorbed probing or target molecules, and the global dielectric properties of a liquid medium, dielectric solid matrix, or dielectric substrate with dissolved, embedded, or adsorbed particles, respectively. Attachment of biomolecules to the nanoparticle surface due to physical adsorption or covalent binding via thiol-modified sites is called functionalization [2], and the functionalized nanoparticles are often called bioconjugates. Until quite recently, the colloidal gold nanosphere bioconjugates were used in the majority of biomedical applications [3]. New activities have been further motivated by recent advances in metal nanoparticle synthesis, including nonspherical and/or inhomogeneous particles such as gold nanoshells [4], nanorods [5], "nanorice" [6], "nanostars", etc. These new nanostructures allow for easy tuning of their spectral, scattering, and absorption properties. Furthermore, the collective electromagnetic response of multiparticle ensembles also shows rich optical properties and great promise to meet the rigorous demands of biodiagnostics and nanomedicine.

Here we discuss the optical properties and possible applications of two popular types of nanoparticles, viz. gold nanorods and silica/gold or polystyrene/gold nanoshells. Inhomogeneous broadening of the extinction spectra caused by the particle polydispersity and the surface-electron scattering has been studied by Westcott et al. [7]. By contrast to this study, we report on the mechanisms of spectral broadening in polydisperse ensembles as probed by the *differential light scattering* technique. For gold nanorods, our consideration is focused on the depolarized light scattering by usual small rods and on the scaling properties of multipole resonances exhibited by larger particles. The optics of interacting nanoparticles is exemplified by a self-assembled monolayer of nanoshells. It has been reported [8] that the extinction spectrum of a silver particle monolayer exhibits sharp resonance peak related to excited quadrupole and suppressed dipole resonances. Our simulations and experiments show that this feature of the monolayer collective response has a general physical basis and does not depend on the single-particle properties. In the final section of this report

we discuss shortly some up-to-date biomedical applications of functionalized plasmon-resonant nanoparticles.

2 Gold nanorods

In the Rayleigh (dipole) approximation, a small gold or silver nanorod exhibits two plasmon resonances corresponding to the excitation of a particle along and perpendicular to its major geometrical axis. In the dipole approximation, the resonance wavelengths are given by expression $\lambda_{\mathrm{P},\perp} = \lambda_p \sqrt{\varepsilon_{ib} + (1/L_{\mathrm{P},\perp} - 1)\varepsilon_m}$, where λ_p is the bulk electron plasma wavelength, ε_{ib} is the interband contribution of valence electrons to the bulk dielectric function, $L_{\mathrm{P},\perp}$ are the so-called geometrical depolarization factors, and ε_m is the dielectric function of the surrounding medium. The geometrical depolarization factors strongly depend on the particle shape, so the LPR peak position can easily be tuned by variation in the particle aspect ratio.

It is well known (van de Hulst, 1957; Kerker, 1969) that the depolarization ratio of the scattered intensities $I_{\mathrm{vh}} / I_{\mathrm{vv}}$ cannot exceed 1/3 for "usual" small randomly oriented particles. However, for plasmon-resonant particles, this constrain does not hold and the upper limit for depolarization ratio is equal to ¾ [9, 10]. Our theoretical analysis, based on the Rayleigh approximation[1] and the exact T-matrix calculations, together with experimental measurements confirmed the existence of unusual depolarization properties of gold nanorods.

To date, the dipole plasmon resonances of metal nanorods have been studied in details both theoretically and experimentally. During past 5-8 years, there appeared several observations of multipole plasmon excitations in gold and silver nanowires deposited onto a substrate (see, e.g., [11] and references therein) and gold nanorods suspended in water [12]. Here we report on the relationships between the multipole plasmons of nanorods and their size, shape, and orientation with respect to polarized incident light. We have found that the multipole resonance wavelengths as a function of the aspect ratio divided by the resonance number collapse onto one linear curve [13] (Fig. 1). This scaling property is explained by using the plasmon standing wave concept [14].

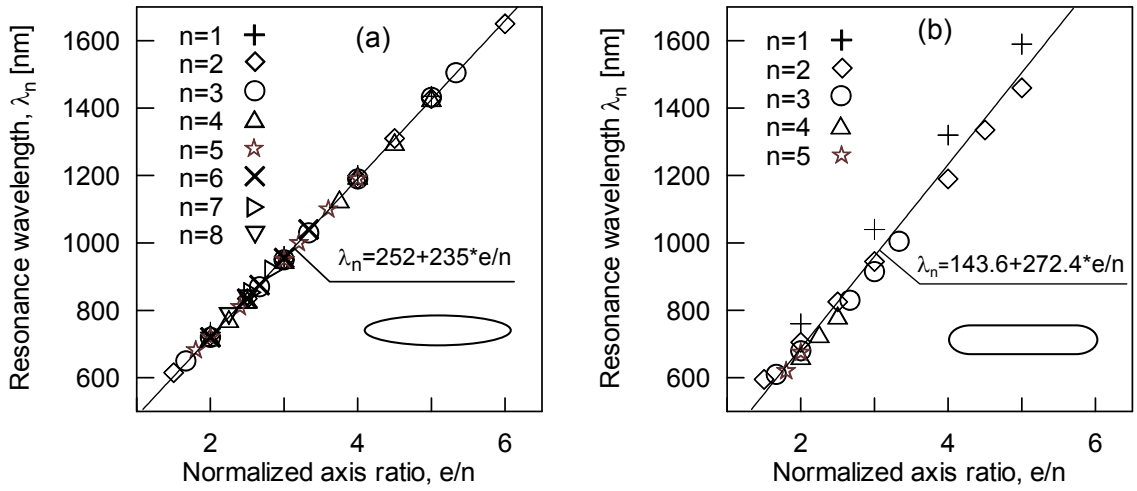

Fig. 1. The linear scaling of multipole resonance wavelengths λ_n *vs* normalized aspect ratio e/n. Calculations for randomly oriented gold spheroids (a) and s-cylinders (b) in water. The particle diameter $d = 80$ nm, the aspect ratio $e = L/d$ = 2-20 (a), 2-12 (b), and the extinction resonance number $n = 1-8$ (dipole, quadrupole, etc.).

[1] Recently, our conclusions about upper depolarized ratio limits for metal and dielectric particles were reproduced by Calander et al. (Chemical Physics Letters **434**,326–330 (2007)) by using a similar Rayleigh approximation analysis.

3 Silica/Gold nanoshells

The effects of the gold nanoshells structural polydispersity and the surface electron scattering in a thin metal layer on the resonance light scattering spectra are studied theoretically and experimentally for the silica/gold nanoshell water colloids. To test the calculations experimentally, two samples of nanoshells (designated 1 and 2) were synthesized. According to the dynamic light scattering data, the sample 1 particles have a 90-nm diameter of core and a broad shell thickness distribution (with an average value of 30 nm), whereas the sample 2 particles have a 70-nm diameter of core and a narrow shell thickness distribution (with an average value of 12 nm). For sample 1, the inhomogeneous broadening of the scattering spectrum is completely determined by the polydispersity; therefore, the bulk constants of gold can be used in simulation of the particle spectra. For sample 2, the main mechanism of the broadening is related to the limitation of the free path of electrons, whereas the contribution from the shell thickness distribution can be neglected.

Recently, Chumanov's group [8] reported on some interesting optical properties of interacting silver nanospheres assembled into 2D array and possessing the dipole and quadrupole single-particle resonances. Here we extend these observations for several kinds of nanostructures to illustrate the general physical basis of the dipole resonance suppression phenomenon. The extinction, scattering, and absorption spectra of silver and gold nanosphere and nanoshell 2D monolayers were calculated by the generalized multiparticle Mie solution. Because of the coherent interaction among particles in the array, the dipole band of extinction disappeared and only the quadruple component of the spectra was observed. In the experimental section, we examined the suspensions and 2D self-assembled arrays of nanoshells with a silica core diameter of 210 nm and a gold shell thickness of 28 nm. Although the dipole resonance suppression phenomenon was not as spectacular as in the case of silver nanospheres, we observed qualitative agreement between the experimental and theoretical data.

4 Biomedical applications

Both the gold nanorods and nanoshells are exceptionally biocompatible nanomaterials, which surface can be easily functionalized by key probe molecules such as antibodies, oligonucleotides, biotin, protein A, lectins, enzymes, etc. Such hybrid nanoparticle-molecule structures are basic build blocks for biosensorics, targeted drug or gene vectors delivery, photothermal therapy, and biomaterial imaging based the dark-field light microscopy, laser confocal microcopy, or OCT techniques. Recent reported examples are application of these techniques to cancer cell experiments in vitro [15] and OCT imaging with gold nanoshells and nanorods [16].

Last year, at St.-Petersburg ELSN-9 Conference, we demonstrated a short dark-filed microscopy movie to visualize the dynamic behavior and interaction of gold nanorods and rat macrophages. Quite recently, Cortie group reported on successful photothermal destruction of murine microphages labeled with gold-nanorod-monoclonal-antibody conjugates [17].

In this report, we discuss our recent first application of silica-gold nanoshells to a solid-phase dot immunoassay [18]. The assay principle is based on staining of a drop (1μL) analyte on a nitrocellulose membrane strip by using silica/gold nanoshells conjugated with biospecific probing molecules. Experimental example is human IgG (hIgG, target molecules) and protein A (probing molecules). For usual 15-nm colloidal gold conjugates, the minimal detectable amount of hIgG is about 4ng. By contrast, for nanoshell conjugates (silica core diameter of 70 nm and gold outer diameter of 100 nm) we have found significant increase in detection sensitivity and the minimal detectable amount of hIgG is about 0.5 ng. This finding is explained by the difference in the monolayer particle extinction.

Finally, we provide an illustration of erythrocyte and living bacteria imaging with silica-gold nanoshells as resonance-scattering labels. In this case, nanoshells are seen as bright red dots against a dark background, except for yellow areas of aggregation, where nanoshells are in close proximity and the plasmon resonance wavelength is changed.

Acknowledgments

This research was partially supported by grants No. 05-02-16776 (RFBR), RNP.2.1.1.4473 and contracts No. 02.513.11.3043 and 02.512.11.2034 (the Ministry of Science and Education of RF). BK was supported by grants from the President of the Russian Federation (no. MK 2637.2007.2) and INTAS YS Fellowship (№06-1000014-6421).

References

[1] M.M. Cheng et al. "Nanotechnologies for biomolecular detection and medical diagnostics," Curr. Opin. Chem. Biol. **10**, 11-19 (2006).

[2] W.R. Glomm, "Functionalized gold nanoparticles for applications in bionanotechnology," J. Dispers. Sci. Technol. **26**, 389-414 (2005) .

[3] M.A. Hayat (Ed.). *Colloidal Gold: Principles, Methods and Applications*. (Academic Press, San Diego, 1989, V. 1.; V. 2; 1990, V. 3.).

[4] L.R. Hirsch et al. "Metal nanoshells," Ann. Biomedical Engineering, **34**, 15-22 (2006).

[5] C.J. Murphy et al. "One-dimensional colloidal gold and silver nanostructures," Inorg. Chem. **45**, 7544-7554 (2006).

[6] H. Wang et al. "Nanorice: A hybrid plasmonic nanostructure," Nano Lett. **6**, 827-832 (2006).

[7] S.L. Westcott et al. "Relative contributions to the plasmon line shape of metal nanoshells," Phys. Rev. B **66**, 155431 (2002).

[8] S. Malynych and G. Chumanov, "Coupled planar silver nanoparticle arrays as refractive index sensors," J. Opt. A: Pure Opt. **8**, 144-147 (2006).

[9] N.G. Khlebtsov et al ."Can the light scattering depolarization ratio of small particles be greater than 1/3?" J. Phys. Chem. B **109**, 13578-13584 (2005).

[10] N.G. Khlebtsov et al. "Depolarization of light scattered by gold nanospheres and nanorods," Opt. Spectrosc. **100**, 448-455 (2006).

[11] G. Laurent et al. "Surface enhanced Raman scattering arising from multipolar plasmon excitation," J. Chem. Phys. **122**, 011102 (2005).

[12] E.K. Payne et al. "Multipole plasmon resonances in gold nanorods," J. Phys. Chem. B **110**, 2150–2154 (2006).

[13] B.N. Khlebtsov, A.G. Melnikov, and N.G. Khlebtsov, "On the extinction multipole plasmons in gold nanorods," J. Quant. Spectr. Radiat. Transfer (2007, in press).

[14] G. Schider et al. "Plasmon dispersion relation of Au and Ag nanowires," Phys Rev B **68**, 155427 (2003).

[15] P.K. Jain, I.H. El-Sayed, and M.A. El-Sayed, "Au nanoparticle target cancer," Nanotoday, **2**, 18-29 (2007).

[16] C. Loo et al. "Gold nanoshell bioconjugates for molecular imaging in living cells," Opt. Lett. **30**, 1012-1014 (2005); A. L. Oldenburg et al. "Plasmon-resonant gold nanorods as low backscattering albedo contrast agents for optical coherence tomography," Optics Express, **14**, 6724-6738, 2006.

[17] D. Pissuwan et al. "Targeted destruction of murine macrophage cells with bioconjugated gold nanorods," J. Nanoparticle Research (2007) DOI 10.1007/s11051-007-9212-z.

[18] B.N. Khlebtsov et al. "A solid-phase dot assay using silica/gold nanoshells," Nanoscale Research Letters **2**, 6-11 (2007).

Optical characteristics of composite ellipsoidal solid-phase aerosols with variable carbon content

Miroslav Kocifaj,[1] and Gorden Videen[2]

[1] *Astronomical Institute, Slovak Academy of Sciences, Dúbravská 9, 845 04 Bratislava, Slovak Republic, astromir@savba.sk*

[2] *US Army Research Laboratory, AMSRD-ARL-CI-EM, 2800 Powder Mill Road, Adelphi, MD 20783-1197, E-mail: gvideen@science.uva.nl*

Abstract

The optical behavior of three-component carbonaceous ellipsoidal aerosols is analyzed. Compared to compact ellipsoids, the fragmented particles show enhanced backscatter and linear polarization. Employment of EMTs may lead to overestimation of both the asymmetry parameter and efficiency factor for absorption, but bulk Q_{ext} is only slightly influenced. Typically the compact particles, whose absorbing component has the largest air-carbon interface, absorb less efficiently than particles with random fragmentation.

1 Introduction

Fine submicron-sized aerosols can occur in both the solid phase and the liquid phase. Such particles are too small to settle rapidly or to be washed out by rain, but they are still sufficiently large to avoid coagulation processes. Thus their survival time in the atmosphere is quite long. Solid-phase aerosols are almost typically non-spherical and are rarely homogeneous. While the prevailing constituents of aerosol particles can be constantly identified in some territories, the internal structure of such particles is a notoriously unknown quantity and depends on many factors participating in processes of particle formation. The optical response of the particles (having known size, shape, orientation and composition) to the incident electromagnetic radiation is still uncertain due to the variety of possible internal mixing of individual materials.

Basically, it is impossible to describe the realistic shapes of ambient aerosols. Instead, it is more convenient to characterize the prevailing morphology by means of aspect ratio ε that relates the largest and smallest characteristic sizes of arbitrarily shaped particle. One of the easiest ways to simulate non-spherical particles having different aspect ratios is to employ mathematically well-defined geometries, like ellipsoids. Then, the ratio of the major semiaxis a to the minor semiaxis b (i.e. the aspect ratio) may vary from $a/b \approx 1$ (for nearly spherical particles) to $a/b >> 1$ (for needle-like particles) or $a/b << 1$ (for disk-like particles) [1].

We present results of numerical simulations of the optical behavior of carbonaceous non-spherical particles with random as well as non-random internal mixing of individual materials. The numerical study is based on the discrete dipole approximation (DDA). At present, many excellent numerical tools are available to calculate optical properties of non-spherical particles, yet there is still a lack of methods applicable for composite particles. Therefore a set of effective medium theories (EMTs) was developed to overcome computational difficulties (typical e.g. for DDA). However, the correctness of EMTs is questionable and their usage may result in errors.

We perform numerical light-scattering simulations for ellipsoidal aerosol particles composed of ammonium sulfate, organic matter and black carbon. Organic matter typically influences the atmospheric radiation through both scattering and absorption. Elemental carbon includes strongly light-absorbing material and is thought to yield large positive radiative forcing. Ammonium sulfates represent a quite important aerosol constituent in urban atmospheres.

2 Computational model

Generally speaking, EMTs approximate the optical properties of the inhomogeneous scatterer by those of a homogeneous particle of the same shape. The advantage of an EMT is that a homogeneous particle can be calculated much more easily and rapidly than a heterogeneous particle. One of the easiest, but physically not-well-justified EMTs is volume (mass) weighted mixing for which the resulting refractive index m of a particle is given as follows: $m = \sum_j m_j f_j$, where m_j is the refractive index of j-species and f_j is its volume fraction. To render principal differences between the EMT-based approach and regular (DDA-based) calculation, we consider the volume weighted mixing rule.

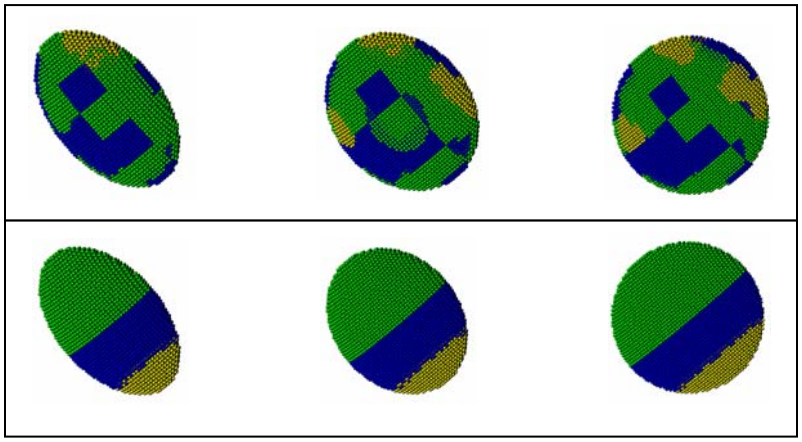

Figure 1: Applied particle models for the low-carbon case. Top shows particles with materials randomly distributed. Bottom shows particles with materials in clumps.

The basic particle model we incorporated into numerical scheme coincides with typical urban aerosols composed of ammonium sulfates (volume content ~ 50%, refractive index 1.52-0.0*i*), organic matter (volume content ~ 40%, refractive index 1.46-0.016*i*), and black carbon with approximately 10% volume content and refractive index 1.75-0.3*i* [2]. However, under some conditions the carbon can occur as an abundant component with volume fraction 20-30%. These situations are studied as "high carbon content case" (where organic matter is varied between 20-40% of particle volume, and ammonium sulfate ranges from approximately 40% to 50 % of particle volume). To check the simultaneous effect of asphericity and material configuration on particle optical properties, we model the aspect ratios of rotationally symmetric particles to be close to 1.4 - 1.6 as this range is well applicable to tropospheric particles [3].

Two basic approaches are employed to simulate the internal mixing of materials: a) the individual pieces of different constituents are distributed randomly in the particle body and b) the individual constituents are not scattered over the particle volume but are rather clumped together into compact blocks (Fig. 1). For both models we calculate the optical characteristics (phase function, polarization and efficiency factors for scattering, absorption and extinction, and asymmetry parameter) using the EMT approximation that assumes the effective refractive index is the volume-averaged refractive index of the components [4]. We analyze particles with *i*) prolate, *ii*) moderate, and *iii*) oblate forms. The classification is based on the mutual relation of particle sizes in X, Y, and Z, which are in our case given as follows: *i*) 1.6/1.0/1.0, *ii*) 1.6/1.3/1.1, *iii*) 1.6/1.6/1.0. All computations are made for incident monochromatic radiation with wavelength $\lambda = 0.525$ μm.

3 Numerical results and discussion

When computing the optical properties of composite randomly oriented particles we especially paid attention to modeling the phase function, polarization and efficiency factors for scattering Q_{sca}, absorption Q_{abs}, extinction Q_{ext}, and asymmetry parameter g. The computer model of the particle is expanded or contracted to produce scattering calculations for particles of different size. The precision of the DDA scattering calculations approximately depends on parameter $|m|kd$, where d is the inter-dipole separation, k is the wave number ($k = 2\pi/\lambda$) and m is the complex refractive index of the particle. To guarantee that scattering calculations are sufficiently accurate, the parameter given above should be less than 1. We increased the number density of dipoles always when necessary to satisfy this requirement.

The computational results show slight differences between optical properties of particles built from compact homogeneous blocks and particles composed of randomly mixed pieces of material constituents (Fig. 2). As expected the most affected quantity is Q_{abs}: particles with characteristic random material configuration absorb more efficiently than particles built from compact blocks (refer to DDA calculations presented in Fig. 2). We discussed this in [5] for very small particles. As known from macrophysical studies the light transmitted into a material generally is increased if the media on either side of the interface have similar refractive indices. The air-carbon interface

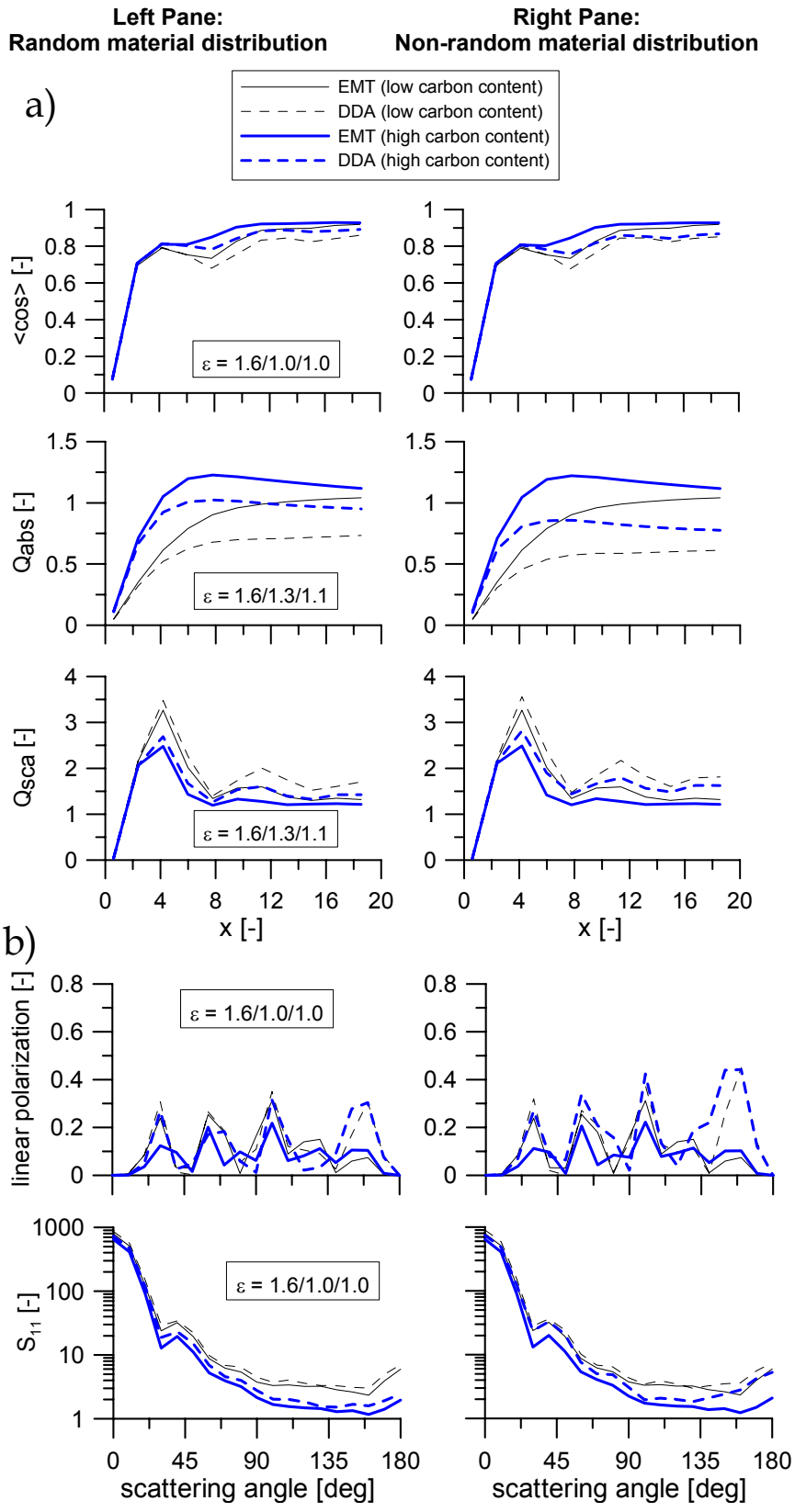

Figure 2: Optical properties of three-component carbonaceous ellipsoidal particles: a) Bulk properties and b) scattering response of x = 6 particles.

tends to reflect more light than the ammonium sulphate-carbon (or organic matter-carbon) interface. Therefore three-segment compact ellipsoids, whose absorbing component has the largest air-carbon interface absorb less efficiently than randomly fragmented ellipsoid.

Compared with DDA results, the volume-weighted EMT results overestimate both the asymmetry parameter and absorption efficiency, and usage of the EMT results in a quite evident reduction of scattering efficiency. Altogether these effects tend to cancel, leaving the extinction efficiency Q_{ext} the most accurate quantity reproduced using EMTs. Discrepancies in the behavior of linear polarization and phase function is observed at large scattering angles for particles whose size is comparable to the wavelength of incident radiation: 1) the fragmented ellipsoids show a bit larger linear polarization than the compact ellipsoid, and also 2) the fragmented ellipsoids with high-carbon content scatter more in the backward direction than the compact ellipsoid. This can be due to reduced absorption or additional internal interactions.

Acknowledgments

This work has been supported by a Grant No. 1/3074/06 of the Scientific Grant Agency VEGA.

References

[1] N. V. Voshchinnikov, V. B. Il'in, Th. Henning, B. Michel, V. G. Farafonov, "Extinction and polarization of radiation by absorbing spheroids: shape/size effects and benchmark results," J. Quant. Spectrosc. Rad. Transfer **65**, 877-893 (2000)

[2] H. Horvath, M. Kasahara, P. Pesava, "The size distribution and composition of the atmospheric aerosol at a rural and nearby urban location," Journal of Aerosol Science **27**, 417–435 (1996)

[3] M. I. Mishchenko, A. A. Lacis, B. E. Carlson, L. D. Travis, "Nonsphericity of dust-like tropospheric aerosols: implications for aerosol remote sensing and climate modeling," Geophys. Res. Lett. **22**, 1077-1080 (1995)

[4] L. Kolokolova, B. Å. S. Gustafson, "Scattering by inhomogeneous particles: microwave analog experiments and comparison to effective medium theories," J. Quant. Spectrosc. Rad. Transfer **70**, 611-625 (2001)

[5] M. Gangl, M. Kocifaj, G. Videen, H. Horvath, "Light absorption by coated nano-sized carbonaceous particles," Atmosph. Environ. (under review, 2007)

Application of the modified method of discrete sources for solving the problem of wave scattering by group of bodies.

A.G.Kyurkchan, S.A.Manenkov

Moscow Technical University of Communications and Informatics,
Aviamotornaya, 8A, 111024, Moscow, Russia
tel:+7-495 -2737509, e-mail: kyurkchan@yandex.ru

Abstract

The new method for solving the problem of wave diffraction on a group of bodies of revolution is presented. The method is based on the simple algorithm and it allows to calculate the electromagnetic field and the pattern with high accuracy.

1 Introduction

The modified method of discrete sources (MMDS), offered in the paper [1], has been subsequently applied for solving a wide class of problems of diffraction theory, and in all the cases high efficiency of the method [2] has been shown. The uniform way of construction of the carrier of discrete (auxiliary) sources by means of analytical deformation of border of a scatterer is the main idea of the method. Thus a priori information of properties of analytical continuation of diffraction field inside the scatterer is materially used.

The major practical issue is how to apply MMDS for solving the problem of wave diffraction on a closely located group of bodies. In consequence of diffraction interaction of the bodies the picture of arrangement of the singularities of the analytical continuation of wave field inside each scatterer can significantly differ from that which takes place in the case of a single body. In the case of close location of the scatterers singular points start "to be multiply", i.e. the singularities inside one body generate the singularities inside the other. In the paper some modification of MMDS is realized. This makes the method efficient for solving the problem of wave diffraction on a closely located group of bodies. The essence of this modification is that the carrier of discrete sources for each body is constructed using usual scheme of MMDS. However the sources surrounding the singular points, which appear because of the interaction between the scatterers, are appended in addition to the basic sources. In the paper the effective numerical algorithm for finding the singularities based on the continuation by a parameter is offered.

2 The statement of the problem and main relations.

Let the group of two bodies of revolution is located on one axis and bounded by surfaces S_1 and S_2. We choose the system of coordinates so that the axis z coincides with the axis of revolution of the bodies. Assume, that the impedance boundary condition on the surfaces of the scatterers is satisfied:

$$\vec{n}_p \times \vec{E} = Z_p \vec{n}_p \times (\vec{n}_p \times \vec{H}), \quad p = 1,2\,, \tag{1}$$

where Z_p is the impedance on the surface S_p and $\vec{n}_p$ is the outward normal. The secondary field, everywhere outside the domains of the bodies, obeys the homogeneous Maxwell equations and the attenuation condition at infinity.

Let's introduce the local systems of coordinates connected with each of the scatterer. We choose the origins of the systems inside the surfaces S_1 and S_2. Then the secondary field is equal to the sum of the fields scattered by each body:

$$\vec{E}^1 = \frac{\eta}{i} \nabla_p \times \nabla_p \times \sum_{p=1}^{2} \int_{\Sigma_p} \vec{J}_p G_p d\sigma, \tag{2}$$

$$\vec{H}^1 = k \cdot \nabla_p \times \sum_{p=1}^{2} \int_{\Sigma_p} \vec{J}_p G_p d\sigma, \tag{3}$$

where

$$G_p = \frac{\exp(-ikR_p)}{4\pi kR_p}, \quad R_p = \left|\vec{r}_p - \vec{r}'_p\right|, \quad \vec{r}'_p \in \Sigma_p, \quad p = 1,2. \tag{4}$$

Here Σ_p is the auxiliary surface of revolution located inside the initial surface S_p of the p-th body, $\vec{J}_p$ is the unknown current distributed on the surface Σ_p, k is the wave-number, η is the wave impedance of the medium. The expressions for the electric and magnetic field components in the spherical coordinate system connected with the given body, are presented in [2]. Similarly to the paper [2] we pass to the parametrical representation of the surfaces of the scatterers. Then for the surfaces S_1 and S_2 we get:

$$x_p = r_p \sin\theta_p \cos\varphi, \quad y_p = r_p \sin\theta_p \sin\varphi, \quad z_p = r_p \cos\theta_p, \quad p = 1,2, \tag{5}$$

where $r_p = r_p(\theta_p)$ are the equations of these surfaces in the local spherical coordinates. The auxiliary surface Σ_p has the following equations:

$$x'_p = \rho_p \sin\alpha_p \cos\varphi, \quad y'_p = \rho_p \sin\alpha_p \sin\varphi, \quad z'_p = \rho_p \cos\alpha_p, \tag{6}$$

where

$$\alpha_p = \arg\xi_p(t_p), \quad \rho_p = \left|\xi_p(t_p)\right|, \quad \xi_p(t_p) = r_p(t_p + i\delta_p)\exp(it_p - \delta_p), \quad p = 1,2. \tag{7}$$

In the formulas (7) δ_p is the positive parameter responsible for the degree of deformation of the contour of the p-th body cross-section, $t_{1,2} \in [0,\pi]$. The choise of the parameters δ_p is described in [2]. By analogy with the paper [2] we present the unknown currents on the surfaces $\Sigma_{1,2}$ in the form:

$$\vec{J}_p = \vec{I}_p / (\chi_p \rho_p \sin\alpha_p), \quad \chi_p = \sqrt{\rho_p^2(\alpha_p) + \rho'(\alpha_p)^2}, \tag{8}$$

where strokes mean the derivatives with respect to the corresponding arguments and

$$\vec{I}_p = I_{p1} \frac{\rho'_p(\alpha_p)}{\rho_p(\alpha_p)} \vec{i}_{\rho_p} + I_{p1} \vec{i}_{\alpha_p} + I_{p2} \vec{i}_{\beta}, \quad p = 1,2. \tag{9}$$

From the formulas (2) - (9) it is easy to get the system of integral equations relative to the Fourier harmonics of four unknown currents $I_{11}^m, I_{12}^m, I_{21}^m, I_{22}^m$. In the matrix form the system looks like:

$$\mathbf{KI} = \mathbf{B}, \tag{10}$$

Where the matrix consists of four blocks:

$$\mathbf{K} = \begin{pmatrix} \mathbf{K}_{11} & \mathbf{K}_{12} \\ \mathbf{K}_{21} & \mathbf{K}_{22} \end{pmatrix}, \tag{11}$$

where each block is:

$$\mathbf{K}_{pq} = \begin{pmatrix} \int_0^{\pi} K_{11}^{pq}(\theta_p, t_q) I_{q1}^m(t_q) dt_q & \int_0^{\pi} K_{12}^{pq}(\theta_p, t_q) I_{q2}^m(t_q) dt_q \\ \int_0^{\pi} K_{21}^{pq}(\theta_p, t_q) I_{q1}^m(t_q) dt_q & \int_0^{\pi} K_{22}^{pq}(\theta_p, t_q) I_{q2}^m(t_q) dt_q \end{pmatrix}, \quad p,q = 1,2, \quad m = 0, \pm 1, \pm 2... \tag{12}$$

The kernels K_{ij}^{pq} of the equations are similar to those presented in [2].

3 Numerical algorithm and some results.

The usual scheme of the numerical solution of the system (10) is described in [2]. Let's consider the problem of finding the singularities of the scattered field under diffraction on the closely located group of bodies. Assume that the body of revolution with the smooth border is placed near the other body, which is sharp-pointed. Thus, it is supposed, that the second body singularity is situated close to the surface of the smooth one. We name this singular point as the singularity-source. Suppose, that given singular point has polar coordinates (r_0, θ_0) in the coordinate system connected with the smooth body. As mentioned above, the singularity-source generates the additional singular point (singularity-image) inside the smooth scatterer, which would be absent under diffraction on this single body. To find the coordinates of the singularity-image we use the method of continuation by a parameter. As this parameter the distance r_0 is used. The coordinates of the singularity-source are also found numerically. The equation defining the coordinates of the singularity-image inside the smooth body has the following form:

$$f(\theta) e^{-i\theta} = r_0 e^{-i\theta_0}, \tag{13}$$

where $f(\theta)$ is the equation of the contour of the smooth body cross-section in the polar coordinate system connected with given body. The equation (13) defines the value of the complex angle θ corresponding to the singularity-image. The polar coordinates of this point are accordingly equal to:

$$r_i = |\xi(\theta)|, \quad \theta_i = \arg \xi(\theta), \quad \xi(\theta) = f(\theta) e^{i\theta}. \tag{14}$$

For further solution of the problem we surround all the singularities-images with the circles of the small radius. When these circles rotate they represent the toroidal surfaces with round sections. Thus the integrals over these toroidal surfaces are added to the expressions (2) and (3) for the scattered field. This gives rise to the additional discrete sources in the presentation for the secondary field.

Comparison of the stated algorithm with the pattern equations method (PEM) presented in the paper [3] has been performed. As an example we have considered the diffraction of the plane wave

$$\vec{E}^0 = \vec{i}_x \exp(-ikz), \ \vec{H}^0 = \frac{1}{\eta} \vec{i}_y \exp(-ikz) \tag{15}$$

on two identical superellipsoids. The equation of the contour of the superellipsoid cross-section is:

$$\left(\frac{x}{a}\right)^{2s} + \left(\frac{z}{c}\right)^{2s} = 1 \tag{16}$$

The sizes of the bodies are $ka = 2.5$, $kc = 5$ and $s = 10$. The minimal distance between the surfaces of the bodies is $kd = 0.02$. In Fig. 1 the angular dependence of the module of the pattern for the concerning group of bodies (solid curve) is presented. The dashed curve demonstrates the results obtained by means of PEM. It follows from the figure that the results of calculations coincide with high accuracy.

Fig. 2 illustrates the advantages of the modified MMDS in comparison with the usual algorithm, which does not consider the singularities-images inside the smooth body generated by the singularities of the other body with rough border. The figure shows the residual of the boundary condition on the contour

of the cross-section of the spheroid near to which the double-cone is located. The double-cone is modeled by the generalized superellipsoid of the following kind:

$$\left(\frac{z-\nu x}{c}\right)^{2s}+\left(\frac{z+\nu x}{c}\right)^{2s}=1. \qquad (17)$$

Axial incidence of the plane wave (15) is considered. The sizes of the bodies have the following values: semi axes of the spheroid are $ka=4,\ kc=2$, the maximal sizes of the double-cone along the coordinate axes are equal to 4, the parameter $\nu=1$ and $s=10$. The distance between the surfaces of the bodies is $kd=0.1$. Curve 1 in the figure corresponds to the standard MMDS, and curve 2 does to the modified algorithm considering the singularity-image on the small axis of the spheroid. The number of the additional sources surrounding the singularity-image is equal to 7. Note, that the full number of discrete sources in both cases are identical and equal to 267. It follows from the figure that the level of the residual obtained by the modified MMDS much less the level of the residual obtained with the use of the standard MMDS.

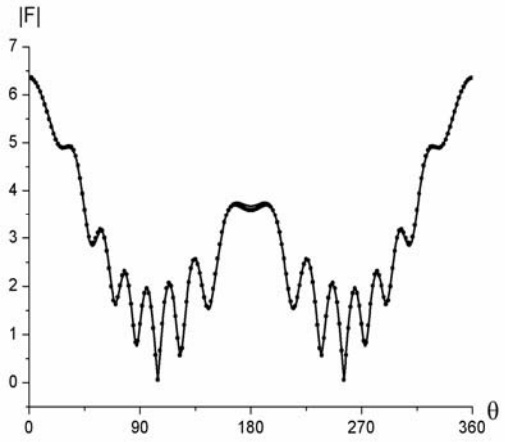

Fig.1

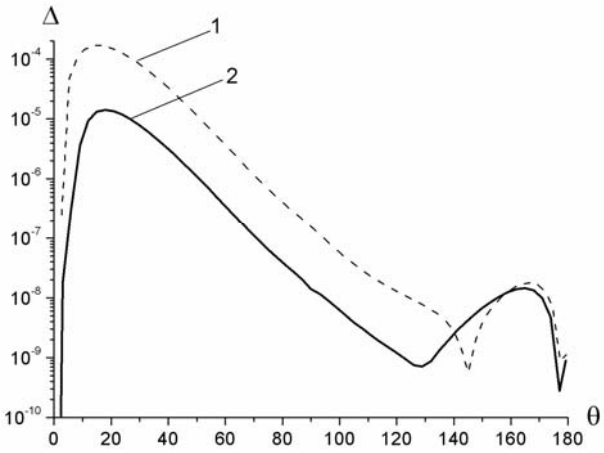

Fig.2

Acknowledgments

This work was supported by the Russian Foundation for Basic Researches (grants 06-02-16483 and 05-02-16931).

References

[1] A.G.Kyurkchan, S.A.Minaev, A.L.Soloveychik. “A modification of the method of discrete sources based on prior information about the singularities of the diffracted field”, Radiotekh. Electron., **46**, 666-672 (2001).

[2] A.P.Anyutin, A.G.Kyurkchan, S.A.Manenkov, S.A.Minaev. “About 3D solution of diffraction problems by MMDS”, JQSRT, **100**, 26-40 (2006).

[3] A.G.Kyurkchan, E.A.Skorodumova, “Modeling the characteristics of the waves scattering by a group of scatterers”, JQSRT, **100**, 207-219 (2006).

Solving the diffraction problem of electromagnetic waves on objects with a complex geometry by the pattern equations method

Alexander G. Kyurkchan, Elena A. Skorodumova

Moscow Technical University of Communication and Informatics, Aviamotornaya Street 8a, 111024, Moscow, Russian Federation,
tel: +7 (495) 236-2267, e-mail: kyurkchan@yandex.ru

Abstract

The new method for solving the diffraction problem on objects with a complex geometry is offered. The problem is reduced to solving an algebraic system of equations with respect to the expansion coefficients of the scattering patterns by using of a series expansion of the scattering patterns in vector spherical harmonics. It's shown, that the method possesses high convergence rate. Examples of modeling of the scattering patterns of objects by the combination of last of objects of the more simple form (fragments of a complex objects) are considered. Reliability of the results obtained is validated by the using of the Optical theorem.

1 Introduction

The problem of effective modeling of the scattering characteristics of electromagnetic waves by objects with a complex geometry remains actual, because there are practically no effective methods of its solution. One of the most effective modern techniques for solving of a series of the diffraction problems is the pattern equations method (PEM). In particular, the high efficiency of this technique was demonstrated by solving of the diffraction problem for a group of bodies and for objects with a complex structure in an acoustical case [1]. One of important advantages of the PEM is its weak dependence of convergence rate of the computational algorithm on a distance between scatterers. In this paper, this technique is extended to an electromagnetic case.

2 Statement of the problem and it's solution

Consider the problem of waves scattering of the primary monochromatic electromagnetic field $\vec{E}^0$, $\vec{H}^0$ on a scattering objects with a complex geometry with latter to be presented as a combination of objects of more simple structure. Let's consider the case of two reflecting objects, for determinacy. It's possible to use this approach for any number of objects.

Let the impedance boundary conditions are set on surfaces S_j, $j=1,2$:

$$\left(\vec{n}_j \times \vec{E}\right)\Big|_{S_j} = Z_j\left[\vec{n}_j \times \left(\vec{n}_j \times \vec{H}\right)\right]_{S_j},$$

where Z_j – surface impedance, $\vec{n}_j$ – the unit normal vector to surface S_j, $\vec{E} = \vec{E}^0 + \vec{E}_1^1 + \vec{E}_2^1$, $\vec{H} = \vec{H}^0 + \vec{H}_1^1 + \vec{H}_2^1$ – the total field, $\vec{E}_j^1$, $\vec{H}_j^1$ – the secondary (diffraction) field, which satisfies to a homogeneous system of the Maxwell's equations everywhere outside of S_j ($\zeta = \sqrt{\mu/\varepsilon}$ – the wave impedance of a medium), and also to the Sommerfeld's condition on infinity

Let's take advantages by series expansion of the scattering patterns in vector spherical harmonics for reduction of an initial problem to a system of algebraic equations:

$$\vec{g}_j(\theta_j,\varphi_j) = \vec{F}_j^E(\theta_j,\varphi_j) = -\sum_{n=1}^{\infty}\sum_{m=-n}^{n} a_{nm}^j i^n \left(\vec{i}_r \times \vec{\Phi}_{nm}^j(\theta_j,\varphi_j)\right) - \sum_{n=1}^{\infty}\sum_{m=-n}^{n} b_{nm}^j i^n \zeta\, \vec{\Phi}_{nm}^j(\theta_j,\varphi_j),$$

where

$$\vec{\Phi}_{nm}^j(\theta_j,\varphi_j) = \vec{r}_j \times \nabla P_n^m(\cos\theta_j)\exp(im\varphi_j)$$

$P_n^m(\cos\theta_j)$ – associated Legendre functions [2], and functions $\vec{F}_j^E(\theta_j,\varphi_j)$ – are scattering patterns of electric field, satisfying in a so-called far zone (for $kr_j >> 1$) to asymptotical relations as:

$$\vec{E}_j^1 = \frac{\exp(-ikr_j)}{r_j}\vec{F}_j^E(\theta_j,\varphi_j) + O\left(\frac{1}{(kr_j)^2}\right).$$

Thus, our purpose is a deriving of an algebraic system for coefficients a_{nm}^j, b_{nm}^j, which can be expressed as following integrals:

$$a_{nm}^j = -\frac{\zeta}{4\pi}N_{nm}\int_{S_j}\left(\vec{n}_j'\times\vec{H}\right)_{S_j}\overline{\vec{e}}_{nm}^e(r_j',\theta_j',\varphi_j')\,ds_j', \tag{1}$$

$$b_{nm}^j = \frac{\zeta}{4\pi}N_{nm}\int_{S_j}\left(\vec{n}_j'\times\vec{H}\right)_{S_j}\overline{\vec{h}}_{nm}^e(r_j',\theta_j',\varphi_j')\,ds_j', \tag{2}$$

where the following labels are introduced:

$$N_{nm} = \frac{(2n+1)}{n(n+1)}\frac{(n-m)!}{(n+m)!},$$

$$\overline{\vec{e}}_{nm}^e(r_j,\theta_j,\varphi_j) = \nabla\times\nabla\times\left(\vec{r}_j\overline{\chi}_{nm}^j(r_j,\theta_j,\varphi_j)\right),\ \overline{\vec{h}}_{nm}^e(r_j,\theta_j,\varphi_j) = \frac{ik}{\zeta}\nabla\times\left(\vec{r}_j\overline{\chi}_{nm}^j(r_j,\theta_j,\varphi_j)\right),$$

$$\overline{\chi}_{nm}^j(r_j,\theta_j,\varphi_j) = j_n(kr_j)P_n^m(\cos\theta_j)\exp(-im\varphi_j),$$

$j_n(k\rho_j)$ – are the Bessel spherical functions of the first kind [2], line means a sign of complex conjugation.

As a result, with the using of expansions of the wave field:

$$\vec{E} = \vec{E}^0 + \sum_{\nu=1}^{\infty}\sum_{\mu=-\nu}^{\nu} a_{\nu\mu}^1\vec{H}_{\nu\mu}^{h1}(r_1,\theta_1,\varphi_1) - b_{\nu\mu}^1\vec{H}_{\nu\mu}^{e1}(r_1,\theta_1,\varphi_1) + a_{\nu\mu}^2\vec{H}_{\nu\mu}^{h2}(r_2,\theta_2,\varphi_2) - b_{\nu\mu}^2\vec{H}_{\nu\mu}^{e2}(r_2,\theta_2,\varphi_2),$$

$$\vec{H} = \vec{H}^0 + \sum_{\nu=1}^{\infty}\sum_{\mu=-\nu}^{\nu} a_{\nu\mu}^1\vec{H}_{\nu\mu}^{e1}(r_1,\theta_1,\varphi_1) + b_{\nu\mu}^1\vec{H}_{\nu\mu}^{h1}(r_1,\theta_1,\varphi_1) + a_{\nu\mu}^2\vec{H}_{\nu\mu}^{e2}(r_2,\theta_2,\varphi_2) + b_{\nu\mu}^2\vec{H}_{\nu\mu}^{h2}(r_2,\theta_2,\varphi_2),$$

where the wave spherical functions are expressed by the following relations:

$$\vec{H}_{nm}^{hj} = \nabla\times\nabla\times(\vec{r}_j\psi_n^m(\theta_j,\varphi_j)),\ \vec{H}_{nm}^{ej} = \frac{ik}{\zeta}\nabla\times(\vec{r}_j\psi_n^m(\theta_j,\varphi_j)),$$

$$\psi_n^m(\theta_j,\varphi_j) = h_n^{(2)}(kr_j)P_n^m(\cos\theta_j)\exp(im\varphi_j),$$

$$j = 1,\ 2,$$

$h_n^{(2)}(kr_j)$ – are the Hankel spherical functions of the second kind [2], and integral relations for coefficients a_{nm}^j, b_{nm}^j (1)-(2) we shall obtain the system of an algebraic equations of PEM:

$$\begin{cases} a_{nm}^j = a_{nm}^{j0} + \sum_{\nu=1}^{\infty}\sum_{\mu=-\nu}^{\nu}\left(G_{nm,\nu\mu}^{jj,aa}a_{\nu\mu}^j + G_{nm,\nu\mu}^{jj,ab}b_{\nu\mu}^j + G_{nm,\nu\mu}^{jl,aa}a_{\nu\mu}^l + G_{nm,\nu\mu}^{jl,ab}b_{\nu\mu}^l\right), \\ b_{nm}^j = b_{nm}^{j0} + \sum_{\nu=1}^{\infty}\sum_{\mu=-\nu}^{\nu}\left(G_{nm,\nu\mu}^{jj,ba}a_{\nu\mu}^j + G_{nm,\nu\mu}^{jj,bb}b_{\nu\mu}^j + G_{nm,\nu\mu}^{jl,ba}a_{\nu\mu}^l + G_{nm,\nu\mu}^{jl,bb}b_{\nu\mu}^l\right), \\ n = 1,2,...;\ |m| < n,\ j,l = 1,2,\ j \neq l. \end{cases}$$

All the coefficients in this system represent summation of two components: corresponding values when the impedance is equal to zero $Z_j = 0$, and additional addends, caused by difference of the value of impedance from zero.

3 An examination of the convergence of calculation algorithm

Our investigations has shown, that for the scatterers with an analytic boundary (spheres) four or five valid significant figures are already established when $N = 9 = 1.5kd_{1,2}$ even at the minimum

distance between objects ($kr = 6.1$) (where d – is the maximum size of the scatterer). However in the case of bodies with nonanalytic boundary (cylinders) three or four valid significant figures are established only at $N = 2.1\ kd_{1,2}$.

These investigations has shown, that the convergence rate of the calculation algorithm remains almost the same high when scattering bodies are coming close together up to their contact, like in previously described acoustical case [1]. This fact allows us extend the PEM to solving the diffraction problem for scatterers with a complex geometry by their representation as a combination of objects of more simple form at minimum consumption of the computer resources.

4 Examination of mutual influence of objects

The difficulty of solving of the diffraction problem on a group of bodies consists in necessity to consider interaction of objects, which is related with rereflections between them. Fig. 1 illustrates dependence of integral scattering cross sections:

$$\sigma = \frac{1}{4\pi} \int_0^{2\pi} \int_0^{\pi} |\vec{F}^E(\theta, \varphi)|^2 \sin\theta d\theta d\varphi$$

for two superellipsoids with $ka_{1,2} = 1$, $kc_{1,2} = 2$, $Z_{1,2} = 0$ on a distance between them, where $\vec{F}^E(\theta,\varphi)$ – is the scattering pattern for two bodies with (curve 1 and 2) and without taking into account the mutual influence, respectively. With increasing of the distance between objects the value of the common integral scattering cross section come close to summation of cross sections of separate bodies (curve 3). Besides, one can see on these figures, when bodies coming together there is a diminution of the aggregate cross section, calculated without taking into account the mutual influence. This can be explained by the "partial accumulation" of the power of an incident wave in the area between mirrors during the average period. Curve 4 corresponds to the integral cross section of superellipsoid of double size, to which the aggregate cross section of two bodies at their contact is coming close.

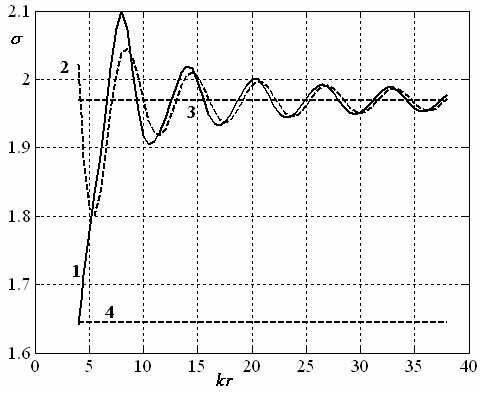

Figure 1.

5 Examination of possibility of the scattering characteristics modeling for bodies with a complex geometry

Let's carry out examination of the proposed method, based on comparison of scattering pattern of a single body with scattering pattern of the object, composed of halves of these bodies. Figures 2a and 2b show examples of such comparison for superellipsoids with $ka_{1,2} = 4$, $kc_{1,2} = 8$ for various values of the impedance. Fig. 2a corresponds to the value of the impedance equal to zero $Z_{1,2} = 0$, and fig. 2b – $Z_{1,2} = \zeta$, in both cases for the perpendicular incidence of wave. Figures show, that the differences of corresponding patterns are very small.

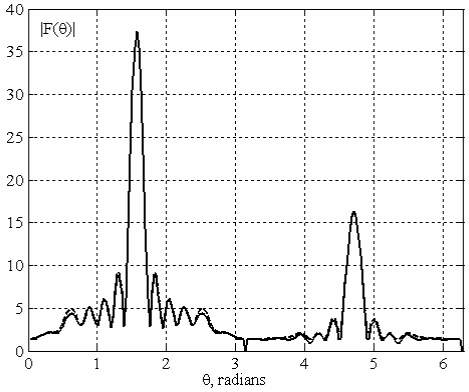

Figure 2a.

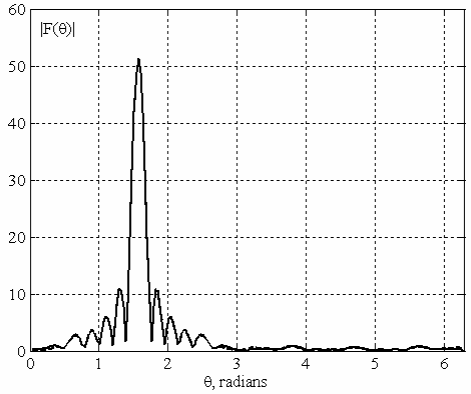

Figure 2b.

5 Verifying of the validity of the optical theorem

One of the methods of an estimation of the validity of the solution of the diffraction problem is verifying of fulfillment of the optical theorem, according to which [3]:

$$-\mathrm{Im}\left\{\vec{F}^{E}(\theta=\theta_0,\,\varphi=\varphi_0)\cdot\vec{p}\right\}=\frac{1}{2\lambda}\int_0^{2\pi}\int_0^{\pi}|\vec{F}^{E}(\theta,\,\varphi)|^2\sin\theta d\theta d\varphi\,,$$

where (θ_0,φ_0) – angles of incidence of a primary wave, $\vec{p}$ – a polarization vector, λ – a wave length.

Table 1. Verifying of the validity of the optical theorem for two objects at perpendicular incidence of a wave

Two spheres, $ka_{1,2}=3$			Two cylinders, $ka_{1,2}=3$, $kh_{1,2}=6$		
kr	σ	$-\mathrm{Im}\left\{F_\theta^E(\theta_0,\varphi_0)\right\}$	kr	σ	$-\mathrm{Im}\left\{F_\theta^E(\theta_0,\varphi_0)\right\}$
6.1	9,03726456130122	9,03726456130087	6.1	14.2118	14.3938
7	9,69071815232501	9,69071815232500	7	15.8345	15.6466
10	9,90163562078583	9,90163562078574	10	14.9745	14.9084

Table 1 shows, that for two spheres the accuracy of fulfillment of the optical theorem practically coincides with the machine precision of evaluations. However for cylinders the accuracy is noticeably lower, that can be explained by nonanalytic boundaries of scatterers, but also is quite acceptable.

Acknowledgements

This work was supported by Russian Foundation for Basic Research, Project No. 06-02-16483.

References

[1] A. G. Kyurkchan and E. A. Skorodoumova, "Modeling the characteristics of the waves scattering by a group of scatterers," Journal of Quantitative Spectroscopy and Radiative Transfer. **100**, 207-219 (2006).

[2] N.Ya.Vilenkin, *Special Functions and Representations Group Theory*, (Nauka, Moscow, 1965 (in Russian)).

[3] C. F. Bohren and D. R. Huffman, *Absorption and Scattering of Light by Small Particles* (Wiley, New York, 1983).

Solution of wave diffraction problems by method of continued boundary conditions combined with pattern equation method

A.G.Kyurkchan[1], N.I.Smirnova[1]

[1] *Moscow Technical University of Communication and Informatics, Aviamotornaya Street 8A, 111024, Moscow, Russian Federation*
tel:+7 (495) 236-2267, e-mail: kyurkchan@yandex.ru

Abstract

The integral-operator equation of the pattern equation method is deduced using a method of the continued boundary conditions. Generally speaking the deduced equation has the approximate character, however it is applicable for the solution of diffraction problems at smaller restrictions on scatterer geometry, than the rigorous equation. Numerical examples are considered.

1 Introduction

For almost 15 years the pattern equations method (PEM) has been successfully applied to the solution of the broad spectrum of wave diffraction and propagation problems. However, essential limitation of the method is that in it's strict formulation it is not applicable to the solution of diffraction problems on bodies with non analytical (in particular, piece-smooth) boundary caused by divergence of Sommerfeld-Weil integral representation in singular points of a wave field. The method of continued boundary conditions (MCBC) suggested recently allows to overcome this limitation. The trick is that according to MCBC, the boundary condition is satisfied not on boundary S of scatterer, but on some surface S_δ, covering S and separated from it by some sufficiently small distance δ. It leads to the approximate statement of a problem, however, as a result all difficulties related to singular points of a wave field on scatterer boundary in case it has breaks, corners, edges, etc., as well as difficulties related to singularity of the corresponding integral equation kernels are removed. Computational algorithm thus becomes significantly simpler and practically universal.

PEM integral-operator equation (in general approximate), which can be deduced using MCBC, is applicable under more general assumptions of scatterer geometry, than the exact equation of the method. For compactness we consider a diffraction problem on perfectly conducting scatterer. However the basic ideas of this approach are entirely extended to the vector problems.

2 Derivation of PEM integral-operator equation

It has been shown [1,2], that in framework MCBC the boundary problem can be reduced to the solution of Fredholm integral equation of the Ist, and IInd kind with smooth kernel. In particular, in case of perfectly conducting scatterer MCBC gives the following equation

$$\vec{J}_\delta = \vec{J}^0_\delta - \left(\vec{n} \times \frac{k}{4\pi} \int_S \left(\vec{J} \times \nabla G_0 \right) ds' \right) \Bigg|_{S_\delta}, \qquad (1)$$

where $\vec{J} = (\vec{n} \times \vec{H})\big|_S$, $\vec{J}_\delta = (\vec{n} \times \vec{H})\big|_{S_\delta}$, $\vec{J}^0_\delta = (\vec{n} \times \vec{H}^0)\big|_{S_\delta}$, and $\vec{H}^0$, $\vec{H}^1$, $\vec{H} = \vec{H}^0 + \vec{H}^1$ are primary, scattered and total magnetic field vectors respectively, $G_0 = \dfrac{\exp(-ikR)}{kR}$ is free-space Green function, $R = |\vec{r} - \vec{r}'|$.

By multiplying both parts of the Eq. (1) on $\exp\{ik\rho_\delta(\theta,\varphi)\cos\gamma\}$, $\cos\gamma=[\sin\alpha\sin\theta\cos(\beta-\varphi)+\cos\alpha\cos\theta]$, integrating on S_δ and taking advantage of generalized Sommerfeld-Weil representation for function G_0:

$$G_0=\frac{1}{2\pi i}\int_0^{2\pi}\int_0^{\pi/2+i\infty}\exp(-ikr\cos\alpha+ikr'\cos\hat{\gamma})\sin\alpha\,d\alpha\,d\beta,$$

were

$$\cos\hat{\gamma}=\sin\alpha\sin\hat{\theta}\cos(\beta-\hat{\varphi})+\cos\alpha\cos\hat{\theta},\ \cos\hat{\theta}=\sin\theta\sin\theta'\cos(\varphi-\varphi')+\cos\theta\cos\theta',$$

$$\sin\hat{\theta}\cos\hat{\varphi}=\sin\theta'\sin(\varphi'-\varphi),\ \sin\hat{\theta}\sin\hat{\varphi}=\sin\theta\cos\theta'-\cos\theta\sin\theta'\cos(\varphi-\varphi'),$$

we obtain the following integral-operator equation of PEM relative to the scattering pattern $\vec{F}^E(\alpha,\beta)$

$$\vec{F}_\delta^E(\alpha,\beta)=\vec{F}_\delta^{0E}(\alpha,\beta)+\frac{k}{8\pi^2 i}\int_{S_\delta}e^{ik\rho_\delta(\theta,\varphi)\cos\gamma}\Big\{\vec{n}\times\Big[\nabla\times\int_0^{2\pi}\int_0^{\pi/2+i\infty}e^{-ikr\cos\alpha}\hat{\vec{F}}^E(\alpha',\beta';\theta,\varphi)\times \sin\alpha'\,d\alpha'\,d\beta'\Big]\Big|_{S_\delta}\Big\}ds. \tag{2}$$

Here $\vec{F}_\delta^E(\alpha,\beta)=\int_S\vec{J}_\delta(\vec{r})\exp[ik\rho_\delta(\theta,\varphi)\cos\gamma]ds$, $\hat{\vec{F}}^E(\alpha',\beta';\theta,\varphi)=\int_S\vec{J}(\vec{r}')\exp[ik\rho(\theta',\varphi')\cos\hat{\gamma}]ds'$ is the generalized scattering pattern [3].

Generally speaking the Eq. (2) is approximate, since at its derivation it was assumed, that $\vec{F}^E(\alpha,\beta)\cong\vec{F}_\delta^E(\alpha,\beta)$. However this equation is now applicable to the diffraction problems on bodies with non-analytical boundary. If boundary S is analytical the obtained equation becomes exact. It is interesting to note, that integral-operator equation of PEM cannot be derived from standard current Fredholm integral equation of a II[nd] kind even for bodies with analytical boundary because of the simple layer potential normal derivative jump.

If scatterer is weakly non-convex [3], it is more appropriate to use the equation Eq. (2) for solving diffraction problem, since the corresponding computation algorithm converges quite fast [3]. However, in case of strongly non-convex scatterers or thin screens, the Eq. (1), which is usually solved using local approximation of the sought current $\vec{J}(\vec{r}')$, is more suitable.

3 Numerical examples

The scattering pattern of plane electromagnetic wave propagating at angles $\varphi_0=0$, $\theta_0=0$ incident on a circular cylinder with a radius *ka*=3 and height *kh*=10 was calculate using the Eqs. (1) and (2). Results of calculations have graphically coincided. The maximal number *N* of the spherical harmonic used at unknown scattering pattern approximation in the Eq. (2) has been set 15, and number of basic functions *M*, used for approximation of unknown current in the Eq. (1) was set 128. The accuracy of the results obtained with Eq. (1) was evaluated by the residual of the boundary condition, calculated in points between collocation points. This residual is shown on figure. 1.

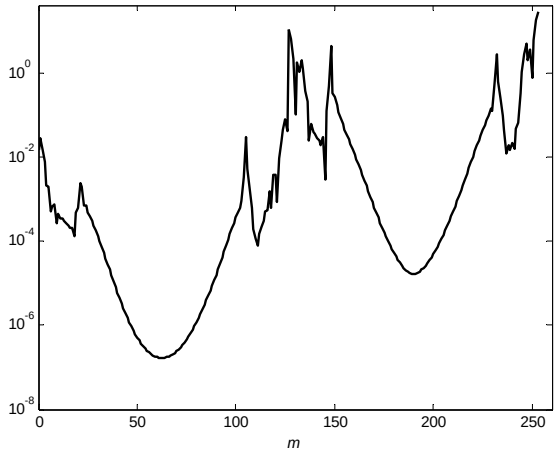

Figure 1: The residual for a circular cylinder with a radius *ka*=3 and height *kh*=10.

Thus, for bodies which geometry allows Eq. (2) for solving diffraction problem, the later is more suitable. However, as mentioned above, using approximation Eq. (3) for reducing Eq. (2) to algebraic system to solve, for example, diffraction problem on thin screen, is not acceptable. If we approximate the pattern $\vec{F}^E(\alpha,\beta)$ in Eq. (2) by sum

$$\vec{F}^E(\alpha,\beta)=\sum_{n=1}^{N}\vec{J}(\vec{r}_n)\exp[ik\rho_n(\theta,\varphi)\cos\gamma],$$

where $\vec{r}_n$ are the position vectors of the points Ω_n, situated everywhere dense on *S*, i.e. $\overline{\{\Omega_n\}_{n=0}^{\infty}}=S$, Eq. (2) leads to algebraic system with ill-conditioned matrix. In such situation using Eq. (1) is more expedient for solution boundary problem.

Let's consider now a diffraction problem, for which Eq. (2) is inapplicable. Solution of diffraction problem for plane wave at $\theta_0=0$ was obtained on a parabolic mirror defined as $\rho(\theta)=f/\cos^2(\theta/2)$, where *f* is the focal length, *kf*=20. Figures 2 and 3 show the scattering pattern in the plane $\varphi=[0,\pi]$ for F_θ^E (solid) and in the plane $\varphi=[\pi/2,3\pi/2]$ for F_φ^E (dashed) and the residual of the boundary condition, calculated in points between collocation points, respectively, obtained at *M*=64, *Q*=1, $\vec{p}=\vec{i}_x$. It can be seen that the solution has the acceptable accuracy.

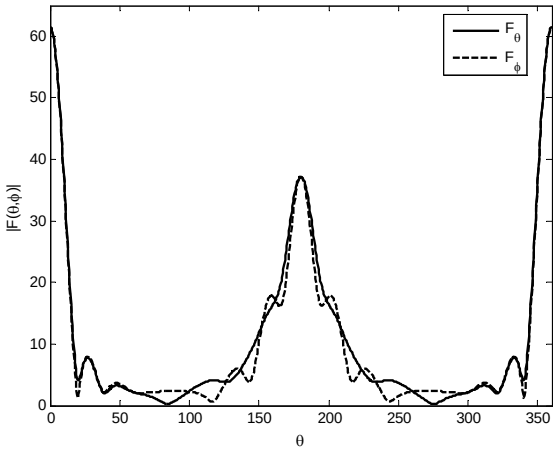

Figure 2: The scattering pattern for a parabolic mirror with *kf*=20.

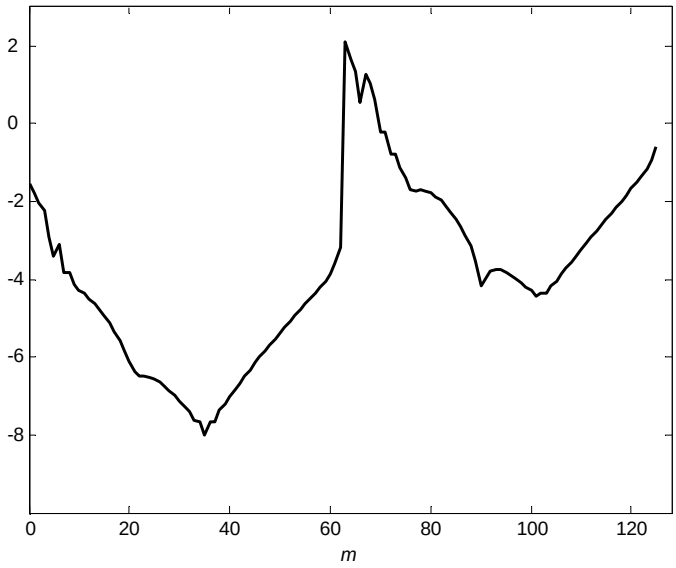

Figure 3: The residual for a parabolic mirror with *kf*=20.

4 Conclusion

Thus, MCBC allows the reduction of a boundary value problem not only to the integral equations with a smooth kernel with respect to sources density on scatterer surface, but also to equations with respect to a scattering pattern of a body, i.e. to a field characteristic in a long-distance zone. This gives the reason to think MCBC one of the most universal method for solving diffraction problems.

Acknowledgments

This work was supported by the Russian foundation of basic researches, project № 06-02-16483.

References

[1] A.G.Kyurkchan, N.I.Smirnova, "Solution of diffraction problems using the methods of continued boundary conditions and discrete sources", Journal of Communication Technology and Electronics, **50**, 1139-1146, (2005).

[2] A.G.Kyurkchan, N.I.Smirnova, "Solution of wave diffraction problems on impedance scatterers by method of continued boundary conditions", JQSRT, (2007) (in press).

[3] Do Dyk Tkhang, A.G.Kyurkchan, "Efficient Method for Solving the Problems of Wave Diffraction by Scatterers with Broken Boundaries", Acoustical Physics, **49**, 43-50 (2003).

[4] C. F. Bohren and D. R. Huffman, *Absorption and Scattering of Light by Small Particles* (Wiley, New York, 1983).

Rigorous Derivation of Superposition *T*-matrix Approach from Solution of Inhomogeneous Wave Equation.

Pavel Litvinov[1], Klaus Ziegler[2]

[1] *Institute of Radio Astronomy of NASU, 4 Chervonopraporna St., Kharkiv, 61002, Ukraine*
[2] *Institut für Physik, Universität Augsburg, D-86135 Augsburg, Germany.*
tel: +38 (057) 7061414, e-mail: Litvinov@ira.kharkov.ua

Abstract

The problem of electromagnetic scattering by a system of particles is considered. Starting from the integral solution of the inhomogeneous wave equation, the equations for Green's and transition operators are derived. By expanding the free-space dyadic Green's function in terms of spherical wave functions, equations for determining the matrix elements of the dyadic transition operators for system of particles are obtained. The relations between the matrix elements of the dyadic transition operator and Waterman's *T* matrix are established.

1 Introduction

Waterman's *T*-matrix formalism is widely used in acoustic and electromagnetic scattering problems [1]-[4]. For the problem of electromagnetic scattering by aggregated (composite) particles the superposition *T*-matrix approach has been developed (see, for example [2], [4]).

Alternative methods for treating the electromagnetic scattering problem are the quantum-mechanical potential scattering approach [3], [5] and recently developed self consistent Green's function formalism [6]. In [6] it is shown that, for suitable choice of expansion functions, the matrix elements of interaction operator are related with Waterman's T-matrix.

In this paper we present rigorous and systematic derivation of the superposition *T*-matrix approach, which directly follows from the inhomogeneous wave equation. Starting from the complete integral solution of the inhomogeneous wave equation for a time harmonic field, we obtain first the equations for the Green's and transition operators. Then, expressing the free space dyadic Green's function in terms of spherical wave functions and separating variables, we find the equation for determining the matrix elements of transition operator $\overleftrightarrow{T}$ for a system of particles using the matrix elements of $\overleftrightarrow{T}$ for isolated particles. We show that for divergence free electric field the matrix elements of $\overleftrightarrow{T}$, expressed in spherical wave functions, directly connected to Waterman's *T* matrix.

2 Equation for particle-centered matrix elements of the dyadic transition operator $\overleftrightarrow{T}$

Let us consider electromagnetic scattering by a system of nonmagnetic scatterers assuming, as usual, that the scatterers are embedded in an infinite, homogeneous, linear, isotropic, nonmagnetic and nonabsorbing host medium. For this problem, it is well-known that everywhere in space the time harmonic electric field satisfies the inhomogeneous differential equation [2]:

$$\nabla\times\nabla\times\mathbf{E}(\mathbf{r})-k^2\mathbf{E}(\mathbf{r})=\mathbf{J}(\mathbf{r}). \tag{1}$$

Here

$$\mathbf{J}(\mathbf{r})=\mathbf{J}_0(\mathbf{r})+k^2(\tilde{m}^2(\mathbf{r},\omega)-1)\mathbf{E}(\mathbf{r}), \tag{2}$$

$$\mathbf{J}_0(\mathbf{r})=\begin{cases}0, & \mathbf{r}\notin V_{sour},\\ \mathbf{J}_0(\mathbf{r}), & \mathbf{r}\in V_{sour},\end{cases} \tag{3}$$

$$\tilde{m}(\mathbf{r},\omega)=\begin{cases}1, \ \mathbf{r}\in V_h, \\ \tilde{m}_i(\mathbf{r},\omega)=\dfrac{m_i(\mathbf{r},\omega)}{m}=\dfrac{k_i(\mathbf{r},\omega)}{k}, \ \ \mathbf{r}\in V_i,\end{cases} \tag{4}$$

where $\mathbf{J}_0(\mathbf{r})$ is a source of radiation, V_{sour} is volume of the source of radiation, V_h and V_i are the volumes of the host medium and the *i*-th particle, respectively, $\tilde{m}_i(\mathbf{r},\omega)$ is the complex refractive index of the *i*-th particle relative to that of the host medium, m and $m_i(\mathbf{r},\omega)$ are the refractive indices of the host medium and the *i*-th particle, respectively. k and $k_i(\mathbf{r},\omega)$ are the wave numbers in the host medium and inside the *i*-th particle, respectively.

The complete solution of Eq.(1) (see, for example [2]) is as follows:

$$\mathbf{E}(\mathbf{r})=\mathbf{E}_{inc}(\mathbf{r})+\int_V \vec{G}_0(\mathbf{r},\mathbf{r}')\vec{U}(\mathbf{r}')\mathbf{E}(\mathbf{r}')d^3\mathbf{r}', \tag{5}$$

where $\vec{G}_0(\mathbf{r},\mathbf{r}')$ is the free space dyadic Green's functions, $\vec{U}(\mathbf{r}')$ is scattering potential [3], [5].

Eq. (5) can be written as follows:

$$\mathbf{E}(\mathbf{r})=\int_V \vec{G}(\mathbf{r},\mathbf{r}_0)\mathbf{J}_0(\mathbf{r}_0)d^3\mathbf{r}_0, \tag{6}$$

where $\vec{G}(\mathbf{r},\mathbf{r}_0)$ is dyadic Green's function for whole system of scatterers. Introducing the transition operator, related with the *i*-th particle and transition operators, related with the *i*-th and *j*-th particles (see for example, [5]), one can write for $\vec{G}(\mathbf{r},\mathbf{r}_0)$:

$$\vec{G}(\mathbf{r},\mathbf{r}_0)=\vec{G}_0(\mathbf{r},\mathbf{r}_0)+\sum_{i,j}\int_{V_i}\int_{V_j}\vec{G}_0(\mathbf{r},\mathbf{r}_i')\vec{T}_{ij}(\mathbf{r}_i',\mathbf{r}_j'')\vec{G}_0(\mathbf{r}_j'',\mathbf{r}_0)d^3\mathbf{r}_i'd^3\mathbf{r}_j''. \tag{7}$$

Here $\vec{T}_{ij}(\mathbf{r}_i',\mathbf{r}_j'')$ is transition operator, related with particles *i* and *j*.

$$\vec{T}_{ij}(\mathbf{r}_i',\mathbf{r}_j'')=\vec{T}_0^i(\mathbf{r}_i',\mathbf{r}_i'')\delta_{ij}+\int_{V_i}\vec{T}_0^i(\mathbf{r}_i',\mathbf{r}_i''')d^3\mathbf{r}_i'''\sum_{k\neq i}\int_{V_k}\vec{G}_0(\mathbf{r}_i''',\mathbf{r}_k''')\vec{T}_{kj}(\mathbf{r}_k''',\mathbf{r}_j'')d^3\mathbf{r}_k'''. \tag{8}$$

$\vec{T}_0^i(\mathbf{r}_i',\mathbf{r}_i''')$ is transition operator, related with particles *i* [3], [5]. Let us separate variables $\mathbf{r}$ and $\mathbf{r}_i'$ ($\mathbf{r}_0$ and $\mathbf{r}_j''$ etc.) in Eqs.(7), (8) and express $\vec{G}_0$ in terms of spherical wave functions. Then Eq.(7) can be written in the following form:

$$\vec{G}(\mathbf{r},\mathbf{r}_0)=\vec{G}_0(\mathbf{r},\mathbf{r}_0)-k^2\sum_{i,j}\sum_{lml'm'}\vec{g}_{lm}^{(1)}(k\mathbf{r}_i)\vec{T}_{lml'm'}^{ij}\vec{g}_{l'm'}^{(2)*T}(k\mathbf{r}_j^0), \tag{9}$$

$$\vec{g}_{lm}^{(1)}(k\mathbf{r}_i)=\left(\vec{I}+\frac{\nabla\otimes\nabla}{k^2}\right)\psi_{lm}^{(1)}(k\mathbf{r}_i), \tag{10}$$

$$\psi_{lm}^{(1)}(k\mathbf{r}_i)=h_l^{(1)}(kr_i)Y_{lm}(\vartheta_i,\varphi_i), \tag{11}$$

$\psi_{lm}^{(1)}(k\mathbf{r}_i)$ are scalar spherical wave functions, $(r_i,\vartheta_i,\varphi_i)$ are spherical coordinates of the radius-vector $\mathbf{r}_i$ in the coordinate system $\{x_i,y_i,z_i\}$ associated with the *i*-th particle.

$\vec{T}_{lml'm'}^{ij}$ are the matrix elements of the dyadic transition operator $\vec{T}_{ij}(\mathbf{R}_i+\mathbf{R}_i',\mathbf{R}_j+\mathbf{R}_j'')$:

$$\vec{T}_{lml'm'}^{ij}=\int_{V_i}\int_{V_j}Rg\psi_{lm}^*(k\mathbf{R}_i')\vec{T}_{ij}(\mathbf{R}_i+\mathbf{R}_i',\mathbf{R}_j+\mathbf{R}_j'')Rg\psi_{l'm'}(k\mathbf{R}_j'')d\mathbf{R}_i'd\mathbf{R}_j'', \tag{12}$$

$$Rg\psi_{lm}(k\mathbf{R}_i')=j_l(kR_i')Y_{lm}(\beta_i',\alpha_i'), \tag{13}$$

where $Rg\psi_{lm}(k\mathbf{R}_i')$ are scalar regular spherical wave functions.

The matrix $\vec{T}_{lml'm'}^{ij}$ is a tensor of 2-nd rank (dyad) associated with the particles *i* and *j* (the particle-centered matrix). It contains all possible scattering processes occurring while wave propagates from the particle *j* to the particle *i*. The matrices $\vec{T}_{lml'm'}^{ij}$ are independent of the incidence and scattering directions as

well as of the polarization state of the incident field. They depend only on the configuration of the system of particles, the properties of the component particles, their orientation, etc.

For the matrix elements $\vec{\vec{T}}^{0i}_{lml'm'}$, associated with isolated particles, we can write similar to (12) the following relation:

$$\vec{\vec{T}}^{0(i)}_{lml'm'} = \int_{V_i}\int_{V_i} Rg\psi^{*}_{lm}(k\mathbf{R}'_i)\vec{\vec{T}}^{i}_{0}(\mathbf{R}_i+\mathbf{R}'_i,\mathbf{R}_i+\mathbf{R}''_i)Rg\psi_{l'm'}(k\mathbf{R}''_i)d\mathbf{R}'_i d\mathbf{R}''_i\,. \tag{14}$$

Using the definitions (12), (14) and the addition theorems for scalar spherical wave functions (see, for example, [7]), from Eq.(8) we have the following equation for matrix $\vec{\vec{T}}^{ij}_{lml'm'}$:

$$\vec{\vec{T}}^{ij}_{lml'm'} = \vec{\vec{T}}^{0(i)}_{lml'm'}\delta_{ij} + \sum_{l_1m_1}\vec{\vec{T}}^{0(i)}_{lml_1m_1}\sum_{k\neq i}\sum_{l_2m_2}\vec{\vec{H}}_{l_1m_1l_2m_2}(k\mathbf{r}_{ki})\vec{\vec{T}}^{kj}_{l_2m_2l'm'}\,, \tag{15}$$

$$\vec{\vec{H}}_{l_1m_1l_2m_2}(k\mathbf{r}_{ki}) = ik(-1)^{l_2+m_2}\sum_{l_3m_3}\vec{\vec{g}}^{(1)}_{l_3m_3}(k\mathbf{r}_{ki})c(l_3m_3\,|\,l_1m_1\,|\,l_2-m_2)\,, \tag{16}$$

$$c(l_3m_3\,|\,l_1m_1\,|\,l_2-m_2) = i^{l_1+l_2-l_3}\,4\pi\sqrt{\frac{(2l_1+1)(2l_2+1)}{4\pi(2l_3+1)}}C^{l_30}_{l_10l_20}C^{l_3m_3}_{l_1m_1l_2-m_2}\,, \tag{17}$$

$C^{l_30}_{l_10l_20}$ and $C^{l_3m_3}_{l_1m_1l_2-m_2}$ are Clebsh-Gordan coefficients [7].

2 Relation between Waterman's *T* matrix and the matrix elements of the dyad transition operator $\vec{\vec{T}}$

Eq.(9) for Green's function and Eqs.(12),(14)-(16) for the matrix elements of the transition operators are obtained for the following conditions: the Green's function must satisfy vector wave equation and must be limited at infinity. Thus $\vec{\vec{G}}_0(\mathbf{r},\mathbf{r}_0)$ and $\vec{\vec{G}}(\mathbf{r},\mathbf{r}_0)$ are not divergence free and contain both transverse and longitudinal parts. For the system of uncharged particles electromagnetic field outside of source region is purely transverse. Thus in Eq.(9) and Eqs.(12), (14)-(16) one has left just the divergence free transverse part of $\vec{\vec{G}}_0(\mathbf{r},\mathbf{r}_0)$ and $\vec{\vec{G}}(\mathbf{r},\mathbf{r}_0)$. For the transverse part of Green's function from Eq.(9) we can write following equation:

$$\begin{aligned}\vec{\vec{G}}^{tr}(\mathbf{r},\mathbf{r}_0) = \vec{\vec{G}}^{tr}_0(\mathbf{r},\mathbf{r}_0) + ik\sum_{LML_1M_1}\frac{(-1)^{M_1}}{L(L+1)L_1(L_1+1)}\Big\{&T^{11}_{LML_1M_1}\mathbf{M}_{LM}(k\mathbf{r})\otimes\mathbf{M}_{L_1-M_1}(k\mathbf{r}_0)\\ &+T^{12}_{LML_1M_1}\mathbf{M}_{LM}(k\mathbf{r})\otimes\mathbf{N}_{L_1-M_1}(k\mathbf{r}_0)+T^{21}_{LML_1M_1}\mathbf{N}_{LM}(k\mathbf{r})\otimes\mathbf{M}_{L_1-M_1}(k\mathbf{r}_0)+T^{22}_{LML_1M_1}\mathbf{N}_{LM}(k\mathbf{r})\otimes\mathbf{N}_{L_1-M_1}(k\mathbf{r}_0)\Big\},\end{aligned} \tag{18}$$

$$T^{11}_{LML_1M_1} = \sqrt{L(L+1)L_1(L_1+1)}\;\;T^{LL_1}_{LML_1M_1} = ik\int_V\int_V Rg\mathbf{M}^{*}_{LM}(k\mathbf{R}')\;\vec{\vec{T}}(\mathbf{r}'+\mathbf{R}',\mathbf{r}''+\mathbf{R}'')Rg\mathbf{M}_{L_1M_1}(k\mathbf{R}'')d^3\mathbf{R}'d^3\mathbf{R}'', \tag{19}$$

$$T^{12}_{LML_1M_1} = \sqrt{L(L+1)L_1(L_1+1)}\left(-i\sqrt{\frac{L_1}{2L_1+1}}T^{LL_1+1}_{LML_1M_1}+i\sqrt{\frac{L_1+1}{2L_1+1}}T^{LL_1-1}_{LML_1M_1}\right) = ik\int_V\int_V Rg\mathbf{M}^{*}_{LM}(k\mathbf{R}')\;\vec{\vec{T}}\;Rg\mathbf{N}_{L_1M_1}(k\mathbf{R}'')d^3\mathbf{R}'d^3\mathbf{R}'', \tag{20}$$

$$T^{21}_{LML_1M_1} = \sqrt{L(L+1)L_1(L_1+1)}\left(i\sqrt{\frac{L}{2L+1}}T^{L+1L_1}_{LML_1M_1}-i\sqrt{\frac{L+1}{2L+1}}T^{L-1L_1}_{LML_1M_1}\right) = ik\int_V\int_V Rg\mathbf{N}^{*}_{LM}(k\mathbf{R}')\;\vec{\vec{T}}\;Rg\mathbf{M}_{L_1M_1}(k\mathbf{R}'')d^3\mathbf{R}'d^3\mathbf{R}'', \tag{21}$$

$$\begin{aligned}T^{22}_{LML_1M_1} &= \frac{\sqrt{L(L+1)L_1(L_1+1)}}{(2L+1)(2L_1+1)}\left(\sqrt{LL_1}T^{L+1L_1+1}_{LML_1M_1}+\sqrt{(L+1)(L_1+1)}T^{L-1L_1-1}_{LML_1M_1}-\sqrt{L(L_1+1)}T^{L+1L_1-1}_{LML_1M_1}-\sqrt{(L+1)L_1}T^{L-1L_1+1}_{LML_1M_1}\right)\\ &= ik\int_V\int_V Rg\mathbf{N}^{*}_{LM}(k\mathbf{R}')\;\vec{\vec{T}}(\mathbf{r}'+\mathbf{R}',\mathbf{r}''+\mathbf{R}'')Rg\mathbf{N}_{L_1M_1}(k\mathbf{R}'')d^3\mathbf{R}'d^3\mathbf{R}'',\end{aligned} \tag{22}$$

In Eqs.(19)-(22) the dyadic transition operator $\vec{\vec{T}}$ for the system of particles is defined by Eq.(8) whereas for isolated particles it is the transition operator related with a particle [5]. $\mathbf{M}_{lm}(k\mathbf{r})$, $\mathbf{N}_{lm}(k\mathbf{r})$ are vector spherical wave functions [2]. In (19)-(22) the matrix elements $T^{ll_1}_{LML_1M_1}$ ($l = L, L \pm 1$) are related with cyclical components $T^{qq_1}_{lml_1m_1}$ (q and q_1 take values $0, \pm 1$)) of $\vec{\vec{T}}_{lml_1m_1}$ (see Eq.(12), Eq.(14)) by the equations:

$$T^{ll_1}_{LML_1M_1} = ik\sum_{mm_1}\sum_{qq_1}(-1)^{q+q_1} C^{LM}_{lm1-q} C^{L_1M_1}_{l_1m_1 1-q_1} T^{qq_1}_{lml_1m_1}, \qquad T^{qq_1}_{lml_1m_1} = \frac{1}{ik}\sum_{LML_1M_1}(-1)^{q+q_1} C^{LM}_{lm1-q} C^{L_1M_1}_{l_1m_1 1-q_1} T^{ll_1}_{LML_1M_1} \tag{23}$$

From Eqs.(5), (6), (18) one can obtain the expansions for scattered and incident fields:

$$\mathbf{E}_{sc}(\mathbf{r}) = \sum_{LM}(p_{LM}\mathbf{M}_{LM}(k\mathbf{r}) + q_{LM}\mathbf{N}_{LM}(k\mathbf{r})), \qquad \mathbf{E}_{inc}(\mathbf{r}') = \sum_{LM}(a_{LM} Rg\mathbf{M}_{LM}(k\mathbf{r}') + b_{LM} Rg\mathbf{N}_{LM}(k\mathbf{r}')), \tag{24}$$

where scattering coefficients are related with expansion coefficients of incident field through the matrix elements (19)-(22) $T^{pn}_{LML_1M_1}$:

$$\begin{pmatrix} p_{LM} \\ q_{LM} \end{pmatrix} = \frac{1}{L(L+1)}\sum_{L_1M_1}\begin{pmatrix} T^{11}_{LML_1M_1} & T^{12}_{LML_1M_1} \\ T^{21}_{LML_1M_1} & T^{22}_{LML_1M_1} \end{pmatrix}\begin{pmatrix} a_{L_1M_1} \\ b_{L_1M_1} \end{pmatrix} \tag{25}$$

Thus the matrix elements of transition operator, which are defined by the relations (19)-(22), are the elements of Waterman's T matrix and the matrix elements of $\vec{\vec{T}}$ defined by the relations (12), (14) are related with Waterman's T matrix by relations (19)-(22) and (23). Consequently, for the elements of T matrix we have a similar to (15) equation, that allows calculating the T matrix for system of particles using T matrices for individual particles of the system.

3 Conclusion

In this paper the matrix elements of $\vec{\vec{T}}$ we expressed in terms of spherical wave functions. As a result, Eq.(15) for the particle-centered T matrices ($\mathbf{T}^{ij}$) is obtained for the condition: the smallest spheres circumscribing particles must not overlap with each other. These restrictions are known in the superposition T-matrix approach as well [2]. But the expression in terms of spherical wave functions is not the only possible one. For example, other possible expressions are the expressions in terms of spheroidal or cylindrical wave functions. Being expressed in terms of such function the T matrices for the cluster of particles must satisfy the following condition: the smallest spheroids (smallest cylinders) circumscribing particles must not overlap with each other. Note that independently of the chosen expansion functions, Eq.(15) for $\mathbf{T}^{ij}$ in the matrix form must be the same, since they are the consequence of more general equations (8) for operators. The key condition is that in the chosen function basis, one could separate variables for the Green's function.

Acknowledgments
We thank M.I. Mishchenko and V.P. Tishkovets for valuable discussions.

References

1. Waterman P.C., Phys. Rev. D., Vol.3, pp. 825-839, 1971.
2. Mishchenko M.I., Travis L.D. and Lacis A.A., "Scattering, Absorption and Emission of Light by Small Particles". Cambridge University press, 2002.
3. Tsang L., Kong J.A., Ding K.-H., "Scattering of electromagnetic waves. Advanced topics". Wiley, New York, 2001.
4. Mackowski D.W., Mishchenko M.I., J. Opt. Soc. Am, Vol.13, pp.2266-2278, 1996
5. Tsang L., Kong J.A., J. Appl. Phys, Vol.51, pp.3465-3485, 1980.
6. Rother T., Optics Communications, Vol.251, pp.270-285, 2005.
7. Varshalovich D.A, Moskalev A.N, and Khersonskii V.K., "Quantum Theory of Angular Momentum", World Scientific, Singapore, 1988.

Light modulation by polymer-dispersed liquid crystal films with small nematic droplets

Valery A. Loiko, Alexander V. Konkolovich, and Polina G. Maksimenko

B.I. Stepanov Institute of Physics of the National academy of sciences of Belarus
Nezalezhnasti Avenue 68, 220072, Minsk, Belarus
Tel: +375(17)2842894, fax: +375(17)2840879; e-mail: loiko@dragon.bas-net.by

Abstract

Light propagation through a polymer-dispersed liquid crystal film with nanosized nematic liquid crystal droplets is considered under the Rayleigh-Gans approximation. Multiple light scattering is taken into account by means of the Foldy-Twersky integral equation. Polarization state of the coherent component of the transmitted light is investigated for films with bipolar droplets. Conditions for circular and linear polarization implementation are obtained and discussed. The results are compared with known experimental data.

1 Introduction

Polymer films with encapsulated liquid crystal (LC) droplets are promising materials for various electro-optical devices, where light modulation is required. Typically droplets of submicron-to-micron sizes are used. Recently films with small droplets as compared with the wavelength of incident light have attracted particular attention of researchers. These films possess weak light scattering and enable one to control the polarization and phase of transmitted light in the visible and infrared regions.

A polymer-dispersed liquid crystal (PDLC) film is a polymer film with embedded LC droplets [1]. This film is placed between two transparent plates with deposited transparent electrodes. We consider liquid crystals with positive birefringence and bipolar structure of molecular arrangement inside the droplets [1, 2]. Each droplet is characterized by an axial vector. This vector is commonly called by a droplet director. It determines the direction of the droplet optical axis. Under applied voltage, LC molecules are reoriented to be aligned along the direction of the electric field and the optical axis of a droplet is rotated (an LC droplet is reoriented). Thus one can change optical properties of a PDLC film by varying the applied voltage. Numerous devices, such as light modulators, optical shutters, TV projection systems, displays, colour filters, polarizers, etc., are developed on this principle. No rigorous theory relating parameters of a PDLC film, applied voltage, and characteristics of transmitted light has been developed yet. Researchers deal with models, which are valid for specific kinds of the films. Typically the transmittance of PDLC films is considered [1, 3].

We investigate the polarization state of light transmitted through a PDLC film with nanosized nematic droplets. Particular attention is paid to the conditions providing linear or circular light polarization.

2 Model to describe polarization state

Consider a PDLC film with small nonabsorbing nematic LC droplets randomly distributed in a polymer binder. Let this film be illuminated by a monochromatic linearly polarized plane wave normally to its surface along z-axis. The x- and y-axes are in the plane of the film. The droplet directors are partially oriented along the x-axis. The azimuth angles of the droplet directors are uniformly distributed over the interval $[-\varphi_d^{\max}, \varphi_d^{\max}]$.

An important characteristic of a PDLC film is the distribution of LC molecules inside droplets. As mentioned above, each LC droplet is characterized by an axial vector called by the director of a droplet. To describe the alignment of LC molecules, we use order parameters [1], namely S is the molecular order

parameter of an LC; S_d is the order parameter of a droplet (it describes the alignment of LC molecules inside the droplet); S_x, S_y and S_z are the components of the order parameter tensor of the PDLC film [4]. These components show the orientation degree of droplet directors in the laboratory coordinate system. Light scattering by a single LC droplet is described under the Rayleigh-Gans approximation. Multiple scattering of waves is taken into consideration by means of the Twersky theory [5].

Components $E_{e,o}$ of the coherent transmitted field can be written as follows:

$$E_{e,o} = a_{e,o} \cos \Phi_{e,o}, \tag{1}$$

where $a_{e,\,o}$ are the amplitudes and $\Phi_{e,\,o}$ are the phases of the extraordinary and ordinary waves, respectively. They depend on the PDLC film parameters [4, 6]:

$$a_{e,o} = \exp(-\frac{1}{2}\gamma_{e,o} l)\begin{pmatrix}\cos\alpha \\ \sin\alpha\end{pmatrix}, \tag{2}$$

$$\Phi_{e,o} = \frac{klc_v}{2}\left(\frac{2n_o^2 + n_e^2}{3n_p^2} - 1 + \frac{2\left(n_e^2 - n_o^2\right)}{3n_p^2} SS_d S_{x,y}\right). \tag{3}$$

Here $\gamma_{e,\,o}$ are the extraordinary and ordinary extinction indices, respectively; l is the thickness of the film; α is the polarization angle of the incident light; k is the module of the wave vector of the incident light in the polymer; c_v is the volume concentration of the LC in the film; n_e and n_o are the refractive indices of the LC; n_p is the refractive index of the polymer. Using Eqs. (1) - (3), one can investigate characteristics of light transmitted through a PDLC film with small LC droplets.

3 Polarization of transmitted light

Using Eq. (1), we analyze characteristics of polarization states of transmitted light. In general case, light is elliptically polarized. Define ellipticity η as a ratio of the minor semiaxis of the polarization ellipse to the major one and azimuth ξ as the angle between the major semiaxis and x-axis, counted from the x-axis counterclockwise.

$$\eta = \sqrt{\frac{\left(a_e \sin\xi\right)^2 + \left(a_o \cos\xi\right)^2 - a_e a_o \sin 2\xi \cos\Delta\Phi}{\left(a_e \cos\xi\right)^2 + \left(a_o \sin\xi\right)^2 + a_e a_o \sin 2\xi \cos\Delta\Phi}}, \tag{4}$$

$$tg\,2\xi = 2\frac{a_e a_o}{a_e^2 - a_o^2}\cos\Delta\Phi. \tag{5}$$

Here $\Delta\Phi$ is the phase shift between the extraordinary and ordinary components:

$$\Delta\Phi = \frac{lkc_v}{3}\frac{\left(n_e^2 - n_o^2\right)}{n_p^2}\frac{\sin\left(2\varphi_d^{\max}\right)}{2\varphi_d^{\max}}\left(1 - S_z\right)SS_d. \tag{6}$$

Consider conditions providing the linear polarization of transmitted light. Light is linearly polarized, when at least one of the following conditions is fulfilled:

i. Polarization angle α is equal to 0 or $\pi/2$. In this case, the transmitted light retains the initial polarization state.
ii. Phase shift $\Delta\Phi$ between extraordinary and ordinary waves is equal to 0. Then the transmitted light is polarized as the incident light as well.

iii. Phase shift ΔΦ is equal to π. In this case, the light is linearly polarized. The polarization angle is determined as follows:

$$\xi_{lin} = \operatorname{atan}\left(\exp\left(\frac{-k^3}{8\pi\langle V\rangle} g\left(\frac{2n_o^2 + n_e^2 - \left(n_e^2 - n_o^2\right)SS_d}{3n_p^2} - 1 + \frac{2\pi\varphi_d^{\max}}{lkc_v \sin\left(2\varphi_d^{\max}\right)}\right)\right)\tan^{-1}\alpha\right) + \frac{\pi}{2}. \quad (7)$$

Here $\langle V\rangle$ is the mean volume of LC droplets; *g* is the function determined by the droplet shape, size, and configuration of LC molecules inside the droplet [4]. Function *g* can be calculated analytically for several special cases, but in general it should be computed numerically. To simplify the problem, we assume that the LC droplets are of spherical shape. In the case of very small LC droplets, angle ξ_{lin} linearly depends on angle α ($\xi_{lin} = \pi - \alpha$).

The dependence of angle ξ_{lin} on mean droplets radius $\langle R\rangle$ and polarization angle α is shown in Fig. 1.

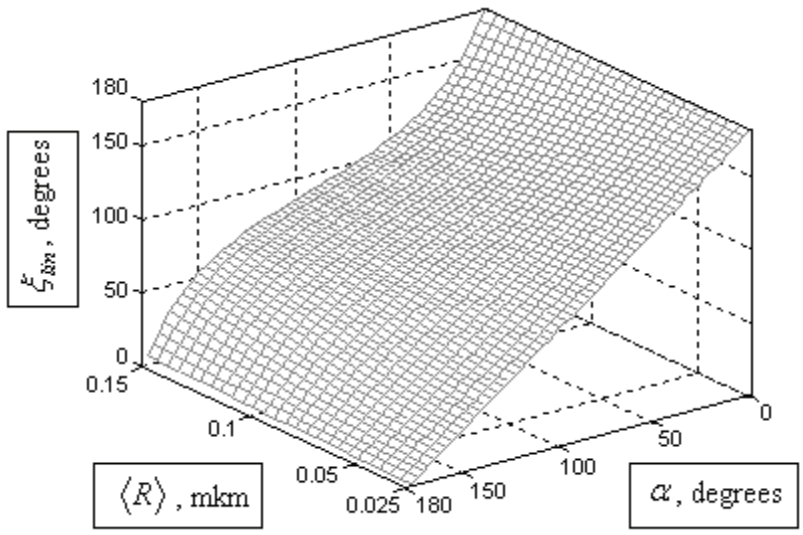

Figure 1: Polarization angle ξ_{lin} of transmitted light vs mean radius $\langle R\rangle$ of LC droplets and polarization angle α of incident light.

Now consider conditions providing the circular polarization of transmitted light ($\eta = 1$). The solution of Eq. (4) shows that the transmitted light is circularly polarized if phase shift $\Delta\Phi = \pi/2$ and the incident light is polarized at the angle:

$$\alpha_{circ} = \arctan\left(\exp\left(\frac{-k^3}{16\pi\langle V\rangle} g\left(\frac{2n_o^2 + n_e^2 - \left(n_e^2 - n_o^2\right)SS_d}{3n_p^2} - 1 + \frac{\pi\varphi_d^{\max}}{lkc_v \sin\left(2\varphi_d^{\max}\right)}\right)\right)\right). \quad (8)$$

Polarization angle $\alpha'_{circ} = \pi - \alpha_{circ}$ also provides circular light polarization. Figure 2 illustrates the dependence of the ellipticity on polarization angle α and on the strength of electric field *E* applied to the film. There are two polarization angles for each mean radius, when the ellipticity equals to unity. The ellipticity peaks correspond to the strength of the electric field, at which the condition of $\Delta\Phi = \pi/2$ is implemented. The mean radius of LC droplets can be estimated by the polarization angles.

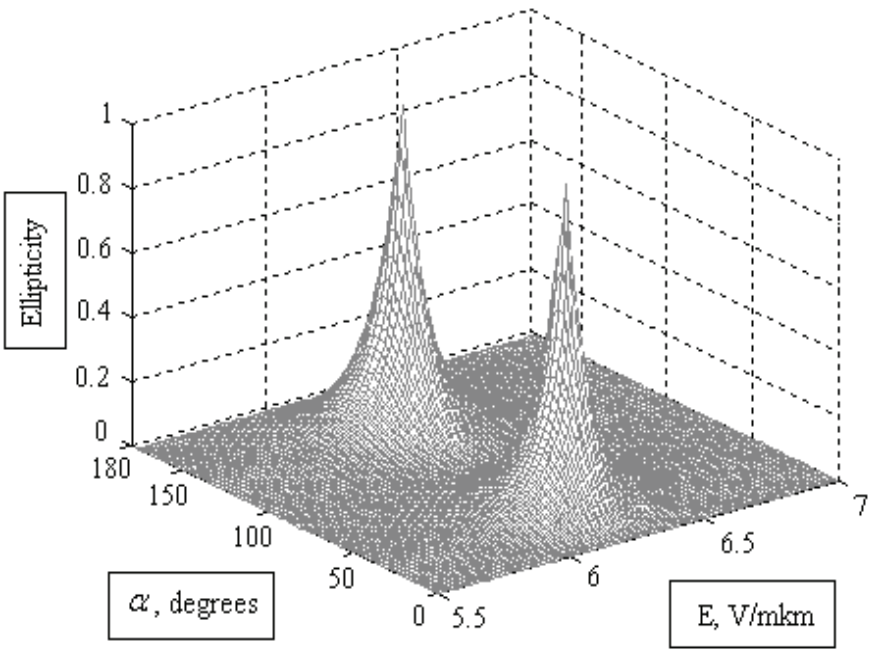

Figure 2: Ellipticity η vs polarization angle α of incident light and strength E of applied electric field.

4 Conclusion

The model to describe polarization state of light transmitted through a PDLC film with nanosized bipolar LC droplets is developed. Polarization characteristics of transmitted light are analyzed. The conditions providing circular and linear polarization of transmitted light are derived and investigated. The results can be used to estimate the mean radius of fine LC droplets in the film. There is a reasonable agreement between the theoretical data and the known experimental results.

References

[1] F. Simoni, *Nonlinear Optical Properties of Liquid Crystals* (World Scientific, Singapore, 1997).

[2] V. A.Loiko, V. I. Molochko, "Influence of the director field structure on extinction and scattering by a nematic liquid crystal droplet," Appl. Opt. **38**, 2857-2861 (1999).

[3] V. A. Loiko, V. V.Berdnik, "Multiple scattering in polymer dispersed liquid crystal films," Liq. Cryst. **29**, 921-927 (2002).

[4] V. A. Loiko, A. V. Konkolovich, "Polarization of light transmitted through a polymer film with nanosized droplets of liquid crystal," JETP **99**, 343-351 (2004).

[5] A. Isimaru, *Waves Propagation and Scattering in Randomly Nonisotropic Media* (Academic Press, New York, 1978).

[6] V. A. Loiko, A. V. Konkolovich, and P. G. Maksimenko, "Polarization and phase of light transmitted through polymer-dispersed liquid crystal film," J. of the SID **14,** 595-601 (2006).

Mononuclear cells morphology for cells discrimination by the angular structure of scattered light

Valery A. Loiko,[1] Gennady I. Ruban,[1] Olga A. Gritsai,[1]
Vladimir V. Berdnik,[2] and Natalia V. Goncharova[3]

[1] *Stepanov Institute of Physics of the NASB, Nezavisimosti avenue 68, 220072, Minsk, Belarus*
[2] *Centre of aerospace researches "Agroresource", K. Marx str. 65, 420015, Kazan, Russia*
[3] *Centre of Hematology and transfusiology, Dolginovsky avenue 160, 223059, Minsk, Belarus*
tel: +375 (17) 284-2894, fax: +375 (17) 284-0879, e-mail: o.gritsai@dragon.bas-net.by

Abstract

The morphology of peripheral blood mononuclear cells (lymphocytes and monocytes) of normal adult individuals is investigated by the methods of specialized light microscopy. The geometrical parameters of cells are analyzed. The possibility of optimization of mononuclear cells separation by light scattering is discussed. Obtained results can be used for the cells discrimination by the angular structure of scattered light.

1 Introduction

Biological particles can be characterized by the angular structure of scattered light. Flow cytometry is a modern technique for particle identification, which deals with the light scattering data. It is widely used for diagnostics of different diseases as well. In flow cytometer the particles are analyzed with the rate up to 5000 per second. In conventional flow cytometers the cells are identified by the intensity of forward ($1°<\theta<3°$) and sideward ($65°<\theta<115°$) scattered light and fluorochrom emission. In the scanning flow cytometer the cells are classified by the intensity of light scattered in a wide interval of angles ($5°<\theta<120°$) [1, 2].

The angular structure of scattered light strongly depends on geometrical and optical particle parameters, namely, size, shape, internal structure, and refractive index. The aim of our investigations is to give a detail description of cells morphology to solve the problem of cells discrimination by the angular structure of scattered light [3]. In our previous work the morphology of lymphocytes was investigated [4]. Here the data on monocytes are presented and the comparison of geometrical parameters of lymphocytes and monocytes is carried out. The possibility of mononuclear cells discrimination by light-scattering profiles is discussed.

2 Cells morphology. Results and discussion

Monocytes of peripheral blood of healthy individuals are investigated by the methods of light microscopy using a Leica DMLB2 microscope. A cellular suspension is sandwiched between the object plate and cover slip as in a microcuvette. To recognise monocytes CD14 –phycoerythrin –staining is used. The differential interference contrast and fluorescence modes are applied. The lens with 100^X magnification and numerical aperture of 1.25 are used. We analyse cell morphology with a Leica image processing software IM 1000. The image of peripheral blood monocytes is presented in Figure 1.

Our observations show, that the shape of lymphocyte and lymphocyte nucleus is slightly elongated or round. Usually the nucleus occupies the most part of lymphocyte (about 80%). The mean value of the ratio between the major axes (maximum linear sizes) of lymphocyte and its nucleus is 1.2. Lymphocyte sizes vary in the range from 4.8 to 11.8 microns. The lymphocyte nucleus sizes vary in the range from 4.1 to 8.3 microns. The mean value of lymphocyte size is about 7.5 microns and the mean value of lymphocyte nucleus size is about 6.2 microns [4].

The shape of monocyte is usually round, but the shape of monocyte nucleus is more complicate. The nucleus occupies about 65% of monocyte. The mean value of the ratio between the major axes of monocyte and its nucleus is 1.5. The sizes of monocytes and their nuclei are measured. The histograms of size distribution of monocytes and their nuclei are constructed. The mean value of monocyte size is 9.87 microns and the mean value of monocyte nucleus size is about 6.44 microns. The investigation demonstrates that the monocyte nucleus is eccentric as well as the lymphocyte one. The intervals of lymphocyte, monocyte, and their nuclei sizes are overlapped.

Figure 1: Peripheral blood monocytes.

Peripheral blood mononuclear cells can be identified by the angular structure of light scattered in the forward hemisphere. The difference in morphology of lymphocytes and monocytes results in the sideward scattering. To separate lymphocytes and monocytes the intensity of sideward scattered light is used. To

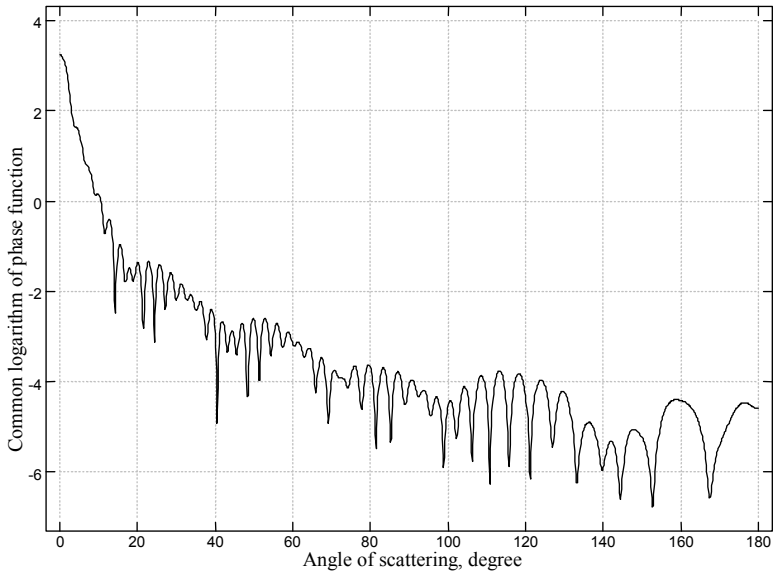

Figure 2: The calculated angular dependence of light scattering intensity for lymphocyte. Diameter of cell is 10.4μm, diameter of nucleus is 8.2μm, refractive index of cell is 1.37, and refractive index of nucleus is 1.39. Refractive index of medium is 1.35. Wavelength of incident light is 0.633μm.

optimize the problem of the cells identification, it is important to estimate the range of angles where the difference in light scattering patterns of lymphocytes and monocytes has maximum. We simulate the scattering from mononuclear cells by bi-layered spherical particles [5] (cell with nucleus) using the results of our experimental data on sizing of the cells. Obtained results show that, the main difference in scattering profiles of lymphocytes and monocytes takes place in the backward hemisphere. It is determined by the difference in cell-nucleus ratios of the cells. As we indicated above, the mean cell-nucleus ratios for lymphocyte and monocyte are 1.2 and 1.5, respectively.

The angular dependences of light scattered by bi-layered spherical particles with close external diameters are shown in Figures 2 and 3. These figures demonstrate that the cell-nucleus ratio has the maximal effect on the light scattering intensity in the range of angles from 125 to 150 degrees.

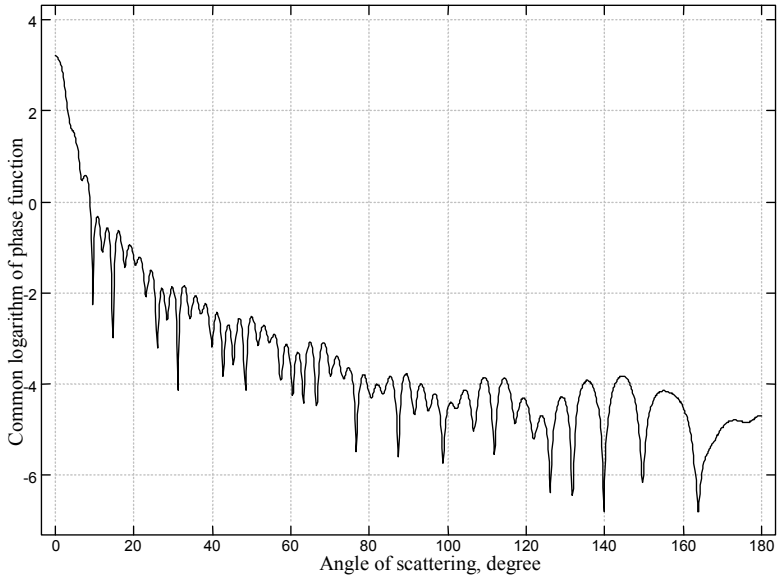

Figure 3: The calculated angular dependence of light scattering intensity for monocyte. Diameter of cell is 9.87μm, diameter of nucleus is 6.44μm, refractive index of cell is 1.37, and refractive index of nucleus is 1.39. Refractive index of medium is 1.35. Wavelength of incident light is 0.633μm.

3 Conclusion

To solve the inverse light scattering problem [6-8] of cells discrimination the optical models of cells are necessary. For construction the adequate optical model one has to know the cells morphology. The peripheral blood mononuclear cells of healthy adult individuals are investigated by the methods of specialized light microscopy. The geometrical parameters of lymphocytes and monocytes are presented. It is shown, that the cell-nucleus ratios for lymphocyte and monocyte are noticeably different. It results in the angular patterns of scattered light mainly in the backward hemisphere. The obtained data can be used to optimize the mononuclear cells discrimination by the light scattering intensity.

Acknowledgments

This research was supported by the Programme of basic research of Belarus ”Modern technologies in medicine” and partially sponsored by NATO’s Scientific Affairs Division in the framework of the Science for Peace Programme.

References

[1] V. P. Maltsev, K. A. Semyanov, *Characterization of Bio-Particles from Light Scattering* (VSP, Utrecht, 2004).

[2] V. P. Maltsev, "Scanning flow cytometry for individual particle analysis," Rev. Sci. Instruments **71**, 243-255 (2000).

[3] G. I.Ruban, V. A. Loiko, O. A.Gritsai, et al, "Investigation of human white blood cells: application to scanning flow cytometry," Proceed. SPIE. **6284**, 6284OH-1-6284OH-5 (2006).

[4] V. A. Loiko, G. I.Ruban, O. A.Gritsai, et al, "Morphometric model of lymphocyte as applied to scanning flow cytometry," J. Quant. Spectr. Radiat. Transfer. **102**, 73-84 (2006).

[5] V. Babenko, L. A. Astafyeva, V. N. Kuzmin, *Electromagnetic Scattering in Disperse Media* (Springer, Berlin, 2003).

[6] V. V. Berdnik, R. D.Mukhamedjarov, and V. A. Loiko, "Characterization of optically soft spheroidal particles by multiangle light-scattering data by use of the neural-networks method," Opt. Lett. **29**, 1019-1021 (2004).

[7] Z. Ulanowski, Z. Wang, P. H. Kaye, and I. K. Ludlow, "Application of neural networks to the inverse light scattering problem for spheres," Appl. Opt. **37**, 4027-4033 (1998).

[8] V. Berdnik, V. Loiko, K. Gilev, A. Shvalov, and V. Maltsev, "Characterization of spherical particles using high-order neural networks and scanning flow cytometry," J. Quant. Spectr. Radiat. Transfer. **102**, 62-72 (2006).

Optically driven micromachines: design and fabrication

Vincent L. Y. Loke, Timo A. Nieminen, Theodor Asavei, Norman R. Heckenberg and Halina Rubinsztein-Dunlop

School of Physical Sciences, The University of Queensland,Queensland, 4072 Australia
tel: +617 33653463, fax: +617 33651242, e-mail: loke@physics.uq.edu.au

Abstract

We design and fabricate optically driven micromachines which find the applications in microfluidics, manipulation of biological cells, microchemistry etc. The micromachines are driven by tightly focused laser beams. To aid the design of micromachines, we employ a number of modeling methods such as the Mie theory, the point matching method, finite difference methods, discrete dipole approximation (FDFD), sometimes in combination, to simulate the light scattering from the individual components. The micromachines prototypes are fabricated using a two-photon polymerization process.

1 Introduction

A 'micromachine', as we have defined it, may be a number of microdevices working in conjunction with one another or it may be as simple as a single rotor trapped by a tightly focused laser beam. For example, a single birefringent vaterite sphere is used to determine the viscosity of it's surrounding liquid medium by means of measuring its rotational speed and the torque applied by the trapping laser beam that carries spin angular momentum. We fabricate micromachine components with complex shapes using a two-photon polymerization process [1]. The components are generally about 1-9μm in size. The design of the micromachines are aided by computational simulations of the scattered field from which the torques and forces can be calculated. A survey on micromachines can be found on [2].

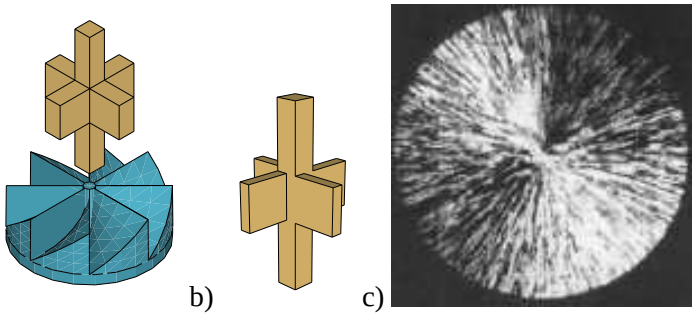

Figure 1: a) DOE and 'cross' rotor. b) 'Cross' rotor with offset blades. c) Spherulitic sphere.

2 Micromachines

There are a number ways a microrotor can be spun using its structure in combination with the nature of the incident tightly focused laser beam. Upon passing through a diffractive optical element (DOE) with 8 blaised blades as per figure 1a, a gaussian beam will aquire orbital angular momentum of $8\hbar$ per photon. The beam then can be used to spin a 'cross' rotor as shown in figure 1a. However, if the 'cross' rotor has

offset blades (figure 1b), it will spin with just a gaussian incident beam due to the asymmetric forces at the blades.

A focused laser beam with spin angular momentum can be used to transfer torque to the birefringent object. The bifringent object works a waveplate to change angular momentum of the beam. Although, the spherulitic sphere in figure 1c is not uniformly birefringent, a nett birefringence is sufficient for the effect to take place.

3 Fabrication

A 3D microstructure is fabricated by curing the resin to the required shape [1]. This involves pulsing the the individual voxels of the structure with a femtosecond laser. Two coverslips, which sit on a pedestal, (figure 2) support the resin. The pedestal is moved in the required x, y and z direction such that each voxel is cured one at a time. When all the voxels are cured, the uncured resin is washed away with acetone, and we are left with the 3D structure.

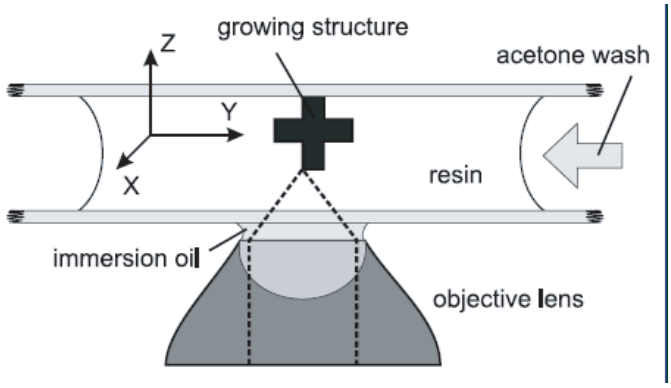

Figure 2: Two-photon polymerization fabrication.

4 Simulation Methods

We have used the FDFD/T-matrix method [3] to calculate the torque imparted on a vaterite particle by any given trapping beam with spin angular momentum. For larger and more complex structures, we have found the DDA method [5] to be suitable. Nonetheless, as the target model gets larger, we begin to hit the limit of available memory; the need for memory saving methods arises.

We developed a method to exploit the rotational symmetry of a target structure [4], whereby the interaction matrix of the DDA linear equations can be compressed to $1/m^2$ to that or the original size, where m is the order of rotational symmetry. The matrix can be further compressed by a factor of 4 by exploiting mirror symmetry. This is achieved by only constructing the interaction matrix from the reduced number of dipoles (figure 3) but still aggregating the contributions from their symmetrical counterparts. Once the linear equations are solved, the polarizations of the other dipoles can be calculated easily from just applying the appropriated rotations or 'reflections' which are merely phase corrections. This holds for the case of plane wave illumination. However, to generalize for arbitrary illumination, we would need to incorporate this method with the T-matrix [6].

We propose to exploit the rotational symmetry of the DOE in figure 4a. However the repeated 'wedge' (figure 4b) of the DOE presents the problem where there are sharp edges where we may need prohibitively

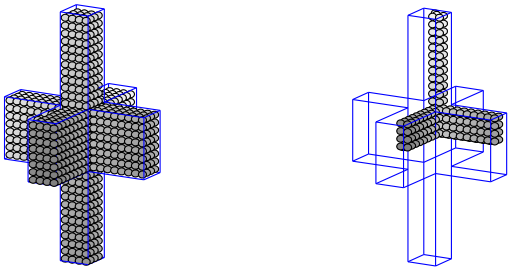

a) b)

Figure 3: a) Dipoles representing target 'cross' rotor. b) Reduced number of dipoles due to symmetry.

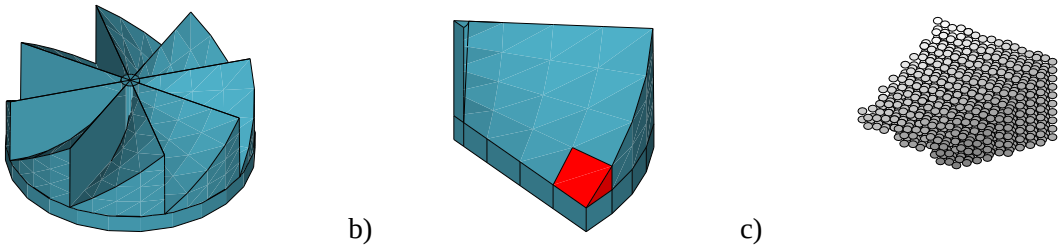

a) b) c)

Figure 4: a) Diffractive optical element (DOE). b) DOE segment. c) Precalculated block.

small (because of memory requirements) lattice spacing for the dipoles. To overcome this, we would divide the DOE segment into smaller blocks and precalculate the overall polarizability of the blocks using relatively small dipoles (figure 4c). The polarizability of those blocks that are repeated throughout the segment need not be calculated again. Effectively, we calculate the polarizability of arbitrarily shaped dipoles. We then assemble the DOE segment and hence apply the same symmetry method as for the cross to model the whole DOE.

5 Conclusion

The fabrication and design of micromachines can be made more efficient with the aid of computational modelling methods; the cycle time between design, fabrication and testing is greatly reduce due to the capability of modeling methods to realistically calculate the scattered fields and hence torques and forces. This means that a bulk of the testing can be done on the computer even before the first fabricated prototype is produced. The flexibility of modeling methods such as DDA allows for the design of exotic structures.

References

[1] G. Knöner and J. Higuet and S. Parkin and T. A. Nieminen and N. R. Heckenberg and H. Rubinsztein-Dunlop, "Two-photon polymerization process for optically driven micromachines", Proc. SPIE 6038, 208.216 (2006)

[2] T. A. Nieminen and J. Higuet and G. Knoener and V. L. Y. Loke and S. Parkin and W. Singer and N. R. Heckenberg and H. Rubinsztein-Dunlop, “Optically Driven Micromachines: Progress and Prospects”, Proceedings of SPIE 6038:237-245 (2006).

[3] V. L. Y. Loke and T. A. Nieminen and A. M. Bra´nczyk and N. R. Heckenberg and Halina Rubinsztein-Dunlop, “Modelling optical micro-machines”, Proc. 9th International Conference on Electromagnetic and Light Scattering by Non-Spherical Particles, June 59, 2006, St. Petersburg, Russia, N. Voshchinnikov (ed).

[4] V. L. Y. Loke and T. A. Nieminen and N. R. Heckenberg and Halina Rubinsztein-Dunlop, “Modelling optical micro-machines”, Proc. DDA Workshop, Intitut für Werkstofftechnik, Bremen, 23 March, 2007.

[5] B. T. Draine and P. T. Flatau, “Discrete-dipole approximation for scattering calculations”, J. Opt. Soc. Am. A, Vol. 11, No. 4, p1491, (1994).

[6] D. W. Mackowski, “Discrete dipole moment method for calculation of the T-matrix for nonspherical particles”, J. Opt. Soc. Am. A, Vol. 19, No. 5, p881-893, (2002).

Direct Simulation of Scattering and Absorption by Particle Deposits

Daniel W. Mackowski

Auburn University, Department of Mechanical Engineering
Auburn, AL 36849, USA
tel: +1 (334) 844-3334, fax:+1 (334) 844-3307, email: mackodw@auburn.edu

1 Introduction

The present paper is concerned with the prediction of the radiative absorption and scattering behavior of a layer of densely packed, wavelength–sized particles. This problem has relevance to a number of engineering and scientific applications, e.g., estimation of the effect of particle deposits on heat exchanger surfaces, modeling the reflection properties of pigment coatings and dust layers, and prediction of Anderson localization in discretely inhomogeneous media.

A well–developed understanding exists for calculation of the single (or isolated) scattering and absorption properties of particles – encompassing simple shapes (such as Lorenz–Mie theory for spheres) to more sophisticated methods for nonspherical and inhomogeneous particles [1]. In the situations of interest here, e.g., particle deposits, paint pigments, composite materials, etc., the particle concentrations can become sufficiently high so that prediction of the particle optical properties via single–scattering formulations becomes suspect. Specifically, under such conditions the electric field incident on a particle can have significant contributions due to scattering from neighboring particles (so–called near field interactions) and the far field scattering can be modified by the correlated positions existing among the close–packed particles (far field interference). These two effects are typically referred to together as dependent scattering, and generally become significant for particle volume fractions $f > 0.01$ and/or particle clearance/wavelength ratios less than 0.5 [2]; such conditions typically involve packed deposits of particles having size parameters $x = 2\pi a/\lambda$ (where a is a characteristic radius of the particle and λ is the radiation wavelength) on the order of unity or less.

Initial investigations on dependent scattering primarily dealt with the propagation of a coherent wave through a particulate medium, with the objective of identifying an effective propagation constant (or, equivalently, complex refractive index) of the medium which describes the attenuation of the coherent wave via absorption and scattering by the particles [3, 4]. In principle, it is possible to exactly calculate, via analytical superposition methods, the absorption and scattering properties of neighboring particles provided the single–scattering properties are known. A review of the superposition method, as applied to spherical particles, is given in Ref. [5]. Until now, the application of the superposition method has primarily been to determine the optical properties of aggregated particles containing a finite number of spheres. A few investigations have been conducted which compared direct simulations of wave propagation in large ensembles of spheres – as exactly calculated with the superposition method – to effective medium theories [6, 7]. Effective medium theories have also been coupled to the superposition method, with the objective of developing efficient methods for computation of scattering properties of nonspherical particles [8, 9].

The objective of this paper is to demonstrate the feasibility of using exact methods to directly simulate the absorption and scattering properties of a plane layer of densely–packed spheres that are exposed to an incident source of radiation. Such methods could provide benchmark calculations for gauging the accuracy of effective medium/radiative transfer equation (RTE) models as applied to thin deposits or coatings of particles. Since the exact methods also provide a detailed description of the electric field distribution both within and external to the particles, calculations of this sort would also be useful in the examination of localization phenomena in random media. The motivation for this approach stems from the fact that the computational algorithms for wave interactions among spheres have progressed to the point that direct calculations involving large–scale ensembles – i.e., sphere systems that are adequately large to represent a radiative continuum – have become tractable on typical desktop PCs [5].

The particle layer in this investigation will be represented by a large, yet obviously finite, number of spheres that are arranged in set positions. The thickness of the layer will be a fixed parameter in the

simulations, yet the lateral extent should be sufficiently large to represent an infinite expanse of particles. Meeting this condition is difficult – if not impossible – when the 'target' of spheres is exposed to a transverse plane wave. In this case the lateral extent of the layer will always have an effect on the far–field scattering pattern, due to diffraction at the edges. This problem is bypassed by using a focussed beam of radiation as the exciting (or probing) source, in which the width of the beam is smaller than the lateral size of the layer.

2 Formulation

The system under examination consists of an ensemble of N_S spheres, each characterized by a size parameter $x_i = \mathrm{k}a_i$, a complex refractive index $m_i = n_i + ik_i$, and a position (X_i, Y_i, Z_i) for $i = 1, 2, \ldots N_S$. The incident field consists of a focussed beam which propagates in a direction $\theta = \beta_0$ and $\phi = \alpha_0$ relative to the target coordinate frame and is focussed at a point X_0, Y_0, Z_0. Along the focal plane (which contains the focal point and is perpendicular to the propagation direction) the beam is approximated as a linearly polarized transverse wave, i.e.,

$$\mathbf{E}_{inc}(X', Y', 0) \approx \hat{\mathbf{x}} \exp\left(-\frac{X'^2 + Y'^2}{\omega_0^2}\right) \tag{1}$$

in which ω_0 is the beam width parameter and the primed coordinates denote the rotated coordinate system that is centered on the focal point and with a z' axis pointing in the propagation direction.

The solution method used to obtain the scattered field is a direct extension of Lorenz/Mie theory. The total field external to the spheres is represented as a sum of fields scattered from the individual spheres in the ensemble plus the incident field;

$$\mathbf{E}_{ext} = \mathbf{E}_{inc} + \sum_{i=1}^{N_S} \mathbf{E}_{sca,i} \tag{2}$$

The incident field is represented as a regular vector spherical harmonic (VSH) expansion centered about an arbitrary origin, whereas each of the scattered fields is represented by an outgoing VSH expansion centered about the origin of the sphere. Application of the continuity equations at the surface of each sphere, and utilization of the addition theorem for VSH, results in a system of equations for the expansion coefficients for the individual scattered fields;

$$\frac{1}{\overline{a}^i_{np}}\, a^i_{mnp} - \sum_{\substack{j=1 \\ j\neq i}}^{N_S} \sum_{n'=1}^{L_i} \sum_{m'=-n'}^{n'} \sum_{p'=1}^{2} H^{i-j}_{mnp\,m'n'p'}\, a^j_{m'n'p'} = g^i_{mnp} \tag{3}$$

In the above, a^i_{mnp} and g^i_{mnp} denote the expansion coefficients, of order n, degree m, and mode p ($= 1, 2$ for TM/TE) for the scattered and incident fields centered about sphere i, H^{i-j} is a translation matrix which transforms an outgoing VSH centered about origin j into an expansion of regular VSH about i, and $\overline{a}^i_{np}$ denote the Lorenz/Mie coefficients for sphere i, which are a function of the sphere size parameter x_i and refractive index m_i.

The present application is concerned primarily with the propagation of a collimated beam into a particulate medium. Accordingly, conditions are sought which minimize the spreading of the beam waist as a function of Z'. Such conditions will correspond to relatively large $\mathrm{k}\,\omega_0$, which is equivalent to a large diffraction length/spot size ratio $(2\pi\omega_0^2/\lambda)/\omega_0$. Fortunately, such conditions also allow a relatively simple formula for the focal–point centered VSH expansion coefficients for the incident beam via the localized approximation. The expansion coefficient for the beam centered about a sphere origin i, i.e., g^i_{mnp}, can then be obtained by application of the VSH addition theorem [10, 11].

The complete scattering and absorption properties of the system can be obtained from the solution to Eq. (3). Such properties include the absorption cross sections of the individual spheres and the bulk absorptive and reflective properties of the slab as a whole.

3 Results and Discussion

The target used in this work consisted of a cylindrical slab of spheres that were packed into a tetrahedral lattice. The axis of the cylinder is taken to be the Z direction, and the radius (which is proportional to the

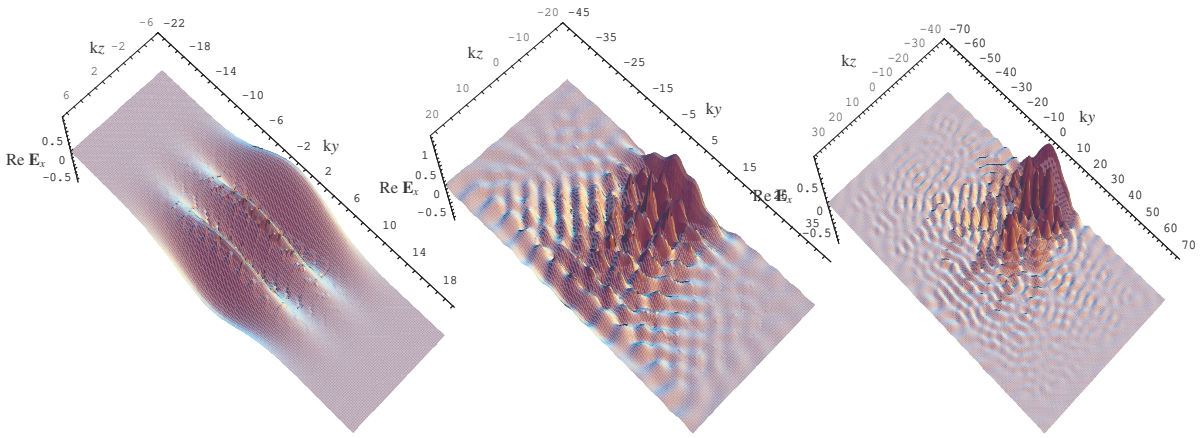

Figure 1: Re $(\hat{\mathbf{x}} \cdot \mathbf{E})$ vs. position on the $Y' - Z'$ plane. Sphere size parameter $x_S = 1$ (l), 4 (c), 8 (r), refractive index $m = 1.6 + 0.02i$.

number of spheres in the X and Y directions) is chosen to be several times larger than the incident beam width ω_0. The incident beam was characterized by a dimensionless beam width parameter of $\mathrm{k}\,\omega_0 = 10$.

Shown in Fig. (1) are surface plots of the X–component of electric field in the $Y - Z$ plane, calculated for sphere size parameters of $x_S = 1$, 4, and 8. The sphere refractive index is $m_S = 1.6 + 0.02i$ for all cases. The sphere matrix consists of 5 sphere layers in the Z direction, and the incident beam is focussed in the center of the matrix and was incident parallel to the z axis (representing normal incidence on the slab). The number of spheres in the slab depended on the size parameter, with a smaller x_S requiring more spheres in order to extend the slab radius past the width of the beam. For $x_S = 1$ and 8 the model required 1760 and 275 spheres. The latter case used a truncation order of $L = 11$ for the sphere scattered field expansions, which corresponded to 44,000 complex–valued equations for the set of scattering coefficients in Eq. (3). Electric field components were calculated using the superposition of Eq. (2) if the point was external to the spheres, or using the Lorenz/Mie relations to relate the internal to external fields for points interior to the spheres.

One point to make regarding Fig. (1) is that it demonstrates the veracity of the formulation and computations. The particular plane chosen for the surface plots splits the spheres intersected by the plane in half, and accordingly the sphere surfaces will be tangential to the x direction along the plane. Since the tangential components of electric field are continuous at the sphere surface, the plots should demonstrate a continuity in electric field from the exterior to interior regions. This behavior is completely consistent with the calculation results. Relatively close inspection of Fig. (1) is needed to discern the sphere positions by virtue of the small jumps in electric field that occur at the sphere edges, which are due to truncation errors in the series solution (most noticeably for the $x_S = 1$ case).

The results in Fig. (1) show that the slab of spheres with $x_S = 1$ behaves as a homogeneous medium, in that the profile of the incident beam is largely unperturbed as it propagates through the slab. This behavior is somewhat surprising: an effectively homogeneous medium would be expected for $x_S \ll 1$, for which the simulation would become equivalent to a discrete dipole model for a homogeneous slab, yet the $x_S = 1$ spheres do not behave as dipoles. Indeed, three harmonic orders (N_O) were needed to represent the scattered fields from the spheres, as opposed to a single TM order for the dipole. A relevant condition behind the apparent homogenous behavior has to do with the fact that the sphere radius, for this case, is significantly smaller than the width of the incident beam. Because of this, a relatively large population of spheres are excited by the beam. The scattered field produced by the spheres – and the resulting interference of fields – will therefore be averaged over the large group of scattering sources, resulting in a net field which is not strongly dependent on position in the slab. This behavior is in keeping with the Quasi–Crystalline Approximation in effective medium models [4].

Conversely, the results for $x_s = 4$ and 8 show that the field within the slab for larger size parameters can become highly dependent on position. The peaks in the field amplitudes are associated with the focussing of

internal fields within the individual spheres, and this effect becomes more pronounced as the size parameter increases. For both $x_S = 4$ and 8, the effects of multiple scattering among the spheres leads to a broadening – or diffusion – of the field with increasing depth into the medium. For the smaller size parameter the field distribution remains symmetrical in the $y - z$ plane – which would be expected due to the symmetrical conditions imposed on the problem – yet for $x_S = 8$ the field distribution appears to take on a chaotic structure.

The distribution of absorption in the medium – which allows for determination of the bulk absorption coefficient – as well as the reflectivity of the slab and the far–field scattering behavior will be presented at the meeting.

References

[1] M. I. Mishchenko, L. D. Travis, and A. Macke. T matrix methods and its applications. In M. I. Mishchenko, J. W. Hovenier, and L. D. Travis, editors, *Light Scattering by Nonspherical Particles: Theory, Measurements, and Applications*, chapter 6. Academic Press, 2000.

[2] C. L. Tien. Thermal radiation in packed and fluidized beds. *ASME J. Heat Transfer*, 110:1230–1242, 1988.

[3] V. N. Bringi, V. V. Varadan, and V. K. Varadan. Coherent wave attenuation by a random distribution of particles. *Radio Sci.*, 17:946–952, 1982.

[4] P. C. Waterman and N. E. Pedersen. Electromagnetic scattering by periodic arrays of particles. *J. Appl. Phys.*, 59:2609–2618, 1986.

[5] K. A. Fuller and D. W. Mackowski. Electromagnetic scattering by compounded spherical particles. In M. I. Mishchenko, J. W. Hovenier, and L. D. Travis, editors, *Light Scattering by Nonspherical Particles: Theory, Measurements, and Applications*, chapter 8. Academic Press, 2000.

[6] L. Tsang, C. Mandt, and K. H. Ding. Monte Carlo simulation of the extinction rate of dense media with randomly distributed dielectric spheres based on solution to Maxwell's equations. *Opt. Lett.*, 17:314–316, 1992.

[7] L. M. Zurk, L. Tsang, K. H. Ding, and D. P. Winebrenner. Monte Carlo simulations of the extinction rate of densely packed spheres with clustered and nonclustered geometries. *J. Opt. Soc. Amer. A*, 12:1772–1781, 1995.

[8] D. W. Mackowski. An effective medium method for calculation of the T matrix of aggregated spheres. *J. Quant. Spectrosc. Radiat. Transfer*, 70:441–464, 2001.

[9] D. W. Mackowski. Discrete dipole moment method for calculation of the T matrix for nonspherical particles. *J. Opt. Soc. Amer. A*, 19:881–893, 2002.

[10] A. Doicu and T. Wriedt. Computation of the beam–shape coefficients in the generalized Lorenz–Mie theory by using the translational addition theorem for spherical vector wave functions. *Appl. Opt.*, 13:2971–2978, 1997.

[11] A. Doicu and T. Wriedt. Plane wave spectrum of electromagnetic beams. *Opt. Comm.*, 136:114–124, 1997.

Coherence effects in systems of Dipolar Bi-Spheres

O. Merchiers[1] , F. Moreno[1], J.M. Saiz[1] and F. González[1]

[1] *Universidad de Cantabria, Grupo de Óptica, Departamento de Física Aplicada, Avda de los Castros, 39005 Santander, Spain*
tel: +34 942 201868, fax: +34 942 201402, e-mail: olivier.merchiers@unican.es

Abstract

We study the behavior of the Negative Polarization Branch (NPB), using a scattering system which consists of two dipolar scatterers separated by a fixed distance and freely floating in space. For such a system, a resonance spectrum is obtained if one plots the scattering cross-section as a function of the polarizability. The excited resonances correspond with specific oscillation modes of the electric (and magnetic) dipole moments and arise due to the interaction between the dipoles. We show that the NPB can be generated if the system is put into the right resonance mode, but can also be suppressed if placed in a so called longitudinal mode. The effect of a magnetic permeability different from one on the NPB will also be considered.

1 Introduction

Coherence effects in or close to the backscattering direction have been the focus of attention of many researchers involved in the theoretical and experimental analysis of the propagation of electromagnetic waves in random dense media where multiple scattering is important. On one hand we have the enhancement of the scattered intensity in the backward direction (EBS) and on the other hand we have the polarimetric opposition effects. Based on observations, two types of opposition effects are usually distinguished. The first one, often called the polarization opposition effect (POE) which appears as a narrow asymmetric branch and the second one, often referred to as negative polarization branch (NPB) and appears as a wide symmetric branch around the backward direction in the linear polarization coefficient (LPC) [1,2]. It is considered that the coherent backscattering mechanism is responsible for the EBS, the POE and the NPB [3]. However, it is assumed that the coherent backscattering is not the only contribution to the NPB. These phenomena have been observed in experiments related to the scattering of unpolarized electromagnetic radiation by astronomical objects [1] and have also been reproduced in laboratory experiments with both volume and surface geometries [2,3].

In this work we present a study of the previously cited NPB using a model constituted by two dipoles separated by a fixed distance. We will call this system a Dipolar Bi-sphere (DBS). This simple model has already been introduced by other authors to study coupling resonances [4] and the EBS [5]. The aim of this contribution is to study the effect of coupling resonances of the DBS on the coherence effects [6], for both non-magnetic ($\mu = 1$) and magnetic particles ($\mu \neq 1$). The reason why we introduce the magnetic permeability in our study is because of the high interest for metamaterials during the last six years. While only very recently those materials have been seen to operate in the visible region [7] and only for slab geometries, an early theoretical study by Kerker et al. [8] showed that small spheres with $\mu \neq 1$ have some very interesting scattering properties. Herein lays the interest of studying scattering systems with magnetic properties.

2. Theory

To obtain the scattered electromagnetic field from our system, we used a generalized version of the coupled dipole method [9] which was introduced by Mulholland et al. in [10]. This generalized method

enables us to compute the scattered electric field when the scatterers have a magnetic permeability different from 1. However, the method can equally well be applied for particles with $\mu = 1$. The method consists in writing each electric ($\mathbf{d}_i$) and magnetic dipole moment ($\mathbf{m}_i$) as a contribution of the incident field and the dipole moments induced by the rest of the particles. One has then to solve the system of 2N linear vector equations in $\mathbf{d}_i$ and $\mathbf{m}_i$ given by

$$\begin{aligned} \mathbf{d}_i &= \alpha^e{}_i \mathbf{E}^o{}_i + \sum_{i \neq j}^{N} \alpha^e{}_j \left[\mathbf{C}_{ij}\mathbf{d}_j - \sqrt{\frac{\varepsilon_o}{\mu_o}}\mathbf{G}_{ij}\mathbf{m}_j \right] \\ \mathbf{m}_i &= \alpha^m{}_i \mathbf{H}^o{}_i + \sum_{i \neq j}^{N} \alpha^m{}_j \left[\mathbf{C}_{ij}\mathbf{m}_j + \sqrt{\frac{\mu_o}{\varepsilon_o}}\mathbf{G}_{ij}\mathbf{d}_j \right] \end{aligned} \tag{1}$$

where $\boldsymbol{C}_{ij}$ and $\boldsymbol{G}_{ij}$ are the interaction matrices and $\alpha^e{}_j$ and $\alpha^h{}_j$ are the electric and magnetic polarizabilities respectively. Once the electric and magnetic dipole moments are obtained by matrix inversion, the scattered electric field is easily obtained.

The calculations are made for N_T random orientations of the scattering system, we then obtain an averaged value of scattering cross-section σ_S.

3. Results

3.1 Particles with $\mu = 1$

In figure 1(a) we show the averaged scattering cross section for $\varepsilon = -2.013$, $\mu = 1$ and P-polarized incident light versus the interparticle distance r between the particles. The results for the S-polarization are identical due to symmetry. As can be seen in figure 1a, successive resonances are excited. Each one of these resonances correspond to a specific oscillation mode of the dipoles.

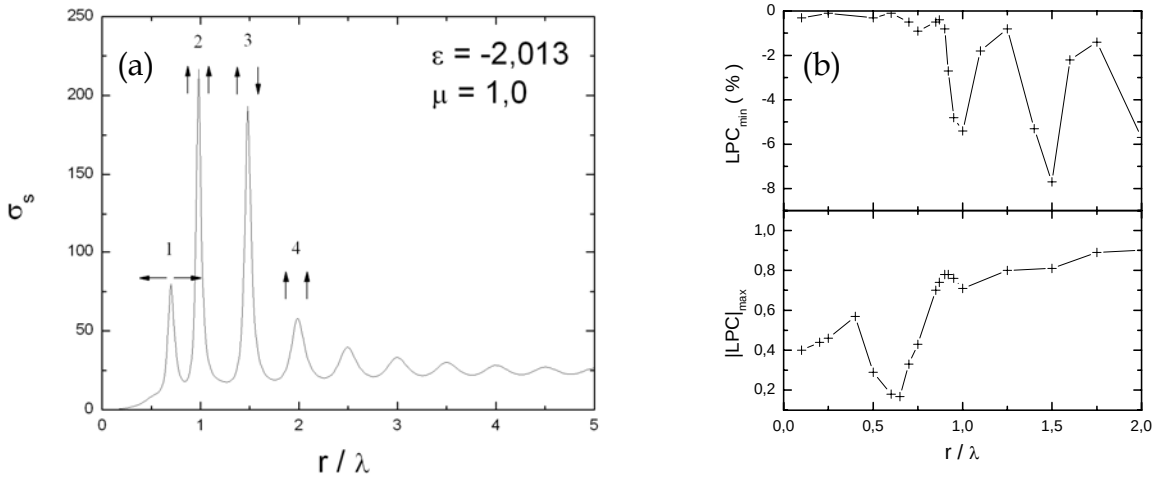

Figure 1: (a) Scattering cross-section σ_S as a function of the interparticle distance for $\varepsilon = -2.013$, $\mu = 1$. The arrows show the oscillation mode for each dipole when placed in the corresponding resonance. (b) LPC_{min} and $|LPC|_{max}$ obtained for totaly unpolarized incident radiation.

Figure 1(b) represents two aspects of the linear polarization coefficient (LPC). LPC_{min} represents the minimum of the LPC in the interval of scattering angles from 0º to 180º and $|LPC|_{max}$ is the maximum of the absolute value of the LPC in the same interval. We see that the peaks (2), (3) and (4) of figure 1(a) correspond to minima in the LPC_{min}. This means that the resonances (2), (3) and (4) produce NPB. This is not the case for resonance (1), which instead creates a minimum in the plot of $|LPC|_{max}$ vs r. From figure 1, we could thus deduce that for an interparticle distance $r = \lambda$, the produced NPB is entirely generated by the contribution of mode (2). However, an other analysis based on the eigenvector decomposition of the local dipole moments (see equation (2)) shows that the anti-symmetrical state does also contribute to the NBP.

$$|d\rangle = \sum_{n=1}^{3N} \frac{|n\rangle\langle n|\mathbf{E}_o\rangle}{1-w_n} \tag{2}$$

where $|n\rangle$ and w_n are the eigenvectors and eigenvalues respectively of the total interaction matrix. $|\mathbf{E}_o\rangle$ represents the incident field. These vectors have all *3N* elements and contain the oscillation modes or the incident electric field on each particle.

3.2 Particles with $\mu \neq 1$

In the previous section we saw that the coupling between two electric dipoles produces four types of modes: transversal and longitudinal modes, where both of them have symmetric and anti-symmetric variants. If we now introduce magnetic dipoles ($\mu \neq 1$), new modes appear. We still have the purely electric longitudinal modes, but now we have also their purely magnetic counterpart. The transversal modes appear now as mixed electric and magnetic states.

As an example, we will choose here $\mu = -1.6$. The scattering cross section as a function of interparticle distance is represented in figure 2(a). We observe similarities but also differences between this case and the previous one with $\mu = 1$. The peak centred in $r/\lambda = 1.5$ is now the most important. As can be seen from figure 2(a), the mode corresponding with interparticle distance $r/\lambda = 1.5$ has anti-symmetrical electric and symmetric magnetic components.

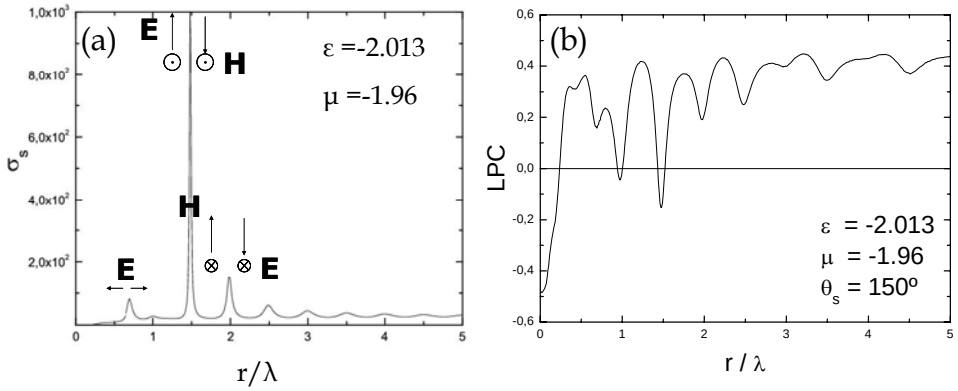

Figure 2: (a) Scattering cross-section σ_S as a function of the interparticle distance for $\varepsilon = -2.166$ and $\mu = -1.6$. (b) LPC obtained for totally unpolarized incident radiation.

In the LPC plot we see for $r/\lambda = 1.5$ a strong minimum with negative values, which indicates a negative polarization branch. This plot was obtained for a scattering angle of $\theta_S = 150º$ which is the direction where the minimum of the NPB usually occurs. The same happens for $r/\lambda = 1.0$. In $r/\lambda = 0.7$, the linear

polarization doesn't become negative which indicates again a qualitative difference between the resonances.

4 Conclusions

We studied the resonance spectra and the linear polarization coefficient of a Dipolar Bi-Sphere as a function of the interparticle distance where the constituents can be considered magnetic or non-magnetic. Depending on the type of excited resonance, we can or cannot produce a negative polarization branch. In the case of non-magnetic particles with $r/\lambda = 1.0$, we found that both the transversal symmetrical and anti-symmetrical states do contribute to the negative polarization branch.

For magnetic particles the highest peak was found for $r/\lambda = 1.5$ corresponding with an anti-symmetric electric and symmetric magnetic mode and produces NPB.

These results point out that not only the presence of multiple scattering is important, but that the oscillation mode plays also a fundamental role.

Acknowledgements

The authors wish to thank the Dirección General de Enseñanza Superior for its financial support (FIS2004-06785). Olivier Merchiers wishes to thank the University of Cantabria for his research grant.

References

[1] G. Videen, Y. Yatskiv, and M. Mishchenko, eds., Photopolarimetry in Remote Sensing, vol. 161 of NATO Sci Series, Kluwer, Dordrecht, 2004.

[2] Y. Shkuratov, A. Ovcharenko, E. Zubko, O. Miloslavskaya, K. Muinonen, J. Piironen, R. Nelson, W. Smythe, V. Rosenbush, and P. Helfenstein, Icarus **159**, 396-416 (2002).

[3] Y. Shkuratov, A. Ovcharenko, E. Zubko, H. Volten, O. Muñoz, and G. Videen, J. Quant. Spectr. Rad. Transf. **88**, 267-284 (2004).

[4] V.A. Markel, Journal of Modern Optics **39**(4), 853-861 (1991).

[5] F. Ismagilov and Y. Kravtsov, Waves in Random Media **3**, 17-24 (1993).

[6] F. Moreno, O. Merchiers, and F. González, Optics Letters **30**, 2194-2196 (2005).

[7] G. Dolling, M. Wegener, C. M. Soukoulis and S. Linden, Optics Letters **32**, 53-55 (2007)

[8] M. Kerker, D.-S. Wang, and C.L. Giles, JOSA **3**, 765-767 (1982)

[9] S. Singham and C. Bohren, J. Opt. Soc. Am. A **5** (11), 1867-1872 (1988).

[10] G.W. Mulholland, C.F. Bohren, and K.A. Fuller, Langmuir **10** (8), 2533-2546 (1994).

Remote sensing of tropospheric aerosols from space: from AVHRR to Glory APS

Michael Mishchenko, Igor Geogdzhayev, Brian Cairns, and Jacek Chowdhary

NASA GISS, 2880 Broadway, New York, NY 10025, USA
tel: +1 (212) 678-5590, fax: +1 (212) 678-5622, mmishchenko@giss.nasa.gov

Abstract

Analysis of the long-term Global Aerosol Climatology Project dataset reveals a likely decrease of the global optical thickness of tropospheric aerosols by as much as 0.03 during the period 1991–2005. This recent trend mirrors the concurrent global increase in solar radiation fluxes at Earth's surface and may have contributed to recent changes in surface climate. Existing satellite instruments cannot be used to determine unequivocally whether the recent trend is due to long-term global changes in the natural or anthropogenic aerosols. It is thus imperative to provide uninterrupted multidecadal monitoring of aerosols from space with dedicated instruments like the Glory Aerosol Polarimetry Sensor in order to detect long-term anthropogenic trends potentially having a strong impact on climate.

Recent observations of downward solar radiation fluxes at Earth's surface have shown a recovery from the previous decline known as global "dimming" with the "brightening" beginning around 1990. The increasing amount of sunlight at the surface profoundly affects climate and may represent diminished effects of certain counter-balances of the greenhouse warming, thereby making it more evident during the past decade.

It has been suggested that tropospheric aerosols have contributed significantly to the switch from solar dimming to brightening via both direct and indirect aerosol effects. It has further been argued that the solar radiation trend mirrors the estimated recent trend in primary anthropogenic emissions of SO_2 and black carbon, which contribute significantly to the global aerosol optical thickness (AOT). Therefore, it is important to provide a direct and independent assessment of the actual global long-term behavior of the AOT. We accomplish this by using the longest uninterrupted record of global satellite estimates of the column AOT over the oceans, the Global Aerosol Climatology Project (GACP) record (http://gacp.giss.nasa.gov). The latter is derived from the International Satellite Cloud Climatology Project (ISCCP) DX radiance dataset composed of calibrated and sampled Advanced Very High Resolution Radiometer (AVHRR) radiances.

The solid black curve in Fig. 1 depicts the global monthly average of the column AOT for the period August 1981 – June 2005. The two major maxima are caused by the stratospheric aerosols generated by the El Chichon (March 1982) and Mt Pinatubo (June 1991) eruptions, also captured in the Stratospheric Aerosol and Gas Experiment (SAGE) stratospheric AOT record. The quasi-periodic oscillations in the black curve are the result of short-time aerosol variability.

The red line traces the overall behavior of the column AOT during the eruption-free period from January 1986 to June 1991. It shows only a hint of a statistically significant tendency and indicates that the average column AOT value just before the Mt Pinatubo eruption was close to 0.142. After the eruption, the GACP curve is a superposition of the complex volcanic and tropospheric AOT temporal variations. However, the green line reveals a clear long-term decreasing tendency in the tropospheric AOT. Indeed, even if we assume that the stratospheric AOT just before the eruption was as large as 0.007 and that by June 2005 the stratospheric AOT became essentially zero (*cf.* the blue curve), still the resulting decrease in the tropospheric AOT during the 14-year period comes out to be 0.03. This trend is significant at the 99% confidence level.

Figure 2 shows the difference between the GACP AOT averaged over the periods 2002–2005 and

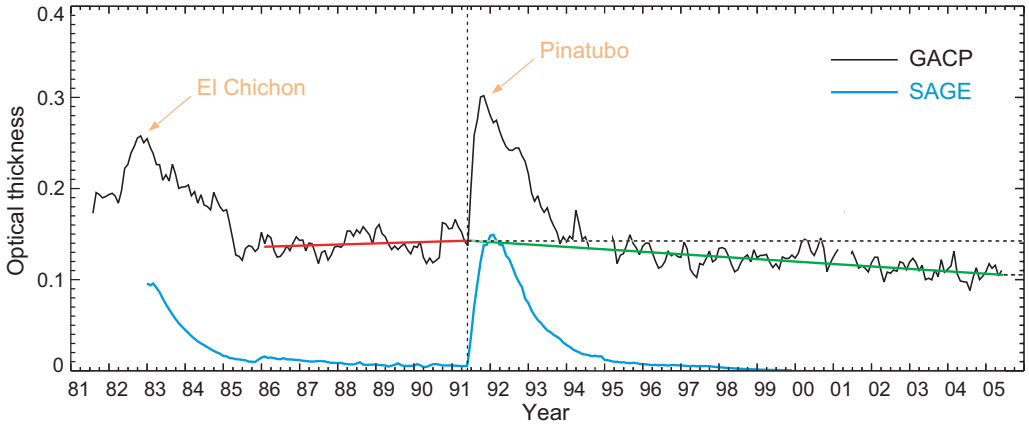

Fig. 1. GACP record of the globally averaged column AOT over the oceans and SAGE record of the globally averaged stratospheric AOT.

1987–1990. As expected, this map reveals increased aerosol loads in Asia and reduced pollution in Europe. Another interesting trend is the significant reduction in the amount of dust aerosols coming from the Sahara desert.

Admittedly, AVHRR is not an instrument designed for accurate aerosol retrievals from space. Among the remaining uncertainties is radiance calibration which, if inaccurate, can result in spurious aerosol tendencies. Similarly, significant systematic changes in the aerosol single-scattering albedo or ocean reflectance can be misinterpreted in terms of AOT variations. However, the successful validation of GACP retrievals using precise sun-photometer data taken from 1983 through 2004 indicates that the ISCCP radiance calibration is likely to be reliable. This conclusion is reinforced by the close correspondence of the calculated and observed TOA solar fluxes. Furthermore, the GACP AOT record appears to be self-consistent, with no drastic intra-satellite variations, and is consistent with the SAGE

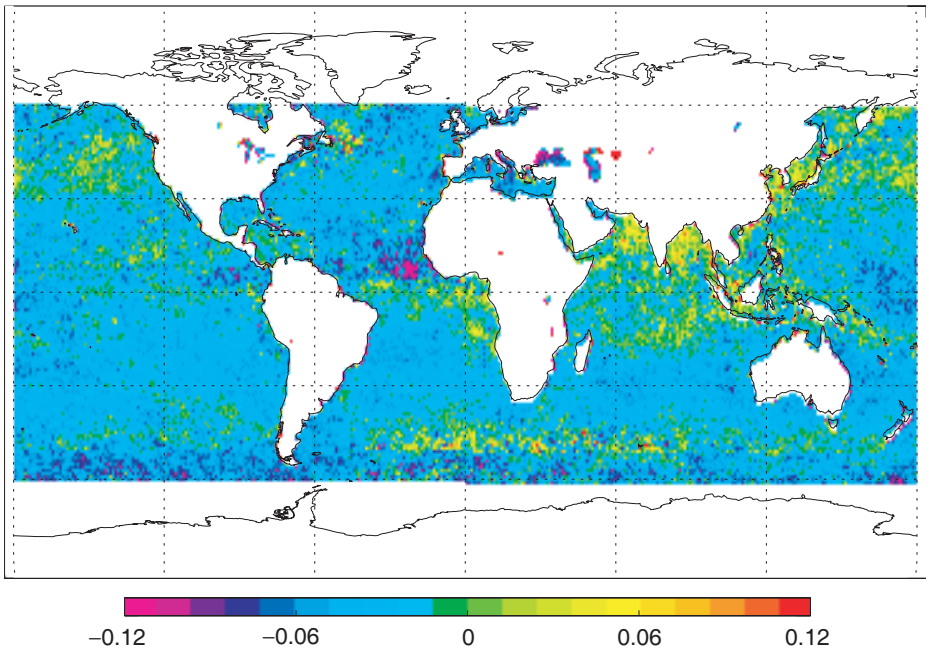

Fig. 2. Aerosol optical thickness difference between the early 2000s and late 1980s.

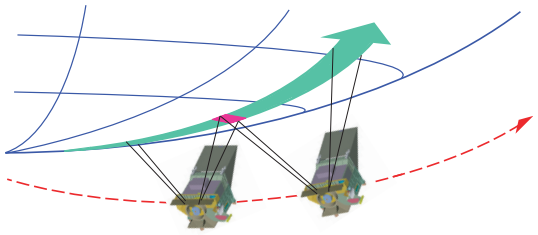

Fig. 3. Along-track multi-angle APS measurements via 360º scanning from the sun-synchronous polar-orbiting Glory spacecraft.

record.

The unique advantage of the AVHRR dataset over the datasets collected with more advanced recent satellite instruments is its duration, which makes possible reliable detection of statistically significant tendencies like the substantial decrease of the tropospheric AOT between 1991 and 2005. With all the uncertainties, the global tropospheric AOT decrease over the 14-year period is estimated to be at least 0.02. This change is consistent with long-term atmospheric transmission records collected in the Former Soviet Union.

Our results suggest that the recent downward trend in the tropospheric AOT may have contributed to the concurrent upward trend in the surface solar fluxes. Neither AVHRR nor other existing satellite instruments can be used to determine unequivocally whether the recent AOT trend is due to long-term global changes in the natural or anthropogenic aerosols. This discrimination would be facilitated by an instrument like the Aerosol Polarimetry Sensor (APS) scheduled for launch in December 2008 as part of the NASA Glory Mission (http://glory.giss.nasa.gov).

The key measurement requirements for the retrieval of aerosol and cloud properties from photopolarimetric data are high (i.e., fine) accuracy, a broad spectral range, and observations from multiple angles, including a method for reliable and stable calibration of the measurements. The APS measurement approach to ensure high accuracy in polarimetric observations employs Wollaston prisms to make simultaneous measurements of orthogonal intensity components from the same scene. The broad spectral range of APS is provided by dichroic beam splitters and interference filters that define nine spectral channels centered at the wavelengths λ = 410, 443, 555, 670, 865, 910, 1370, 1610 and 2200 nm. The critical ability to view a scene from multiple angles is provided by scanning the APS IFOV along the spacecraft ground track (Fig. 3) with a rotation rate of 40.7 revolutions per minute with angular samples acquired every 8 ± 0.4 mrad, thereby yielding ~250 scattering angles per scene. The scanner assembly also allows a set of calibrators to be viewed on the side of the scan rotation opposite to the Earth. The APS on-board references provide comprehensive tracking of polarimetric calibration throughout each orbit, while radiometric stability is tracked monthly to ensure that the aerosol and cloud retrieval products are stable over the period of the mission.

Since APS shares many design features with its aircraft predecessor, the Research Scanning Polarimeter (RSP), the latter can be expected to provide a close model of the future APS performance. Examples of the fidelity of the AOT, size distribution, and absorption estimated from the APS type of remote-sensing measurement during seven different flights are shown in Fig. 4. In panel (a) we see that the spectral AOT values retrieved from polarimetric measurements agree well with those measured by ground-based sunphotometers over an AOT range from 0.05 to more than 1. The absence of spectrally-dependent biases in these retrievals also demonstrates the reliability of the size distribution estimate for both small and large modes of a bimodal aerosol distribution. Comparisons have also been made between in situ and retrieved size distributions and have also been found to agree extremely well (difference in aerosol effective radius of less than 0.04 μm).

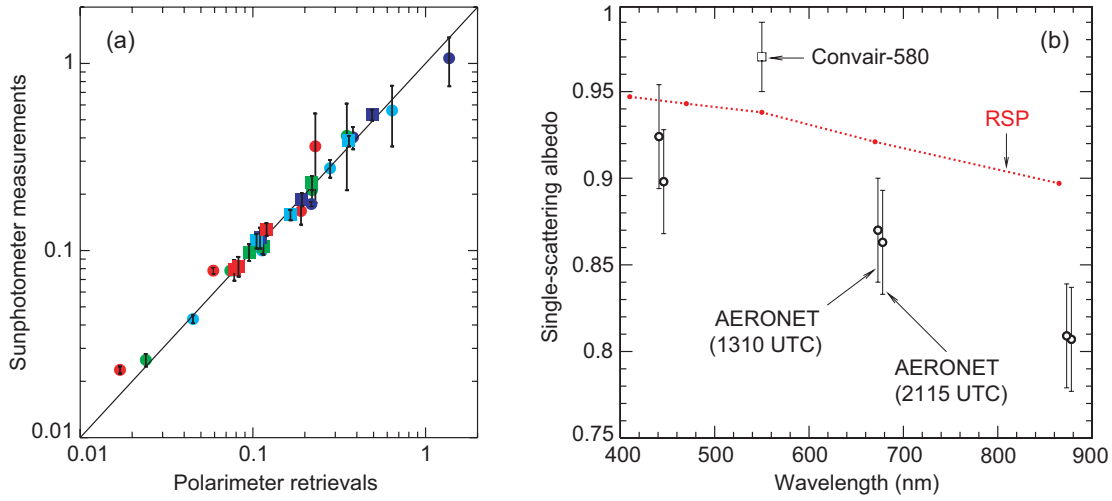

Fig. 4. (a) Optical thickness comparison. Sunphotometer measurements at 410/443, 500, 673, and 865 nm shown as blue, turquoise, green, and red symbols, respectively, are compared with RSP retrievals for the same wavelength. The circular symbols are for retrievals over land while the square symbols are for retrievals over ocean. Error bars are only shown for the sunphotometer measurements. (b) Single-scattering albedos as a function of wavelength. The red dotted line shows the best-estimate values retrieved from RSP data. Also included are estimates from data collected during Convair-580 flight 1874 and from the AERONET data.

The aerosol single-scattering albedo (SSA) can also be estimated from polarimetric measurements because of the differing sensitivities of polarized and unpolarized reflectances to aerosol absorption. In Fig. 4(b), the SSA derived from polarimetry is compared with *in situ* and ground-based sky radiance estimates. The discrepancy between these estimates may be related to the loss of particles in the sampling system for *in situ* measurements, humidification of the *in situ* extinction (but not the absorption) coefficients, and uncertainties in the SSA retrieval from sky radiances that may be caused by horizontal variability in the aerosol burden. Nonetheless the polarimetric estimate of SSA is consistent with the other measurements given their inherent uncertainties. Overall, Fig. 4(b) illustrates the complexity of retrieving SSA from both *in situ* and remote-sensing measurements and suggests that the validation of SSA retrievals from APS data will be a challenging task.

Acknowledgments

This research was funded by the NASA Radiation Sciences Program managed by Hal Maring and by the NASA Glory Project.

Scattering of light by concave-hull-transformed Gaussian particles

Karri Muinonen and Hannakaisa Erkkilä

Observatory, Kopernikuksentie 1, P.O. Box 14, FI-00014 University of Helsinki, Finland
tel: +358 9-19122941, fax: +358 9-19122952, e-mail: Karri.Muinonen@helsinki.fi

Abstract

We study light scattering by angular and faceted random particles using the discrete-dipole and geometric-optics methods. For describing the particle shapes, we introduce a concave-hull transformation and apply it to the Gaussian-random-sphere geometry. We describe other potential applications for the concave-hull transformation.

1 Introduction

Naturally occurring small particles provide a world of varying shapes. The Gaussian-random-sphere geometry can be utilized in the modeling of irregular shapes [1]. Based on the Gaussian geometry, first steps are here taken toward modeling angular and faceted shapes. Knowing the scattering characteristics of angular and faceted particles is important, e.g., in solar-system remote sensing.

For modeling the angular and faceted shapes, we define a concave hull: For an arbitrary three-dimensional object, the concave hull coincides with the inner surface formed by a sphere rolling over the object. The concave hull varies as a function of a single scale parameter, the radius of the generating sphere. In the limits of infinitesimal and infinite radii, the concave hull approaches the original shape and the convex hull of the object, respectively. In defining the concave hull, we thus mimic a mechanical profilometer sensing the shape of the object.

We parameterize the concave-hull transformation by the ratio of the generating-sphere radius to a typical radius of the object. For the Gaussian geometry, we utilize the ratio of the generating-sphere radius to the ensemble mean radius, denoting that ratio by h. It follows that the relative curvature radii of the concave-hull concavities cannot be smaller than h. The present concave hull is related to the internal tangenting spheres introduced in [2] to represent the volumes of sample Gaussian particles. For an illustration of the concave-hull transformation, see Fig. 1 for shapes generated with $h = 0$, $h = 2$, and $h = 2 \cdot 10^4$.

In what follows, we show the first application of the concave-hull transformation in discrete-dipole and geometric-optics light-scattering computations.

2 Scattering by concave-hull-transformed Gaussian particles

We parameterize the Gaussian-random-sphere particle with two statistical parameters, the radial-distance standard deviation σ and covariance-function power-law index ν [2]. We assess two pairs of these parameters: first, $\sigma = 0.2$ and $\nu = 2$; and, second, and $\sigma = 0.3$ and $\nu = 4$.

For both geometric-optics and discrete-dipole computations, the complex refractive index of the particles is fixed at $m = 1.55 + i10^{-4}$. For the geometric-optics computations, the size parameter is $x = ka = 100$, where k is the wave number and a is the mean radius of the Gaussian-random-sphere particles. For the discrete-dipole computations concerning individual sample particles in Fig. 1 in random orientation, the equal-volume-sphere size parameter is $x_{\rm ev} = 5$.

The geometric optics computations are carried out for 700 sample shapes with 700 rays incident on each sample particle in random orientation, totaling altogether 490,000 rays. For $\sigma = 0.2$ and $\nu = 2$, decreasing

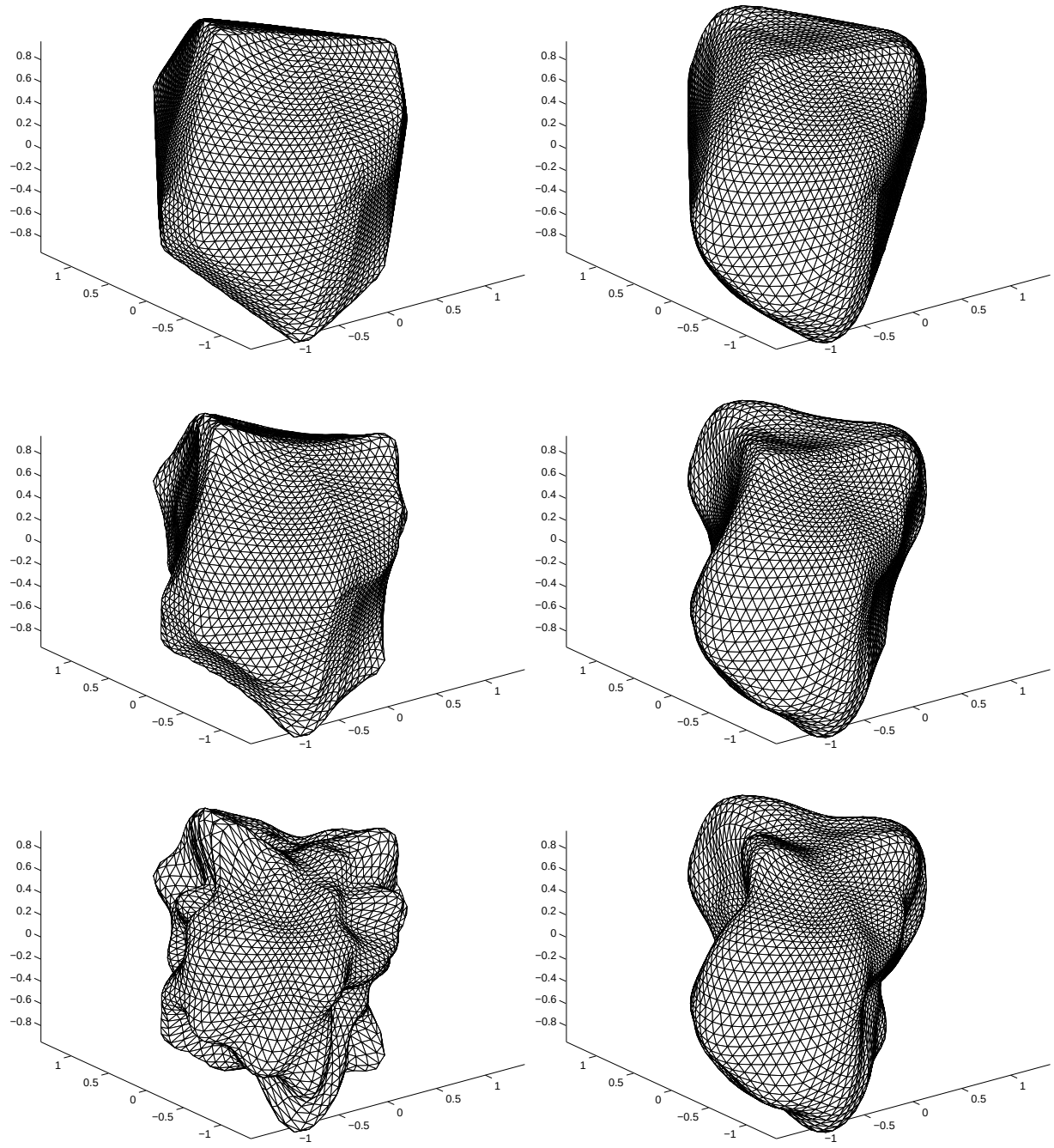

Figure 1: Example shapes corresponding to the Gaussian-random-sphere radial-distance standard deviations and covariance-function power-law indices $\sigma = 0.2$ and $\nu = 2$ (left) as well as $\sigma = 0.3$ and $\nu = 4$ (right). We show the original shapes (bottom; $h = 0$) and their concave hulls generated with spheres of scale radii $h = 2$ (middle) and $h = 2 \cdot 10^4$ (top).

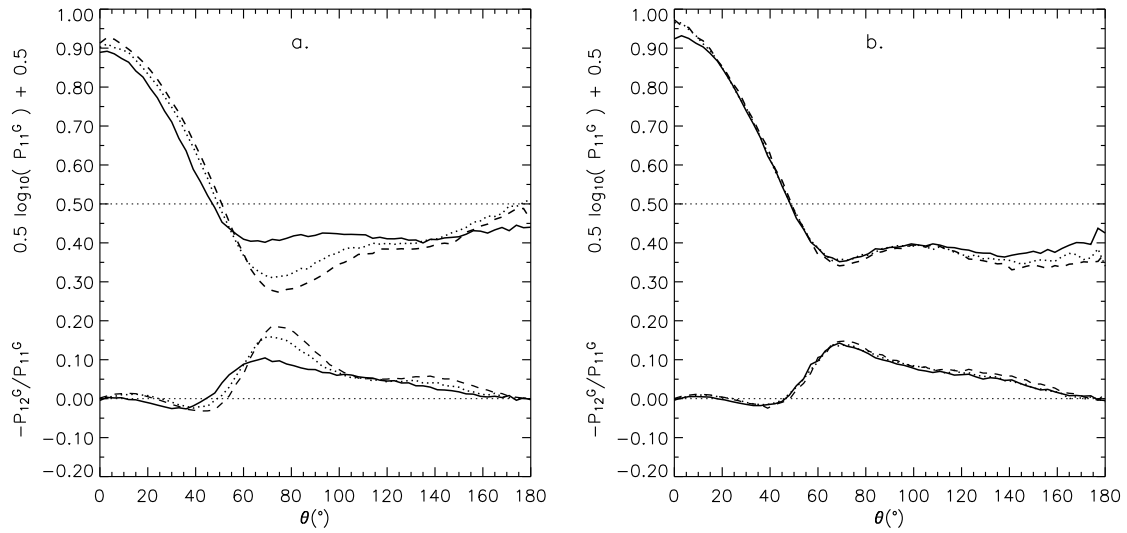

Figure 2: Ensemble-averaged geometric-optics scattering-phase-matrix elements $P_{11}^{\rm G}$ (top) and $-P_{12}^{\rm G}/P_{11}^{\rm G}$ (bottom) for random particles originating with (a) $\sigma = 0.2$ and $\nu = 2$ as well as (b) $\sigma = 0.3$ and $\nu = 4$ for the size parameter $x = 100$ and refractive index $m = 1.55 + i10^{-4}$. The solid, dotted, and dashed lines refer to the Gaussian particles and their concave-hull-transformed counterparts with $h = 2$ and $h = 2 \cdot 10^4$, respectively.

concaveness results in increasing steepness of the geometric-optics scattering phase function toward the backscattering direction and increasing degree of linear polarization in the intermediate scattering angles (Fig. 2a). Clearly, the rougher interface more efficiently neutralizes the polarization characteristics. For $\sigma = 0.3$ and $\nu = 4$, the scattering characteristics are perhaps surprisingly independent of the concavities (Fig. 2b).

The discrete-dipole computations are carried out for the shapes depicted in Fig. 1 in 1008 orientations (mimicking random orientation) using the DDSCAT code [3]. For $\sigma = 0.2$ and $\nu = 2$, the discrete-dipole computations show a trend that is the opposite to that in the geometric-optics computations: decreasing concaveness results in decreasing degree of linear polarization for unpolarized incident light in the intermediate scattering angles (Fig. 3a). It is plausible that the original surface with smaller-scale irregularities results in a more pronounced positive polarization due to the electric dipole moments induced in the irregularities. Note the backscattering peaks and negative polarization branches close to backscattering (Figs. 3a and 3b; for explanation, see [2, 4]).

3 Discussion

There are a number of potential applications for the concave-hull geometry presently introduced. The concave hull is unambiguously defined for particles that are aggregates of constituent smaller grains although, in practice, it can become challenging to compute their concave hulls. For rough solid surfaces, for which the convex hull has little significance, the concave hull can be highly useful. For rough particulate surfaces, the concave hull allows studies of porosity as a function of surface height and the concave-hull scale parameter. Finally, for macroscopic objects such as asteroids, the concave hull can help in determining the scale-dependent density of the object.

We have studied light scattering by concave-hull-transformed Gaussian-random-sphere particles showing angular and faceted geometries with the help of the discrete-dipole and geometric-optics methods. The

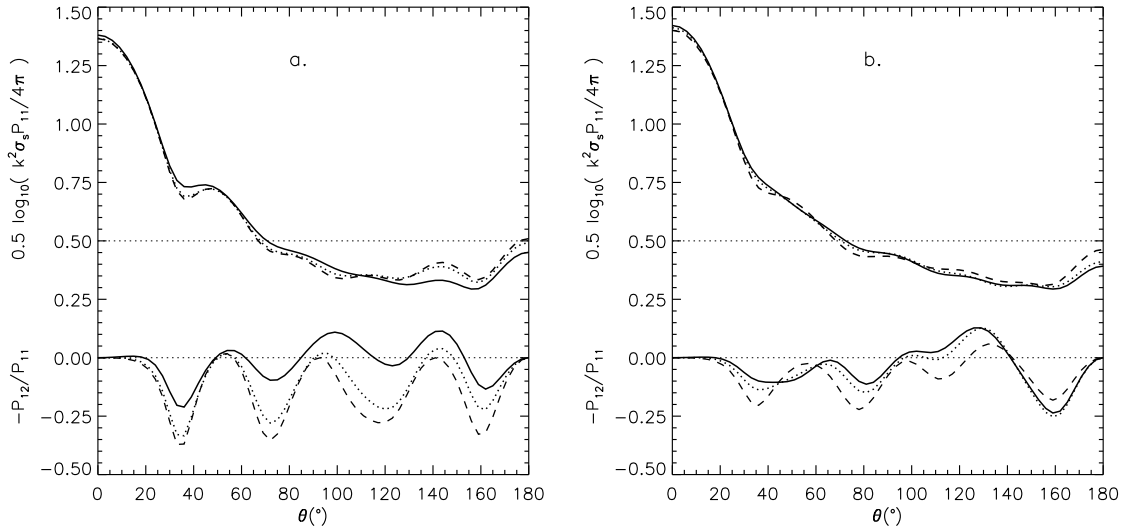

Figure 3: Discrete-dipole scattering-phase-matrix elements $k^2\sigma_s P_{11}/(4\pi)$ (top; σ_s is the scattering cross section) and $-P_{12}/P_{11}$ (bottom) for the particles left and right in Fig. 1 for the equal-volume size parameter $x_{ev} = 5$ and refractive index $m = 1.55 + i10^{-4}$. The solid, dotted, and dashed lines refer to the bottom, middle, and top particle geometries in Fig. 1, respectively.

concave-hull geometry offers a promising tool to study the effects of concavities on the scattering characteristics of nonspherical particles.

Acknowledgments

Research supported, in part, by the Academy of Finland.

References

[1] K. Muinonen, T. Nousiainen, P. Fast, K. Lumme, and J. I. Peltoniemi, "Light scattering by Gaussian random particles: ray optics approximation," *JQSRT* **55**, 577-601 (1996)

[2] K. Muinonen, E. Zubko, J. Tyynelä, Yu. G. Shkuratov, and G. Videen, "Light scattering by Gaussian random particles with discrete-dipole approximation," *JQSRT*, in press (2007)

[3] B. T. Draine, and P. J. Flatau, "User Guide to the Discrete Dipole Approximation Code DDSCAT 6.1," http://arxiv.org/abs/astro-ph/0409262v2 (2004)

[4] J. Tyynelä, E. Zubko, G. Videen, and K. Muinonen, "Interrelating angular scattering characteristics to internal electric fields for wavelength-scale spherical particles," *JQSRT*, in press (2007)

Simplex inversion of asteroid photometric lightcurves

Karri Muinonen and Johanna Torppa

Observatory, Kopernikuksentie 1, P.O. Box 14, FI-00014 University of Helsinki, Finland
tel: +358 9-19122941, fax: +358 9-19122952, e-mail: Karri.Muinonen@helsinki.fi

Abstract

We develop simplex inversion methods for asteroid photometric lightcurves in the case of limited and/or sparsely distributed observations. We show that the methods can be utilized in the computation of asteroid spins and convex shapes described using a finite number of triangles.

1 Introduction

In asteroid lightcurve inversion, the shape and spin of the asteroid as well as its scattering properties are solved for. Conventionally, the shape model is a convex polyhedron, where the free parameters are either the individual polyhedron facet areas or the coefficients of the spherical-harmonics series describing the Gaussian curvature of the surface [1]. Spin and shape models can be obtained using relative photometry by applying simple scattering laws, such as a combination of the Lommel-Seeliger and Lambert laws. Scattering properties can usually be assumed to be homogeneous over the surface. Extensive results of asteroid lightcurve inversion have been published by, e.g., Torppa et al. [2]. Deriving the scattering parameters of more complicated scattering laws constitutes a challenge. As an inverse problem, it is not as stable as plain spin and shape determination, and improvements in the available scattering models are called for (e.g., [3, 4]).

In Sect. 2, we describe the main features of the current simplex algorithms aimed at statistical inversion of asteroid spins, shapes, and scattering properties (see also [5]). We present some first results in Sect. 3, and Section 4 contains the conclusions and future prospects.

2 Simplex inversion

Whereas conventional lightcurve inversion consists of two parts, that is, the derivation of the normal-vector distribution and the subsequent derivation of the convex shape from the normal vectors, in simplex inversion, the convex shape solution is directly searched for. There are four parameters for the spin characteristics: the rotational period, the ecliptic longitude and latitude of the rotational pole, and the rotational phase of the object at a given time. The shape is specified using triangles with the Cartesian coordinates of the nodes as free parameters. Altogether, there are $3 + 3N$ free parameters where N is the number of nodes, the rotational phase becoming redundant because of the general shape model. The initialization of the simplex can be accomplished, e.g., by using prolate spheroids. For a detailed description of downhill simplex minimization, the reader is refered to Press et al. [6].

The simplex minimization allows for a flexible incorporation of conditions on the shape to be searched for. At each iteration step, the convexity of the shape is verified, returning a rejection for concave solutions. Solutions are constrained into a realistic regime in radial distances, that is, only radial distances within $[0.3, 1.0]$ are presently accepted. Solutions are further constrained by the requirement that the triangle mesh be mathematically well defined during the minimization.

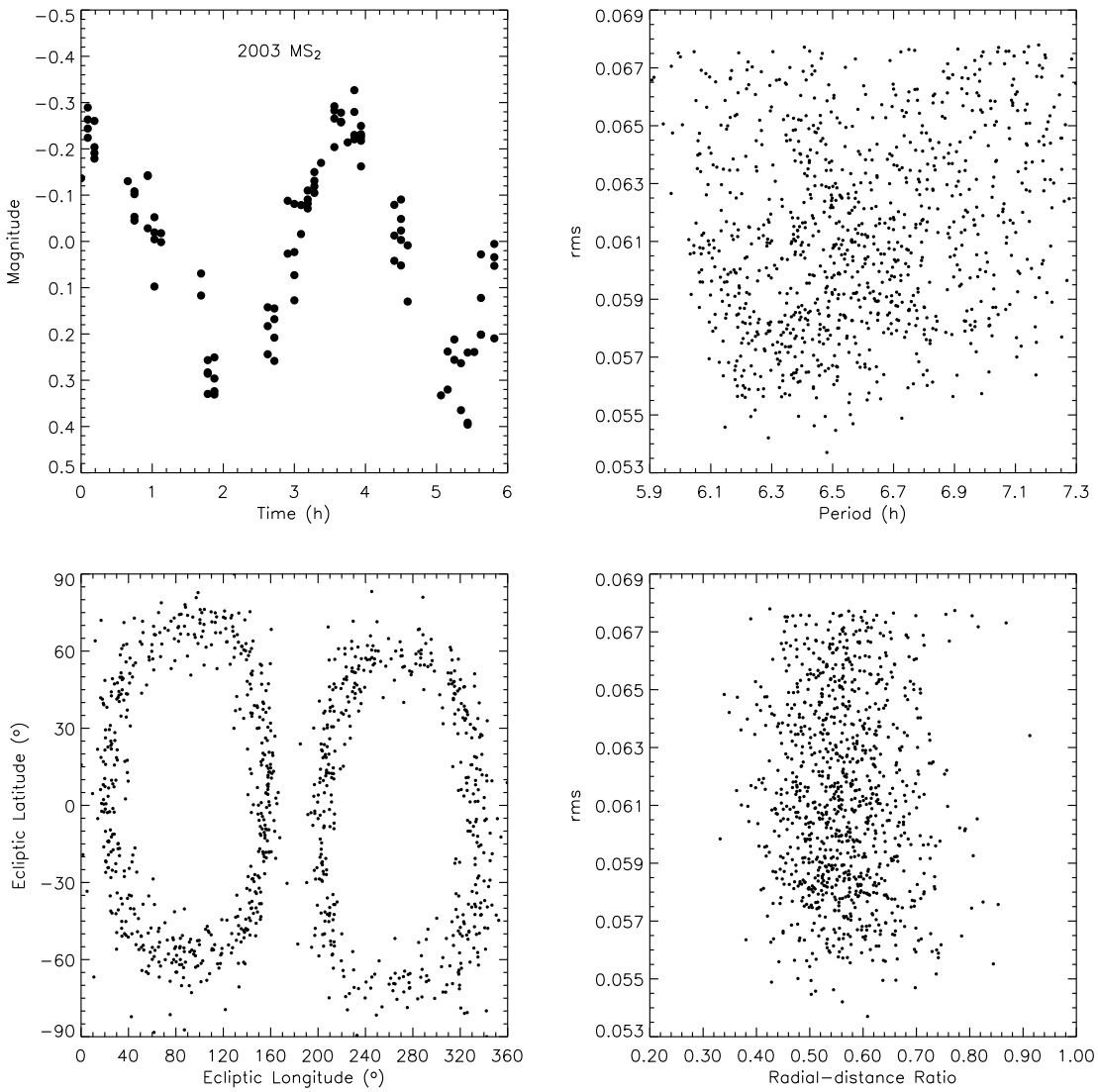

Figure 1: The original lightcurve observations (top left), rotational periods vs. rms (top right), pole longitudes vs. latitudes (bottom left), and ratios of minimum and maximum nodal radial distances vs. rms (bottom right) for the near-Earth object 2003 MS_2 as obtained by simplex inversion.

3 Results and discussion

We have applied the simplex inversion methods to the limited lightcurve observations of the near-Earth objects 2003 MS_2 and (1981) Midas, and to the extensive observations of (1580) Betulia. In all cases, we have succeeded in obtaining realistic spin and convex shape solutions within reasonable computing times.

In Fig. 1, we depict a distribution of 1000 sample solutions for 2003 MS_2 based on the single lightcurve observed at the Nordic Optical Telescope (NOT) [5]. The inverse problem entails the derivation of three spin parameters and 42 shape parameters, the Cartesian coordinates of the 14 nodes in the discretized shape (there are 24 triangular facets involved). The low-resolution characterization of the shape is justified by the limited data and the success of the inverse method in yielding acceptable fits to the data (at best, the rms difference is 0.054). Simplex inversion indicates forbidden regions in the pole orientation and a ratio of minimum-to-maximum nodal radial distances within $0.55 \pm 0.0.15$.

Figure 2 shows four sample shapes for (1981) Midas based on altogether eight lightcurves [8, 7, 5] spanning 18 years with three differing illumination and observation geometries. Using 54 shape parameters (32 triangles), the rms values of the sample solutions varied from 0.048 (top left) to 0.055 (bottom right). For (1580) Betulia, using the same number of parameters, we have obtained tentative solutions with rms values of 0.05-0.06.

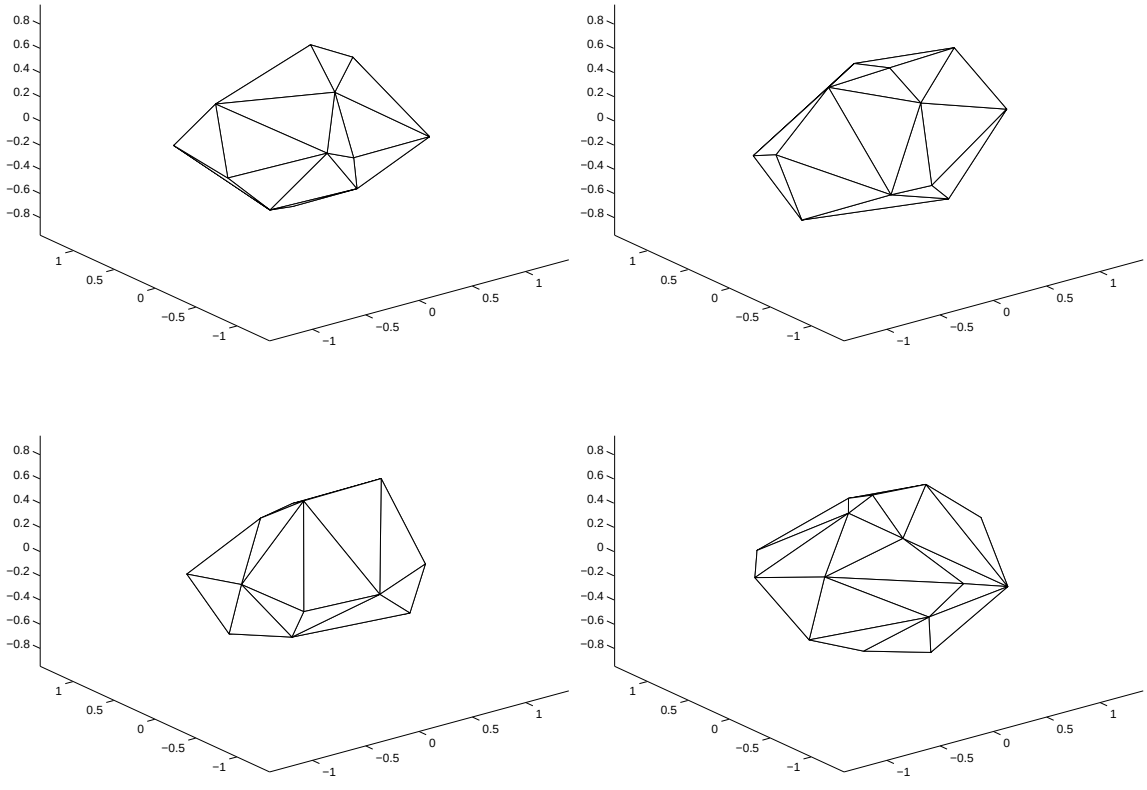

Figure 2: Four sample shapes for the near-Earth object (1981) Midas as derived by simplex inversion.

4 Conclusions

We have developed simplex inversion methods for deriving asteroid spins, shapes, and scattering properties from photometric lightcurve observations using general convex shapes. With the help of the novel methods, we have successfully assessed both limited and extensive lightcurve observations of three near-Earth objects. In the future, we will compare the simplex and conventional inversion methods, and plan to apply the methods to the forecoming sparse photometric observations by the ESA Gaia mission (launch in 2011).

Acknowledgments

We thank the Nordic Optical Telescope (NOT). Most of the data utilized have been obtained using ALFOSC, which is owned by the Instituto de Astrofisica de Andalucia (IAA) and operated at the Nordic Optical Telescope under agreement between IAA and the Astronomical Observatory of Copenhagen. Research supported, in part, by the Academy of Finland.

References

[1] M. Kaasalainen, J. Torppa, and K. Muinonen, "Optimization methods for asteroid lightcurve inversion. II. The complete inverse problem," *Icarus* **153**, 37-51 (2001)

[2] J. Torppa, M. Kaasalainen, T. Michalowski, T. Kwiatkowski, A. Kryszczynska, P. Denchev, and R. Kowalski, "Shapes and rotational properties of thirty asteroids from photometric data," *Icarus* **164**, 346-383 (2003)

[3] K. Muinonen, J. Piironen, Yu. G. Shkuratov, A. Ovcharenko, and B. E. Clark, "Asteroid photometric and polarimetric phase effects," in: *Asteroids III* (W. Bottke, R. P. Binzel, A. Cellino, P. Paolicchi, Eds., University of Arizona Press, Tucson, Arizona, U.S.A.), 123-138 (2002)

[4] H. Parviainen, and K. Muinonen, "Rough-surface shadowing for self-affine random rough surfaces," *JQSRT*, in press (2007)

[5] K. Muinonen, J. Torppa, J. Virtanen, J. Näränen, J. Niemelä, M. Granvik, T. Laakso, H. Parviainen, K. Aksnes, Z. Dai, C.-I. Lagerkvist, H. Rickman, O. Karlsson, G. Hahn, R. Michelsen, T. Grav, P. Pravec, and U. G. Jørgensen, "Spins, shapes, and orbits for near-Earth objects by Nordic NEON," in *Proceedings of IAU Symposium No 236, Near-Earth Objects, our Celestial Neighbors: Opportunity and Risk* (A. Milani, G. Valsecchi, and D. Vokrouhlicky, eds.), in press, 12 pp (2007)

[6] W. H. Press, B. P. Flannery, S. A. Teukolsky, and W. T. Vetterling, *Numerical Recipes, The Art of Scientific Computing, Second Edition* (Cambridge University Press, Cambridge, Massachusetts) (1994)

[7] S. Mottola, G. de Angelis, M. di Martino, A. Erikson, G. Hahn, and G. Neukum, "The near-Earth objects follow-up program: First results," *Icarus* **117**, 62-70 (1995)

[8] W. Z. Wisniewski, T. M. Michalowski, A. W. Harris, and R. S. McMillan, "Photometric observations of 125 asteroids," *Icarus* **126**, 395-449 (1997)

The scattering matrix of large Libyan desert particles

Olga Muñoz[1], Hester Volten[2], Joop Hovenier[3], Timo Nousiainen[4], Karri Muinonen[5], Daniel Guirado[1], Fernando Moreno [1], and Rens Waters.[3]

[1] *Instituto de Astrofísica de Andalucía (CSIC), Granada, Spain. olga@iaa.es*
[2] *RIVM - National Institute of Public Health and the Environment, Bilthoven, Netherlands*
[3] *Astronomical Institute "Anton Pannekoek", University of Amsterdam,Netherlands.*
[4] *Department of Physical Sciences, University of Helsinki, Finland,*
[5] *Observatory, University of Helsinki, Finland*

Abstract

We measured the complete scattering matrix as a function of the scattering angle of a Sahara dust sample which was collected from the upper part of a dune in Libya (hereafter Libyan dust sample). This sample mainly consists of large particles since small particles were blown up by the wind. Measurements were done at a wavelength of 632.8 nm in the angle range 4-174 degrees. The Libyan dust sample has $r_{\rm eff}$ = 124.75 μm and $v_{\rm eff}$ = 0.15. Therefore, it is an interesting test case for the Ray Optics Approximation (ROA) that provides accurate results for particles with curvature radii much larger than the wavelength. In addition to the ROA we investigate whether a ray-optics method employing Gaussian random shapes [1] can reproduce the experimental scattering matrix for the Libyan dust sample. Moreover, we use a modified ROA model that takes the small-scale surface roughness and internal inhomogeneities of the particles into account using heuristic ad hoc schemes [2]. Model particle shapes used in the simulations are based on a statistical shape analysis of our sample.

1 Libyan dust particles

Desert dust particles have irregularly round shapes with small-scale surface roughness. Examples of images of particles of our Libyan dust sample taken with a Field Emission Scanning Electron Microscope (FESEM) and an optical microscope are shown in Fig. 1, panels (a) and (b), respectively. A statistical shape model called the Gaussian random sphere geometry [1, 3] was adapted to characterize the shape of the particles in the sample. The shape analysis was performed exactly as in [4] for quasi-spherical ice crystals.

The normalized projected-surface-area distribution, $S(logr)$ was measured using a Fritsch laser particle sizer [5] that employs a diffraction method without making any assumptions about the refractive indices of the particles. The measured $S(logr)$ was transformed into a normalized number distribution as a function of r, $n(r)$. From the retrieved number distribution we obtained the values of the effective radius, $r_{\rm eff}$=124.75 μm, and effective variance, $v_{\rm eff}$=0.15 [6]. For modeling purposes we fitted a trimodal lognormal number distribution to the retrieved normalized number distribution, $n(r)$, of our sample as $n(r) = \sum_{i=1}^{3} n_i(r)$, with

$$n_i(r) = \frac{f_i}{\sqrt{2\pi} ln(10) log(\sigma_i) r} exp\left\{ -\frac{[log(r) - log(R_i)]^2}{2 log(\sigma_i)^2} \right\}, \quad (1)$$

where f_i is a dimensionless parameter, σ_i the geometric standard deviation, and R_i the geometric mean radius. In Fig. 2 we present the retrieved normalized number distribution together with the best-fit trimodal lognormal number distribution.

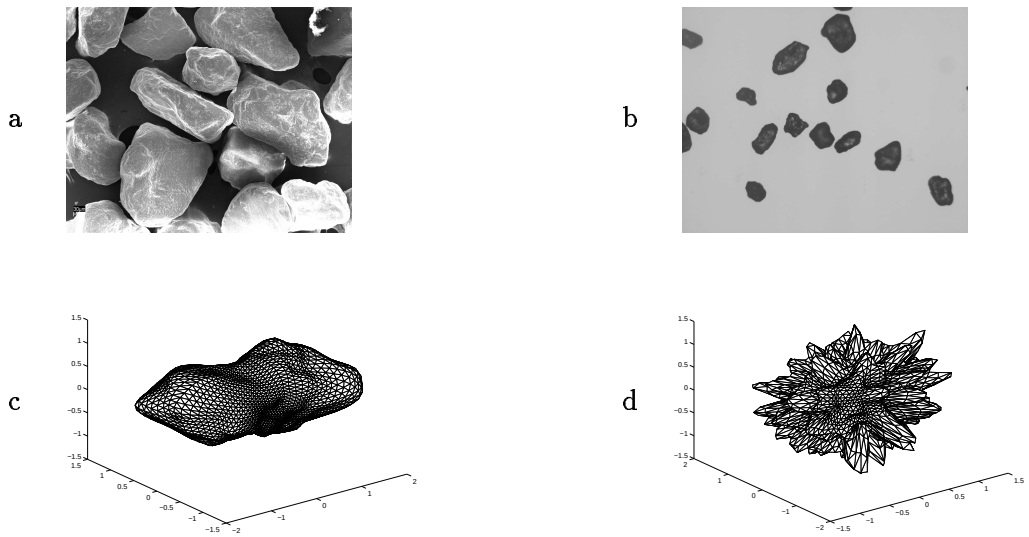

Figure 1: FESEM (a), and optical microscope images (b) of the Libyan dust sample. Panels (c) and (d) present images of a realistic and a unrealistic spiky model particle, respectively.

2 Results and discussion

In Fig. 3 we present the measured scattering matrix elements, $F_{i,j}$, as a function of the scattering angle for the Libyan dust sample at 632.8 nm. The measurements were performed with the Amsterdam light scattering facility [7]. F_{11} is normalized to unity at 30 degrees. The measured scattering matrix follow the general trends presented by irregular mineral particles (see e.g. [8]).

The measured results for the Libyan dust sample were used to investigate whether the Ray Optics Approximation, ROA, can reproduce its scattering matrix as a function of the scattering angle. Firstly, we analyzed our experimental results with the traditional ROA method by varying the real and imaginary parts of the refractive index. As mentioned, model particle shapes were based on a shape analysis of the particles. Fig. 1, panel (c) presents an image of our retrieved model particle. We could not obtain simultaneous good fits for all scattering matrix elements by systematically changing the value of the real and imaginary parts of the refractive index for realistic shapes (dashed gray lines, Fig. 3). Encouraged by the success obtained in previous simulations [8, 2], we tried to improve our fits by enhancing the surface roughness of the particles i.e. the spikiness of our model particles (Fig. 1, panel (d)). The assumption of these unrealistically spiky particles improved the fits especially for $F_{11}(\theta)$ and $F_{22}(\theta)/F_{11}(\theta)$ (solid gray lines, Fig. 3). Apparently, spikiness can actually mimic diffuse surface scattering.

Secondly, we studied the effects of including Lambertian surface elements to simulate diffuse surface scattering and internal Lambertian screens to incorporate the effect of internal inhomogeneity. The ROA simulation with the best-fit Lambertian parameters improved the agreement with the measurements for $F_{11}(\theta)$, $F_{22}(\theta)/F_{11}(\theta)$, and $F_{34}(\theta)/F_{11}(\theta)$ (dashed black lines, Fig. 3). The improvement required, however, the decrease of the value of the imaginary part of the refractive index k to $4{\cdot}10^{-5}$ from the first-guess value $4{\cdot}10^{-4}$. In any case even by including the Lambertian schemes, we could not get reasonably good fits for all elements of the scattering matrix as functions of the scattering angle. Further, we tried to improve the fits to the experimental data by assuming unrealistic spiky particles with the inclusion of Lambertian schemes. The increase of the spikiness (Fig. 1, panel (d)), produces better fits for almost all elements of the scattering matrix (solid black lines, Fig. 3).

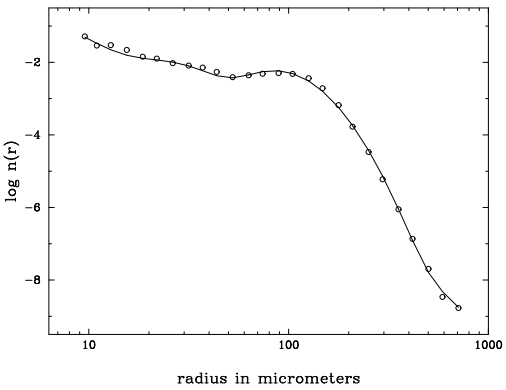

Figure 2: Fitted trimodal log-normal size distribution (solid line) and the normalized number distribution, $n(r)$ (circles), as deduced from the normalized projected-surface-area distribution. The fit resulted in the following parameters: f_1=200.63, f_2=0.24, f_3=0.45; σ_1=4.5, σ_2=1.5, and σ_3=1.4; R_1=9.0 10^{-2}, R_2=28.8, and R_3=96.5 (μm). Number distributions for radii below about 10 micron were found to be below detection limits.

Nousiainen et al. [2] obtained good agreement with the measurements on another Sahara dust sample already included in the *Amsterdam Light Scattering Database,* by assuming realistic shapes when the Lambertian schemes were applied. In that case, the r_{eff} and v_{eff} were equal to 8.2 μm and 4.0, respectively. Due to computational limitations, the size distribution had to be truncated so that particles smaller than 2 μm were not taken into account. Still, there was a relatively high contribution to the scattering by small particles. Apparently, the contribution of those small particles could mimic the scattering effects of the small-scale surface roughness. Another possibility could be that the surface roughness characteristics of the former Sahara dust sample are different from those of the Libyan dust sample. All our results clearly show that the single-scattering properties of the Libyan dust particles cannot be accurately modeled without accounting for the effects of surface roughness. Further, our study shows that to do that properly we need something different from the Lambertian elements. A more detailed account of the measurements and model calculations will be published [9].

References

[1] Muinonen, K., T. Nousiainen, P. Fast, K. Lumme, and J.I. Peltoniemi, Light scattering by Gaussian random particles: Ray Optics approximation, *J. Quant. Spectrosc. Radiat. Transfer, 55,* 577-601, 1996.

[2] Nousiainen, T., K. Muinonen, and P. Räisänen, Scattering of light by large Saharan dust particles in a modified ray optics approximation, *J. Geophys. Res., 108,* D1, 405, dor:10.1029/2001JD001277, 2003.

[3] Muinonen, K., Light scattering by stochastically shaped particles, in *Electromagnetic and Light Scattering by Nonspherical Particles,* edited by M.I. Mishchenko, J.W. Hovenier, and L.D. Travis, pp. 323-352, Academic, San Diego, Calif., 2000.

[4] Nousiainen, T., and MacFarquhar G.M., Light Scattering by Quasi-Spherical Ice Crystals, *J. Atmosph. Sc., 61,* Issue 18, 2229-2248, 2004.

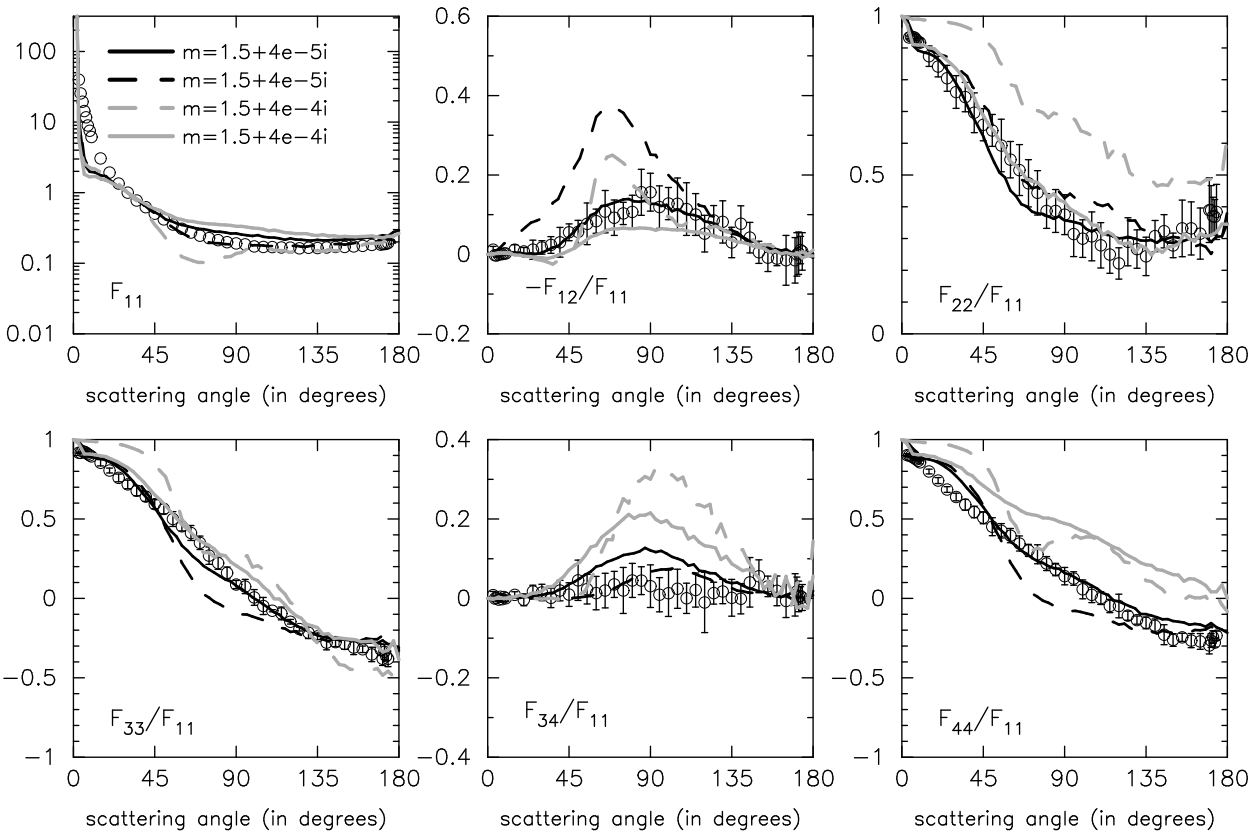

Figure 3: Measured scattering matrix elements as functions of the scattering angle at 632.8 nm for the Libyan sand sample (circles). The measurements are presented together with the best-fit cases. Dashed an solid gray lines correspond to traditional ROA calculations for realistic and unrealistic shapes of the particles, respectively. Dashed and solid black lines correspond to ROA calculations including Lambertian elements for realistic and unrealistic shapes of the particles, respectively.

[5] Konert, M. and Vandenberghe, J., Comparison of laser grain size analysis with pippette and sieve analysis: a solution for the underestimation of the clay fraction. Sedimentology 44, 532-535, 1997.

[6] Hansen, J. E., and L. D. Travis, Light scattering in planetary atmospheres, *Space Sci. Rev., 16,* 527-610, 1974.

[7] Hovenier, J. W., H. Volten, O. Muñoz, W.J. van der Zande, and L.B.F.M. Waters, Laboratory studies of scattering matrices for randomly oriented particles: potentials, problems, and perspectives, *J. Quant. Spectrosc. Radiat. Transfer, 79-80,* 741-755, 2003.

[8] Volten, H., O. Muñoz, E. Rol, J. F. de Haan, W. Vassen, J. W. Hovenier, K. Muinonen and T. Nousiainen, Scattering matrices of mineral aerosol particles at 441.6 nm and 632.8 nm, *J. Geophys. Res., 106,* 17375-17401, 2001.

[9] Muñoz, O., H. Volten, J.W. Hovenier, T. Nousiainen, K. Muinonen, D. Guirado, F. Moreno, and L.B.F.M. Waters, Scattering matrix of large Saharan dust particles: experiments and computations, *J. Geophys. Res.,* in press.

Soft X-ray spectroscopy at small to medium phase angles: Theoretical and empirical studies

Jyri Näränen[1], Hannu Parviainen[1], Kim Nygård[2], and Karri Muinonen[1]

[1]*Observatory, P.O. Box 14, FI-00014 University of Helsinki, Finland*
[2]*Department of Physical Sciences, P.O. Box 64, FI-00014, University of Helsinki, Finland*
e-mail: naranen@astro.helsinki.fi

Abstract

A study of phase-angle, particle-size, and packing-density-related phenomena affecting soft X-ray spectroscopy of atmosphereless planetary bodies is presented. Both numerical modelling and laboratory measurements are included in the study. The surface properties, such as particle size and illumination geometry are found to have an effect for the total emission from the surface observed and on the measured fluorescent characteristic elemental ratios.

1 Introduction

Soft X-ray spectroscopy is a tool that has been used in planetary research since the Apollo 15 lunar mission [1]. It is used for providing global maps of elements such as silicon, iron, and calcium, which have characteristic fluorescent emission lines in the soft X-ray energy region (~0.5-10 keV, i.e., wavelengths of 2.5-0.12 nm). These maps are then used to deduce the rock types and even mineralogy of the surface, with the help of instruments from other wavelengths. The standard practice is to normalize the elemental abundances in the spectrum to some characteristic emission line, e.g., Si Kα.

The fluorescent emission from atmosphereless planetary surfaces is induced mainly by solar emission which, although highly variable in soft X-rays, is weak compared to visible wavelengths. Therefore, soft X-ray spectroscopy is useful only for inner solar-system bodies, i.e., Mercury, the Moon, and near-Earth objects (NEOs).

Spacecraft-based X-ray spectroscopy is limited to small phase angles (the angle between the light source and observer as seen from the surface), i.e., close to the backward direction. The most noticeable phenomena in soft X-rays take place close to the forward direction, e.g., Bragg scattering and by anomalous diffraction. Therefore, the backward direction has been left relatively unstudied.

Historically, the detectors used aboard the planetary missions for measuring the X-ray spectrum have been quite limited in both spectral and spatial resolution. However, with the advent of the next-generation space-based imaging X-ray spectrometers, such as MIXS aboard the ESA mission to Mercury BepiColombo (launch due in 2013), the resolution will improve dramatically imposing new challenges on the data analysis. One of these challenges is the fact that the instruments will begin to observe the surface elements with well defined illumination geometries. As is well known in the visible wavelengths, surface properties such as regolith grain size (distribution), packing density, as well as illumination geometry etc. affect scattering from the medium.

In the soft X-ray wavelengths, the situation is complicated due to the high energy (short wavelength) of the radiation, introducing a new realm of physics compared to visible wavelengths. The physical interactions occur mostly between photons and single atoms in the regolith. Therefore, the bulk elemental composition of the material plays an important role.

Some work has been carried out to understand the particle-size and phase-angle-related phenomena in soft X-ray spectroscopy (e.g., [2], [6]), but more detailed analyses are needed to allow a correct use of future high-spatial-resolution soft X-ray spectrometers in planetary science.

2 Theoretical modelling

We have developed a Monte Carlo ray-tracing code for modelling X-ray scattering and fluorescence phenomena in atmosphereless planetary regoliths[4] [7]. The current model assumes a medium consisting of spherical particles, a good assumption considering the very short wavelengths, with fixed particle size and packing densities. The code computes the first-order fluorescence from the particles induced by incident radiation. We use a simulated solar X-flare spectrum as input spectrum to allow realistic simulated spectra. At the moment, the code allows two different elements in the same medium with arbitrary elemental ratios.

Our theoretical work and the first results were introduced in Näränen et al.[4]. They reported a strong dependence of the fluorescent radiation on the particle size, smaller particles producing more fluorescence, as well as a smaller dependence on the phase angle. An opposition effect was also seen to arise due to shadowing. An interesting result for planetary research is also that elemental ratios seemed to change as a function of the viewing geometry. All of the simulations were performed with the illumination source fixed in the direction of the normal of the surface.

Scattering, which produces most of the background signal in soft X-ray spectroscopy, has not yet been included in the simulation. It will soon be implemented, as it is required for the correct evaluation of the fluorescent lines. Secondary fluorescence (characteristic emission is allowed to induce fluorescence at lower energies), realistic particle size distribution, and capability to produce spectra instead of integrated output will also be addressed.

We exclude particle processes such as particle-induced X-ray emission (PIXE) from our modelling, at least at this phase, to limit the amount of free parameters in the simulations. For comparing the theoretical results with those from the laboratory measurements (see next section) this is a valid assumption. However, for analysing the data from planetary missions, also the particle processes need to be included.

3 Laboratory experiments

To complement the theoretical work, we started laboratory experiments in multiangular soft X-ray spectroscopy in March 2007. The experimental setup used was originally built for the scientific ground calibration of ESA SMART-1 lunar mission X-ray Solar Monitor (XSM)[3]. It consists of a cylindrical vacuum chamber (63 cm in diameter, 30 cm tall), inside of which all the measurements are performed, and a titanium light source (0.5 mA and 10 kV for the initial measurements). Near vacuum (4 mbar) is necessary, as soft X-rays are readily absorbed in air. The X-rays are directed inside the vacuum chamber through a collimator tube which has two apertures and an aluminium window. The experimental setup is illustrated in Figure 1.

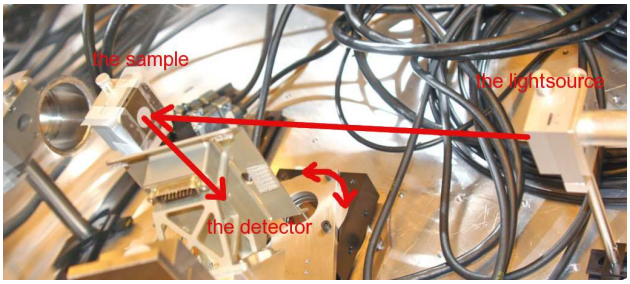

Figure 1: The experimental setup used for the initial measurements. The distance between the light source and the sample is 33 cm and the distance between the sample and the detector varied between 12.8 and 18 cm. The detector can be rotated remotely along the rotation axis indicated.

The first measurements that are reported here were performed on two samples of the same material but different grain size distributions ($< 75\mu$m an $75 - 250\mu$m). The sample material was basalt with olivine,

which is considered to be a good spectral lunar highlands analogue material in the visible wavelengths. We have studied the sample materials previously in the visible wavelengths for, e.g., effects of extremes of packing density and surface roughness on the opposition effect [5]. Due to the present experimental setup restrictions, the samples had to be compressed into pellets with a packing density of 0.6±0.05. We measured the samples at four different phase angles; 16.6, 22.8, 30.2, and 38.8 degrees. For the first measurements, we limited the studies to nadir illumination geometries. In order to gain acceptable photon statistics, we measured each angle for more than 5 hours. The only measureable characteristic fluorescent lines in the samples were iron and calcium Kα lines (Fig. 2).

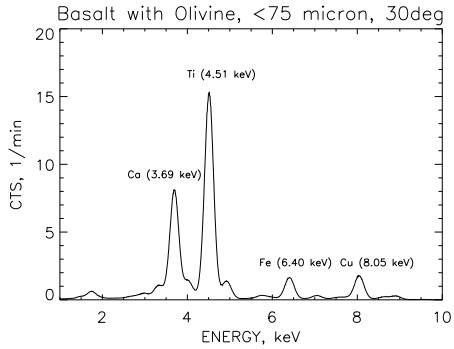

Figure 2: Spectrum measured for olivine-rich basalt sample (< 75μm) at phase angle of 30 degrees. The titanium line is produced by the light source and the copper line by the sample holder.

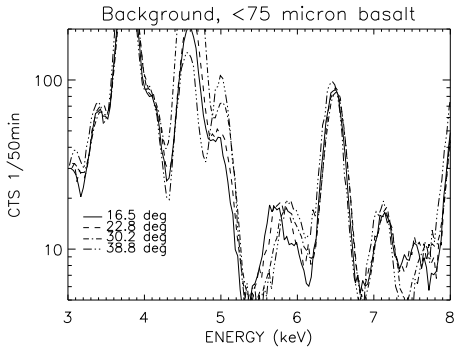

Figure 3: The scattering background of the < 75μm sample at different phase angles. There are systematic phase-angle dependent scattering phenomena. Note also the dependence of fluorescence on the phase angle.

The data were analyzed using custom-written IDL programs. The spectral lines were modeled with Gaussian functions and the maximum values of the functions were taken as data points. The effective area of the detector as a function of off-axis angle and energy was corrected for.

During 2007, we aim to continue the measurements with significant improvements in the experimental setup, including moving the sample to the center of the detector field of view.

4 Results

We report new theoretical results, including nadir-pointing simulations (observing direction normal to the surface) and results of changing the mixing ratio of elements in the medium. Even a small addition of iron in calcium-rich medium can cause a noticeable increase in the observed characteristic X-ray flux as illustrated in Fig. 5.

The initial results from the laboratory measurements are also reported. A significant increase in observed iron abundance relative to calcium is observed as a function of phase angle (Fig. 4). The results are qualitatively similar to those reported by Okada[6]. The results, if confirmed in more detailed studies, can have profound implications for the analysis of high spatial resolution soft X-ray planetary spectra.

Assessing the particle-size effect in the laboratory requires a more careful analysis and calibration of the data (as it deals with absolute values) than studying the relative intensities of elements.

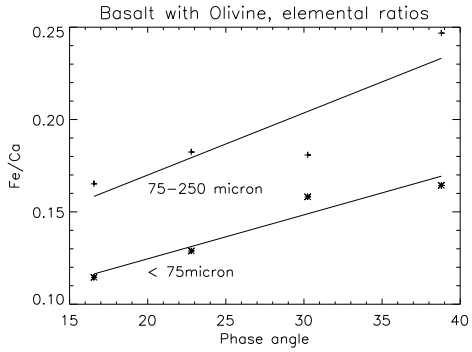

Figure 4: Measured elemental ratios of the two samples as a function of phase angle. The line represents the best linear least-squares fit to the data.

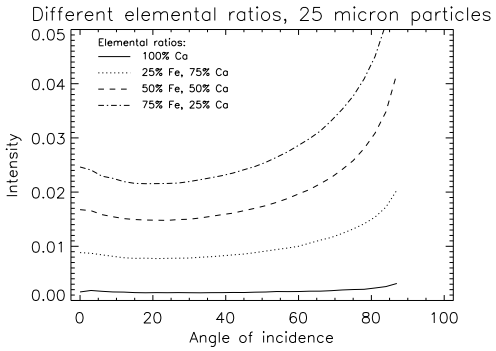

Figure 5: Total fluorescent emission from media with varying elemental ratios. Iron dominates the total output flux which can be at least partly explained by the fact that iron has over twice the fluorescent yield of calcium.

5 Conclusions

Our results show that in order to obtain accurate information from planetary soft X-ray spectroscopy, viewing-geometry-relatedphenomen need to be understood and taken into account. Particle size, packing density, and phase-angle-related phenomena in the spectrum create basis for solving the direct problem, i.e., of how to best calibrate the effects out of the data. But, in addition, they can also be used as input for the inverse problem (with data from other wavelengths as well) of actually gaining geometrical information of the surface. Our theoretical modelling and laboratory experiments are part of that endeavour that is just beginning.

6 Acknowledgements

We would like to thank Juhani Huovelin and Lauri Alha for helpful discussions on X-ray instrumentation, and for providing us with the simulated solar spectrum model. This work has been partly funded by the Academy-of-Finland grant 210607.

References

[1] I. Adler, J. Trombka, J. Gerard, P. Lowman, R. Schmadebeck, H. Blodget, E. Eller, L. Yin, R. Lamothe, P. Gorenstein, and P. Bjorkholm, Apollo 15 geochemical X-ray fluorescence experiment: Preliminary report Science 175 (1972) 436-440.

[2] W. A. Hockings, Particle- and grain-size measuremnt by X-ray fluorescence, Powder Technol. 3 (1969) 29-40

[3] J. Huovelin, L. Alha, H. Andersson, T. Andersson, R. Browning, D. Drummond, B. Foing., M. Grande, K. Hämäläinen, J. Laukkanen, and 10 co-authors, The SMART-1 X-ray solar monitor (XSM): calibrations for D-CIXS and independent coronal science, P&SS 50 (2002) 1345-1353

[4] J. Näränen, H. Parviainen, and K. Muinonen, X-ray fluorescence modelling for Solar-System regoliths: Effects of viewing geometry, particle size, and surface roughness, Proceedings of IAU Symposium 236, Cambridge University Press, in press

[5] J. Näränen, S. Kaasalainen, J. Peltoniemi, S. Heikkilä, M. Granvik, and V. Saarinen, Laboratory photometry of planetary regolith analogs. II. Surface roughness and extremes of packing density, A&A 426 (2004) 1103-1109

[6] T. Okada, Particle size effect in X-ray fluorescence at a large phase angle: Importance of elemental analysis of asteroid Eros(433), 35th Lunar and Planetary Science Conference (2004) 1927

[7] H. Parviainen & K. Muinonen, Rough-surface shadowing of self-affine random rough surfaces, JQSRT in press

Impact of particle shape on composition dependence of scattering

Timo Nousiainen

University of Helsinki, Department of Physical Sciences, P.O. Box 64 (Gustaf Hällströminkatu 2), FI-00014 University of Helsinki, Finland
tel: +358 (9) 191-51064, fax: +358 (9) 191-50860, e-mail: timo.nousiainen@helsinki.fi

Abstract

The impact of particle shape on how scattering depends on the refractive index m is studied. The goal is to find out whether spherical model particles provide an accurate estimate for the m-dependence of scattering by nonspherical particles. The results indicate that this is very unlikely especially when small m intervals are considered.

1 Introduction

The assumption of spherical shape is still widely used in many applications where the single-scattering properties of nonspherical particles are involved. For example, all climate models presently use aerosol optics based on spherical aerosol particles. Kahnert et al.[1] show that this is likely to be a major error source in climate simulations.

The same spherical-particle approximation (SPA) is also used when estimating the impact of other error sources connected to aerosol particles, such as their uncertain refractive index m. The m-uncertainty has been considered the single most important source of error in assessing the direct climate forcing effect of dust aerosols[2]. This conclusion has been reached by use of the SPA, yet it is altogether unclear how well spherical model particles can represent the m-dependence of scattering by nonspherical particles. The shapes of dust particles vary, and it seems plausible to expect a shape distribution to smooth out different dependencies, implying that the SPA might over-estimate the m-dependence. The purpose of the present study is to assess the m-dependence of nonspherical particles and the ability of the SPA to estimate it.

2 Modeling aspects

To address the issue, the m-dependence of scattering was computed for a variety of spheroids, including spheres. Scattering simulations were carried out using the T-matrix implementation of the exact Extended Boundary Condition Method by Mishchenko[3].

The computations were performed for four different size parameters, 17 different shapes, and 14 different refractive indices (seven different values for both the real and the imaginary part of the refractive index, one being fixed when the other was varied). The values used are given in Table 1. The size parameter $x = kr$, where k is the wavenumber

Table 1: Parameters defining the properties of model particles used in the simulations.

Parameter	Values
x	1, 5, 10, 20
Re(m)	1.45, 1.50, 1.55, 1.60, 1.65, 1.70, 1.75
Im(m)	0.0001, 0.0002, 0.0005, 0.001, 0.002, 0.005, 0.01
ϵ	1.0, 1.2, 1.4, 1.6, 1.8, 2.0, 2.2, 2.4, 2.6

in vacuo, was based here on the surface-equivalent radius r; control runs with volume-equivalent radius in selected test cases showed that the results of the investigation are not significantly affected by the choice of size equivalence. The spheroid shapes were defined using the aspect ratio ϵ, which is the ratio of major-to-minor axis. The same ϵ were used for both oblate and prolate spheroids. A narrow, uniform size distribution within $\pm 1\%$ of the speficied size was used to damp interference effects.

3 Results

The analysis described here is limited to the asymmetry parameter g, which is an important parameter for radiative fluxes and sensitive to particle shape.

The results showed that the m-dependence of g varies for different spheroids. For many spheroids it was actually stronger than for spheres, so it was not obvious that the dependence would be weaker for a shape distribution of spheroids than for the corresponding spheres. To address that, two different shape distributions were used for shape averaging, an equiprobable and a weighed shape distribution. In the former, all different spheroids were added together by weighing only by their corresponding scattering cross sections. The latter is the '$n = 3$' shape distribution introduced in [4], which gives much more weight to strongly elongated spheroids, and appears to mimic single-scattering properties of an ensemble of irregularly shaped particles quite well.

Figure 1 shows the results obtained regarding the dependence on the imaginary part of the refractive index, Im(m). It is seen that for $x \leq 5$, g depends on Im(m) similarly in each case. For $x \geq 10$, both distributions of spheroids are more sensitive to Im(m) than the sphere is. In each case, g is a monotonic function of Im(m).

Figure 2 illustrates the dependence of g on the real part of the refractive index, Re(m). Again, for $x \leq 5$, the dependence is simple and monotonous, but now it is spheres that show higher sensitivity (quite extreme at $x = 5$, actually). For larger x the dependencies become more complicated; neither spheres nor spheroids show monotonic dependence. At $x = 10$, the dependence for the weighed spheroid distribution seems to have the opposite sign to that for spheres or the equiprobable shape distribution of spheroids. At $x = 20$ both spheroid distributions have only a weak g-dependence on Re(m), g decreasing with increasing Re(m), while g for spheres is a non-monotonous and quite varying function of Re(m).

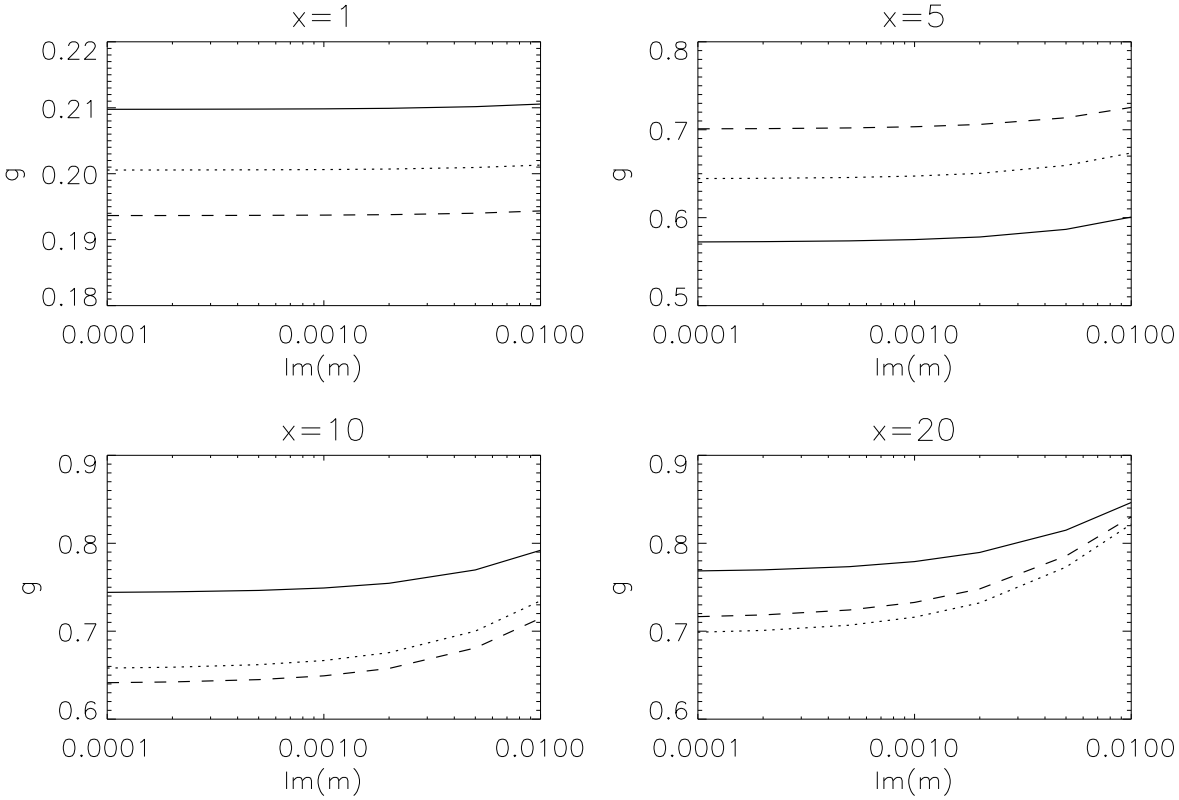

Figure 1: Dependence of the asymmetry parameter g on the imaginary part of the refractive index, Im(m), for spheres (solid line), equiprobable shape distribution (dotted line), and weighed shape distribution (dashed line).

4 Conclusions

The results show that, somewhat surprisingly, the dependence of the asymmetry parameter g on the refractive index m is not necessarily stronger for spheres than for a shape distribution of spheroids. Spheroids appear to be more sensitive to changes in Im(m) than spheres are, whereas for Re(m) the opposite tend to be true. Moreover, the dependence of g on m seems to depend much on the size parameter x.

However, the m-dependence of g is much more consistent and conservative for spheroids than for spheres. This is especially true for the dependence on Re(m) at large x, where g for spheres can change very fast as a function of Re(m). Thus, for example, if one uses spheres to estimate how much an uncertainty in m affects the impact of nonspherical particles on radiative fluxes, the result obtained may even have the wrong sign. Of course, in most practical applications one need to consider dependencies over a size distribution, which is likely to improve the performance of spheres to some degree.

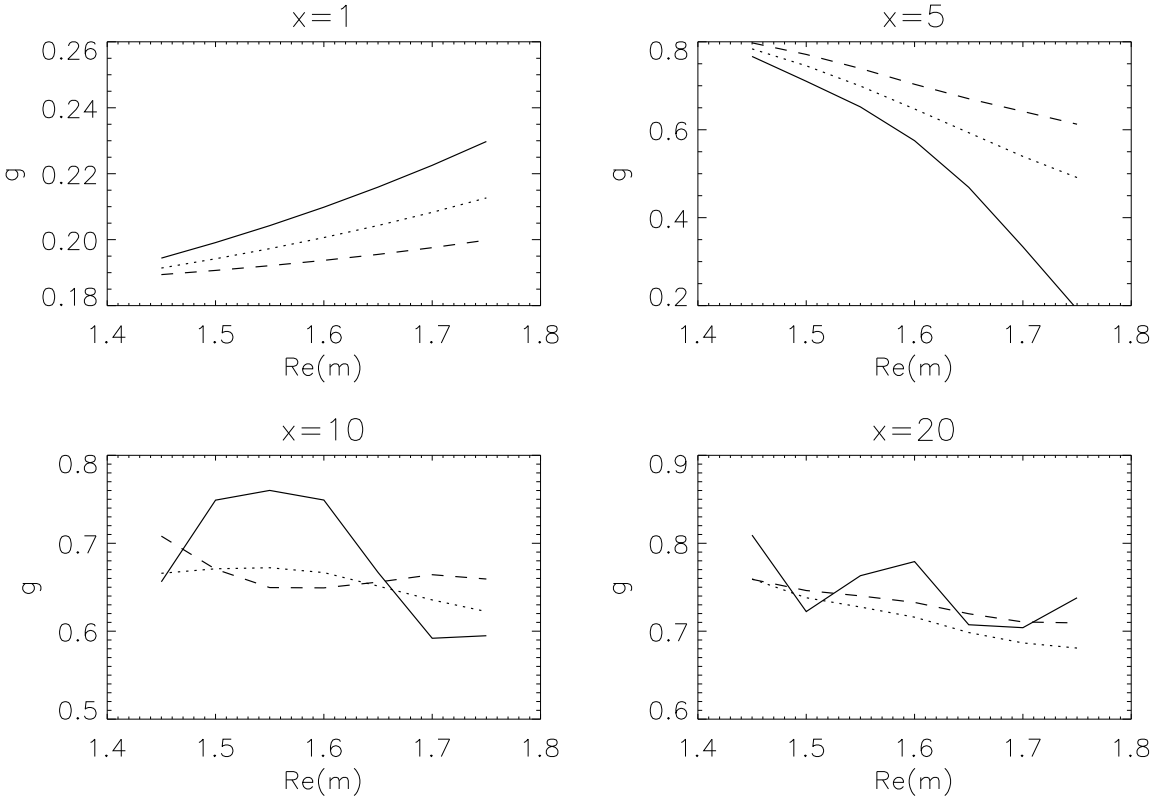

Figure 2: Same as Fig. 1 but for the real part of the refractive index, Re(m).

References

[1] M. Kahnert, T. Nousiainen, P. Räisänen, Mie simulations as an error source in mineral aerosol radiative forcing calculations, Quart. J. Roy. Meteor. Soc. 133, (in press).

[2] G. Myhre, F. Stordal, Global sensitivity experiments of the radiative forcing due to mineral aerosols, J. Geophys. Res. 106 (2001) 18193–18204.

[3] M. I. Mishchenko, L. D. Travis, Capabilities and limitations of a current Fortran implementation of the T-matrix method for randomly oriented rotationally symmetric scatterers, J. Quant. Spectrosc. Radiat. Transfer 60 (1998) 309–324.

[4] T. Nousiainen, M. Kahnert, B. Veihelmann, Light scattering modeling of small feldspar aerosol particles using polyhedral prisms and spheroids, J. Quant. Spectrosc. Radiat. Transfer 101 (2006) 471–487.

Reduction of iterations for the linear equation solutions in DDA

- application for the orientation averaging of irregularly shaped particles -

Yasuhiko Okada,[1] Tadashi Mukai,[1] Ingrid Mann,[1]
Sano Itaru,[2] and Sonoyo Mukai[2]

[1] *Graduate School of Science, Kobe University*
1-1 Rokkodai, Nada Kobe 657-8501 Japan
[2] *Faculty of Science and Technology, Kinki University,*
3-4-1 Kowakae, Higashi-Osaka, 577-8502, Japan
tel: +81 (78) 803-6566, fax: +81 (78) 803-6483, e-mail: yasokada@gmail.com

Abstract

We introduce the method to shorten the number of iterations required in the linear equation solutions of DDA. In the linear equation solution in DDA, the solution is iteratively solved. We give the initial guess, which is close to the actual solution infered from parameters close to the selected one. We apply the method for the orientation averaging of scattering properties of non-symmetric particles. The method reduces the number of iterations into less than 10% for non-symmetric particles with moderate shape variations against the direction of incident light when the interval of the grid angles is set as 5 degree. On the other hand, non-symmetric particles with high shape variations against the direction of incident lights shows iteration ratio of less than 25%.

1 Introduction

Discrete Dipole Approximation (DDA) is a powerful tool to treat light scattering problems of irregularly shaped particles [1]. In the DDA calculations, the shape is described with a number of dipoles, then the multiple interactions of the incident light between the dipoles are solved. Compared with other methods, DDA has the advantage in treating shape with dipoles making the calculation possible for irregularly shaped particles without any symmetry. On the other hand, the disadvantage of DDA is that the linear equations are required to be solved for every variations in the parameter of the particle (e.g. size, shape, refractive index, etc.) and for the direction of incident lights.

In order to apply the calculation of DDA into the remote sensing, such as retrieval of atmospheric aerosol properties, cometary dust, and dust on the surface of Asteroids, reduction of the DDA calculations for parameter variations of the particles are indispensable. In this study, we apply the method to reduce the iterations in the DDA calculation for the variations in the particle orientation.

2 Reduction of the iterations

In the DDA calculation, the polarizability of all the dipoles are solved based on the iterative method (e.g. Conjugate Gradient Method) [1]. In the iterative method, the initial value of the dipole polarizability (hereafter as initial guess) is set arbitrarily (e.g. CMPLX(0.0, 0.0)) since the solution of the linear equations (i.e. dipole polarizability) is not known at the beginning of the iteration.

Muinonen and Zubko (2006) proposed the method to give the initial guess by extrapolating from the results of similar size or of similar refractive index to the selected parameter of the particle. This is because, small variations in the size or in the refractive index are considered to have only small influence in the polarizability of dipoles. Then the calculated initial guess is close to the solution of the selected

parameter resulting in the reduction of iterations. In their study, extrapolation are used to calculate the initial guess of the polarizability for size variations or for variations in refractive indices.

In this study, we apply the same method for the orientation averaging of scattering properties. For the orientation variations, the interpolation of the initial guess is always possible by using values in both sides of the selected orientation. Since the interpolation is considered more accurate than extrapolation, the proposed method has more advantage in the proximity of the initial guess to the solution. We use spline interpolation [3] to calculate the initial guess of the selected orientation from the results of orientations close to the selected one.

We define the orientations, with which the interpolation is conducted, as "grid angles". Before the calculation with the proposed method, the dipole polarizabilities for grid angles are calculated with the DDA method and are stored into the files. Then, the calculation with the proposed method is performed after interpolating initial guess from the stored polarizabilities of grid angles close to the selected orientation.

We define "iteration ratio" as the ratio between the number of iterations in proposed method and those in original calculation to investigate the efficiency of the method applied for orientation variation. We use public domain DDA code "DDSCAT6.1" developed by Dr. Draine and his colleague [1].

3 Efficiencies and Accuracies

As non-symmetric particles, we use "Gaussian Sphere (hereafter as GSP)" and "Overlapping mixture of multiple tetrahedra (hereafter as OMMT)" as shown in Fig.1. The former is produced to have moderate surface roughness with the selected parameters of Gaussian Sphere while the latter shape has high surface roughness causing high orientation dependence of the shape against the direction of incident light. The GSP described originally with a number of triangular facets [4] are converted into the shape described with dipoles following Muinonen et al. (in Press) [5]. OMMT is created by using the tetrahedra composed of dipoles, which is produced with "calltarget" program in DDSCAT6.1 [1], then, by sequentially adding randomly rotated tetrahedra into the particle.

In the DDSCAT6.1, the angle of the particles against the direction of incident light is configured with *beta*, *theta* and *phi* [1]. In this study, we arbitrarily set theta=20.0 and phi=15.0, then rotate the particles in the direction of beta from 0 to 360 degree.

In this study, we set grid angles as 5 degree. Therefore the precalculation of dipoles for 73 grid angles are required. After calculating for 73 grid angles, we performed the calculation with the proposed method with interpolation. The interpolation for orientations is conducted by using 8 grid angles close to the selected angle. The "8" is arbitrarily chosen in this study. We investigate for the particle size parameter for the equivolume sphere as 7.0. The refractive index is selected as m=1.60 + 0.01i.

Fig.2 shows the iteration ratio for GSP and for OMMT. The iteration ratios are less than 10% for GSP and less than 25% for OMMT. This iteration ratio depends on the interval of grid angles, which is set as 5 degree in this study. We also investigate the iteration ratio for GSP and OMMT with the grid angle interval of 10 degree. The result (not shown here) is that the iteration ratio is increased for the central angle between grid angles, while for the orientations close to the grid angles, the iteration ratio become small similar to those shown in Fig. 2.

In order to investigate the accuracies of calculated scattering properties, we have compared scattering properties calculated 1) with original DDASCAT and 2) those with the proposed method for the angles *beta* from 0 to 360 degree with the step of 0.5 degree. Fig.3 shows the example of the comparison of absorption (*Qabs*) and scattering properties (*Qsca*) of the OMMT for the variation of the *beta* angles. Fig.4 shows the comparison for the scattering function S11 and polarization -S12 / S11 where *beta*=113.5 for OMMT. The errors (i.e. $|Q_{original} - Q_{proposed}| / Q_{original} * 100$ [%]) caused by the proposed method are less than 0.013%, 0.08%, 0.09%, 5.58% for Qabs, Qsca, S11, -S12 / S11, respectively. The errors of S11 and -S12 / S11 for different *beta* angles are also in the same order.

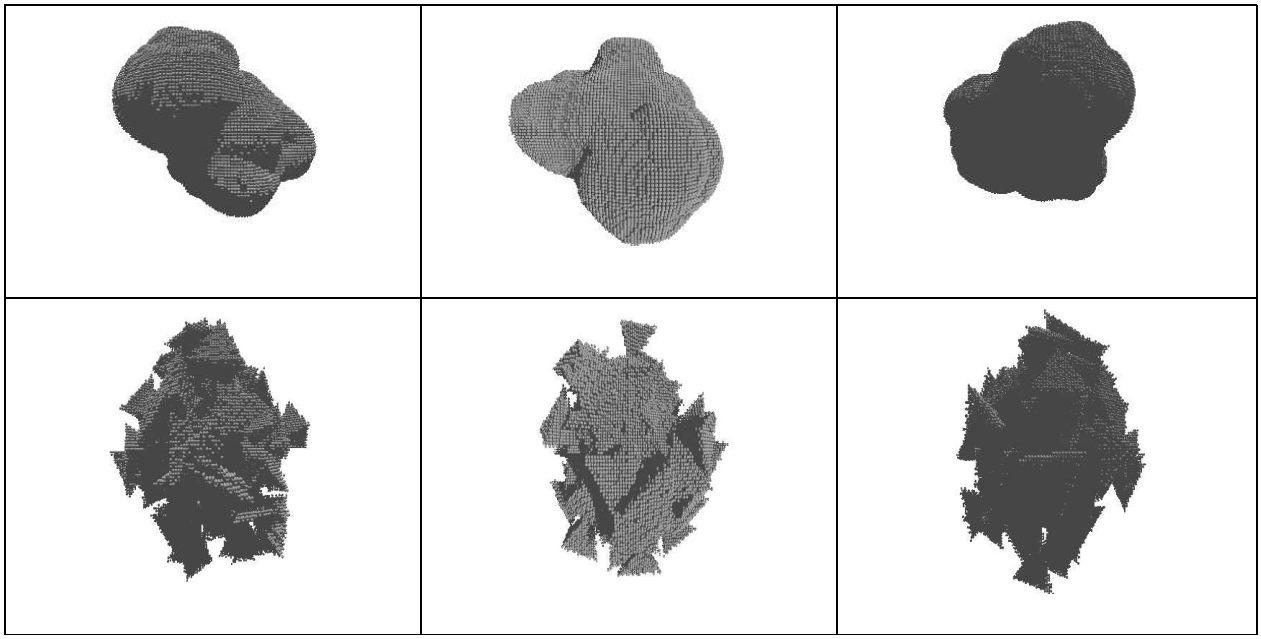

Figure 1: Shapes of the particles composed of a number of dipoles shown in XY (left), YZ (middle), and XZ plane (right). Gaussian sphere (upper panel) and overlapping mixture of multiple tetrahedra (lower panel) are considered.

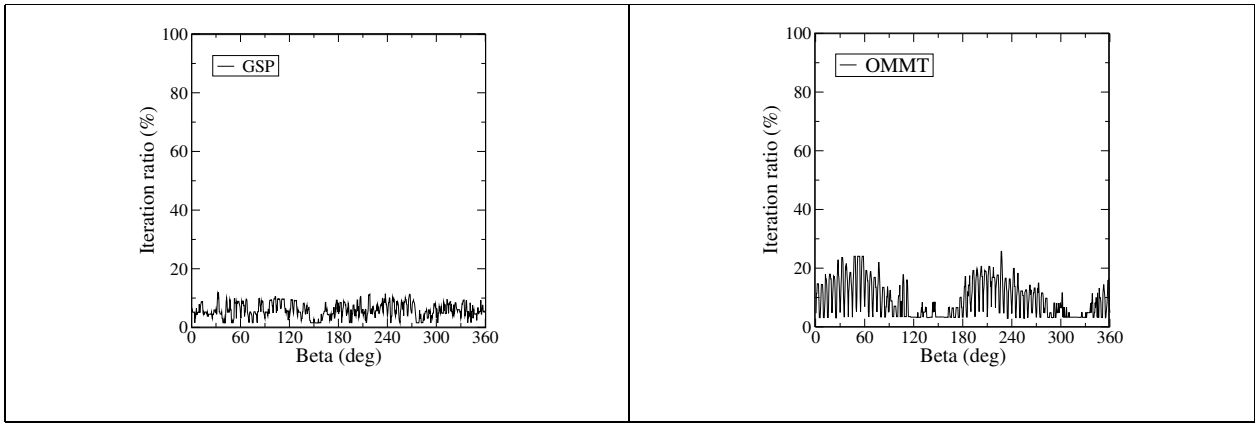

Figure 2: The iteration ratio for GSP and OMMT where the interval of grid angles is 5 degree.

4 Summary

The reduction method of the iterations in the linear equations are applied for the orientation variations of irregularly shaped particles. Non-symmetric particles with moderate orientation dependence of the shape (i.e. Gaussian Sphere) have gained large advantage with the iteration ratio of less than 10%. While, non-symmetric particles with large orientation dependence of the shape (i.e. OMMT) has also gained advantage with iteration ratio of less than 25%. We have known that the iteration ratio becomes larger for larger intervals of grid angles at central angles between grid angles. We are now trying to devise efficient division of orientation angles to reduce total number of iterations in DDA calculations in order to conduct DDA calculation efficiently for the 3D orientation averaging.

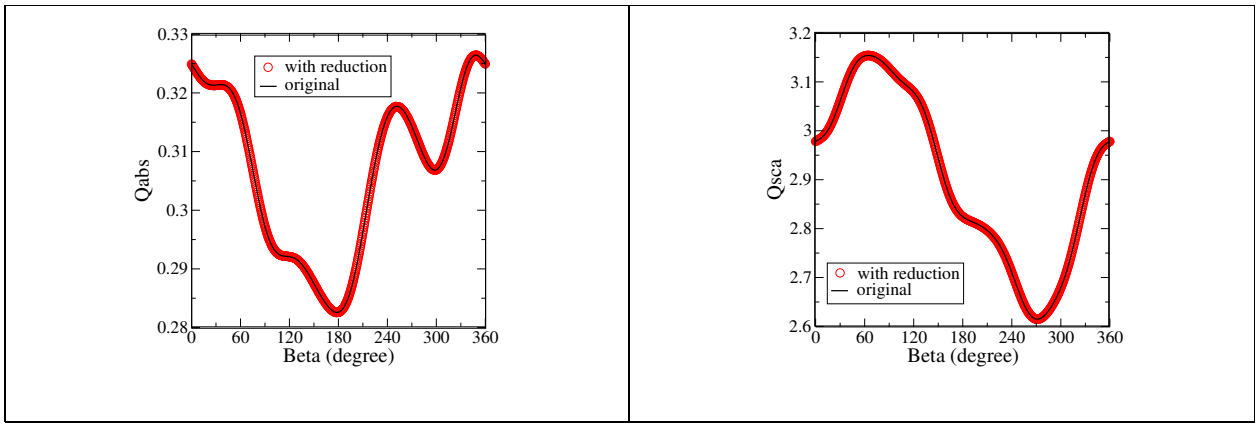

Figure 3: The comparison of Qabs and Qsca of OMMT for the original and the proposed method

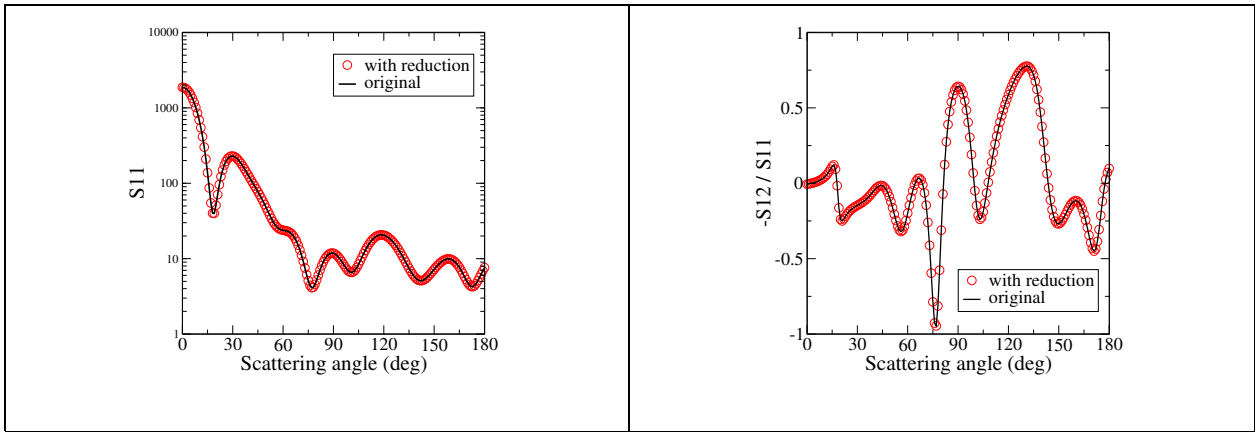

Figure 4: The comparison of S11, and -S12 / S11 of OMMT where *beta*=113.5.

Acknowledgments

Some of the data analysis were performed on the general common use computer system at the Astronomical Data Analysis Center (ADAC) of the National Astronomical Observatory of Japan. DDSCAT6.1 is provided from http://www.astro.princeton.edu/~draine/. This research is supported by “The 21st Century COE Program of Origin and Evolution of Planetary Systems” of the Ministry of Education, Culture, Sports and Technology (MEXT).

References

[1] Draine BT, and Flatau PJ. 2004, "User Guide to the Discrete Dipole Approximation Code DDSCAT 6.1", http://arxiv.org/abs/astro-ph/0409262v2.

[2] Muinonen K, Zubko E, Optimizing the discrete-dipole approximation for sequences of scatterers with identical shapes but differing sizes or refractive indices, JQSRT, 2006;100:288-294.

[3] S.A. Teukolsky, W.T. Vetterling, B.P. Flannery, W.H. Press, Numerical Recipes in Fortran 77: The Art of Scientific Computing (Cambridge University Press, 1992)

[4] Muinonen K, Nousiainen T, Fast P, Lumme K, Peltoniemi JI. Light scattering by Gaussian random particles: ray optics approximation. JQSRT 1996;55:577-601.

[5] Muinonen K, Zubko E, Tyynela J, Shkuratov Yu-G, Vidden G, Light scattering by Gaussian random particles with discrete dipole approximation, JQSRT (in Press)

Aerosol optical properties assessed by an inversion method using the solar principal plane for non-spherical particles

F. J. Olmo[1,2], A. Quirantes[1], H. Lyamani[1,2] and L. Alados-Arboledas[1,2]

[1]*Dpto. Física Aplicada, Universidad de Granada, Fuentenueva s/n, 18071-Granada, Spain.*
[2]*Centro Andaluz de Medio Ambiente (CEAMA), Avda. del Mediterráneo s/n, 18071, Granada, Spain.*
Tel: +34-958-240023, fax: +34-958-243214, e-mail: fjolmo@ugr.es

Abstract

Adequate modeling of light scattering by nonspherical particles is one of the major difficulties in remote sensing of atmospheric aerosols, mainly in desert dust events. In this paper we test a parameterization of the particle shape in size distribution, single scattering albedo, phase function and asymmetry parameter retrieval from direct and sky-radiance measurements, based on the model skyrad.pack taking into account the principal plane measurements configuration. The method is applied under different Saharan dust outbreaks. We compare the results with those obtained by the almucantar measurements configuration. The results obtained by both methodologies agree and make possible to extend the parameter retrieval to different zenith angles.

1 Introduction

Modeling the impact of mineral dust aerosols on radiative net flux is of particular interest in climate research, because mineral dust aerosols can have a strong direct climate forcing effect. Thus, this is especially relevant in southern Europe and in some Atlantic islands [1]. North African dust is injected into the atmosphere through resuspension processes at the source areas, and it is then transported at different altitudes (from sea level up to 4-6 km), being the maximum dust transport in summer when large quantities of dust are carried across the Mediterranean basin to Europe and the Middle East and across the Atlantic ocean to the Caribbean, the southeastern United States, and the midlatitude western North Atlantic. In winter, there is also considerable transport when large quantities of dust are carried toward South America and sporadically to Western Europe. As example, in 2001 was recorded 77 days with African episode at the Iberian Peninsula [1].

The satellite sensors provide a global coverage, but the retrieval algorithms to determine atmospheric aerosol characteristics used need validation so they can be tested and improved. In the last decades, there have been continuous efforts to establish inversion algorithms for determining the columnar aerosol optical properties of suspended aerosol polydispersions from ground measurements of solar extinction and almucantar sky radiance, taking into account spherical or spheroid particles approximation (i.e. [2-5]). The columnar aerosol properties of interest are: size distribution, phase function, asymmetry parameter, single scattering albedo and refraction index. Nevertheless it would be convenient to include nonsphericity features for improving the retrieval qualities in particular for large dust particles. Scattering phase function, including scattering angles larger than 90º, are important because this angular range of scattering determines the aerosol effect on climate and is used for remote sensing. Aerosol scattering at large angles 100º-140º is affected by the particle shape. The results show that the use of spheres causes considerably larger sky radiance errors for mineral particles than the use of spheroids, and the effect is particularly pronounced at Top of Atmosphere (TOA), which is most relevant for satellite remote sensing computations. Thus, different authors have shown that in presence of mineral particles the modeled phase function of spheres strongly deviates from that of non-spherical particles. Simulations based on spherical model particles were found to give TOA spectral radiance results with an error range that is larger by a factor of 4 than those results obtained with spheroidal shape distributions [6].

On the other hand, using the almucantar sky radiance data the authors show that the single scattering albedo can be retrieved with reasonably high accuracy only for high aerosol loading and large solar

zenith angles (i.e. [3], [7]). But the aerosol load can change along the day also due to the different local sources or meteorological conditions. To extend the columnar aerosol properties derived by inversion methods along the day, including scattering angles larger than 90^o, in this work we test a parameterization of the particle shape in size distribution, phase function, single scattering albedo and asymmetry parameter retrievals from direct and sky-radiance measurements, based on the model skyrad.pack using the principal plane approximation. The method is applied under different atmospheric conditions, including Saharan dust outbreak. We compare the results with those obtained by the well tested almucantar inversion using the spheroids particles approximation [3-5].

2 Instrumentation

For this study we use solar extinction and diffuse sky radiance measured with a CIMEL CE-318 at Granada, Spain (37.18ºN, 3.58ºW and 680 m a.m.s.l.). The instrument is part of AERONET network [8]. This instrument obtains solar transmissions, aureole and sky radiances observations through a large range of scattering angles from the Sun through a constant aerosol profile. The solar transmission measurements are performed at 340, 380, 440, 500, 670, 870, 940 and 1020 nm to retrieve the aerosol optical depth, and the sky radiance measurements are carried out at 440, 670, 870 and 1020 nm by means of almucantar and principal plane observations. Together with the AERONET calibration procedures, Langley plots at high location in Sierra Nevada Range (2200 m msl) have been made to determinate the spectral extraterrestrial voltage for this instrument. The aerosol optical depth was derived from the total optical depth subtracting the Rayleigh, O_3 and NO_2 contributions. The total uncertainty in aerosol optical depth and sky radiance measurements are $\leq \pm 0.01$ and $\leq \pm 5\%$, respectively [8].

3 Methods

The retrieved information from sky radiance at large scattering angles requires accurate correction for the effects of multiple scattering and for the contribution of light reflected from the Earth's surface and scattered downward in the atmosphere. Nakajima et al. [2] developed and applied an inversion scheme that includes accurate radiative transfer modeling to account for multiple scattering (Skyrad.pack code). The method use specified wavelengths, selected outside the gas absorption bands, in order to reduce the radiative transfer problem to a pure scattering problem. The inversion procedure uses the normalized sky radiance (almucantar and principal plane configuration) and the aerosol optical depth measured by means of a method that requires absolute calibration. The connection between the optical measurements and the aerosol features occurs through the radiative transfer equation in a multiple-scattering scheme for a one-layer plane-parallel atmosphere. The code is developed originally for spherical particles and Olmo et al. [5] was adapted the methodology including a shape mixtures of randomly oriented spheroids using the almucantar measurement configuration. In this paper, we also modified this method including the same parameterization of the particle shape to calculate the efficiency factor for extinction and the phase function using the principal plane measurement configuration. All scattering angles in the range measured, which depend on the measurement time, were used to retrieve the aerosol volume radius distribution in the radius interval 0.06-10 μm.

The EBCM, or T-matrix [9], theory has been used to calculate light scattering calculations for nonspherical matrices (kernel matrices) instead of previously used Mie simulations by Nakajima. Both incident and scattered electric fields can be expanded in vector spherical wave functions. Incident and scattered expansion field coefficients can be related by means of a transition (T) matrix, whose elements depend on the particle's size, shape and orientation. In the case of randomly oriented, axially symmetric particles, the T-matrix is calculated for the so-called natural reference frame (z axis along the particle symmetry axis) and results are then averaged for all particle orientations. T-matrix sizes have been chosen so that phase matrix elements are calculated with an accuracy of 10^{-3}; cross sections are accurate to within one part in 10^4 [10]. Accordingly, we defined in code the aerosol single-scattering properties as functions of the volume size distribution of randomly oriented polydisperse spheroids, and we have computed the kernel matrices for randomly oriented prolate and oblate

spheroids, using equiprobable distributions, following the recommendations of Dubovik et al [3].

For the complex refractive index we have selected for each experimental case a unique value independent of wavelength. The selected value is the one that minimize the residuals between the measured and the simulated radiances. We assumed a Lambertian surface with a constant albedo in the wavelength range. The procedure allows the retrieval of particle size distributions, the complex refractive index, the single scattering albedo, the phase function and the asymmetry parameter.

4 Results

In order to verify how representative are the retrieval improvements of the method using the principal plane configuration we processed several measurements data (extinction and sky radiance –almucantar and principal plane-) collected at Granada in different atmospheric conditions. Figure 1 shows the comparison of the aerosol size distributions retrieved using the two spheroids scattering models in a day influenced by desert dust. We can appreciate the good agreement for the range of radius where the codes are applicable. Figure 2 shows the codes comparison for the columnar single scattering albedo (670nm) for July 31 (2006), also influenced by a Saharan dust outbreak. In addition, this day is influenced by the local pollution due to the traffic emissions that affect the aerosol absorption proper-

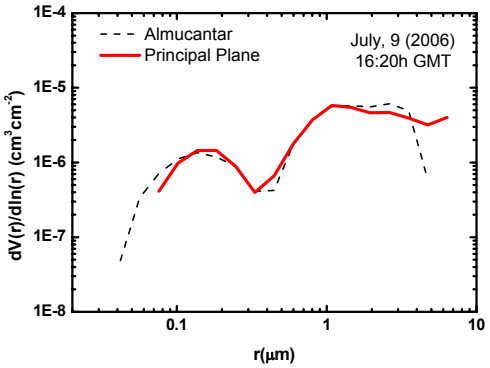

Fig. 1.- Aerosol size distribution at Granada in a day with Saharan dust influence.

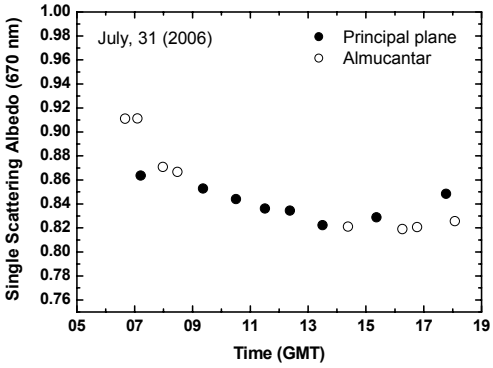

Fig. 2.- Single scattering albedo evolution at Granada in a day with Saharan dust influence.

ties decreasing the single scattering albedo along the day. Figures 3 shows the asymmetry parameter evolution (670nm) derived by the two methods for July 31 (2006). Both results display that the columnar aerosol properties derived by the principal plane inversion agree with the almucantar inver-

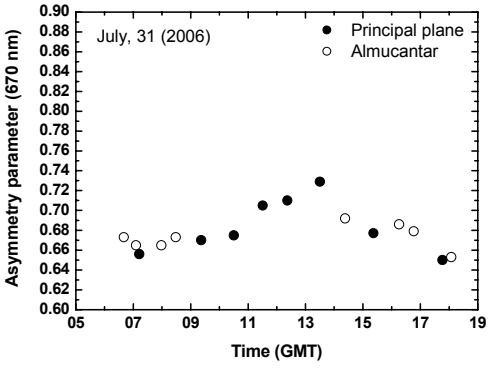

Fig. 3.- Asymmetry parameter evolution at Granada in a day with Saharan dust influence.

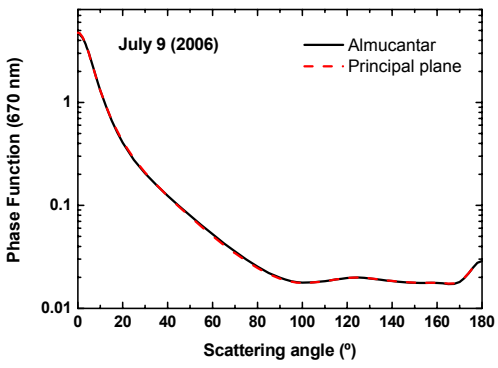

Fig. 4.- Aerosol phase function at Granada in a day influenced by desert dust.

sion using the spheroids approximation. Figure 4 shows the comparison of the phase function (670nm) also derived by the two methods for measurements close in time. As we can observe, the result for the phase function also agrees from sky-radiance aureole and for scattering angles higher than 90^o.

5 Conclusions

We have modified the skyrad.pack code to take into account the non-sphericity of the aerosol particles as polydisperse, randomly oriented spheroids (equiprobable distributions of oblate and prolate), to retrieve the columnar aerosol optical properties from measurements of extinction and sky atmospheric radiances –almucantar and principal plane- at Granada (Spain). The aerosol size distributions, single scattering albedo, asymmetry parameter and phase function obtained by the two methods have been compared for different atmospheric conditions (Saharan dust influence). The results of the two methods agree well, showing the feasibility of extending the retrieval of atmospheric aerosol optical properties along the day, not only for large solar zenith angles. Nevertheless, this study is only a first attempt to explore the columnar aerosol optical properties with this method. We also plan to explore the parameters taking into account different particle aspect-ratio and computing more accurate spheroids kernel matrices.

Acknowledgement

This work was supported by La Dirección General de Ciencia y Tecnología from the Education and Research Spanish Ministry through Projects CGL2004-05984-C07-03 and FIS2005-06860-C02-01, and by Andalusian Regional Government through Project P06-RNM-01503. Also, we thank Professor Nakajima for the software code SKYRAD.PACK.

References

[1] M. Escudero et al., “Wet and dry African dust episodes over eastern Spain”, J. Geophys. Res., 110, D18S08, doi: 10.1029/2004JD004731 (2005).

[2] T. Nakajima, G. Tonna, R. Rao, P. Boi, Y.J. Kaufman, B.N. Holben, “Use of sky brightness measurements from ground for remote sensing of particulate polydispersions”, App. Opt., **35**, 15, 2672-2686 (1996).

[3] O. Dubovik, B.N. Holben, T. Lapyonok, A. Sinyuk, M.I. Mishchenko, P. Yang, I. Slutsker, “Non-spherical aerosol retrieval method employing light scattering by spheroids”, Geophys. Res. Lett., **29**, N10, 10.1029/2001GL014506 (2002).

[4] O. Dubovik et al., “Application of spheroid models to account for aerosol particle nonsphericity in remote sensing of desert dust”, J. Geophys. Res., 111, D11208, doi: 10.1029/2005JD006619 (2006).

[5] F.J. Olmo, A. Quirantes, A. Alcántara, H. Lyamani, L. Alados-Arboledas, “Preliminary results of a non-spherical aerosol method for the retrieval of the atmospheric aerosol optical properties”, J. Quant. Spectr. Radiat. Transfer, 100, 305-314 (2006).

[6] M. Kahnert, T. Nousiainen, B. Veihelmann, “Spherical and spheroidal model particles as an error source in aerosol climate forcing and radiance computations : A case study for feldespar aerosols”, J. Geophys. Res., 110, D18S13, doi: 10.1029/2004JD005558 (2005).

[7] D.H. Kim et al., “Aerosol optical properties over east Asia determined from ground-based sky radiation measurement”, J. Geophys. Res., 109, D02209 (2004).

[8] B.N. Holben, T.F. Eck, I. Slutsker et al., “AERONET-A federated instrument network and data archive for aerosol characterization”. Rem. Sens. Environ., **66**, 1-16 (1998).

[9] M.I. Mishchenko, “Light scattering by randomly oriented axially symmetric particles”, J. Opt. Soc. Am. A **8**, 871-882 (1991); Errata **9**, 497 (1992)

[10] M.I. Mishchenko, “Light scattering by size-shape distributions of randomly oriented axially symmetric particles of a size comparable to a wavelength”, Appl .Opt. **32**, 4652-4666 (1993)

Light Scattering from Rough Thin Films: DDA Simulations

Hannu Parviainen and Kari Lumme

Observatory, P.O. box 14, FIN-00014, University of Helsinki, Finland
e-mail: hannu@astro.helsinki.fi

Abstract

Light scattering properties of rough thin circular films of constant thickness are studied using the discrete-dipole approximation. Effects on the intensity distribution of the scattered light due to different statistical roughness models, model dependant roughness parameter, and uncorrelated small-scale porosity of the inhomogeneous media are investigated. The effects due to inhomogeneity of the scattering media are compared with the analytic approximation by Maxwell Garnett and the results are found to agree well with the theory.

1 Introduction

The latest advances in computing power and numerical methods—such as the distribution of the geometry to different computing nodes as in the ADDA-code [1]—has allowed the DDA simulations of objects with ever extending sizes. We are approaching the range where we can study the wave-optic effects due to the rough boundaries between extended media of different physical properties (i.e. rough-surface scattering), together with the volume effects from the internal structure of the scattering media. This study considers computationally light rough-surface analogs, deformed thin circular films, which allow us to study the wave-optics effects due to surface roughness, and to investigate the volume scattering effects to some extent.

Rough Thin Films The film geometry is represented as a thin circular slab of constant thickness t along the z-axis. The deformation along the z-axis is modeled by a two-dimensional homogeneous isotropic random field $h(x, y)$ [2]. The distribution of heigths follows Gaussian statistics, and is defined by the standard deviation σ. The generation of the geometry realizations is based on the spectral synthesis method [3].

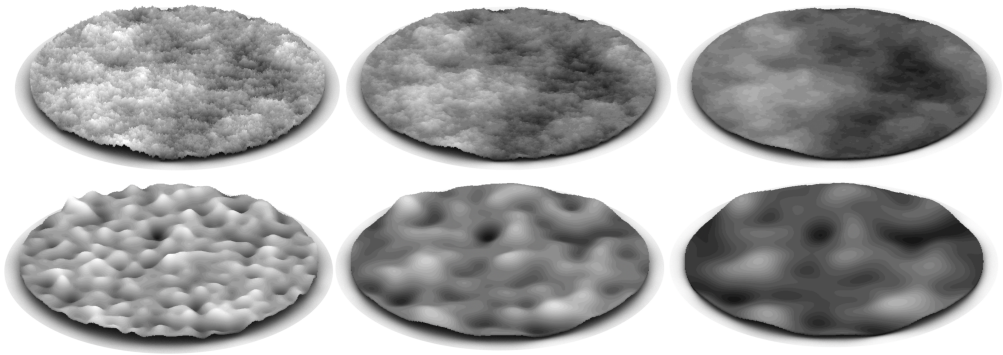

Figure 1: In the upper row we show the fBm model, in the lower the Gc model. Horizontal roughness parameter changes from left to right as $H = 0.25,\ 0.5,\ 0.9$ and $\frac{l}{L} = 0.215,\ 0.5,\ 0.75$.

As in [4], two different types of roughness models were chosen for the study: fractional Brownian motion (fBm) and Gaussian correlation (Gc). The two models are shown in Fig. 1. Gc-surfaces show roughness features of a certain scale, determined by the correlation length l, while the fBm-surfaces are of self-affine nature showing roughness features in all scales, distribution determined by the Hurst exponent H. For brevity, both l and H are denoted in the following text by a horizontal roughness parameter τ.

2 Simulations

2.1 Numerical Methods

Simulations were carried out using a modified version of the DDSCAT-code [5] by B. Draine, and the results were verified against the ADDA-code [1]. The modifications consisted of inclusion of several F90 features into the F70-code, such as dynamical allocation of memory for more convenient working with geometries of varying sizes. The modifications were tested not to affect the simulation results.

The geometry was discretized into cells of 0.025 μm width and height. The radius of the circular film was 5.0 μm, and the thickness of the film was set to 4 cells, corresponding to 0.1 μm. This discretization scheme leads to effective radius A_{eff} of 1.12, and size parameter x of 12.64 for the value of $\lambda = 0.557\mu m$ used in the simulations. Only the effects due to the horizontal roughness parameter were studied, and the amplitude of the roughness deformations in the z-axis was considered as constant, $\frac{\sigma}{L} = 0.01$.

Geometries with packing density $\rho < 1$ were generated by randomly removing $n \times n \times n$ dipole chunks from the solid geometries. While this method lacks the elegance of using, e.g., a random field to define ρ, it allows us to study the scattering dependency of the films due to the varying size of the voids in a simple and well-determinated manner.

The Sepeli computing cluster of the Finnish IT center for science (CSC) was used to carry out the simulations. The memory usage for a single geometry was around 4-6 GB, and computation time varied from several tens of minutes to hours, depening on the packing density and the index of refraction of the scattering medium.

2.2 Simulation Sets

The main focus of the study was on the the behaviour of the scattered intensity $M_{11}(\theta_i, \phi_i, \theta_e, \phi_e)$—where (θ_i, ϕ_i) are the angles of incidence, (θ_e, ϕ_e) the angles of emergence— as a function of the horizontal roughness parameter and composition of the scattering media. The simulations were divided into five sets, each studying different aspects of the scattering problem. For each value of the studied variable, the results are averaged over 30 geometry realizations to obtain statistically meaningful results. When possible (i.e., for normal incident radition, sets 1-4), the averaging is also carried out over 20 values of ϕ_e, thus giving $M_{11}(\theta_e)$ as an average of 600 samples.

Set 1 studied the behaviour of $M_{11}(\theta_e)$ as a function of the horizontal roughness parameter and density of the medium for normal incident radiation ($\theta_i = 0$). The simulations were carried out for five values of τ ($\frac{l}{L} = [0.25,\ 0.3,\ 0.4,\ 0.5,\ 0.75]$ for the Gc model, $H = [0.25,\ 0.375,\ 0.5,\ 0.625,\ 0.9]$ for the fBm model), and three values of packing density ($\rho = [1.0,\ 0.5,\ 0.3]$) for a void size of a single dipole.

Set 2 considered the effects due to the imaginary part of the refraction index. Simulations were carried out for films with $\rho = 1.0$, $n = 1.5$, $k = [0.01i,\ 0.1i,\ 1i]$ and $H = [0.5,\ 0.625]$.

Set 3 treated the approximation of the inhomogeneous media by a homogeneous one with an average index of refraction using the Maxwell Garnett relation [7, 6]. Simulations were carried out for films with $\rho = 1.0$, $H = [0.5,\ 0.625]$, and $N = n + ik$ computed using the Maxwell Garnett relation.

Set 4 was a follow-up study for the sets 1 and 3. The behaviour of the scattered intensity was studied as a function of the size of square-shaped voids. Simulations were carried out for films with $\rho = 0.5$, $H = 0.5$, with size of the voids $n = [2,\ 4,\ 8]$ dipoles.

Set 5 was a follow-up study for the set 1. The simulations of the set 1 were carried out for $\theta_i = 15°$, and no averaging over ϕ_e was done. This was to test the consistency of the results obtained from the set 1, especially the behaviour of the specular reflectance as a function of varying ρ.

3 Results and Discussion

3.1 Results

Figures 2 and 3 sum up the primary results of the simulations. In Fig. 2 is shown the effects due to varying density, horizontal roughness parameter and different roughness model. Figure 3 illustrates the agreement of results between porous media and solid media with index of refraction computed using the relation by Maxwell Garnett, as well as the effects due to increasing void-size. The most prominent results are:

1. The Gc and the fBm models lead to rather a different distribution of the backward scattered intensity. For the fBm model, the transition from the specular reflection to diffuse is smoother than with Gc model. For both models, the specular peak smoothens when the mean scale of the roughness increases. This agrees with the theories based on wave-optics: the directional-diffuse component of the scattered radiation starts to dominate when the scale of the roughness approaches the scale of the wavelength.

2. Approximation of the inhomogeneous media using solid geometry with the relation by Maxwell Garnett agrees with the simulations. The shape of the reflectance is not sensitive to the inhomogeneities of scale $\frac{l}{\lambda} \approx 0.05$, even for a loose geometry with $\rho = 0.3$. Decreasing density is manifested as a multiplicative factor constant over θ_e, with minor differences in the shape of the reflectance distribution.

3. While the thinness of the geometry prevents us from studying the volume scattering effects in depth, basic conclusions can be made from the behaviour of the reflectance as a function of void size. From Fig. 3b. we see that the results deviate from the effective medium approximation along with the increasing void size, but the relative deviation reduces near the specular direction. Nevertheless, more simulations for off-normal incidence and significantly increased thickness are required for a serious study of the effects due to size distribution of the inhomogeneities.

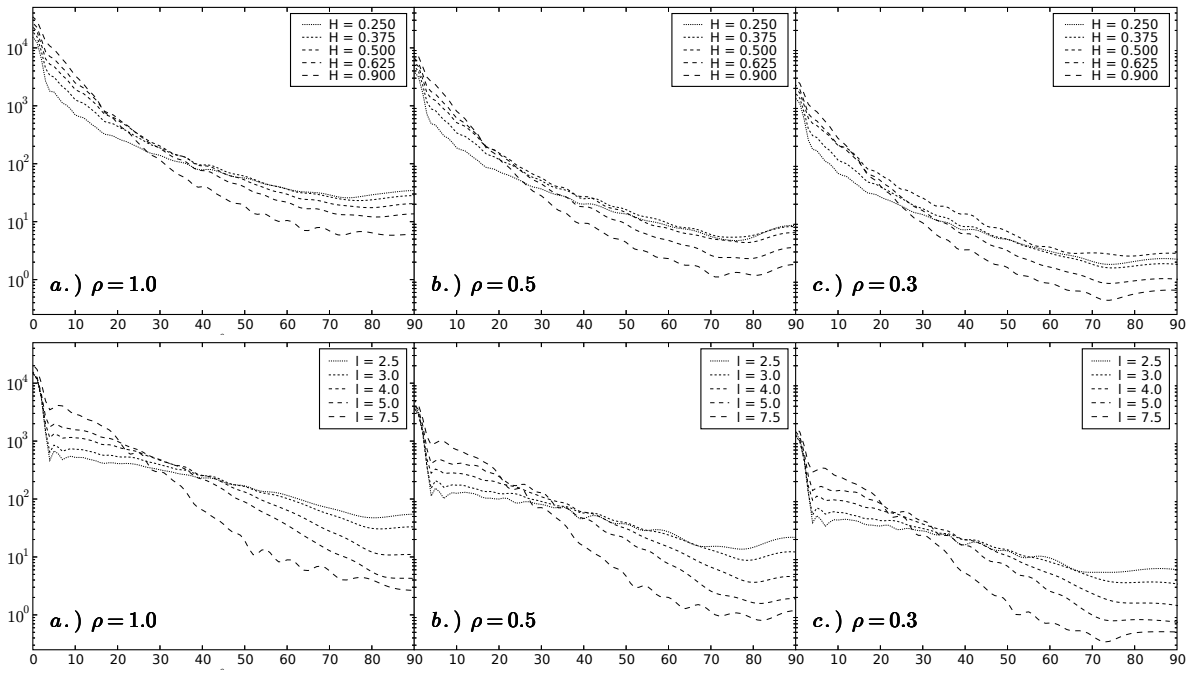

Figure 2: Distribution of the scattered intensity (M_{11}) as a function of θ_e computed for the films with fBm roughness and Gc roughness and normal incident radiation.

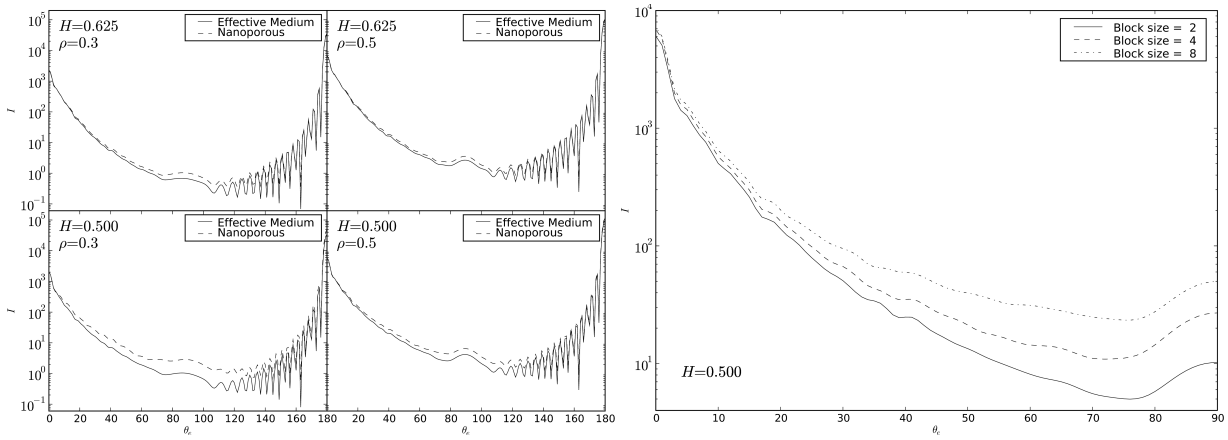

Figure 3: On the left, distribution of scattered intensity for inhomogeneous films with $\rho = [0.5,\ 0.3]$, and solid films with effective index of refraction. On the right, the effects due to the increasing void size.

3.2 Discussion

The study considered light scattering from simple nanoporous media, that is, inhomogeneous media with pore size in the nanometer range and simplified pore structure. The results can be generalized to situtations where the pore size is very small compared to other structures of the media—such as the surface roughness—and to the wavelength of the radiation. The results can not be generalized to particulate media with coherent particle structure, or to porous media with pore structure exceeding the scale of the wavelength.

Possible sources of error include the dominance of the surface dipoles over the total dipole count of the volume, and the use of normal incidence. The latter makes the separation between backscattering, directional-diffuse and the specular reflectance effects impossible

For a scattering object to be considered analogous to a surface, we must have $\frac{r}{t} >> 1$. Here r is the radius of the cylinder, and t the thickness. This is especially important for off-normal incident radiation, since the cylinder walls contribute to the scattering. Nevertheless, to include realistic volume scattering effects, we would like to have $t >> \lambda$, where λ is the wavelength of the radiation. With DDSCAT, The size of the geometry is restricted by the available memory of a single computing node. This imposes a strict limit to the geometry thickness. This limit can be raised by applying codes with capability to slice the geometry between different nodes, such as ADDA. Geometry slicing will allow us to maximize $\frac{r}{t_s}$ for a single computing node, where t_s is the thickness of a slice, and use appropriate number of nodes to achieve the total thickness.

The use of more extended rough-surface analogs will allow for the comparison between the different analytic wave-optics approximations for random rough surfaces [8] and independent numerical simulations.

References

[1] M. A. Yurkin, A. G. Hoekstra, "User Manual for the Discrete Dipole Approximation Code 'Amsterdam DDA'", 2007

[2] R. J. Adler, *The Geometry of Random Fields*, Wiley, 1981.

[3] H. P. Parviainen, *Ray tracing model for light scattering from self-affine random rough surfaces*, Master's thesis, University of Helsinki (2006).

[4] H. P. Parviainen, K. Muinonen, "Rough-surface shadowing of self-affine random rough surfaces", J. Quant. Spectros. Radiat. Transf. (2007), doi:10.1016/j.jqsrt.2007.01.025.

[5] B. T. Draine, "The discrete-dipole approximation and its application to interstellar graphite grains", ApJ **333**, 848 (1988).

[6] C. F. Bohren, D. R. Huffman, *Absorbtion and Scattering of Light by Small Particles*, Wiley, 1998

[7] J. C. Maxwell Garnett, "Colours in Metal Glasses and in Metallic Films", Phil. Trans. R. Soc. A **203**, 385 (1904)

[8] T. M. Elfouhaily, C.-A. Guérin, "TOPICAL REVIEW: A critical survey of approximate scattering wave theories from random rough surfaces", Waves in Random Media 14, 1 (2004).

Coherent backscattering effects with Discrete Dipole Approximation method

Antti Penttilä[1] and Kari Lumme[1]

[1]*Observatory, P.O. box 14, FIN-00014 University of Helsinki, Finland*
fax: +358 9 1912 2952, e-mail: Antti.I.Penttila@helsinki.fi

Abstract

We use the Discrete Dipole Approximation method to simulate light scattering from a dense cloud of wavelength-sized spherical particles. We will mimic the set-up that was used in recent articles from Mishchenko et al.[1, 2] where the superposition T-matrix method was used to simulate the scattering characteristics. We will show that the same demonstration of the evolution of the coherent backscattering phenomena can be produced with the Discrete Dipole Approximation.

1 Introduction

The coherent backscattering (CB) or the weak localization effect of electromagnetic waves has been studied both theoretically and with laboratory experiments, and recently also by numerical simulations[1, 2, and the references therin]. Mishchenko et al.[1, 2] have used the superposition T-matrix method to study the scattering characteristics from a dense cloud of wavelength-sized uniform spheres. They were able to simulate scattering from systems with up to 240 spheres. Mishchenko et al. make the (probably legitimate) claim, that they were able to show the evolution of the CB effect directly for the first time.

The superposition T-matrix method has some practical limitations in its convergence and the size of the system in [1, 2] is the largest that can be computed with current implementations and computing resources. On the other hand, the Discrete Dipole Approximation (DDA) method, among some other methods, can also be used to compute scattering from a cloud of spheres. Currently, there is only one implementation of the DDA as far as we know, the "Amsterdam DDA" (ADDA) code[3], that can handle as large systems as in the experiment by Mishchenko et al. The reason for this is that the ADDA can be run in parallel computing clusters where the system matrix in DDA can be divided among the operating memory banks of different processors. The other DDA codes suffer from the limitation of the available operating memory in single processor environments.

In this article we will show that the DDA approach can produce the same results as the superposition T-matrix implementations with the same set-up as in [1, 2]. The idea behind this is that once the applicability of the DDA is verified in this case, it can be used in larger or more complicated problems when studying the CB. The T-matrix approach is limited to solids with rotational symmetries, while the DDA can be used with arbitrary geometry. In the future it could be studied, e.g., if the CB effect needs a cloud of separated constituents, or could it also be produced by e.g. a large single random and porous particle.

2 Numerical results

We will mimick the set-up in [1, 2] and place either 80 or 160 spheres with size parameter $kr = 4$ randomly inside a large sphere with size $kR = 40$, where r and R are the radii of the small and large spheres and k is the wave number $k = 2\pi/\lambda$. The refractive index of the particles is 1.32.

This experiment uses just one realization of the random particle positions. With T-matrix method the scattering is averaged over all orientations of the system, thus producing different 'views' to the system. The

DDA method is not capable to produce exact orientation averaging, but the DDA computations can be run with different target orientations and then averaged, producing an estimate of random orientation scattering.

Currently, we have computed 22 different orientation directions placed systematically in spherical coordinates (θ, ϕ). In the DDA method the different rotations of the scattering plane in some orientation direction (θ_i, ϕ_i) are cheap to compute and we have used 256 different planes, making a total of 22x256=5632 orientations. Because one of the rotational angles is so overrepresented in the orientation averaging, the deviation in the random orientation estimate is larger than in the case of more balanced systematic sampling over the rotation angles.

The results of the simulations are presented in Figs. 1 and 2. In Fig. 1 are the scattering characteristics for both the 80- and 160-sphere systems computed with both the T-matrix and the DDA method. The elements of the Mueller matrix are labeled with $a_1, \ldots, a_4$ for diagonal elements and with b_1 for element $(1, 2)$ and $(2, 1)$ and with b_2 for element $(3, 4)$ and $-(4, 3)$. Different combinations of these elements are presented, e.g. intensity a_1 in subfigs. (a) and (e), and linear polarization $-b_1/a_1$ in subfigs. (d) and (l).

3 Conclusions

Mishchenko et al.[1, 2] analyze the behavior of the different scattering characteristics of the sphere clusters in question. Most obvious signs of the coherent backscattering phenomena in these clusters are seen in the peaks in the backscattering region in intensity (Fig. 1(e)) and in different polarizations states in Figs. 1(f)-(k). It is clear that the DDA method produces the same effects and is therefore well applicable in CB studies. The errors due to the limited number of orientations, as seen in Fig. 2 are still large, but will decrease as more orientations are computed.

The CPU times needed for the DDA computations are much larger than for the T-matrix method. Roughly estimated CPU-time for the T-matrix solution of the 80-sphere problem is $\sim$ 100 CPU-hours[2] with a modern PC. CPU-time for one orientation (with 256 scattering planes) with the ADDA code was $\sim$ 70 CPU-h. For 22 orientations it was roughly 1500 CPU-h, and at least twice this much orientations would be needed for the result to fit better to the exact results from the T-matrix method. Nevertheless, the available computing resources grow rapidly and the flexibility of the DDA method with arbitrary geometry does make the DDA approach very advantageous.

Acknowledgments

I would like to thank M. Mishchenko for providing me the data from the T-matrix simulations.

References

[1] M.I. Mishchenko and L. Liu. Weak localization of electromagnetic waves by densely packed many-particle groups: Exact 3d results. JQSRT, doi:10.1016/j.jqsrt.2007.01.039, 2007.

[2] M.I. Mishchenko, L. Liu, D.W. Mackowski, B. Cairns, and G. Videen. Multiple scattering by random particulate media: exact 3d results. Optics Express, in press, 2007.

[3] M.A. Yurkin, V.P. Maltsev, and A.G. Hoekstra. The discrete dipole approximation for simulation of light scattering by particles much larger than the wavelength. JQSRT, doi:10.1016/j.jqsrt.2007.01.033, 2007.

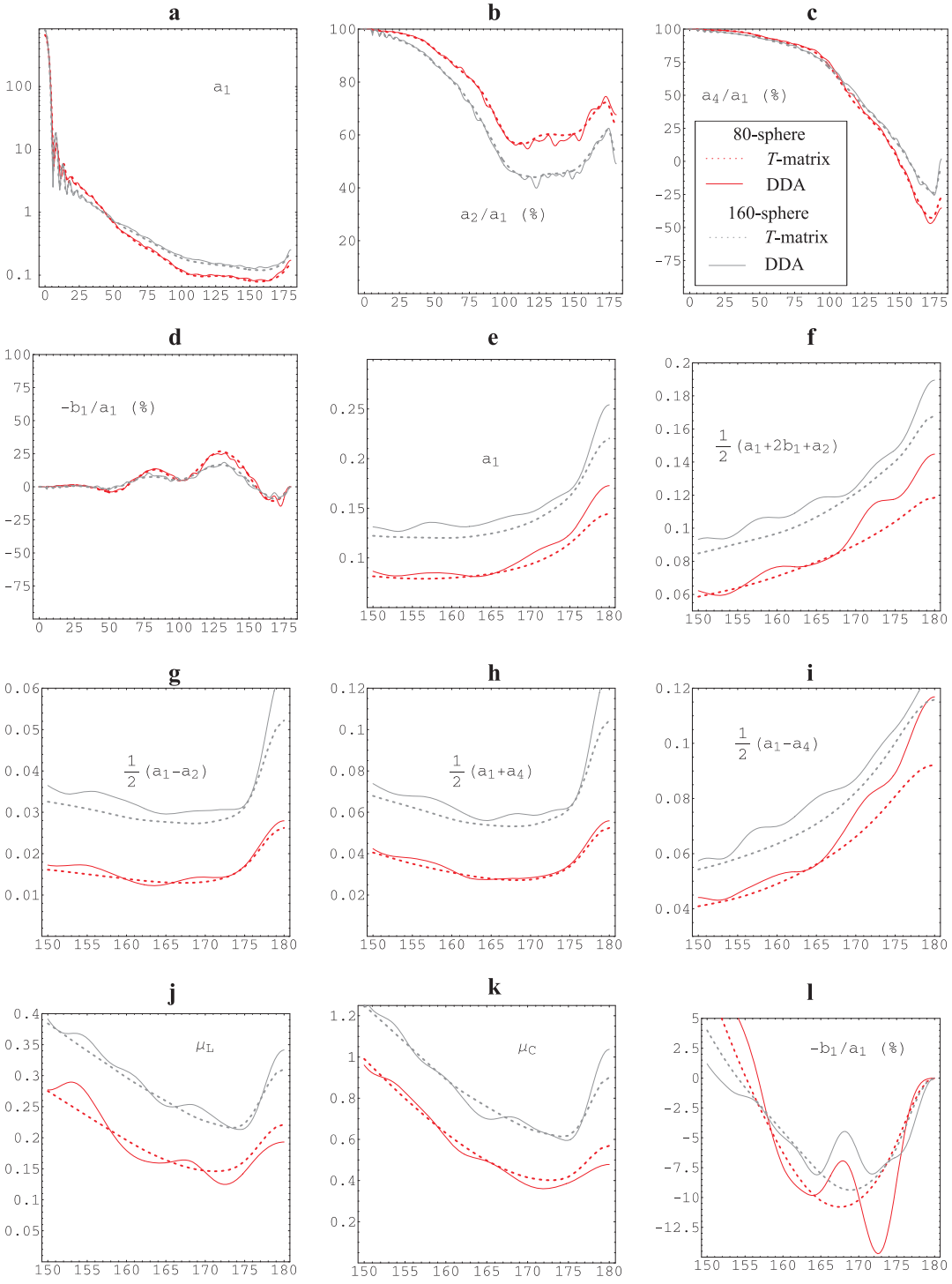

Figure 1: Different scattering characteristics for both the 80- and 160-sphere systems computed with the *T*-matrix or the DDA method as a function of the scattering angle.

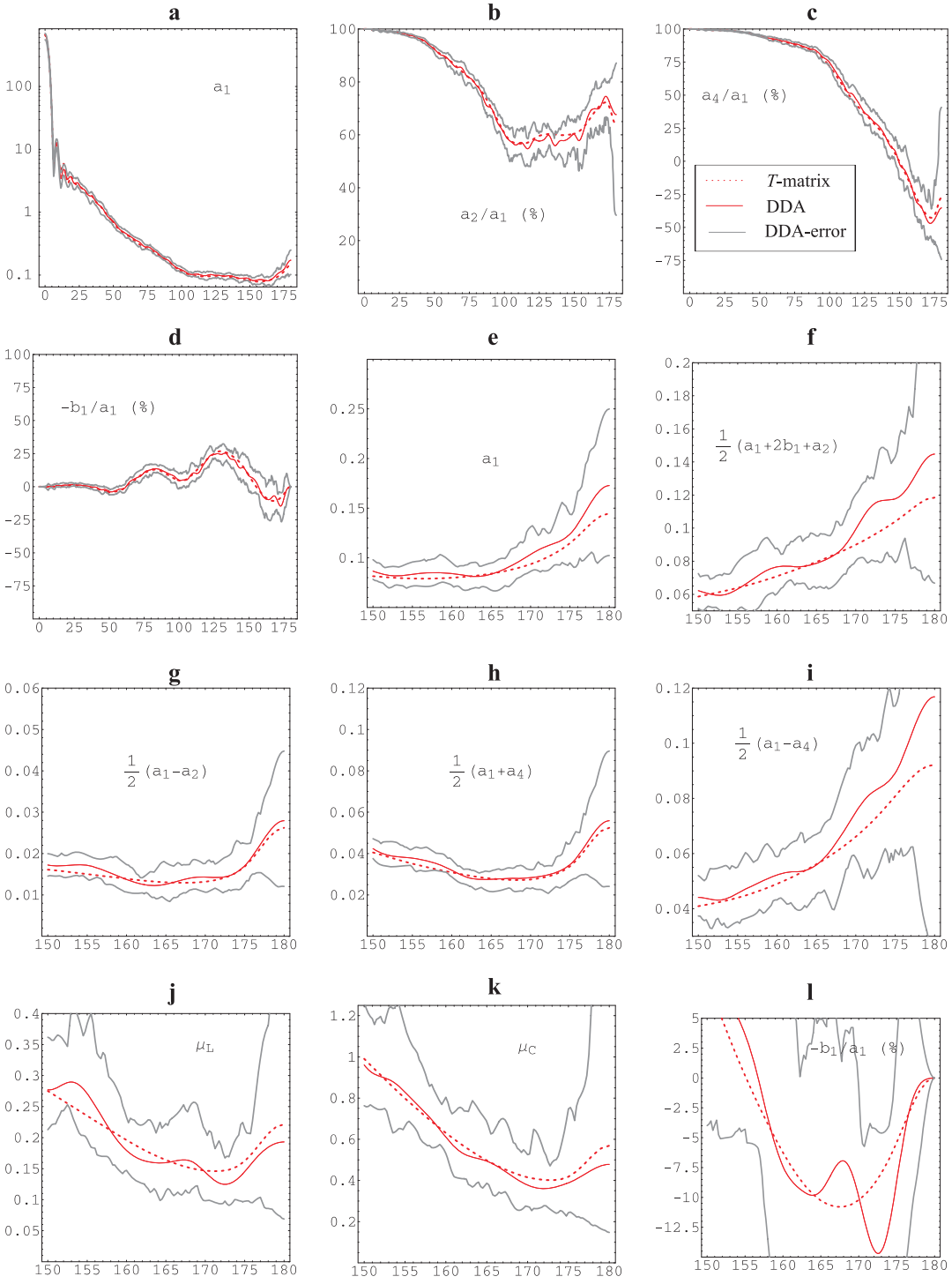

Figure 2: Scattering characteristics for the 80-sphere system and a typical error of the DDA orientation averaging. The lower and upper error lines are the 4th smallest and largest values in the 22 orientations at that scattering angle. This non-parametric error estimate encloses 64 % of the observations. The widely used mean-$\pm$-σ -error encloses 68 % of obervations, but it is symmetric while the errors in e.g. backscattering region in subfigs. (g) and (h) are not.

Applying *Sh*-matrices to two merging spheres

Dmitry Petrov,[1] Yuriy Shkuratov,[1] Gorden Videen[2,3]

[1]*Astronomical Institute of Kharkov V.N. Karazin National University. 35 Sumskaya St, Kharkov, 61022, Ukraine, phone +38-057-707-50-63,* petrov@astron.kharkov.ua
[2]*Army Research Laboratory AMSRD-ARL-CI-EM, 2800 Powder Mill Road Adelphi Maryland 20783 USA*
[3]*Astronomical Institute "Anton Pannekoek," University of Amsterdam, Kruislaan 403, 1098 SJ Amsterdam, The Netherlands*

Abstract

The introduction of the *Sh*-matrices in the *T*-matrix method allows the shape-dependent parameters to be separated from size- and refractive-index-dependent parameters. In many case this allows analytic solutions of the corresponding surface integrals to be obtained. In this manuscript we derive and analyze the analytical solution for merging spheres at different degrees of merging.

1 Introduction

The *T*-matrix method is widely used for calculations of scattering properties of non-spherical particles [1]. In the *T*-matrix method, the incident and scattered electric fields are expanded in series of vector spherical wave functions, and then a relation between the expansion coefficients of these fields is established by means of a transition matrix (or *T* matrix). *T*-matrix elements depend on the optical and geometrical parameters of the scatterers and do not depend on the illumination/observation geometry, so the *T*-matrix approach allows for the separation of the influence of illumination/observation parameters and inner properties of a scattering object such as its size, shape parameters, and refractive index. Our modification of the *T*-matrix approach (specifically we use here the Extended Boundary Condition Method) consists of a further development, namely, we separate the contributions of the different inner parameters of the scattering object [2-6].

2 *Sh*-matrices

Mathematically our approach consists of introducting the so-called *Sh*-matrices, which depend on the scattering object shape only. The elements of the *T*-matrix can be expressed through the *Sh*-matrix elements. For example, the elements $RgJ^{11}_{mnm'n'}$ and $J^{11}_{mnm'n'}$ of the *T*-matrix for particles with an axis of symmetry are found with the following equations (see designations in [1,2]):

$$\mathrm{Rg}J^{11}_{mnm'n'} = -2\pi\delta_{mm'} i(-1)^{m'-m} A_{nn'} \int_0^{\pi} d\theta \left\{ \sin\theta \left[\pi_{m'n'}(\theta)\tau_{mn}(\theta) + \pi_{mn}(\theta)\tau_{m'n'}(\theta) \right] j_{n'}(m_0 R(\theta)) j_n(R(\theta)) (R(\theta))^2 \right\}, \quad (1)$$

$$J^{11}_{mnm'n'} = -2\pi\delta_{mm'} i(-1)^{m'-m} A_{nn'} \int_0^{\pi} d\theta \left\{ \sin\theta \left[\pi_{m'n'}(\theta)\tau_{mn}(\theta) + \pi_{mn}(\theta)\tau_{m'n'}(\theta) \right] j_{n'}(m_0 R(\theta)) h_n(R(\theta)) (R(\theta))^2 \right\}. \quad (2)$$

Calculating these elements numerically requires much time, especially if we consider an ensemble of particles polydisperse in size or refractive index. We have suggested modifications making such calculations much easier. For example, the elements $RgJ^{11}_{mnm'n'}$ and $J^{11}_{mnm'n'}$ can be expressed using the *Sh*-matrix as follows [2]:

$$\mathrm{Rg}J^{11}_{mnm'n'}\left(X,m_0\right)=X^{n+n'+2}\left(m_0\right)^{n'}\sum_{k_1=0}^{\infty}\frac{\left(Xm_0\right)^{2k_1}}{k_1!\Gamma\left(n'+k_1+\frac{3}{2}\right)}\sum_{k_2=0}^{\infty}\frac{\left(X\right)^{2k_2}}{k_2!\Gamma\left(n+k_2+\frac{3}{2}\right)}\mathrm{Rg}Sh^{11}_{mnm'n',k_1+k_2}\,, \tag{3}$$

$$J^{11}_{mnm'n'}\left(X,m_0\right)=X^{-n+n'+1}\left(m_0\right)^{n'}\sum_{k_1=0}^{\infty}\frac{\left(Xm_0\right)^{2k_1}}{k_1!\Gamma\left(n'+k_1+\frac{3}{2}\right)}\sum_{k_2=0}^{\infty}\frac{\left(X\right)^{2k_2}}{k_2!\Gamma\left(-n+k_2+\frac{1}{2}\right)}Sh^{11}_{mnm'n',k_1+k_2}\,, \tag{4}$$

where $X=2\pi r/\lambda$ is the size parameter, r is the size of the major axis of a particle, λ is the wavelength of incident light; m_0 is the refractive index of the particle, *Sh* and Rg*Sh* are the shape matrices or just *Sh*-matrices:

$$\mathrm{Rg}Sh^{11}_{mnm'n'k}=-2\pi^2\delta_{mm'}i\frac{\left(-1\right)^{m'-m+k}}{2^{2k+n'+n+2}}A_{nn'}\int_0^{\pi}d\theta\left\{\sin\theta\left[\pi_{m'n'}\left(\theta\right)\tau_{mn}\left(\theta\right)+\pi_{mn}\left(\theta\right)\tau_{m'n'}\left(\theta\right)\right]\left(R_0\right)^{2k+n+n'+2}\right\} \tag{5}$$

$$Sh^{11}_{mnm'n'k}=2\pi^2\delta_{mm'}\frac{\left(-1\right)^{m'-m+n-1+k}}{2^{2k+n'-n+1}}A_{nn'}\int_0^{\pi}d\theta\left\{\sin\theta\left[\pi_{m'n'}\left(\theta\right)\tau_{mn}\left(\theta\right)+\pi_{mn}\left(\theta\right)\tau_{m'n'}\left(\theta\right)\right]\left(R_0\right)^{2k-n+n'+1}\right\} \tag{6}$$

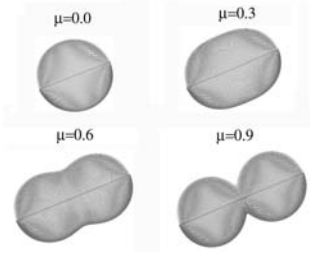

Figure 1: Examples of merging spheres for different values of μ.

where $R_0=\frac{R(\theta)}{X}$, $R(\theta)$ is the shape function of axi-symmetric particles in spherical coordinates; θ is the polar angle. Thus the *Sh*-matrices depend on the shape of the scattering particle only, and are independent of the particle size and refractive index, so they need to be calculated only once. Moreover in many cases the integrals in (5) and (6) can be calculated analytically, e.g., for Chebyshev particles [3], bi-spheres (osculating spheres), and capsules [5], and finite circular cylinders [6]. We here study the analytic solution for two merging spheres at different degrees of merging (see Fig. 1). The shape of the merging spheres of the same diameter is described by the equation $R_0(\theta)=\sqrt{1+\mu\cos 2\theta}$, where θ is the polar angle in a spherical coordinate system centered midway between the two sphere centers, $\mu<1$ is the parameter of merging. At $\mu=0$ the particle is a single sphere and at $\mu=1$ it is an osculating spheres (Fig. 1). Examples of analytical expressions for the elements of *Sh*-matrix are

$$\mathrm{Rg}Sh^{11}_{mnm'n',k}=-2\pi^2\delta_{mm'}i\frac{\left(-1\right)^{m'-m+k}}{2^{2k+n'+n+2}}A_{nn'}I^{(1)}_{mnm'n'}\left(2k+n+n'+2\right),\ Sh^{11}_{mnm'n',k}=2\pi^2\delta_{mm'}\frac{\left(-1\right)^{m'-m+n-1+k}}{2^{2k+n'-n+1}}A_{nn'}I^{(1)}_{mnm'n'}\left(2k-n+n'+1\right)$$

$$I^{(1)}_{mnm'n'}(z)=m\left[\frac{n'\sqrt{(n'+1)^2-m'^2}}{2n'+1}I^{(\theta)}_{mnm'n'+1}(z)-\frac{(n'+1)\sqrt{n'^2-m'^2}}{2n'+1}I^{(\theta)}_{mnm'n'-1}(z)\right]+m'\left[\frac{n\sqrt{(n+1)^2-m^2}}{2n+1}I^{(\theta)}_{mn+1m'n'}(z)-\frac{(n+1)\sqrt{n^2-m^2}}{2n+1}I^{(\theta)}_{mn-1m'n'}(z)\right]$$

$$I^{(\theta)}_{mnm'n'}(\mu,z)=(-1)^{n+n'}\Xi_m\Xi_{m'}n!\sqrt{(n-|m|)!(n+|m|)!}n'!\sqrt{(n'-|m'|)!(n'+|m'|)!}\times$$

$$\sum_{k=0}^{n-|m|}\frac{(-1)^k}{k!(n-k)!(n-|m|-k)!(|m|+k)!}\sum_{k'=0}^{n'-|m'|}\frac{(-1)^{k'}}{k'!(n'-k')!(n'-|m'|-k')!(|m'|+k')!}\ ,\ \Xi_m=\begin{cases}1, m\ge 0\\(-1)^m, m<0\end{cases}$$

$$\left[I^{(C1)}_{mnm'n'}\left(\mu,2n-2k-|m|+2n'-2k'-|m'|-1,2k+|m|+2k'+|m'|-1,z\right)\right]$$

$$I^{(C1)}_{mnm'n'}(\mu,\eta,\nu,z)=(1+\mu)^{\frac{z}{2}}\sum_{n=0}^{\infty}(-4)^n\left(\frac{2\mu}{1+\mu}\right)^n\frac{\frac{z}{2}\left(\frac{z}{2}-1\right)\mathrm{K}\left(\frac{z}{2}-n+1\right)}{n!}\Omega(\eta+2n,\nu+2n),\ \Omega(\eta,\nu)=\frac{\Gamma\left(\frac{\eta+1}{2}\right)\Gamma\left(\frac{\nu+1}{2}\right)}{2\Gamma\left(\frac{\eta+\nu}{2}+1\right)}.$$

It can be shown that at $\mu \to 1$ the expressions tend to corresponding formulas for osculating spheres [5]. We also note that such a system of spheres has been examined previously using the *T*-matrix method [7], but performing numerical integrations over the surface integrals.

3 Results

Calculations using the analytical solution are represented in Figs. 2 and 3. One can see the development of the interference structure arising from varying μ in Figure 2.

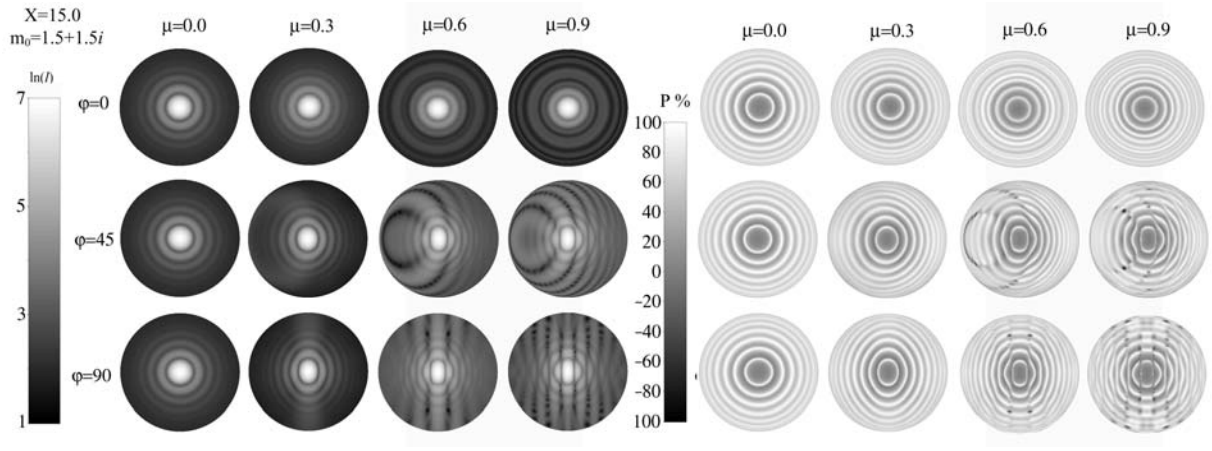

Figure 2: Maps of the forward-scattering hemisphere intensity (left panel) and polarization degree (right panel) produced by merging spheres at several fixed orientations (φ = 0° is the case when the incident light is parallel to the major particle axis). The refractive index of the particle and size parameter is $m_0 = 1.5+1.5i$ and $X = 15.0$.

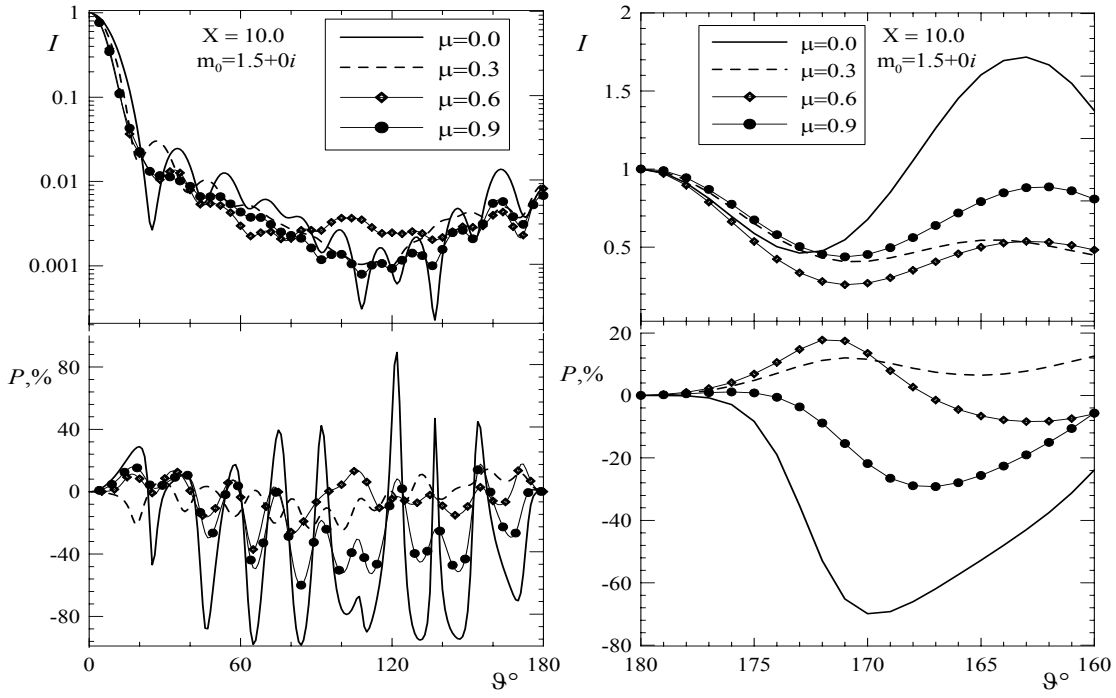

Figure: 3 Phase dependence of intensity and polarization degree for merging spheres at different degree of merging. The (a) entire and (b) narrow backscatter ranges of scattering angles are presented.

Figure 3 shows orientation-averaged intensities and polarizations for different merging parameter μ. Previous studies have shown that the negative polarization branch of a single sphere can be damped significantly by the presence of another sphere [8]. For the parameters of Figure 3, no backscattering phenomena are obvious for the single sphere. When the system evolves into two osculating spheres none develop.

4 Conclusion

In the framework of the *T*-matrix method we have used the *Sh*-matrices to find an analytical solution for a system composed of merging spheres. Sample results show that the interference between the spheres becomes obvious even for a relatively large degree of merging $\mu > 0.5$. In a system for which no backscattering effects were obvious for a single sphere, none become apparent when the system evolves into two merging spheres even for large values of μ.

References

[1] M. I. Mishchenko, L. D. Travis, D. W. Mackowski, "T-matrix computations of light scattering by nonspherical particles: a review", J. Quant. Spectrosc. Rad. Transfer, **55,** 535–575. (1996).

[2] D. Petrov, E. Synelnyk, Yu. Shkuratov and G. Videen, "The *T*-matrix technique for calculations of scattering properties of ensembles of randomly oriented particles with different size," J. Quant. Spectrosc. Rad. Transfer **102**, 85-110. (2006).

[3] D. V. Petrov, Yu. G. Shkuratov, G. Videen, "Analytical light-scattering solution for Chebyshev particles," J. Opt. Soc. Am. A (2007) in press.

[4] D. Petrov, Yu. Shkuratov, E. Zubko, G. Videen, "*Sh*-matrices method as applied to scattering by particles with layered structure," J. Quant. Spectrosc. Rad. Transfer, (2007) in press.

[5] D. Petrov, G. Videen, Yu. Shkuratov, M. Kaydash, "Analytic *T*-matrix solution of light scattering from capsule and bi-sphere particles: Applications to spore detection," J. Quant. Spectrosc. Rad. Transfer (2007) in press.

[6] D. Petrov, Yu. Shkuratov, "Application of *Sh*-matrices in light scattering by circle cylinder," Optics and Spectroscopy (2007) in press.

[7] M.I. Mishchenko, G. Videen, "Single-expansion EBCM computations for osculating spheres," J. Quant. Spectrosc. Radiat. Transfer **63**, 231-236 (1999).

[8] D.W. Mackowski and M.I. Mishchenko, "Calculation of the *T* matrix and the scattering matrix for ensembles of spheres," J. Opt. Soc. Am. A 13, 2266-2278 (1996).

Photometry of powders consisting of dielectric and metallic spheres at extremely small phase angles

V. Psarev,[1,2] A. Ovcharenko,[1,2] Yu. Shkuratov,[1,3] I. Belskaya[1], G. Videen,[4,5] A. Nakamura,[6] T. Mukai,[6] Y. Okada[6]

[1]*Astronomical Institute of V.N. Karazin Kharkov National University, 35 Sumskaya St, Kharkov, 61022, Ukraine tel. +38-057-700-5349. e-mail: pva@astron.kharkov.ua*

[2]*Main Astronomical Observatory of NASU, 27 Akademika Zabolotnogo St., 03680, Kyiv, Ukraine*

[3]*Radioastronomical Institute of NASU, 4 Chervonopraporova, Kharkov, 61002, Ukraine*

[4]*Army Research Laboratory AMSRL-CI-EM, 2800 Powder Mill Road Adelphi Maryland 20783 USA*

[5]*Astronomical Institute ''Anton Pannekoek'', University of Amsterdam, Kruislaan 403, 1098 SJ Amsterdam, The Netherlands*

[6]*Graduate School of Science and Technology and Department of Earth and Planetary Sci., Faculty of Science Kobe University, Nada, Kobe 657-8501, Japan*

Abstract

We present results of our photometric measurements of three samples of particulate surfaces consisting of dielectric and metallic spheres at extremely small phase angles. Monolayers of the spheres show satisfactory coincidence with the results of Mie-theory calculations. In particular, no opposition effect of the monolayer was found at the phase angle range 0.008 – 1.6° in accordance with Mie theory prediction. On the other hand, thick layers of the spheres reveal the opposition effect at phase angles less than 0.8°. In the case of dielectric spheres the opposition spike is due to the coherent-backscattering effect; whereas, for iron particulate surfaces the main contributor is perhaps the shadow-hiding effect. Measured dependencies do not allow us to separate these effects.

1 Introduction

The motivation of this study is an astrophysical problem: Photometric observations of Kuiper belt objects reveal a prominent brightness opposition spike that is very narrow [1]. These objects are observed at very small phase angles (< 2°) and to reproduce these conditions in a laboratory requires the use of very small angular apertures of the light source and the receiver. Using an old laboratory of our Institute, which had been exploited as an analog processor for Fourier transformation of large images, we have constructed a laboratory laser photometer to study extremely small phase angles; this setup provides measurements in the range 0.008 – 1.6° [2]. This instrument allows us to measure the scattering properties of structural analogs of the surfaces of Kuiper belt objects. First of all it allows studies of the opposition spike effect in a wide physical context. For example, we here compare phase dependencies of intensity for dielectric and metallic small spherical particles that form a monolayer and thick layer in order to study the opposition effect related to the shadowing and coherent backscatter enhancement.

2 Instrument, measurements, and samples

Using the laser extra-small-phase-angle photometer we investigate the opposition effect of complicated surfaces in a vertical and horizontal position in the range of phase angles 0.008 – 1.6°. The extremely small phase angles are feasible due to small linear apertures of the light source (a laser) and receiver (photomultiplier Hamamatsu H5783-01) and the large distance from the light source and detector to the

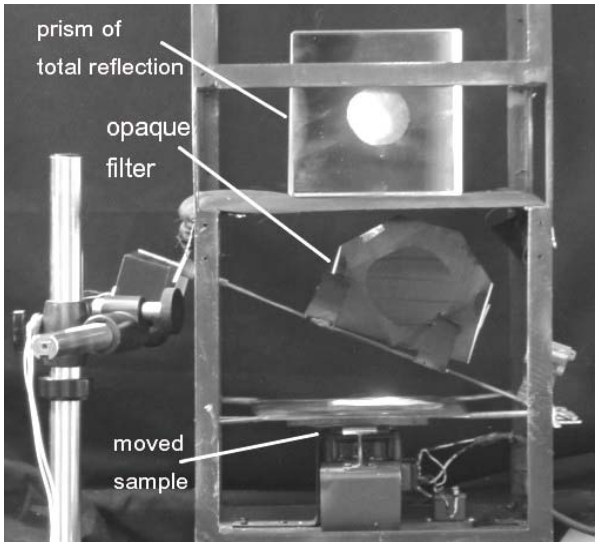

Figure 1: The sample block of the instrument.

scattering surface (samples) that is 25 m. The linear diameter of the apertures is 2 mm. In the laboratory we use a clean-room environment that helps eliminate scattering by dust particles in air, which is very important for small-phase-angle measurements covering a large distance. In these measurements we use a gas monomodal non-polarized laser (50.0 mW) with wavelength 0.658 μm as a light source. All measurements are carried out in full darkness. For light detection we use a pinhole camera, a circular cone with a truncated top [2]. The linear diameter of the samples we use is about 7 cm. A checking procedure includes measurement of the light background from the small totally reflecting prism of the light source that is used in the optical scheme to turn the laser beam. We make this check by bringing the detector aperture to the laser beam (toward minimal phase angles). We change the phase angle by moving the detector block. The block consists of the pinhole camera with the photomultiplier inside and a coaxial guiding spyglass. The spyglass is needed for aligning the sample after a phase-angle displacement of the detector block. Each sample is measured at least twice at increasing and decreasing phase angles. Coincidence of these two dependencies is an indicator of the reproducibility of the measurements. An important verification is to estimate parasitic light scattering by dust in air for low-albedo samples at extremely small phase angles. To test we use as a sample an optical filter that absorbs light at the laser wavelength (Fig. 1). We tilt the filter so the specular reflection is diverted from the detector. Thus we obtain the signal from the dust in air [2]. To avoid problems with speckle pattern we move samples during measurements providing averaging. Figure 1 shows an image of the sample block in the mode allowing measurements of horizontal surfaces; for such measurements a large, totally reflecting prism (10×10 cm) is used to direct the laser beam vertically. The sample is mounted on a moveable spring hanger.

We here study metallic and dielectric materials (Fig. 2). We use two iron powders. One sample consists of small spheres whose average size is 2 μm. The distribution covers a range from a tenth micron to 4 μm. The second sample consists of coarse particles of different sizes whose average is 150 μm, which reveals very complicated surface structure of the particles. The characteristic scale of the particle surface

roughness is several microns. The dielectric sample is composed of 1 μm silica spheres (see Fig. 2). We show results of measurements of the samples in Fig. 3. Each point of these phase curves (open circles and crosses) is a result of averaging three measurements. The duration of each measurement is 2 s; at this time the movement of the spring hanger shown in Fig. 1 produces good averaging of the speckle pattern. We measured thick layers of the powders with a thickness ≈ 5 mm. In addition we measured thin (mono) layers that were prepared by drying an alcohol suspension of the particles on a substrate, a dark leatherette with frost coating, that does not have any opposition features. The albedo of the thick layer samples was determined at 1° phase angle and is given relative to the photometric standard Halon [3]. The bright (dielectric) sample shows very high albedo, higher than that of Halon. The iron samples have albedos near 21 % and 32 %, respectively, for the coarse grain sample and the fine sphere powder.

3 Results and discussion

Figure 3a shows that the thick layer sample of silica spheres has a very prominent opposition spike at phase angles less than 1.0°. This spike is related to the coherent backscattering effect that is ubiquitously observed in nature, e.g., [4]. This spike is similar to what was observed for some Kuiper belt objects. The monolayer of the small spheres does not show the opposition effect, and these results are consistent with the Mie theory shown prediction as a solid line; thus, the scatter from the monolayer is dominated by single-particle scattering. For Mie theory modeling we use $m = 1.45 + 0i$ and $3.57 + 4.02i$ [5], respectively, for dielectric and metallic spheres. It should be emphasized that the monolayer phase curves were calculated with a weighted subtraction of the phase dependence of the substrate.

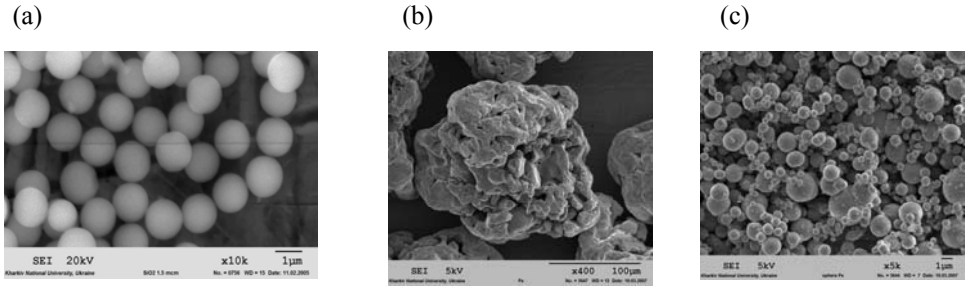

Figure 2: Electron microscope photographs of samples used. Silica spheres with size ≈ 1.0 μm (a), iron powder with coarse particles having complicated surface structure (b), and iron spheres with average diameter 2 μm (c).

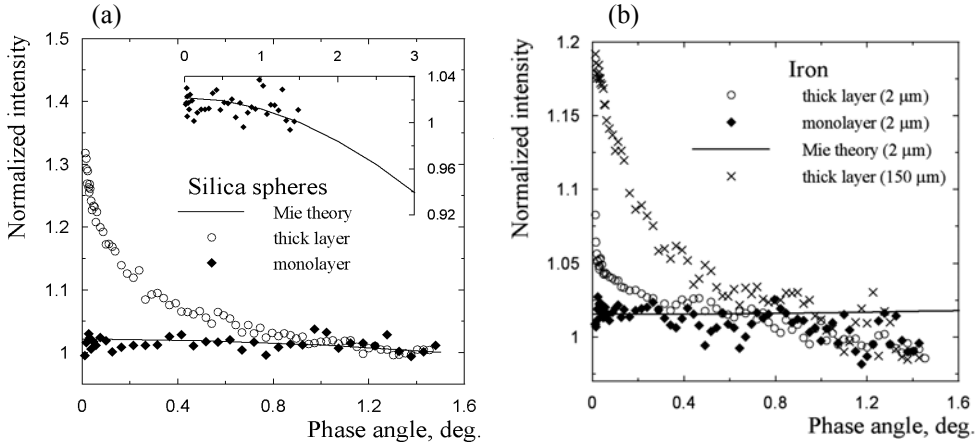

Figure 3: Photometric phase curves for silica spheres (a) and iron particles (b). Open circles and points designate measurements, respectively, for thick and thin layers. Solid lines correspond to calculations with Mie theory. Crosses represent measurements for thick layer of coarse iron particles. All the dependencies are normalized at 1.4°. The insert demonstrate the Mie theory curve at wider range of phase angles.

The sample of coarse iron grains shows a spectacular opposition feature; whereas, the iron sphere sample demonstrates only a small amplitude and very narrow opposition peak starting from 0.2° (Fig. 3 b). The particulate surface consists of coarse iron grains that have two scales of roughness: the first one is produced by the grains and the second one is related to the complicated surface structure of the grains (Fig. 2). It is well-known that surfaces with such a hierarchical structure produce much more prominent shadow-hiding effect than single scale roughness [6]. We suppose that the spike seen in Fig. 3 b for the sample of coarse iron particles is related at least partially to this double-shadowing. This spike also may have a contribution from the coherent backscatter effect. This contribution can be estimated from the phase dependence of the small-sphere sample that forms a non-hierarchical particulate surface. Like in the case of the small dielectric particles, the independent iron spheres reveal a very neutral behavior of brightness over the phase-angle range. This can be seen for monolayer measurements that are in good agreement with the Mie theory.

4 Conclusion

We have initiated research with a new laboratory laser photometer covering an extremely small phase-angle range (0.008 – 1.6°). Our measurements of dielectric and metallic spheres have shown a narrow opposition spike of the samples at phase angle less than 0.8°. From measurements at such small phase angles, we are not able to determine whether the brightness spike is produced by metallic or dielectric surfaces. From comparison of our measurements with the Mie theory we also may conclude that the scattering from a thin layer (monolayer) of particles on a dark substrate is dominated by single-particle scattering at such small phase angles.

Acknowledgement

This work was partially supported by the Ministry of Education and Science of Ukraine (agreement No H/14 – 2002).

References

[1] I.N. Belskaya, J.L. Ortiz, P. Rousselot, V. Ivanova, G. Borisov, V.G. Shevchenko, N. Peixinho. “Low phase angle effects in photometry of trans-neptunian objects: 20000 Varuna and 1996 TO66.” Icarus 184, 277-284. (2006).

[2] V. Psarev, A. Ovcharenko, Y. Shkuratov, I. Belskaya, G. Videen. “Photopolarimetry of surfaces with complicated structure at extremely small phase angles.” 9th Conference on Electromagnetic and Light scattering by Nonspherical Particles. June 5 – 9, Russia, St. Petersburg, pp. 235-238. (2006).

[3] V. Weidner, J. Hsia, “Reflection properties of pressed polytetrafluoroethylene powder,” J. Opt. Soc. Am. 71. 856-861. (1981).

[4] Yu. Shkuratov, G. Videen, M. Kreslavsky, I. Belskaya, A. Ovcharenko, V. Kaydash, V. Omelchenko, N. Opanasenko, E. Zubko. “Scattering properties of planetary regoliths near opposition”, in: Photopolarimetry in Remote Sensing / Eds. G. Videen, Ya. Yatskiv, and M. Mishchenko. NATO Science Series. Kluwer Academic Publishers, London. pp. 191-208. (2004).

[5] H. Yolken J. Kruger. “Optical constant of iron in the visible region.” J. Opt. Soc. Am. 55, 842-846. (1965).

[6] K. Muinonen, D. Stankevich, Y. Shkuratov, S. Kaasalainen, J. Piironen. “Shadowing effect in clusters of opaque spherical particles.” J. Qunt. Spectrosc. Rad. Transfer. 70. 787-810. (2001).

Correction factors for a total scatter/backscatter nephelometer

A. Quirantes[1], L. Alados-Arboledas[1,2], F. J. Olmo[1,2]

[1]*University of Granada, Department of AppliedPhysics,*
[2]*Centro Andaluz de Medio Ambiente (CEAMA), Avda. del Mediterráneo s/n, 18071, Granada, Spain.*

Fuentenueva s/n, 18071-Granada, Spain
tel: +1 (34) 958-240019, fax: +1 (34) 958-243214, e-mail: aquiran@ugr.com

Abstract

Total aerosol scattering and backscattering atmospheric values are typically obtained with an integrating nephelometer. Due to design limitations, measurements usually do not cover the full (0º-180º) angular range, and correction factors are necessary. The effect of angle cutoff is examined for a range of particle size distributions and refractive indices. Scattering data for sub-micron particles can be corrected by the use of a modified Anderson approximation, while data for larger particle distributions can be approximated by a function of the effective size parameter. Such approximation will help more accurate corrections for angle range.

1 Introduction

In order to determine the influence of atmospheric aerosols on climate, visibility and photochemistry, several key aerosol properties are required. These include the aerosol light extinction, single scattering albedo, backscattering fraction and asymmetry parameter. Integrating nephelometers are well suited for this kind of measurements., but only on the condition that operation procedures are followed to minimize practical limitations. Such procedures include accurate calibration and consistent sampling practice, as well as corrections for nonlambertian and truncation errors.

In this paper, the influence of limited angular range measurement (7º-170º) on scattering and backscattering values is analyzed. The need for a correction factor to account for such truncation has been studied [1], but only a limited set of refractive indices and particle size distributions (PSD) was considered, and nonsphericity effrects were neglected. An alternative approach, based on the assumption that the diffraction forward-scattering peak is the same for spherical and nonspherical particles of the same projected area, combines experimental measurements in the 5º-173º angular range with a Lorenz-Mie calculations of the forward scattering (0º-5º) peak. The resulting phase function and that determined experimentally yield similar values for the asymmetry parameter [2].

The purpose of the present work is to provide a more complete set of correction factors for scattering measurements on particle size distributions of both spheres and spheroids.

2 Theory

Light scattering values (extinction, scattering, backscattering coefficients) were calculated at five different refractive indices. Mie theory was used for spheres, and T-matrix was used for randomly oriented prolate and oblate spheroids. The numerical angle integration needed to calculate the correction factors was done by substraction of the forward (0º-7º) and the backward (170º-180º) contributions from the full integrals, e.g.:

$$C^*_{sca} = \tfrac{1}{2} C_{sca}\left(1 - \int_{0^o}^{7^o} p(\vartheta)\sin\vartheta\, d\vartheta - \int_{170^o}^{180^o} p(\vartheta)\sin\vartheta\, d\vartheta\right) \quad (1)$$

for the scattering cross section. Results were then size-averaged assuming a power-law distribution:

$$p(x) = \begin{matrix} Cx^{-3} & x_1 \le x \le x_2 \\ 0 & otherwise \end{matrix} \quad (2)$$

where x stands for the equivalent-volume size parameter in the case of spheroids. A correction ratio F_s=Csca/Csca* was adopted as a measure of the effect of angular range limitation. Instead of using integration limits (x_1,x_2), PSDs are represented by the effective size parameter x_{eff} and the effective variance $<_{eff}$, as they have been found to best characterize any plausible PSD [3]:

$$x_{eff} = \frac{\int_{x_1}^{x_2} x^3 p(x)dx}{\int_{x_1}^{x_2} x^2 p(x)dx} \qquad \nu_{eff} = \frac{\int_{x_1}^{x_2} x^2 (x - x_{eff})^2 p(x)dx}{x_{eff}^2 \int_{x_1}^{x_2} x^2 p(x)dx} \quad (3)$$

The maximum $x_{eff,}$ $<_{eff}$ values for spherical PSDs were chosen as 100 and 10, respectively. Large as they might seem, they are sometimes found airborne, for instance as the combustion products of powdered coal in a power plant, or in the aftermath of large volcanic eruptions [4]. For the case of nonspherical scatterers, computer limitations impose a maximum equivalent-sphere-volume size parameter restriction of about 61-62, thus limiting the range of effective value parameters. In all cases, light scattering parametere were calculated to a minumum accuracy of 10^{-5}.

2 Results

Correction factors for scattering F_s have been compared to the Angstrom exponent over the 8_1 to 8_2 range, defined as follows:

$$\alpha = \frac{-\ln\left[C_{sca}(\lambda_1)/C_{sca}(\lambda_2)\right]}{\ln(\lambda_1/\lambda_2)} \quad (4)$$

(for the present work, 8_1=450 nm, 8_2=700 nm). The near-forward (0-7º) scattering is quite insensitive to shape effects for moderately wide PSDs, so the dependence of nonsphericity on the correction factor can be expected to be small. This effect has been observed in our results. For all but the narrowest size distributions, F_s values for equivalent-volume-size spheroidal particle distributions are identical to those for spheres to within 1-2%. This result has been confirmed for all five refractive index values, at sizes for which T-matrix calculations converged, and for $<_{eff}\exists 0.2$. This supports the view that particle populations of interest can be regarded as spheres as far as scattering correction factors is concerned.

The correction factor F_s can be partially approximated in the form $F_s=a+b\forall$ (Anderson approximation), as Fig 1 shows ($\forall>0.5$ zone). The validity of this approximation depends on both $<_{eff}$ and *m*, and covers only the sub-micrometer size range, but the approximation itself is $<_{eff}$-independent and depends on the value of the refractive index alone. For the smallest size distributions, the correction factor can be better approximated by the Rayleigh-limit value 1.01717.

For lower $\forall$ values, (higher effective size parameters), an Anderson-like approximation is unworkable. The reasons are clear from Fig. 1. First, the functions become multivalued. Second, even in the case of the widest PSDs (where the curve can be represented as another lineal function), such a fitting would have a large slope, so a small uncertainty in the value of $\forall$ could results in large F_s errors. In those cases, the monotonic behavior of the F_s -x_{eff} curve allows for an approximation in the form F_s =a+bLn(x_{eff}) or F_s =c+d*x_{eff}, the range of validity depending on the PSD and *m* value.

The correction factor for backscattering F_b is not monotonic and cannot be easily represented by a lineal function of either x_{eff} or Ln(x_{eff}), but it is in general a small amount. For nonspherical scatterers, it has values in a small range, F_b =1.01-1.02 for nonspherical particles, as the example of Fig. 2 shows. Only for the smallest PSDs (x_{eff}<1) is a higher correction factor needed, as it slowly increases towards the Rayleigh limit 1.02314. Spherical scatterers show a larger F_b range (except the high-absorbing case, *m*=1.6+i0.6). This result suggests that a correction based on Mie theory yields worse results than not correcting at all. Only when a natural particle population can be regarded as spherical should Mie-based corrections be considered.

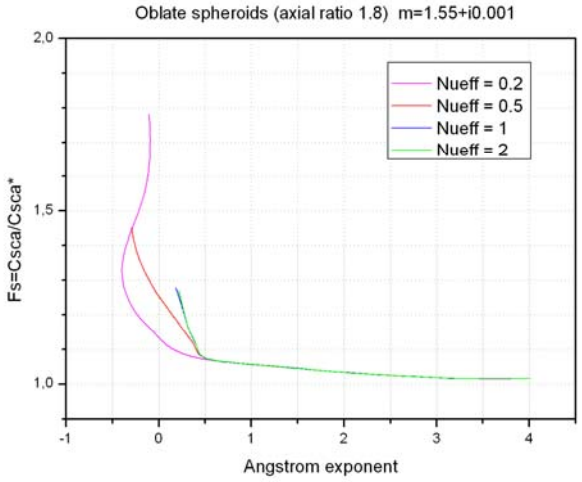

Figure 1: Scattering correction factor

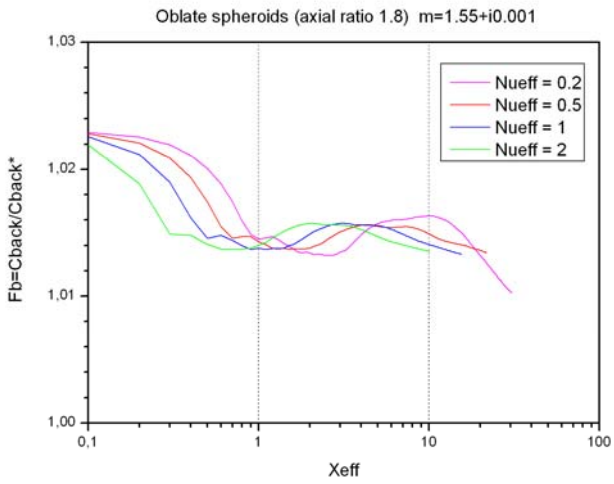

Figure 2: Backscattering correction factor

Acknowledgments

This work was supported by La Dirección General de Ciencia y Tecnología from the Education and Research Spanish Ministry through Projects CGL2004-05984-C07-03 and by Andalusian Regional Government through Project P06-RNM-01503. Financial support from the Spanish Ministry of Science and Education (Grant FIS2005-06860-C02-01) is gratefully acknowledged.

References

[1] T. L. Anderson, J. A. Ogden, "Determining aerosol radiative properties using the TSI 3563 integrating nephelometer" Aerosol Sci. Technol. **29**, 58-69 (1998)

[2] L. Liu, M. I. Mishchenko, J. W. Hovenier, H. Volten, O. Muñoz, "Scattering matrix of quartz aerosols: comparison and synthesis of laboratory and Lorenz-Mie results". JQSRT **79-80**, 911-920 (2003)

[3] J. E. Hansen, L. D. Travis, "Light scattering in planetary atmospheres" Space Sc. Rev. **16**, 527-610 (1974)

[4] O. Muñoz, H. Volten, J. F. de Haan, W. Vassen, J. W. Hovenier, "Experimental determination of scattering matrices of randomly oriented fly ash and clay particles at 442 and 633 nm" J. Geophys. Res. **106**, 22.833-22.844 (2001)

Light scattering properties of a spheroid particle illuminated by an arbitrarily shaped beam

K. F. Ren,[1] F. Xu,[1,2] X. Cai,[2]

[1] *UMR 6614/CORIA, CNRS – Université & INSA de Rouen*
av. de l'Université, 76801 Saint-Etienne du Rouvray, France
[2] *Institute of Particle and Two-phase Flow Measurement Technology, University of Shanghai for Science and Technology, 516 Jungong Rd, Shanghai 200093, China*
tel: +33(0)232953743, fax: +33(0)232953794, e-mail:fang.ren@coria.fr

Abstract

The theories to predict the light scattering properties, such as the scattering diagram, the rainbow angles, the absorption, scattering and extinction cross sections, as well as the radiation pressure forces of a spheroid illuminated by an arbitrarily located, oriented and shaped beam are presented and numerical results are given for different parameters of the particle and the beam.

1 Introduction

The particles encountered in many practical processes, such as the droplets in spray atomization and biological cells, are not spherical. Their optical properties are more or less different from those of spherical ones. The model of spheroid particle is a first order approximation of those non-spherical particles in order to improve the relevant measurement techniques, to better characterize the real particles and to understand the formation of them. When the particle is illuminated by a focused laser beam as in optical tweezers and its size is larger or at the order of radius of the incident beam the non-homogeneous illumination must be considered.

Based on the rigorous solution of Maxwell equations[1] Asano has studied the scattering properties of a spheroid particle when it is illuminated by a plane wave[2]. Barton[3] and Xu *et al*[4-5] have treated the scattering of a laser beam by a spheroid particle in the framework of generalized Lorenz-Mie theory (GLMT). But the rigorous theories are hardly be applied to large particle because of numerical difficulties. The geometrical optics approximation (GOA) is just appropriate to treat such a problem. Lock has studied the diffraction and specular reflection[6] as well as the transmission and cross-polarization effects[7] for an arbitrarily oriented spheroid in the case of plane wave illumination. Xu *et al*, on the other hand, have extended this approach to the scattering of a spheroid for the on-end incidence of a Gaussian beam which permits to predict the scattering diagram in all direction and the rainbow angle for a spheroid of an arbitrary aspect ratio[8].

In this communication we will present the light scattering properties calculated by the rigorous model for small particle and by geometrical optics approximation for large one.

2 Generalized Lorenz-Mie Theory for arbitrarily oriented shaped beam

In General Lorenz-Mie Theory (GLMT), an arbitrarily oriented, located and shaped beam is expanded in spheroidal vector wave functions $\mathbf{M}_{mn}^{(i)}$ and $\mathbf{N}_{mn}^{(i)}$ with two sets of beam shape coefficients $G_{n,TM}^{m}$ and $G_{n,TE}^{m}$. Then all scattering properties can be expressed by the scattering coefficients of the particle A_n^p and B_n^p. For example, the radiation pressure forces are given by:

$$C_{pr,x}=\frac{\lambda^2}{4\pi}\sum_{p=1}^{+\infty}\sum_{n=p-1\neq 0}^{+\infty}\sum_{n'=p}^{+\infty}\mathrm{Re}\left[L_{nn'}^{p-1}\left(2U_{nn'}^{p-1}-S_{nn'}^{p-1}\right)+L_{n'n}^{-p}\left(2U_{n'n}^{-p}-S_{n'n}^{-p}\right)+iM_{nn'}^{p-1}\left(2V_{nn'}^{p-1}-T_{nn'}^{p-1}\right)+iM_{n'n}^{-p}\left(2V_{n'n}^{-p}-T_{n'n}^{-p}\right)\right],$$

$$C_{pr,y}=\frac{\lambda^2}{4\pi}\sum_{p=1}^{+\infty}\sum_{n=p-1\neq 0}^{+\infty}\sum_{n'=p}^{+\infty}\mathrm{Im}\left[L_{nn'}^{p-1}\left(2U_{nn'}^{p-1}-S_{nn'}^{p-1}\right)+L_{n'n}^{-p}\left(2U_{n'n}^{-p}-S_{n'n}^{-p}\right)+iM_{nn'}^{p-1}\left(2V_{nn'}^{p-1}-T_{nn'}^{p-1}\right)+iM_{n'n}^{-p}\left(2V_{n'n}^{-p}-T_{n'n}^{-p}\right)\right],$$

$$C_{pr,z}=\frac{\lambda^2}{4\pi}\sum_{p=-\infty}^{+\infty}\sum_{n=|p|\neq 0}^{+\infty}\sum_{n'=|p|\neq 0}^{+\infty}\mathrm{Re}\left[J_{nn'}^{p}\left(O_{nn'}^{p}+P_{nn'}^{p}\right)+ipK_{nn'}^{p}\left(Q_{nn'}^{p}-R_{nn'}^{p}\right)\right],$$

where the coefficients $J_{nn'}^{p}\sim V_{nn'}^{p}$ are all expressed in the beam shape coefficients $G_{n,TM}^{m}$ and $G_{n,TE}^{m}$ and the scattering coefficients of the particle A_n^p and B_n^p.

Fig. 1 presents the radiation pressure force $C_{\mathrm{pr,z}}$ predicted for a sphere, a prolate and an oblate spheroid. The incidence and polarization angles are assumed to be 0°. The relative refractive index of the particle $\hat{m}$ =1.5. The dashed line is for a prolate spheroid of the semi-minor axis equal to the radius of the projection area (b=R) and the dotted line is for an oblate spheroid of the semi-major axis equal to the radius of the projection area (a=R). We find that the oscillation of the prolate spheroid is much weaker for laser beam illumination than for plane wave case.

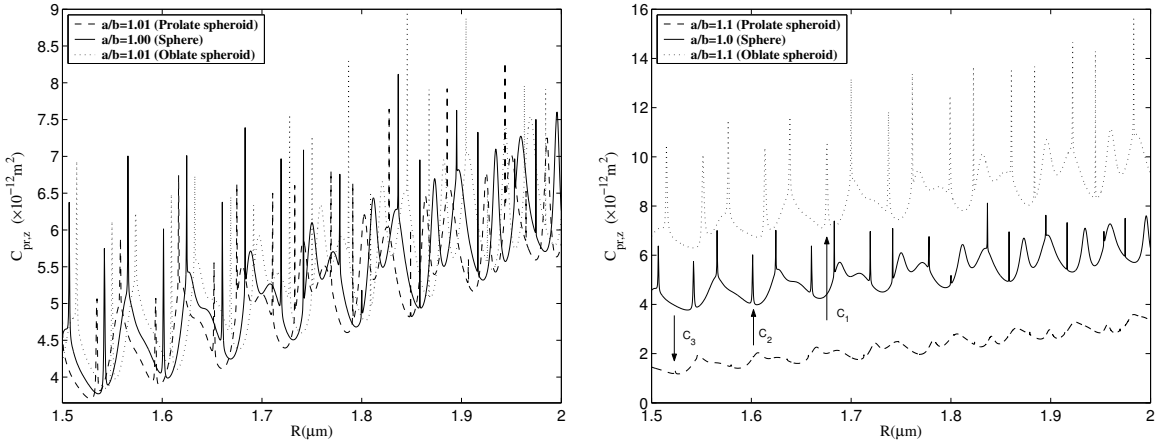

(a) plane wave incidence (b) beam incidence case

Figure 1. Longitudinal radiation pressure cross section $C_{\mathrm{pr,z}}$ exerted by the plane wave on the spheroid. For clarity and convenient identification, the RPCS curves of the prolate and oblate spheroids have been offset by the factors 2×10^{-12}, -2×10^{-12} respectively.

On the other hand, according to the discontinuity of the electromagnetic field, the surface force can also be calculated by the GLMT. We can then predict the deformation of a biological cell in the optical tweezers for example.

3 Extension of geometrical optics approximation

In the extension geometrical optics approximation (EGOA)[8], a shaped beam is considered as a bundle of rays. Each of them is reflected or refracted at the surface of the particle. The scattered wave is then the sum of all the rays in considering the amplitude and the phase of each ray.

The scattering intensity I_j of j^{th} ray in the far-field at an observation point of distance r from the particle center is given by:

$$I_j=\frac{I_0}{(kr)^2}i_j(\theta)=\frac{I_0}{(kr)^2}\left|S_j(\theta)\right|^2$$

where the complex amplitude $S_j = S_d + \sum_{p=0}^{\infty} S_{j,p}$, S_d is the diffracted contribution, S_j is the amplitude of the ray of order *p*.

It should be pointed out that when the particle is illuminated by a shaped beam, the phase in the complex amplitude is composed of three parts: the phase shift due to the optical path $\phi_{p,PH}$, the phase shift due to the focal lines (inside and out of the sphere) $\phi_{p,FL}$ and that due to the wave front curvature of the shaped beam ϕ_G:

$$\phi_p = \left(\frac{\pi}{2}\right) + \phi_{p,PH} + \phi_{p,FL} + \phi_G$$

A scattering diagram of a sphere illuminated by a Gaussian beam calculated by GLMT and EGOA for the on-axis case. We find that when the beam radius is smaller than the particle radius the agreement of the two methods is very good. But when the beam is much larger than the particle radius the discrepancy becomes remarkable around the rainbow angle and 90°.

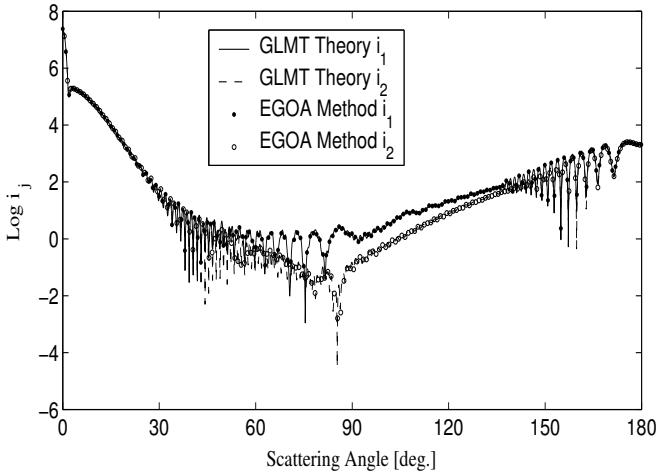

Figure 2. Comparison of the scattering intensities calculated by GLMT and EGOA for a pure water droplet of refractive index $m = 1.33$ and radius $a = 25$ μm illuminated by a Gaussian beam of waist radius $w_0 = 10$ μm and wavelength $\lambda = 0.6328$ μm. The particle is located at the center of the beam.

It is well known that the rainbow angle is very sensitive to the form of the particle. Möbius has proposed a model to predict the rainbow position of a spheroid of aspect ratio near unity. With the EGOA we can predict the rainbow angle for any aspect ratio.

The primary rainbow position of a spheroid of water droplet (m=1.33) with on-end incidence of a Gaussian beam predicted by EGOA is shown in Fig. 3. We can distinct three zones. When the aspect ratio is less than 1.4 the rainbow angle increases as function of the aspect ratio and the formation mechanism is the same as for a spherical particle. There is no primary rainbow when the aspect ratio is between 1.4 and 1.65. The rainbow reappears for the spheroid of aspect ratio larger than 1.65. The rainbow angle decreases as function of the aspect ratio and the formation mechanism is not the same. We find also that the rainbow position is not sensitive to the beam radius.

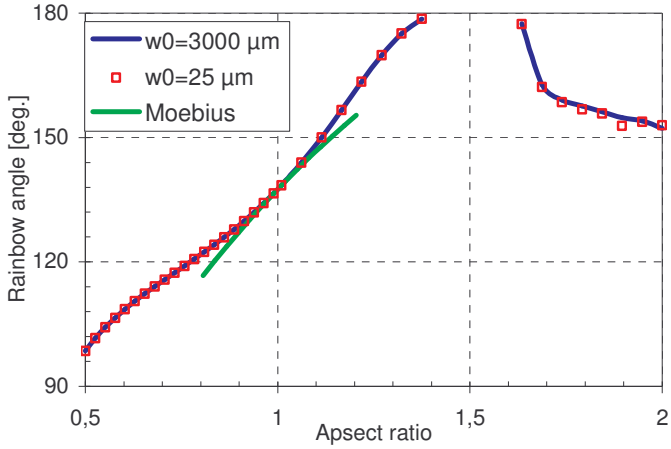

Figure 3. Primary order rainbow position versus aspect ratio, predicted by EGOA method for a spheroid droplet of projection radius R=100µm and illuminated by the Gaussian beam of waist radii w_0=25, and 3000µm, respectively.

4 Conclusion

The light scattering properties of a spheroid illuminated by a shaped beam can be predicted by the rigorous theory in the framework of generalized Lorenz-Mie theory for relatively small particle or by geometrical optics approximation for large particle. Some numerical results are exemplified.

References

[1] S. Asano and G. Yamamoto, "Light scattering by a spheroid particle," *Appl. Opt*. **14**(1), 29–49 (1975).

[2] S. Asano, "Light scattering properties of spheroidal particles" *Appl. Opt.* **18**(5), 712-723 (1979).

[3] J. P. Barton, "Internal and near-surface electromagnetic fields for a spheroidal particle with arbitrary illumination," *Appl. Opt.* 34, 5542-5551 (1995).

[4] F. Xu, K. F. Ren, X. Cai, G. Gouesbet and G. Grehan, "Generalized Lorenz-Mie theory for arbitrarily oriented, located and shaped beam scattering by a homogeneous spheroid", *J. Opt. Soc. Am. A*, 24(1), 119-131 (2007).

[5] F. Xu, K. F. Ren, G. Gouesbet, X. Cai and G. Grehan, "Theoretical prediction of radiation pressure force exerted on a spheroid by an arbitrarily shaped beam", *Physical Review E*, 026613, (2007)

[6] J. A. Lock, "Ray scattering by an arbitrarily oriented spheroid. I. Diffraction and specular reflection," *Appl. Opt*. 35, 500–514 (1996).

[7] J. A. Lock, "Ray scattering by an arbitrarily oriented spheroid. II. Transmission and cross-polarization effects," *Appl. Opt*. 35, 515–531 (1996).

[8] F. Xu, K. F. Ren, X. Cai and J. Shen, "Extension of geometrical-optics approximation to on-axis Gaussian beam scattering. II. By a spheroidal particle with end-on incidence", *Appl. Opt,*. 45(20), 5000-5009 (2006).

Identification of radiative parameters of dense scattering media with polarization analysis

RIVIERE Nicolas[1], HESPEL Laurent[1]

[1] *Onera, Theoretical and Applied Optics Department*
Light Interaction with Matter, Imaging and detection Laser Systems Unit
2 avenue Edouard Belin, BP4025, 31055 Toulouse cedex 4, France
tel: +33 562 25 26 24, fax: +33 562 25 25 88, e-mail: nicolas.riviere@onera.fr

Abstract

Predicting the radiative properties of diluted scattering media and determining the BRDF-BTDF for dense scattering media require a good estimation of microphysical parameters such as particle size distribution. Polarized light scattering bears information that can favor the characterization of these media. Our study aims to introduce polarized data into the optimization scheme to find the optical thickness, the albedo, and the Mueller matrix. Direct 1D codes (adding-doubling) and 3D codes (Monte Carlo) have been developed to solve the polarized radiative transfer equation (VRTE). After a study of sensitivity, we adopt the inversion strategy. The optical thickness, albedo and others parameters which describe the Mueller matrix are identified recursively and coupled by optimization methods. The particle size distribution is then extracted from the Mueller matrix. After numerical validation of this concept, an experimental validation is conducted on reference media, using a specifically developed system (MELOPEE bench).

1 Introduction

Optical properties of scattering media are important for several applications like remote sensing, climatology, biomedical imaging, spray or paint coating... Considering absorbing and scattering made-man media, some effects as multiple scattering should be investigated. Three ways of study are possible: measurements, direct modeling by radiative transfer or electromagnetic methods, and identification of radiative parameters. In this paper, we choose an identification of the radiative parameters for spherical particles in cell or coating media. Simulation of scattering properties requires a good knowledge of the Particle Size Distribution (PSD), the shape or the optical indexes. Moreover, dense scattering and absorbing media can be affected by dependent effects. Therefore, direct modeling is quite difficult to perform. Radiative parameter identification is a useful tool to look into scattering media but a lot of works consider unpolarized data [1-2]. It generally implies the optical thickness (OT) to be known and functions which represent the scattering parameters to be simplified. Then, the identification is more difficult for high optical thickness. This paper's aim is to improve actual optimization schemes in order to develop a robust method and to analyze the contribution of polarized data to a better and simultaneous estimation of all the radiative parameters (OT, albedo and Mueller matrix).

2 Identification of radiative parameters

We already demonstrated that the polarization state after scattering gives information to characterize scattering media [3]. The Stokes-Mueller formalism is selected to describe the evolution of the polarization of the light. In fact, it uses real quadratic values directly measured by detectors. The degree of polarization is represented by the ratio between the second and the first elements of the scattered Stokes vector. During an optimization process, it allows to be free from the uniqueness of the solution when we consider a multiple scattering media.

2.1 Optimization principle

To represent the Mueller matrix (**M**) efficiently in an optimization scheme with limited CPU time, we consider particles randomly oriented. **M** can be describe by a Legendre polynomial decomposition where μ is the cosine of the quadratic angle.

$$\mathbf{M} = \begin{bmatrix} M_{11} & M_{12} & 0 & 0 \\ M_{12} & M_{22} & 0 & 0 \\ 0 & 0 & M_{33} & M_{34} \\ 0 & 0 & -M_{34} & M_{44} \end{bmatrix}, \; M_{ij} = \sum_{n=0}^{N} (2 \cdot n + 1) \cdot a_n \cdot P_n(\mu) \tag{1}$$

There is no assumption on particles but this method needs too many parameters to represent the Mueller matrix (*e.g.* 240 parameters if $r_g = \lambda$ for spherical particles). If optical indexes and particle morphology are known, a second way consists in building a base of scattering matrices against the radius. During the optimization, we make an integration over the PSD. It is a sum of log-normal distributions each represented by 3 parameters (f, r_g, s_g).

$$n(r) = \sum f \cdot \frac{1}{(2\pi)^{1/2} \cdot r \cdot \ln(s_g)} \cdot e^{-\frac{(\ln(r) - \ln(r_g))^2}{2 \cdot \ln^2 s_g}} \tag{2}$$

The general optimization scheme is described by Figure 1. First, we model the polarized scattered light using "direct" codes. We consider an heterogeneous and 1D media with N homogeneous layers. The Vectorial Radiative Transfer Equation (1D-VRTE) is solved by an adding-doubling method and a Fourier decomposition of the radiance [4]. We take into account the layers' modification as the optical index. In this study, the method is limited to flat interfaces with unpolarized or linearly polarized incident beam. The approach is validated with referenced analytical data [5] and by comparison to data generated by a Monte Carlo model (3D). Then, we define an objective function to make a comparison between referenced (*e.g.* experimental) and simulated data. The minimization of this function is done by considering optimization methods (quasi-Newton or simulated annealing process).

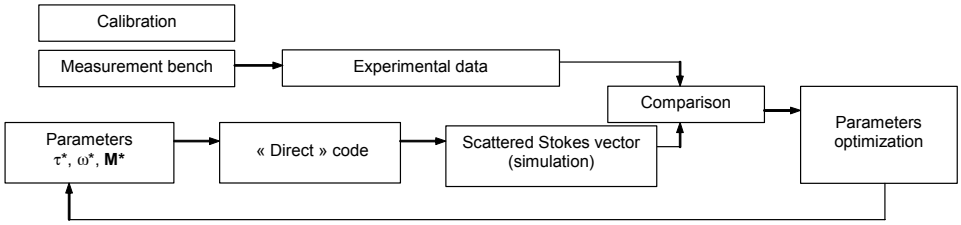

Figure 1: General optimization scheme.

2.2 Sensitivity analysis

This section aim is to determine the domain of validity for an objective function used in the optimization process. The analysis is restricted to spherical particles and to two polarized data of interest witch are the BRDF-BTDF ($\mu.I$) and the degree of linear polarization (*DOLP* or *Q/I*). The study is performed considering a non polarized incident radiance ($\vec{L}_{inc} = (1,0,0,0)^T$) and an incident vector collimated with the normal of the surface ($\mu_{inc} = 1$). Both polarized data ($\mu.I$ and *Q/I*) are invariant for all azimuth planes. The normalized sensitivity coefficient is proportional to the scattered-Stokes-vector derivative and is defined by Eq. (3). This value is calculated for each interest parameters described above.

$$C_{S,normalized} = \frac{x_j}{L_{scattered,i}} \cdot \frac{\partial L_{scattered,i}}{\partial x_j} \tag{3}$$

Then, it may be deduced a restricted angular range (*cf.* Table 1) where the objective function of each parameter should be done. The originality of our study is that all angular ranges are not dependent on each other in order to steer clear of parameters dependence in the optimization process. The BRDF-BTDF is used to make the objective function depending on the albedo whereas the degree of depolarization is used for the OT determination.

Table 1: angular range.

	OT	Albedo	PSD (r_g)
$\mu \, . \, I$ reflected	-	-0.75<μ<-0.25	-1<μ<-0.75
$\mu \, . \, I$ transmitted	-	0<μ<0.25	0.75<μ<1
Q/I reflected, if albedo ~ 1	-0.5<μ<0 if OT<1.5	-	-
	-1<μ<-0.5 if OT>1.5	-	-
Q/I reflected, if albedo ≠ 1	-0.5<μ<0	-	-
Q/I transmitted	-	-	0.75<μ<1

The global objective function F is a sum of functions defined for each parameter: $F = \alpha_{OT} \cdot F_{OT} + \alpha_{\omega} \cdot F_{\omega} + \alpha_{PSD} \cdot F_{PSD}$. This conditioning problem advantage is that the optimization is improved. Nevertheless, we must weight the sum in the global objective function (α_i).

2.3 Numerical validation of the optimization

Referenced data are generated by numerical models. First, each objective function is validated and then the global objective function is tested. Parameters are identified with less than 10% of accuracy.

However, some limits appear in this approach. For high OT it is more difficult to retrieve the albedo or the PSD (*cf.* Figure 3a). Furthermore, the particle optical index should be known. The error is quite equal to 50% when the optical index is set to 1.65 instead of 1.58 for latex particles. In fact, phase functions are mainly affected by its value. Considering measurement noise simulated by a standard deviation, the OT is well optimized but the albedo is more difficult to be assessed (*cf.* Figure 3b).

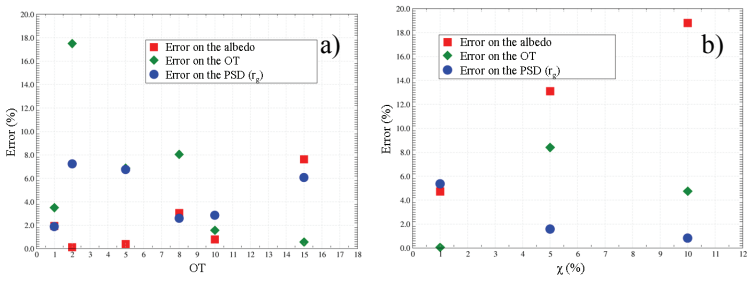

Figure 3: Error on the retrieved parameters according to the value of the OT (a) and to the standard deviation parameter χ (b).

3 Optimization based on experimental data

We intend also to validate experimentally the method. A polarized light scattering measurement setup based on the work of Kuik *et al*. [6] was developed. This automated setup could measure in the incident plane both the polarized BRDF-BTDF and the degree of linear polarization on a cross polarized way. Direct measurements of the optical thickness on a dedicated way are also available. The calibration is done using referenced materials like spectralon or calibrated latex particles into an analysis cell. This part of our study will be explained in detail during the oral session. A first experimental validation is performed with latex particles into an analysis cell (r_g = 530 nm). The albedo is assumed to be equal to 1 (no absorption). The measured OT on the dedicated experimental setup is equal to 2.1. The retrieved values after optimization on the 3 parameters (OT, albedo and PSD) are displayed on Table 2.

Table 2: Retrieved values of the OT, the albedo and the PSD.

	OT	Albedo	PSD (r_g)
Retrieved values	2.13	0.96	0.517 nm
Error	4%	4%	3%

5 Conclusion and perspectives

To conclude, this approach involves a good efficiency of the optimization scheme with limited CPU time. Moreover, we have verified the identification method sturdiness for several perturbing phenomenon even for a high optical thickness. The inverse approach has been assessed by numerous numerical simulations in order to determine its validity domain. The retrieved parameters accuracy derived from the optimized outputs is less than 10%. A numerical validation of this concept is actually performed with non-spherical particles. All of these results will be presented in the oral session. We also intend to expend the experimental validation of this method on scattering media made of non-spherical particles. Calibrated media made of non-spherical particles will then be used in the future.

References

[1] L. Hespel, S. Mainguy, J.J. Greffet, “Radiative properties of scattering and absorbing dense media: theory and experimental study”, JQSRT **77**, 193-210 (2003).

[2] Yu. Shkuratov, A. Ovcharenko, E. Zubko, H. Volten, O. Muñoz, G. Videen, “The negative polarization of light scattered from particulate surfaces and of independently scattering particles”, JQSRT **88**, 267-284 (2004).

[3] N. Rivière, L. Hespel, G. Gréhan, “Schemes of calculations and measurements of polarized radiative properties of dense media with intermediate optical thickness”, ELS8, 278-281 (2005).

[4] K.F. Evans, G.L. Stephens, “A new polarized atmospheric radiative transfer model”, JQSRT **46**, 413-423 (1991).

[5] K.L. Coulson, J.V. Dave, Z. Sekera, “Tables related to radiation emerging from a planetary atmosphere with Rayleigh scattering, University of California press, Berkeley, 1960.

[6] F. Kuilk, P. Stamnes, J.W. Hovenier, “Experimental determination of scattering matrices of water droplets and quartz particles”, Appl. Opt. **30**, 4872-4881 (1991).

Circular and linear polarization of comet C/2001 Q4 (NEAT). Why circular polarization in comets is predominantly left-handed?

V. Rosenbush,[1] N. Kiselev,[1] N. Shakhovskoy,[2] S. Kolesnikov,[3]
V. Breus,[3]

[1] *Main Astronomical Observatory of National Academy of Science of Ukraine, Zabolotnoho str.27, 03680 Kyiv, Ukraine*
[2] *Crimean Astrophysical Observatory, 98409 Nauchny, Crimea, Ukraine*
[3] *Astronomical Observatory of Odessa National University, T. G. Shevchenko Park, 65014 Odessa, Ukraine*
tel: +380-44-5262147, fax: +380-44-5262147, e-mail: rosevera@mao.kiev.ua

Abstract

We present the results of new polarimetric observations of comet C/2001 Q4 (NEAT). Measurements of circular and linear polarization were made with the 2.6-m Shain telescope of the Crimean Astrophysical Observatory on May 21–23, 2004. A significant correlation between variations of circular and linear polarization measured along the cuts through the coma and nucleus of the comet was found. It means that single scattering of light on aligned non-spherical dust particles can produce circular as well as linear polarization. We call particular attention to the fact that the measured circular polarization in four comets, 1P/Halley, C/1995 O1 (Hale–Bopp), D/1999 S4 (LINEAR) and C/2001 Q4 (NEAT), was predominately left-handed. This question is discussed in the frame of light scattering by optically active organic particles.

1 Introduction

Circular polarization is sensitive to the shape, structure, and composition of the scatterers and thus may provide further proof of a complex structure of cometary grains and put constraints on their shape and composition. However, the measurements of circular polarization in comets are still rare. Attempts to detect circular polarization in comets C/1969 T1 (Tago–Sato–Kosaka), C/1973 E1 (Kohoutek), C/1974 C1 (Bradfield), and C/1975 VI (West) were unsuccessful [1,2]. Notably nonzero circular polarization was measured only for comets 1P/Halley [3], C/1995 O1 (Hale–Bopp) [4,5], and D/1999 S4 (LINEAR) [6]. Therefore it is still unclear if circular polarization is an inherent feature of all comets. In this connection any new attempt to detect of circular polarization in comets is critically important.

2 Observations and data reduction

Measurements of circular polarization in comet C/2001 Q4 (NEAT) (hereafter Q4 (NEAT)) were made with a one-channel photoelectric photometer-polarimeter mounted at the 2.6-m Shain telescope of the Crimean Astrophysical Observatory. The photopolarimeter works on the same principle as was described by Shakhovskoj et al. [7]. However, instead of four counters we used eight ones for registration of impulses. It allowed us to measure simultaneously both circular and linear polarization of the comet.

The comet was observed during three nights on May 21–23, 2004. The wide-band R filter and 10 arcsec diaphragm (4350 km at the comet) were used. The phase angle, the heliocentric and geocentric distances of the comet were $\alpha \approx 76°$, $r \approx 0.97$ AU, and $\Delta \approx 0.60$ AU respectively. The comet had the straight gas tail orientated at position angle PA=100.5° and the dust jet located approximately orthogonally to the gas tail. This comet was very active. The measurements of the total intensity and parameters determining the circular and linear polarization of the scattered light were made along cuts

over the coma. The diaphragm was placed on the northern side of the coma in such a way that each cut passed through the nucleus. The cuts over the coma were determined by proper motion of the comet at position angle $PA = 189.4°$ and passed along the dust jet. The single exposure time was 4 s and each cut consisted of 64 measured points that corresponds to approximately 9000 km at the distance of the comet. To improve the signal-to-noise ratio, we obtained from 15 to 20 cuts during a given observational night which were subsequently summarized. The results in the form of distributions of total intensity I, degree of circular P_c and linear P_l polarization, and position angle of the polarization plane θ_r relative to the scattering plane are presented in Fig. 1. Each data point is result of averaging over the area 2000×4350 km along the cuts.

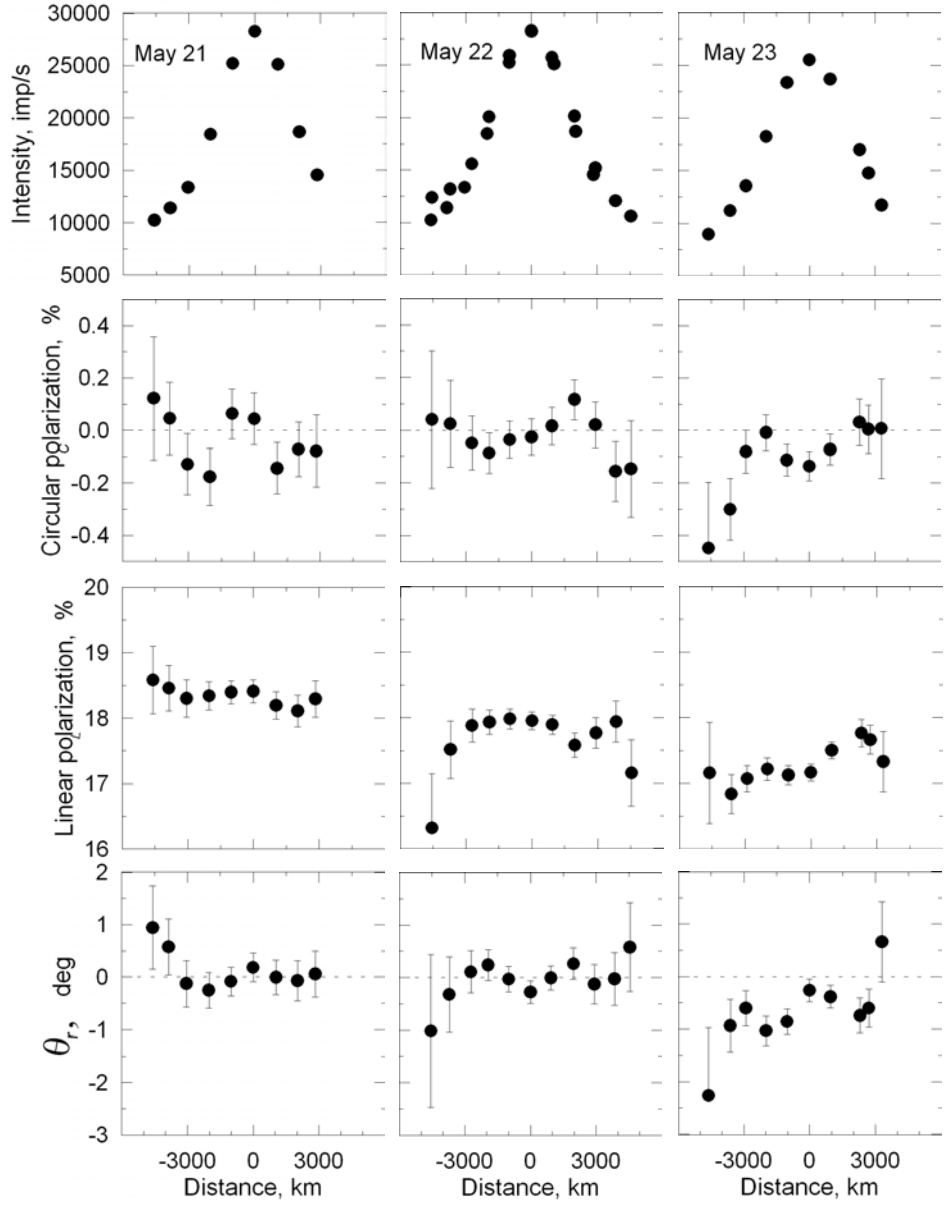

Figure 1: Distribution of intensity I, degree of circular and linear polarization and position angle of the polarization plane relative to the scattering plane θ_r along the cuts in coma of comet Q4 (NEAT).

3 Results and discussion

As Fig. 1 shows, the variations of circular polarization along the cuts correlate with the changes of parameters of linear polarization P_l and θ_r. We have found that the coefficients of correlation between P_c and P_l are 0.740, –0.225, and 0.618 on May 21, 22, and 23 respectively, while the coefficients of correlation between P_c and θ_r for the same dates are 0.762, –0.405, and 0.705. A significant correlation between these parameters means that there is a common reason which gives rise to changes in circular and linear polarization of the comet. Such reason may be aligned non-spherical particles. It is generally believed that scattering of light on aligned non-spherical particles is most effective mechanism for producing circular polarization in comets. Thus, the same changes of the parameters of linear and circular polarization along the coma testify that there is significant component of polarization that is not related to the scattering plane and can be explained by inhomogeneity or anisotropy of dust medium in which the particles are partly aligned.

The measurements of circular polarization in comet Q4 (NEAT) as well as in three others (Halley, Hale–Bopp, and S4 (LINEAR)) show that the left circularly polarized light was mainly observed over the coma. This effect is well seen in Fig. 2.

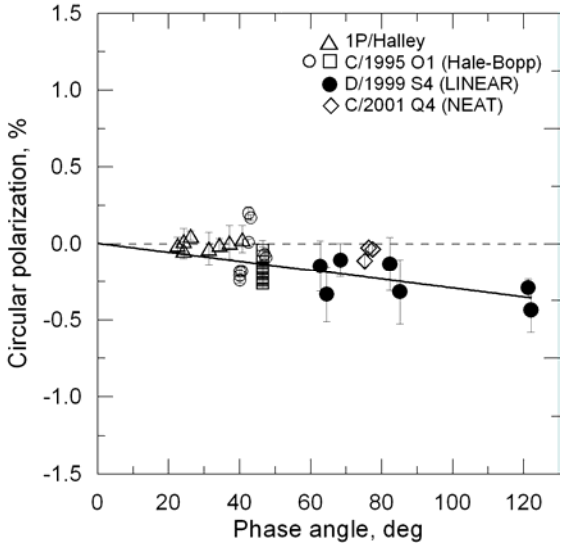

Figure 2: Composite phase-angle dependence of circular polarization for comets Q4 (NEAT), S4 (LINEAR), Hale–Bopp, and Halley. Data for comets Halley and Hale–Bopp are taken from [3, 5].

Circular polarization indicates a violation of symmetry in the medium. However, circular polarization may appear as a result of intrinsic asymmetry of the particles themselves, i.e. scattering of light by particles composed of optically active materials. Optically active substance has different refractive indexes for right- and left-circularly polarized light and therefore light of different handiness has different speed in the medium that leads to separation of left- and right-handed polarized waves and rotation of the plane of linearly-polarized light [8]. These effects are especially strong for organic molecules since they are not only optically active, but also possess circular dichroism, i.e. such substances have different absorption for left- and right-handed circular polarization [9]. It is known that complex organic molecules exist in two forms: L (left-handed) and D (right-handed). For terrestrial biomolecules, there are only L-amino acids and D-sugars. For a long time it was believed that asymmetry in the number of L and D biomolecules, i.e. homochirality, has Earth origin and relates to the birefringence of some Earth minerals. But then L-enantiometric excess was found in amino-acids from the Murchison and Murrey meteorites

[10], suggesting an origin in the pre-solar nebula. This idea was confirmed when the high degree of circular polarization was measured in star-forming regions [11]. The origin of homochirality is explained by illumination of cosmic organics by circularly polarized light in protoplanetary nebulae. In that case chiral organics should be found not only in meteorites but also in other primitive bodies, including comets. Predominantly left-handed circular polarization in comets may testify in favour of L-enantiometric excess in cometary organics.

4 Conclusion

We present the results of the measurements of circular and linear polarization in comet Q4 (NEAT). The correlation between the degree of circular polarization and the degree and plane of linear polarization was found. We have also revealed that all comets with a significant value of circular polarization show a common feature, namely predominantly left-handed circularly polarized light. It testifies in favor of L-enantiometric excess in cometary organics.

Acknowledgments

We are very grateful to I. L. Andronov for the POLAROBS code. V. Rosenbush acknowledges SOC of the ELS-10 for the financial support.

References

[1] G. W. Wolf, "A search for elliptical polarization in starlight," Astron. J. **77**, 576–583 (1972).

[2] J. J. Michalsky, "Optical polarimetry of Comet West 1976 VI," Icarus. **47**, 388–396 (1981).

[3] A. Dollfus and J.-L. Suchail, "Polarimetry of grains in the coma of P/Halley I. Observations," Astron. Astrophys. **187**, 669–688 (1987).

[4] V. K. Rosenbush, N. M. Shakhovskoj, and A. E. Rosenbush, "Polarimetry of comet Hale–Bopp: Linear and circular polarization, stellar occultation," Earth, Moon, Planets. **78**, 381–386 (1997).

[5] N. Manset and P. Bastien, "Polarimetric observations of comets C/1995 O1 Hale–Bopp and C/1996 B2 Hyakutake," Icarus. **145**, 203–219 (2000).

[6] V. Rosenbush, L. Kolokolova, A. Lazarian et al., "Circular polarization in comets: Observations of comet C/1999 S4 (LINEAR) and tentative interpretation," Icarus. **186**, 317–330 (2007).

[7] N. M. Shakhovskoj, I. L. Andronov, S. V. Kolesnikov, and A. V. Khalevin, "Methodics of measurements of circular polarization by using one-channel photopolarimeter," Izvest. Krymskoy Astrofis. Obs. **97**, 91–100 (2001).

[8] C. F. Bohren and D. R. Huffman, *Absorption and Scattering of Light by Small Particles* (Wiley, New York, 1983).

[9] R. Wolstencroft, G. Tranter, and D. Le Pevelen, *Diffuse reflectance circular dichroism for the detection of molecular chirality: An application in remote sensing flora*,. In: Bioastronomy 2002: Life Among the Stars (R. Norris, F. Stootman, Eds.) pp. 149–156, (Astron. Soc. of the Pacific, San Francisco, 2002), (2004).

[10] S. Pizzarello and G. Cooper, "Molecular and chiral analyses of some protein amino acid derivatives in the Murchison and Marray meteorite," Meteor. Planet. Sci. **36**, 897–909 (2001).

[11] J. H. Hough, J. Bailey, A. Chrysostomou et al., "Circular polarization in star-forming regions: possible implications for homochirality," Adv. Space. Res. **27**, 313–322 (2001).

Anisotropy Parameters for *Chlorophytum* leaf Epidermis

Sergey Savenkov,[1] Ranjan S. Muttiah,[2] Viktor V. Yakubchak,[1] Alexander S. Klimov[1]

[1] *Department of Radio Physics Taras Shevchenko University, Kiev, Ukraine, e-mail: sns@univ.kiev.ua,*

[2] *Depts. Environmental Science & Geology , Texas Christian University, Fort Worth, Texas 7612, USA tel: +1 (817) 257-6272, fax: +1 (817) 257-7789, e-mail: r.muttiah@tcu.edu*

Abstract

Mueller polarization experiments on the epidermis layer of the chlorophytum leaf are presented. Three anisotropy parameters (from among the six) are presented and interpreted.

1 Introduction

Plant leaves have been fine tuned by evolution to capture red and blue photon energy from the sun, transfer electron energy without radiation loss from chlorophyll to chlorophyll molecule to reaction centers, and convert that energy to photosynthetic products. The electric potential required to split water occurs across the thylakoid membrane at these reaction centers. A chlorophyll molecule consists of a porphyrin ring, and a pytol tail. The plane of the poryphyrin ring with respect to the incident electric vector determines the singlet state of the π-orbital electron. In general, the majority of the chlorophyll molecules in mesophyll cells aren't preferentially aligned but rather randomly oriented, except perhaps for the chlorophyll molecules in the PSI and PSII reaction centers [1]. First light must transmit through the leaf surface – which can contain waxes and hairs, and epidermis cells before it reaches the carbohydrate factories in mesophyll cells. Like all plant cells, the epidermis has an outer cell wall providing structural rigidity; buildings are only as good as the strength of their walls. We know much about the biochemical reactions, and atomic scale structures of the molecules regulating photosynthesis [2]. Yet we don't know much about the role that light properties have played in constraining the structure and location of cells and molecules in the leaf. We know from other instances in nature that bees use the polarization of the sky for navigation; UV sensitive rhodopsin is preferentially oriented in specialized microvilli in the dorsal part of the compound eye helping focus and detect plane polarized light. Many other arthropods also seem to use polarization to navigate their way about [3-4].

Do plants control incident light polarization?

2 Method

In order to elucidate the role played by the epidermis cells in controlling light polarization, we performed Mueller polarimetry experiments as shown in Fig.1. The laser beam (λ = 630 nm) was normally transmitted through the epidermis layer and imaged on a 512 x 512 CCD camera after microscopic magnification. Epidermis layers from the mid-section were mechanically separated from *Chlorophytum* leaves, and experiments repeated for 10 samples. The polarimeter consisted of two main parts: sensing channel and receiving channel. The sensing channel produced incident radiation in various states of polarization: a source of electromagnetic radiation with isotropic (completely unpolarized or circularly polarized) polarization 1, ideal polarizer and quarter-wave phase plate 3, both with computer controlled azimuth of orientation. The receiving channel represented an arrangement for Stokes vector components (Stokes-polarimeter 5): a continuously turning quarter-wave phase plate, fixed analyzer, and, photodetector (number 7). The six parameters characterizing anisotropy and depolarization of epidermis

were generated from the inverse polarimetric technique given in Savenkov et al. [5-6]: Δ ($0 \le \Delta \le 2\pi$) is the phase shift between two orthogonal linear components of electric vector of incident light, α ($0 \le \alpha \le 2\pi$) is the azimuth of linear phase anisotropy (linear birefringence), φ ($0 \le \varphi \le 2\pi$) is the phase shift between two orthogonal circular components of incident light or measures circular phase anisotropy (circular birefringence), P ($0 \le P \le 1$) is the relative absorption of two linear orthogonal polarizations, and γ ($0 \le \gamma \le 2\pi$) is the azimuth of linear amplitude anisotropy (linear dichroism); R ($-1 \le R \le 1$) is the relative absorption of two orthogonal circular polarizations of circular amplitude anisotropy (circular dichroism). Finally entropy [7] which characterizes depolarization was calculated. For additional details on entropy derivation, the reader is referred to [7].

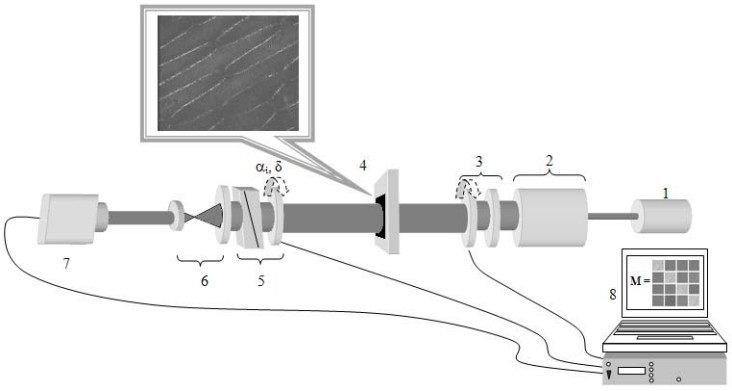

Figure 1: Polarimeter setup.

We present results for P, γ, and Δ [5].

3 Results & Discussion

Figure 2a shows the linear dichroism P: the cell walls have about equal absorption for both components of electric vector, where as, the cell cytosol and vacuole absorbed one of the electric vectors. Figure 2b, which shows the orientation γ of linear dichroism, suggests random orientation (or size) except on cell wall, except along the cell wall. Figure 3a for linear birefringence Δ is due to the differences in the chemical make up of the cell wall and cytosol/vacuole. From entropy (Figure 3b), we surmise light goes directly through the cytoplasm of the cells without being multiply scattered inside the cell i.e., the polarization state of the preferentially absorbed electric vectors is not altered. The poincare sphere (Figure 3c) for leaf without the epidermis (generated from a separate experiment) showed that relative to the epidermis, the internal cells in the leaf were highly depolarizing the incident light: once the electric vector (either E_x or E_y, but not both) entered the inner leaf, it was multiply scattered/absorbed. Figure 4 shows a more magnified view of the epidermis cells. The cell walls are composed of a plasma membrane on the surface of which a primary network of cellulose cross linked with glycans forms microfibrils which is embedded in a secondary network of pectic polysaccharides, which in turn is inside a structural protein or phenylpropanoid network [1]. The pectin matrix regulates wall porosity, and cellulose synthesis occurs *outside* the plasma membrane. The proteins, pectins and other other chemicals for the secondary and tertiary networks are synthesized inside the cell in the endoplasmic reticulum, and golgi apparatus which are then exported to the surface in vesicles. The tiny specks in Figure 4 likely shows the vesicles, golgi apparatus, or the endoplasmic reticulum. Our results open up an interesting discussion. The cell walls are very thin, not more than 100 nm. Our results suggest that the epidermis cytoplasm does control the polarization state of incident light.

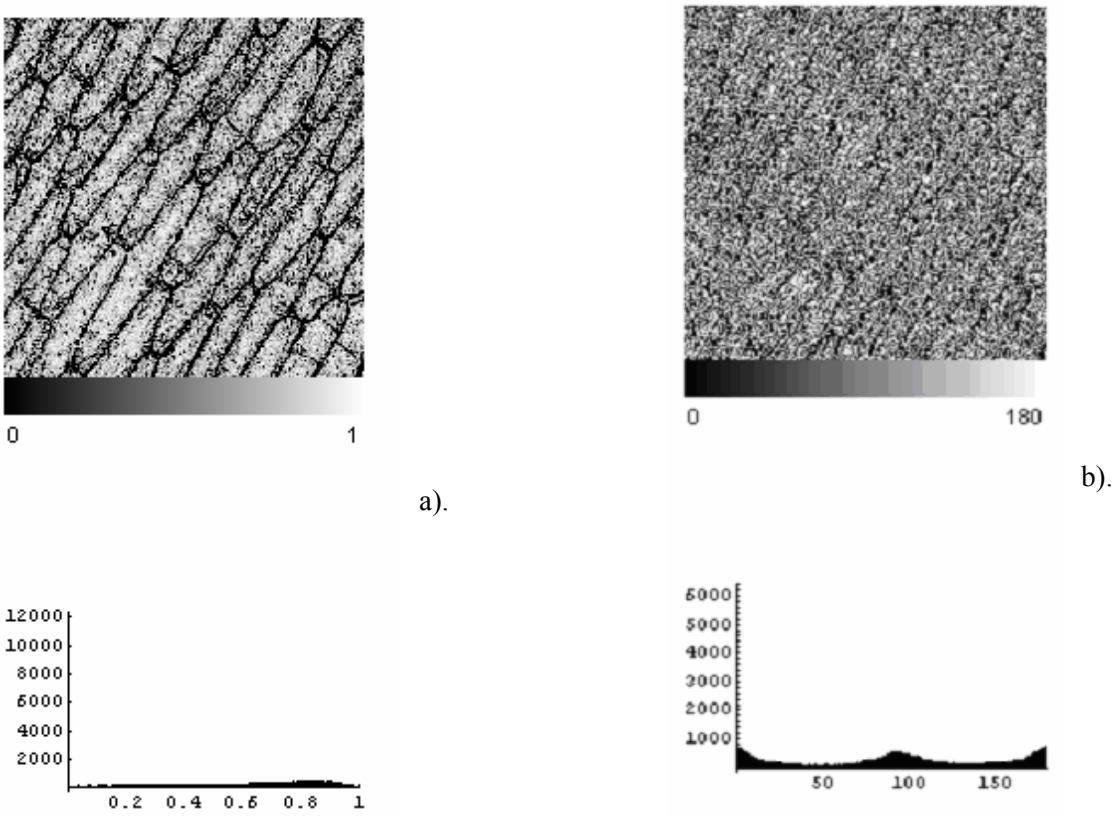

Figure 2a: Dichroism parameter and histogram of values; b: angle of dichroism and histogram for light transmission through epidermis.

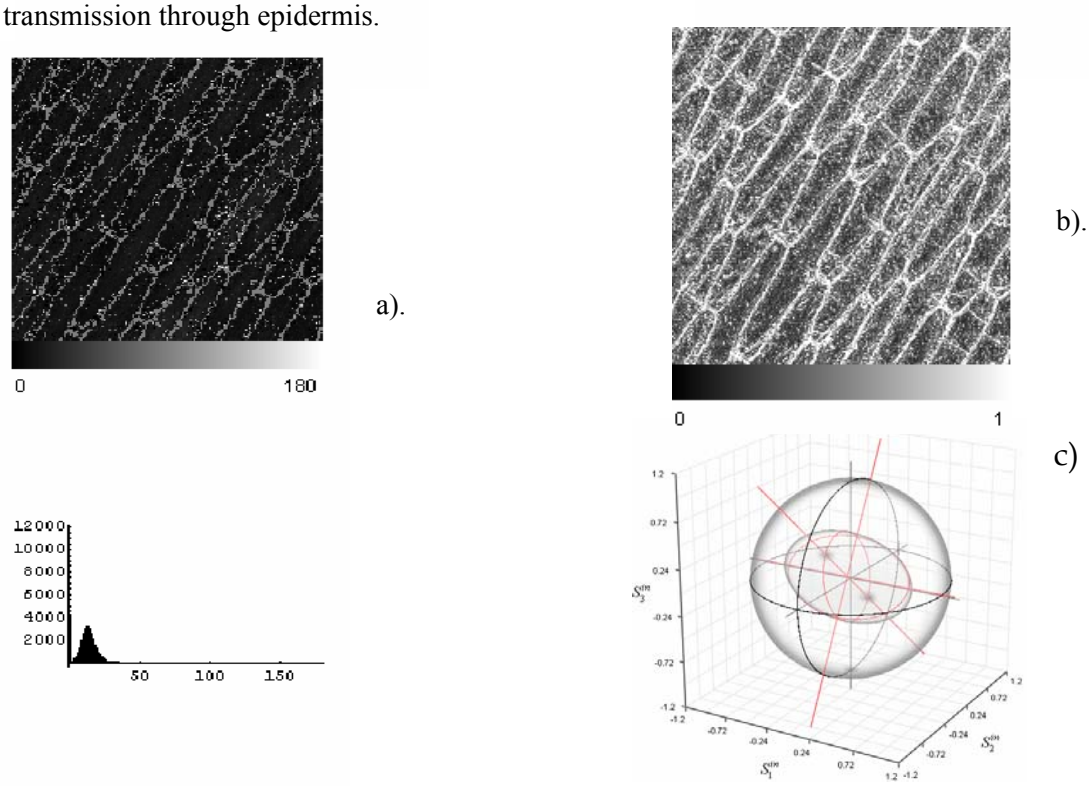

Figure 3a: Phase shift for linear anisotropy; b: Entropy, and c: Poincare sphere (the outer sphere represents incident light) for leaf without epidermis.

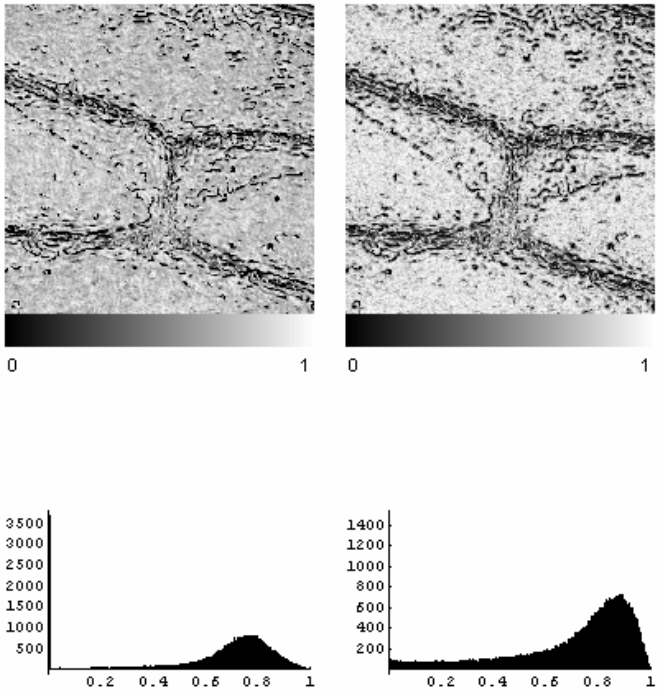

Figure 4: Magnified view of the area between two epidermis cells for amplitude of linear polarization anisotropy; the histogram of values is shown below.

4. Conclusion

Our polarization experiments are the first ever observations on the polarization optics of leaf epidermis. It is highly likely that the epidermis "filters" the incident sunlight to a specific polarization state.

References

[1] P. S. Nobel, Biophysical Plant Physiology and Ecology, W.H. Freeman & Co, New York (1983).

[2] B.B. Buchanan B.B., W. Gruissem, and R.L. Jones, Biochemistry & Molecular Biology of Plants, American Society of Plant Physiologists, Rockville, Maryland (2000).

[3] R. Wehner, "Ant's celestial compass system: Spectral and polarization channels" In: Orientation and Communication in Arthropods (Ed., M. Lehrer), pp. 145-185, Birkhauser-Verlag, Berlin (1997).

[4] M. Dacke, D.-E.,Nilsson, E.J. Warrant, A.D. Blest, M.F. Land, and D.C.O'Carroll. Built-in polarizers form part of a compass organ in spiders. Nature **401**: 470-473, 1999.

[5] S.N. Savenkov, V.V. Mar'enko, E.A. Oberemok and O.I. Sydoruk, "Generalized matrix equivalence theorem for polarization theory," Phys. Rev. E **74**, 056607 (2006).

[6] S.N. Savenkov "Optimization and structuring of the instrument matrix for polarimetric measurements," Opt. Engineering. **41**, 965-972 (2002).

[7] S.R. Cloude, "Groupe theory and polarization algebra," Optik **75**, 26-36 (1986).

Matrix model of inhomogeneous medium with generalized birefringence

Sergey N.Savenkov,[1] Konstantin E.Yushtin,[1] Ranjan S. Muttiah,[2] Viktor V. Yakubchak[1]

[1] *Taras Shevchenko Kiev National University, Department of Radiophysics, 64, Volodymyrska street, 01033 Kyiv, Ukraine, e-mail: sns@univ.kiev.ua*
[2] *Texas Christian University, Department of Geology, Fort Worth, Texas*

Abstract

We derive the Mueller matrix for single scattering from inhomogeneous medium characterized by simultaneous linear and circular birefringence. Simulations for $I_{\min}/I_{\max}$ showed a simple dependence on wavelength of incident radiation.

1 Introduction

The Mueller matrix is a rich source of information about the properties of media investigated in a wide variety of disciplines [1-3]. And unique experimental methods are being rapidly developed to measure the matrix. The challenge is to interpret the measured Mueller matrix, and relate the matrix elements to observable phenomena. A polarization model for anisotropic media aids in these interpretations.

Mueller matrices for homogeneous anisotropic media are well known [4]. There are four basic anisotropies characterizing the homogeneous anisotropy of deterministic media: linear and circular dichroism, and linear and circular birefringence. Inhomogeneous media can depolarize the incident radiation, and, therefore, can not be directly described in terms of these four basic anisotropy properties. In [5], we derived and analyzed the Mueller matrix model for the rough plate parallel slab with linear birefringence. The main goal this paper is to derive the single scatter Mueller matrix model for an inhomogeneous medium with simultaneous linear and circular birefringence.

2 Theory

The geometry of the problem is given in Fig. 1. The object under discussion is a slab of anisotropic medium located in the $z = 0$ plane. Inhomogeneity of the slab is specified by variation of its thickness $h(\boldsymbol{\rho})$ which sets the conditions for single scattering; $h(\boldsymbol{\rho})$ is assumed to follow a known statistical model – a uniform Gaussian process:

$$f(h) = \left(2\pi\sigma_h^2\right)^{-1/2} \exp\left\{-\left(h-\bar{h}\right)^2 / 2\sigma_h^2\right\} \tag{1}$$

with mean thickness $\bar{h}$, mean-square deviation σ_h, and correlation coefficient between screen thickness at two points given by:

$$\gamma_h(\boldsymbol{\rho}_-) = \frac{\overline{h(\boldsymbol{\rho}_1)\cdot h(\boldsymbol{\rho}_2)}}{\sigma_h^2} = \exp\left\{-\frac{\boldsymbol{\rho}_-^2}{\rho_0^2}\right\}, \tag{2}$$

where, the distance between points is given by: $\boldsymbol{\rho}_- = \boldsymbol{\rho}_2 - \boldsymbol{\rho}_1$. The correlation radius is ρ_0.

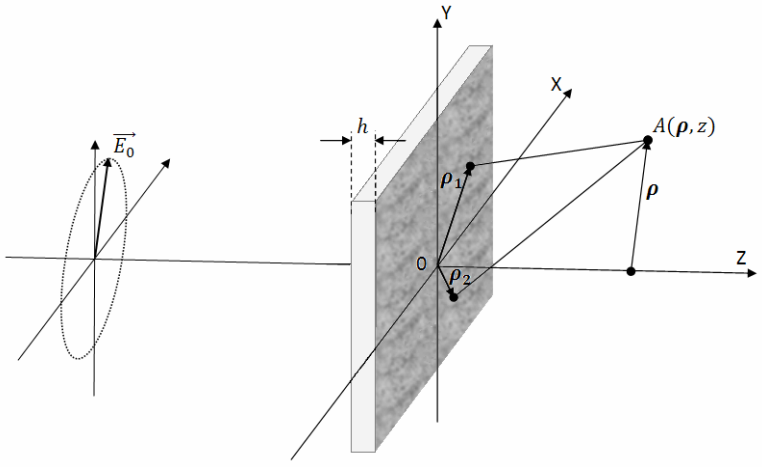

Fig. 1. Geometry for anistropic medium.

Anisotropy of the medium is given by its polarization eigen states, and the corresponding eigen values. Interaction of radiation with such medium is described by its Jones matrix written in eigen coordinate system (UOV) by:

$$\mathbf{J}^{eigen} = \begin{bmatrix} \exp(-i\phi_u) & 0 \\ 0 & \exp(-i\phi_v) \end{bmatrix} = \begin{bmatrix} g_u & 0 \\ 0 & g_v \end{bmatrix} \tag{3}$$

Where, $g_{u,v}$ are the corresponding eigen values which are the complex transmittance coefficients of radiation in eigen polarization states.

We will consider the case when fast eigen polarization of the studied object is associated with basis vector OU. We assume that field distribution of incident radiation to be Gaussian in the plane normal to its propagation direction, with the center of the beam located in the $z = 0$ plane:

$$\mathbf{E}^{in}(\boldsymbol{\rho}) = \mathbf{E}^{in} \exp\{-\boldsymbol{\rho}^2 / a^2\}, \tag{4}$$

Here, $\mathbf{E}^{in}$ denotes Jones vector in the center of the beam; a is the beam's radius. It has been shown in [5], that the Mueller matrix in the eigen coordinate system in the far field limit is (refer to [5] for definition of variables):

$$\mathbf{M}^{eigen} = \begin{pmatrix} \Phi_{11}+\Phi_{22} & \Phi_{11}-\Phi_{22} & 0 & 0 \\ \Phi_{11}-\Phi_{22} & \Phi_{11}+\Phi_{22} & 0 & 0 \\ 0 & 0 & \Phi_{12}+\Phi_{21} & i(\Phi_{12}-\Phi_{21}) \\ 0 & 0 & -i(\Phi_{12}-\Phi_{21}) & \Phi_{12}+\Phi_{21} \end{pmatrix}, \tag{5}$$

where:

$$\Phi_{uv}(\boldsymbol{\rho}, z) = \frac{1}{2}\left(\frac{kaw}{2z}\right)^2 \Phi_{uv}^{brf}\left[(1-\eta_{uv})\exp\left\{-\left(\frac{k\boldsymbol{\rho}w}{2z}\right)^2\right\} + \frac{\eta_{uv}}{\tilde{\sigma}_{uv}^2 w^2 + 1}\exp\left\{-\frac{1}{\tilde{\sigma}_{uv}^2 w^2 + 1}\left(\frac{k\boldsymbol{\rho}w}{2z}\right)^2\right\}\right];$$

$$\Phi_{uv}^{\text{brf}} = \exp\{ik(n_u - n_v)\bar{h} - k^2\sigma_h^2(n_u - n_v)^2/2\};\ w = \left\{\frac{1}{2a^2} + \frac{a^2k^2}{8z^2}\right\}^{-1/2}$$

$$\sigma_{uv}^2 = k^2\sigma_h^2(n_u - 1)(n_v - 1),\ \tilde{\sigma}_{uv}^2 = \frac{\sigma_{uv}^2}{\eta_{ij}\rho_0^2},\ \eta_{uv} = 1 - \exp\left(-\sigma_{uv}^2\right)$$

In the general case, the Jones matrix in the laboratory coordinate system can be presented as:

$$\mathbf{J}^{\text{lab}} = g_1\mathbf{B}\begin{pmatrix}1 & 0\\ 0 & 0\end{pmatrix}\mathbf{B}^{-1} + g_2\mathbf{B}\begin{pmatrix}0 & 0\\ 0 & 1\end{pmatrix}\mathbf{B}^{-1} = \sum_{u=1}^{2} g_u\boldsymbol{\beta}^u\ , \tag{6}$$

where, $\boldsymbol{\beta}^u = \mathbf{B}\begin{pmatrix}\delta_{u,1} & 0\\ 0 & \delta_{u,2}\end{pmatrix}\mathbf{B}^{-1}$.

If eigenvectors χ_1 and χ_2, ($\chi = E_2/E_1$) are known, then the transformation matrix $\mathbf{B}$ is:

$$\mathbf{B} = \frac{1}{\sqrt{\chi_2 - \chi_1}}\begin{pmatrix}1 & 1\\ \chi_1 & \chi_2\end{pmatrix}. \tag{7}$$

The Jones (as well as Mueller-Jones) matrix model of homogeneous anisotropic medium characterized by simultaneous linear and circular birefringence is defined by the first Jones' equivalence theorem [6,7]:

$$\mathbf{J}_{Lin}(\alpha,\delta)\,\mathbf{J}_{Cir}(\varphi) = \begin{bmatrix}\cos^2\alpha + \sin^2\alpha\exp(-i\delta) & \cos\alpha\sin\alpha(1-\exp(-i\delta))\\ \cos\alpha\sin\alpha(1-\exp(-i\delta)) & \cos^2\alpha\exp(-i\delta) + \sin^2\alpha\end{bmatrix}\begin{bmatrix}\cos\varphi & -\sin\varphi\\ \sin\phi & \cos\varphi\end{bmatrix}. \tag{8}$$

Then, the medium's eigenvectors $\begin{bmatrix}1 & \chi_{1,2}\end{bmatrix}^T$ can be calculated as:

$$\chi_{1,2} = \frac{-\xi \pm \eta}{\kappa}, \tag{9}$$

where,

$$\begin{aligned}\xi &= \sin\frac{\delta}{2}\cos(2\alpha - \phi), \quad \eta = \sqrt{1 - \left(\cos\frac{\delta}{2}\cos\phi\right),^2}\\ \kappa &= \sin\frac{\delta}{2}\sin(2\alpha - \phi) - i\cos\frac{\delta}{2}\sin\phi\end{aligned} \tag{10}$$

and matrices $\boldsymbol{\beta}^u$ from Eq.(6) are:

$$\boldsymbol{\beta}^1 = \frac{1}{2}\begin{pmatrix}1 + \frac{\xi}{\eta} & \frac{\kappa}{\eta}\\ \frac{\eta^2 - \xi^2}{\eta\kappa} & 1 - \frac{\xi}{\eta}\end{pmatrix};\quad \boldsymbol{\beta}^2 = \frac{1}{2}\begin{pmatrix}1 - \frac{\xi}{\eta} & -\frac{\kappa}{\eta}\\ \frac{\xi^2 - \eta^2}{\eta\kappa} & 1 + \frac{\xi}{\eta}\end{pmatrix}. \tag{11}$$

And finally, from Eqs.(5) and (6) after some algebra, the Mueller matrix model, in the laboratory reference, for the inhomogeneous medium with generalized birefringence in single scattering case for large inhomogeneities given by $\sigma_h > \sqrt{7}/2\pi\left[(n_1 - n_2)^{-1}\lambda\right]$ [5], is:

$$\mathbf{M} = \begin{pmatrix}
\Phi_{11} + \Phi_{22} & \frac{\xi}{\eta}(\Phi_{11} - \Phi_{22}) & \frac{\mathrm{Re}\kappa}{\eta}(\Phi_{11} - \Phi_{22}) & \frac{\mathrm{Im}\kappa}{\eta}(\Phi_{11} - \Phi_{22})\\
\frac{\xi}{\eta}(\Phi_{11} - \Phi_{22}) & \frac{\xi^2}{\eta^2}(\Phi_{11} + \Phi_{22}) & \frac{\xi\,\mathrm{Re}\kappa}{\eta^2}(\Phi_{11} + \Phi_{22}) & \frac{\xi\,\mathrm{Im}\kappa}{\eta^2}(\Phi_{11} + \Phi_{22})\\
\frac{\mathrm{Re}\kappa}{\eta}(\Phi_{11} - \Phi_{22}) & \frac{\xi\,\mathrm{Re}\kappa}{\eta^2}(\Phi_{11} + \Phi_{22}) & \frac{(\mathrm{Re}\kappa)^2}{\eta^2}(\Phi_{11} + \Phi_{22}) & \frac{\mathrm{Re}\kappa\,\mathrm{Im}\kappa}{\eta^2}(\Phi_{11} + \Phi_{22})\\
\frac{\mathrm{Im}\kappa}{\eta}(\Phi_{11} - \Phi_{22}) & \frac{\xi\,\mathrm{Im}\kappa}{\eta^2}(\Phi_{11} + \Phi_{22}) & \frac{\mathrm{Re}\kappa\,\mathrm{Im}\kappa}{\eta^2}(\Phi_{11} + \Phi_{22}) & \frac{(\mathrm{Im}\kappa)^2}{\eta^2}(\Phi_{11} + \Phi_{22})
\end{pmatrix}. \tag{12}$$

3 Discussions

As can be seen from Eq.(12), the matrix $\mathbf{M}$ is singular i.e., $\mathbf{M}$ exhibits dependence of output intensity on input polarization. From the fact that matrix $\mathbf{M}$ is non-deterministic, there are no input polarizations for which the intensity of output radiation is equal to zero. Maximum and minimum values of output intensities are obtained for input radiation with polarizations describing by the following Stokes vectors respectively:

$$\mathbf{S}^{\max,\min} = \left[\xi^2 + |\kappa|^2 \quad \pm\xi \quad \pm \mathrm{Re}(\kappa) \quad \pm \mathrm{Im}(\kappa)\right]^T . \tag{13}$$

The ratio of minimum and maximum output intensities is therefore:

$$\frac{I_{\min}}{I_{\max}} = \frac{\Phi_{11}}{\Phi_{22}} \tag{14}$$

Figure 1 presents the results of simulations performed to study the dependence of ratio $I_{\min}/I_{\max}$ versus wavelength from 0.4 to $1.0\,\mu m$. The data for refractive indices for this simulation was taken from [8] for paratellurite TeO_2.

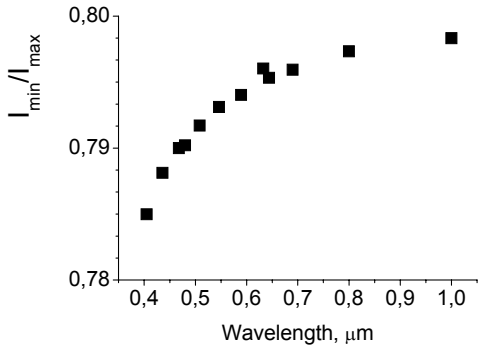

Figure 1. Dependence of ratio $I_{\min}/I_{\max}$ versus wavelength for TeO_2

References

[1] C.F. Bohren, E.R. Huffman, *Absorption and scattering of light of light by small particles* (Wiley, New York, 1983).

[2] M.I. Mishchenko, J.W. Hovenier, and Travis L.D., *Light scattering by nonspherical particles* (Academic Press, San Diego, 2000).

[3] A.A. Kokhanovsky, *Polarization optics of random media* (Praxis Publishing, Chichester, 2003).

[4] R.M. Azzam, N.M. Bashara, *Ellipsometry and polarized light* (North Holland, New York, 1987).

[5] S.N. Savenkov, R.S. Muttiah, K.E. Yushtin and S.A. Volchkov, "Mueller-matrix model of an inhomogeneous, linear, birefringent medium: Single scattering case," JQSRT, doi:10.1016/j.jqsrt.2007.01.29.

[6] H. Hurwitz, R.C. Jones, "A new calculus for the treatment of optical systems. II. Proof of three general equivalence theorem," J. Opt. Soc. Am. **31**, 493-499, (1941).

[7] H. Hammer, "Characteristic parameters in integrated photoelasticity: an application of Poincare's equivalence theorem," J. Modern Optics **51**, 597-618 (2004).

[8] N. Uchida, "Optical properties of single-crystal paratellurite (TeO_2)," Phys Rev. B **4**, 3736-3745 (1971).

Backscattering linear depolarization ratio of laboratory generated ice clouds composed of pristine and complex-shaped ice crystals

Martin Schnaiter, Roland Schön, Ottmar Möhler, Harald Saathoff, and Robert Wagner

Forschungszentrum Karlsruhe, Institute of Meteorology and Climate Research,
PO Box 3640, 76021 Karlsruhe, Germany
tel: +49 (7247) 82-6079, fax: +49 (7247) 82-4332, e-mail: martin.schnaiter@imk.fzk.de

Abstract

Artificial ice clouds have been generated in the laboratory by using the large cloud simulation chamber AIDA of Forschungszentrum Karlsruhe. Experiments have been conducted in the 0C to -30C temperature range. Temperature and saturation ratio regimes with distinct predominating ice crystal habits in a varying ice crystal complexity could be identified by probing the ice clouds with a contact-free, single particle imaging device developed in our institute. Backscattering linear depolarization ratio measurements have been performed on the overall ice cloud simultaneously to single ice crystal characterization. A clear dependence of the linear backscattering depolarization ratio on the ice crystal habit was observed. Ice clouds composed predominantly of compact columnar crystals exhibit a higher depolarization ratio than clouds composed of thin plate-like crystals. Ice crystal growth at high ice saturation ratios increases the particle complexity and lowers the depolarization ratio.

1 Introduction

Quantifying the role of cirrus clouds in the climate system requires the determination of the microphysical properties like size and habit of cirrus ice particles and their radiative properties in the infrared and visible region [1]. Fundamental knowledge of scattering, absorption, and polarization properties of ice crystals is also required for reliably retrieving the microphysical particle properties of visible and subvisible cirrus clouds from remote sensing data. Especially the knowledge of the link between the backscattering depolarization ratio δ of ice crystals and their size and habit is a prerequisite for the interpretation of LIDAR remote sensing measurements of cirrus clouds. Interpretations of LIDAR depolarization data usually rely on results from ray tracing models that calculate laser depolarization ratios for large pristine ice crystals, i.e. hexagonal columns and plates [2]. These models predict backscatter depolarization ratios in the range from 0.1 to 0.65, depending on the size and shape (aspect ratio) of the crystals [2, 3]. Depolarization generally becomes larger for larger ice crystals and is larger for columns compared to plates [3]. Moreover, it was found that the depolarization ratio of columns will be significantly reduced, if the basal facets become distorted, e.g. by the formation of pyramidal inversions (like in “hollow” columns) [4]. Although thin plates and “hollow” columns are also not very effective in depolarizing laser light, low depolarization ratios ($0.1<\delta<0.3$) frequently observed in cirrus clouds by *Sassen and Benson* [5] were attributed to the existence of supercooled water droplets and to crystal orientation due to gravitational sedimentation. However, the authors concluded that the linear depolarization ratio of more realistic, complex-shaped ice crystals might differ significantly from that of pristine and simplified crystal geometries modeled so far.

In order to shed some light on the depolarization capabilities of ice clouds with ice crystal shapes that closely resemble those found in natural ice clouds, we started to run well-defined ice crystal growth and characterization campaigns at the large cloud simulation chamber AIDA of Forschungszentrum Karlsruhe. Such campaigns became feasible after the development and installation of two new instruments at the chamber in 2006, namely the in situ laser scattering and depolarization device

SIMONE and the contact-free single particle imaging probe PHIPS. A brief introduction of these instruments is given in section 2. Experimental results are discussed in section 3.

2 Experimental methods

The experiments were conducted at the cloud simulation chamber AIDA [6] in the temperature range of 0C to -30C and at initially ambient pressure. The chamber was humidified to near ice saturated conditions prior to the experiments. Water vapor concentration within the chamber is determined by a long-path tunable diode laser spectrometer. Small seed ice crystals with sizes of a few micrometers were generated outside of AIDA by mixing a cold gas stream containing crystalline ammonium sulfate aerosol particles with warm and moist air in a turbulent mixing chamber with a temperature maintained at -60C. By directing the resulting ice particle/air flow into the AIDA chamber an ice crystal number concentration of about 1 to 10 cm^{-3} can be generated within 10 minutes in the huge AIDA volume of 84 m^3. Ice saturated or supersaturated conditions can be achieved by a controlled expansion of the chamber gas and, thus, a controlled cooling of the chamber volume. Overall homogeneous conditions within the chamber are assured by a mixing fan at the bottom of the chamber.

Light scattering measurements

The laser light scattering and depolarization instrument SIMONE uses a cw semiconductor laser with an emission wavelength of λ=488 nm to generate a polarized and collimated light beam which is directed horizontally along the 4 meter diameter of the cylindrically shaped AIDA chamber. The polarization vector of the light beam can be arbitrarily changed by using a liquid crystal polarization rotator in front of the laser head, but is usually aligned parallel to the scattering plane. The latter is defined by the light beam and the overlapping detection apertures of two telescope optics that probe scattered light from the chamber interior from the 1.8° and 178.2° directions. The intersection between the laser beam and the detection apertures defines a detection volume of 7 cm^3 in the center of the chamber. The intensity of light scattered in forward direction is measured by a photomultiplier. The backscattered light is decomposed by a Glan-Laser prism according to the parallel and perpendicular components with respect to the incident laser polarization. The corresponding intensity components $I_\perp$ and $I_\parallel$ are measured by two photomultipliers. From these measurements the backscattering linear depolarization ratio δ is determined by

$$\delta = I_\perp - I_\perp^{bg} / I_\parallel - I_\parallel^{bg} ,$$

with $I_\perp^{bg}$ and $I_\parallel^{bg}$ the background intensities of the particle-free chamber.

Ice particle habit characterization

Bright field microscopic imaging of single ice crystals was conducted online using the novel PHIPS imaging instrument. The PHIPS instrument is installed underneath the aluminum chamber within the temperature controlled housing of AIDA. It vertically extracts chamber air via a 10 mm in diameter stainless steel flow tube that extents to about 200 mm into the chamber volume. A stable sampling flow of 10 SLM is maintained by a flow controller backed by a vacuum pump. When a cloud particle passes the detection volume of the instrument, which is defined by the intersection of the laser beam cross section and the field of view of an optical detector, scattered light generates a trigger pulse that opens the shutter of the microscopy unit and fires – with a short delay – the flash lamp. The half width of the flash is only 10 ns. In this way an 8 times magnified bright field image of the moving ice crystal is generated without any motion blurring. The system has an optical resolving power of about 2 µm and a depth of field of about 150 µm. The magnified image of the particle is captured by a 1392×1024 pixel CCD camera with 6.45×6.45 μm^2 pixel size. This results in a field of view of about 1.1×0.8 mm^2 with a pixel resolution of 0.8 µm in the object plane. Image processing algorithms have been developed for automated analysis of

the geometric properties of the particles, like projected area, sphere equivalent diameter, roundness and aspect ratio.

3 Results

An example of an ice growth experiment is shown in Figure 1. The experiment was started at a temperature of -5C. Ice crystals with columnar shapes are expected in this temperature range [7]; pristine habits for a growth near ice saturation and complex shapes (like "hollow" columns or needles) for a growth at intermediate and high saturation ratios. Within the first 300 sec experiment time supercooled water droplets were sprayed by a two-component nozzle directly into the chamber to gradually increase the ice saturation ratio by droplet evaporation. Ice saturated conditions were eventually achieved at about 300 sec experiment time.

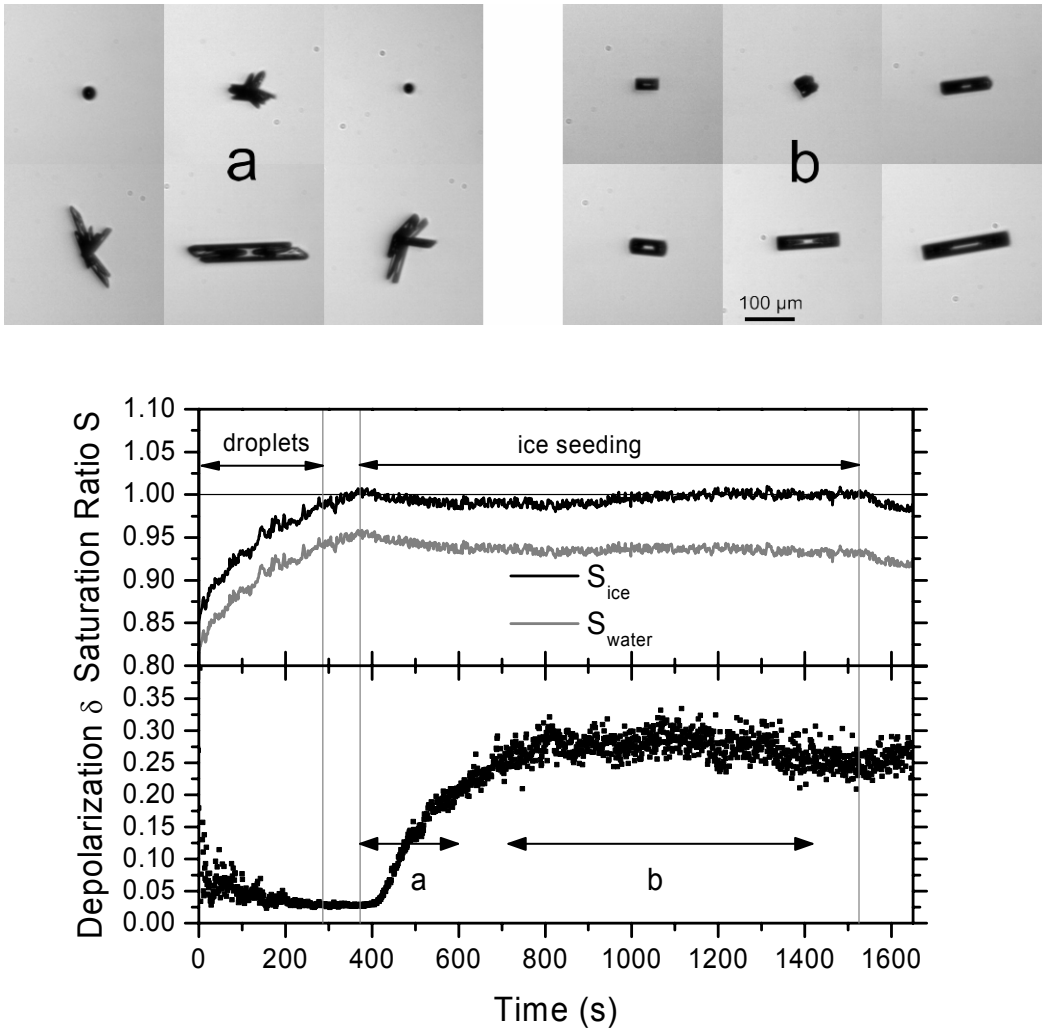

Figure 1: Ice growth experiment conducted at an initial temperature of -5C. See text for details.

Note that the saturation ratios given in Figure 1 are mean values. Locally, the saturation ratios might differ from these values due to temperature and water vapor inhomogeneities, especially near the injection positions of the water droplets and the seed ice crystals. The presence of a droplet cloud is reflected by a

low depolarization ratio δ in Figure 1. Ice seeding was started roughly 1 minute after the water droplet injection has been stopped. Thus, small seed ice crystals were added to an evaporating water cloud. To maintain ice saturated conditions in the chamber during ice seeding, the chamber gas was slowly expanded by pumping, resulting in a temperature drop to -7.5C during 300 to 1500 sec experiment time. Immediately after the beginning of the seed ice addition a mixed phase cloud was observed for a short time period of about 60 to 100 sec by PHIPS (first row of plate (a) in Figure 1). Needles and almost "hollow" columns were indeed observed in this period of high saturation ratio as expected from [7]. After the water droplets have been evaporated the remaining ice cloud was predominantly composed of "hollow" columns and bundles of needles (shown in the second row of plate (a)), which results in a low depolarization ratio of only about 0.1 to 0.15. Newly added seed ice crystals then grew at lower saturation ratios which resulted in a gradual change of the cloud composition between 500 and 700 sec experiment time. An uniform cloud predominantly composed of rather solid columns with less structural complexity was eventually achieved at about 700 sec experiment time. By keeping the saturation ratio at about ice saturation while continuously feeding new seed ice crystals, a stable cloud could be maintained over about 900 sec (plate (b) of Figure 1). A significantly higher depolarization ratio of about 0.3 was measured during this time period of compact, solid crystals. In further experiments, conducted in temperature regions where the ice crystals grow into plate-like shapes (-12C and -25C), we measured very low depolarization ratios of 0.1 or even less. Such ice clouds cannot easily be distinguished from supercooled water clouds by LIDAR applications. Our experimental results confirm, at least qualitatively, the trends in the ray tracing modeling results by *Takano and Liou* [4] and *Noel et al.* [2], i.e. very low δ values in case of very thin plates and a strong decrease of δ by the formation of basal inversions in case of columns. However, for the distorted ice crystals shown in plate (a) of Figure 1, we measured a significantly lower depolarization ratio of $0.1<\delta<0.15$ than modeled so far for columns with deep inversions in the basal facets ($\delta=0.24$).

Acknowledgments

This work is funded by the Helmholtz-Gemeinschaft Deutscher Forschungszentren as part of the program "Atmosphere and Climate".

References

[1] Y. Zhang, A. Macke, and F. Albers, "Effect of crystal size spectrum and crystal shape on stratiform cirrus radiative forcing", Atmos Res **52**, 59-75, (1999).

[2] V. Noel, D.M. Winker, M. McGill, and P. Lawson, "Classification of particle shapes from lidar depolarization ratio in convective ice clouds compared to in situ observations during CRYSTAL-FACE", J Geophys Res-Atmos **109**, doi:10.1029/2004JD004883, (2004).

[3] K.N. Liou, Y. Takano, and P. Yang, *Light Scattering and Radiative Transfer in Ice Crystal Clouds: Applications to Climate Research*, in *Light Scattering by Nonspherical Particles*, M. Mishchenko, J.W. Hovenier, and L.D. Travis, Editors. 2000, Academic Press: San Diego. p. 417-449.

[4] Y. Takano and K.N. Liou, "Radiative-Transfer in Cirrus Clouds .3. Light-Scattering by Irregular Ice Crystals", Journal of the Atmospheric Sciences **52**, 818-837, (1995).

[5] K. Sassen and S. Benson, "A midlatitude cirrus cloud climatology from the facility for atmospheric remote sensing. Part II: Microphysical properties derived from lidar depolarization", Journal of the Atmospheric Sciences **58**, 2103-2112, (2001).

[6] O. Möhler, P.R. Field, P. Connolly, S. Benz, H. Saathoff, M. Schnaiter, R. Wagner, R. Cotton, M. Krämer, A. Mangold, and A.J. Heymsfield, "Efficiency of the deposition mode ice nucleation on mineral dust particles", Atmos Chem Phys **6**, 3007-3021, (2006).

[7] K.G. Libbrecht, "The physics of snow crystals", Rep Prog Phys **68**, 855-895, (2005).

Detection of dust grains vibrations with a laser heterodyne receiver of scattered light

Yuriy Serozhkin, Olexiy Kollyukh, and Yevgen Venger

V. Lashkaryov Institute of Semiconductor Physics
41 Nauky Prospect, Kyiv 03028, Ukraine
Tel./Fax: +38 (044) 525 61 79; e-mail: yuriy.serozhkin@zeos.net

Abstract

A laser heterodyne receiver of scattered light was used to detect dust grains vibrations. We made experiments for estimation of the technique sensitivity. The vibrations were excited in cigarette smoke with a loudspeaker. The results obtained indicate that dust grains vibrations with amplitude of about 30 nm can be detected.

1 Introduction

Heterodyne detection of scattered light is one of the most informative techniques used for investigation of the static and dynamic characteristics of micron and submicron particles. The parameters of modern laser heterodyne receivers of scattered radiation make it possible to detect nanoparticles and nanoclusters [1]. Application of heterodyne detection of scattered light when studying various biological objects *in vivo* seems very promising [2].

The objective of our work is to estimate feasibility of investigation of the dynamic characteristics of microparticles with a laser heterodyne detector of scattered radiation. We determined the potentialities of this technique and carried out pilot experiments on determination of vibrational amplitude for microparticles (cigarette smoke, colophony smoke) exposed to external actions.

2 Estimation of technique sensitivity

Let us estimate the laser heterodyne receiver capabilities when measuring vibrations of dust grains. The signal-to-noise ratio (S/N) of heterodyne detector peaks under conditions when its sensitivity is determined by shot noise [4, 5]:

$$\left(\mathrm{S/N}\right)_{\mathrm{power}} \approx \frac{\eta P_s}{h\nu\Delta F}. \tag{1}$$

Here P_s is the detected signal power, h Planck's constant, ν radiation frequency, η detector quantum efficiency, and ΔF pass bandwidth of the receiver. Then the expression for the minimal detected signal power $P_{s,\,\mathrm{min}}$ (S/N = 1) is

$$P_{s,\,\mathrm{min}} \approx \frac{h\nu}{\eta}\Delta F. \tag{2}$$

When the wavelength is 0.6328 μm, η =0.5, losses in the receiving optical system up to 60%, and pass bandwidth of the receiver 10 kHz, then one obtains $P_{s,\,\mathrm{min}} \approx 1\times10^{-14}$ W. If the entrance aperture cross section is 1 cm^2, probing radiation power 1 mW, and distance to the scattering surface 50 cm, then the power coming to the detector input will be about 6×10^{-8} W (with the assumption that the surface scattering is isotropic and albedo is 0.8). Thus, a signal scattered from a surface with albedo of about 1×10^{-5} can be detected at a distance of 50 cm. If the scatterer is an assembly of 5 μm grains, with single albedo of 0.5 and the distance between particles of about 100 μm, then the resulting albedo of a layer about 0.5 mm thick will be 0.6×10^{-2}. In this case, the signal from radiation scattered by the dust layer will

be 600 times the threshold of sensitivity, so one obtains S/N = 0.6×10^3. It can be shown that the S/N ratio at a frequency of scattering surface vibration is determined by the following expression:

$$(\mathrm{S/N})_{\omega_i \pm \Omega} \approx \left(\frac{2\pi}{\lambda} a\right)^2 \frac{P_s}{P_{s,\ \min}}. \tag{3}$$

Here ω_i is the difference between the heterodyne and probing radiation frequencies, a amplitude of scattering surface vibrations, and Ω vibrational frequency of the surface. For vibrational amplitude of 10 nm, the ratio S/N ≈ 6; this means that one can easily detect in-phase vibrations of particles in a layer of about 0.5 mm thick.

3 Experimental setup

The threshold of sensitivity of our detector was 2×10^{-14} … 2×10^{-12} W (depending on the pass bandwidth); the detector sensitivity to vibrations of a surface (with albedo of 0.8) at a distance of 1 m was no worse than 0.1 nm (in the 10 kHz band). The probing and heterodyne beams of the detector were formed with acoustooptical shift of laser radiation frequency in the same direction by the frequencies Fs and Fh, respectively. As a result, the information signal (which is formed when the frequencies of the radiation from heterodyne and that scattered by particles are mixed in the photodetector) is a phase-modulated signal whose carrier frequency $F_s - F_h$ is about 10 MHz.

Digitization of that phase-modulated signal was made with a two-channel A/D converter AD6600. Extraction of quadrature components digital heterodyning, decimation and filtration were performed with a digital filter/receiver AD6620. The information on phase value and rate (and consequently on the scattering surface displacement and velocity) was extracted by calculating the modified function atan2 of the ratio between the in-phase and quadrature components of a phase-modulated signal.

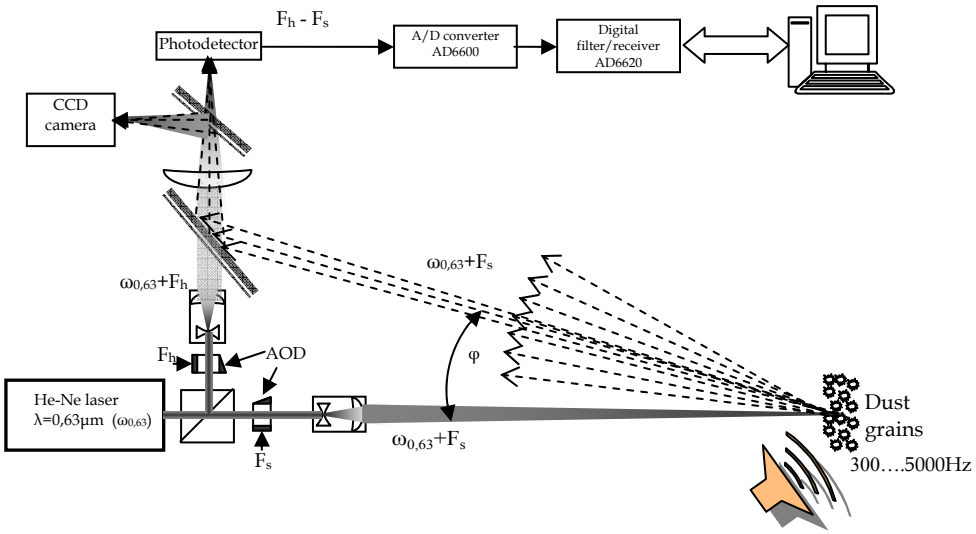

Figure 1: The experimental setup.

The experimental setup (Figure 1) involved a laser heterodyne receiver and a volume for dust component (cigarette smoke, colophony smoke) bleeding. A loudspeaker (to excite vibrations of air with dust component) was located in the above volume. A probing laser beam was focused (through a window) at a chosen point inside the dust cloud at a distance of about 50 cm from the collecting aperture. The focal spot diameter was 100…200 μm. A TV camera was used for visual focusing at a chosen region of the dust cloud. The detector was a bistatic optical system (with an angle $\varphi \approx 5^o$ between the transmission and reception optical axes), so there was a depth of focus for such detector: object shifting led to change in the

scattered spot position relative to the heterodyne spot, thus resulting in signal decrease. For the angle of about 5^o and distance of 50 cm, the depth of focus was 0.25…0.5 mm. One can state that the information signal was formed by scattering from those particles which occupied a region whose cross section was equal to the focal spot diameter and whose length was about five times that diameter.

4 Experimental results

Before measuring particle vibrations, we have measured piezoelectric cell vibrations (of the known amplitude) to refine the measurement procedure and receiver calibration. Shown in figure 2a is the spectrum of the $F_s - F_h$ signal obtained at scattering from the vibrating surface of piezoelectric cell (vibrational amplitude of 10 nm and frequency of 1 kHz). Figure 2b presents the signal spectrum after phase recovery and attenuation of low frequencies with a 6^{th} order filter (the cutoff frequency of 200 Hz). Such measurements were performed for different frequencies and amplitudes of surface vibrations.

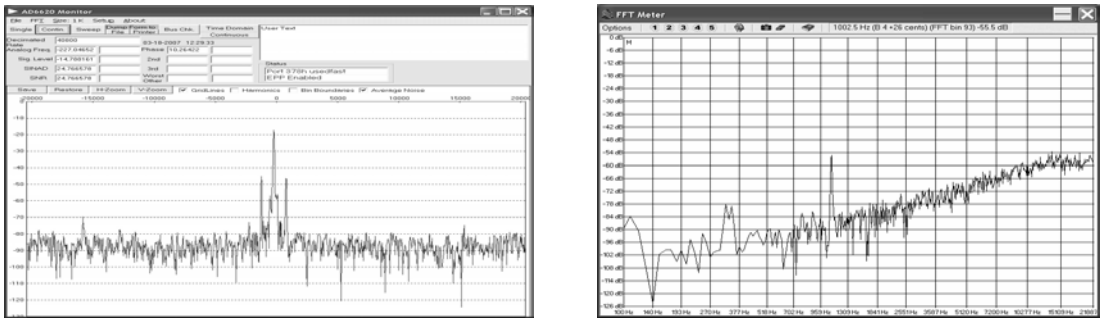

a) b)

Figure 2: Frequency spectrum signal from light, scattered by piezoelectric cell vibrations

When measuring particles vibrations, the probing beam was focused at a point inside the dust cloud at a distance of several millimeters from the inlet window. Shown in figure 3 are trails of the probing beam in the dust cloud and heterodyne spot (in center, a 10^4-fold attenuation). After the information collection area is chosen and detector is set, the heterodyning intensity is increased up to the operating level (about 50 μW). The diameter of the beam entering the dust cloud is 0,3 mm. The bright spots on the right are formed due to scattering from the inlet window surfaces.

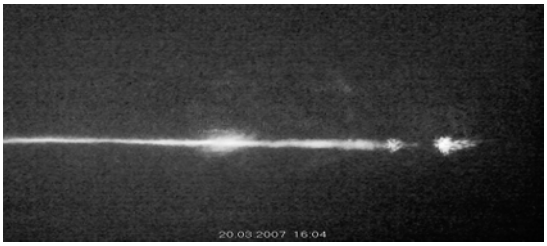

Figure 3: Trails of the probing beam in the dust cloud

Figure 4a presents the spectrum of the $F_s - F_h$ signal obtained at scattering from cigarette smoke exposed to sound action from a loudspeaker (power of 0.1 W at a frequency Ω = 1 kHz). The components with the above frequency appear in the spectrum of the $F_s - F_h$ signal (Fig. 4a). The spectrum is broadened considerably due to chaotic motion of the particles. Figure 4b presents the signal spectrum after phase recovery and attenuation of low frequencies with a 6^{th} order filter (the cutoff frequency of 200 Hz). Such measurements were performed for different frequencies and power of loudspeaker.

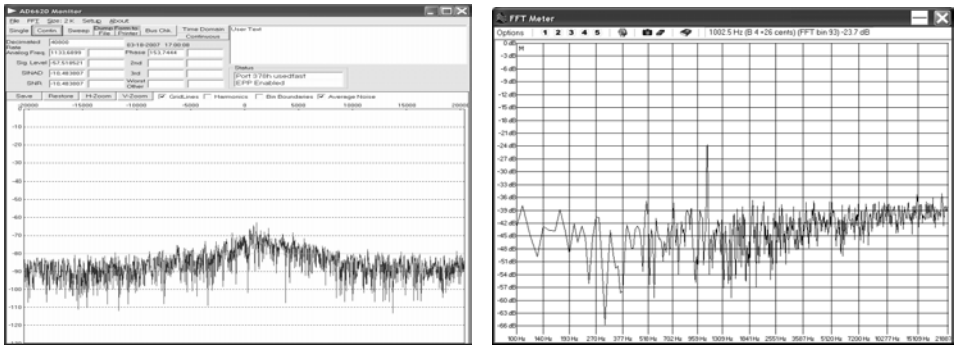

4a 4b

Figure 4: Frequency spectrum signal from light, scattered by smoke

From figure 4b it is visible, that the noise level at measuring a scattering from a smoke makes quantity about 40 dB. It corresponds to vibration amplitude about 30 nm.

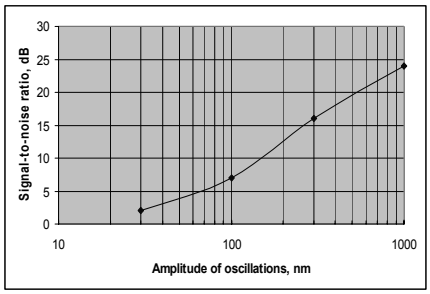

Figure 5: Signal-to-noise ratio for vibration of grains

In figure 5 is presented the dependence of the signal/noise ratio from a vibration amplitude of grains.

5 Conclusion

We developed a laser heterodyne detector of scattered radiation to be applied for investigation of the dynamic characteristics (vibrational amplitude and frequency) of dust grains in a dust cloud. Such detector makes it possible to register micron particles vibrations with amplitude of 30 nm.

References

[1] Stéphane Berciaud, Laurent Cognet, Gerhard A. Blab, and Brahim Lounis. Photothermal Heterodyne Imaging of Individual Nonfluorescent Nanoclusters and Nanocrystals, Phys. Rev. Lett. 93, 257402 (2004)

[3] Gross M, Goy P, Forget BC, Atlan M, Ramaz F, Boccara AC, Dunn AK. Heterodyne detection of multiply scattered monochromatic light with a multipixel detector. Opt. Lett. 2005 Jun 1; Vol. 30, No. 11, pp. 1357-1359.

[3] Oliver, B.M. (1961). Signal-to-noise ratio in photoelectric mixing. Proc. IEEE, 49(12):1960–1961.

[4] M. C. Teich and R. Y. Yen, "On the Signal-to-Noise Ratio for Optical Heterodyne Detection," J. Appl. Phys. **43**, 2480-2481 (1972).

Researching the physical conditions in Jupiter atmosphere using remote sensing methods

O.S. Shalygina, V. V. Korokhin, L.V. Starukhina, E. V. Shalygin, G. P. Marchenko,

Yu. I. Velikodsky, O. M. Starodubtseva and L. A. Akimov

Astronomical Institute of Kharkov V.N. Karazin National University,
Sumskaya Ul., 35, Kharkov 61022, Ukraine
tel: +38 (057) 700-53-49, fax: +38 (057) 700-53-49, e-mail: ksusha@astron.kharkov.ua

Abstract

New results of studying the north-south asymmetry in polarization of light reflected by Jupiter are presented. On the basis of 24-year (1981-2004) observational period, anticorrelation between asymmetry of Jupiter polarization and insolation has been found. The mechanism of influence of seasonal variations (with temperature changes) on north-south asymmetry of polarization has been proposed. Our estimates show that components of Jovian stratospheric haze which consists of polycyclic aromatic hydrocarbons (PAH) (crystal naphthalene, phenanthrene) particles may be formed by homogeneous nucleation. Temperature variations in Jupiter stratosphere have strong effect on PAH condensation; benzene does not condensate at T > 120 K. We have found that fluxes of solar cosmic rays may influence upon concentration of aerosol haze particles only through series of chemical reactions that produce source material for aerosol formation.

1 Seasonal variations of the north-south asymmetry of polarization

Remote sensing methods are effective for researching the atmosphere of the planets. The main mechanism of polarization origin in planetary atmospheres is the light scattering on electrons, atoms, molecules and aerosols. Light reflected by Jovian atmosphere is polarized in various atmosphere layers. Studying the distribution of polarization parameters over the planet disk and analysis of their temporal changes may promote to obtain new information about physical conditions in Jupiter atmosphere. As known, ground-based and cosmic polarimetric observations of Jupiter in visual spectrum range show the dependence of linear polarization degree *P* on phase angle and polarization increasing with latitude (even at zero orbital phase angle): polarization degree increases from zero (equatorial regions) to 7-8% (polar regions). Also it is known, that there is a north-south asymmetry of linear polarization at Jupiter [1-4].

To explain these observational facts, we have started regular polarimetric observations of Jupiter in 1981. In our previous works [e.g. 2], on the basis of Jupiter photopolarimetric observations in opposition at blue light during 1981-1999, seasonal variations of north-south asymmetry (P_N-P_S) of linear polarization *P* in polar regions and anticorrelation between P_N-P_S and insolation have been found. Parameter of asymmetry P_N-P_S is defined as a difference between values of linear polarization degree on north and south at the latitudes ±60° at the central meridian. P_N-P_S data are well organized if plotted in accordance with Jupiter's orbital location and there is some relation between P_N-P_S and insolation [2]. We are continuing our studying: 1) our new observations were used; 2) our old data (1981-1998) have been reprocessed using new improved technique; 3) Hall and Riley data [3] (1968-1974) (ultraviolet, visual spectrum range) are involved for analysis. New variant of P-asymmetry dependences on Jupiter's orbital location are presented in the Fig.1. To investigate the nature of the dependence the approximations have been made using different functions. Earlier, in paper [2], we used sinusoidal function with period 180°, but this approximation was difficult for physical interpretation. For new data the approximation by this function is unsuccessful. At the same time, one-periodic functions make a good approximation: sinusoid (Fig.1, Fig.2, curve *1*) gives significant decrease of dispersion in comparison with approximation by con-

stant according to F-criterion with confidence probability 0.76 and "saw-shape" function (P_N–P_S = 1.83–0.005L_S, for 160°<L_S<520°, period is 360°) with 0.96.

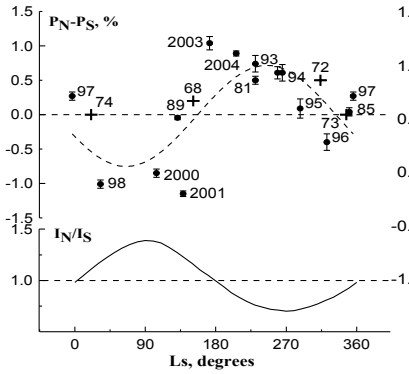

Figure 1.

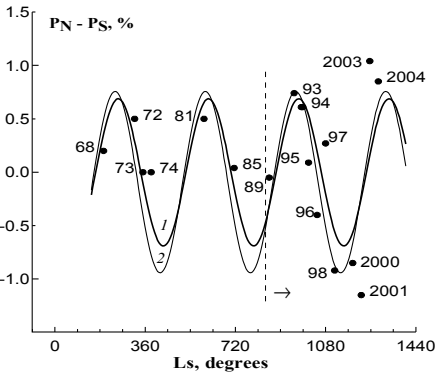

Figure 2.

Figure 1: Dependence of North-South asymmetry of polarization P_N-P_S on planetocentric orbital longitude of the Sun Ls (upper plot). Points correspond to the data obtained by averaging from our observations, crosses are the Hall and Riley data 1968-74 [2]. Bars are errors of mean. Dashed line is approximating curve: P_N-P_S= -0.67sin(L_S+0.32°) + 0.05. Solid line is theoretically calculated asymmetry of insolation of polar regions (intensity ratio I_N/I_S at latitudes ±60°).

Figure 2: Approximation of P_N-P_S dependence on Ls (for continuous Ls axis) by different functions: (1) sinusoid calculated over all observational data, (2) sinusoid calculated only using CCD observations.

To check stability of solution, we have carried out the experiment: approximative function was found only on part of data obtained using the CCD (1989-2004) (Fig.2, curve *2*). Obtained dependence, prolonged to small values of Ls, shows a good agreement with our earlier data and Hall and Riley data. So, one might assert that *periodic* variations of polarization are exist.

Correlation coefficient between P_N-P_S and I_N/I_S is -0.7, i.e. there is significant *anticorrelation*. Our earlier assumption [2] is confirmed by new data and we can speak about *seasonal variations* of polarization.

2 Causes of seasonal variations of Jupiter polarization

We assume that variations of insolation are the principal cause of the seasonal variations of polarization. Jupiter has a small axial tilt (about 3 degrees). However, the orbital eccentricity of 0.05 results in 20% variation in the dilution factor $1/r^2$ values due to the change of the distance r from the Sun. Besides, the perihelion and maximum of Jovian latitude of the Sun are almost coinciding in time. These factors produce significant seasonal fluctuations of the incident solar radiation and result in north-south asymmetry in insolation and temperature. Thus, seasonal variations of stratospheric temperature appear: temperature difference at the polar regions in Jupiter's atmosphere may vary in the range ±25 K [5, 6].

As known, observational data and theoretical modeling indicate the presence of stratospheric aerosol haze on p ~ 20 mbar pressure level with greatest abundance at polar regions [7,8]. This haze conceivably consists of benzene and polycyclic aromatic hydrocarbons (PAH) like naphthalene, phenanthrene, pyrene [8]. Model calculations [9] estimate the mean radius of haze particles r=1-1.5 μm. We have shown in [10] that main contribution in registered polarization in Jovian polar regions is produced by the light reflected from underlying surface (clouds) and then scattered on aerosol haze particles. Aerosols of this haze may be in unstable state, and temperature changing may influence on forming/dissociation of particles.

Anticorrelation of polarization asymmetry and insolation may be caused by following mechanism. Because of essential heating of thin stratospheric aerosol layer (during Jovian summer) the substance of haze may leave state of supersaturated vapor. Condensation becomes slower, concentration of particles decreases and polarization also decreases (as known, the rate of condensation decreases when temperature increases). Thus, possible scenario of polarization asymmetry appearance is: seasonal variations of insolation are led to –> seasonal variations of temperature –> changes of activity of aerosol formation –> aerosol concentration changes –> polarization changes –> changes of north-south asymmetry of linear polarization.

2.1 Temperature effect on aerosol haze formation

Average temperature in polar regions of Jovian stratosphere is about 150 K [8]. This temperature is lower than triple points of naphthalene and benzene (359 K and 278 K, respectively), so they may produce crystal nucleus from gaseous phase. Let's consider homogeneous particle nucleation (i.e. proceeding without additional condensation centers). Equilibrium condition for nuclei of a crystal with radius r and surrounding gas is defined as following [11]:

$$r = r_c = \frac{2\alpha\Omega}{\Delta\mu(T,\xi)} \quad , \tag{1}$$

where r_c – critical radius (nuclei with smaller radius evaporate, and bigger ones grow); Ω is specific volume of molecule in crystal; $\mu = kT\xi$ is chemical potential; $\xi = \ln[p(T)/p_0(T)]$ is supersaturation, $p(T)$ is vapor pressure in atmosphere; $p_0(T)$ is saturated vapor pressure; α is surface tension coefficient; for particles in solid phase α is close to the value in liquid phase near melting temperature.

Eq. (1) is unstable. For formation of a nucleus with radius r, the system should overcome potential barrier G:

$$\Delta G(\xi, r) = -\frac{4}{3}\pi r^3 \frac{\Delta\mu(T,\xi)}{\Omega} + 4\alpha\pi r^2 \quad , \tag{2}$$

where G is Gibbs potential. Homogeneous nucleation takes place when radius of critical nucleus is close to molecular sizes; at the same time, supersaturation ξ is about or larger than 1. For example, for naphthalene (α=30 erg/cm^2) at T=150 K and ξ = 10 critical radius r_c = 6 Å, i.e., in Jovian stratosphere homogeneous nucleation can occur.

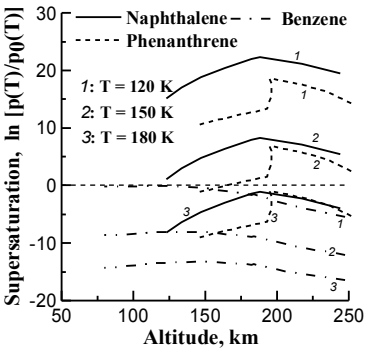

Figure 3: Altitude distributions of PAH supersaturation for different Jovian temperatures.

To study the effect of temperature changes on PAH formation, we used altitude concentration profiles from [8]. Temperature values for calculations (Fig.3) were selected because of average temperature at the pressure level 20 mbar (probable aerosol haze location) is 150 K [12], and its season changes in north and south Jupiter polar regions reach up to ±30 K [6]. Our estimates show (Fig.3) that temperature changes have strong effect on processes of homogeneous nucleation in Jupiter stratosphere: benzene does not condensate at T>120 K (negative supersaturation means vapour undersaturation), whereas probability of naphthalene and phenanthrene nucleation at T=120 K and T=150 K is considerable.

2.2 Mechanism of the effect of irregular factors (solar cosmic rays) on aerosol haze

We have investigated influence of solar wind, solar cosmic rays and X-rays on Jupiter polarization. One can see (Fig.4), there is some relation between P_N-P_S and solar cosmic rays flux (protons, E>10 MeV). Marked points (1998, 2000, 2001) greatly deviate from general group. In what way extremely large flux of high-energy protons registered in this years had influence on increasing of polarization values? First, high-energy protons may increase concentration of ions that participate in chemical reactions, which can enhance synthesis of source material (PAH molecules) for aerosol formation. Second, the ions may serve as additional condensation centers of aerosols. At last, chemical reactions stimulated by additional ionization of the atmosphere occur with heat release or absorption, which may result in temperature change at high altitudes (similar effect is well known for the Earth stratosphere [13]). This can change aerosol concentrations and, consequently, polarization values at both poles. Because of nonlinear dependence of vaporization-condensation processes on temperature, the stratosphere aerosol concentration is different in both polar regions, which may produce polarization asymmetry. Only second mechanism (nucleation in gas containing ions) can be described quantitatively. Gibbs potential in this case is:

$$\Delta G(\xi, q, r) = -\frac{4}{3}\pi r^3 \frac{\Delta\mu(T,\xi)}{\Omega} + 4\alpha\pi r^2 - \frac{q^2}{2}\frac{\varepsilon-1}{\varepsilon}\left(\frac{1}{r^*} - \frac{1}{r}\right) \quad , \tag{3}$$

where r is the radius of charged sphere, r^* is the ion radius; q is ion charge, and ε is dielectric permeability of nucleus. The new term on the right in Eq.(3) describes screening of a charge q by growing particle.

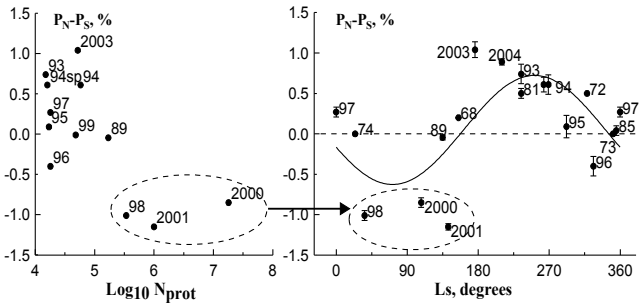

Figure 4.

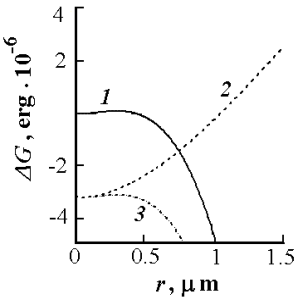

Figure 5. a

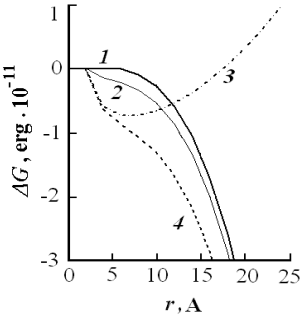

Figure 5. b

Figure 4: Comparison of solar cosmic rays flux (amount of high energy protons, GOES-10 data) with polarization asymmetry (left) and Fig.1 (right).

Figure 5: Thermodynamic potential ΔG (ξ,q,r) changing of system which content nucleus with radius r was formed on ion with charge q (q in charges of electron): a: small supersaturation, big charges, r~μm, ΔG (0.01,0,r) (1), ΔG (0.001,103,r) (2), ΔG (0.01,103,r) (3), b: high supersaturation, real charges, r near molecular sizes, ΔG (8,0,r) (1), ΔG (8,1,r) (2), ΔG (0.01,2,r) (3), ΔG (8,2,r) (4).

Assuming ε = 2.3, r^* = 2 Å the plots in Fig. 5 have been obtained. As shown in Fig. 5a, additional domain of stability (local minimum of function G (ξ,q,r)) does not appear in the range of our interests (particles sizes ~1 μm) even for unreally great charges (Fig. 5a, lines *2*, *3*). At real values of charges (1-2 charge of electron), stability appears only very close to molecular sizes (Fig. 5b, line *3*), i.e. only charged molecular clusters (not particles) can be stable (not evaporating and not growing). Thus, mechanism of aerosol particles formation on charges is not effective.

3 Conclusion

(1) There is an anticorrelation between polarization asymmetry and insolation Jupiter's atmosphere. (2) Seasonal variations of insolations (through variations of temperature) is the principal cause of variations of north-south asymmetry of polarization. (3) Jovian stratospheric haze which consists of PAH (naphthalene, phenanthrene) particles may be formed by homogeneous nucleation. (4) Temperature variations in Jovian stratosphere have strong influence on PAH condensation; benzene does not condensate at T>120K. (5) Flux of solar cosmic rays may influence on concentration of aerosol haze particles only through series of chemical reactions that produce source material for aerosol formation.

References

[1] T. Gehrels, B. M. Herman, T. Owen, Astron. J. **74**, 190-199 (1969). [2] O. M. Starodubtseva, L. A. Akimov, V. V. Korokhin, Icarus. **157**, No 2, 419-425 (2002). [3] J. S. Hall, L. A Riley, Icarus. **29**, 231-234 (1976). [4] C. J. Braak et al., Icarus. **157**, 401-418 (2002). [5] R. F. Beebe, R. M Suggs, T. Little, Icarus.**66**, 359-365 (1986). [6] J. Caldwell, R. D. Cess, B. E. Carlson, Astrophys. J. **234**, L155-L158 (1979). [7] R. A. West, Icarus. **75**, 381-398 (1988). [8] A. J. Friedson, Ah-San Wong, Yuk. L Yung, Icarus. **158**, № 2, 389-400 (2002). [9] K.G Kemp et al., Icarus. **35**, №2, 263-271 (1978). [10] Goryunova O.S. et al., Kinematics and Physics of Celestial Bodies, **5**, 443-447 (2005). [11] A. A. Chernov "Modern Crystallography III", Springer, 3-120 (1984). [12] L. M. Trafton et al., Astrophys. J. **421**, 816-827 (1994). [13] J. Xanthakis et al., Πρακτικα τησ ακαδημιασ αθηνω. **55**, 362-371 (1980).

Mapping the Moon in P_{min}

Yu. Shkuratov,[1] N. Opanasenko,[1] A. Opanasenko,[1] E. Zubko,[1,2] Yu. Velikodsky,[1]
V. Korokhin,[1] and G. Videen[3,4]

[1]*Astronomical Institute of V.N. Karazin Kharkov National University, 35 Sumskaya St, Kharkov, 61022, Ukraine*
tel. +38-057-700-5349. e-mail: shkuratov@astron.kharkov.ua

[2]*Institute of Low Temperature Science, Hokkaido University Kita-ku North 19 West 8, Sapporo 060-0819, Japan*

[3]*Astronomical Institute "Anton Pannekoek", University of Amsterdam, Kruislaan 403, 1098 SJ Amsterdam, The Netherlands*

[4]*Space Science Institute, 4750 Walnut St. Suite 205, Boulder CO 80301, USA*

Abstract

At small phase angles the Moon reveals a wide negative polarization branch whose inversion angle is 22° and whose average amplitude is 1%. We present results of polarimetric mappings of the Moon in P_{min} at a phase angle near 11°. The observations in the red and blue spectral bands were carried out with the Kharkov 50-cm telescope at the Maidanak Observatory (Middle Asia) using a Canon-350D camera and polarizing filter. A thorough calibration of the camera array (flat field and so on) allows for the reliable detection of significant variations of $|P_{min}|$ over the lunar surface, from 0.2 to 1.6 %. Smallest $|P_{min}|$ are characteristic of young bright craters; the parameter $|P_{min}|$ is the highest for the lunar highland and bright mare areas.

1 Introduction

The lunar surface is illuminated by solar radiation that is not polarized. Upon scattering the radiation becomes polarized and the polarization degree P varies with the phase angle α. In particular at small phase angles the wide negative polarization branch with $|P_{min}| \approx 1$ %, $\alpha_{min} \approx 11°$, and inversion angle equal 22° is observed [1-3] ($P = \frac{I_\perp - I_\parallel}{I_\perp + I_\parallel}$, where $I_\parallel$ and $I_\perp$ are intensities measured, respectively, at parallel and perpendicular orientations of the analyzer axis with respect to the scattering plane). The negative polarization is observed for different particulate surfaces, an example of which is the lunar regolith.

Telescope polarimetric observations of the Moon are still rare. One of the reasons for this is the lack of motivation due to poor interpretation of previous lunar polarimetry. There are only three large surveys [1,2,4,5] of discrete polarimetric measurements. Results in imaging lunar polarimetry also are meager, though recently it was shown that this method suggests at large phase angles an effective diagnostic tool for determination of compositional heterogeneity of particles of the lunar surface [6]. There has been only one attempt to carry out imaging polarimetry of the Moon at small phase angles where the polarization degree is negative [7]. That investigation [7] has shown noticeable variations of $|P_{min}|$ over the lunar surface, approximately from 0.2 to 1.8 %. Although the diagnostic meaning still remains unclear, we further develop the approach of [7] using more accurate maps of $|P_{min}|$ whose initial images have higher spatial resolution.

2 Observations

The observations in the red and blue spectral bands were carried out with the Kharkov 50-cm telescope at the Maidanak Observatory (Middle Asia) using a Canon-350D camera and polarizing filter. The Observatory is characterized with very good astro-climate conditions, many nights of clear sky and very small atmosphere turbulence. The polarimetric measurements were made at a phase angle near 11° that is close to α_{min} for the Moon. The flat fields of the system "camera array + filters + telescope" at two spectral channels (red: λ_{eff} = 0.63 μm and blue: λ_{eff} = 0.48 μm) were measured and then taken into account. A thorough calibration allows the reliable detection of significant variations of $|P_{min}|$ over the lunar surface, which are in quantitative agreement with our previous discrete and mapping measurements [2,4,7]. We present results of our polarimetric measurements of the Moon in P_{min} for several areas of the lunar nearside. Figures 1-4 present images of albedo, $|P_{min}|$ in blue light, and the ratio $|P_{min}|_{red}$ / $|P_{min}|_{blue}$ for 4 areas of the lunar nearside. The higher the parameter $|P_{min}|$, the brighter the details of the $|P_{min}|$ map. All variations of the parameter $|P_{min}|$ correspond to specific morphological features of the lunar surface, which is a strong argument that we are studying a real physical effect and not an artifact. The $|P_{min}|_{red}$ / $|P_{min}|_{blue}$ ratio is higher for mare surface. Bright highland craters do not show up on the $|P_{min}|_{red}$ / $|P_{min}|_{blue}$ images. This probably is related to the fact that the lunar highland is more spectrally neutral, than mare regions.

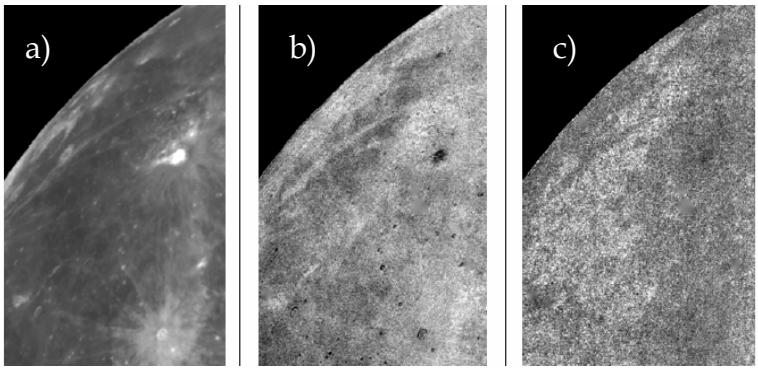

Figure 1: Images of a) albedo, b) $|P_{min}|$ in blue light, and c) ratio $|P_{min}|_{red}$ / $|P_{min}|_{blue}$ for the northwestern portion of the lunar disk. The bright spot on right side of the albedo image is the crater Aristarchus.

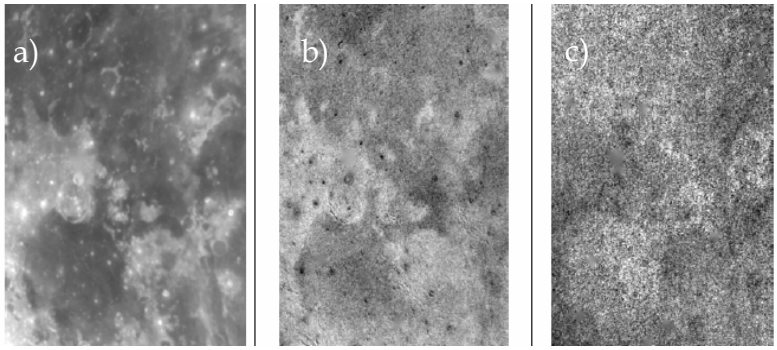

Figure 2: Images of a) albedo, b) $|P_{min}|$ in blue light, and c) the ratio $|P_{min}|_{red}$ / $|P_{min}|_{blue}$ for the southwestern portion of the lunar disk including Mare Humorum.

3 Results and discussion

Comparing the albedo and $|P_{min}|$ images in Fig. 1-4, one can see that for the low albedo domain there is a direct correlation between $|P_{min}|$ and albedo (the brighter the lunar detail, the higher its $|P_{min}|$), while for bright lunar areas (young craters) the correlation is inverted. Unfortunately, the interpretation basis for the $|P_{min}|$ variations is not sufficiently developed to explain these observations. From laboratory experiments

we know that the wide negative polarization branch values of $|P_{min}|$ is a function of particulate surface albedo and particle size [3,8,9]. The brighter the particulate surface, the higher, the incoherent multiple scattering, hence, the lower $|P_{min}|$ should be. On the other hand, the smaller the particle size, the deeper the negative polarization branch, i.e. higher $|P_{min}|$. Thus the inverse correlation between albedo and $|P_{min}|$ can be attributed to the multiple scattering reducing $|P_{min}|$ as well as the fact that young (bright) craters are composed of particles coarser than those of the mature regoliths. It is more difficult to interpret the direct correlation at the low albedo domain. This correlation exists regardless of the effect of multiple scattering. An explanation of the direct correlation can be related to the scattering properties of single particles. Using the DDA method we calculated the polarization phase curves (Fig. 4, left panel) for aggregated particles (Fig. 4, right panel) averaged over orientation at different values of the imaginary part (Im(m)) of the refractive index m. As can be seen $|P_{min}|$ increases with decreasing absorption Im(m). Many different series of such calculations show the same. We suppose that this effect could be responsible for the direct correlation between albedo and $|P_{min}|$ in the low-albedo domain, when multiple scattering is small.

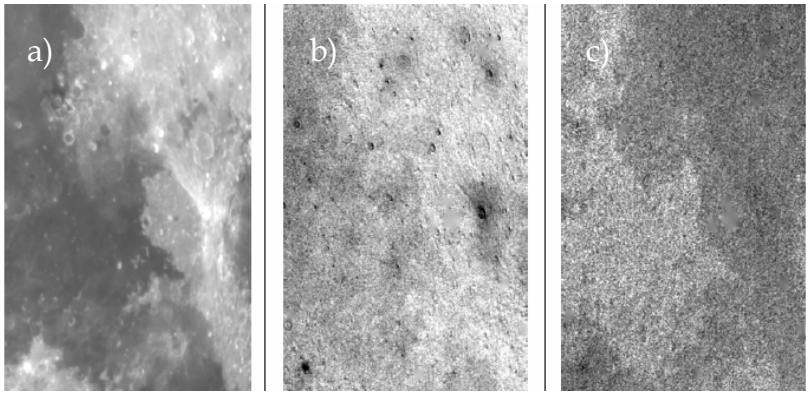

Figure 3: Images of a) albedo, b) $|P_{min}|$ in blue light, and c) the ratio $|P_{min}|_{red}$ / $|P_{min}|_{blue}$ for the eastern portion of the lunar disk. The bright spot on the right side of the albedo image is the crater Proclus.

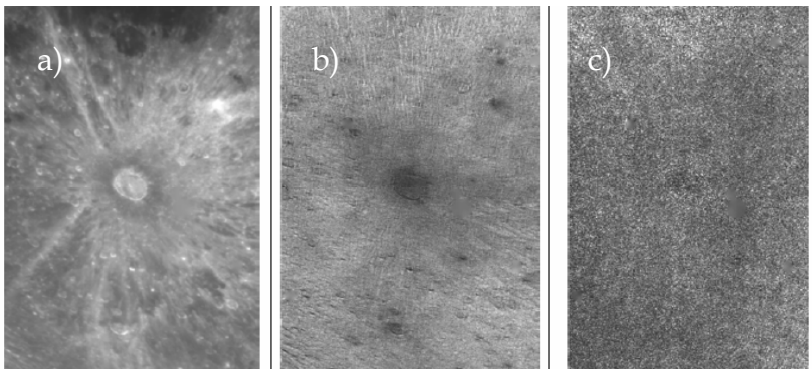

Figure 4: Images of a) albedo, b) $|P_{min}|$ in blue light, and c) the ratio $|P_{min}|_{red}$ / $|P_{min}|_{blue}$ for the southern portion of the lunar disk. In the center of the albedo image one can see the crater Tycho.

The northwestern portion of the lunar nearside that includes the craters Aristarchus and Kepler is shown in Fig. 1. The crater Aristarchus reveals a low polarization degree, as small as 0.6 % in blue light. Unexpectedly the Reiner gamma formation (left lower corner) shows up as a unit with relatively high $|P_{min}|$. Figure 2 presents albedo and polarimetric images for the southwestern portion of the lunar disk including Mare Humorum (left lower portion of the frame). Two low $|P_{min}|$ areas can be seen in the frame, near the upper edge and again a bit to right and below the center. These areas are not peculiar in albedo. For the image in Fig. 2 the border between highlands and maria is clearly seen in the $|P_{min}|$ image. The eastern portion of the lunar disk is presented in Fig. 3. The crater Proclus and its ray system conspicuously show up on this scene, $|P_{min}|_{blue} \approx 0.4$. No trace of the crater and rays may be found on the

image $|P_{min}|_{red}$ / $|P_{min}|_{blue}$. The same is observed for the crater Tycho (Fig. 4). We note that in many cases nearby young craters with the same albedo reveal very different values of $|P_{min}|$.

4 Conclusion

We have presented the first results of our polarimetric measurements of the Moon at a phase angle near 11°. The observations in the red and blue spectral bands were carried out with the Kharkov 50-cm telescope at the Maidanak Observatory using a Canon-350D camera and polarizing filter that provides reliable detection of significant variations of $|P_{min}|$ over the lunar surface, from 0.2 to 1.6 %. The smallest $|P_{min}|$ are characteristic of young bright craters; the parameter $|P_{min}|$ is highest for highland and bright mare areas. In many cases bright young craters with the similar albedo reveal very different values of $|P_{min}|$.

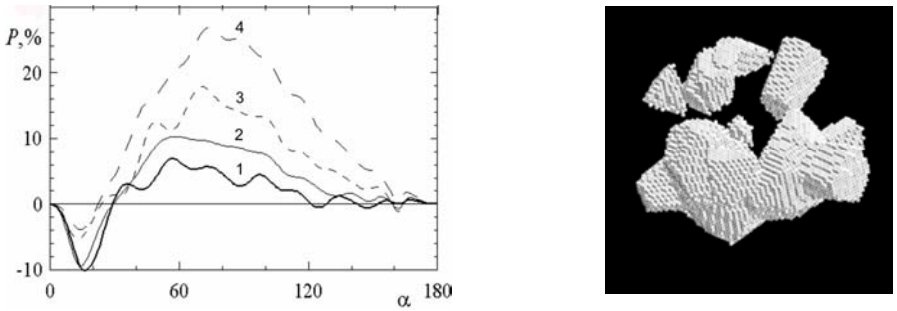

Figure 5: Polarization phase curves (left panel) calculated for aggregate particles (right panel) at Re(m) = 1.5, $X = 2\pi r/\lambda = 10$, where r is the radius of circumscribed sphere and λ is the wavelength. Curves 1-4 correspond to Im(m) = 0, 0.02, 0.05, and 0.1, respectively.

References

[1] A. Dollfus, E. Bowell "Polarimetric properties of the lunar surface and interpretation. I. Telescope observation". Astron. Astrophys. 10. 29-53 (1971).

[2] Yu.G. Shkuratov, N.V. Opanasenko, M.A. Kreslavsky "Polarimetric and photometric properties of the Moon: Telescope observation and laboratory simulation. 1. The negative polarization". Icarus 95. 283-299 (1992).

[3] Yu. Shkuratov, G. Videen, M. Kreslavsky, I. Belskaya, A. Ovcharenko, V. Kaydash, V. Omelchenko, N. Opanasenko, E. Zubko. "Scattering properties of planetary regoliths near opposition", in: Photopolarimetry in Remote Sensing / Eds. G. Videen, Ya. Yatskiv, and M. Mishchenko. pp. 191-208. (NATO Science Series. Kluwer Academic Publishers, London. 2004).

[4] N. V. Opanasenko, Yu. G. Shkuratov "Simultaneous polarimetry and photometry of the Moon". Solar System Research 28, 233-254 (1994).

[5] O. I. Kvaratskhelia "Spectropolarimetry of the lunar surface and its ground samples". Bull. Abastumani Astrophys. Obser. V.64. Tbilisi. (1988). 312 p.

[6] Yu. Shkuratov, N. Opanasenko, E. Zubko, Ye. Grynko, V. Korokhin, C. Pieters, G. Videen, U. Mall, A. Opanasenko. "Multispectral polarimetry as a tool to investigate texture and chemistry of lunar regolith particles". Icarus 187. 406–416 (2007).

[7] N. V. Opanasenko, A. A. Dolukhanyan, Yu. G. Shkuratov, D. G. Stankevich, M. A. Kreslavsky, V. G. Parusimov. "Polarization map of the Moon at the minimum of the negative branch". Solar System Research 28, 98-105 (1994).

[8] Yu. Shkuratov, A. Ovcharenko, E. Zubko, O. Miloslavskaya, R. Nelson, W. Smythe, K. Muinonen, J. Piironen, V. Rosenbush, P. Helfenstein. "The opposition effect and negative polarization of structurally simulated planetary regoliths." Icarus 159. 396-416 (2002).

[9] Yu. Shkuratov, S. Bondarenko, A. Ovcharenko, C. Pieters, T. Hiroi, H. Volten, O. Munos, G. Videen. "Comparative studies of the reflectance and degree of linear polarization of particulate surfaces and independently scattering particles." JQSRT 100, 340-358 (2006).

Pattern equation method based on Wilcox representation

N.I.Smirnova[1], A.G.Kyurkchan[1]

[1] *Moscow Technical University of Communication and Informatics,*
Aviamotornaya Street 8A, 111024, Moscow, Russian Federation
tel:+7 (495) 310-3575, e-mail: nadya-ussr@yandex.ru

Abstract

The variant of the pattern equation method, based on representation of a wave field by Atkinson-Wilcox expansion, is proposed for the solution of wave diffraction problem on compact scatterers. The basic integral-operator equation of the method is deduced and it's algebraization is obtained. Limitations on scatterer geometry, at which algebraic system can be resolved by a reduction method, are established. The analytical solution of plane wave diffraction problem on a sphere is obtained and it is shown, that it merges into the known classical solution at some special value of one of the method parameters. The suggested approach is illustrated by numerical example.

1 Introduction

The pattern equation method (PEM), for the first time suggested by the author in 1992 [1,2], subsequently has been successfully applied to the solution of the wide range of the waves scattering and propagation problems. At present moment about 30 papers dedicated to PEM application to the solution of various diffraction theory problems have been published in the leading journals. Some aspects of the method were also applied by other authors (see, for example, [3-5]).

Original variant of PEM is based on the plane wave representation of diffracted field by Sommerfeld-Weil integral [1, 2, 6]. The method is universal enough, and the algorithms based on it converge very fast.

However, the original method is poorly suitable for the solution of diffraction problems when the characteristic sizes of a scatterer are much greater than wavelength. The approach allowing to overcome this difficulty is developed below. The new approach is based on the wave field representation by a Atkinson-Wilcox series [7]. It is shown [8], that this series, converge in the area $r > 2\sigma/k$, where r is radial spherical coordinate, σ is a growth parameter of the scattering pattern [8,9] and k is a wavenumber. However, when the scatterer sizes are much greater than wavelength, Atkinson-Wilcox series, which are reduced to the first few summands, can be treated as asymptotic expansion [10].

2 The statement of the problem and its solution

So, lets consider a scalar diffraction problem on a compact scatterer, bounded by a surface S. We assume for definiteness, that Dirichlet boundary condition is satisfied on S. Thus, we seek a wave field function $u^1(\vec{r})$, as the solution of the following problem:

$$\Delta u^1 + k^2 u^1 = 0, \quad \vec{r} \in \mathbf{R}^3 \setminus \bar{D}, \quad (u^0 + u^1)\big|_S = 0, \tag{1}$$

where D is an area inside S, u^0 is an incident (primary) wave. Function u^1 should also satisfy a Sommerfeld condition of radiation on infinity [11].

In spherical coordinates (r,θ,φ) function $u^1(\vec{r})$ has the following representation [7]:

$$u^1(r,\theta,\varphi) = \frac{e^{-ikr}}{kr} \sum_{j=0}^{\infty} \frac{g_j(\theta,\varphi)}{(kr)^j}, \tag{2}$$

where $g_0(\theta,\varphi) \equiv g(\theta,\varphi)$ is the pattern of wave field (the scattering pattern), and functions $g_j(\theta,\varphi)$ for $j > 0$ are determined by recurrent relations

$$g_j(\theta,\varphi)=\frac{i}{2j}[j(j-1)g_j(\theta,\varphi)+\mathrm{D}g_j(\theta,\varphi)],\quad j=1,2,3,\ldots, \tag{3}$$

in which $\mathrm{D}\equiv\frac{1}{\sin\theta}\frac{\partial}{\partial\theta}\left(\sin\theta\frac{\partial}{\partial\theta}\right)+\frac{1}{\sin^2\theta}\frac{\partial^2}{\partial\varphi^2}$ is the Beltrami operator [11,12].

We can combine the relations Eq. (2) and Eq. (3) using operator W (we call it Wilcox operator) so, that $u^1(r,\theta,\varphi)=W\left[g(\theta,\varphi)\right]$.

In case of Dirichlet boundary condition the following representation is valid

$$g(\alpha,\beta)=-\frac{k}{4\pi}\int_S\left.\frac{\partial u}{\partial n}\right|_S\exp\left(ikr\big|_S\cos\gamma\right)ds, \tag{4}$$

here $u=u^0+u^1$ is a full field, $\frac{\partial}{\partial n}$- differentiation in the direction of external normal to S, $\cos\gamma=\sin\alpha\sin\theta\cos(\beta-\varphi)+\cos\alpha\cos\theta$, $r\big|_S=\rho(\theta,\varphi)$ is the equation of a surface S in spherical coordinates.

Let's introduce the following notations:

$$v(\theta,\varphi)=-\frac{k}{4\pi}d_nu,\quad v^0(\theta,\varphi)=-\frac{k}{4\pi}d_nu^0,\quad v^1(\theta,\varphi)=-\frac{k}{4\pi}d_nu^1, \tag{5}$$

where $d_nu\equiv\kappa\rho\left.\frac{\partial u}{\partial n}\right|_S=\left.\left(\rho^2\sin\theta\frac{\partial u}{\partial r}-\rho'_\theta\sin\theta\frac{\partial u}{\partial\theta}-\frac{\rho'_\varphi}{\sin\theta}\frac{\partial u}{\partial\varphi}\right)\right|_{r=\rho(\theta,\varphi)}$, $\kappa=\sqrt{\left(\rho^2+\rho'^2_\theta\right)\sin^2\theta+\rho'^2_\varphi}$.

Using these notations, representation (4) can be rewritten as follows

$$g(\alpha,\beta)=\int_0^{2\pi}\int_0^{\pi}v(\theta,\varphi)\exp\left(ik\rho(\theta,\varphi)\cos\gamma\right)d\theta d\varphi. \tag{6}$$

Combining Eq. (6) and Wilcox operator introduced above, finally we have

$$g(\alpha,\beta)=g^0(\alpha,\beta)-\frac{k}{4\pi}\int_0^{2\pi}\int_0^{\pi}d_nW\left[g(\theta,\varphi)\right]\exp\left(ik\rho(\theta,\varphi)\cos\gamma\right)d\theta d\varphi. \tag{7}$$

Here $g^0(\theta,\varphi)$ is the integral similar to Eq. (6), where the function $v^0(\theta,\varphi)$ is used instead of $v(\theta,\varphi)$.

Thus, the relation Eq. (7) is the sought integral-operator equation of PEM.

Let's algebraize the problem. For this purpose we shall expand function $g(\theta,\varphi)$ on some basis. For example, using the spherical harmonics, we shall have $g(\theta,\varphi)=\sum_{n=0}^{\infty}\sum_{m=-n}^{n}a_{nm}P_n^m(\cos\theta)e^{im\varphi}$, $g_j(\theta,\varphi)=\sum_{n=0}^{\infty}\sum_{m=-n}^{n}a_{nm}^jP_n^m(\cos\theta)e^{im\varphi}$. Using Eq. (3) it is easy to establish, that $a_{nm}^j=\frac{\left(n+\frac{1}{2},j\right)}{(2i)^j}a_{nm}$, where $\left(n+\frac{1}{2},j\right)=\begin{cases}\frac{1}{j!}\prod_{s=1}^{j}\left[n(n+1)-s(s-1)\right], j=1,2,\ldots\\ 1,\quad j=0\end{cases}$ is Hankel symbol [13]. Using the notation

$$\frac{e^{-ikr}}{kr}\sum_{j=0}^{J}\frac{\left(n+\frac{1}{2},j\right)}{(2ikr)^j}\equiv h_n^J(kr), \tag{8}$$

expansion Eq. (2) can be rewritten as follows

$$u^{1J}(r,\theta,\varphi)=\sum_{n=0}^{\infty}\sum_{m=-n}^{n}a_{nm}h_n^J(kr)P_n^m(\cos\theta)e^{im\varphi}. \tag{9}$$

The index "*J*" means, that in relation Eq. (9) only first (*J*+1) summands of the sum Eq. (8) are kept, therefore it is now approximate. From Eq. (9) and Eq. (5) we have

$$d_nu^{1J}(\theta,\varphi)=\sum_{n=0}^{\infty}\sum_{m=-n}^{n}a_{nm}\left[k\rho^2(\theta,\varphi)h_n^{J'}(k\rho)P_n^m(\cos\theta)\sin\theta-\rho'_\theta h_n^J(k\rho)\frac{dP_n^m}{d\theta}\sin\theta-\frac{im}{\sin\theta}\rho'_\varphi h_n^J(k\rho)P_n^m(\cos\theta)\right]e^{im\varphi}. \tag{10}$$

3 Bodies of revolution

Let's consider, for example, a case of a body of revolution, i.e. a situation, when $\rho(\theta,\varphi)=\rho(\theta)$. Let also u^0 be the field of a plane wave, i.e.

$$u^0 \equiv e^{-ikr\cos\gamma_0} = \sum_{n=0}^{\infty}\sum_{m=-n}^{n}(-i)^n(2n+1)\frac{(n-m)!}{(n+m)!}j_n(kr)P_n^m(\cos\theta)P_n^m(\cos\theta_0)e^{im(\varphi-\varphi_0)},$$

where $\cos\gamma_0=\sin\theta_0\sin\theta\cos(\varphi_0-\varphi)+\cos\theta_0\cos\theta$, θ_0,φ_0 are incident angles. In this case the equation Eq. (7) is reduced to the following algebraic system

$$a_{nm}^J = a_{nm}^0 + \sum_{\nu=|m|}^{\infty} G_{nm,\nu m}^J a_{\nu m}^J, \quad n=0,1,2,...;\ m=0,\pm1,...\pm n, \tag{11}$$

where $G_{nm,\nu m}^J = -i^n\frac{(2n+1)}{2}\frac{(n-m)!}{(n+m)!}\delta_{\mu m}\int_0^{\pi}[k^2\rho^2(\theta)h_\nu^{J\prime}(k\rho)P_\nu^m(\cos\theta)\sin\theta -$

$$-k\rho'_\theta h_\nu^J(k\rho)\frac{dP_\nu^m}{d\theta}\sin\theta]j_n(k\rho)P_n^m(\cos\theta)d\theta, \tag{12}$$

$$a_{nm}^0 = i^n\frac{(2n+1)}{2}\frac{(n-m)!}{(n+m)!}e^{-im\varphi_0}\int_0^{\pi} j_n(k\rho)P_n^m(\cos\theta)\sum_{\nu=|m|}^{\infty}(-i)^\nu(2\nu+1)\frac{(\nu-m)!}{(\nu+m)!}P_\nu^m(\cos\theta_0)\times$$

$$\times[k^2\rho^2(\theta)j_\nu{}'(k\rho)P_\nu^m(\cos\theta)\sin\theta - k\rho'_\theta j_\nu(k\rho)\frac{dP_\nu^m}{d\theta}\sin\theta]d\theta. \tag{13}$$

For sphere ($\rho(\theta)=a$) at $\theta_0=\varphi_0=0$ from Eq. (12) and Eq. (13) we obtain

$$G_{nm,\nu\mu}^J = -\delta_{\mu m}\delta_{\nu n}i^n k^2a^2 j_n(ka)h_n^{J\prime}(ka),\ a_{nm}^0 = -k^2a^2(2n+1)j_n(ka)j_n'(ka)\delta_{m0}. \tag{14}$$

Solving system Eq. (11) using Eq. (14), we obtain

$$a_{nm}^J = -\frac{k^2a^2(2n+1)j_n(ka)j_n'(ka)\delta_{m0}}{1+i^nk^2a^2j_n(ka)h_n^{J\prime}(ka)}. \tag{15}$$

The obtained solution (taking into account the remark after the formula Eq. (9)) is approximate. The solution Eq. (15), as well as initial relations Eqs. (9) - (14), become exact, if in (8) J is replaced by n. Thus expression $i^{n+1}h_n^J(kr)$ turns into spherical Hankel function $h_n^{(2)}(kr)$, and an expression Eq. (15) becomes

$$a_{nm} = -i(2n+1)\frac{j_n(ka)}{h_n^{(2)}(ka)}\delta_{m0}, \tag{16}$$

which coincides with classical result [14].

Figure 1 shows the scattering patterns of sphere with radius *ka*=21, calculated using the exact solution Eq. (16) (a continuous curve at *N*=40, a dotted curve at *N*=20) and approximate solution Eq. (15) (a dashed curve). *N* is the maximal number of value *n* in series for the scattering pattern. Parameter *J* in Eq. (15) has been set to 20. Good agreement between exact and approximate (at *J*=20) results is observed.

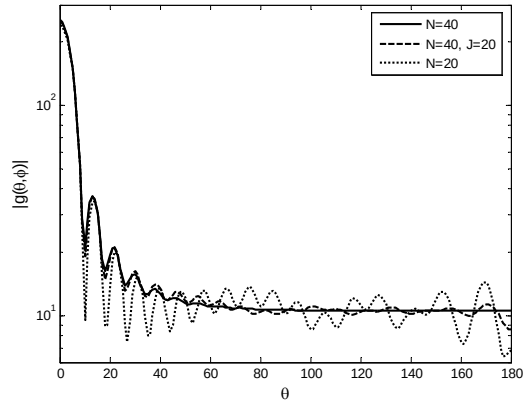

Figure 1: The scattering patterns of sphere with radius ka=21.

4 Conclusion

Thus, we obtained an already known variant of PEM, if in relations Eqs. (9) - (12) we replace J by n. However, fixing J on any finite value we achieve an alternative approach, allowing, as we just demonstrated, to solve (although approximately) problems of waves scattering by bodies with sizes considerably larger than incident field wavelength. The proposed approach can be easily extended to other kinds of boundary conditions, and also on vector scattering problems.

Acknowledgments

This work was supported by the Russian Foundation for Basic Research, project № 06-02-16483.

References

[1] A.G.Kyurkchan, "A new integral equation in the diffraction theory", Soviet Physics Doklady. **37**, 338-340, (1992).

[2] A.G.Kyurkchan, "About one method of the solution of waves diffraction problems on the scatterers of finite sizes", Physics Doklady. **39**, 728-731, (1994).

[3] A.Hizal, A.Marincic, "New rigorous formulation of electromagnetic scattering from perfectly conducting bodies of arbitrary shape", Proc. IEE. **117**, 1639-1647, (1970).

[4] M.Ochmann, "The full-field equations for acoustic radiation and scattering", J. Acoust. Soc. Amer. **105**, 2574-2584, (1999).

[5] V.B.Il'in, A.A.Loskutov, V.G.Farafonov, "Modification and investigation of T-matrix method", Comp. Math. Math. Phys. **44**, 329-348, (2004).

[6] Do Dyk Tkhang, A.G.Kyurkchan, "Efficient method for solving the problems of wave diffraction by scatterers with broken boundaries", Acoustical Physics. **49**, 43-50 (2003).

[7] C.H.Wilcox, "An expansion theorem for electromagnetic fields", Comm. on Pure and Appl. Mathem. **9**, 115-134. (1956).

[8] A.G.Kyurkchan, "On the exact value of the radius of convergence of the Wilcox series", Soviet Physics Doklady. **36**, 567-569, (1991).

[9] V.F.Apeltsin, A.G.Kyurkchan, *Analytical properties of wave fields* (Moscow State University, Moscow, 1990).

[10] V.A.Borovikov, B.E.Kinber, *The Geometrical Theory of Diffraction* (Svyaz, Moscow, 1978).

[11] R.Courant, *Partial Differential Equations* (Wiley, New York, 1962).

[12] M.Abramowitz, I.A.Stegun, *Handbook of Mathematical Functions* (National Bureau of Standards, New York, 1964).

[13] A.Sommerfeld, *Partielle Differentialgleichungen der Physik* (Leipzig, 1948).

[14] C. F. Bohren and D. R. Huffman, *Absorption and Scattering of Light by Small Particles* (Wiley, New York, 1983).

The Effect of Particle Size, Composition, and Shape on Lidar Backscattering

Anu-Maija Sundström, Timo Nousiainen, and Tuukka Petäjä

University of Helsinki, Department of Physical Sciences,
P.O.Box 68 , 00014 University of Helsinki, Finland

Abstract

The optical properties of urban aerosol particles are calculated using exact methods at 910 nm wavelength under different assumptions about particle composition and shape. Results show that spherical particles backscatter light on the average about 40 percent more than the corresponding nonspherical particles, the difference generally being larger for larger particles. In contrast, changing the particle composition from water to silicate increases backscattering by about a factor of three. Typical values for absorptivity seem to have negligible impact on backscattering.

1 Introduction

Accurate modeling of light scattering properties of aerosol particles is essential to conduct reliable remote sensing observations. Although it is well known that the scattering properties of nonspherical particles can be significantly different from those of spherical particles, assumption of spherical particles is still widely used in remote sensing applications. This can lead to large errors when retrieving aerosol optical properties with lidar inversions, especially if dust particles are present (e.g [1]).

The aim of this work was to study the effect of particle size, shape, and composition on lidar backscattering in an urban environment. On one hand, sensitivity studies based on optical modelling were conducted to estimate the relative importance of different physical factors affecting backscattering of light by aerosol particles. On the other hand, modeled backscattering values were compared with lidar measurements. To facilitate the comparison, the lidar measurements were conducted in a vicinity of aerosol in situ measurement site.

2 Methods

A lidar measures backscattering that is the sum of all scatterers - air molecules, aerosol particles and hydrometeors - within the measurement volume. To solve the lidar equation (e.g. [2]), the relation between volume backscattering coefficient β, and volume extinction coefficient σ has to be known. Physically β describes how much light is scattered in the backward direction from a measurement volume and is defined ultimately by particles' phase function and scattering cross section. Similarly, σ describes the total amount of energy removed from the incident field and is defined by particles' extinction cross section. Most common solution to the lidar equation is to assume a linear relation between β and σ, which is usually called the lidar ratio R (e.g. [2]).

To study how physical properties of aerosol particles affect the lidar signal (or β, σ, and R), we need to know how the optical properties of the particles (e.g. phase function, scattering and extinction cross sections) depend on their physical properties, i.e. particles' composition and shape. For simplicity, the effect of particle composition was only studied for spheres. Mie

simulations were carried out varying both the real and the imaginary part of the refractive index. For the real part, values of 1.5 and 1.3 were used. The former value is representative of many dust aerosol types as well as sea salt and ammonium sulphate, whereas the latter is close to that for liquid water. For the imaginary part, values of 0.0 and 0.001 were used. The former is used for nonabsorbing aerosol, whereas the latter is considered a representative effective value for the expected mixture of the aerosol in Urban Helsinki.

Likewise, when the effect of particle shape was studied, particle composition was assumed to be fixed. Since no shape information was available, a modeling approach for solid urban aerosol particles could not be developed. Thus, we assumed that their optical properties can be computed using the modeling approach for dust aerosol as in [3]. The optical properties of irregularly shaped urban aerosol particles were described by a distribution of randomly oriented spheroids. As suggested in [3] for dust particles, we used the shape distribution that weights most heavily the most elongated spheroids in the distribution.

The measurements were conducted at the Kumpula campus of the University of Helsinki, which is located in a heterogeneous urban area about 5 km away from the center of Helsinki. The lidar measurements were carried out using a vertically pointing Vaisala CL31 ceilometer, which is an elastic backscatter lidar that operates at 910 nm wavelength. Particle *In Situ* measurements at ground level were conducted 250 m from the lidar site. Aerosol size distributions were obtained by combining results from two different instruments (Differential Mobility Particle Sizer DMPS and Aerosol Particle Sizer APS) that together covered particle diameters ranging from 3 nm to 20 μm.

3 Results

Three rainless days from summer 2005 were selected to these sensitivity studies. For each day the effective radius r_{eff} and variance v_{eff} from the measured size distribution was calculated, as well as the values of β, σ, and R. In addition the value of β measured with lidar was determined.

Both the composition (excepting absorption) and shape had a substantial effect on backscattering. The values of β, σ, and R for water droplets were on average 0.33, 0.53, and 0.62 times the values for spherical silicates, respectively. Similarly, for nonspherical particles the values of optical parameters were on average 0.60, 0.79, and 0.76 times the values for spherical particles. In Fig. 1 the difference in these quantities due to composition and shape are expressed as a water/silicate and nonspherical/spherical ratios. In both cases the results also depended on the particle size but in different way. The effect of composition on σ increased with decreasing values of r_{eff}, whereas the effect of particle shape on β increased with increasing values of r_{eff}.

In addition theoretically calculated values for β were compared with backscattering measured with lidar, denoted as β_{meas}. To define only the aerosol contribution to β_{meas} , backscattering from hydrometeors and molecules had to be excluded. The molecular contribution to β_{meas} was assumed to be constant, at sea level and at 910 nm wavelength $1.855 \cdot 10^{-7}$ $m^{-1}srad^{-1}$ [4]. Hydrometeors were excluded simply by choosing to study days when no rain, drizzle or mist was observed. The comparisons revealed that theoretically calculated values for β were on average 3.6 and 2.1 times higher than β_{meas}, if aerosol particles were assumed to be spherical or nonspherical silicates, respectively.

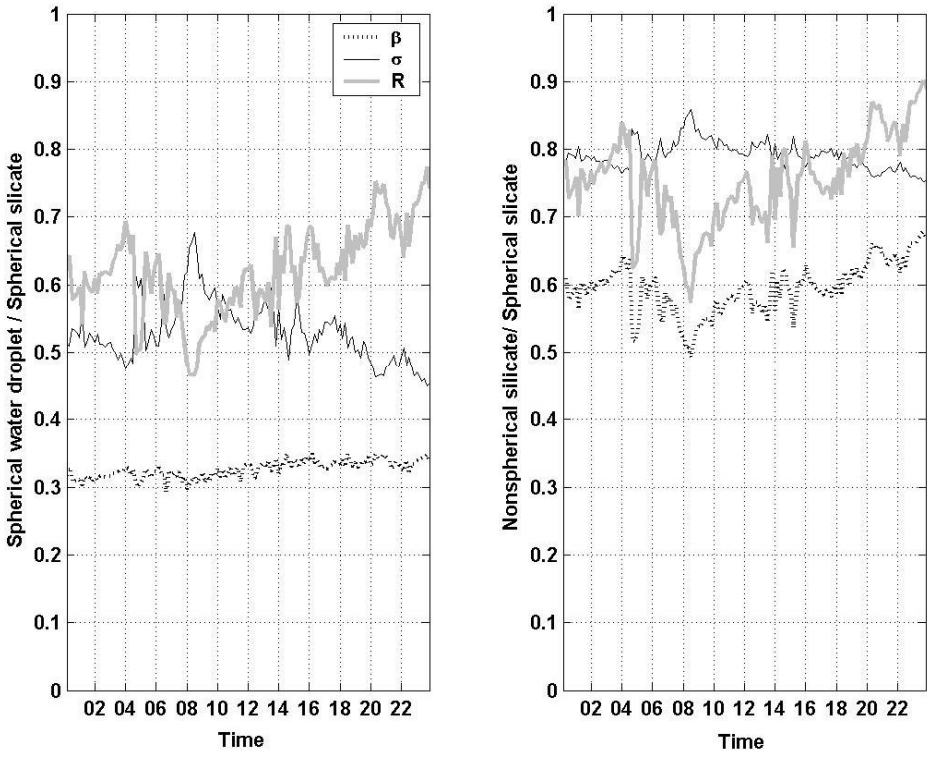

Figure 1. The effect of particle composition (right panel) and shape (left panel) on theoretically calculated β, σ, and R during one example day, represented as a water/silicate and nonspherical/spherical ratios. For water droplets the value of refractive index was m=1.3+i0.0 and for silicates m=1.5+i0.0.

4 Conclusion

Results showed that particle composition (with the exception of absorption) and shape had substantial effect on backscattering. A connection of these effects to the variation in size distribution was also observed.

The agreement between theoretically calculated and lidar measured backscattering was found to be better for nonspherical than for spherical silicates. It should be noted, however, that such a comparison is meaningful only if the in situ-measured particle size distribution can be considered representative for the particle size distribution in the lidar's measurement volume. In our case, this depends not only on possible local aerosol sources, but also on ambient meteorological conditions. Further, differences could be caused by calibration-related issues related to lidar, or an uncertain sampling efficiency for the DMPS and APS instruments.

References

[1] Mishchenko, M. I., L. D. Travis, R. A. Kahn, and R. A. West, 1997: Modeling phase functions for dustlike tropospheric aerosols using a shape mixture of randomly oriented polydisperse spheroids. *J. Geophys. Res.*, **102**, 16831–16847.

[2] Klett, J., 1981: Stable analytical inversion solution for processing lidar returns. *Appl. Opt.*, **20**, 211–220.

[3] Nousiainen, T., M. Kahnert, and B. Veihelmann, 2006: Light scattering modeling of small feldspar aerosol particles using polyhedral prisms and spheroids. *J. Quant. Spectrosc. Radiat. Transfer*, **101**, 471–487, doi:10.1016/j.jqsrt.2006.02.038.

[4] Measures, R. M., 1984: *Laser remote sensing: fundamentals and applications*. Wiley, New York, 510 pp.

Backscattering of light from a layer of densely packed random medium

Victor P. Tishkovets

Institute of Radioastronomy of NASU, 4 Chervonopraporna St., Kharkov 61002. Ukraine

E-mail: tishkovets@ira.kharkov.ua

Abstract

The theory of light scattering by systems of nonspherical particles is applied to derive equations corresponding to incoherent (diffuse) and interference parts of radiation reflected from the medium. A solution of the system of linear equations describing the light scattering by a system of particles is represented by iteration. The symmetry properties of the T-matrices and of the translation coefficients for the vector Helmholtz harmonics lead to the reciprocity relation for an arbitrary iteration. This relation is applied to consider the backscattering enhancement phenomenon. In the exact backscattering direction the relation between incoherent and interference parts is identical to that for sparse media.

The problem of light scattering by densely packed discrete random media is important for many areas of science and technology. In particular this problem is of interest to astrophysics. The surfaces of the majority of atmosphereless solar system bodies are covered with regolith and the interpretation of optical observations of them must be based on an adequate theory of light scattering by a densely packed medium. Some of these bodies exhibit the opposition effect (or the effect of coherent backscattering [1,2]). The effect of coherent backscattering has been observed in numerous laboratory experiments as well [2]. It is caused by the constructive interference of multiple scattered waves traveling in a discrete medium in a certain direct and reversal trajectories [1,2]. The well known Saxon's reciprocity relation [3] is applied to investigate of the effect of coherent backscattering. Although the Saxon's reciprocity relation is valid for arbitrary finite scatterers including systems of particles, it is valid only in the far-field zone of the scatterers. In theoretical analysis of multiple scattering of waves by media this relation can be applied only for sparse media whose particles are located in the far-field zones of the each other. Because of this, the effect of coherent backscattering is comparatively well studied for such media. In particular, for sparse media a relation between the incoherent and coherent parts of scattered light in the exact backscattering direction has been obtained [4,5]. This relation allows one to calculate the amplitude of the interference peak of the coherent backscattering effect using the vector radiative transfer equation only [4]. Equations for describing the angular dependence of the interference part of multiply scattered waves by a layer of sparse medium of randomly oriented arbitrary particles have been obtained in [6,7].

In this work the theory of light scattering by densely packed systems (aggregates) of nonspherical particles is applied to study the light scattering by densely packed media. It is assumed that the $\mathbf{T}$-matrices of all aggregate particles are known in their local coordinate systems and that the smallest circumscribing spheres of all particles do not overlap with each other. A solution of the system of equations describing scattering of waves by particles is represented by a method of iteration. It is shown that the symmetry properties of the $\mathbf{T}$-matrices and of the translation coefficients of the vector Helmholtz harmonics lead to the reciprocity relation for an arbitrary iteration. For the amplitude matrix of an iteration this relation is identical to the Saxon's reciprocity relation. For example, let $S_{pn}^{(j,\sigma,s)}(\mathbf{k}_0,\mathbf{k}_{sc})$ be the amplitude scattering matrix for the wave propagating in the direction $\mathbf{k}_0$ with initial polarization n, scattered first by particle s, then by particle σ and finally by particle j in the direction $\mathbf{k}_{sc}$ with final

polarization p. (Here the so-called CP-representation is used in which the polarization indexes $n, p = \pm 1$). In this case the reciprocity relation can be written as

$$S_{pn}^{(j,\sigma,s)}(\mathbf{k}_0, \mathbf{k}_{sc}) = S_{np}^{(s,\sigma,j)}(-\mathbf{k}_{sc}, -\mathbf{k}_0). \quad (1)$$

The symmetry relation for the amplitude scattering matrix (1) is applied to consider the backscattering enhancement phenomenon for macroscopically homogeneous, isotropic and mirror-symmetric medium. Let the medium be in form of plane-parallel layer and the upper boundary of the medium coincides with the plane $(x_0 y_0)$ of the coordinate system $\hat{\mathbf{n}}_0$ (Fig.1). In the paper bold letters with carets $\hat{\mathbf{n}}_i$ denote right-handed coordinate systems (x_i, y_i, z_i) with the z_i-axes along the vectors $\mathbf{n}_i$. The scattering matrix, which transforms the Stokes parameters of the incident light into those of the scattered light is supposed to be in the form:

$$S_{pn\mu\nu} = S_{pn\mu\nu}^{(L)} + S_{pn\mu\nu}^{(C)}. \quad (2)$$

Here matrix $S_{pn\mu\nu}^{(L)}$ describes the diffuse (incoherent) part of scattered light and matrix $S_{pn\mu\nu}^{(C)}$ describes the coherent (interference) part. $p, n, \mu, \nu = \pm 1$.

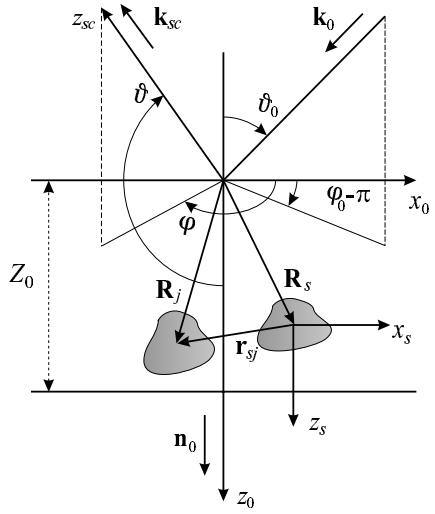

Figure 1. Geometry of scattering of light by a layer.

Equations for matrixes $S_{pn\mu\nu}^{(L)}$ and $S_{pn\mu\nu}^{(C)}$ are obtained using the quasi-crystalline approximation and an approach described in [6,7]. Radii of the circumscribing spheres of all particles are assumed to be identical.

$$S_{pn\mu\nu}^{(L)} = \frac{\eta}{k_0} \sum_{LMlm} \frac{(2L+1)(2l+1)}{4} D_{Mp}^{*L}(\varphi, \vartheta, 0) D_{m\mu}^{l}(\varphi, \vartheta, 0) \int_0^{k_0 Z_0} B_{LMlm}^{(z)(pn)(\mu\nu)} \exp\left(\frac{\tau z}{\cos\vartheta}\right) dz, \quad (3)$$

where η is the concentration of particles, $k_0 = 2\pi/\lambda$, $\tau = 2\,\mathrm{Im}(m_{eff})$, $m_{eff} = \mathrm{Re}(m_{eff}) + i\,\mathrm{Im}(m_{eff})$ is the effective refractive index of the medium, Z_0 is the thickness of the medium. Matrix $S_{pn\mu\nu}^{(L)}$ is defined per unit area of the upper boundary of the medium. $D_{Mn}^{L}(\varphi, \vartheta, \gamma)$ is the Wigner function, $\varphi, \vartheta, \gamma$ are the Euler angles determining the rotation from the coordinate system $\hat{\mathbf{n}}_0$ into coordinate system $\hat{\mathbf{k}}_{sc}$ (Fig.1).

Coefficients $B_{LMlm}^{(z)(pn)(\mu\nu)}$ are determined from the system of equations

$$B_{LML_1M_1}^{(z)(pn)(\mu\nu)} = \exp\left(-\frac{\tau z}{\cos\vartheta_0}\right)\sum_{lml_1m_1} t_{LMlm}^{(pn)} t_{L_1M_1l_1m_1}^{*(\mu\nu)} D_{mn}^{l}(\varphi_0,\vartheta_0,0) D_{m_1\nu}^{*l_1}(\varphi_0,\vartheta_0,0) +$$
$$+\eta \sum_{qq_1lml_1m_1} t_{LMlm}^{(pq)} t_{L_1M_1l_1m_1}^{*(\mu q_1)} \sum_{l_2m_2l_3m_3} \int g(r) B_{l_2m_2l_3m_3}^{(y)(qn)(q_1\nu)} H_{lml_2m_2}^{(q)}(\hat{\mathbf{n}}_0,\hat{\mathbf{r}}) H_{l_1m_1l_3m_3}^{*(q_1)}(\hat{\mathbf{n}}_0,\hat{\mathbf{r}}) d\mathbf{r}, \quad (4)$$

where $y = z + k_0 r\cos\omega$, the angle ω $(0 \le \omega \le \pi)$ is measured from the direction $\mathbf{n}_0$ (see Fig.1), $q, q_1 = \pm 1$, $g(r)$ is the pair distribution function, $H_{lml_2m_2}^{(q)}(\hat{\mathbf{n}}_0,\hat{\mathbf{r}})$ are the translation coefficients for the vector Helmholtz harmonics (see, for example, [6]). Integration in Eq.4 is over the whole volume of the medium. $t_{LMlm}^{(pn)} t_{L_1M_1l_1m_1}^{*(\mu\nu)} = \left\langle t_{LMlm}^{(j)(pn)} t_{L_1M_1l_1m_1}^{*(j)(\mu\nu)} \right\rangle$ where the angular brackets denote averaging over particle orientation and particle properties,

$$t_{LMlm}^{(j)(pn)} = -i^{l-L}\sqrt{\frac{2l+1}{2L+1}}\left[T_{MLml}^{11(j)} + nT_{MLml}^{12(j)} + pT_{MLml}^{21(j)} + pnT_{MLml}^{22(j)}\right], \quad (5)$$

and $T_{MLml}^{kw(j)}$ $(k,w = 1,2)$ are the elements of the $\mathbf{T}$-matrix of j-th particle. For sparse media Eqs.(3),(4) can be transformed into the classical vector radiative transfer equation [4,6,7], and in the case of normal illumination of semi-infinite medium of densely packed identical spherical particles they can be transformed into the equations obtained in Ref.8.

$$S_{pn\nu\mu}^{(C)} + S_{pn\nu\mu}^{(1)} = \frac{\eta}{k_0}\sum_{LMlm} \frac{(2L+1)(2l+1)}{4} D_{Mp}^{*L}(\varphi,\vartheta,0) D_{m\mu}^{l}(\pi+\varphi_0,\pi-\vartheta_0,0) \int_0^{k_0 Z_0} F_{LMlm}^{(z)(pn)(\mu\nu)} \exp\left(-i\varepsilon z\right) dz, \quad (6)$$

where

$$\varepsilon = \frac{m_{eff}-1}{\cos\vartheta} + \frac{m_{eff}^{*}-1}{\cos\vartheta_0}, \quad (7)$$

and coefficients $F_{LMlm}^{(z)(pn)(\mu\nu)}$ are determined from the system of equations

$$F_{LML_1M_1}^{(z)(pn)(\mu\nu)} = \exp\left(i\varepsilon^{*} z\right)\sum_{lml_1m_1} t_{LMlm}^{(pn)} t_{L_1M_1l_1m_1}^{*(\mu\nu)} D_{mn}^{l}(\varphi_0,\vartheta_0,0) D_{m_1\nu}^{*l_1}(\pi+\varphi,\pi-\vartheta,0) +$$
$$+\eta \sum_{qq_1lml_1m_1} t_{LMlm}^{(pq)} t_{L_1M_1l_1m_1}^{*(\mu q_1)} \sum_{l_2m_2l_3m_3} \int g(r) F_{l_2m_2l_3m_3}^{(y)(qn)(q_1\nu)} H_{lml_2m_2}^{(q)}(\hat{\mathbf{n}}_0,\hat{\mathbf{r}}) H_{l_1m_1l_3m_3}^{*(q_1)}(\hat{\mathbf{n}}_0,\hat{\mathbf{r}}) \exp\left(i\mathbf{r}(\mathbf{k}_0+\mathbf{k}_{sc})\right) d\mathbf{r}. \quad (8)$$

Matrix $S_{pn\nu\mu}^{(1)}$ in Eq.(6) corresponds to the single scattering (the first term on the r.h.s. of Eq. (8)). For sparse media Eqs.(6),(8) can be transformed into the equations obtained in Refs.6,7.

In the case of $\mathbf{k}_{sc} = -\mathbf{k}_0$ the system (8) is identical to the system (4). Therefore the following equation is valid

$$S_{pn\mu\nu}^{(L)} = S_{pn\nu\mu}^{(C)} + S_{pn\nu\mu}^{(1)}. \quad (9)$$

This equation exactly reproduces Eq.(19) in Ref.9 for sparse media. In the case of $\mathbf{k}_{sc} \ne -\mathbf{k}_0$ the multiplier $\exp\left(i\mathbf{r}_{js}(\mathbf{k}_0+\mathbf{k}_{sc})\right)$ in Eq.(8) rapidly oscillate and the contribution of the second term of this equation tends to zero. As result the matrix $S_{pn\nu\mu}^{(C)}$ in Eq. (6) differs from zero only in the narrow area of scattering angles near the direction $\mathbf{k}_{sc} = -\mathbf{k}_0$. In intensity of scattered light this matrix describes a narrow interference peak centered in the exact backscattering direction.

Eqs.(3)-(8) describe the incoherent (diffuse) and coherent parts of reflected radiation from a plane parallel layer of densely packed particles. For sparse media these parts determine the reflection matrix of light. For such media the incoherent part corresponds to the sum of the ladder diagrams and is described by the vector radiative transfer equation [4]. The interference part of scattered radiation corresponds to the sum of the cyclical diagrams and is described by equations obtained in [6,7]. In the intensity of scattered light, this part appears as a narrow peak centered at the exact backscattering direction. In the exact backscattering direction the interference part is related with incoherent part by a simple equation [4,5,9]. The same equation (Eq.(9)) is valid for densely packed media as well. However, for densely packed media, the equations describing the incoherent and coherent parts are much more complex. Complexity of the equations is caused by the correlation between particles and by the inhomogeneity of waves near the particles. The inhomogeneity of waves near the particles is described by the coefficients of the addition theorem for the vector Helmholtz harmonics. For sparse media these coefficients have a simple form and describe the propagation of spherical waves between particles [6,7]. For densely packed media of particles comparable in sizes to the wavelength, the equations for incoherent and coherent parts describe only a part of scattered radiation. Additional part of scattered radiation for such media can come, for example, from the interference of waves scattered by neighboring particles and interference of waves of different orders of scattering [8]. Unfortunately, consideration of such interferences is a very complicated problem and is far from being satisfactory resolved even for qualitative analysis.

References

[1] Yu.N. Barabanenkov, Yu.A Kravtsov, V.D. Ozrin, and A.I. Saichev, "Enhanced backscattering in optics," Progr. Opt. **29,** 65-197 (1991).

[2] V.L. Kuz'min, and V.P. Romanov, "Coherent phenomena in light scattering from disordered systems," Phys. Usp. **39,** 231-260 (1996).

[3] D.S. Saxon, "Tensor scattering matrix for the electromagnetic field," Phys.Rev. **100**, 1771-1775 (1955).

[4] M.I. Mishchenko, L.D. Travis, and A.A. Lacis, *Multiple Scattering of Light by Particles. Radiative Transfer and Coherent Backscattering.* (Cambridge University Press, 2006).

[5] M.I. Mishchenko, "Polarization effect in weak localization of light: calculation of the copolarized and depolarized backscattering enhancement factors," Phys. Rev. B. **44,** 12597-12600 (1991).

[6] V.P. Tishkovets, "Multiple scattering of light by a layer of discrete random medium: backscattering," J. Quant. Spectrosc. Radiat. Transfer. **72,** 123-137 (2002).

[7] V.P. Tishkovets, and M.I. Mishchenko, "Coherent backscattering of light by a layer of discrete random medium," J. Quant. Spectrosc. Radiat. Transfer. **86,** 161-180 (2004).

[8] V.P. Tishkovets, K. Jockers, "Multiple scattering of light by densely packed random media. Dense media vector radiative transfer equation," J. Quant. Spectrosc. Radiat. Transfer. **101,** 54–72 (2006).

[9] M.I. Mishchenko, "Enhanced backscattering of polarized light from discrete random media: calculations in exactly the backscattering direction," J. Opt. Soc. Am. A., **9**, 978-982 (1992).

Interrelating angular scattering characteristics to internal electric fields of wavelength-scale Gaussian particles

Jani Tyynelä,[1] Evgenij Zubko,[2,3] Gorden Videen,[4,5] and Karri Muinonen[1]

[1]*Observatory, PO. Box 14, FI-00014 University of Helsinki, Finland (WWW: http://www.astro.helsinki.fi)*
[2]*Institute of Low Temperature Science, Hokkaido University, Kita-ku North 19 West 8, Sapporo060-0819,Japan*
[3]*Astronomical Institute, Kharkov National University, 35 Sumskaya Street, Kharkov, 61022, Ukraine*
[4]*Army Research Laboratory, AMSRL-CI-EM, 2800 Powder Mill Road, Adelphi, Maryland 20783, U.S.A.*
[5]*Astronomical Institue "Anton Pannekoek", Kruislaan 403, NL-1098 SJ Amsterdam, The Netherlands*

Abstract

We study the effect of internal electric field on the scattered field by modifying the electric field components of the discretized internal field of the particle. The internal fields for incident *X*-polarized and *Y*-polarized wave have been computed for a Gaussian-random-sphere particle using Discrete Dipole Approximation. The incident field propagates in the direction of the Z-axis. We show that both the Z- and X-component of the internal field cause negative polarization, the Z-component directly and the X-component through constructive interference between the contributions from different parts of the particle interior. The former component has a more pronounced influence on the overall polarization, while the latter component dominates the negative linear polarization close to the backscattering direction and is additionally seen to be responsible for the backscattering enhancement in intensity.

1 Introduction

Two ubiquitous light-scattering phenomena observed in atmosphereless solar-system bodies near opposition are the backward enhancement in scattered intensity and the negative linear polarization extending to some 20 degrees from the exact backscattering direction. The negative polarization seems to be largely due to single-particle scattering (e.g., [1]) but, close to backscattering, the coherent-backscattering mechanism plays an important role (e.g., [2]). Mechanisms responsible for the negative polarization of single particles have been suggested by, e.g., Muinonen et al. [3]. In the case of spherical particles, they hypothesize that, for a linearly X-polarized incident field propagating in the direction of the Z-axis, negative polarization arises from both the X- and Z-component of the internal field. The negative polarization of the Z-component arises due to non-destructive interference in the scattering plane defined by the wave and polarization vectors of the incident field (Y = 0; Fig. 1b). In the perpendicular plane X = 0 (Fig. 1a), the contribution is canceled. The negative polarization of the X-component arises due to constructive interference in the plane Y = 0 (Fig. 2b) between the cells divided by the planes X = 0 and Y = 0. In the perpendicular plane X = 0 (Fig. 2a), the linear polarization is positive, but the interference typically varies.

2 Computation of the scattered field

The effect of interference in the particle interior on the scattering characteristics is here studied by dividing the interior into equi-spaced cells parallel to the planes X = 0 and Y = 0, first into quadrants and then further into sixteen cells. The contributions from the radiating cells are calculated incoherently. The method described above was applied previously to spherical particles [4] and it was noted that the interference between different parts of the interior were responsible for the negative polarization and the backward enhancement. For the study, we have chosen a Gaussian-random-sphere particle with size parameter for the

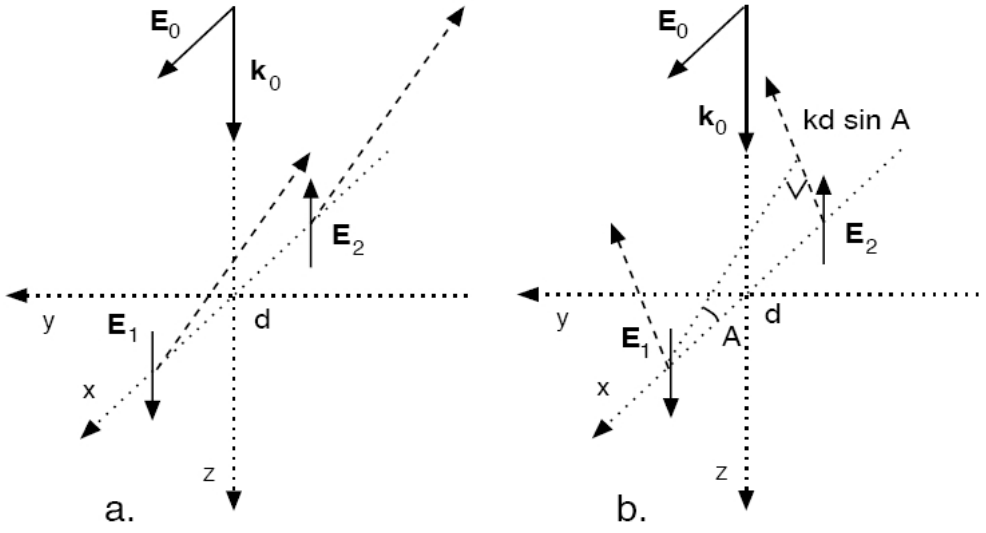

Figure 1: We illustrate the negative-polarization mechanism based on the Z-component of the internal electric field with odd parity: a) in the $X = 0$ plane, the scattered waves from the dipoles interfere destructively (phase difference $\Delta\phi = \pi$);b) in the $Y = 0$ plane, the interference between the waves varies depending on the distance d and phase difference $\Delta\phi = \pi + kd\sin(\pi - \theta)$, giving rise to negative linear polarization (see [3]).

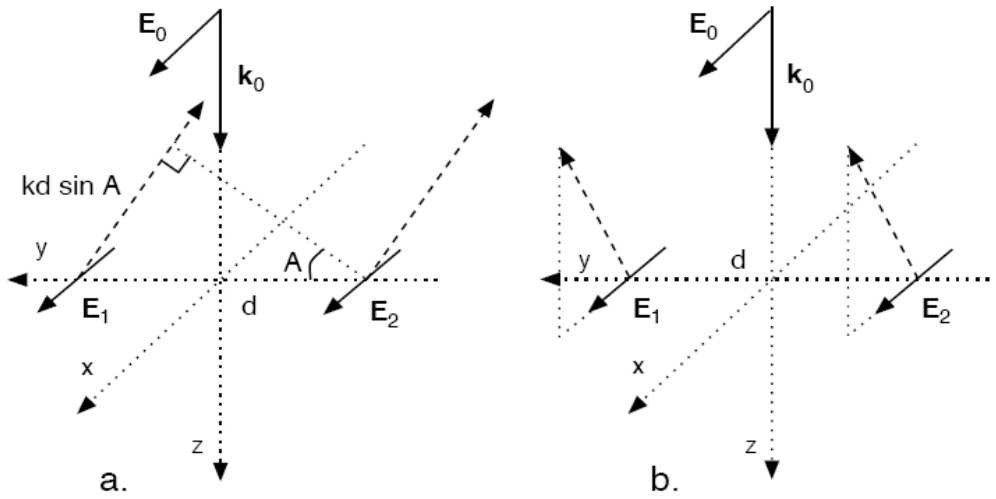

Figure 2: We illustrate the backward enhancement and the negative-polarization mechanism based on the X-component of the internal electric field with even parity: a) in the $X = 0$ plane, the scattered waves from the dipoles interfere destructively with phase difference $\Delta\phi = \pi + kd\sin(\pi - \theta)$; b) in the $Y = 0$ plane, the waves interfere constructively for all scattering angles (see [3]).

circumscribing sphere $x = 12$, the refractive index $m = 1.5 + 0.1i$, the relative standard deviation of radius $\rho = 0.245$ and the power-law index of the covariance function $\nu = 4$.

For the Gaussian-random-sphere particle, the internal fields for X- and Y -polarized incident field are obtained from a DDA simulation using the code by Zubko et al. [5]. The scattered field is calculated in XZ- and YZ-planes and an azimuthal averaging is carried out by rotating the particle with respect to the Z-axis for one hundred evenly distributed orientations. The size parameter grid for the internal field is $\Delta x = 0.375$.

3 Results and discussion

We investigate the effect of the different components of the internal field on the total intensity $I_{\|} + I_{\perp}$ and the linear polarization $P = (I_{\perp} - I_{\|})/(I_{\perp} + I_{\|})$ of the scattered field.

Figures 3a and 3c depict the total intensity normalized to one at $\theta = 0°$ and Figures 3b and 3d depict the linear polarization for the Gaussian-random-sphere particle. For the upper plots, the case of unmodified internal field is shown with thin solid line and the case of omitting the Z-component of the internal field is shown in thick solid line. For the lower plots, the case of unmodified internal field is shown with thin solid lines, the case of both omitting the Z-component of the internal field and dividing the interior into quadrants is shown in dashed line and the case of both omitting the Z-component of the internal field and dividing the interior into sixteen cells is shown in thick solid line.

As can be seen, the effect of omitting the Z-component of the internal field increases the linear polarization dramatically, but does not eliminate the negative polarization near backscattering region. When the interior is divided into quadrants, the polarization becomes positive for all scattering angles. Division further into sixteen cells does not have as profound an effect on polarization in this case, but for the total intensity, the effect is evident. As the interior is divided into four incoherently radiating parts, the relative backward enhancement in intensity diappears. The results reinforce the idea that the mechanisms described above are responsible for the negative polarization also for non-spherical particles. The computations will be extended to larger numbers of Gaussian particles.

References

[1] H. Volten, O. Munoz, E. Rol, J. de Haan, W. Vassen, and J. Hovenier, 'Scattering matrices of mineral aerosol particles at441.6 nm and 632.8 nm," J. Geophys. Res. 106, 17375-17401 (2000)

[2] K. Muinonen, 'Coherent backscattering of light by complex random media of spherical particles: numerical solution," Waves in Random Media, 365-388 (2004)

[3] K. Muinonen, E. Zubko, J. Tyynelä, Yu. G. Shkuratov, and G. Videen, 'Light scattering by Gaussian random particles with discrete-dipole approximation," JQSRT, in press (2007)

[4] J. Tyynelä, E. Zubko, G. Videen, and K. Muinonen, 'Interrelating angular scattering characteristics to internal electric fields for wavelength-scale spherical particles," JQSRT, in press (2007)

[5] E. Zubko, Y.G. Shkuratov, G. Videen, and K. Muinonen, 'Effects of interference on the backscattering properties of irregularly shaped particles using DDA," in Proceedins of the 9th Conference on Electromagnetic and Light Scattering by Nonspherical Particles: Theory, Measurements and Applications, 287-290 (2006)

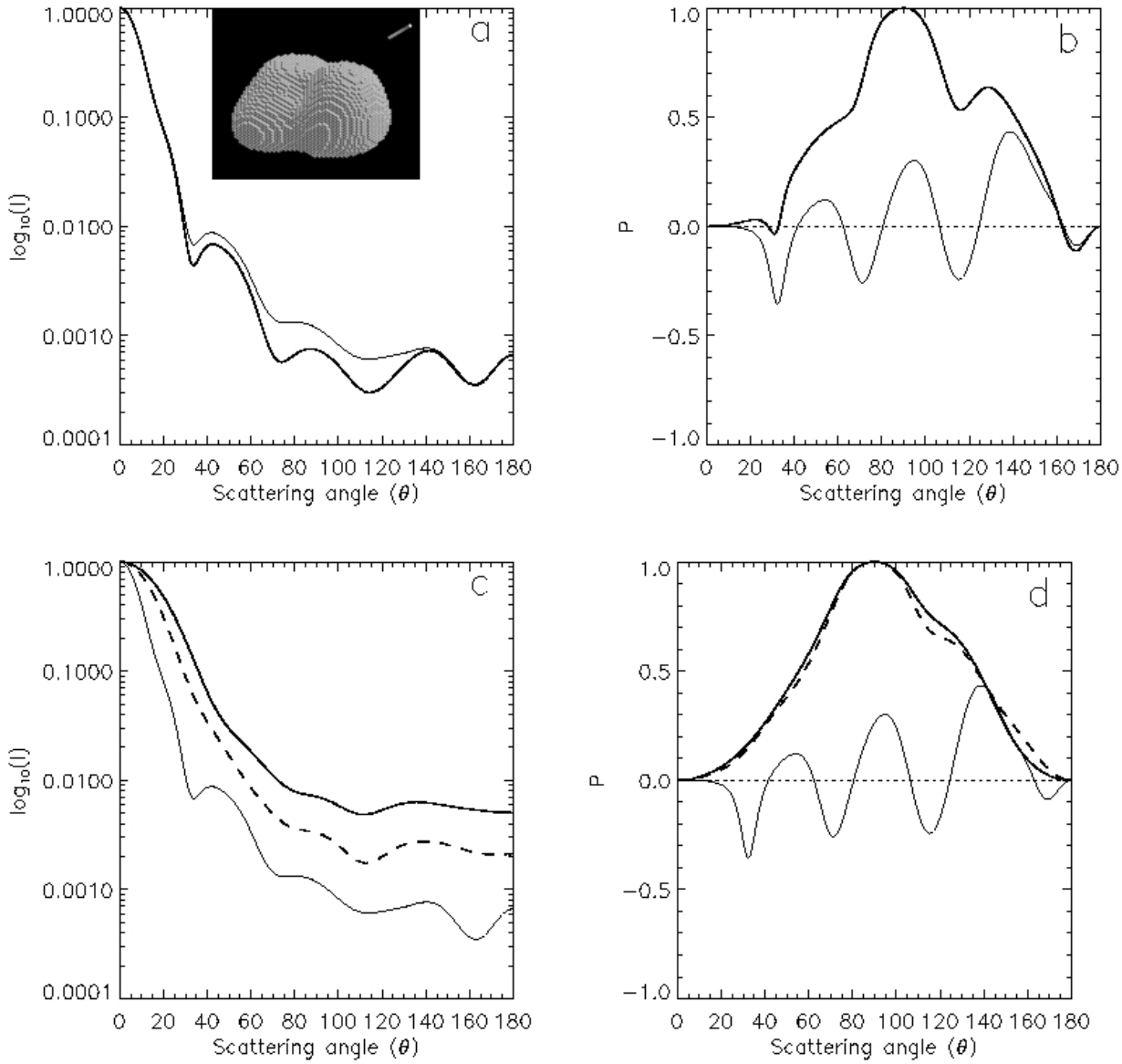

Figure 3: We plot the total intensity $I_{\|} + I_{\perp}$ (a) and $P = (I_{\perp} - I_{\|})/(I_{\perp} + I_{\|})$ (b) in the case of the unmodified internal field (thin solid line) and when $E_Z = 0$ (thick solid line). Also, we plot the total intensity (c) and P (d), when $E_Z = 0$ and the particle interior is divided into quadrants (thick dashed line), sixteen cells (thick solid line), and the unmodified internal field (thin solid line). An image of the sample Gaussian-random-sphere particle is shown in plot a. The parameters for the particle are $x = 12$, $m = 1.5 + 0.1i$, $\rho = 0.245$ and $\nu = 4$.

Characterization of Small Ice Crystals Using Frequency Analysis of Azimuthal Scattering Patterns

Z. Ulanowski,[1] C. Stopford,[1] E. Hesse,[1] P.H. Kaye,[1] E. Hirst,[1]
and M. Schnaiter,[2]

[1] *STRI, University of Hertfordshire, Hatfield AL10 9AB, United Kingdom.*
[2] *IMK-AAF, Forschungszentrum Karlsruhe, 76344 Eggenstein-Leopoldshafen, Germany.*
tel: +44 1707 284604, fax: +44 1707 284185, e-mail: z.ulanowski@herts.ac.uk

Abstract

Azimuthal scattering patterns obtained from ice crystals using the Small Ice Detector 2 are examined. They are converted to frequency spectra using Fast Fourier Transform. To classify the shape of the crystals, the spectra are compared to theoretical ones computed for a range of hexagonal crystal shapes, including hollow ones, of various aspect ratios.

1 Introduction

Cloud particle shape is important from the point of view of both atmospheric dynamics and radiative properties. For this reason, many *in situ* probes for shape characterization have been developed. Most of them rely on direct imaging of particles onto a variety of 1D or 2D sensors, so their resolution is limited by the usual optical constraints. Consequently, large gaps in knowledge exist for smaller ice crystals, where the resolution of imaging probes is insufficient. Yet these particles are highly important, especially in the context of radiative properties of clouds and cloud feedbacks [1]. Moreover, many imaging probes do not reveal fine detail, such as the roughness of crystals or whether they are hollow or not – both highly significant properties [2,3]. The Small Ice Detector 2 (SID-2) probe was developed at University of Hertfordshire to provide information on the size and shape of single particles approximately 1 to 50 μm in size by measuring the spatial distribution of scattering. Discriminating between droplets and non-spherical ice crystals is straightforward, since the former produce highly symmetric scattering patterns and the latter generally do not [4]. It is also possible to derive more detailed information about particle shape [5]. The present work attempts to extend the shape analysis to various classes of ice crystals, with special emphasis on solid and hollow hexagonal prisms of various aspect ratio.

2 Small Ice Detector Mk. 2

SID-2 collects scattering patterns from single particles passing through a 532 nm wavelength laser beam with elliptical cross-section. The detector is a hybrid photodiode (HPD) custom-manufactured by B.V. DEP, Netherlands. The HPD is a segmented silicon photodiode mounted in a vacuum tube with a photocathode, and has photoelectron gain of up to several thousands, depending on the acceleration voltage. It contains 27 independently sensed photodiode elements – Fig. 1. In the present study only the outer detector ring was used, comprising the elements 9 to 32 and subtending scattering angles 10 to 20°.

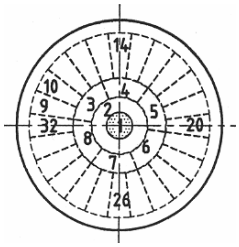

Figure 1: SID-2 detector. The centre corresponds to forward scattering. The elements 3 to 8 are paired.

3 Theoretical scattering patterns

Two dimensional (2D) scattering patterns have been computed using the Ray Tracing with Diffraction on Facets (RTDF) model [6,7]. The fundamental shape was a hexagonal prism with basal faces replaced by inverted (hollow) hexagonal pyramids of varying depth: 0, 10, 25 and 49% of the prism length. The aspect ratio (length to diameter) of the prisms was 3, 1 and 0.2, to represent columns, compact prisms and thin plates, respectively – giving 12 classes in total. For each shape, 2D scattering patterns for 40 different orientations were computed - Fig. 2. The central dark area in the 2D plot in Fig. 2 is due to the exclusion of the scattering on the projected outline of the particle, which in the current versions of the RTDF model is computed as Fraunhofer diffraction on a circular aperture, which would not represent 2D scattering correctly. However, this region is not seen by the outer ring of the SID-2 detector, so the present analysis is not affected. The 2D patterns were converted to the SID-2 detector outer-ring responses by integrating over corresponding angles, to give 24-element azimuthal scattering patterns. The patterns were then converted to angular frequency spectra using fast Fourier transform (FFT) and taking the magnitude of the Fourier coefficients of order 1 to 12 normalized to the coefficient of order 0 – Fig. 2.

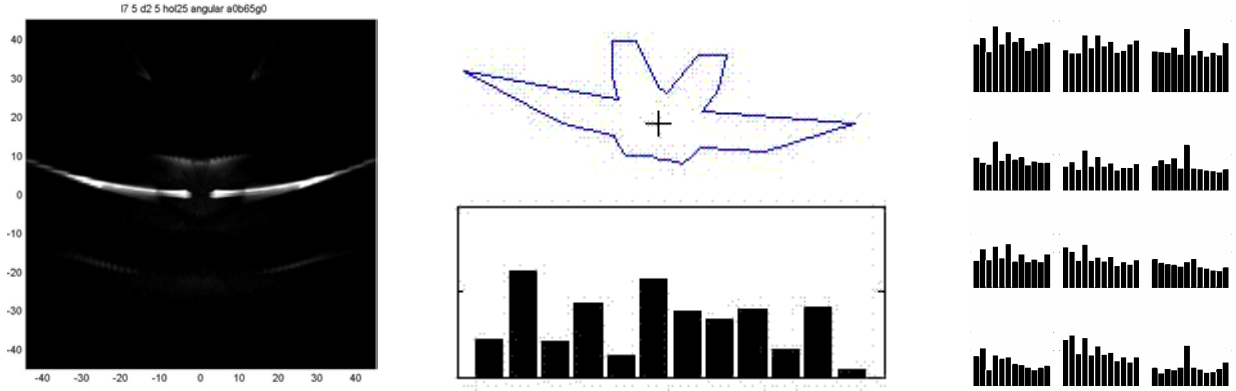

Figure 2: (left) Scattering computed for a prism with 25% basal indentations: 2D pattern extending up to 45°. (centre) Corresponding polar plot of square root of the outer ring response, and FFT coefficients (order 1-12) for the pattern. (right) FFT spectra for the 12 prism shapes averaged over 40 orientations - the aspect ratio decreases from left to right and the cavity depth from bottom to top.

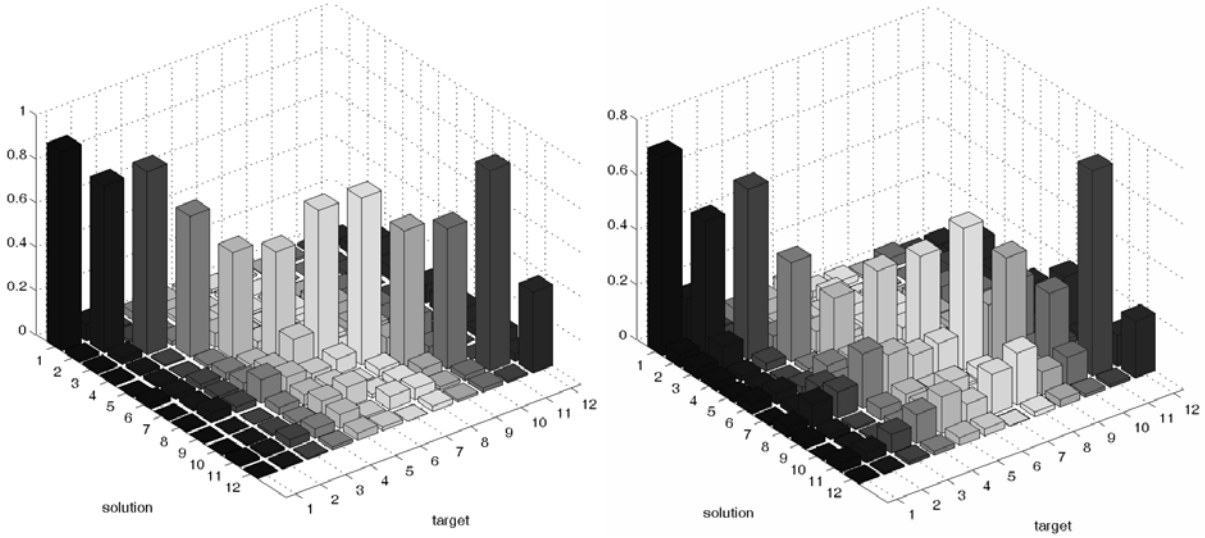

Figure 3: Fitted solution matrix for the 12 computed classes of hexagonal prisms, with 40 orientations in each class, and corrupted by random noise with signal to noise ratio of 2.4 (left) and 1.8 (right).

As a test, each shape class (40 orientations) of the theoretical FFT spectra was corrupted by adding varying amounts of random noise and fitted using a least squares method to uncorrupted spectra. This procedure produced 12x12 "solution matrices" giving proportions of spectra assigned to each class. It was found that the spectra were classified correctly even for large noise levels, but with increasing "leakage" into wrong classes for increasing noise – Fig. 3. The solution matrices were algebraically inverted to produce "deconvolution" matrices for each noise level, to allow the correction of solution sets.

4 Measurements

4.1 Ice analogue measurements

SID-2 scattering patterns were recorded from ice analogue crystals [2,8] by ejecting single crystals from a needle electrode [9]. Examples are shown in Fig. 4, together with the corresponding FFT spectra.

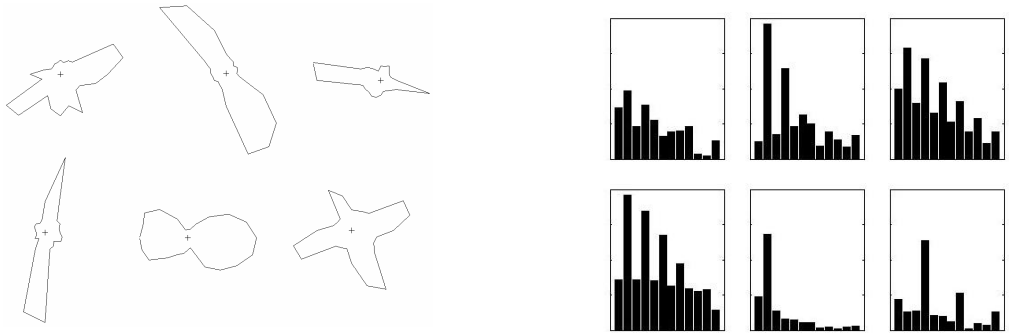

Figure 4: Azimuthal scattering patterns (left) and FFT spectra (right) from 5 ice analogue prisms and a 4-arm rosette (lower right corner).

4.2 AIDA cloud chamber measurements

Ice crystal measurements were done at the AIDA cloud chamber of Forschungszentrum Karlsruhe during the HALO-01 ice nucleation campaign in March 2007. AIDA can be operated as an expansion cloud chamber to study the formation of ice clouds down to temperatures of about -90°C [10]. During experiment 17 hexagonal plates were grown at temperature of –28°C and low supersaturation by injecting seed ice crystals into the chamber. FFT spectra from SID-2 data at time=910s were fitted to theoretical spectra from the 12 shape classes using a least squares method, and then deconvolved. The solutions were consistent with the presence of thick plates with 10% cavities – Fig. 5.

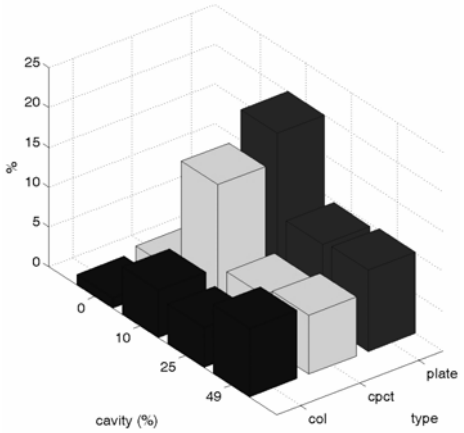

Figure 5: Crystal shape classification for HALO-01 exp. 17 obtained by fitting FFT spectra.

4 Conclusion

A theoretical database of 2D light scattering patterns for 12 classes of hexagonal prisms with different aspect ratios and cavity depth was computed using the RTDF method. The 2D patterns were converted into azimuthal ones and then into angular frequency spectra using FFT. The spectra were found to be characteristic of particle shape and they can be used as a basis for shape classification, even for data strongly contaminated by noise. Experimental spectra from ice crystals were obtained using the SID-2 probe in the AIDA cloud chamber and fitted using a least squares method to the database to derive ice crystal shape. The shape classification can be improved by a deconvolution of solutions using inverted theoretical solution matrices obtained for levels of noise characteristic of the given experimental conditions.

Acknowledgments

This work was carried out with funding from the Natural Resources Research Council, with further support from the European ACCENT network.

References

[1] T. J. Garrett, H. Gerber, D. G. Baumgardner, C. H. Twohy, and E. M. Weinstock, “Small, highly reflective ice crystals in low-latitude cirrus,” Geophys. Res. Lett, **30**, 2132 (2003).

[2] Z. Ulanowski, E. Hesse, P. H. Kaye and A. J. Baran, “Light scattering by complex ice-analogue crystals,” J. Quantit. Spectr. Rad. Transf. **100**, 382-392 (2006).

[3] C. G. Schmitt, J. Iaquintaa, and A. J. Heymsfield, "The asymmetry parameter of cirrus clouds composed of hollow bullet rosette-shaped ice crystals from ray-tracing calculations," J. Appl. Meteor. Climat. **45**, 973-981 (2006).

[4] E. Hirst, P. H. Kaye, R. S. Greenaway, P. R. Field, and D. W. Johnson, “Discrimination of micrometre-sized ice and super-cooled droplets in mixed-phase cloud,” Atmos. Environ. **35**, 33-47 (2001).

[5] E. Hirst, P. H. Kaye, and Z. Wang-Thomas, “A Neural Network based Spatial Light Scattering Instrument for Hazardous Airborne Fiber Detection**,”** Appl. Opt. **36**, 6149-6156 (1997).

[6] A. J. M. Clarke, E. Hesse, Z. Ulanowski, and P. H. Kaye, “A 3D implementation of ray tracing combined with diffraction on facets,” J. Quantit. Spectr. Rad. Transf. **100**, 103-114 (2006)

[7] E. Hesse, A. J. M. Clarke, Z. Ulanowski and P. H. Kaye, “Light scattering by ice crystals modelled using the Ray Tracing with Diffraction on Facets method,” EGU General Assembly, Vienna (2007).

[8] Z. Ulanowski, E. Hesse, P. H. Kaye, A.J. Baran, R. Chandrasekhar, “Scattering of light from atmospheric ice analogues,” J. Quantit. Spectr. Rad. Transf. **79-80C**, 1091-1102 (2003).

[9] E. Hesse, Z. Ulanowski, and P. H. Kaye, “Stability characteristics of cylindrical fibres in an electrodynamic balance designed for single particle investigation,” J. Aerosol Sci. **33**, 149-163 (2002).

[10] O. Möhler, P. R. Field, P. Connolly, S. Benz, H. Saathoff, M. Schnaiter, R. Wagner, R. Cotton, M. Krämer, A. Mangold, A.J. Heymsfield, “Efficiency of the deposition mode ice nucleation on mineral dust particles,” Atmos. Chem. Phys. **6**, 3007–3021 (2006).

Comparison of LS Methods Using Single Expansions of Fields

Alexander A. Vinokurov[1], Victor G. Farafonov[1], Vladimir B. Il'in[2]

[1] *St. Petersburg University of Aerocosmic Instrumentation, Bol. Morskaya 67, St. Petersburg, 190000 Russia*

[2] *St. Petersburg University, Universitetskij pr., 28, St. Petersburg, 198504 Russia*

tel: +7 (812) 428-4264, fax: +7 (812) 428-7129, e-mail: ilin55@yandex.ru

Abstract

The light scattering methods expanding the fields in terms of wave functions are widely applied due to their high efficiency. We compare some of these methods, namely the extended boundary condition, separation of variables, and point matching ones, considering their theoretical and practical applicability. Though the methods look alike because of their use of the same expansions of the fields, it is found that these approaches differ in important aspects.

1 Introduction

The approaches using single expansions of the fields in terms of wave functions to solve the light scattering problem are the extended boundary condition (EBCM), separation of variables (SVM), and point matching (PMM) methods [1, 2]. They give solutions widely used because of their high speed and accuracy.

These approaches seem to be very similar as they search for the problem solution in the form of the *same* field expansions with the expansion coefficients being derived from solution of the systems of linear algebraic equations. The main difference of the methods is their use of different problem formulation which leads as a result to different systems. In the EBCM the fields and Green function expansions are substituted into the boundary condition presented in the surface integral form; in the SVM the field expansions are substituted into the boundary condition written in the usual (differential) form; in the PMM any of the above forms can be used, but the system is derived from minimization of a residual of the boundary condition considered in selected points at the scatterer surface (see [2] for more details).

In this work we compare the methods using the spherical function basis by considering their theoretical and practical applicability ranges. In the latter case the questions of accuracy and computational time are concerned. Note that though the EBCM, SVM, and PMM represent the fields in the same way, a different number of terms in the expansions may be required by the methods to reach the same accuracy.

2 Theoretical aspects

From the theoretical point of view, applicability of the approaches is determined by *convergence* of the field expansions and *solvability* of the systems used to derive the expansion coefficients.

The convergence of the expansions of the scattered and internal fields at a distance d from the coordinate origin does not depend on the methods used and occurs if and only if

$$\max\{d^{\mathrm{sca}}\} < d \quad \text{and} \quad d < \min\{d^{\mathrm{int}}\}, \tag{1}$$

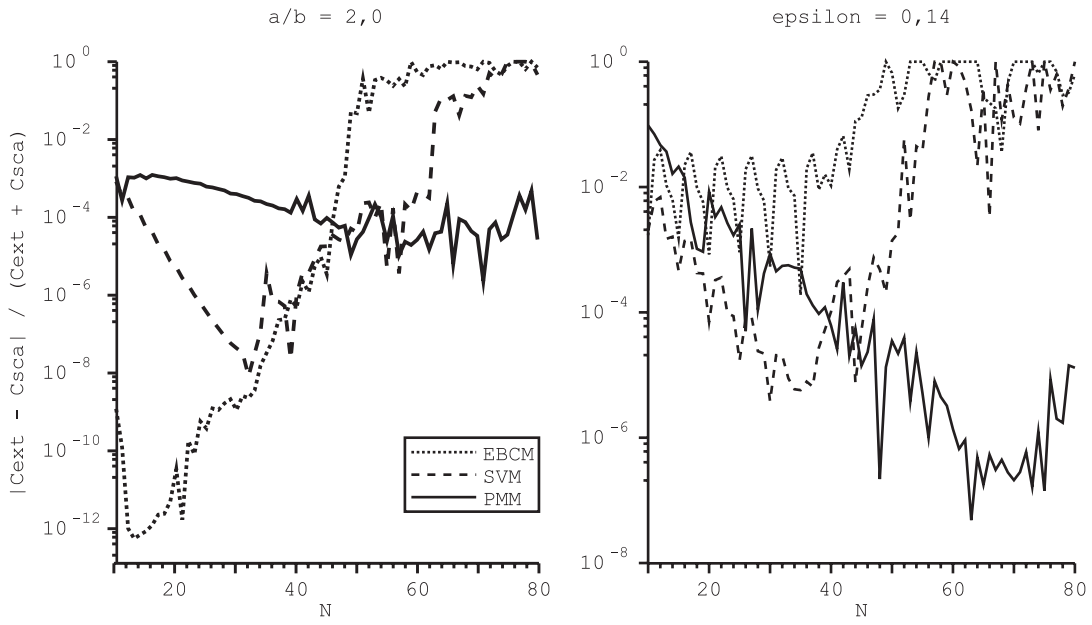

Figure 1: The dependence of the code accuracy measure δ on the number of terms kept in the field expansions N for spheroids with the aspect ratio $a/b = 2$ (left panel) and Chebyshev particles with $n = 5$ and $\varepsilon = 0.14$ (right panel). For both scatterer types, refractive index is $m = 1.5$, the diffraction parameter $x_{\rm v} = 1$, and the radiation incidence angle $\alpha = 10°$.

where $d^{\rm sca}$ and $d^{\rm int}$ are the distances to singularities of analytic continuations of the fields (see [3] for more details).

The solvability of the system arising in the EBCM takes place provided (see the discussion in [2])

$$\max\{d^{\rm sca}\} \; < \; \min\{d^{\rm int}\}. \tag{2}$$

For the SVM, a similar analysis has not yet been performed, though at least the EBCM system can be obtained within the SVM [3]. The system arising in the PMM is always solvable, as it is positively determined (see, e.g., [2]).

It should be added that the convergence is important for calculations of the fields in the near field zone (note that the condition (2) is always weaker than the condition (1)). The solvability plays the main role in the far field zone where the field expansions should converge. For instance, any EBCM calculations of the field characteristics in this zone converge only if the condition (2) is satisfied [2]. Note also that the conditions (1), (2) do not depend on such scatterer characteristics as refractive index and diffraction parameter as only the geometrical parameters are involved.

3 Practical aspects

We have developed a homogeneous set of codes based on the methods under consideration. Their accuracy in the far field zone was studied by using the relative difference of the extinction and scattering cross sections $\delta = |C_{\rm ext} - C_{\rm sca}| / (C_{\rm ext} + C_{\rm sca})$ calculated for nonabsorbing particles.

The typical behaviour of accuracy of the codes with a changing number of terms kept in the expansions N is shown in Fig. 1. For spheroids, the EBCM solution well converges with growing N and gives as high accuracy as $\sim 10^{-12}$ for $N \approx 16$. For $N \gtrsim 16$, the system is ill-conditioned and the

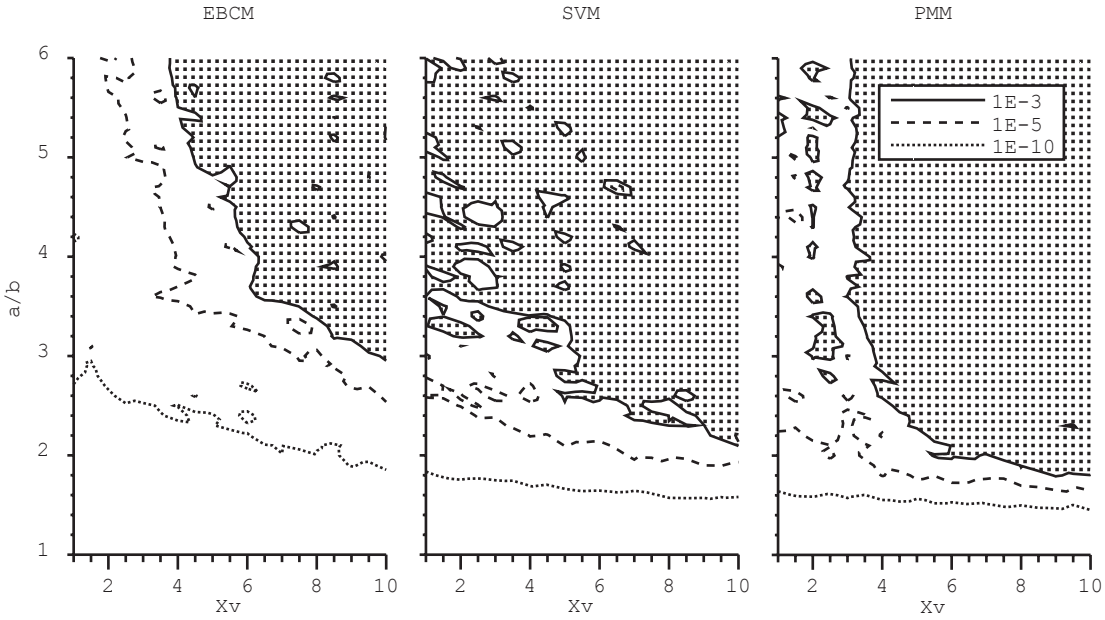

Figure 2: Dependence of δ on prolate spheroid parameters a/b and $x_{\rm v}$ ($\alpha = 10^\circ$, $m = 1.5$).

accuracy quickly drops with increasing N. The same behaviour is observed for the SVM solution, though it reaches maximum accuracy when $N \sim 30$. For the PMM solution, the convergence is even slower and numerical problems appearing at $N \gtrsim 40$ limit its practical applicability.

Note that for any spheroids all 3 methods are mathematically correct [2]. The situation is a bit different for axisymmetric Chebyshev particles having the surface equation $r(\theta) = r_0(1 + \varepsilon \cos n\theta)$, where θ is an angle of the spherical coordinates, r_0 the radius of a unperturbed sphere, ε its deformation amplitude, n the number of surface maxima.

The EBCM solvability condition (2) is satisfied in a certain region of the geometrical parameters of the particles, and in particular for $\varepsilon < 0.14$, when $n = 5$ [2]. Our calculations well confirm this, e.g. Fig. 1 shows that accuracy of the EBCM on average does not grow with increasing $N < 40$. Meantime the SVM and PMM solutions converge for $N < 35$ and $N < 65$, respectively. Thus, despite the large similarity of the EBCM and SVM (see the discussions in [2,3]), their theoretical applicability conditions differ in principle as definitely the solvability of the SVM is not determined by the EBCM condition (2).

A systematic numerical comparison of the methods is still absent in the literature. As a first step of such comparison in Fig. 2 and 3 we consider the regions of the parameters of spheroids and Chebyshev particles where the methods can provide a given accuracy. The figures allow one to see the practical applicability of the methods. For spheroids, the EBCM is generally preferable to other 2 methods. In contrast, for Chebyshev particles, the SVM and PMM look better (the former needs less terms and hence is faster, however the latter can give higher accuracy). Therefore, in a general case it is worth to combine these 3 methods keeping in mind that their codes differ by a few dozen operators.

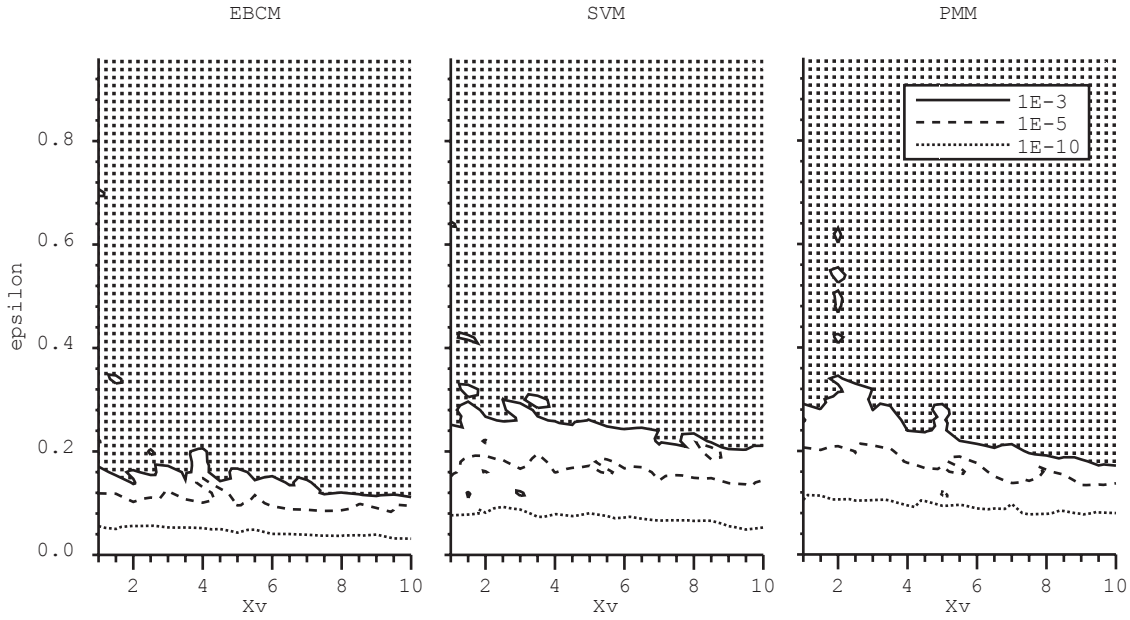

Figure 3: Dependence of δ on Chebyshev particle parameters ε and $x_{\rm v}$ ($n = 5$, $\alpha = 10^\circ$, $m = 1.5$).

4 Conclusions

We have compared 3 methods utilizing single field expansions in terms of spherical wave functions. It is found that despite a very large similarity of the EBCM and SVM their theoretical applicability ranges are different in principle.

Extensive calculations have shown that the methods well supplement each other, and as the codes differ by a few operators it is worth to combine them.

Our preliminary results of similar comparison of the methods, when the spheroidal functions were used for the field expansions, led to the same conclusions.

Acknowledgements

The work was supported by a grant of the RFFI. V.I. acknowledges a support by the grants RNP 2.1.1.2852, NSh 8542.2006.2 and RFBR N 07-02-00831.

References

[1] M. I. Mishchenko, J. Hovenier, and L. D. Travis (eds), *Light Scattering by Nonspherical Particles*, (Academic Press, San Francisco, 2000).

[2] V. G. Farafonov, V. B. Il'in, "Single light scattering: computational methods," In: A. Kokhanovsky (Ed.) *Light Scattering Reviews*, (Springer-Praxis, Berlin, 2006), pp. 125–177.

[3] V. G. Farafonov, A. A. Vinokurov and V. B. Il'in, "Comparison of light scattering methods using the spherical basis," Opt. Spectrosc. **102**, N6 (2007).

On the polarizing efficiency of the interstellar medium

N. V. Voshchinnikov[1] and H. K. Das[2]

[1]*Astronomy Department and Sobolev Astronomical Institute,*
St. Petersburg University, Universitetskii prosp., 28, St. Petersburg, 198504 Russia
[2]*IUCAA,Post Bag 4, Ganeshkhind, Pune 411 007, India*
tel: +7 812-428-4263, fax: +7 812-428-7129, e-mail: nvv@astro.spbu.ru

Abstract

We consider the wavelength dependence of the ratio of the linear polarization degree to extinction (polarizing efficiency) for aligned spheroidal particles. Size/shape/orientation effects are analyzed. The comparison of the theory with the polarizing efficiency of the interstellar medium observed in several directions permits to restrict the range of the model parameters.

1 Interstellar extinction and polarization

The reddening and linear polarization of stellar radiation occurs when it passes through interstellar clouds. Interstellar extinction grows with the radiation wavelength decrease while interstellar linear polarization reaches a maximum in the visual part of spectrum and declines at shorter and longer wavelengths (see [1], [2] and Fig. 1, left panel). Interstellar linear polarization indicate that non-spherical grains aligned in large-scale magnetic fields are present in the Galaxy. These data contain information about the interstellar magnetic fields and properties of dust grains. A correlation between observed interstellar extinction and polarization shows that the same particles are responsible for both phenomena.

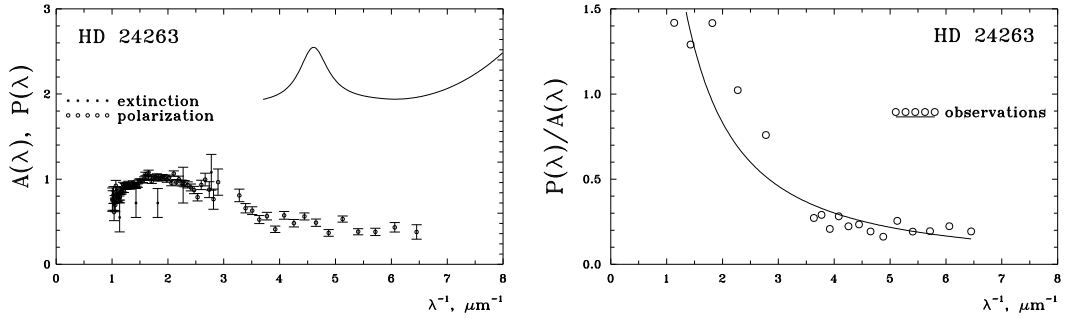

Figure 1: Interstellar extinction and polarization curves for star HD 24263 (left panel) and the polarizing efficiency of the interstellar medium in the direction of this star (right panel; solid curve shows the power-law approximation $P/A \propto \lambda^{1.47}$.). Observational data were taken from [3] (extinction) and [4] (polarization).

The modelling of these phenomena usually includes the consideration of normalized extinction $E(\lambda - \mathrm{V})/E(\mathrm{B} - \mathrm{V})$ and normalized polarization given by Serkowski's curve $P(\lambda)/P_{\max} = \exp[-K \ln^2(\lambda_{\max}/\lambda)]$ (see, e.g., [5] and discussion in [1], [2]). In such case, it is difficult to apply the dust-phase abundances and alignment theory for restriction of grain properties. It seems better to compare with observations the absolute extinction and theoretical polarizing efficiencies.

The *polarizing efficiency* of the diffuse interstellar medium is defined as the ratio of the percentage polarization (P) to the extinction (A) observed at the same wavelength $P(\lambda)/A(\lambda)$. There exists an empirically found upper limit on this ratio

$$P_{\max}/A(\mathrm{V}) \lesssim 3\%/\mathrm{mag}\,, \qquad (1)$$

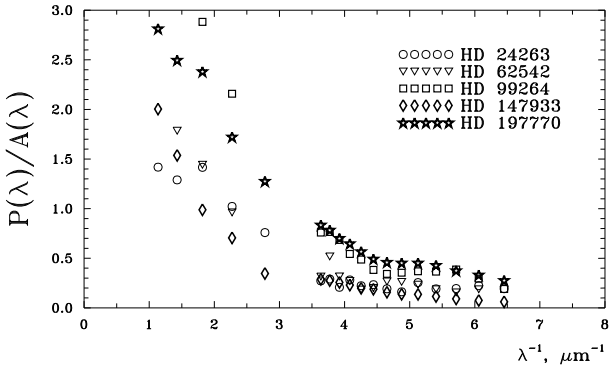

Figure 2: Polarizing efficiency of the interstellar medium in the direction of five stars. Observational data were taken from [3] (extinction) and [4] (polarization).

where $P_{\max}$ is the maximum degree of linear polarization which is reached near the wavelength $\lambda_{\max} \approx 0.55\,\mu$m (see [1], [2] for more discussion).

As a preliminary we chose five stars located not far than 500 pc[1] with measured UV polarization [4], then found the extinction (data published in [3] were mainly used) and calculated the ratio $P(\lambda)/A(\lambda)$. The obtained polarizing efficiencies are shown in Fig. 2. Note that, apparently, first presentation of the observational data in the similar form was made by Whittet [6, Fig. 9] who gave the average normalized dependence $P(\lambda)/A(\lambda) \cdot A_{\rm V}/P_{\max}$.

Here, we compare the observed polarizing efficiencies with the theoretical ones produced by rotating spheroidal grains of different composition, size, shape and porosity for various degrees and directions of grain alignment.

2 Modelling

Let us consider non-polarized light passing through a dusty cloud of rotating spheroidal grains. Rotating interstellar grains are usually partially aligned (see, e.g., [7]). Imperfect alignment is also supported by the fact that values of the polarizing efficiencies calculated for non-rotating or perfectly aligned particles are generally higher than the empirically estimated upper limit given by Eq. (1) [2, 8].

The extinction in stellar magnitudes and polarization in percentage can be found as [2]

$$A(\lambda) = 1.086 N_{\rm d} \langle C_{\rm ext} \rangle_\lambda \,, \qquad P(\lambda) = N_{\rm d} \langle C_{\rm pol} \rangle_\lambda 100\% \,, \tag{2}$$

where $N_{\rm d}$ is the dust grain column density and $\langle C_{\rm ext} \rangle_\lambda$ and $\langle C_{\rm pol} \rangle_\lambda$ are the extinction and linear polarization cross sections, respectively, averaged over the grain orientations

$$\langle C_{\rm ext} \rangle_\lambda = \left(\frac{2}{\pi} \right)^2 \int_0^{\pi/2} \int_0^{\pi/2} \int_0^{\pi/2} \pi r_V^2 \, Q_{\rm ext} \, f(\xi, \beta) \, d\varphi d\omega d\beta \,, \tag{3}$$

$$\langle C_{\rm pol} \rangle_\lambda = \frac{2}{\pi^2} \int_0^{\pi/2} \int_0^{\pi} \int_0^{\pi/2} \pi r_V^2 \, Q_{\rm pol} \, f(\xi, \beta) \, \cos 2\psi \, d\varphi d\omega d\beta \,. \tag{4}$$

Here, r_V is the radius of a sphere with the same volume as spheroidal grain, β is the precession-cone angle for the angular momentum $\mathbf{J}$ which spins around the magnetic field direction $\mathbf{B}$, φ the spin angle, ω the precession angle (see Fig. 1 in [8]). Quantities $Q_{\rm ext} = (Q_{\rm ext}^{\rm TM} + Q_{\rm ext}^{\rm TE})/2$ and $Q_{\rm pol} = (Q_{\rm pol}^{\rm TM} - Q_{\rm ext}^{\rm TE})/2$ are the efficiency factors for the non-polarized incident radiation, $f(\beta, r_V)$ is the cone-angle distribution.

We consider so-called imperfect Davies–Greenstein (IDG) orientation described by the function $f(\xi, \beta)$ which depends on the alignment parameter ξ and the angle β

$$f(\xi, \beta) = \frac{\xi \sin\beta}{(\xi^2 \cos^2\beta + \sin^2\beta)^{3/2}} . \tag{5}$$

[1] We suggest that these stars are seen through one interstellar cloud.

The parameter ξ is a function of the particle size r_V, the imaginary part of the grain magnetic susceptibility χ'' (= $\varkappa\omega_{\rm d}/T_{\rm d}$, where $\omega_{\rm d}$ is the angular velocity of grain), gas density $n_{\rm g}$, the strength of magnetic field B and dust ($T_{\rm d}$) and gas ($T_{\rm g}$) temperatures

$$\xi^2 = \frac{r_V + \delta_0(T_{\rm d}/T_{\rm g})}{r_V + \delta_0}, \quad \text{where} \quad \delta_0^{\rm IDG} = 8.23\,10^{23}\frac{\varkappa B^2}{n_{\rm g}T_{\rm g}^{1/2}T_{\rm d}}\,\mu\text{m}. \tag{6}$$

The angle ψ in Eq. (4) is expressed via the angles φ, ω, β and Ω (angle between the line of sight and the magnetic field, $0^\circ \le \Omega \le 90^\circ$). Note that for the case of the perfect DG orientation (PDG, perfect rotational or 2D orientation) the major axis of a non-spherical particle always lies in the same plane. For PDG, integration in Eqs. (3), (4) is performed over the spin angle φ only.

3 Results and discussion

The calculations have been made for prolate and oblate rotating spheroids of several sizes and aspect ratios consisting of astronomical silicate (astrosil) and amorphous carbon (AC1). Some results for prolate particles are plotted in Figs. 3 and 4. They show the polarizing efficiency in the wavelength range from the infrared to far ultraviolet. The observational dependence $P(\lambda)/A(\lambda)$ for two stars is given for comparison. The value of δ_0 for IDG orientation is typical of diffuse interstellar medium [8]. Calculations for porous grains are made using the Bruggeman mixing rule for refractive index and particles of same mass as compact ones. Note that calculated efficiencies can be considered as upper limits because some populations of grains (spherical, non-oriented) may give the contribution into extinction but not to polarization.

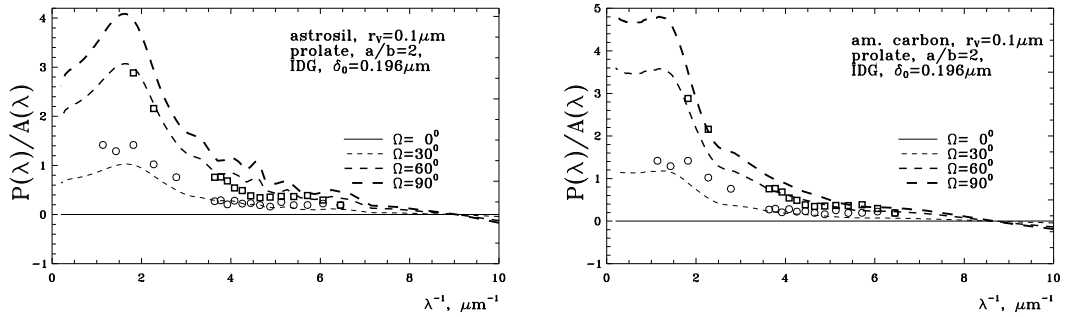

Figure 3: Wavelength dependence of polarizing efficiency for homogeneous rotating spheroidal particles of astronomical silicate and amorphous carbon. The effect of variations of particle composition and direction of alignment is illustrated. The open circles and squares show the observational data for stars HD 24263 and HD 99264, respectively.

From Figs. 3, 4 one can conclude that the wavelength dependence of polarizing efficiency is mainly determined by the particle composition and size. Variations of other parameters influence on the value of efficiency (the dependence of P/A is scaled). The growth of the efficiencies $P(\lambda)/A(\lambda)$ takes the place if we increase angle Ω (direction of alignment), parameter δ_0 (degree of alignment) or aspect ratio a/b (consider more elongated or flattened particles) and decrease particle porosity P or particle size r_V.

The resulting relationships will be applied for detailed comparison of the theory with observations.

Acknowledgments

The work was partly supported by grants NSh 8542.2006.2, RNP 2.1.1.2152 and RFBR 07-02-0000 of the Russian Federation.

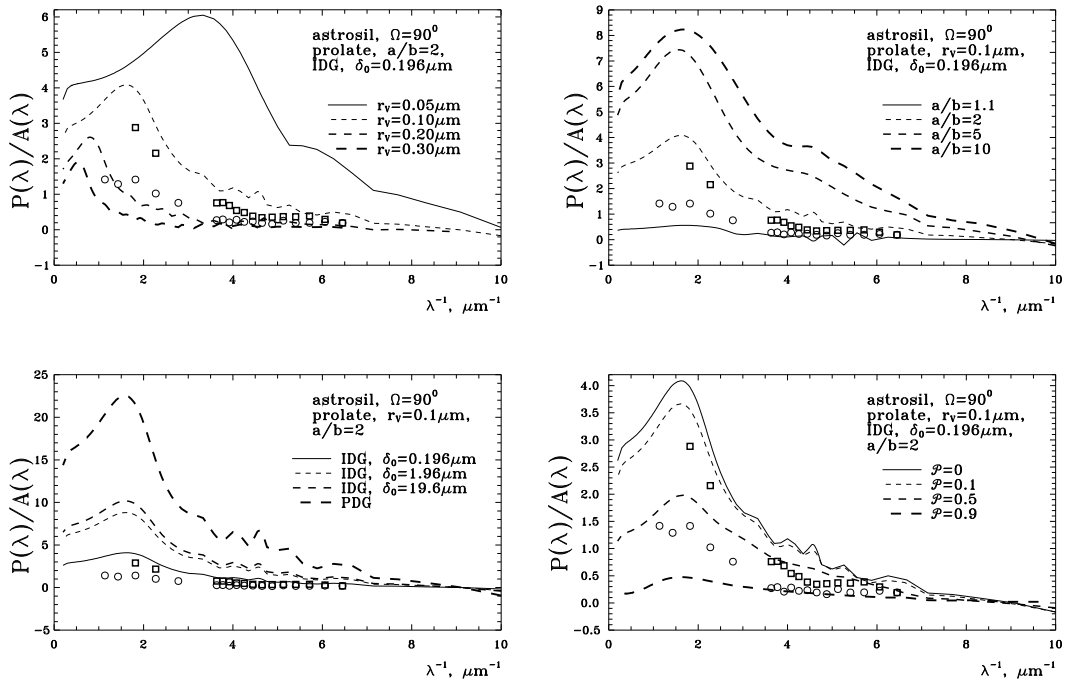

Figure 4: Wavelength dependence of polarizing efficiency for homogeneous rotating spheroidal particles of astronomical silicate. The effect of variations of particle size, shape, porosity and degree of alignment is illustrated. The open circles and squares show the observational data for stars HD 24263 and HD 99264, respectively.

References

[1] D. C. B. Whittet, "Dust in the Galactic Environments," Second Edition, Institute of Physics Publishing, Bristol (2003).

[2] N. V. Voshchinnikov, "Optics of Cosmic Dust. I," Astrophys. Space Phys. Rev., **12**, 1–182 (2004).

[3] L. A. Valencic, G. C. Clayton, and K. D. Gordon, "Ultraviolet extinction properties in the Milky Way," ApJ, **616**, 912–924 (2004).

[4] C. M. Andersen et al., "Ultraviolet interstellar linear polarization of galactic starlight I. Observations by the Wisconsin Ultraviolet Photo Polarimeter Experiment," AJ, **112**, 2726–2743 (1996).

[5] M. J. Wolff, G. C. Clayton, and M. R. Meade, "Ultraviolet interstellar linear polarization I. Applicability of current grain models," ApJ, **403**, 722–735 (1993).

[6] D. C. B. Whittet, "Continuum polarization of starlight," in: Polarimetry of the Interstellar Medium, ASP Conf. Ser., **97**, 125–142 (1996).

[7] A. Lazarian, "Tracing magnetic fields with grain alignment," JQSRT, in press (2007).

[8] N. V. Voshchinnikov, "Determination of dust properties and magnetic fields from polarimetric and photometric observations of stars," Astron. Nachr., **310**, 265–271 (1989).

Status of the Remote Sensing of Martian Aerosols

M. J. Wolff,[1] R. T. Clancy,[2] and M. D. Smith[3]

[1] *Space Science Institute,*
18970 Cavendish Road, Brookfield, WI 53045 USA
[2] *Space Science Institute, Bald Head Island, NC 28461 USA*
[3] *NASA Goddard Space Flight Center, Greenbelt, Maryland 20771 USA*
tel: +1 (262) 790-1356, fax: +1 (262) 781-8052, e-mail: wolff@spacescience.org

Abstract

We present a brief overview of the current state of the remote sensing of Martian aerosols, including an even briefer historical context as provided by the pre-1990 missions (i.e., Mariner 9, Viking, Phobos). We also outline the new directions that aerosol studies can (and should) take as a result of data sets now being acquired.

1 Introduction

The recent (and continuing) confluence of data from Mars-based spacecraft offers significant opportunities to improve our understanding of Martian aerosols. Such advancements are (and will continue to be) motivated by more than the simple acquisition of additional data. More specifically, the flotilla of Mars-based spacecraft provide the powerful combination of multi-wavelength coverage (ultraviolet through the thermal infrared) and systematic spatial/temporal sampling (e.g., seasonal coverage including nadir, "emission phase function", limb views). When such data are combined with robust, sophisticated radiative transfer and electromagnetic scattering algorithms, one is able to explore/constrain aspects of Martian aerosols that would not have been possible even only a few years ago. Given the list of current (and recently) operating platforms -- Mars Global Surveyor (MGS, deceased Nov. 2006), Mars Odyssey, Mars Express (MEx), Mars Exploration Rovers (MER, Spirit and Opportunity), and the recently arrived Mars Reconnaissance Orbiter (MRO) -- and the availability of computing resources, the primary inhibitor in Martian aerosol studies is the small number of people engaged in it. It is the beginning of a very exciting time and we hope that this presentation will stimulate you to consider working on the many aspects of Martian aerosols. We encourage everyone to contact us (wolff@spacescience.org) with any questions that you might have regarding the Mars data available for the synthesis of state-of-the-art electromagnetic scattering and radiative transfer analyses.

2 What We Will Say

In order to properly frame the current epoch of remote sensing within previous efforts, we begin with a review of aerosol remote sensing from Mariner 9, Viking 1 and 2 (both landers and orbiters), Phobos missions. To some degree, this represents a "classic" phase of Martian aerosol work. We follow up with the "neoclassical" period, which we define as ending before the arrival of Mars Express and the landing of the Mars Exploration Rovers. For these two distinct epochs remote sensing, we highlight both the results and the limitations of the datasets, including the algorithms previously employed. Finally, for the remainder of the time (hopefully, at least 50% of the total allocation), we concentrate on the current period of observations. In keeping with the silliness of our nomenclature, we refer to it as the "modern" era. One defines this period by both the capabilities of the spacecraft as well as the focus/capability of the algorithms available for remote sensing studies. As a result, we group the individual components of the remaining presentation in the following manner.

2.1 "Ground-Truth," Simultaneous, and Novel Observations

Remote sensing observations of the Martian atmosphere do not easily lend themselves to the notion of ground truth. While one might consider a high fidelity measurement from a surface platform (such as optical depth from direct solar imaging) to represent some degree of ground truth, connecting a series of orbital spacecraft observations to those of a surface station requires a temporal, as well as a spatial, overlap to account for the dynamical nature of the atmosphere. While concept of an ``overflight'' was first exploited during the Viking era, these observations were fundamentally limited by two aspects: the absence of multi-instrument coordinated (i.e., simultaneous, or nearly so) observations, and the lack of similar instrument capabilities on both the surface and the orbital platforms (See [1] for a brief historical review). Fortunately, one is able to remedy such issues in the current epoch through the use of MEx or MGS (in orbit) in conjunction with MER (on the surface). In addition to "ground-truth," the combination of MGS-MEX and MER instruments provides for leveraged atmospheric studies. That is to say, by combining the data from both platforms, one obtains a more complete picture than would be possible from analysis of each dataset independently. As an example, Figure 1 shows the differing sensitivity of an orbital thermal IR spectrometer (Thermal Emission Spectrometer – TES – onboard MGS) versus an upward viewing surface instrument (Minature TES -- Mini-TES – onboard MER). It is only with the Mini-TES that one becomes sensitive to the "scattering" aspect of the aerosols (ignoring limb geometry for now). We will present additional detail of how this can be exploited, with one set of results being an improved set of effective indices of refraction for Martian dust aerosols (shown in Figure 2). A final aspect of these type of observations is the physical scales captured by the solid angles of each orbital geometry, e.g., the view of ice clouds. Athough the "cirrus-like" aspect of Martian ice clouds, as seen in Figure 3, has been inferred from microphysical retrievals and orbital imaging, it is only with high resolution surface observations that the morphological similarity is seen.

2.2 Multi-spectra, "high" spectral resolution Emission Phase function

The emission phase function (EPF) observation sequence traces its origin to the Viking era, with significant application found during the neoclassical MGS operations. However, both of these datasets suffer from spatial registration and spectral issues that prevent the full exploitation of their capability for aerosol studies. Fortunately, with the advent of MRO and its Compact Reconnaissance Imaging Spectrometer for Mars, both of these two problems can be overcome. We outline the available datasets and the progress-to-date with respect to both dust and water ice aerosols.

2.3 Limb Observations (including Occultations)

From an electromagnetic scattering point of view, limb observations hold extreme promise in that this geometry accentuates both the important of particle size and shape. From a remote sensing retrieval point of view, one's enthusiasm may be damped by the same factors as combined with the spectre of vertically variation in such particle properties as well as the aerosol number density. As such, this type of observation was taken extensively by MGS, limb observations represent one of the "untapped" reservoirs of Martian aerosol work. Thus, these data represent one of the exciting "new" areas for Martian aerosols. We again outline the available datsets and provide the progress-to-date review. We also include a synopsis of the stellar occultation observations that are part of the MEx dataset.

Acknowledgments

This work is funded by National Aeronautics and Space Administration (NASA) through the MER and MRO projects, A portion of which was carried out at the Jet Propulsion Laboratory, California Institute of Technology, under a contract with NASA.

References

[1] M. J. Wolff et al. and 11 co-authors 2006, Constraints on dust aerosols from the Mars Exploration Rovers Using MGS Overflights and Mini-TES," Journal of Geophysical Research - Planets, 111, E12S17, doi:10.1029/2006JE002786.

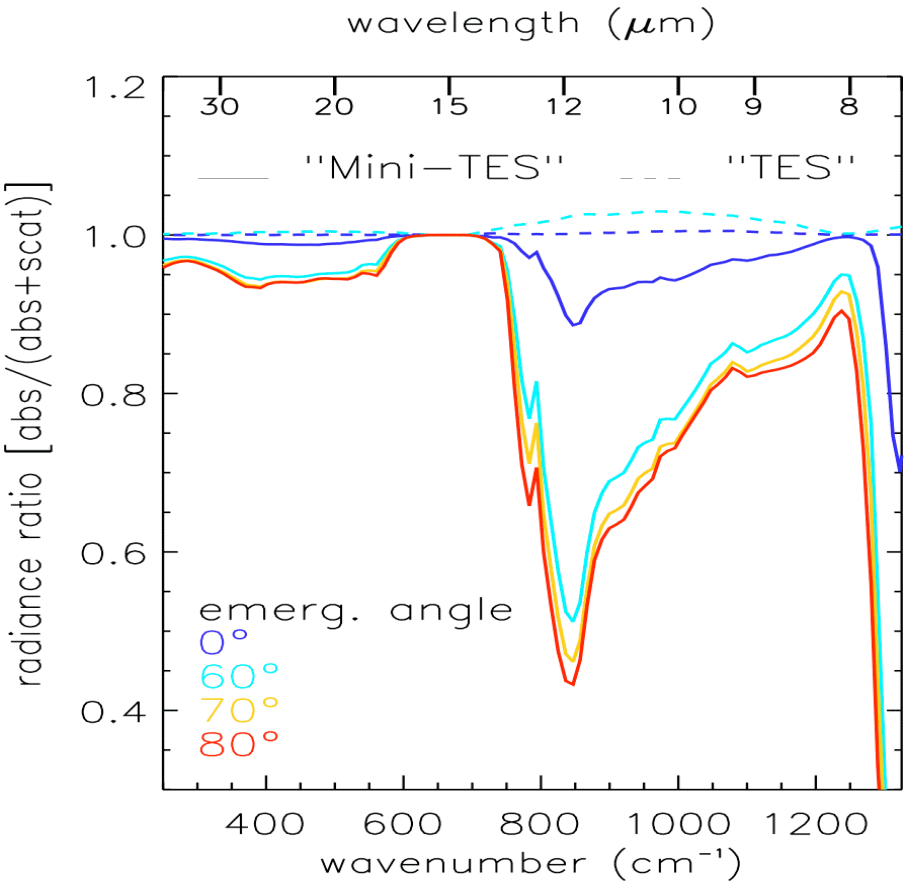

Figure 1 – The effect of scattering: MGS/TES versus MER/Mini-TES observing geometries. Synthetic spectra are calculated using the temperature profile from the Sol 46 of the Spirit mission (late southern summer), but using a 9.3 micron dust optical depth 0.3 (See [1] for more details). For convenience, we give only the emergence angles as defined for TES viewing geometry; for Mini-TES atmospheric viewing, the emergence angles are the supplement to those of TES (i.e., $e_{\text{Mini-TES}} = 180\text{-}e_{\text{TES}}$). The ratio plotted is that of the ``absorbing atmosphere'' radiance relative to the full multiple scattering radiance. The solid lines represent the Mini-TES view (downwelling) while the dashed lines show the TES view (upwelling). The relative importance of scattering between the two view points is quite distinctive.

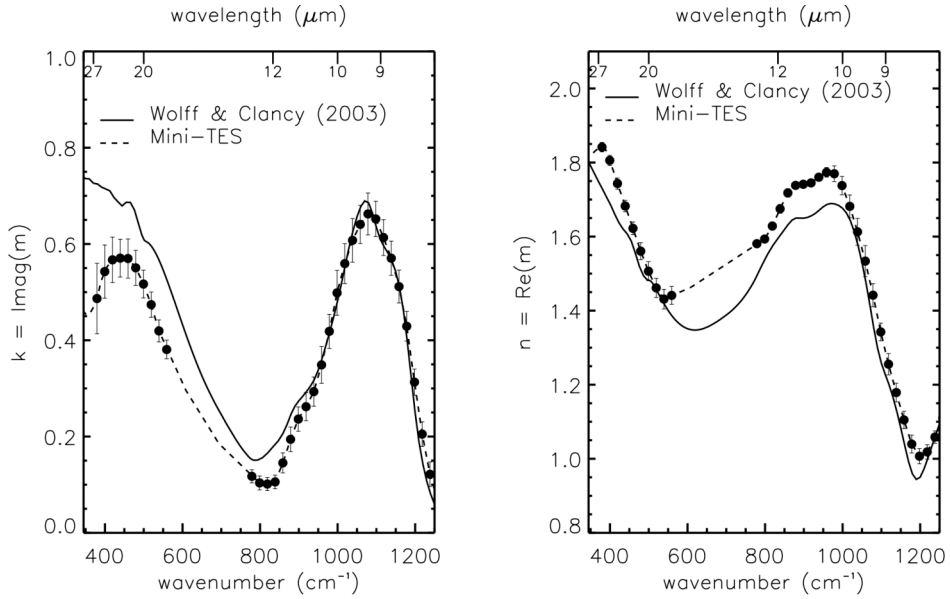

Figure 2 Complex indices of refraction from the combined TES-Mini-TES overflight analyses. Left Panel: Imaginary indices of refraction (dashed line, k = Im(m)) compared with the starting values (solid line) from Wolff and Clancy (2003). The filled circles indicate the position of each Mini-TES channel, with the error bars representing the averaged formal retrieval precision and the standard deviation among the k values from all seven datasets, added in quadrature assuming no correlation. Right Panel: As for Left Panel, but for the real indices of refraction.

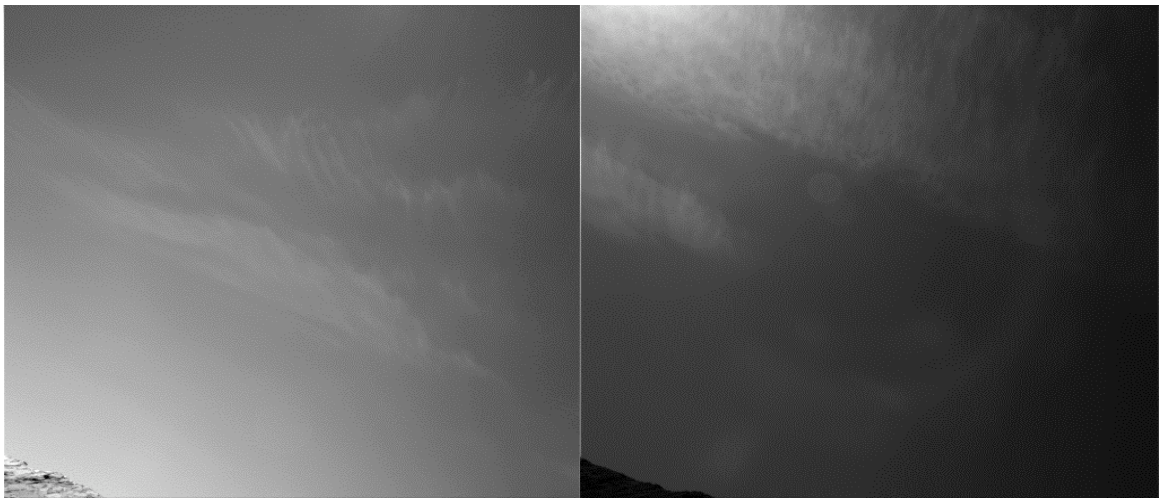

Figure 3 – Opportunity Navcam images of clouds obtained on sols 290 (Top) and 291 (Bottom). Although the cirrus-like nature of the clouds was expected from previous observational and modeling efforts, the morphological similarities to terrestrial cirrus remains striking (well, at least to me).

New *Scattering Information Network* project for the light scattering community

Thomas Wriedt,[1] Jens Hellmers[2]

[1] *Institut für Werkstofftechnik,*
Badgasteiner Str.3, D-28359 Bremen, Germany
[2] *Verfahrenstechnik, Universität Bremen*
Postfach 330440 ,D-28334 Bremen, Germany
tel: +49 (421) 218-2507, fax: +49 (421) 218-2507, e-mail: thw@iwt.uni-bremen.de

Abstract

Current international research needs efficient exchange of information. To constantly keep information for the light scattering community up to date, to start a project for a new *Scattering Information Network* has been proposed. The history and the concept of the project will be reported.

1 Introduction

With current international research efficient and fast exchange of information is needed. The internet can help in many respects but Google and other search engines only may not provide all the information that is needed. Therefore information web sites have been set up by members of the community over the years.
All this web sites provide relevant information to the community, but relevant information is quite disperse, quite diverse, and it is difficult to keep all information up to date.
One reason for this is of cause that most of these enthusiasts can care for these web sites only in their spare time. Because of this we felt that we should care for a new *Scattering Information Network* web site full time. We applied for funding of this new web site by the German Research Foundation (DFG). In the next section we will give a short overview of existing web information, following that we will report on the history of the project and we shortly outline the concept of the new web site we currently have in mind.

2 Existing information web sites

In this section we give a short overview over existing information web sites which are intended for the light scattering community or which may of interest for all researchers working in this field. For the light scattering community there is the *Directory of Members of the Electromagnetic Scattering Community* by M. Mishchenko [1] listing members of the community with their addresses and email data. The *Electromagnetic and Light Scattering by Particles Newsletter* is published regularly by L. Kolokolova. Both the list of *Electromagnetic Scattering Programs* by T. Wriedt [3] and *SCATTERLIB Light Scattering Codes Library* by P. Flatau [4] have been founded at about the same time and mainly focus on providing information on computer programs. But additional information such as information on new book and conferences is also included.
Additionally there is the *Minsk bibliography on light scattering* V. Babenko [5], the *Database of Optical Constants* [6] and the *Amsterdam Light Scattering Database* H. Volten [7]. B. Gustafson provides a *Database of microwave-analog-to-light-scattering data* [8].

3 History of *Electromagnetic scattering programs*

The new project dates back to the internet side *Electromagnetic Scattering Programs* [3] which exists nearly for 14 years. It was started following the first „seminar Mie theory“, which was organized in Clausthal-Zellerfeld, Germany in 1993. This seminar was intended to clarify some problems, which at that time seemed to exist with some computer programs based on Mie theory. The seminar was arranged to compare results from different programs. It soon became clear that problems could easily be solved be using the latest program published by Wiscombe on an ftp server [9]. A first overview of available scattering programs was presented at the seminar and published later [10]. Following the seminar a first *List of available electromagnetic scattering programs* [11] was published on the web server of the Faculty of Production Engineering of the University of Bremen. At that time this web page had the highest number of hits on all web pages of this web server. With the help of the Internet archive www.archive.org the development of this web page can be traced back to 03.12.1998 [12].

4 Concept of new *Information Network*

In this section we like to shortly explain the concept of the new *Scattering Information Network* web site we plan to erect within the next year. The basic features of the information network will include the following topics, which we think are of utmost importance for the community.

- Up to date information related to the subject of light scattering e.g. conference announcements, free jobs.
- General information, answers to frequently asked questions.
- List of scientists and research groups working in the field of light scattering including subjects of research.
- Database of available computer programs.
- A user forum for researchers and students in the field.
- Database of computed T-matrices.
- Database of validated computational results.

One of our favorite topics is the list of available computer programs. We will start with this by updating information from our previous web site *Electromagnetic Scattering Programs* [3]. We will try to retrieve dead or broken links. Another way to recover lost programs is to look at our stored local information or to ask other researchers whether they have a local copy of a web site no longer available. Some older programs are only available in printed form. We will scan and may be “ocr” this printed reports or PhD theses such that we can include these programs in electronic form in the data base.

Another of our favorite topics the data base of computed T-matrices. As a T-matrix includes all information on the scattering process we assume that a data base of T-matrices may be of interest to the light scattering community. Especially with inversion problems to retrieve the shape of a scattering particle where many scattering problems need to be solved a database of T-matrices may help to reduce total computer time. We intend to implement an interface to this database in our T-matrix programs such that a user is asked whether he likes to provide his computed T-matrix to this database. We will also get in touch to other scientists working on the T-matrix method also to include such an interface into their programs. This would of cause need conversion between different types of nomenclature.

This is only a rough outline of the project. We hope that erection of the information network will lead to discussion with interested scientists which will help to improve on the concept.

5 How to contribute

Such a *Scattering Information Network* web site can not be erected without assistance from the scientific community. We therefore would like to invite all scientists working in the field and interested in the project to contribute to the concept first of all. Please send your suggestions and ideas to the authors of this abstract. We welcome any comments on the first draft of the concept we are presenting.

In the later stage of the project we would need editors who like to care for a special topic included in the *Scattering Information Network* e.g. new programs or new books published. We would also be glad if you could send any information which you think is relevant for inclusion in the *Information Network.*

6 Conclusion

During the conference we like to discus how this project can help to cope with the increasing importance of information exchange of a growing community and how the information network should be designed to help international collaboration within the light scattering community working in different scientific disciplines.

Acknowledgments

We would like to acknowledge support of this work by Deutsche Forschungsgemeinschaft DFG.

References

[1] M. Mishchenko: NASA GISS: Directory of Members of the Electromagnetic Scattering Community, http://www.giss.nasa.gov/~crmim/scatter/ .

[2] L. Kolokolova: Electromagnetic and Light Scattering by Particles Newsletter, http://www.astro.ufl.edu/~elsnews/ .

[3] T. Wriedt: Electromagnetic Scattering Programs, http://diogenes.iwt.uni-bremen.de/vt/laser/wriedt/index_ns.html .

[4] P. Flatau: SCATTERLIB Light Scattering Codes Library, http://atol.ucsd.edu/~pflatau/scatlib/ .

[5] V. Babenko: Minsk bibliography on light scattering, http://www.astro.spbu.ru/DOP/4-BIBL/bibl0.html .

[6] Laboratory Astrophysics Group of the AIU Jena: Database of Optical Constants for Cosmic Dust http://www.astro.uni-jena.de/Laboratory/Database/odata.html

[7] H. Volten: Amsterdam Light Scattering Database, http://www.astro.uva.nl/scatter/ .

[8] B. Gustafson: Database of microwave-analog-to-light-scattering data, http://www.astro.ufl.edu/~aplab/database.htm .

[9] W. Wiscombe: Mie code for scattering by dielectric spheres, ftp://climate.gsfc.nasa.gov/pub/wiscombe/Single_Scatt/ .

[10] T. Wriedt, “Available electromagnetic-scattering programs,” IEEE Antennas and Propagation Magazine **36**, 61-63 (1994).

[11] T. Wriedt: List of available electromagnetic scattering programs, http://imperator.cip-iwt.uni-bremen.de/~fg01/laser.html (no longer available) .

[12] Internet Archive of [10]: http://web.archive.org/web/*/http://imperator.cip-iw1.uni-bremen.de/fg01/codes2.html .

Decomposition of objects for light scattering simulations with the null-field method with discrete sources

Thomas Wriedt[1], Roman Schuh[2]

[1] *Institut für Werkstofftechnik,*
Badgasteiner Str.3, D-28359 Bremen, Germany
[2] *Verfahrenstechnik, Universität Bremen*
Postfach 330440 ,D-28334 Bremen, Germany
tel: +49 (421) 218-3503, fax: +49 (421) 218-3350, e-mail: schuh@iwt.uni-bremen.de

Abstract

The null-field method with discrete sources (NFM-DS) is used for the simulation of the light scattering by elongated particles. These particles can be decomposed into several identical parts with a small aspect ratio. The T-matrix computed for a single part is used to compose the T-matrix for the whole particle. For verification purposes the light scattering distributions computed with NFM-DS are compared with results from DDA (discrete dipole approximation).

1 Introduction

Computations of light scattering by elongated particles are needed in various scientific branches such as astrophysics, atmospheric science and especially in optical particle characterization. In optical particle characterization there is interest to detect airborne fibrous particles like mineral, glass or asbestos fibres, which are considered to be serious health hazards. Here high aspect ratios are of special interest and so it is required that a light scattering simulation algorithm can handle them.
The null-field method with discrete sources (NFM-DS) is suitable for the simulation of light scattering by particles with high aspect ratios, like finite fibres or flat discs. The method also can be used for computation of the T-matrix of composite objects [1]. Therefore, it is possible to compose complex particles from basic parts for which the T-matrix is already known.
In this work we examine a new approach to compute scattering by fibres and we will present computational results. The method is described briefly in the next chapter.

2 Null-Field Method with Discrete Sources for Composite Objects

Using discrete sources we can compute scattering by a single fibre having a high aspect ratio. But to compute scattering by two long fibres which stick together in some way would be a multiple scattering problem and to solve this problem using a standard multiple scattering concept combining the T-matrices of both fibres would not be possible because the circumscribed spheres of both fibres would intersect. Also other computational approaches such as DDA, FDTD and related methods might be problematic because if the fibres are not aligned parallel to each other this would blow up the computational domain and increase computer time tremendously.
To overcome this problem we developed a multiple scattering method based on decomposition into basic parts [2]. Each fibre is decomposed into basic parts having a small size parameter and the full scattering problem is solved by combining the T-matrices of all those parts.
In this work we would like to show the feasibility of this new method. It is important to make a computational analysis, because the circumscribing spheres of the basic parts show

intersecting volumes, even if comparatively low. The NFM-DS simulations are verified with DDA simulations (DDSCAT) [3].

3 Simulations results

In the following two examples are presented fibres of circular section composed of four identical basic parts. Each section is a short cylinder of circular cross section.
In Figure 1 the differential scattering cross section (DSCS) of a fibre with the size parameter $kh = 8$ is shown, where k is the wave number $2\pi/\lambda$ and h is the length of the fibre. The diameter of the fibre corresponds to $kd = 2$. The index of refraction values $m = 1.5$. The fibre is composed of four equal sized cylinders with $kh = 2$ and $kd = 2$. The rotational axis of the fibre is aligned on the z-axis. The plane wave is incident along the z-axis and the scattering diagram is plotted on the x-y plane both for incident p- and s-polarization.
The comparison with a corresponding DDA simulation shows good agreement in the DSCS. Small deviations for the p-polarization indicate that the influence of the intersecting circumscribing spheres can not be neglected.
Further simulations with smaller objects but similar configurations show even better or almost perfect agreement between NFM-DS and DDA. It seems obvious that there is an upper limit in size of the composed objects for which the effect of the intersecting circumscribing spheres must not be neglected.

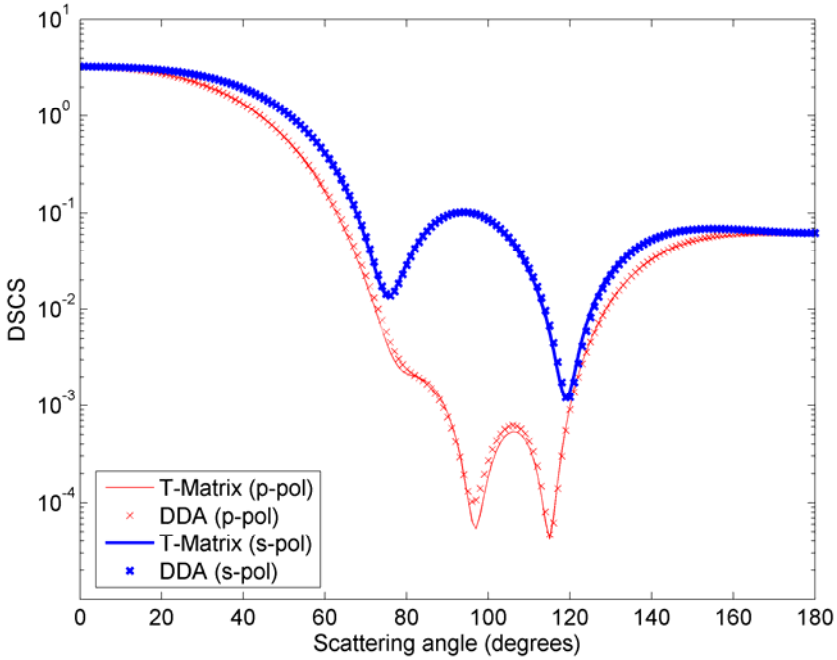

Figure 1: DSCS of a cylindrical particle (length $kh = 8$; diameter $kd = 2$; $m = 1.5$). Comparison of T-matrix and DDA simulations. The T-matrix is composed of 4 identical T-matrices of smaller cylinders with $kh = 2$.

In Figure 2 the differential scattering cross section (DSCS) of a fibre with the size parameter $kh = 16$ is shown. The diameter of the fibre corresponds to $kd = 4$. The index of refraction values $m = 1.5$. The fibre is composed of four equal sized cylinders with $kh = 4$ and $kd = 4$. The rotational axis of the fibre is aligned on the z-axis. The plane wave is incident along the z-axis and the scattering diagram is plotted on the x-y plane both for incident p- and s-polarization.

The comparison with a corresponding DDA simulation shows only good agreement in the forward scattering angle range from 0° to 80°. Strong deviations for both the p-polarization and the s-polarization show the limits of the method of composing the T-matrix from basic parts if the circumscribing spheres of the basic parts intersect.

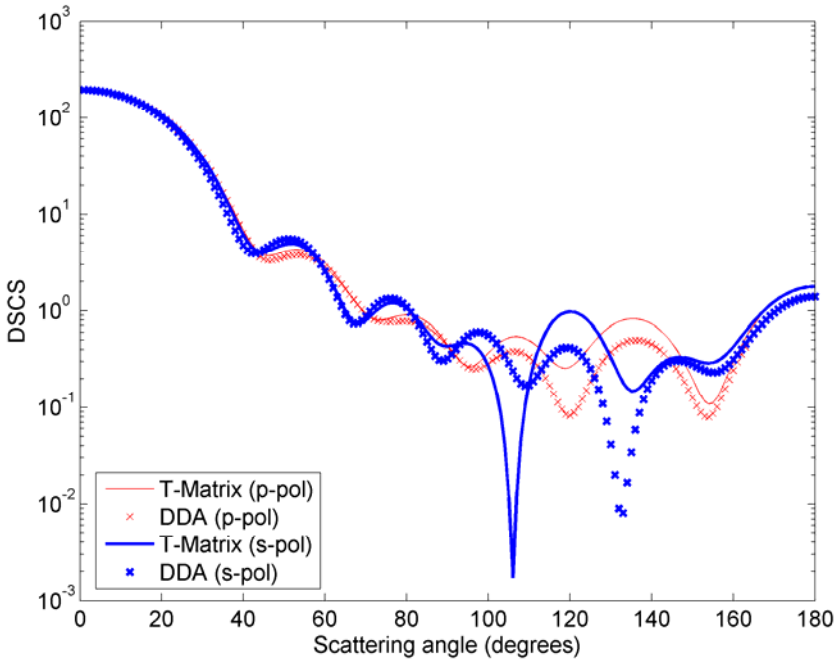

Figure 2: DSCS of a cylindrical particle (length $kh = 16$; diameter $kd = 4$; $m = 1.5$). Comparison of T-matrix and DDA simulations. The T-matrix is composed of 4 identical T-matrices of smaller cylinders with $kh = 4$.

4 Conclusion

It has been shown that the NFM-DS can be used to compute light scattering by composite objects. This makes possible the computation of the light scattering for even more complex objects like torus- or helix-shaped particles. The first computations for simple fibres show the need for further investigations to verify the range of validity of the method.

Acknowledgments

We would like to acknowledge support of this work by Deutsche Forschungsgemeinschaft DFG.

References

[1] A. Doicu, T. Wriedt and Y. Eremin: Light Scattering by Systems of Particles. Null-Field Method with Discrete Sources - Theory and Programs. Springer Verlag Berlin, Heidelberg, New York, 2006.

[2] T. Wriedt: Review of the Null-Field Method with Discrete Sources, JQSRT, in press, 2007.

[3] B. T. Draine, P. J. Flatau, User Guide to the Discrete Dipole Approximation Code DDSCAT 6.1, http://arxiv.org/abs/astro-ph/0409262v2, 2004.

Systematic comparison of the discrete dipole approximation and the finite difference time domain method

Maxim A. Yurkin,[1,2,4] Alfons G. Hoekstra,[1] R. Scott Brock,[3] Jun Q. Lu,[3]

[1] *Faculty of Science, Section Computational Science, of the University of Amsterdam, Kruislaan 403, 1098 SJ, Amsterdam, The Netherlands, tel: +31 (20) 525-7530, fax: +31 (20) 525-7490*
[2] *Institute of Chemical Kinetics and Combustion, Siberian Branch of the Russian Academy of Sciences, Institutskaya 3, Novosibirsk 630090, Russia, tel: +7 (383) 333-3240, fax: +7 (383) 334-2350*
[3] *Biomedical Laser Laboratory, Department of Physics, East Carolina University, East Fifth Street, Greenville, NC 27858-4353, USA, tel: +1 (252) 328-6739, fax: +1 (252) 328-6314*
[4] *e-mail: myurkin@science.uva.nl*

Abstract

We compare the discrete dipole approximation (DDA) and the finite difference time domain (FDTD) method for simulating light scattering of spheres in a range of size parameters x up to 80 and refractive indices m up to 2. Using parallel implementations of both methods, we require them to reach a certain accuracy of scattering quantities. We show that relative performance sharply depends on m with boundary value of 1.4. DDA is faster for smaller m, while FDTD – for larger.

1 Introduction

DDA [1] and FDTD [2] are two of the most popular methods to simulate light scattering of arbitrarily shaped inhomogeneous particles. These methods have a very similar region of applicability; however, they are rarely used together. In a few papers either one method is used to validate the other or they are compared for a few scatterers [3]. We perform a new comparison, which in two respects is more extended than the previous studies. First, we cover a large range of x and m, which includes, e.g., almost the whole range of biological cells (x up to 80). Second, we pre-set the accuracy to be reached by both methods, which makes the performance results more informative.

2 Methods

As a numerical implementation of DDA we have used the ADDA computer code [4] v.0.76, which is capable of running on a cluster of computers (parallelizing a single DDA computation), allowing simulating light scattering by scatterers much larger than a wavelength. In this paper we use the default ADDA settings for dipole polarizability and iterative method (lattice dispersion relation and quasi minimal residual method respectively). The convergence criterion of the iterative solver (required relative residual norm) was set to 10^{-3}, which is larger than the default value but is enough for the accuracy required in this study (as shown by results).

The implementation used for FDTD was developed in the Biomedical Laser Laboratory at East Carolina University [5], based on the methods described by Yang and Liou [2] with numerical dispersion correction [6]. The implementation is written in standard Fortran90 and uses the MPI standard for communications, allowing it to run on a variety of platforms. The incident field used was an approximate Gaussian pulse with an average wavelength equal to the wavelength of interest. Berringer's perfectly matching layer (PML) boundary condition was used to terminate the lattice. To determine the convergence, multiple simulations are carried out, each simulating a time period longer than the previous. The time periods are in increments of the time it takes the incident pulse to travel once across the scattering particle. When the difference in results for two simulations is negligible, or when the differences start to oscillate, the result is said to have converged.

We simulate scattering by spheres with different x and $m = m' + im''$, m'' is fixed at 1.5×10^{-5}. For each sphere we calculated the extinction cross section Q_{ext}, asymmetry parameter g, and Mueller matrix in one

Table 1. Performance results of DDA vs. FDTD for spheres with different x and m'.[a]

m'	x	Time, s		dpl[b]		Used RAM, GB		Iterations[c]	
		DDA	FDTD	DDA	FDTD	DDA	FDTD	DDA	FDTD
1.02	10	1.1	0.6	15	12	0.15	0.02	2	275
	20	11	4.1	20	14	1.4	0.13	4	509
	30	24	17	17	13	2.9	0.28	4	651
	40	78	384	18	22	7.1	2.3	5	1398
	60	453	7026	20	32	30	20	7	4004
	80	691	(40580)	16	(32)	40	(47)	9	(5239)
1.08	10	0.7	2.1	10	18	0.07	0.06	6	453
	20	1.9	25	10	19	0.22	0.30	12	1005
	30	8.7	207	10	19	0.79	0.84	18	2531
	40	19	388	10	20	1.4	2.1	25	1928
	60	31	1196	6.7	18	1.4	4.7	49	2509
	80	129	12215	6.3	22	2.9	18.7	84	4009
1.2	10	0.9	3.2	10	18	0.07	0.07	20	671
	20	3.2	58	7.5	20	0.15	0.44	57	1589
	30	8.7	645	6.7	24	0.22	2.09	146	3321
	40	106	740	7.5	18	0.79	2.09	384	3837
	60	1832	35998	8.4	25	2.9	15.9	1404	13762
1.4	10	4	2.5	15	10	0.15	0.03	78	1047
	20	896	3203	25	37	2.9	3.4	687	10333
	30	7256	3791	17	23	2.9	2.8	5671	11013
	40	10517	(47410)	18	(32)	7.1	(15.7)	2752	(21580)
1.7	10	185	5.5	25	8	0.61	0.03	900	2323
	20	22030	998	35	18	7.1	0.82	5814	13101
	30	(185170)	47293	(37)	30	(25)	10	(12005)	39751
2	10	1261	32	40	11	1.4	0.07	2468	7481
	20	(252370)	6416	(60)	20	(30)	1.7	(14067)	30693

[a] Parentheses indicate that computational method failed to achieve required accuracy for this x and m'.
[b] Number of dipoles or grid cells per incident wavelength.
[c] Number of the iterations and time steps during time marching for DDA and FDTD respectively.

scattering plane (polar angle θ changes from 0° to 180° in steps of 0.25°). From the whole Mueller matrix we analyze only the S_{11} element and the linear polarization $P = -S_{12}/S_{21}$. The spherical symmetry of the problem is used to calculate the Mueller matrix using the result for only one incident polarization [4]. This accelerates the simulation almost twice compared to the general shapes, both for DDA and FDTD. In this study we fix the accuracy required by both methods. We take the crudest discretization that satisfies both of the following: the relative error (RE) of Q_{ext} less than 1%, and the root mean square (RMS) RE of S_{11} less than 25%. All simulations were performed on the Lemieux cluster using 16 nodes (each has 4 Alpha EV6.8 1 GHz processors and 4 GB RAM, http://www.psc.edu/machines/tcs/).

3 Results and discussion

Results of the performance comparison of DDA and FDTD are shown in Table 1. The total computational time describes overall performance. It is determined by two factors: the number of cells in the computational grid and the number of iterations or time steps. The former depends on x and dpl (number of grid cells per wavelength) and determines the memory consumption. Values of dpl can not be directly compared between both methods because the typical values for DDA [1] are twice as small as for FDTD [2]. The same applies to the iteration count in an even greater extent. For some problems one of the methods failed to reach the prescribed accuracy for the given hardware. Results of these simulations are shown in parenthesis.

Table 2. Same as Table 1 but for accuracy results.

m'	x	RE(Q_{ext})		RMSRE(S_{11})		RE(g)		RMSE(P)	
		DDA	FDTD	DDA	FDTD	DDA	FDTD	DDA	FDTD
1.02	10	2.5×10^{-3}	4.3×10^{-3}	0.20	0.17	1.6×10^{-4}	3.6×10^{-4}	0.039	0.043
	20	1.4×10^{-4}	9.3×10^{-4}	0.17	0.22	1.6×10^{-5}	6.9×10^{-5}	0.088	0.095
	30	5.2×10^{-5}	7.9×10^{-3}	0.13	0.22	1.5×10^{-5}	5.3×10^{-5}	0.037	0.10
	40	8×10^{-6}	3.3×10^{-3}	0.19	0.21	4×10^{-6}	1.6×10^{-5}	0.064	0.074
	60	1.6×10^{-4}	5.9×10^{-3}	0.25	0.20	1×10^{-6}	4×10^{-6}	0.071	0.048
	80	1.2×10^{-4}	(4.3×10^{-3})	0.25	(0.33)	3×10^{-6}	(2×10^{-6})	0.074	(0.12)
1.08	10	2.5×10^{-4}	5.5×10^{-3}	0.15	0.064	6.4×10^{-5}	1.2×10^{-4}	0.074	0.024
	20	5.8×10^{-5}	1.0×10^{-2}	0.17	0.063	3.6×10^{-4}	5.2×10^{-5}	0.097	0.061
	30	3.8×10^{-4}	9.3×10^{-3}	0.10	0.054	1.3×10^{-4}	6×10^{-6}	0.062	0.033
	40	2.8×10^{-4}	9.5×10^{-3}	0.083	0.053	5.1×10^{-5}	8.2×10^{-5}	0.11	0.045
	60	2.2×10^{-3}	8.3×10^{-3}	0.16	0.072	2.7×10^{-4}	4.7×10^{-4}	0.14	0.062
	80	3.8×10^{-3}	8.7×10^{-3}	0.13	0.071	9.6×10^{-5}	1.1×10^{-3}	0.13	0.054
1.2	10	7.1×10^{-4}	7.6×10^{-3}	0.073	0.024	6.2×10^{-4}	3.6×10^{-4}	0.059	0.022
	20	5.4×10^{-3}	9.3×10^{-3}	0.13	0.037	3.3×10^{-4}	3.4×10^{-3}	0.11	0.029
	30	2.5×10^{-3}	7.8×10^{-3}	0.16	0.075	3.4×10^{-4}	1.4×10^{-3}	0.14	0.069
	40	3.9×10^{-3}	9.1×10^{-3}	0.19	0.25	1.2×10^{-3}	1.0×10^{-2}	0.15	0.23
	60	2.3×10^{-3}	6.0×10^{-3}	0.13	0.25	1.2×10^{-3}	1.3×10^{-3}	0.14	0.23
1.4	10	7.0×10^{-3}	8.9×10^{-3}	0.13	0.14	8.2×10^{-3}	4.6×10^{-2}	0.059	0.093
	20	9.7×10^{-3}	9.8×10^{-3}	0.23	0.17	1.3×10^{-2}	2.7×10^{-2}	0.095	0.15
	30	7.4×10^{-3}	8.2×10^{-3}	0.24	0.19	5.6×10^{-3}	4.6×10^{-3}	0.24	0.19
	40	7.1×10^{-3}	(1.5×10^{-2})	0.15	(0.24)	7.3×10^{-5}	(2.7×10^{-3})	0.13	(0.097)
1.7	10	5.2×10^{-4}	8.0×10^{-3}	0.12	0.22	3.4×10^{-2}	9.6×10^{-2}	0.097	0.13
	20	1.0×10^{-2}	8.0×10^{-3}	0.12	0.24	1.2×10^{-2}	1.8×10^{-2}	0.086	0.21
	30	(2.0×10^{-2})	1.1×10^{-2}	(0.14)	0.12	(1.5×10^{-2})	1.0×10^{-2}	(0.12)	0.095
2	10	4.7×10^{-3}	8.3×10^{-3}	0.16	0.16	5.1×10^{-3}	2.3×10^{-2}	0.11	0.17
	20	(2.6×10^{-2})	8.3×10^{-3}	(0.086)	0.14	(5.0×10^{-3})	3.1×10^{-2}	(0.098)	0.11

Naturally, both methods require larger computational time for larger x just because the number of grid cells scale cubically with x, if dpl is kept constant. Apart from that, the behavior of the methods is quite different. Dpl required by DDA to reach the prescribed accuracy do not systematically depend on x, except for $m' = 1.7$ and 2. However, dpl does depend on m' – it increases both when m' increases over 1.4 and approaches the unity. The latter is partly artificial because $S_{11}(\theta)$ for soft spheres has very sharp maxima, the position of which depends on the exact shape of the particle. Using the methodology described elsewhere [7] we determined that shape errors constitute 90% of RMSRE of S_{11} for $m' = 1.02$, $x = 20$, and dpl = 10 (data not shown). The number of iterations for DDA is relatively small and only moderately increases with x for $m' = 1.02$ and 1.08. However, for larger m' it rapidly increases both with m' and x. For $m' = 1.7$ and 2 this combines with increasing dpl leading to the sharp increase in computational time.

The behavior of dpl for FDTD is oscillating on the whole range of x and m' studied. On the contrary, the number of time steps increase systematically with both x and m', which is expected. The dependences of the FDTD performance on x and m' are less interdependent than that of DDA. Comparing the overall performance of two methods, one can see that for small m′ and large x DDA is an order of magnitude faster than FDTD, and for large m' vice versa. The boundary value of m' is about 1.4, for which both methods are comparable. They are also comparable for small values of both m' and x. Memory requirements of the two methods are generally similar. However, they naturally correlate with computational time – in most cases the faster method is also less memory consuming.

Accuracy results for several scattering quantities are shown in Table 2. For $m' \geq 1.4$ errors of both Q_{ext} and S_{11} are close to the required values (0.01 and 0.25 respectively) for both DDA and FDTD. However, for smaller m' DDA has relatively small errors of Q_{ext} while FDTD has smaller errors of S_{11}. In other words, performance of DDA is limited by S_{11} (because of the shape errors as discussed above), while performance of FDTD is limited by Q_{ext}. DDA results in several times smaller errors of g, which is correlated with smaller errors of Q_{ext}, and FDTD – in smaller errors of P. We can, therefore, conclude that DDA is generally more accurate for integral scattering quantities while FDTD – for angle-resolved ones. However, that only means that general interrelation between DDA and FDTD as a function of m' may slightly change depending on the certain scattering quantities that are calculated.

4 Conclusion

A systematic comparison of DDA and FDTD for a range of x up to 80 and m' up to 2, using state-of-the-art parallel implementations of both methods, was performed requiring a certain accuracy of the simulated scattering quantities. DDA is an order of magnitude faster for $m' \leq 1.2$ and $x > 30$, while for $m' \geq 1.7$ FDTD is faster by the same extent. $m' = 1.4$ is a boundary value, for which both methods perform comparably. Although these conclusions depend slightly on particular scattering quantity and on the implementations of both methods, they will not change principally unless a major improvement of one of the method is made. For instance, improving iterative solver and/or preconditioning of the DDA would improve the DDA performance for larger m. For the FDTD, a "safe" set of PML parameters were chosen; fine tuning these parameters could lead to a thinner PML and increase performance especially for the larger problem sizes. Also the FDTD code is designed to use memory conservatively; relaxing the memory restrictions would allow faster simulation times at the expense of additional memory use.

The current study is far from being complete, since we do not vary the imaginary part of the refractive index, which is known to significantly influence the performance of the methods. This should be a topic of a future work.

Acknowledgments

J.Q.Lu acknowledges the support of National Institute of Health (grant 1R15GM70798-01) and Teragrid for supercomputer time allocations. M.A.Y. acknowledges support of the Russian Science Support Foundation through the grant "Best PhD-students of Russian Academy of Sciences" and of the administration of the Novosibirsk region.

References

[1] M. A. Yurkin and A. G. Hoekstra, "The discrete dipole approximation: an overview and recent developments," JQSRT (2007), doi:10.1016/j.jqsrt.2007.01.034.

[2] P. Yang and K. N. Liou, "Finite difference time domain method for light scattering by nonspherical and inhomogeneous particles," in *Light Scattering by Nonspherical Particles, Theory, Measurements, and Applications,* M. I. Mishchenko, J. W. Hovenier, and L. D. Travis, eds. (Academic Press, New York, 2000), pp. 173-221.

[3] T. Wriedt and U. Comberg, "Comparison of computational scattering methods," JQSRT **60**, 411-423 (1998).

[4] M. A. Yurkin, V. P. Maltsev, and A. G. Hoekstra, "The discrete dipole approximation for simulation of light scattering by particles much larger than the wavelength," JQSRT (2007), doi:10.1016/j.jqsrt.2007.01.033.

[5] R. S. Brock, X. Hu, P. Yang, and J. Q. Lu, "Evaluation of a parallel FDTD code and application to modeling of light scattering by deformed red blood cells," Opt. Expr. **13**, 5279-5292 (2005).

[6] R. S. Brock and J. Q. Lu, "Numerical dispersion correction in a parallel FDTD code for the modeling of light scattering by biologic cells," to be submitted to Appl. Opt.

[7] M. A. Yurkin, V. P. Maltsev, and A. G. Hoekstra, "Convergence of the discrete dipole approximation. II. An extrapolation technique to increase the accuracy," J. Opt. Soc. Am. A **23**, 2592-2601 (2006).

Sizing non-spherical, evaporating aerosol particles using "white" light resonance spectroscopy

A. A. Zardini and U. K. Krieger

Institute for Atmospheric and Climate Science, ETH Zurich, 8092 Zurich, Switzerland
tel: +41-44-633-4007, E-mail: ulrich.krieger@env.ethz.ch, alessandro.zardini@env.ethz.ch

Abstract

We show how "white" light resonance spectroscopy can be used to measure the evaporation rate of a solid, non-spherical aerosol particle levitated in an electrodynamic balance. The vapor pressure of solid ammonium nitrate (AN), an inorganic salt of relevance for atmospheric science, is calculated and compared with the literature.

1 Introduction

In the field of atmospheric and climate science there is considerable interest in understanding the partitioning between gas and particle phase of chemical species. In particular for semi-volatile substances like ammonium nitrate or certain organic species, the partitioning will strongly influence particulate matter burden in the troposphere. In addition, it will influence the radiative properties of the aerosol and the way it participates to cloud formation and heterogeneous chemistry. In order to predict this partitioning, it is crucial to know the vapor pressure of the compounds under ambient conditions, whereas most established methods rely on high temperatures to achieve a sufficiently high vapor pressure. One possible method to assess very low vapor pressures is to measure evaporation rates of particles, by precisely sizing the particles while evaporating. Recently, we used white light Mie resonance spectroscopy [1] for sizing and measuring the evaporation rates of aqueous solution (hence spherical) aerosol particles. In the present work we extend that method to the case of a solid, non-spherical particle.

2 Experimental setup

The experimental setup used in this study has been described previously in detail [1]. A micrometer-sized aqueous solution particle is levitated in an electrodynamic balance under sufficiently dry conditions until it effloresces whereupon its evaporation under controlled ambient conditions is monitored. The 2-dimensional angular scattering pattern is recorded with a CCD camera to distinguish liquid (spherical) particles from solid (non-spherical) particles. A ball lens type point source LED is used as a "white light" source with high spatial coherence (50 μm source diameter, peak wavelength $\simeq$ 589 nm, spectral bandwidth at 50% $\simeq$ 16 nm, radiant power $\simeq$ 150 μW) using a bestform lens (f = 32 mm, $f\#$ = 2.0) to focus the light on the levitated particle and a pierced mirror to collect the resonance spectra in a backscattering geometry (collection angle 180°±4°). An optical fiber is employed to deliver the backscattered light from the particle to a spectrograph with an array detector as an optical multichannel analyzer.

3 Results and discussion

Figure 1 shows three spectra of a solid, non-spherical AN particle levitated at T=293 K taken at the different times during an evaporation experiment. The spectra show a complex structure of weak optical resonances, but a time series of spectra does not allow easily to discern a shift in the resonance position as it is the case with a spherical particle evaporating. The most pronounced difference between spectra is the different mean backscattered intensity. The

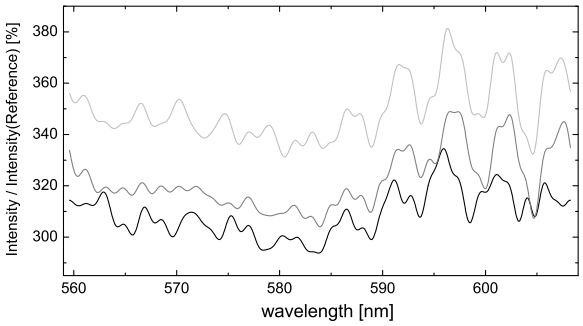

Figure 1: Spectra of a solid AN particle taken at T=293 K, exposure time was 30s. These spectra are taken at the beginning of the experiment (t=2 minutes, black curve), at t=172 minutes (gray curve), and at t=174 minutes (light gray curve).

2-dimensional angular scattering pattern show the same basic features, namely a complex pattern, similar to what has been observed with natural aerosol particles [2], and a significant change in intensity over time periods of seconds. To make a size change of the evaporating non-spherical particle visible in its resonance spectra, we proceed as shown in Fig. 2. Here, panel (a) shows a times series of raw spectra (gray scale intensity coded), with a 120 seconds time lag between consecutive spectra. Clearly, what is most apparent is the change in total intensity from spectrum to spectrum. Most likely, rotational Brownian motion does not lead to a complete orientational averaging within the exposure time of 30 s, and hence the irregular morphology causes the integrated intensity to fluctuate. To eliminate this intensity fluctuations, each single spectrum is separately normalized to its own maximum and minimum of intensity and the result is plotted in panel (b). The most prominent features here are intensity extrema at certain wavelength (roughly regularly spaced) which are not time dependent. Further normalization is

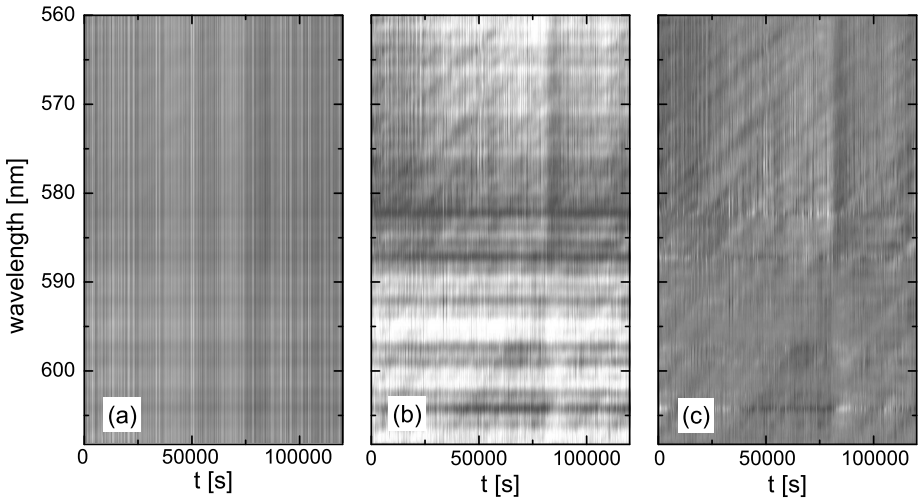

Figure 2: Panel (a) shows the raw spectra of an AN solid particle versus time (wavelength on vertical axis, b/w coded intensity). The intensity of each spectrum are normalized to the same maxima and minima in panel (b). In panel (c) the data of panel (b) are normalized with the mean spectrum of the complete time series.

performed in panel (c) by dividing each spectrum by the mean spectrum of the complete times series. Thus, the non time dependent features are suppressed and intensity bands shifting with time become visible, although not nearly as distinct as in the case of an evaporating liquid, i.e. spherical, particle [1]. Now we assign to such a band a specific size parameter x_0. If we assume the spacing of the bands in wavelength to correspond to that of a Mie-sphere of the same size, we can estimate the initial radius, and follow the temporal evolution of the radius by measuring the wavelength, $\lambda(t)$, of the chosen band at each time which yields then $r(t) = x_0/2\pi\lambda(t)$ [1].

It is difficult to assess the validity of these assumptions from light scattering theory, because we do not know the exact morphology of our effloresced non-spherical particles and an exact treatment would be computationally expensive for a very complex morphology. However, there is indication that effloresced particles are best described as perturbed spheres [2]. To test whether the basic features of Fig. 2 can be reproduced by a simple model of a perturbed sphere, we used the T matrix code of Mackowski and Mishchenko [3] to calculate the random-orientation backscattering intensity of a cluster of spheres shown in Fig. 3, panel (a). Here, we assume that a large sphere at the core does not change its size during evaporation but just a "layer" of small spheres covering the surface of the large sphere. The total radius of the cluster is 2.14 μm for the first simulation decreasing to 1.32 μm with a step size of 0.02 μm. The result of the simulation is very encouraging by showing the same kind of pattern in panel (c) as was observed in the experiments. If we apply the same analysis as for the experimental data to deduce the temporal evolution of the radius, we obtain a radius rate of 0.0274 μm/step, which is 37% higher than the input step size, but still very close. Also, we note that it would be computationally very expensive to perform simulations for the size parameter range of our experimental particles with a more realistic morphology, i.e. more smaller spheres attached to the surface of the inner core sphere. But despite these limitations, we feel that the simulations are reproducing the observations remarkably well, justifying our procedure to evaluate the radius rate.

In order to determine the vapor pressure from the radius change, the following considerations must be taken into account. A solid (or aqueous) evaporating AN particle dissociates in ammonia and nitric acid in the gas phase through the reaction: $NH_4NO_3(s) \rightleftharpoons NH_3(g) + HNO_3(g)$,

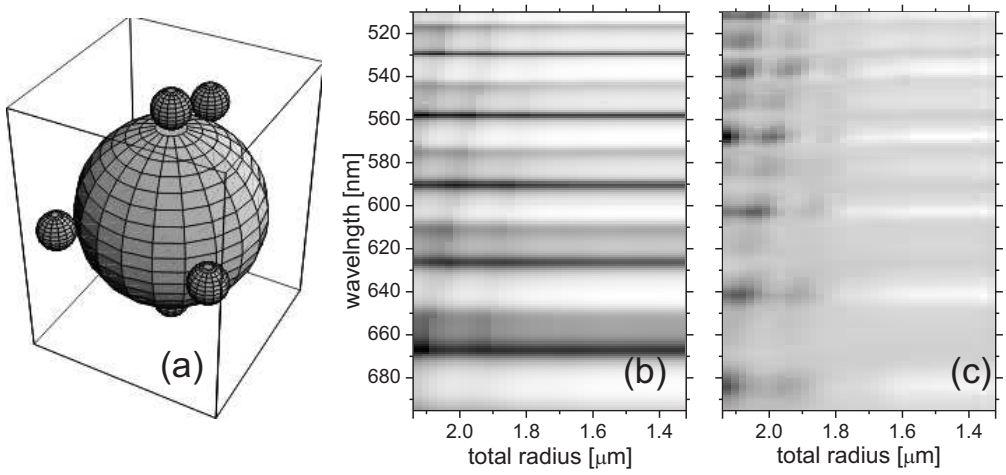

Figure 3: Panel (a) shows the geometry of our simplified model for a perturbed sphere. It consists of a sphere of 1.2 μm radius in the center with 6 attached spheres of smaller radius, decreasing from 0.47 μm to 0.06 μm in radius during the simulation. Panel (b) shows a series of the corresponding simulated spectra with the backscatter intensity gray scale coded. Panel (c) shows the spectra normalized with the mean spectrum of all the simulations, comparable to panel (c) of Fig. 2.

which yields the total pressure in the gas phase as:

$$p_{tot} = p_{NH_3} + p_{HNO_3} = -\frac{1}{2}\frac{dr^2}{dt} RT \frac{\rho_{AN}}{M_{AN}} \left(\frac{1}{D_{NH_3}} + \frac{1}{D_{HNO_3}} \right), \quad (1)$$

where R is the ideal gas constant, T the ambient temperature, ρ_{AN} and M_{AN} the density and molar mass of AN, and D the diffusivities of the two species in the ambient air [1]. We repeated the same experiment as shown in Fig. 2 for different temperatures and a clear temperature dependence of the rate of shift of the intensity bands was evident. The resulting vapor pressures are shown in Fig. 4 together with data from literature. The literature data are extrapolated to lower temperatures in order to compare to our data; the agreement is excellent, but shows also that the enthalpy of evaporation is slightly temperature dependent. **Acknowledgments**:

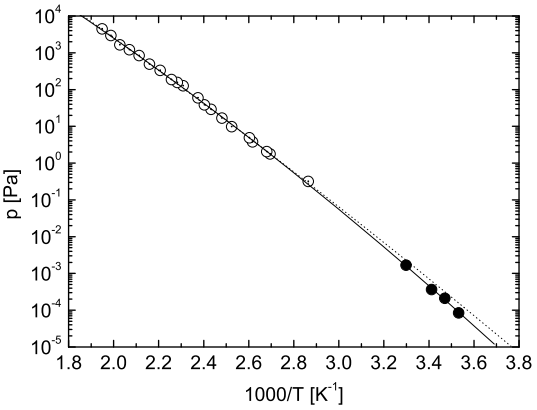

Figure 4: Vapor pressure of a solid AN particle versus inverse temperature. Solid circles: this study; open circles: Brandner et al.[4]; dotted line: extrapolation of the Brandner data to low temperatures; solid line: polynomial 2 nd order fit to all data points.

We acknowledge helpful discussions with Gorden Videen and Thomas Peter and the financial support by the National Science Foundation Switzerland (grant n 200021-100280).

References

[1] A. A. Zardini and U. K. Krieger, "White light Mie resonance spectroscopy used to measure very low vapor pressure of substances in aqueous solution aerosol particles," Opt. Express, **14**, 15, 6951–6962 (2006).

[2] K. B. Aptowicz, R. G. Pinnick, S. C. Hill, Y. L. Pan, and R. K. Chang, "Optical scattering patterns from single urban aerosol particles at Adelphi, Maryland, USA: A classification relating to particle morphologies," J. Geophys. Res., **111**, D12212 (2006).

[3] D. W. Mackowski and M. I. Mishchenko, "Calculation of the T matrix and the scattering matrix for ensembles of spheres," J. Opt. Soc. Am. A, **13**, 2266-2278 (1996).

[4] J. D. Brandner, N. M. Junk, J. W. Lawrence, and J. Robins, "Vapor Pressure of Ammonium Nitrate," J. Chem. Eng. Data, **7**, 2 (1962).

Differences in polarimetric properties of cometary jets and circumnucleus halos

Evgenij Zubko[1,2], Hiroshi Kimura[1], Tetsuo Yamamoto[1], Hiroshi Kobayashi[1]

[1] *Institute of Low Temperature Science, Hokkaido University, Kita-ku North 19 West 8, Sapporo 060-0819, Japan*

[2] *Institute of Astronomy, Kharkov National University, 35 Sumskaya St., Kharkov, 61022, Ukraine*

Abstract

Polarimetry of comets reveals significantly higher polarization in jets than in circumnucleus halos. We hypothesize that this difference arises from distinction in the velocity of dust: particles in jets move out of a nucleus much faster than those in a halo and thus we may observe jet particles in the early stage of their evolution when they are large agglomerates of small grains fastened by a certain amount of ice; velocity of particles in a circumnucleus halo is low enough to be observed in the latter stage of evolution when ice already sublimated totally and agglomerates have been disrupted into constituent grains. Using the discrete dipole approximation we study the influence of disruption of agglomerated dust particles due to ice sublimation on their angular dependence of degree of linear polarization. We found that in a wide range of phase angles the linear polarization of agglomerates of three grains comparable to wavelength covered by ice is visibly higher than polarization of independently scattering constituent grains. This supports our interpretation of the polarimetric observations of comets.

1 Introduction

An approach of a comet to the Sun initiates its coma (a gas-dust atmosphere) whose structure is always inhomogeneous and changes with time. Frequently observed features of the coma are jets, which are high-speed fluxes of gas and dust particles ejected from the surface of the cometary nucleus. The projected velocity of jet particles on an image plane derived from observations of comets is as high as 300–500 m/s [1]. The relatively high speed of jet particles is a result of acceleration of those particles by gas drag. Polarimetry of comets shows that jets are more positively polarized compared with the circumnucleus halo – a bright cloud around a nucleus with a lower polarization [2, 3]. In the range of small phase angles ($\alpha \leq 20°$) in particular, the degree of linear polarization of jets remains substantially positive (i.e., higher), while the circumnucleus halo reveals significant negative polarization i.e., lower, up to –6% near opposition [2, 3]. The authors of [2, 3] associate the higher degree of linear polarization in jets with presence of small grains and/or fluffy aggregates; the lower linear polarization of the circumnucleus region is attributed to more compact dust particles. This seems to be a reasonable explanation because small particles as well as porous aggregates consisting of them reveal essentially higher polarization than compact micron particles which reveal prominent negative polarization branches (NPB) near backscattering [see, e.g., 4].

In this paper, we propose an alternative explanation for the difference in polarimetry of jets and a circumnucleus halo. As it was previously shown with Geometrical Optics Approximation [5, 6], high-absorbing compact irregular particles of size larger than wavelength produce only positive polarization in the entire range of phase angles. Irregular particles comparable to wavelength, however, produce a few stable areas of negative polarization [4, 8]; one of them is in the range of small phase angles. Thus, the polarimetrical difference between a halo and jets may be attributed to a change in size and composition under dust evolution. We investigate the plausibility of this explanation using the discrete dipole approximation (DDA).

2 Model of cometary dust particles

Due to high velocities in jets, we expect to observe fresh large particles preserving ice. On the contrary, particles in the rest of circumnucleus region move significantly slower than those in jets because they are not accelerated by flux of gas. Thus, we observe them in the later stage of evolution when initial large particles are already disrupted into small grains due to total losing of ice. Our interpretation is consistent with polarimetry of comet C/1995 O1 (Hale-Bopp) at a heliocentric distance of 2.9 AU and a phase angle of α=19.6°. Namely, the lengths of four bright jets ranging from 2700 to 5400 km correspond to the distances that dust particles at an average velocity of 400 m/s could cover within 2–4 hours, equivalent to the evaporation timescale for homogenous icy spheres with radius 1 μm.

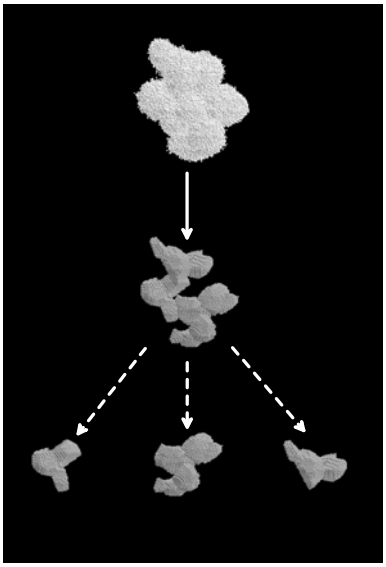

Figure 1: Example image of model particles.

In the present paper, we study the applicability of dust disruption due to ice sublimation to interpretation of the difference in polarimetry between cometary jets and a circumnucleus halo. We assume that particles freshly ejected from a cometary surface are agglomerates of a number of irregular micron grains, filled with ice. Due to this infill the freshly ejected particles could be considered as compact particles significantly larger than visible wavelengths with optically soft inclusions. For instance, refractive indices of an ice infill m=1.313+0i and silicate grains m=1.66+0.0028i at visible wavelength give us the relative refractive index of silicate inclusions in large icy particle as m=1.264+0.0021i. We guess that the features found for compact irregular particles significantly larger than wavelength are also valid, at least in some part, for large particles with optically soft inclusions. We examine here the case when initial particles consist of three irregularly shaped grains. These agglomerated particles are covered with a certain amount of ice. Note that the model fresh particles are only a few times bigger than the constituent grains and, thus, they are still comparable to wavelength.

We compute the scattering of light by particles comparable to wavelength with the DDA method [4, 7, 8]. This is a numerical approach intended for simulation of light scattering by particles comparable to wavelength. The DDA has no restrictions on the shape and internal structure of a particle and thus it is well suitable for the current purpose.

The constituent grains have been generated with help of one of the algorithms described in [4]. For a fixed set of three constituent grains, we build 24 various sample agglomerates. We study separately two kinds of constituent grains: grains of pure silicate (refractive index m=1.66+0.0028i) and grains of a silicate core and an organic mantle (m=1.5+0.1i) with the volume ratio of silicate to organic material being unity. Images of pure silicate grains and one example of the constructed agglomerate are shown in Figure 1. The bottom row shows initial grains separately, whereas the agglomerate constructed from these initial grains is shown in the middle of the figure. Images of core-mantle grains and agglomerates constructed from them are not much different from those shown on Figure 1; the agglomerates are only a little bit bigger and grains have more smoothed shape. Finally, we cover sample agglomerates by icy shell (m=1.313+0i) like it is shown in the top of Figure 1. In the case of pure silicate agglomerates the volume ratio of grains to icy shell is set 1:2 and in the case of agglomerates of core-mantle grains – 1:1. Thus both kinds of particles are covered with equal amount of ice.

3 Results of calculations

We first compute light scattering by agglomerates covered with ice shell and then we consider independent scattering by constituent grains. Comparison of two these cases allows us to estimate clearly

the influence of disruption of sample particles due to ice sublimation on their scattering of light. We have examined different sizes of grains but here we present only results for 1.9 μm grains (this is the size of circumscribing sphere of the largest of three grains at a wavelength of λ=0.5 μm). All cases have been averaged over orientations so that the standard deviation of degree of linear polarization does not exceed 1.5%.

Figure 2 presents the phase dependences of the degree of linear polarization *P* for agglomerates of pure silicate grains (left panel) and for agglomerates of silicate-core organic-mantle grains (right panel). As we expected, all considered cases reveal prominent negative polarization at small phase angles. Qualitatively the same result has been previously received for other kinds of compact particles comparable to wavelength [4, 8]. At the same time, we can see that in comparison with single grains,

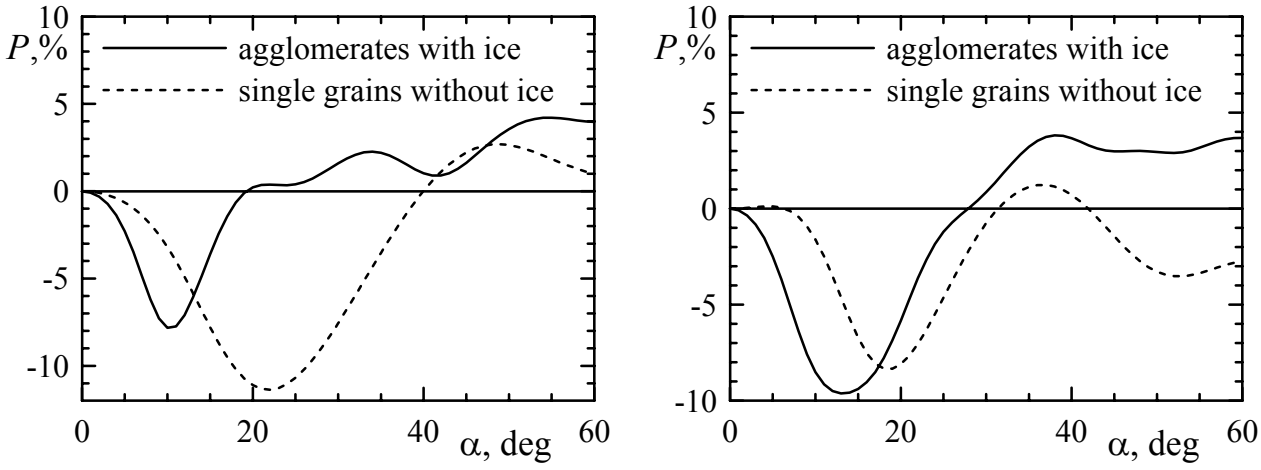

Figure 2: Phase curves of degree of linear polarization of agglomerates covered by ice and single constituent grains. Left panel: pure silicate grains. Right panel: grains with a silicate-core plus organic-mantle structure.

NPB of agglomerates covered by ice shell is shrunk to zero phase angle. The NPB of agglomerates of pure silicate grains is almost two times shallower than NPB of independently scattering grains. Thus, in a wide range of phase angles agglomerates covered by ice shell produce visibly a higher degree of linear polarization than single grains. For pure silicate grains this is the case at phase angles α=15–60° (except for a narrow region near α=45°) and for core-mantle grains α=18–60°.

4 Discussion

At phase angles α≥15°, our simulation qualitatively reproduces the observed difference in polarimetry of jets and a circumnucleus halo. In the range of smaller phase angles α<15°, our simulation does not agree with observations, but we have two reasons to suppose that a larger number of constituent grains will make the NPB of agglomerates shallower. First, as it was shown in experimental measurements of light scattering by single irregular particles and media composed of these particles, the multiple scattering between the particles strongly decreases the NPB [9]. The same dependence has been also found with a DDA simulation of light scattering by agglomerated particles [10]. Another factor is the filling of porous agglomerate by ice, which decreases single scattering by constituent grains and thus their NPB. In future we plan to involve a larger number of constituent grains in order to check our guess.

Acknowledgments

The authors thank Yuriy Shkuratov for illuminating discussion. This research was supported by Grants-in-Aid program of Japan Society for the Promotion of Science and the research grant from Institute of Low Temperature Science (Hokkaido University).

References

[1] J. Warell, C. Lagerkvist, J. S. V. Lagerros, "Dust morphology of the inner coma of C/1995 O1 (Hale–Bopp)" Earth, Moon, and Planets, **78**, 197–203 (1997).

[2] E. Hadamcik, A.C. Levasseur-Regourd, "Dust evolution of comet C/1995 O1 (Hale-Bopp) by imaging polarimetric observations", Astronomy & Astrophysics, **403**, 757–768 (2003).

[3] E. Hadamcik, A.C. Levasseur-Regourd, "Imaging polarimetry of cometary dust: different comets and phase angles". J. Quant. Spectrosc. Radiat. Transfer, **79-80**, 661–678 (2003).

[4] E. Zubko, Yu. Shkuratov, N. Kiselev, G. Videen, "DDA simulations of light scattering by small irregular particles with various structure", J. Quant. Spectrosc. Radiat. Transfer, **101**, 416–434 (2006).

[5] K. Muinonen, T. Nousianen, P. Fast, K. Lumme, and J.I. Peltoniemi, "Light scattering by Gaussian random particles: ray optics approximation." J. Quant. Spectrosc. Radiat. Transfer, **55**, 577–601. (1996).

[6] Ye. Grynko and Yu. Shkuratov, "Scattering matrix calculated in geometric optics approximation for semitransparent particles faceted with various shapes", J. Quant. Spectrosc. Radiat. Transfer, **78**, 319–340 (2003).

[7] A. Penttilä, E. Zubko, K. Lumme, K. Muinonen, M. A. Yurkin, B. Draine, J. Rahola, A. G. Hoekstra, Yu. Shkuratov, "Comparison between discrete dipole implementations and exact techniques", J. Quant. Spectrosc. Radiat. Transfer, *in press* (2007).

[8] E. Zubko, K. Muinonen, Yu. Shkuratov, G. Videen and T. Nousiainen, "Scattering of light by roughened Gaussian random particles", J. Quant. Spectrosc. Radiat. Transfer, *in press* (2007).

[9] Yu. Shkuratov, A. Ovcharenko, E. Zubko, H. Volten, O. Munoz, G. Videen, "The negative polarization of light scattered from particulate surfaces and of independently scattering particles", J. Quant. Spectrosc. Radiat. Transfer, **88**, 267–284 (2004).

[10] E. Zubko, Yu. Shkuratov, K. Muinonen, G. Videen, "Collective effects by agglomerated debris particles in the backscatter", J. Quant. Spectrosc. Radiat. Transfer, **100**, 489–495 (2006).